MSC - 05937

4th ANNUAL EARTH RESOURCES PROGRAM REVIEW

LUME IV
TIONAL OCEANIC AND ATMOSPHERIC
MINISTRATION PROGRAMS AND
. NAVAL RESEARCH
BORATORY PROGRAMS

Presented at the
Manned Spacecraft Center
Houston, Texas

January 17 to 21, 1972

Page intentionally left blank

Page intentionally left blank

FOREWORD

A review of various aspects of the Earth Resources Program was held at the Manned Spacecraft Center, Houston, Texas, January 17 to 21, 1972. Particular emphasis was placed on the results of analysis of data obtained with the Manned Spacecraft Center and other aircraft which have contributed data to the program.

The review was divided into the disciplinary areas of Geology, Geography, Hydrology, Agriculture, Forestry, and Oceanography. Program investigators presented the results of their work in each of these areas. The material presented is published in five volumes:

VOLUME I - NATIONAL AERONAUTICS AND SPACE ADMINISTRATION PROGRAMS

VOLUME II - UNIVERSITY PROGRAMS

VOLUME III - U.S. GEOLOGICAL SURVEY PROGRAMS

VOLUME IV - NATIONAL OCEANIC AND ATMOSPHERIC ADMINISTRATION PROGRAMS AND U.S. NAVAL RESEARCH LABORATORY PROGRAMS

VOLUME V - AGRICULTURE AND FORESTRY PROGRAMS

The review provided a current assessment of the program for both management and technical personnel. Note that the material presented represents the current status of ongoing programs and complete technical analyses will be available at a later date.

Where papers were not submitted for publication or were not received in time for printing, abstracts are used.

FRONT COVER

The map on the front cover depicts the NASA Earth Resources aircraft coverage of the United States through June 1971.

Page intentionally left blank

Page intentionally left blank

CONTENTS OF VOLUME I

Section		Page
	FOREWORD	iii
	AMES RESEARCH CENTER	
1	AMES RESEARCH CENTER SR&T PROGRAM AND EARTH OBSERVATIONS by Ilia G. Poppoff	1-1
	WALLOPS STATION	
2	DEVELOPMENT OF CHESAPEAKE BAY TEST SITE FOR REMOTE SENSING APPLICATIONS by James Bettle	2-1
	GODDARD SPACE FLIGHT CENTER	
3	DEVELOPMENT OF EARTH RESOURCES SURVEY TECHNIQUES AT GSFC - OVERVIEW by William Nordberg	3-1
4	RADIOMETRIC IMAGES OF IR RESTSTRAHLEN EMISSION FROM ROCK SURFACES by Warren A. Hovis	4-1
5	NIMBUS HYDROLOGICAL OBSERVATIONS OVER THE WATERSHEDS OF THE NIGER AND INDUS RIVERS by Vincent V. Salomonson and Norman H. MacLeod	5-1
6	SPECTRAL REFLECTANCE MEASUREMENTS OF PLANT-SOIL COMBINATIONS by Norman MacLeod	6-1
7	ANALYSIS OF MULTISPECTRAL IMAGES SIMULATING ERTS OBSERVATIONS by Nicholas M. Short and Norman H. MacLeod	7-1

Section		Page
8	MICROWAVE EMISSION MEASUREMENTS OF SEA SURFACE ROUGHNESS, SOIL MOISTURE, AND SEA ICE STRUCTURE . . .	8-1
	by P. Gloersen, T. Wilheit, and T. Schmugge	
9	RADIOMETRIC OCEAN COLOR SURVEYS THROUGH A SCATTERING ATMOSPHERE	9-1
	by Robert J. Curran and Warren A. Hovis	
10	A MULTISPECTRAL METHOD OF MEASURING SEA SURFACE TEMPERATURES FROM SATELLITES	10-1
	by William E. Shenk and Vincent V. Salomonson	
	MISSISSIPPI TEST FACILITY	
11	A SUMMARY OF ACTIVITIES OF THE EARTH RESOURCES LABORATORY AT THE MISSISSIPPI TEST FACILITY DURING 1971	11-1
	by Robert O. Piland	
12	SUMMARY OF 1971 WATER REMOTE SENSING INVESTIGATIONS	12-1
	by Edward L. Tilton, III	
13	MISSISSIPPI SOUND REMOTE SENSING STUDY	13-1
	by B. H. Atwell and G. C. Thomann	
14	SUMMARY OF 1971 LAND REMOTE SENSING INVESTIGATIONS . . .	14-1
	by Darden W. Mooneyhan	
15	SUMMARY OF 1971 PATTERN RECOGNITION PROGRAM DEVELOPMENT	15-1
	by Sidney L. Whitley	
	LEWIS RESEARCH CENTER	
16	LEWIS RESEARCH CENTER EARTH RESOURCES PROGRAM	16-1

Section Page

MARSHALL SPACE FLIGHT CENTER

17 ENVIRONMENTAL APPLICATIONS ACTIVITY AT MARSHALL SPACE FLIGHT CENTER 17-1

by Charles T. N. Paludan

LANGLEY RESEARCH CENTER

18 EARTH RESOURCES PROGRAMS AT THE LANGLEY RESEARCH CENTER. PART I. ADVANCED APPLICATIONS FLIGHT EXPERIMENTS (AAFE) AND MICROWAVE REMOTE SENSING PROGRAM 18-1

by Robert N. Parker

19 EARTH RESOURCES PROGRAMS AT THE LANGLEY RESEARCH CENTER. PART II. COASTAL ZONE OCEANOGRAPHY PROGRAM 19-1

by Walter E. Bressette

MANNED SPACECRAFT CENTER

20 MSC SUPPORTING RESEARCH AND TECHNOLOGY 20-1

by Dallas Evans

21 HOUSTON AREA TEST SITE 21-1

by Bryan Erb

22 PUBLIC HEALTH APPLICATIONS OF REMOTE SENSING 22-1

by Charles E. Fuller

23 A BREADBOARD HYBRID MULTISPECTEAL PROCESSING SYSTEM 23-1

by Donald Hayden

24 CONSTRUCTING AND MANIPULATING COLOR IMAGERY FROM DIGITAL DATA 24-1

by J. E. Davis, C. A. Helmke, T. R. Kell, M. J. Arldt, and E. L. Wilson

Section Page

25 SALINITY SURVEYS USING AN AIRBORNE MICROWAVE RADIOMETER 25-1

by J. F. Paris, J. D. Droppleman, and D. E. Evans

26 MICROWAVE BRIGHTNESS TEMPERATURE OF A WINDBLOWN SEA 26-1

by Forrest G. Hall

27 DETECTION OF OIL SPILLS USING 13.3-GHz RADAR SCATTEROMETER 27-1

by Kumar Krishen

CONTENTS OF VOLUME II

Section		Page
	FOREWORD	iii
	UNIVERSITY OF MICHIGAN	
28	A SUMMARY OF MICHIGAN PROGRAM FOR EARTH RESOURCES INFORMATION SYSTEMS	28-1
	by Jon D. Erickson	
29	INFORMATION EXTRACTION TECHNIQUES FOR MULTISPECTRAL SCANNER DATA	29-1
	by William A. Malila, Robert B. Crane, Wyman Richardson, and Robert E. Turner	
30	USER ORIENTED MULTISPECTRAL DATA PROCESSING AT THE UNIVERSITY OF MICHIGAN	30-1
	by Frederick J. Thomson	
31	PREDICTION OF DIRECTIONAL REFLECTANCE OF A CORN FIELD UNDER STRESS	31-1
	by Gwynn H. Suits, Gene Safir, and A. Ellingboe	
32	CLASSIFICATION OF SPATIALLY UNRESOLVED OBJECTS	32-1
	by Richard F. Nalepka, Harold M. Horwitz, Peter D. Hyde, and James P. Morgenstern	
33	EXPERIMENTAL METHODS FOR GEOLOGICAL REMOTE SENSING	33-1
	by Robert K. Vincent	
34	MICHIGAN EXPERIMENTAL MULTISPECTRAL SCANNER SYSTEM	34-1
	by Philip G. Hasell, Jr.	
35	MULTISPECTRAL IMAGING RADAR	35-1
	by L. J. Porcello and R. A. Rendleman	

Section Page

UNIVERSITY OF KANSAS

36 SURFACE CONFIGURATION AS AN EXPLANATION FOR LITHOLOGY-RELATED CROSS-POLARIZED RADAR IMAGE ANOMALIES 36-1

by James R. McCauley

37 THE STATUS OF PARAMETRIC STUDIES IN RADAR AGRICULTURE 37-1

by Stanley A. Morain

38 DATA PROCESSING AT THE UNIVERSITY OF KANSAS 38-1

by Robert M. Haralick

39 RADAR SIGNATURE AND SYSTEMS STUDIES AT KANSAS UNIVERSITY 39-1

by Richard K. Moore

UNIVERSITY OF CALIFORNIA

40 AN INTEGRATED STUDY OF EARTH RESOURCES IN THE STATE OF CALIFORNIA USING REMOTE SENSING TECHNIQUES . . . 40-1

by Robert N. Colwell

SOUTH DAKOTA STATE UNIVERSITY

41 REMOTE SENSING OF SOILS, LAND FORMS, AND LAND USE IN THE NORTHERN GREAT PLAINS IN PREPARATION FOR ERTS APPLICATIONS 41-1

by C. J. Frazee, F. C. Westin, J. Gropper, and V. I. Myers

42 PATTERN RECOGNITION SYSTEM AND PROCEDURES 42-1

by Gerald D. Nelson and David V. Serreyn

COLORADO SCHOOL OF MINES

43 BONANZA PROJECT — 1971 43-1

by Keenan Lee

Section Page

TEXAS A & M UNIVERSITY

44 A COACTIVE INTERDISCIPLINARY RESEARCH PROGRAM WITH NASA 44-1

by John W. Rouse, Jr.

45 SPECTRAL REFLECTANCE MEASUREMENTS OF A VIRUS HOST MODEL 45-1

by Robert W. Toler and N. K. Shankar

UNIVERSITY OF WISCONSIN

46 APPLICATION OF REMOTE SENSING TO WATER RESOURCES PROBLEMS 46-1

by James L. Clapp

PURDUE UNIVERSITY

47 DIFFERENTIATING ELEMENTS OF THE SOIL-VEGETATION COMPLEX 47-1

by M. F. Baumgardner and Staff

48 LAND UTILIZATION AND WATER RESOURCE INVENTORIES OVER EXTENDED TEST SITES 48-1

by Roger M. Hoffer and Staff

49 MEASUREMENTS PROGRAM IN REMOTE SENSING AT PURDUE UNIVERSITY 49-1

by LeRoy F. Silva and Staff

50 DATA PROCESSING I: ADVANCEMENTS IN MACHINE ANALYSIS OF MULTISPECTRAL DATA 50-1

by Philip H. Swain and Staff

51 DATA PROCESSING II: ADVANCEMENTS IN LARGE-SCALE DATA PROCESSING SYSTEMS FOR REMOTE SENSING 51-1

by David Landgrebe and Staff

Section Page

JET PROPULSION LABORATORY

52 OVERVIEW OF THE EARTH RESOURCES PROGRAM OF THE JET PROPULSION LABORATORY 52-1

by Donald P. Burcham

53 MICROWAVE PROPERTIES OF GEOLOGICAL MATERIALS: STUDIES OF PENETRATION DEPTH AND MOISTURE EFFECTS 53-1

by John C. Blinn, III and Jack G. Quade

54 POLARIZATION EFFECTS WITH A COMBINED RADAR-RADIOMETER 54-1

by David Martin

CONTENTS OF VOLUME III

Section		Page
	FOREWORD	iii
	GEOLOGY, MINERAL, AND LAND RESOURCES	
55	AN OVERVIEW OF RESEARCH BY USDI GEOLOGY, MINERAL, AND LAND RESOURCES WORKING GROUP	55-1
	by Douglas Carter	
56	SATELLITE RELAY TELEMETRY IN THE SURVEILLANCE OF ACTIVE VOLCANOES AND MAJOR FAULT ZONES	56-1
	by Jerry P. Eaton and Peter L. Ward	
57	ANALYSIS OF THERMAL PATTERNS OF GEOCHEMICALLY STRESSED TREES AT CATHEART MOUNTAIN, MAINE	57-1
	by F. C. Canney, T. D. Hessin, and W. G. Burge	
58	APPLICATIONS OF INFRARED REMOTE SENSING METHODS TO GEOLOGICAL AND ENGINEERING PROBLEMS OF THE ARCTIC	58-1
	by Gordon W. Greene	
59	GEOLOGIC MATERIAL DISCRIMINATION FROM NIMBUS SATELLITE DATA	59-1
	by H. A. Pohn, T. W. Offield, and Kenneth Watson	
60	NEAR-INFRARED IRON ABSORPTION BANDS: APPLICATIONS TO GEOLOGIC MAPPING AND MINERAL EXPLORATION	60-1
	by Lawrence C. Rowan	
61	MAPPING OF TERRAIN BY COMPUTER CLUSTERING TECHNIQUES USING MULTISPECTRAL SCANNER DATA AND USING COLOR AERIAL FILM	61-1
	by Harry W. Smedes, Harold J. Linnerud, Lawrence B. Woolaver, Ming-Yang Su, and Robert R. Jayroe	

Section		Page
62	FUNCTIONS AND ACTIVITIES OF THE ARIZONA REGIONAL ECOLOGICAL TEST SITE	62-1
	by L. K. Lepley	
63	APPLICATIONS OF REMOTE SENSOR DATA BY STATE AND FEDERAL USER AGENCIES IN ARIZONA	63-1
	by Herbert H. Schumann	
64	REMOTE SENSING ON INDIAN AND PUBLIC LANDS	64-1
	by Grover B. Torbert and Arthur M. Woll	
65	THE REMOTE SENSING OF AIR POLLUTION FROM COAL UTILIZATION	65-1
	by Brian M. Harney, Donald H. McCrea, and Albert J. Forney	
66	REMOTE SENSING OF WET LANDS IN IRRIGATED AREAS	66-1
	by Herbert H. Ham	
67	SHORT PULSE RADAR MEASUREMENTS OF LAYERED ICE AND SNOW	67-1
	by R. S. Vickers and G. C. Rose	
68	EARTH RESOURCES CARTOGRAPHY PROGRAM	68-1
	by Alden P. Colvocoresses	
69	AUTOMATIC THEMATIC MAPPING IN THE EROS PROGRAM	69-1
	by Dean T. Edson	
	GEOGRAPHY, HUMAN, AND CULTURAL RESOURCES	
70	THE GEOGRAPHY AND HUMAN - CULTURAL RESOURCES WORKING GROUP OF THE EROS PROGRAM	70-1
	by Arch C. Gerlach	
71	AN AUTOMATED MAP AND MODEL OF LAND USE IN THE PHOENIX QUADRANGLE	71-1
	by John L. Place	

Section		Page
72	CENTRAL ATLANTIC REGIONAL ECOLOGICAL TEST SITE	72-1
	by Robert H. Alexander	
73	THE CENSUS CITIES PROJECT: A STATUS REPORT FOR 1971	73-1
	by James R. Wray	
74	BUREAU AND AGENCY REPORTS	74-1
	by George L. Loelkes	
	HYDROLOGY AND WATER RESOURCES	
75	HYDROLOGIC APPLICATIONS PROGRAM SUMMARY	75-1
	by Morris Deutsch	
76	SIMULATION STUDIES OF ERTS-A&B DATA FOR HYDROLOGIC STUDIES IN THE LAKE ONTARIO BASIN	76-1
	by Joseph MacDowall, Allan Falconer, and Keith P. B. Thomson	
77	COURT PRECEDENT FOR ACCEPTANCE IN EVIDENCE OF REMOTELY-SENSED DATA AND THEIR INTERPRETATION, CROSS-FLORIDA BARGE CANAL	77-1
	by Aaron L. Higer, Milton C. Kolipinski, and Eldon Lucas	
78	WETLANDS DELINEATION BY SPECTRAL SIGNATURE ANALYSIS AND LEGAL IMPLICATIONS	78-1
	by Richard R. Anderson and Virginia Carter	
79	DISCRIMINATION OF FLUORIDE AND PHOSPHATE CONTAMINATION IN CENTRAL FLORIDA FOR ANALYSES OF ENVIRONMENTAL EFFECTS	79-1
	by A. E. Coker, R. Marshall, and F. Thomson	
80	RELAY OF QUANTITATIVE RESOURCES DATA BY ERTS-A	80-1
	by James F. Daniel	

Section | Page

81 APPLICATIONS OF SPECTROSCOPY TO REMOTE DETERMINATION OF WATER QUALITY. 81-1

by Marvin C. Goldberg and Eugene R. Weiner

82 SPECTRAL REFLECTANCE OF SELECTED AQUEOUS SOLUTIONS FOR WATER QUALITY APPLICATIONS 82-1

by M. R. Querry, R. C. Waring, W. E. Holland, W. Nijm, and G. M. Hale

83 QUANTITATIVE RELATIONSHIP BETWEEN REFLECTANCE AND TRANSPIRATION OF PHREATOPHYTES — GILA RIVER TEST SITE 83-1

by R. C. Culler, J. E. Jones, and R. M. Turner

CONTENTS OF VOLUME IV

Section		Page
	FOREWORD	iii
	NATIONAL OCEANIC AND ATMOSPHERIC ADMINISTRATION	
84	MICROWAVE CHARACTERISTICS OF THE OCEAN SURFACE IN THE 1-10 GHz BAND	84-1
	by Alan E. Strong and Ronald A. Porter	
85	OBSERVATIONS OF OCEANIC WHITE CAPS FOR MODERATE TO HIGH WIND SPEEDS	85-1
	by Duncan B. Ross and Vincent Cardone	
86	THE CONSTRAINT OF SUN GLINT ON VISIBLE DATA GATHERED BY EARTH SATELLITES	86-1
	by Alan E. Strong	
87	SPECIAL DISPLAYS OF SATELLITE INFRARED DATA FOR SEA ICE MONITORING	87-1
	by E. Paul McClain	
88	APPLICATION OF SATELLITE INFRARED MEASUREMENTS TO MAPPING SEA ICE	88-1
	by James C. Barnes	
89	MICROWAVE EMISSION CHARACTERISTICS OF SEA ICE	89-1
	by A. T. Edgerton and G. Poe	
90	REGIONAL STUDIES USING SEA SURFACE TEMPERATURE FIELDS DERIVED FROM SATELLITE INFRARED MEASUREMENTS	90-1
	by Alan E. Strong	
91	FISHERIES RESOURCE IDENTIFICATION AND ASSESSMENT STUDIES	91-1
	by William H. Stevenson	

Section		Page
92	COMPARISON OF REMOTE SENSORS FOR SOIL MOISTURE AND OTHER HYDROLOGIC STUDIES	92-1
	by Donald R. Wiesnet	
93	SOIL MOISTURE MAPPING BY GROUND AND AIRBORNE MICROWAVE RADIOMETRY	93-1
	by G. Poe and A. T. Edgerton	
94	DETERMINATION OF THAWING SNOW AND ICE SURFACES USING EARTH SATELLITE DATA	94-1
	by Donald R. Wiesnet and David F. McGinnis	
95	SNOW STUDIES USING THERMAL INFRARED OBSERVATIONS FROM EARTH SATELLITES	95-1
	by James C. Barnes	
	U. S. NAVAL RESEARCH LABORATORY	
96	LABORATORY INVESTIGATIONS RELATED TO MICROWAVES . . .	96-1
	by Omar H. Shemdin	
97	THE EXTRAPOLATION OF LABORATORY AND AIRCRAFT RADAR SEA RETURN DATA TO SPACECRAFT ALTITUDES	97-1
	by Willard J. Pierson and Richard K. Moore	
98	MISSION 119 PASSIVE MICROWAVE RESULTS	98-1
	by J. P. Hollinger and R. A. Mennella	
99	GROUND TRUTH INVESTIGATIONS FOR AIDJEX 71	99-1
	by William Campbell	
100	APPLICATION OF THERMAL RADIATION DATA TO FISHERY OCEANOGRAPHY	100-1
	by Merritt Stevenson and Forrest Miller	

Section		Page
101	THE CASE FOR OCEAN COLOR	101-1
	by Henry J. Yotko	
102	DETECTION OF OCEAN CHLOROPHYLL FROM EARTH ORBIT . . .	102-1
	by Seibert Q. Duntley	
103	A TECHNIQUE FOR THE REDUCTION AND ANALYSIS OF OCEAN SPECTRAL DATA	103-1
	by Peter G. White	
104	AIRBORNE DIFFERENTIAL RADIOMETER MEASUREMENTS OF CHLOROPHYLL IN WATER	104-1
	by John C. Arvesen	
105	REMOTE MEASUREMENT OF CHLOROPHYLL CONCENTRATION AND SECCHI-DEPTH USING THE PRINCIPAL COMPONENTS OF THE OCEAN'S COLOR SPECTRUM	105-1
	by James L. Mueller	
106	SURFACE TRUTH MEASUREMENTS OF OPTICAL PROPERTIES OF THE WATERS IN THE NORTHERN GULF OF CALIFORNIA	106-1
	by Roswell W. Austin	
107	PRACTICAL UTILITY OF THE BLUE SPECTRAL REGION	107-1
	by Donald S. Ross	
108	EVALUATION OF FACTORS AFFECTING RESOLUTION OF SHALLOW-WATER BOTTOM FEATURES	108-1
	by Curtis C. Mason, Dean R. Norris, and I. Dale Browne	
109	MULTISPECTRAL OBSERVATIONS OF MARINE ENVIRONMENTS	109-1
	by Fabian C. Polcyn	
110	COASTAL AND ESTUARINE APPLICATIONS OF MULTISPECTRAL PHOTOGRAPHY	110-1
	by Edward Yost and Sondra Wenderoth	

Section		Page
111	EFFLUENT MIXING IN THE MISSISSIPPI REGION DELTA, LOUISIANA	111-1
	by James Coleman, Lyn Wright, and Ronald Becker	
112	A STUDY OF TEMPORAL ESTUARINE FLOW DYNAMICS	112-1
	by Robert L. Mairs and Dennis K. Clark	
113	THE TONGUE OF THE OCEAN AS A REMOTE SENSING OCEAN COLOR CALIBRATION RANGE	113-1
	by Leo V. Strees	
114	A PROGRAM TO ASSESS A THERMAL DISCHARGE ON TRINITY BAY, TEXAS	114-1
	by James B. Zaitzeff and Victor S. Whitehead	

CONTENTS OF VOLUME V

Section		Page
	FOREWORD	iii
	AGRICULTURE AND FORESTRY	
115	DEVELOPMENT OF ANALYSIS TECHNIQUES FOR REMOTE SENSING OF VEGETATION RESOURCES	115-1
	by William C. Draeger	
116	RESOURCE ANALYSIS AND LAND USE PLANNING WITH SPACE AND HIGH ALTITUDE PHOTOGRAPHY	116-1
	by Barry J. Schrumpf	
117	THE USE OF KODAK AEROCHROME INFRARED COLOR FILM, TYPE 2443 AS A REMOTE SENSING TOOL	117-1
	by G. R. Cooper, R. L. Bowen, and H. W. Gausman	
118	MEASUREMENTS FROM AIRCRAFT TO CHARACTERIZE WATERSHEDS	118-1
	by Bruce J. Blanchard	
119	DISCRIMINANT ANALYSES OF BENDIX SCANNER DATA	119-1
	by A. J. Richardson, C. L. Wiegand, R. W. Leamer, A. H. Gerbermann, and R. J. Torline	
120	DEVELOPMENT AND FIELD TEST OF AN ERTS - MATCHED FOUR - CHANNEL SPECTROMETER	120-1
	by Frederick P. Weber	
121	MICROSCALE PHOTO INTERPRETATION OF FOREST AND NONFOREST LAND CLASSES	121-1
	by Robert C. Aldrich and Wallace J. Greentree	
122	POTENTIALITY FOR OBTAINING PORIA DISEASE SIGNATURES IN THE OREGON CASCADES FROM ORBITAL ALTITUDES	122-1
	by John F. Wear	

Section		Page
123	PATTERN RECOGNITION OF NATIVE PLANT COMMUNITIES — MANITOU COLORADO TEST SITE	123-1
	by Richard S. Driscoll	
	CORN BLIGHT	
124	CORN BLIGHT WATCH EXPERIMENT RESULTS	124-1
	by C. J. Johannsen, M. E. Bauer, and Staff	
125	THE CORN BLIGHT PROBLEM — 1970 AND 1971	125-1
	by Marvin E. Bauer	
126	CORN BLIGHT REVIEW — SAMPLING MODEL AND GROUND DATA MEASUREMENTS PROGRAM	126-1
	by Richard Allen	
127	AIRCRAFT DATA ACQUISITION	127-1
	by Ronald K. Blilie	
128	1971 CORN BLIGHT WATCH EXPERIMENT DATA PROCESSING, ANALYSIS, AND INTERPRETATION	128-1
	by Terry L. Phillips and Staff	
129	EXPERIMENT RESULTS GROUND MEASUREMENTS, PHOTO AND MULTISPECTRAL MACHINE ANALYSIS	129-1
	by Phillip Swain	
130	DETAILED INTERPRETATION AND ANALYSIS OF SELECTED CORN BLIGHT WATCH DATA SETS	130-1
	by R. F. Nalepka, J. P. Morgenstern, and W. L. Brown	
131	1971 CORN BLIGHT WATCH EXPERIMENT	131-1
	by J. W. Clifton	

MICROWAVE CHARACTERISTICS OF THE OCEAN SURFACE IN THE 1-10 GHz BAND

by

Alan E. Strong
National Oceanic and Atmospheric Administration
Washington, D. C. 20031

and

Ronald A. Porter
Radiometric Technology, Inc.
Wakefield, Massachusetts 01880

INTRODUCTION

The objective of this contract study was to investigate, in considerable detail, the microwave characteristics of calm, rough and foam-covered ocean surfaces and to develop a technique for deriving thermodynamic ocean surface temperatures from brightness temperatures measured by an Earth-orbiting radiometer. This investigation encompassed frequencies in the range 1 to 10 GHz (wavelength range of 30 to 3 cm) and was based on the use of a 1-dimensional geometric optics roughness model (1), including shadowing and multiple scattering of radiant electromagnetic energy. Provision is made, in the model, for characterizing surface roughness through the rms slope-versus-wind velocity relations previously established by other researchers (2). Suitable foam and atmospheric models were superimposed on the roughness model.

A wide variety of operating and environmental parameters were brought into the study, including both horizontal and vertical polarizations, an antenna beam zenith angle range of 0 to 60 degrees, wind velocities from 4 to 20 meters/sec., surface temperatures from 276 to 296 Kelvin, salinities of 24 to 37 parts per thousand, and atmospheric conditions ranging from clear sky to heavy rain. Following preliminary studies, concerned with the dielectric properties of model sea water, specular emissivities, and specular brightness temperatures, an initial frequency optimization analysis was performed, involving a total of twelve frequencies in the above range. Based on the response of brightness temperature to changes in surface temperature, and uncertainties introduced by the atmosphere at higher frequencies, the frequency span was compressed to the range 1.4 - 5 GHz. Concurrently,

the salinity range was reduced to 31 - 37 parts/thousand, thus eliminating river estuaries from further consideration.

Rough ocean brightness temperatures were generated and a physical foam model was established. This presented some unusual problems, due to the limited amount of information available on the physical structure of a given patch of foam, and the precentage coverage of ocean surfaces by foam as a function of wind velocity. A decision was ultimately, made to represent foam as a porous homogeneous mixture of air and sea water. Comparisons were made between theoretical and experimental (3) brightness temperatures, for identical environmental conditions, at 1.4 and 8.4 GHz. The results were excellent for vertical polarization and moderate for horizontal polarization.

The above information, on the radiative properties of rough, foam-covered ocean surfaces, has been analyzed to show the influence of various operating and environmental parameters on brightness temperatures and to bring out the inherent uncertainties in derived surface temperatures. This has led to the selection of optimum radiometer operating parameters and a particular surface temperature sensing technique (4).

SPECULAR EMISSIVITIES AND BRIGHTNESS TEMPERATURES OF SEA WATER

It was realized at the outset of this study that the development of a surface temperature sensing technique would require a broad range of information, to permit optimization of radiometer operating frequency, polarization and viewing angle. This was made necessary by the basic study objective -- to analyze the accuracy with which influencing microwave characteristics of ocean surfaces and environmental conditions must be known to permit sensing sea surface temperatures to within $\pm 2^{\circ}C$ of the correct value.

Listed below are the operating and environmental parameters established for the study.

Frequency range:	1 to 10 GHz (wavelength range of 30 to 3 cm.)
Polarizations:	Linear horizontal and vertical.
Antenna beam zenith angles:	0 to 60 degrees.
Surface temperature range:	276 to 296 degrees Kelvin.
Sea water salinities:	24 - 37 parts/thousand. Later reduced to 31 - 37°/oo.

Ocean roughness model:	1-dimensional geometric optics, taking into account shadowing and multiple scattering.
Wind velocities:	4, 8, 14 and 20 meters/sec.
Foam thickness:	1.7 cm.
Foam coverage:	0.1 - 16% corresponding to wind velocities of 4 - 20 meters/sec.
Atmospheric models:	Clear Sky, Cloud, Moderate Rain (4 mm/hr, Heavy Rain (15 mm/hr).
Stability effects:	Influence of temperature changes, at air-sea interface, on rms wave slope and, hence, brightness temperature.

The Fresnel equations listed below, allow calculation of specular emissivities, for model sea water, utilizing values of dielectric permittivity (see Final Report (1)). Thus, the vertical, ϵ_v, and horizontal, ϵ_h, polarized components are obtained from the following expressions:

$$\epsilon_v = \frac{4(ae' + be'')\cos\varphi}{(e'\cos\varphi + a)^2 + (e''\cos\varphi + b)^2} \qquad (1)$$

$$\epsilon_h = \frac{4a\cos\varphi}{(\cos\varphi + a)^2 + b^2} \qquad (2)$$

where,

$$a = r^{\frac{1}{2}}\cos\gamma$$

$$b = r^{\frac{1}{2}}\sin\gamma$$

$$r = \left[(e' - \sin^2\varphi)^2 + (e'')^2\right]^{\frac{1}{2}}$$

$$\gamma = \tfrac{1}{2}\tan^{-1}\left(\frac{e''}{e' - \sin^2\varphi}\right)$$

φ is incidence angle, degrees

e' is the real part of the dielectric permittivity

and e'' is the imaginary part of the dielectric permittivity.

Figure 1 presents horizontally and vertically polarized specular emissivities as a function of frequency with temperature and salinity and incidence angle as parameters. The emissivity values show a strong relationship to increasing angle; however, at a given angle and temperature, there is a relatively small reduction as salinity increases from 24 to 37°/oo. At both vertical incidence and an angle of 30 degrees, the emissivities gradually increase with frequency, with a maximum change of approximately 0.06 from 1.4 to 9.3 GHz. The two components of polarization, at $\psi = 30°$, depart from the vertical incidence values by approximately 0.04. The curves show clearly the effects of changes in salinity; evidently these effects are minor at frequencies above approximately 3 GHz. There is a rather small temperature dependence in the emissivities.

Computation of specular brightness temperatures, for a given homogeneous material, is a relatively straightforward procedure, once the emissivities and influencing atmospheric properties are known. The expression for specular brightness temperature is,

$$T_B = \left[\epsilon T + (1 - \epsilon)\, T_{s,\,down}\right] t_f + T_{s,\,up} \qquad (3)$$

ϵ is the emissivity of the surface.

$(1 - \epsilon)$ is the reflectivity of a specular surface, under conditions of thermal equilibrium.

T is the surface temperature, °K.

$T_{s,\,down}$ is the sky brightness temperature, as viewed from the surface, °K.

t_f is the atmospheric transmission factor for that part of the atmosphere lying between the surface and the radiometer.

and $T_{s,\,up}$ is the sky brightness temperature of that part of the atmosphere between the surface and the radiometer (radiating upward to the radiometer), °K.

In the above expression, all terms except the temperature, T, are functions of antenna beam zenith angle. Uniform atmospheric conditions are implied.

BRIGHTNESS TEMPERATURES OF ROUGH OCEAN SURFACES

A naturally occurring ocean surface is characterized primatily by by the salinity and temperature of the sea water, the surface roughness,

the foam coverage, and the spray layer. The effect of salinity and temperature on the emission of a specular surface has been discussed (see (4) for more detail), and the effect of a spray layer is outside the scope of this report. Thus, surface roughness and foam coverage remain to be considered.

Figure 2 shows the basic steps in the computation of rough ocean brightness temperatures. The atmospheric radiation and transmission factors generated by the program SKYTEMP are put into the programs ROUGH and FOAM TEMP. The program ROUGH calculates the emissivities and scattering coefficients of an oil-free rough ocean surface and combines them with the atmospheric data to generate brightness temperatures. The program FOAM TEMP has, as input from the FOAM program, the reflectivities of foam-air and foam-water boundaries and the attenuation factor of a foam layer (for further details see (4)). FOAM TEMP then calculates brightness temperatures for a specular layer of foam. The brightness temperatures from FOAM TEMP and ROUGH are then put into ROUGH TEMP which weights them according to the percentage of foam coverage. The output from ROUGH TEMP is the brightness temperature for a rough ocean surface, partially covered with foam.

The thermal emission and reflection characteristics of the ocean depend upon the surface geometry. In the previous section the simplest case of a plane surface was considered. In reality, however, the ocean rarely, if ever, displays a smooth, planar surface. To take into account ocean roughness, a geometrical-optics model of scattering in one dimension, developed by Lynch and Wagner (1), was used. This approach takes into account double-scattering and shadowing effects, unlike the physical-optics model developed by Stogryn (5). At large incidence angles shadowing effects must be taken into account, otherwise significant errors will result.

The Lynch-Wagner approach is essentially a ray-trace analysis which follows a ray from emission through all subsequent intersections with the surface. The infinite set of possible emissions are grouped into subsets according to the number of intersections. In the process, the total emission, visible to the observer, can be represented by the sum of an infinite series in which the first term gives the contribution by direct emission; the second term, the contribution of atmospheric radiation reflecting off the surface once, after emission, and so on. Since shadowing of an emitted ray is equivalent to a surface reflection, the shadowing effects are taken into account in each term. It can be shown that each term in the series is positive; and, therefore, by taking the first and second order terms, one can obtain a lower bound to the emissivity. In similar fashion onc can find a lower bound to the reflectivity which, in turn, gives an upper bound to the emissivity. This is accomplished by expressing the total reflection as a sum of an infinite series, in which the first term gives the contribution of incident

radiation reflecting once off the surface; the second term gives the double reflection contribution; and so on. As in the case of emission, only the first two terms are considered.

It is necessary to assign probability densities to the first and second order terms for emission and reflection. If the assumption is is made that the surface is generated by a stationary random process, neglecting correlation between the two surface scattering points, one can express probability densities as known mathematical functions. It turns out that these functions are related to roughness only through the rms slope of the surface. These probability densities, coupled with expressions for the emissivity of a rough ocean surface, as well as values for scattering coefficients are used to determine the reflected atmospheric radiation.

The proper rms slope, denoted by s_o, applicable to the one-dimensional model is given by,

$$s_o^2 = s_u^2 + s_c^2 \tag{4}$$

where,

s_u = rms slope in the upwind direction,

and s_c = rms slope in the crosswind direction.

According to Cox and Munk (2), the rms slope can be related to wind speed by the following expressions:

$$s_o^2 = \begin{cases} 5.12 \times 10^{-3} W + 0.003 \pm 0.004 & \text{Clean Surface} \\ 1.56 \times 10^{-3} W + 0.008 \pm 0.004 & \text{Oil Slick Surface} \end{cases} \tag{5}$$

where, W. is the wind speed measured at 12.5 meters above the surface, in units of meter/sec.

For frequencies above 2 GHz, the oil-free surface rms slope is used. Below 2 GHz, where the wavelength is at least ten times longer than the maximum dimension of capillary waves, thus making these waves non-contributing to the radiation, the oil slick slope is used because it is known that oil suppresses capillary waves.

SURFACE TEMPERATURE UNCERTAINTY DUE TO UNCERTAINTIES IN ENVIRONMENTAL PARAMETERS

In developing a surface temperature sensing technique it is necessary to determine the optimum operating parameters, namely, the

frequency, polarization and zenith angle that will minimize surface temperature uncertainties caused by environmental parameters i.e., the atmosphere, wind speed and salinity. To accomplish this, surface temperatures are calculated for various operating and environmental conditions. By noting the change in surface temperature, for specified changes in environmental parameters, the errors caused by environmental uncertainties can be determined.

For clarity, consider the following situation. An observer measures a brightness temperature, T_{Bo}, with a radiometer at a particular frequency, polarization and zenith angle. He then wishes to determine the surface temperature. If he knows the exact wave slope distribution, atmospheric condition and salinity, he may calculate a unique surface temperature. However, suppose he is only given ranges for the environmental parametes, that is, he only knows the upper and lower bounds on wind speed, atmospheric condition and salinity. He must, then, calculate surface temperature for eight combinations of extreme value corresponding to the three environmental parameters. The temperatures will represent uncertainties due to environmental uncertainties.

In order to perform an analysis on surface temperature uncertainty, it is necessary to generate a brightness temperature represented by T_{Bo}. Thus, it is necessary to assume values for all the operating and environmental parameters as well as a surface temperature. The latter will be called the reference temperature, T_{ref}. Then, using the corresponding generated value for T_{Bo}, and assuming that it is the brightness temperature measured by the radiometer, the procedure for determining the uncertainties described in the preceding paragraph can be performed.

To be specific, let W_o, A_o and S_o be the lower bounds in the ranges of the wind speed, atmospheric condition and salinity; and let W_1, A_1 and S_1 be the upper bounds. In addition, consider three different values of T_{ref}: 276, 284 and 296°K. Using these reference temperatures, three brightness temperatures are generated as follows:

$$\left.\begin{aligned} T_{Bo}^{1} &= F(f, p, \varphi_o, W_o, A_o, S_o, 276) \\ T_{Bo}^{2} &= F(f, p, \varphi_o, W_o, A_o, S_o, 284) \\ T_{Bo}^{3} &= F(f, p, \varphi_o, W_o, A_o, S_o, 296) \end{aligned}\right\} \qquad (6)$$

where: f is frequency and p is polarization.

Note that it was arbitrarily decided to use the lower bounds of the parameters to generate the assumed brightness temperatures; the upper bounds could have been used as well. Let the values of brightness temperatures, to be used for the linear interpolation, be represented by,

$$\left.\begin{aligned} T_{B1}^{ijk} &= F(f,\ p,\ \varphi_o,\ W_i,\ A_j,\ S_k,\ 276) \\ T_{B2}^{ijk} &= F(f,\ p,\ \varphi_o,\ W_i,\ A_j,\ S_k,\ 284) \\ T_{B3}^{ijk} &= F(f,\ p,\ \varphi_o,\ W_i,\ A_j,\ S_k,\ 291) \\ T_{B4}^{ijk} &= F(f,\ p,\ \varphi_o,\ W_i,\ A_j,\ S_k,\ 296 \end{aligned}\right\} \quad (7)$$

where, i = 0, 1; j = 0, 1; and k = 0, 1. Thus equation (7) actually represents eight different sets of equations; each set can be substituted into the following equation, to find the corresponding surface temperature:

$$ {}^{m}T_o^{ijk} = \begin{cases} 8(T_{Bo}^{m} - T_{B1}^{ijk}) \,/\, (T_{B2}^{ijk} - T_{B1}^{ijk}) + 276; & T_{Bo}^{m} < T_{B2}^{ijk} \\ 7(T_{Bo}^{m} - T_{B2}^{ijk}) \,/\, (T_{B3}^{ijk} - T_{B2}^{ijk}) + 284; & T_{B2}^{ijk} \leq T_{Bo}^{m} < T_{B3}^{ijk} \\ 5(T_{Bo}^{m} - T_{B3}^{ijk}) \,/\, (T_{B4}^{ijk} - T_{B3}^{ijk}) + 291; & T_{B3}^{ijk} \leq T_{Bo}^{m} \end{cases} \quad (8)$$

where, m = 1, 2, or 3 and refers to the reference temperature.

The above equation is simply an extension of equation (5). For each reference temperature, there are eight derivable surface temperatures, corresponding to the eight different commbinations of the upper and lower bounds for wind speed, atmospheric condition and salinity. let ${}^{m}T_o^{max}$ be the highest temperature in the set of eight and ${}^{m}T_o^{min}$ the lowest. Then, these two values will set an upper and lower bound on surface temperature, for a given reference temperature and set of (W_o, W_1, A_o, A_1, S_o, S_1) for specified operational parameters f, p, and φ_o.

Figure 3 shows graphically the procedure for finding ${}^{2}T_o^{max}$ and ${}^{2}T_o^{min}$, for a reference temperature of 284°K. The ranges considered are salinity variations from 31 to 37°/oo, wind variations of 0 to 8 meters/sec., and atmospheric conditions of clear sky to cloud layer. Eight curves are obtained for the various combinations; the curves for the lower bounds of all three environmental parameters are used to generate T_{Bo} from T_{ref}. The vertical dashed line represents T_{Bo}, and every intersection it makes with the family of curves corresponds to a possible surface temperature. ${}^{2}T_o^{max}$ and ${}^{2}T_o^{min}$ are the maximum and minimum possible surface temperatures.

SURFACE TEMPERATURE UNCERTAINTY RESULTING FROM COMBINED ENVIRONMENTAL UNCERTAINTIES

Several environmental parameter uncertainties will now be considered. In this analysis, three reference temperatures will be used: 276°K, 284°K and 296°K. By using three reference temperatures, it is possible to determine the effect of the actual surface temperature on temperature uncertainties.

The information for this section was generated by program OP DEL. the program employs equations (6) through (8) to find a set of surface temperatures for each reference temperature, and for specified environmental conditions. T_o^{max} and T_o^{min} are, then, found for each set and printed out. The surface temperature uncertainty is defined as the difference between T_o^{max} and T_o^{min}. The specified environmental conditions are given by all possible combinations of the following specifications on salinity, atmosphere and wind speed:

S = 31, 33, 37, 31 - 33 and 33 - 37°/oo

A = Clear, Mod. Rain, Heavy Rain, Clear - Mod. Rain, Mod. - Hvy. Rain

W = 0, 4, 8, 14, 20, 0 - 4, 4 - 8, 8 - 14, 14 - 20 meters/sec.

No information is printed out for combinations which do not include at least one uncertainty since, if there are no environmental uncertainties. The operational parameters employed are as follows:

f = 2.5 and 3 GHz

φ_o = 50 and 60 degrees

p = vertical.

The above were chosen as optimum operating parameters in the light of the previous analyses.

Some of the results are shown in Figure 4, for a fixed salinity of 33°/oo. Data at the two frequencies are plotted for two wind ranges, two atmospheric ranges and for φ_o=50. For the fixed salinity 2.5 GHz is the preferred frequency showing a lower surface temperature uncertainty for all reference temperatures.

When a range of salinities is considered it is not as easy to select an optimum frequency. It appears that, for low reference

temperatures, 2.5 GHz is optimum, whereas for high reference temperatures 3 GHz is preferable. Simply stated, 2.5 GHz appears to be the optimum frequency when there is no salinity uncertainty; however, as the salinity uncertainty increases, a higher frequency is required to minimize the surface termperature uncertainty. The plots also indicate that a greater uncertainty is caused by a 4 - 8 meter/sec., range than a 14 - 20 meter/sec., range in wind velocity, and by a change from moderate to heavy rain. Lastly, the positive slope of most of the plots indicate that surface temperature uncertainty is greater for a warm ocean than a cold one.

OPTIMUM OPERATING PARAMETERS AND SURFACE TEMPERATURE UNCERTAINTY

The study indicates that, to minimize the effects of uncertainties in the environmental parameters, vertical polarization should be used, with a nominal zenith angle of 60 degrees. The choice of frequency depends somewhat on the specified environmental conditions. If there is little uncertainty in slainity, say, one or two parts per thousand, then the operating frequency should be 2.5 GHz. However, if the salinity range is greater, the optimum frequency shifts upward toward 3 GHz. In fact, if the ranges in atmosphere and wind speed were small and the salinity range was relatively large an operating frequency of 4 to 5 GHz would be justified. In addition, the salinity effect is enhanced as sea water temperature increases. Thus, if a sizable salinity range is anticipated, the optimum frequency for a warm ocean should be slightly higher than for a cold ocean, to counteract the increased salinity effect. Considering all factors, however, operation at 2.5 GHz appears to be optimum for surface temperature sensing.

Now that the optimum operating parameters have been set, the magnitude of the surface temperature uncertainty may be determined for a specified environmental situation, by referring to the 2.5 GHz, $\varphi_o = 60^o$ data generated. Considering salinity effects only, the ratio of surface temperature uncertainty to salinity uncertainty varies from 0 to 1°K/°/oo, depending on the wind speed and reference temperature. As the reference temperature increases from 276°K, the uncertainty ratio increases by a factor of three to four. In addition, a change in wind speed, from 0 to 20 meters/sec., causes the uncertainty ratio to decrease by approximately a factor of four. The atmosphere appears to have little effect on the value. In the light of this relationship, the following expression has been derived to express the uncertainty ratio as a function of wind speed and reference temperature; the latter can be considered to be surface temperature:

$$R_S = (0.25)\ (1 - 3W/80)\ \left[1 + 3(T - 276)/20\right] \qquad (9)$$

where, W is in meters/sec., and T is in degrees Kelvin. The above equation is a rough approximation and should not be taken as an exact expression.

Turning to wind speed effects, it has been noted that the ratio of surface temperature uncertainty to wind speed uncertainty varies from 0 to 0.9°K/(m/sec.). The ratio is very sensitive to the wind speed range under consideration. For the 0-4 meter/sec., and 4-8 meter/sec., ranges, the ratio has a value of 0.4 to 0.5°K/(m/sec.). The 8-14 meter/sec., range shows the largest ratios, varying from 0.3 to 0.9°K/(m/sec.), and the 14-20 meter/sec., range has the smallest ratios, varying from 0 to 0.2°K/(m/sec.). It would appear that the moderate wind speeds cause a greater uncertainty. The uncertainty ratio increases with reference temperature, approximately doubling as the temperature increases from 276°K to 296°K. The atmosphere and salinity do not have a sizable effect. The following approximate expression shows the uncertainty ratio as a function of wind speed and temperature:

$$R_W = 0.5(1 - |W - 10|/15)\left[1 + (T - 276)/20\right] \qquad (10)$$

where, W is the mid-range wind speed.

The uncertainty due to atmospheric uncertainties ranges from 1.6 to 2.9°K for clear sky to moderate rain, and from 0.6 to 1.3°K for moderate to heavy rain. The uncertainty increases only slightly with temperature and salinity and is inversely proportional to wind speed. The uncertainty can be expressed as,

$$U_A^1 = 2.9 - 0.07W, \quad \text{clear to moderate rain}$$
$$U_A^2 = 1.3 - 0.035W, \quad \text{moderate to heavy rain} \qquad (11)$$

The temperature uncertainty resulting from a combination of environmental uncertainties may be approximated by the sum of the individual uncertainties. Referring to equation (9) through (11), the total uncertainty is given by,

$$U = R_S \, \Delta S + R_W \, \Delta W + U_A^j \qquad (12)$$

in which,

$$j = \begin{cases} 1; & \Delta A = \text{Clear to moderate rain} \\ 2; & \Delta A = \text{Moderate to heavy rain} \end{cases}$$

and,

ΔS = uncertainty in salinity, °/oo

ΔW = uncertainty in wind speed, meters/sec.

and ΔA = uncertainty in atmospheric model.

Thus, the total surface temperature uncertainty, U, depends on both the magnitude of the environmental uncertainties and the mid-range wind speed and surface temperature. In general, high surface temperatures result in high temperature uncertainties.

The determination of surface temperature to within $\pm$ 2°K implies acceptance of a maximum uncertainty of 4°K. Thus, if the difference between the maximum and minimum derived surface temperatures is less than 4°K, a tolerance of $\pm$ 2°K results with respect to a temperature halfway between these values. It is rather difficult to state the conditions under which this tolerance can be satisfied. For instance, if a wind speed range of 0 to 4 meters/sec. is chosen, with an atmosphere range of moderate to heavy rain and salinity range of 31 to 33°/oo, then referring the derived surface temperature uncertainties it is evident that, for reference temperatures of 276°K or 284°K, the $\pm$ 2°K tolerance can be met; however, at 296°K the uncertainty is 4.7°K.

If a $\pm$ 2°K tolerance is to be satisfied under all conditions it will be necessary to reduce the ranges of the environmental parameters. If the salinity is known within 2°/00 and wind speed within 6 meters/sec., and if a somewhat narrower range of atmospheric uncertainty can be achieved, then a $\pm$ 2°K tolerance can be realized for most situations. However, for high surface temperatures in the vicinity of 296°K, these environmental conditions may not be sufficiently narrow. Thus, it appears that supporting sensing or data correlation techniques must be utilized to minimize derived temperature uncertainties under all environmental conditions.

CONCLUSIONS

Several conclusions of importance may be drawn from the results of this study (1). These are as follows:

1. The effects of sea water salinity on emissivities and brightness temperatures become negligible at frequencies above 4 GHz, for maximum salinity uncertainties of 4 parts per thousand.

2. Atmospheric contributions to specular ocean brightness temperatures are considerable, reaching a value of approximately 6°K for vertical polarization, a zenith angle of 45 degrees and clear sky conditions, at all frequencies from 1.4 to 9 GHZ. The contribution is somewhat greater for heavier weather conditions. Thus, atmospheric

effects must be treated with some care, if undue errors are to be avoided in derived surface temperatures.

3. Ocean brightness temperatures show a maximum response to surface temperatures at a frequency of approximately 5 GHz, vertical polarization and zenith angle of 60 degrees. For these conditions, the ratio of the change in brightness temperature to a given change in surface temperature is about 0.6, in the temperature interval 276 - 196°K.

4. At vertical incidence, emissivities decrease slightly with surface roughness, for horizontal polarization, and increase slightly for vertical polarization. The slight reduction in the first-mentioned polarization is probably due to the fact that capillary waves have not been accounted for in the roughness model. Near a zenith angle of 60 degrees, the vertically polarized emissivities cross over and decrease with roughness at angles beyond the cross-over point. A similar cross-over occurs for horizontally polarized emissivities near a zenith angle of 30 degrees.

5. Comparisons between theoretical and experimental rough surface brightness temperatures, without foam, show considerably better agreement for vertical polarization than for horizontal polarization. In the case of vertical polarization, all theoretical values fell within the experimental uncertainty.

6. A foam layer may be realistically modeled as a random porous structure, consisting of 99% air and 1% sea water. The effects of multiple reflections in the foam layer should be taken into account in any future study. In this work, a simplified once-through radiative model, with a single reflection from the underlying water, provided a reasonable basis for determining the brightness temperatures of foam-covered ocean surfaces.

7. Both horizontal and vertically polarized brightness temperatures of rough, foam-covered ocean surfaces are proportional to wind velocity, at frequencies from 1.4 to 5 GHz. In the case of vertical polarization, wind variations have a progressively smaller effect with increasing zenith angle until, in the vicinity of 60 degrees, brightness temperatures are almost independent of wind velocity. At vertical incidence, there is a gradual increase in brightness temperature sensitivity to wind velocity, at both polarizations, as frequency increases from 1.4 to 5 GHz.

8. In a manner similar to the above, the brightness temperatures of rough, foam-covered ocean surfaces are proportional to atmospheric radiation i.e., atmospheric moisture content. The effect is independent of polarization and zenith angle except at angles beyond 40 degrees, for the horizontal component of polarization, where a given increase in

atmospheric moisture causes a somewhat greater increase in over-all brightness temperatures. This is due to relatively higher surface reflectivities in this angular region. A change in atmospheric condition from Clear Sky to Heavy Rain, increases rough ocean brightness temperatures, at vertical incidence, by approximately 0.5°K at 1.4 GHZ; 2°K at 2.5 GHz; 5°K at 4 GHz; and 8°K at 5 GHz.

9. If the effects of atmospheric stability are neglected, an error of 0.8°K or less results in derived surface temperatures, at 2.5 GHz, for the operating and environmental conditions considered in the study.

10. To minimize uncertainties in derived surface temperatures, due to uncertainties in wind speed and atmospheric condition, the optimum operating parameters are: a frequency of 2.5 GHz, vertical polarization and a nominal zenith angle of 60 degrees (slightly smaller errors are expected at an angle of 59 degrees). The derived temperature uncertainties for horizontal polarization are, in general, of such magnitude as to preclude consideration of this polarization for temperature sensing.

11. Surface temperature uncertainties, due solely to salinity uncertainties, can be minimized by operating at a frequency of 4 GHz or above. Thus, the choice of optimum frequency depends on the relative magnitude of the salinity uncertainty compared with other environmental uncertainties. In most cases, involving combined uncertainties, the optimum frequency remains at 2.5 GHz.

12. To satisfy the ± 2°K tolerance on derived surface temperatures, at 2.5GHz, the salinity should be known to within 2 parts/thousand, the wind speed to within 6 meters/sec. (approximately 12 knots) and atmospheric brightness temperature uncertainty to within 1°K, at $_{o} = 60°$, corresponding to approximately the difference between moderate and heavy rain. It would be helpful if the atmospheric uncertainties were reduced to narrower ranges than represented by the difference between clear sky and moderate rain (1.3°K). Thus, a need exists for a supporting technique capable of furnishing some correction for atmospheric effects. Finally, since surface temperature uncertainties increase with absolute temperature, it si important that environmental uncertainties be reduced to a minimum when observing ocean areas at temperatures of 296°K and above.

REFERENCES

1. Lynch, R. J. and R. J. Wagner, "Rough-Surface Scattering: Shadowing, Multiple Scatter, and Energy Conservation: J. Math. Physics, Sept. 1970.

2. Cox, C., and W. Munk, "Statistics of the Sea Surface Derived From Sun Glitter," J. Marine Research, Vol. 13, 1954, pp. 198-227.

3. Hollinger, J. P., "Passive Microwave Measurements of Sea Surface Roughness," IEEE Transactions on Geosciences Electronics, July 1971. Also, private communication on experimental data.

4. Porter, R. A. and F. J. Wentz, "Microwave Radiometric Study of Ocean Surface Characteristics," Final Report, NOAA Contract 1-35140, National Environmental Satellite Service, 1971.

5. Stogryn, A., "The Apparent Temperature of the Sea at Microwave Frequencies," IEEE Transactions on Antennas and Propagation, Vol. AP-15, No. 2, March 1967.

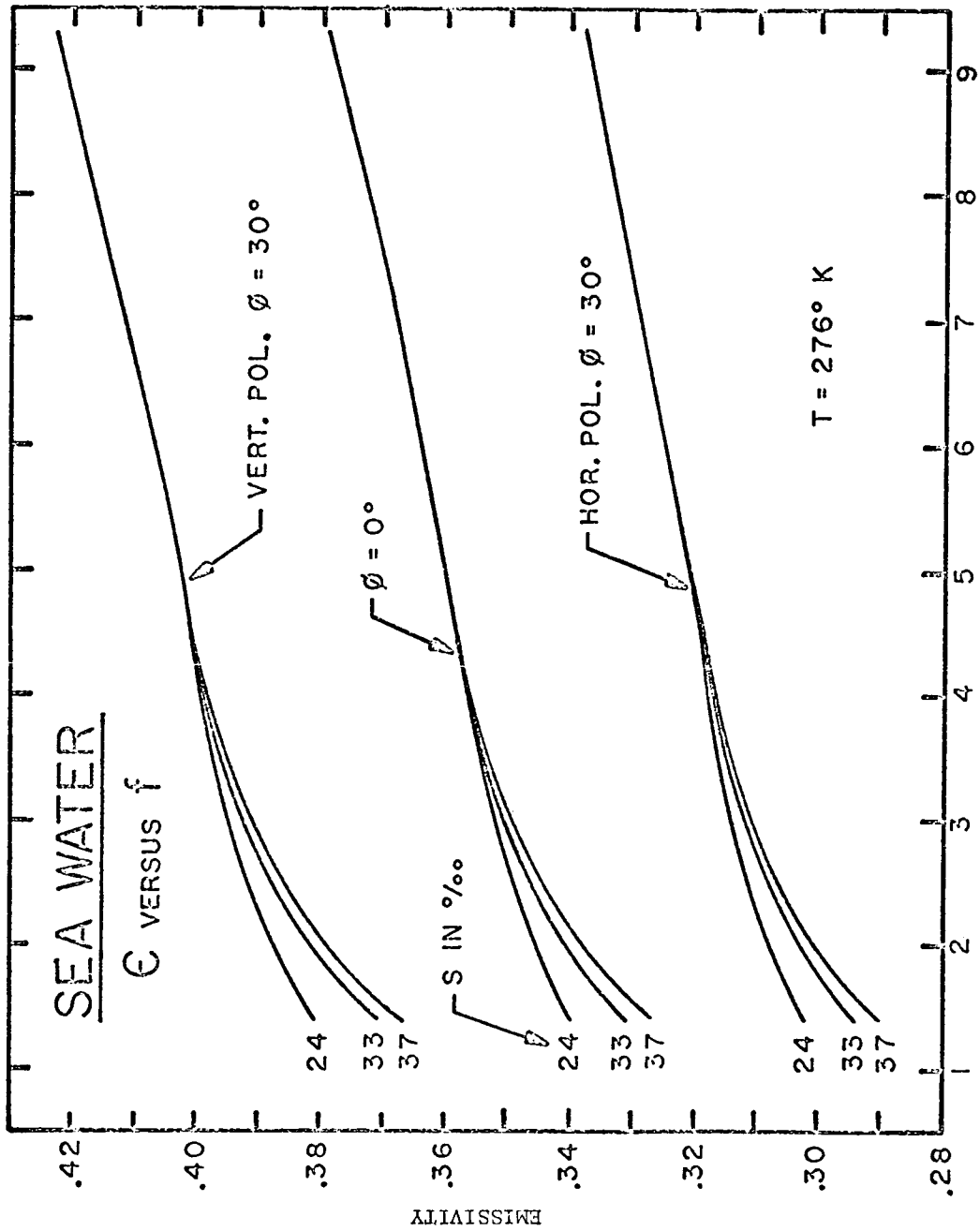

Fig. 1. Specular Emissivity of Model Sea Water versus Frequency for T = 276°K.

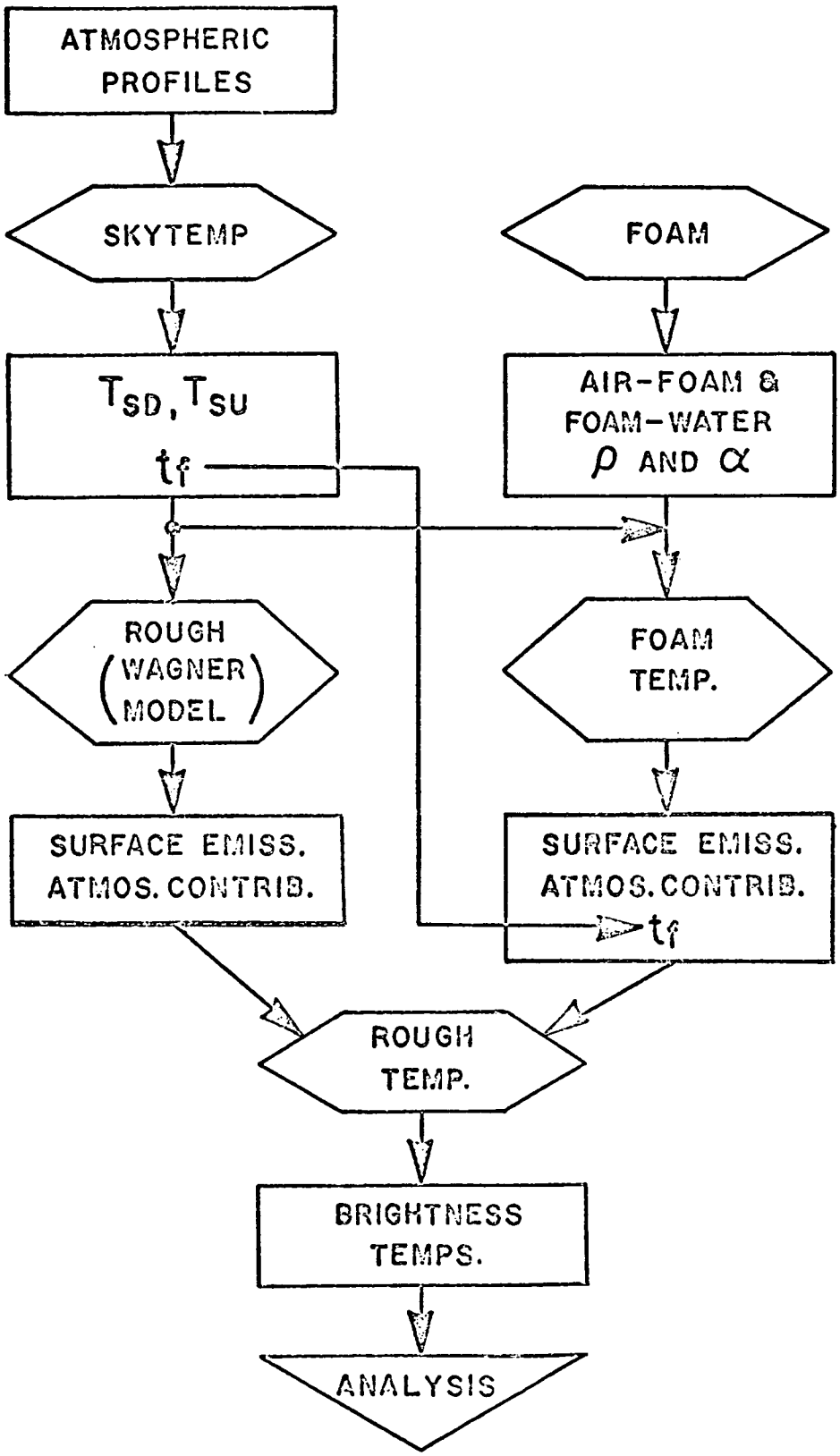

Fig. 2. Flow Chart for Computations of Rough Ocean Brightness Temperatures.

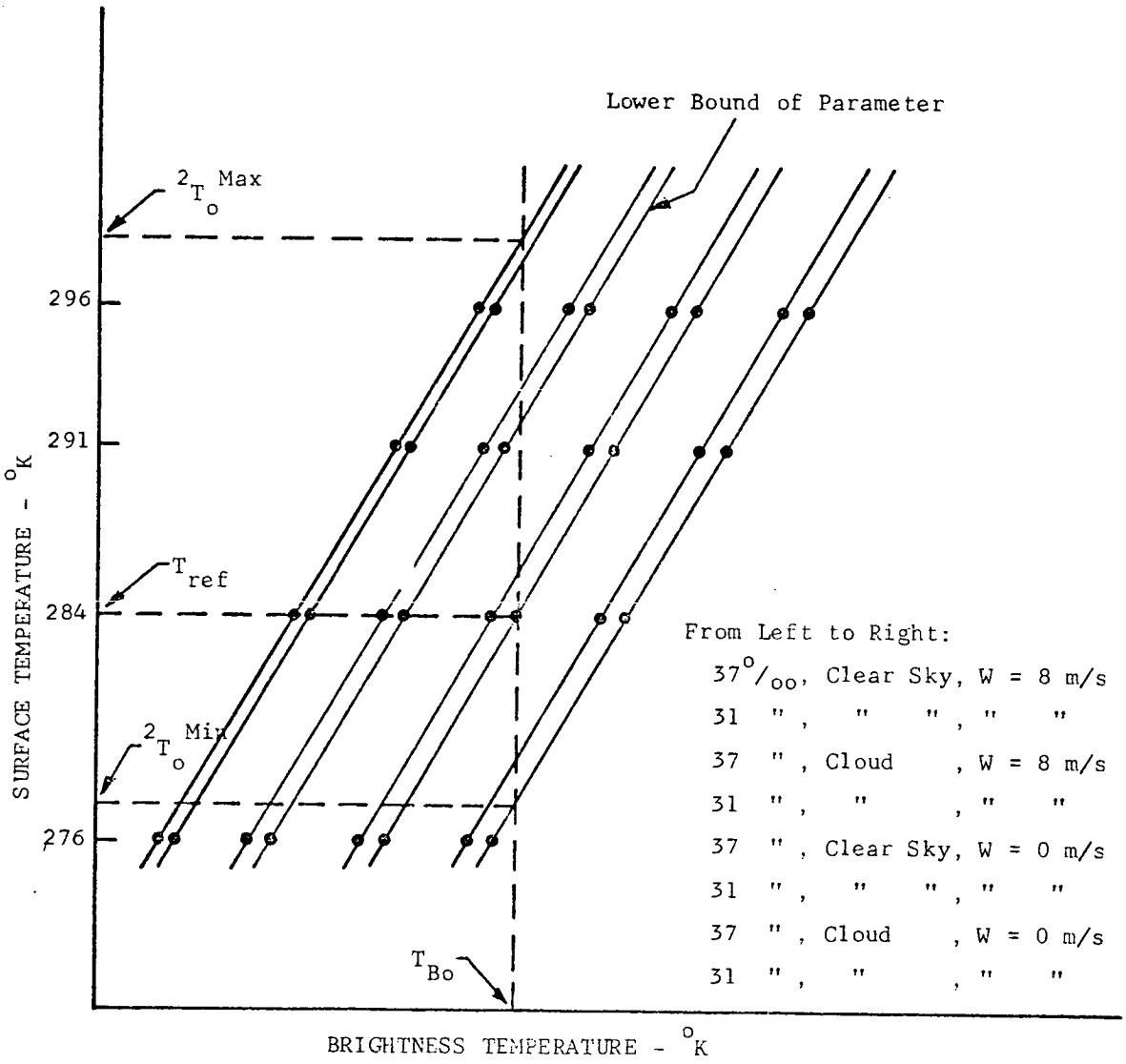

Fig. 3. Derivation of Surface Temperatures from Brightness Temperatures and Determinations of Surface Temperature Uncertainty.

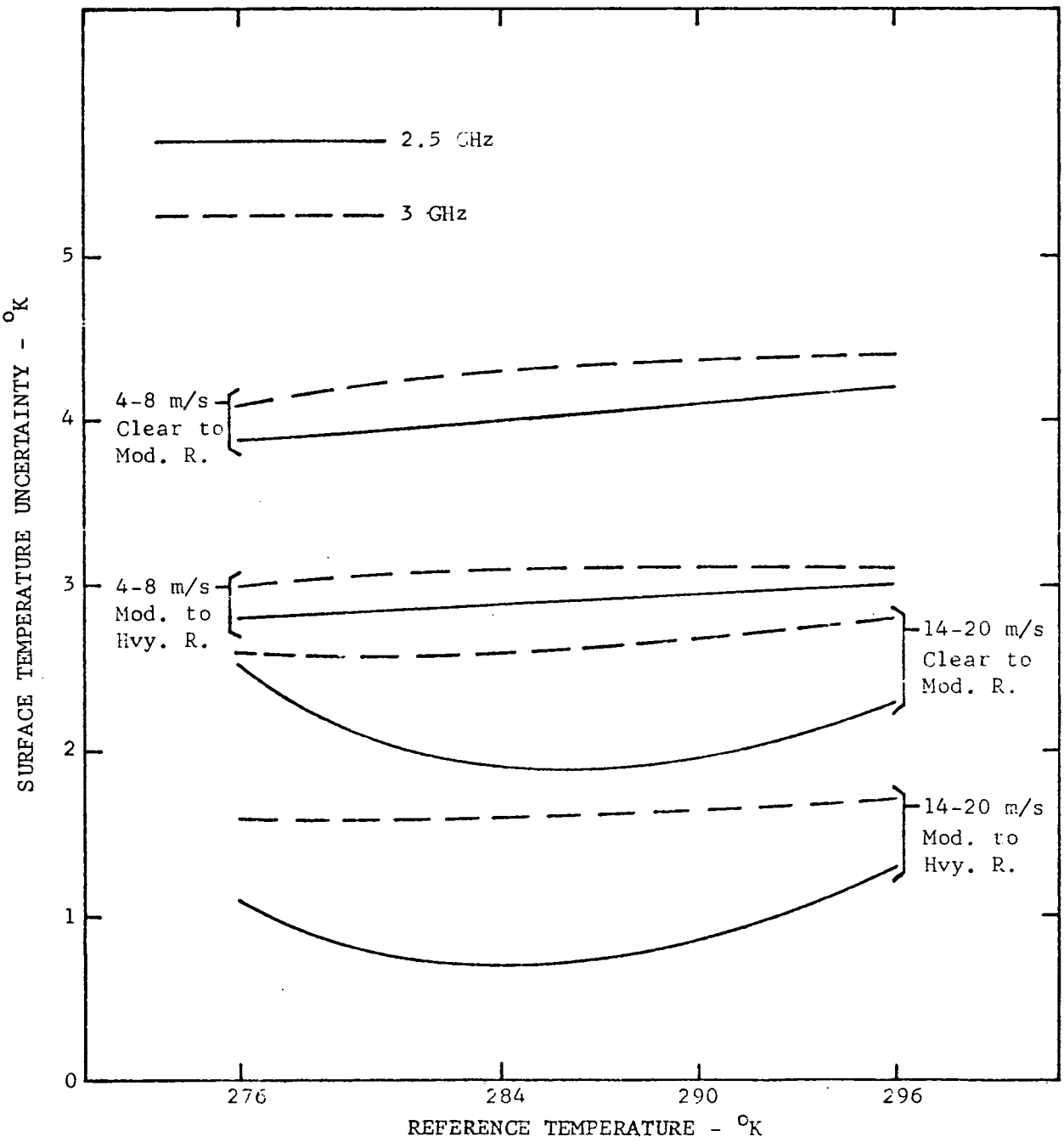

Fig. 4. Surface Temperature Uncertainty versus Reference Temperature for Combined Environmental Uncertainties (ψ_o = 60°, Vert. Pol., S = 33%).

SECTION 85

OBSERVATIONS OF OCEANIC WHITE CAPS FOR MODERATE TO HIGH WIND SPEEDS

by

Duncan B. Ross
National Oceanic and Atmospheric Administration
Atlantic Oceanographic and Meteorological Laboratories
Sea-Air Interaction Laboratory
Miami, Florida

and

Vincent Cardone
Department of Oceanography
and Meteorology
New York University

A series of photographs of sea surface whitecap conditions for wind speeds of 10 to 25 m/sec has been obtained and analyzed for areal coverage of white water. The results are in good agreement with the semiempirical calculations of Cardone based on the wind speed and the development of the wave spectrum only when the contribution of thin foam streaks oriented in the direction of the wind is neglected. Since both the actively forming whitecaps and the thin foam streaks contribute significantly, though perhaps to a differing degree, to the microwave emissivity of the sea surface, it is important that the foam streaks be included in the theory but differentiated from large white caps and foam patches. A simple relationship that accounts for the foam streaks based on the rate of energy transfer, the windspeed, and the wave spectrum is proposed herein. By means of empirically derived constant terms for the microwave signatures of white caps and foam streaks, this theory is adapted to the prediction of the increase in brightness temperature due to foam, with reasonable results to windspeeds of 20 m/sec.

INTRODUCTION

Current models for the prediction of the marine environment, both atmospheric and in the surface layers of the ocean, utilize many concepts developed from experimental results which are often contradictory. Roll (1965) stated that the most critical deficiency in most models is due to a serious lack of suitable, reliable, and repeatable measurements. A second inadequacy in current predictions is the data base input to the model which is often inferior in both quality and quantity. Thus, in order to improve our forecasting capabilities we must improve the models by means of improved experiments and improve both the quality and quantity of the data base input to the model.

The purpose of this paper is to present results of some studies designed to improve the theoretical concepts of white cap production. The motivation for this effort is that measurements of the microwave emissivity of the ocean are eminently suitable for space applications. Depending on the microwave band chosen, oceanographic parameters of temperature, roughness (including foam as well as RMS wave slope) and salinity greatly modulate the observed emissivity or brightness temperature (Paris, 1969, and 1971, and others). Williams (1969) first demonstrated experimentally the influence of foam on the measured microwave emissivity of the sea surface. Droppleman (1970) and Porter and Wentz (1971) have modeled this dependence theoretically and others (Ross, et al., 1970, Nordberg, et al., 1971, and Williams, 1971) have obtained quantitative field measurements of this foam dependence. Cardone (1969) utilized the fresh water whitecap observations of Monahan (1969) to develop a semi-empirical theory relating fresh water white cap density to the local wind speed and the wave spectrum. From the results obtained during the course of this study, Cardone's theory has been extended to include salt water white caps and to account for the effects of thin streaks which begin to appear to a wind speed between 10 and 12.5 m/sec.

DATA ANALYSIS

A series of photographs has been obtained of a variety of sea conditions for wind speeds of 10-25 m/sec and significant wave conditions of 2.5-8 meters. These photographs, all vertically

oriented and obtained from aircraft, have been analyzed for the percentage of the surface covered by actively forming white caps and new foam patches and thin foam streaks oriented in the direction of the wind. The analysis was accomplished by means of a scanning false color densitometer manufactured by Spatial Data, Inc., of Santa Barbara, Calif. This device scans the photograph and divides the grey scales present into 32 different levels. Each level is assigned a false color and the result is displayed on a color television monitor. This display is then subjectively divided into three categories: (1) actively forming white cap and large new foam patches, (2) thin foam streaks elongated in the direction of the wind, and (3) background foam-free water. Selection of the lines of demarcation between each category is aided by replacing each color in turn with the color black until all white caps and foam patches are blacked out. By means of a planimeter circuit, the coverage of these colors is then obtained. The blacking-out procedure is then continued until the foam streaks are completely filled and the areal coverage of the streaks is obtained. The remaining colors and coverage constitute the background sea conditions. Figure 1 shows a typical photograph along with the enhanced version. Because of deficiencies in the photography, it is not possible to precisely determine the lines of demarcation. In addition, spatial variability in foam conditions is significant. As a result, it is necessary to average a large number of photographs in order to obtain a usefully accurate estimate of the white water coverage.

REFERENCE DATA

As attempt has been made in all instances to suppress the variability in the observations due to windspeed variations with height. This is a necessary procedure, as for example, a 15 m/sec wind measured at an elevation of 10 meters would measure approximately 18 m/sec at 19.5 meters elevation and about 22 m/sec at flight altitudes of 150-400 meters depending on stability criteria (air-sea temperature difference). Therefore, all winds reported here have been adjusted to an anemometer height of 20 meters. For data obtained near ocean station vessels, the winds reported by the weather ship on station are used directly since anemometers on these ships are located at 19.5 meters above mean sea level. Where only flight altitude winds are available, a logarithmic profile was assumed

to hold to an altitude of 43.5 meters (see Moskowitz, 1967) and the measured flight level winds were reduced directly to this elevation and then logarithmically to 20 meters. Table I presents the results of this technique for handling winds when measured by means of an inertial navigation system and referenced to surface anemometer winds. It is evident that the technique give reasonable results.

OBSERVATIONS

A tabulation of all foam cover determinations and associated environmental conditions is shown in Table II. According to the measured air-sea temperature differences, all observations are associated with unstable stratification of varying degree. The wind speeds for the data range from 10-25 m/sec so that the low-level Richardson's numbers, a more fundamental measure of stability, indicate only moderately unstable conditions for most observations. Hence, this data set is not as useful for studying the effects of stability on foam cover as other studies of lower wind speeds which cover both positive and negative air sea temperature differences (e.g. Monahan, 1969).

The range of fetches is quite large - the observations in the vicinity of ocean station "I" and southeast of Cape Fear, North Carolina, represent essentially fully developed sea conditions over the wind speed range 10-17 m/sec as observed significant wave heights were close to values given by the Pierson-Moskowitz fully developed sea formulation. The remainder of the high wind observations represent situations in which the fetch was limited by an upwind shoreline and seas were well below the fully developed stage.

The most striking differences between these observations and those at lower wind speeds are the significant contributions of foam streaks to total foam cover for wind speeds above 12 m/sec and the great variability in both streak and whitecap area coverage. The latter characteristic is also indicated in Figure (1), which shows the distribution of whitecap coverage for a typical photograph.

For most cases, histograms of the data depict a weakly bimodal distribution to the whitecap coverage on individual photographs. An examination of each photograph reveals that typically, the large percentage coverage is caused by the presence of a few very large foam patches associated with the relatively infrequent breaking of

waves of relatively long wavelengths. For low flight altitudes particularly, the observations are subject to considerable sampling variability, as these large foam patches contribute significantly to average whitecap coverage. It is likely, therefore, that the 24.7 and 22.7 m/sec North Sea data are biased toward low foam coverage as no large foam patches were evident in the small number of photographs analyzed, yet they were observed visually (by the authors) on these flights. On the other hand, the absence of large foam patches for the 20 m/sec limited fetch observations at short fetch is probably related to the fact that wave breaking is restricted to the relatively high frequency components in the wave spectrum, as the extremely short fetches restrict the development and saturation of larger wave components. The higher aircraft altitudes and larger area viewed per photograph may also have contributed to the smaller variability for the first two sets of photographs taken on this flight.

DEPENDENCE OF FOAM COVER ON WIND SPEED

As with most other wind-wave interaction phenomena, a meaningful dependence of foam cover on wind speed can be determined only from a set of observations representing similar stages of wave development. The five observations noted above between 10 m/s and 17 m/sec, which represent nearly fully developed seas, are thus suitable for this purpose and are shown in Figure (2).

The indicated variation of white cap coverage is in good agreement with an extensive set of observations of salt water white cap coverage at speeds below 10 m/sec as analyzed by Monahan (1971). The solid curve shown in the figure, which also provides a good fit to the high wind speed data for total foam, was also found by Monahan (1971) to provide a good description of the highest oceanic white cap coverage values observed below 10 m/sec. This curve is one of the results of the semiempirical theory for white cap coverage, proposed by Cardone (1969), initially to explain the dependence of fresh water white cap coverage on wind speed, stability, fetch and duration, but later simply extended (Ross and Cardone, 1970), to include salt water effects in the manner proposed by Monahan (1969).

The observations indicate that total foam coverage increases with wind speed at a greater rate than predicted by Cardone's model. However, the discrepancy is largely attributable to the contribution

to foam cover by the streaks, and a simple way to account for the effect of streaks on total foam cover within the context of Cardone's model is presented below.

The observations of percentage white cap coverage shown in Figure (2) for wind speeds above 20 m/sec lie considerably below what would be expected at these wind speeds for both white cap and total foam cover on the basis of the fully developed sea conditions. This behavior seems to be caused by the fetch limitations associated with these data (as well as a low bias due to sampling) as both Monahan's low-speed white cap data and Cardone's model suggest that for a given wind speed, white cap coverage should increase with increasing fetch and reach a maximum for fully developed seas as seen in Figure (3).

The ratio of streak-to-white-cap coverage for this set of data appears to increase linearly with wind speed. In Figure (4) a simple linear relationship above 9 m/sec is shown to fit the data reasonably well, considering the uncertainty in the observed ratio. A portion of this data was obtained on a flight conducted on 27 January 1971 specifically designed to observe the effect of fetch on the growth of the streak and white cap density and the wave spectrum. The meteorological situation along with the flight track flown are shown in Figure (5). The behavior of the streak and white cap density versus fetch for this flight is shown in Figure (6). It can be seen that the growth of the significant wave height and the white cap and streak density are in reasonable agreement with predictions (solid curves) during the early portion of the flight. However, approximately 120 km offshore, there was a drastic decrease in streak density. Figure (7) is a false color enhancement of the ITOS infrared image of 27 January and shows that the edge of the Gulf Stream lay at approximately this location. Whether this phenomenon is somehow related to the Gulf Stream or perhaps to a mesoscale lull in the wind field is unknown, as the aircraft was not equipped with a navigation system capable of resolving small scale changes in windspeed from the flight altitude flown (the aircraft doppler navigation system is inoperative below 300 meters and the Omega system does not have sufficient sensitivity).

The streak-to-white-cap ratio can be interpreted physically in terms of effective increase in the half-life of whitecaps in surface waters due to the presence of streak producing circulations. The ratio can be employed to extend Cardone's semiempirical theory since, as noted by Monahan, foam coverage is proportional to the product

of the whitecap production rate and the half-life of individual whitecaps. Cardone's model calculates, basically, a measure of the whitecap production rate, with the empiricism entering into the model through a description of the effective half-life.

The success of the relationship depends on the assumption that the streak/whitecap ratio is independent of fetch. While this data set is not entirely conclusive in this regard due to the aforementioned anomaly occurring in the vicinity of the Gulf Stream and to unknowns in the wind field, the dominant effect seems to be windspeed. Further efforts, however, must be expended to verify this assumption.

As mentioned earlier, the Cardone model for white cap production is based on the energy dissipated in breaking waves according to the following equation:

$$E = \rho_w \cdot g \cdot \int_0^{\infty} B \cdot S \cdot \delta \cdot df$$

Where E = energy dissipation (ergs/cm^2-sec)
ρ_w = water density
g = gravitational acceleration
B = Miles-Phillips Instability Growth Parameterization
S = Spectral Energy
f = frequency

and $\delta = 1 \quad S \leq S_{oo}$
$\delta = 0 \quad S > S_{oo}$
S_{oo} = Pierson-Moskowitz Fully Developed Spectrum

The empiricism enters in from the data of Monahan and results in the expression for percentage white cap coverage, modified to include salt water effects (Ross and Cardone, 1970), of

$$W_S = .00925 + 1.31 \cdot E$$

Accounting for the streaks by means of the streak/whitecap ratio results in

$$F_T = (1 + R_S)W_S$$

Where F_T = Total Foam Density (% of surface covered by whitecaps plus streaks)
W_S = Salt water whitecap density (%)
R_S = Ratio of streaks to white caps = $-1.99 + .06\ \bar{U}_{20}$
$\bar{U}_{20}$ = Average windspeed measured at an altitude of 20 meters (m/sec)

Ross, et al., (1970) and Nordberg, et al., (1971) from data obtained in March, 1969 have shown that K_W, the rate of increase of the brightness temperature with whitecap density at the Nadir viewing angle, amounts to about 1^oK for a 1% change in whitecap density at 19.5 GHZ. Whether this same figure is correct for the thin foam streaks (which may be largely a single-layered phenomena at the surface) is not known exactly, although it would appear to be somewhat less. Williams (1971), investigating the phenomena in a tank, reports that at 3 cm wavelengths, the emissivity of foam covered water is raised from .4 to .9 with a foam thickness of only 3 mm. This would suggest that the streaks might be equally as important as whitecaps, at least at the higher microwave frequencies. However, it is possible that a streak visible on photography is not altogether a surface phenomena, but also includes light scattered from bubbles suspended just below the surface. If this is the case, streaks would contribute less than whitecaps to changes in the microwave emissivity. In either case, the streak contribution may be represented as some constant, K_S, times the ratio of the streaks to the whitecaps, R_S.

If the whitecap and streak sensitivity are represented in this manner, the change in brightness temperature due to foam may be related to the white cap density according to the expression:

$$\Delta T_B = (K_W + K_S R_S)\, W_S$$

Using the observations of ΔT_B K_W, and W_S obtained during the March, 1969 experiment, and the value of R_S determined above, it is possible to solve for K_S. This was done and a value of $K_S = 0.5$ was obtained.

Application of this equation with predicted values of W_S and the empirically-derived constant terms leads, for example, to a ΔT_B of 5.5^oK and 14.5^oK for fully developed conditions associated with winds of 13 and 16 M/sec respectively, compared to observed differences (Nordberg, et al, 1971) of about 7 and 12^oK. For the 20 M/sec case, the calculation leads to a difference of 18^oK vs 18^oK observed, and for 25 M/sec 70^oK calculated vs 22^oK observed. Neglecting foam streaks entirely, calculated values of 4, 8.5, 8.5, and 26^oK vs observed values of 7, 12, 18, and 22^oK are obtained. The following table presents results of calculations of ΔT_B from the above equations and from the photographic observations, compared to observed differences in microwave brightness temperature.

Windspeed (M/s)	ΔT_B Calc. from Ross-Cardone Model (^oK)	ΔT_B Calc. from Obs. of W.Cps.&St's (^oK)	ΔT_B Observed (^oK)
13	5.5	6.0	7.0
16	14.5	10.0	12.0
20	18.0	15.0	18.0
25	70.0	15.0	22.0

While it is recognized that some of the above results may be influenced by invalid atmospheric assumptions, these are judged to be small as the set of observed brightness temperature differences were carefully selected to be from similar atmospheric conditions. Therefore, it would appear that use of the Ross-Cardone model gives reasonable results for windspeeds to 20 M/sec, but may seriously over-estimate ΔT_B for higher winds under fetch-limited conditions. Thus, the thrust of future experiments must be oriented toward the fetch-limited situations and multi-frequency measurements of the microwave signature of foam streaks, and white caps.

REFERENCES

Cardone, V. J., "Specification of the wind field distribution in the Marine boundary layer for wave forecasting," Geophysics Sci. Lab., New York Univ., New York, Rep. TR 69-1, December, 1969.

Droppelman, J. D., "Apparent microwave emissivity of sea foam," J. Geophys. Res., Vol. 75, Jan. 20, 1970.

Monahan, E. C., "Fresh water whitecaps," J. Atmos. Sci., Vol. 26, No. 9, 1969.

Monahan, E. C., and Zaitlow, E., "Laboratory Comparisons of Fresh-water and Saltwater Whitecaps," J. Geophys. Res., Vol. 74, No. 28, 1969.

Moskowitz, L., "Reduction of ocean wind data by use of drag coefficients with application to various wave forecasting techniques," U. S. Naval Oceanographic Office, IMR 0-66-64, Jan., 1965.

Nordberg, W., Conaway, J., Ross, D.B., and Wilheit, T., "Measurements of Microwave Emission from a foam-covered, wind-driven sea," J. of Atmos. Sciences, Vol. 28, No. 3, April, 1971, pp. 429-435.

Paris, J. F., "Microwave radiometry and its application to marine meteorology and oceanography", Ref. No. 69-II, Dept. of Ocean., Texas A&M Univ., 1969.

Paris, J. F., "Transfer of Thermal microwaves in the atmosphere," Dept. of Met., Texas A&M Univ., May, 1971.

Porter, R. A. and Wentz, F.J. III, Final Report, Radiometric Technology, Inc., Wakefield, Mass., 30 July 1971.

Roll, H. U., "Physics of the Marine Atmosphere", Academic Press Inc., New York, 1965.

Ross, D. B., Conaway, J., and Cardone, V. J., "Laser and microwave observations of sea-surface conditions for fetch-limited 17- to 25- M/S winds," IEEE Trans. on Geoscience Electronics, Vol. GE-8, No. 4, Oct., 1970.

Ross, D. B., and Cardone, V. J., "Laser observations of wave growth and foam density for fetch-limited 25 m/sec winds," Proc. of the Third Annual Earth Resources Program Review, Rep. No. MSC-03742, NASA, MSC, Houston, Texas, Dec., 1970.

Williams, G. F., Jr., "Microwave radiometry of the ocean and the possibility of marine velocity determination from satellite observations." J. Geophys. Res., 74, 1968.

Williams, G. F., Jr., "Microwave radiometry of the ocean, Final Report, Contract N62306-69-C-0301, Rosenstiel School of Marine and Atmospheric Science, Univ. of Mia., Coral Gables, Fla., June, 1971.

TABLE I

LITTON LTN 51 INERTIAL NAVIGATOR WINDS COMPARED TO SURFACE WINDS

Date	Location	Flight Level Wind Speed (m/sec)	Altitude (feet)	Reduced Flt.Level Wind Speed (m/sec)	Measured Surface Wind Speed (m/sec)	Anemometer Height (meters)	Air-Sea Temp. Difference (°C)	Logarithmic Profile Assumption (meters)
3/14/69	N. Sea	25**	500	22.0**	22.7*	20	-3°	45
3/14/69	N. Sea	27.3**	500	25.2**	24.7*	20	-3°	45
3/14/69	N. Sea	27.8**	500	25.8**	25.4*	20	-3°	45
3/14/69	N. Sea	24.2**	500	22.1**	24.0*	20	-3°	45
3/ 6/69	N. Atlantic (I)	17***	1500	15.5	16	20		
3/10/69	N. Atlantic (I)	16***	500	15	16	20	-4°	45
3/11/69	N. Atlantic (I)	20***	750	18	17	20	-3°	45
3/13/69	N. Atlantic (I)	16***	900	13.5	13	20	-2°	45
	N. Atlantic (I)	13.5***	900	13.0	13	20	-2°	45
	N. Atlantic (I)	16.5***	1100	14.8	13	20	-2°	45
	N. Atlantic (I)	15.0***	500	13.5	13	20	-2°	45
3/13/69	N. Atlantic (J)	9***	600	7	6	20	1°	45
2/ 9/70	Hotel	16.5	150	14.8	15.5	20	-1.5°	45
2/11/70	XERBI	5	150	4.5	4	10	0	45
2/16/71	XERBI	7.5	150	7	6-9	Unknown	-2°	45
2/18/71	Hotel	11	150	10	11	20	0	45

* Reduced Geostropic Winds weighted by Surface Beufort and Anemometer Winds
** 20 Minute Average
*** 1 Minute Average

TABLE II - SUMMARY OF OBSERVATIONS

DATE	TIME[1]	PLACE	FLIGHT LEVEL(m)	FETCH (km)	A-S[5] (°C)	WIND[6] SPEED(m/s)	NUMBER of Photos	WHITECAP COVERAGE(%)	WHITECAP STD Deviation	STREAK COVER(%)	STREAK STD.DEV.	TOTAL FOAM Cvr.	RATIO OF STREAKS TO WHITE CAPS
3/10/69	1426-1439	Atlantic[2]	150	740	- 4	15.5	34	6.7	5.1	7.2	2.8	13.9	1.07
3/11/69	1323-1329	Atlantic[2]	230	740	- 3	17.0	33	9.0	6.3	10.7	6.8	19.7	1.20
3/13/69	1057-1116	Atlantic[2]	270	740	- 2	13.4	27	4.2	4.4	3.5	3.2	7.7	.83
3/14/69	1407-1447	North Sea	140	370	- 3	24.7	10	7.1	8.7	25.3	7.5	32.4	3.56
3/14/69	1510	North Sea	140	>500	- 3	22.7	8	6.4	3.3	17.0	3.0	23.4	2.66
3/19/69	0947-1038	North Sea	140	340	- 1	20.6	23	6.2	4.6	18.0	7.0	24.2	2.90
11/14/69	1826-1844	Gulf of Mex.	210	140	-20	13.4	6	4.2	1.1	2.9	2.0	6.2	.69
10/3/70		CaribbeanSea[4]	420	>800	- 1	10.3	13	1.4	.3	0	0	1.4	.00
1/27/71	1452-1454	Atlantic[3]	300	6	- 8	20.0	49	4.2	2.3	12.8	4.9	17.0	3.00
1/27/71	1503-1504	Atlantic[3]	300	75	- 8	20.0	13	5.9	2.9	13.1	6.3	19.8	2.36
1/27/71	1513-1515	Atlantic[3]	110	148	<- 8	20.0	82	4.4	7.0	1.9	3.6	6 3	.43
1/27/71	1522-1524	Atlantic[3]	110	204	<- 8	20.0	63	8.4	10.2	13.4	7.8	21.8	1.60
1/27/71	1535-1538	Atlantic[3]	110	296	<- 8	20.0	66	3.8	4.3	14.3	6 4	18.1	3.76

[1]All times in Greenwich Mean Time
[2]In the vicinity of ocean station "I"
[3]Downwind of Cape Fear, North Carolina
[4]Caribbean Sea
[5]Air-Sea temperature difference
[6]Adjusted to 19.5 meter level

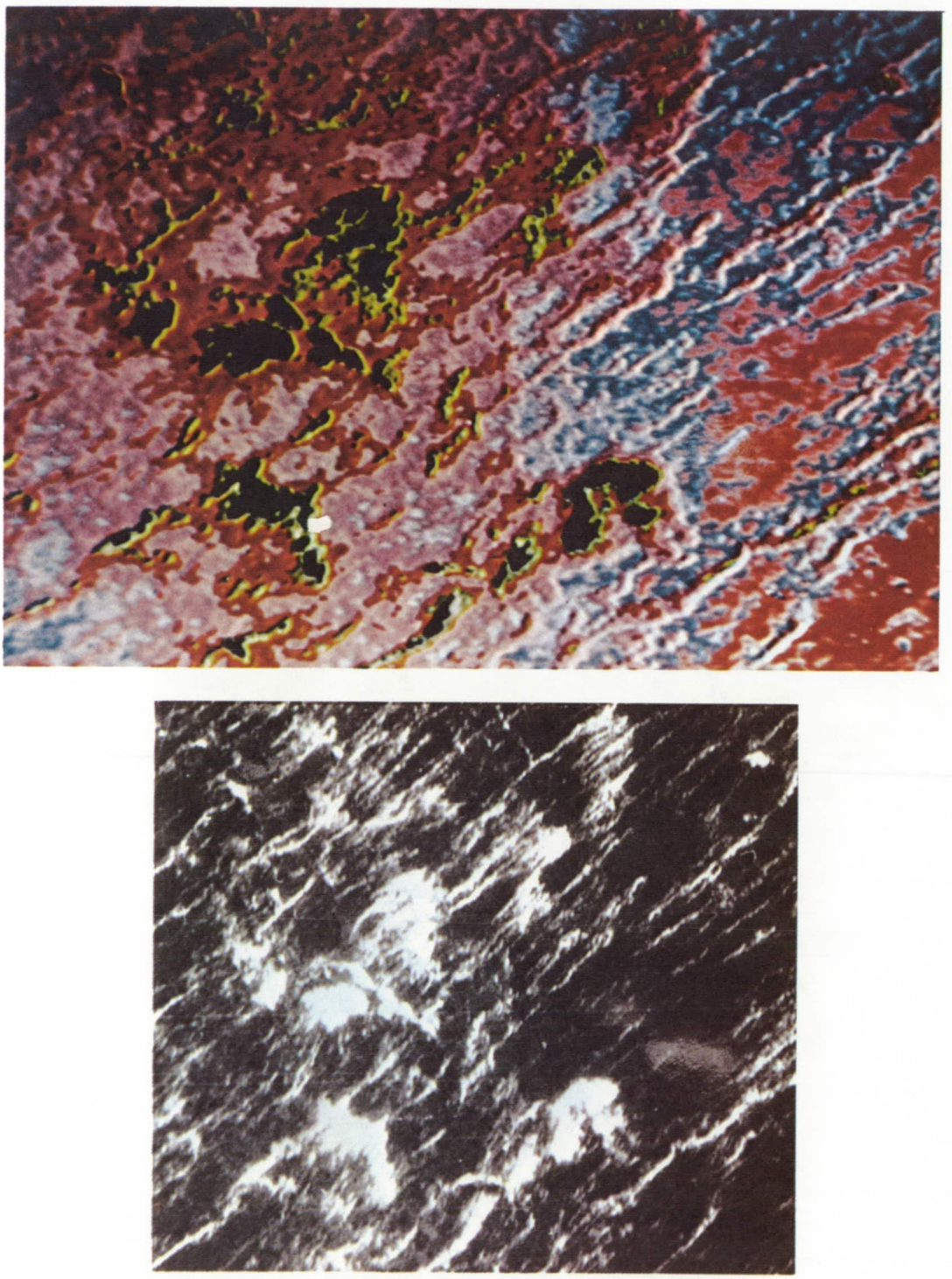

FIGURE 1. False color enhancement of white cap photography for a windspeed of 20 m/s. White caps have been made black while the thin streaks are gold and orange.

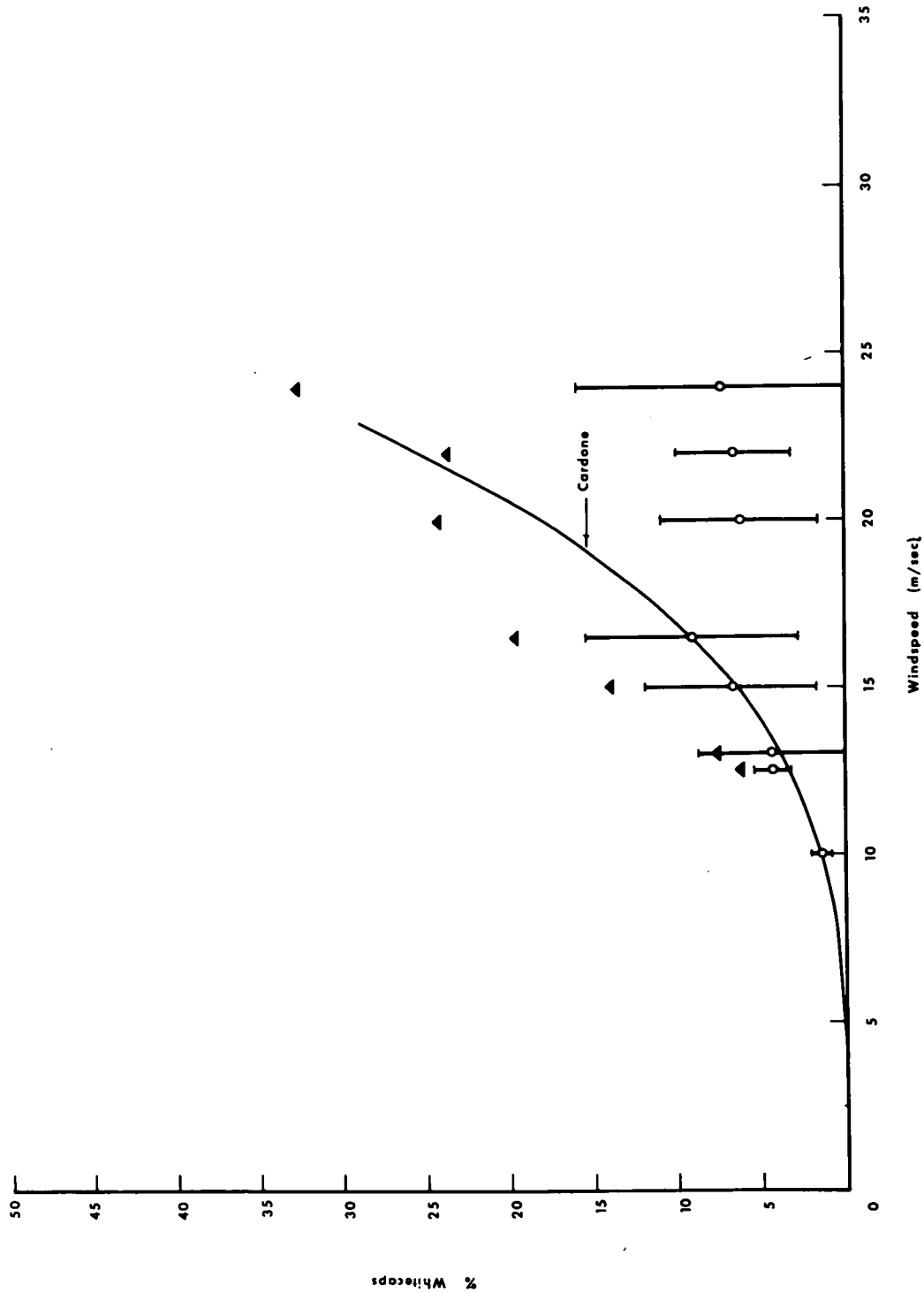

FIGURE 2. Observations of white cap density (open circles) and white caps plus streaks (solid triangles) compared to the predictions of Cardone.

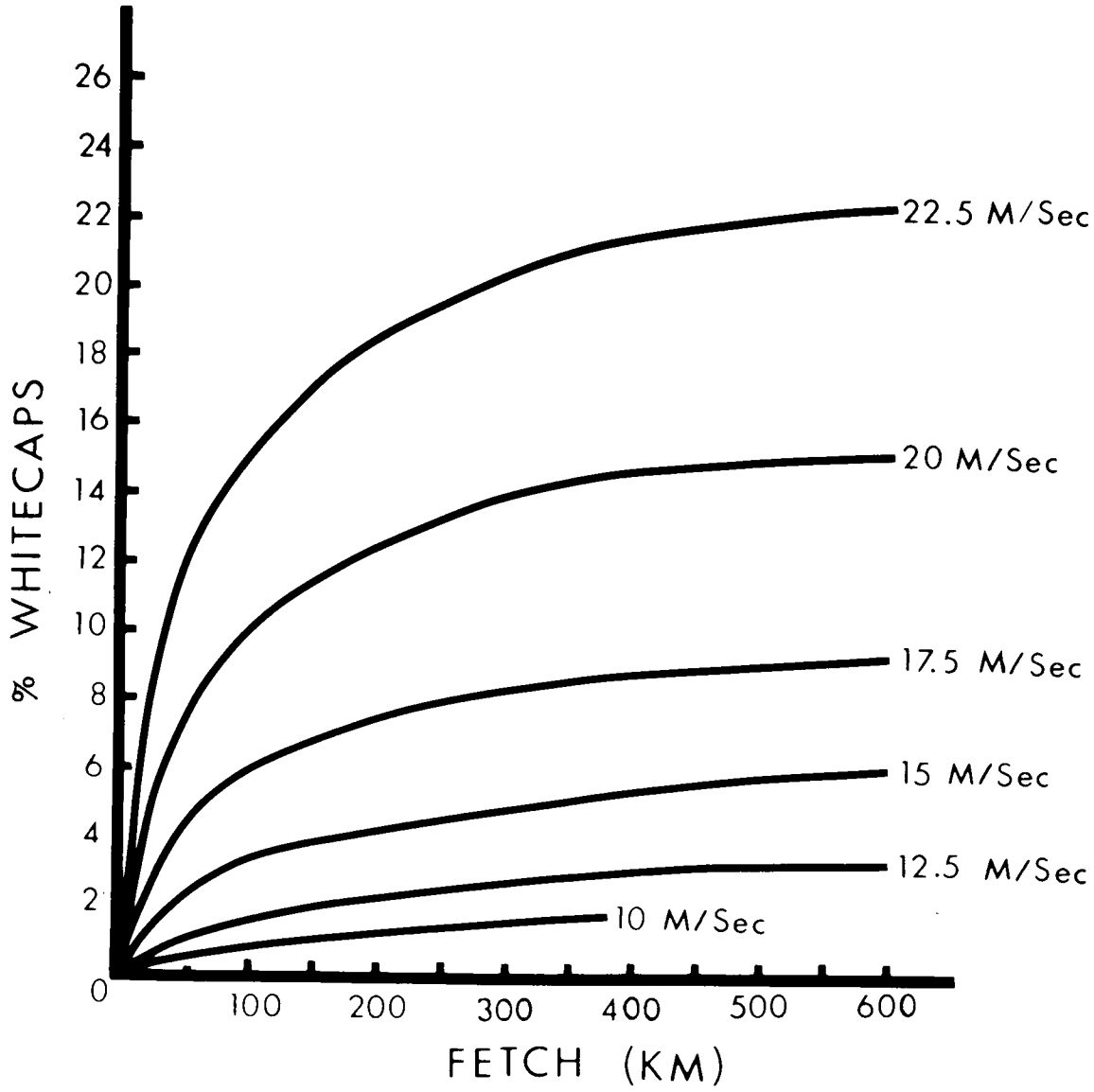

FIGURE 3. Fresh Water White Cap density as a function of fetch according to Cardone (1969).

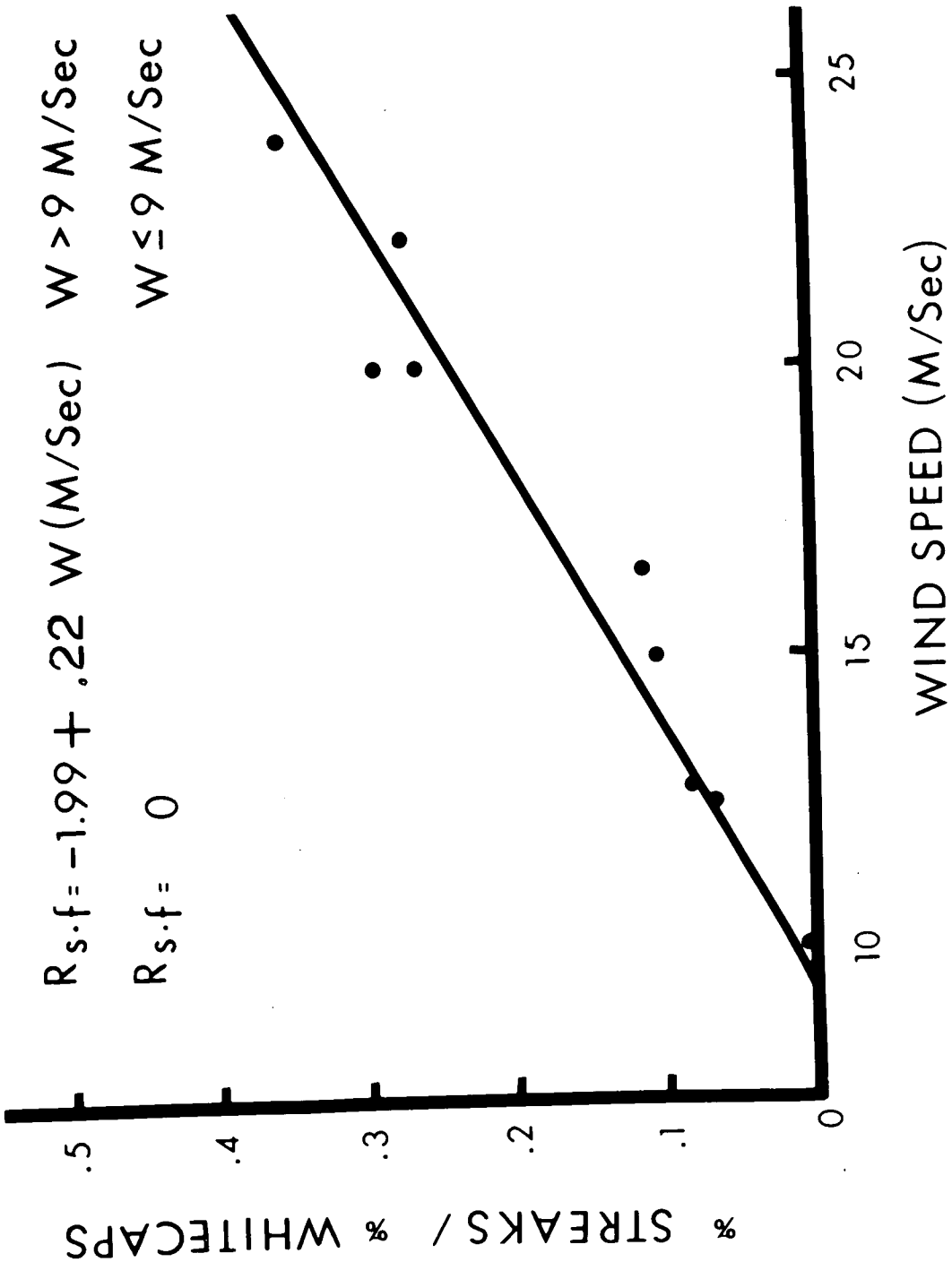

FIGURE 4. Ratio of streaks to white caps vs windspeed.

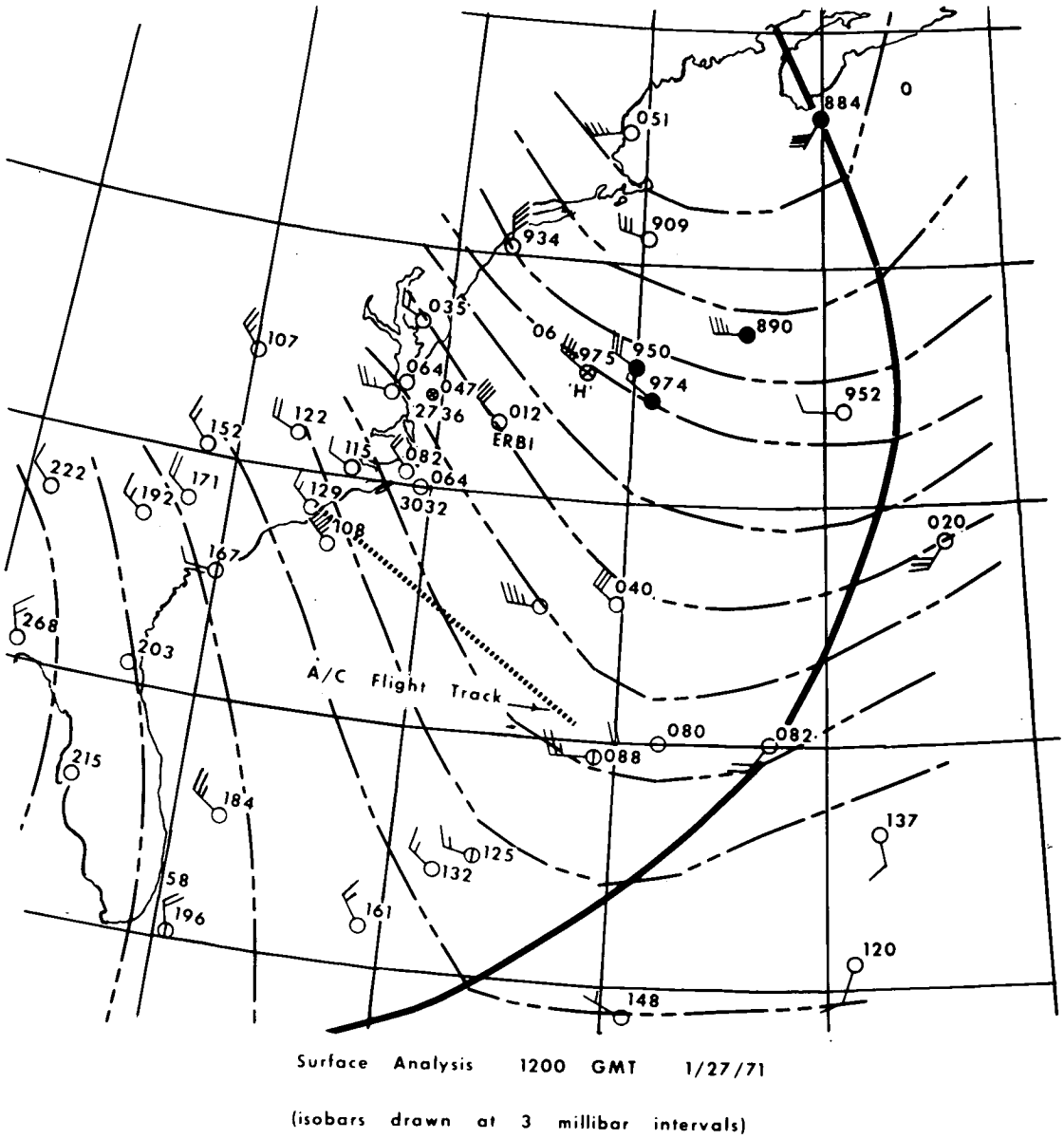

FIGURE 5. Meteorology situation for 27 Jan 71 Fetch Limited Experiment.

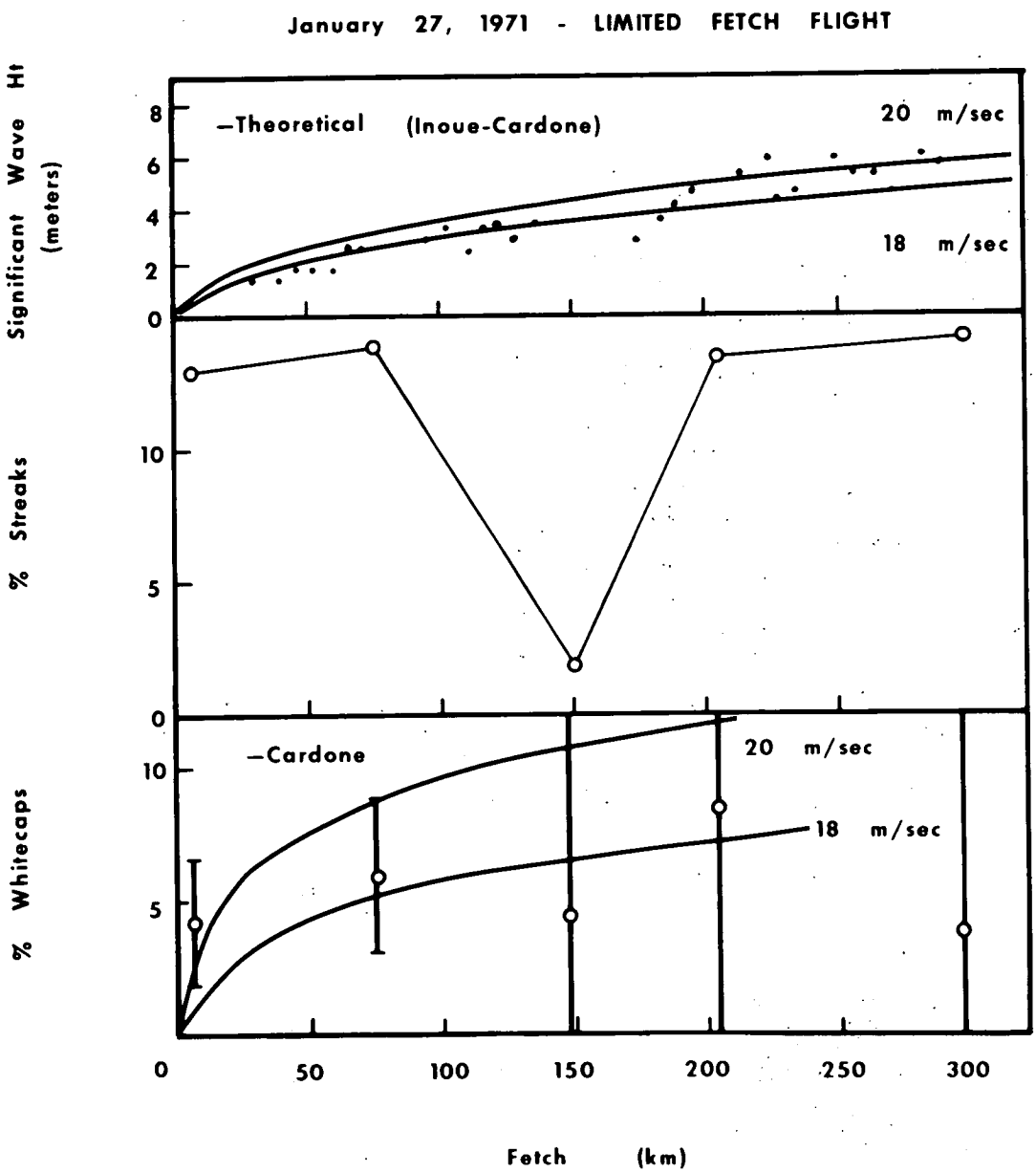

FIGURE 6. Observed behavior of the significant wave height, streak, and white cap density.

FIGURE 7. 32 level false color enhancement of ITOS HRIR Image of 27 Jan 71 showing warm Gulf Stream in red and light blue and cooler shelf waters in black.

SECTION 86

THE CONSTRAINT OF SUN GLINT ON VISIBLE DATA GATHERED BY EARTH SATELLITES

by

Alan E. Strong
National Oceanic and Atmospheric Administration
Washington, D. C. 20031

INTRODUCTION

Viewing Earth's oceans from increasing altitudes results in an expanding sunglint area on the ocean scene. At the equinox an aircraft flying along the equator at 10,000 feet experiences little difficulty viewing a dark ocean from nadir at 1500 local time. From the geosynchronous altitude of ATS (19,300 miles) a similar view of the ocean suffers from sunglint "contamination" at nadir for several hours either side of local noon. Oceanographers hoping to employ environmental satellites at intermediate altitudes for ocean color studies must be aware of and operate with this sunglint constraint when viewing these low radiance levels. This paper presents sunglint simulation from selected satellite orbits in an attempt to optimize the selection of an orbit suitable for ocean color measurements.

SPACE VIEWED OCEAN SUNGLINT

It is important to remember that as the Earth is viewed from increasing altitude the solid angle subtended by Earth decreases. Naturally, the solid angle subtended by the sun remains virtually constant. Such geometric conditions cause the glitter pattern from an ocean to expand in areal extent as the observational altitude increases. This is easily illustrated by comparing the photographs in Figs. 1 and 2. Fig. 1 shows the sunglint pattern over the mid-equatorial Pacific viewed from ESSA 9 altitude (780 n. miles). The ATS-I photograph in Fig. 2 is from the geosynchronous altitude of 19,300 nautical miles. From similar photographs it can be easily demonstrated that although a view of the ocean at nadir at 1400 local time would not be contaminated by glitter, viewing from 780 n. miles would find the glitter area had expanded sufficiently to contaminate nadir.

SUNGLINT SIMULATION FOR AN EARTH ORBITING RADIOMETER

During the preliminary planning phases of satellite oceanographic missions it became obvious that the sun would be a driving function for ocean color measurements. Some recent ocean color work by Duntley (1971) has indicated that a minimum solar zenith angle of 35° is necessary. He stated that the maximum solar zenith is dictated by the various angles involved in contamination of high solar zeniths with sunglint.

We have taken the same model that was developed to simulate the sunglint patterns (Strong and Ruff, 1970) coming from a range of ocean roughnesses and observed by the "old" ESSA vidicon photographs (similar to Fig. 1) and reoriented the model to illustrate the reflection pattern as would be seen by a scanning radiometer (SR). The Improved TIROS Operational Satellite (ITOS) is converting from the vidicon to the SR during 1972. Figure 3 provides an example of visible imagery from the NOAA-1 satellite SR. The curves overlaying the imagery show solar zenith angles at Earth's surface. Since the NOAA satellites are currently ascending across the equator at 1530 local time the higher solar zeniths occur to the west of the subsatellite track (nadir) - north-south lies approximately through the middle of the image. Greenland is apparent at the top of the image. The major water body on this example is the Mediterranean Sea. In the sunglint region over the Mediterranean Sea a narrow band of glitter can be seen to extend from Malta, around the western tip of Sicily, and then northward between Sardinia and Italy. The AVCS picture from ESSA 9 and shown in Fig. 4 was taken within a few minutes of the SR data and illustrates not only the marked difference between the performance of the two sensors but also that the sunglint region off Sicily is indeed free of clouds. Similar anomalous glitter features have been discussed previously (McClain and Strong, 1969) and unveil areas that are devoid of small-scale surface roughness. The concurrent surface weather charts for the Mediterranean area indicate these calm areas most likely mark the center of sea breeze circulations off the coasts - mesoscale high pressure regions.

Employing surface wave slope statistics from Cox and Munk (1956) glitter patterns have been similated for 5 m sec^{-1} and 10 m sec^{-1} surface wind speeds. These patterns, shown in Figs. 5 and 6, were simulated to correspond to the NOAA-1 orbit and imagery shown in Fig. 3. Units represent percent reflectance at the surface and consider no corrections for atmospheric or surface water layer attenuation or scattering. The 0.1% isophote has been included as some oceanographers feel this is the sensitivity to which ocean color sensors need to be sensitive (Clark, et at., 1970).

From the last two figures it is obvious that 1530 local time is not a desirable time to measure ocean color from space as the maximum glint occurs under solar zeniths between 30 and 35 degrees. It is apparent that a near-noon orbit provides the only way to obtain a high solar zenith. Glitter simulation was made for the same altitude (780 n. mi.) but revised to consider an equatorial ascention of local noon. Figure 7 shows the resulting solar zenith curves over the imagery for 25 June. It is interesting to compare the resulting glitter patterns in Figs. 8 and 9 as with those patterns from the afternoon orbit. Wind speeds of 5 m sec^{-1} and 10 m sec^{-1}, respectively, were again simulated. Since the glint falls nearly beneath the satellite more reflected energy reaches the satellite sensor. However, large areas either side of the glitter have a high solar zenith that should permit ocean color measurements outside the glitter pattern that was simply not possible from the afternoon orbit. The 0.1% isophote for the 5 m sec^{-1} simulation never exceeds a 15° satellite viewing angle from nadir.

CONCLUSIONS

It appears from the ocean sunglint simulations presented that ocean color sensing from satellite may be most productive during a near-noon polar orbit. Sunglint along the subsatellite track will contaminate much of the ocean view out to 10 to 15 degrees either side of nadir but useful data either side of the nadir-oriented glint will be possible under the necessary high solar illumination. If fact, some limited oceanic observations may be possible under 5 and 10 degree solar zenith angles.

With a good dynamic range sensor, surface roughness measurements could be made throughout the glitter region. Two advantages are available for noon-viewed glitter (1) reflectance is maximized, and (2) the central location migrates least with changing wind speed (this effect can be seen by comparing Figs. 5 and 6 with 8 and 9). These two features make point reflectance measurements more strongly wind dependent and reduce the wind speed uncertainty when compared with satellite measurements before or after local noon.

REFERENCES

1. Duntley, S. W., August 1971 briefing to NASA's Earth Observatory Satellite Mission Review Group at Goddard Space Flight Center.

2. Strong, A. E. and I. S. Ruff, 1970. Utilizing satellite-observed solar reflections from the sea surface as an indicator of surface wind speed, Remote Sensing of Environment, 1: 181-185.

3. McClain, E. P. and A. E. Strong, 1969: On cluomalous dark patches is satellite-viewed sunglint areas, Monthly Weather Review, 97(12): 875-884.

4. Cox, C. and W. Munk, 1956: Slopes of the sea surface deduced from photographs of sun glitter, Bulletin Scripps Institute of Oceanography, 6(9): 401-488.

5. Clark, G. L., Ewing, G. C. and C. J. Lorenzen, 1970: Spectra of backscattered light fromthe sea obtained from aircraft as a measure of chlorophyll concentration, Science, 167 (3921).

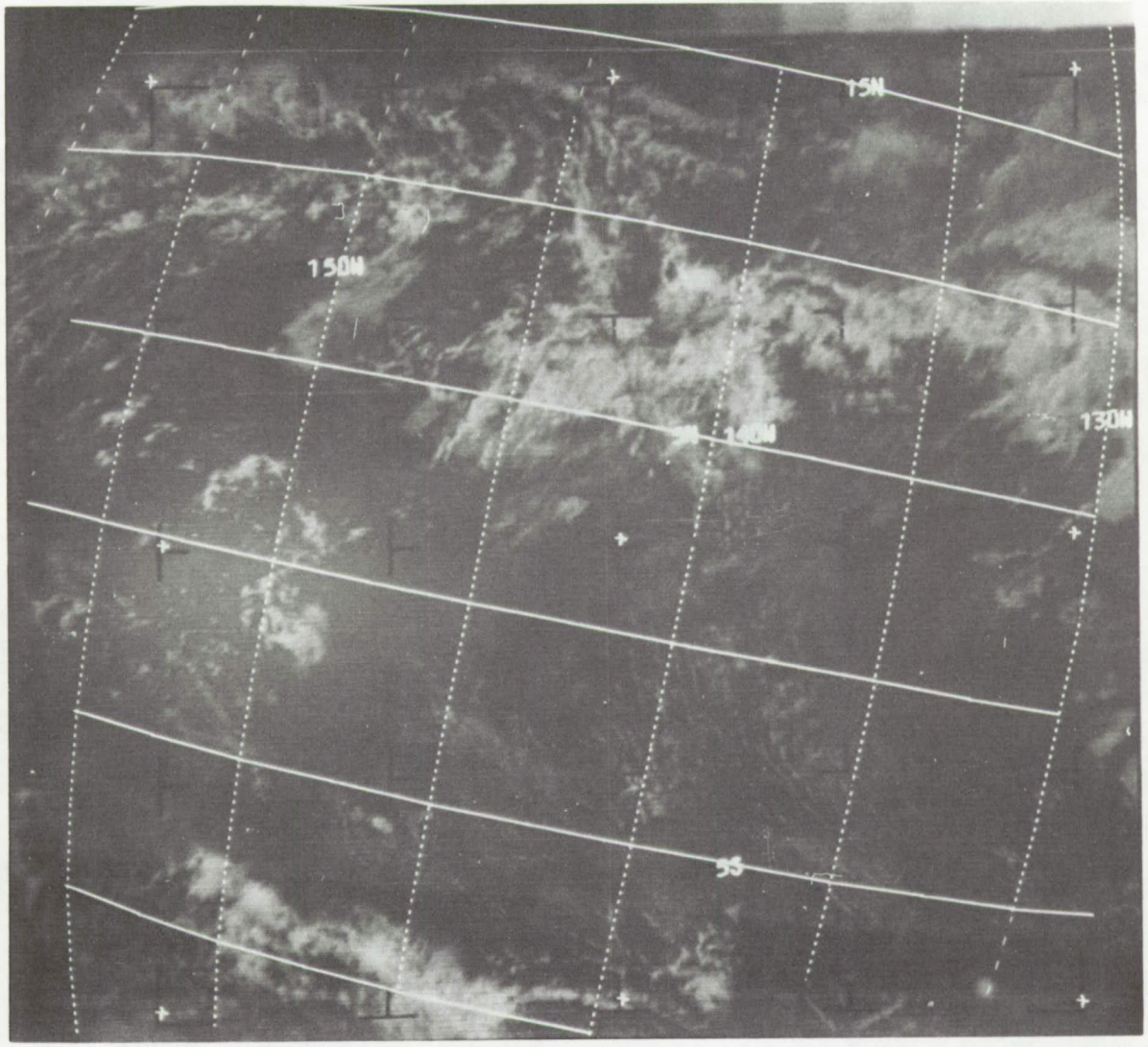

Fig. 1. ESSA 9 AVCS Photograph, 28 October 1971. Compare sunglint coverage of ocean scene in Fig. 1 with Fig. 2.

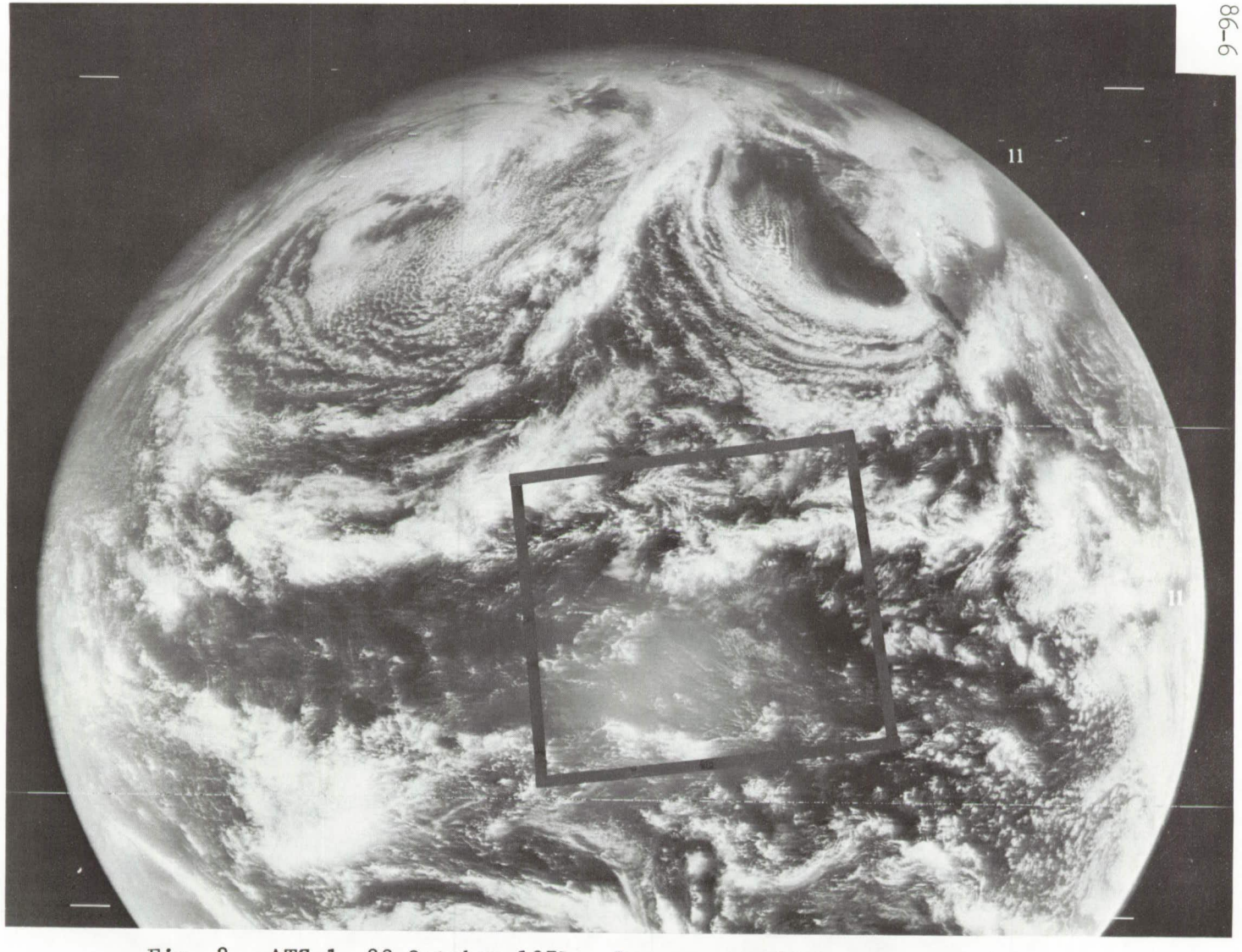

Fig. 2. ATS 1, 28 October 1971. Compare sunglint coverage of ocean scene in Fig. 2 with Fig. 1. Box shows approximate area covered by Fig. 1.

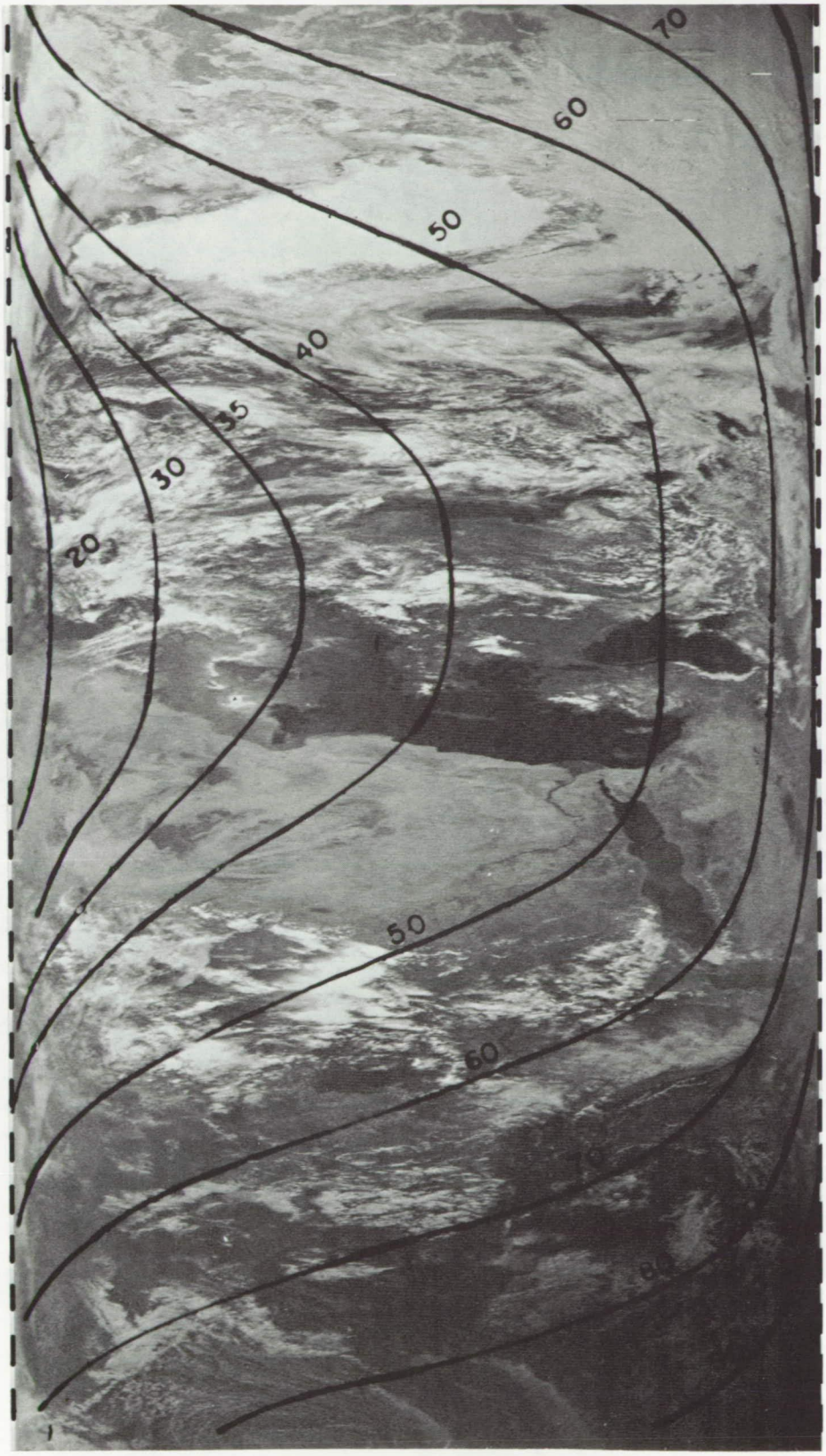

Fig. 3. NOAA-1 Scanning Radiometer Visible Imagery, 25 June 1971. Note sunglint in Mediterranean Sea. Solar zenith angles are Earth-located for 1530 local time, 780 nautical mile orbit.

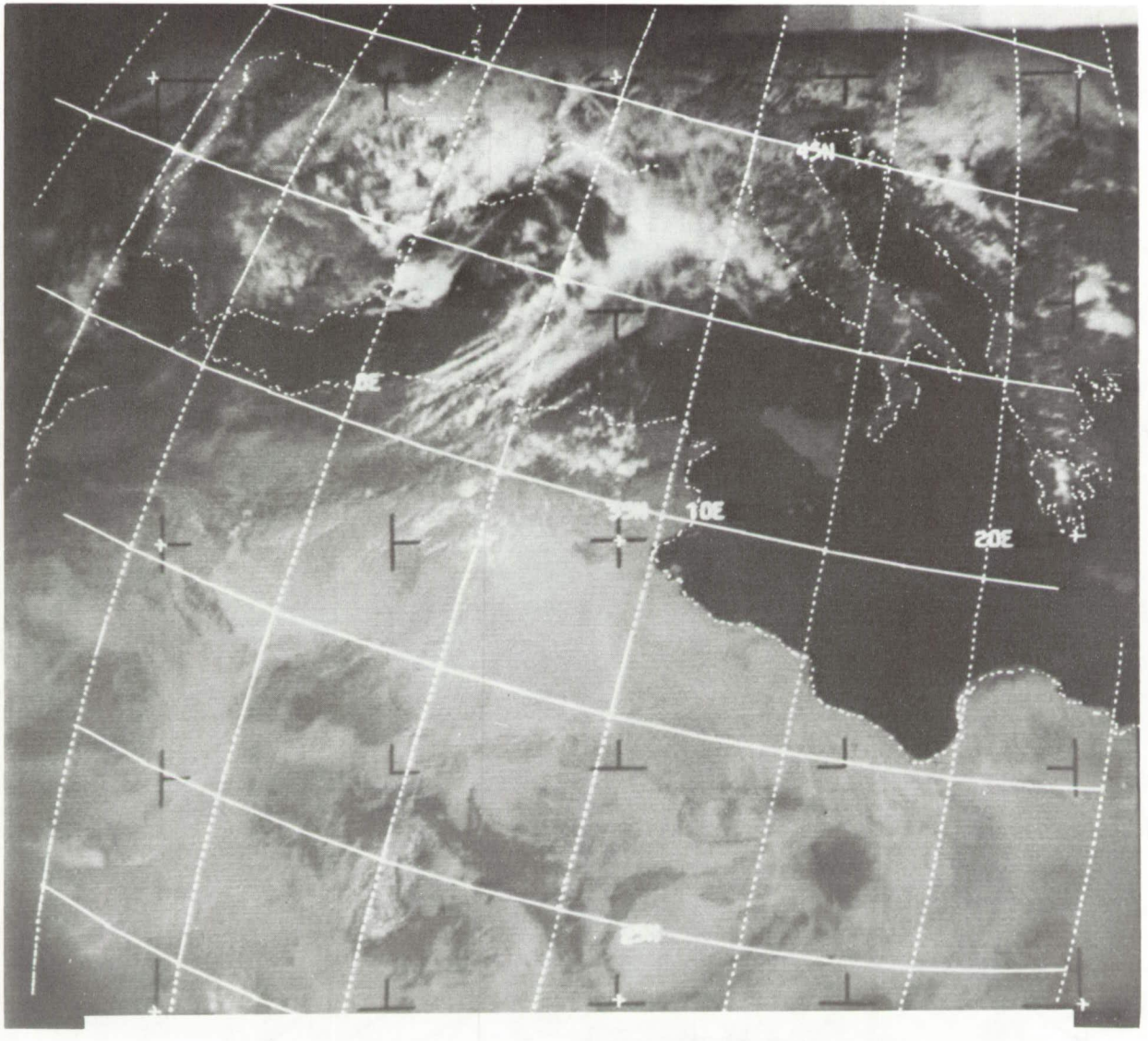

Fig. 4. ESSA 9 AVCS Photograph. 25 June 1971. Taken approximately same time as imagery over Mediterranean shown in Fig. 3. Note clear sky mode over Sicily.

Fig. 5. NOAA-1. Visible Imagery with reflectance ratio for surface under 5 m sec^{-1} wind.

Fig. 6. Same as Fig. 5 but for 10 m sec^{-1} wind.

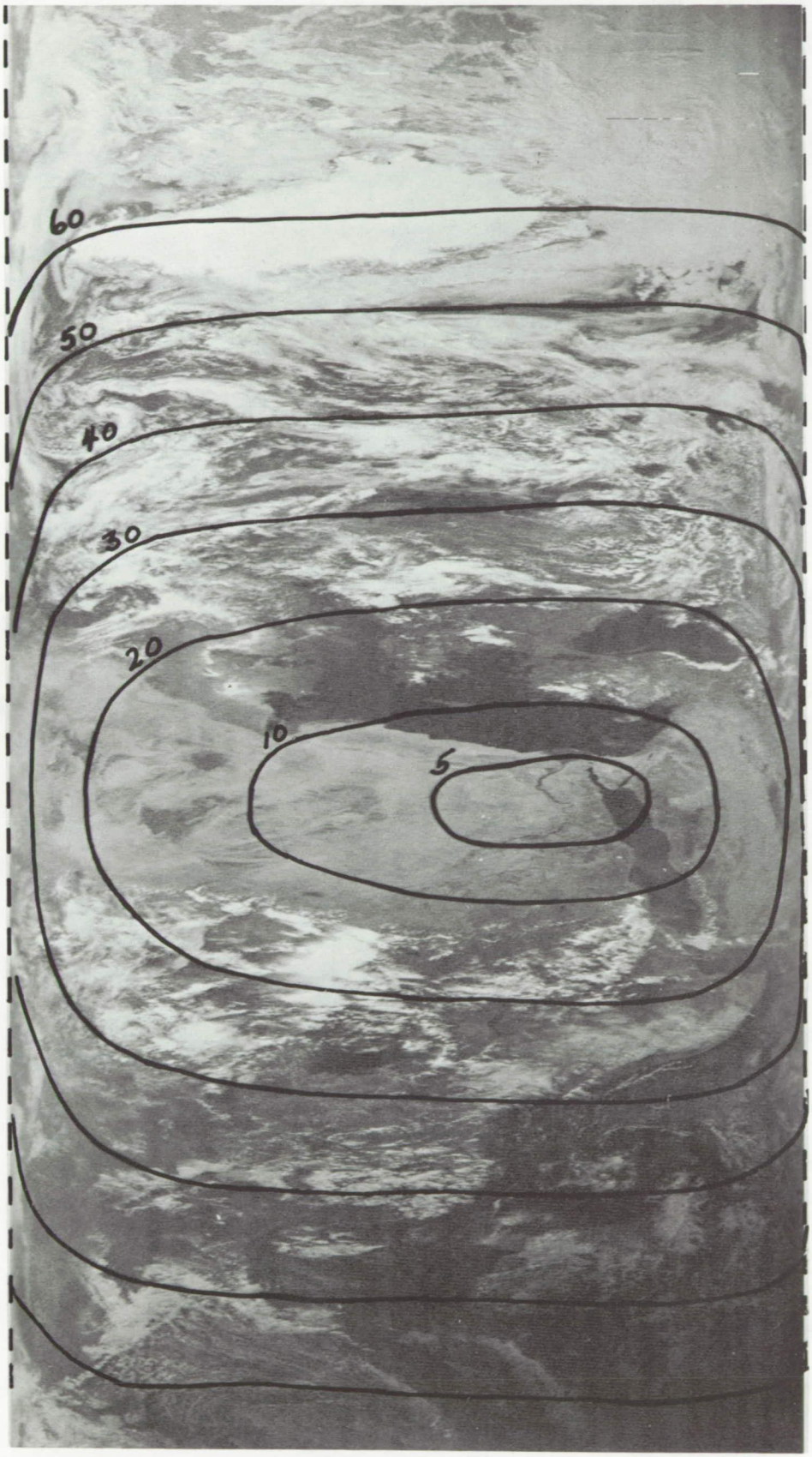

Fig. 7. NOAA-1 imagery with simulated solar zeniths for noon orbit at 780 n. miles.

Fig. 8. Reflectance ratios for Fig. 7 simulation with surface wind of 5 m sec^{-1}.

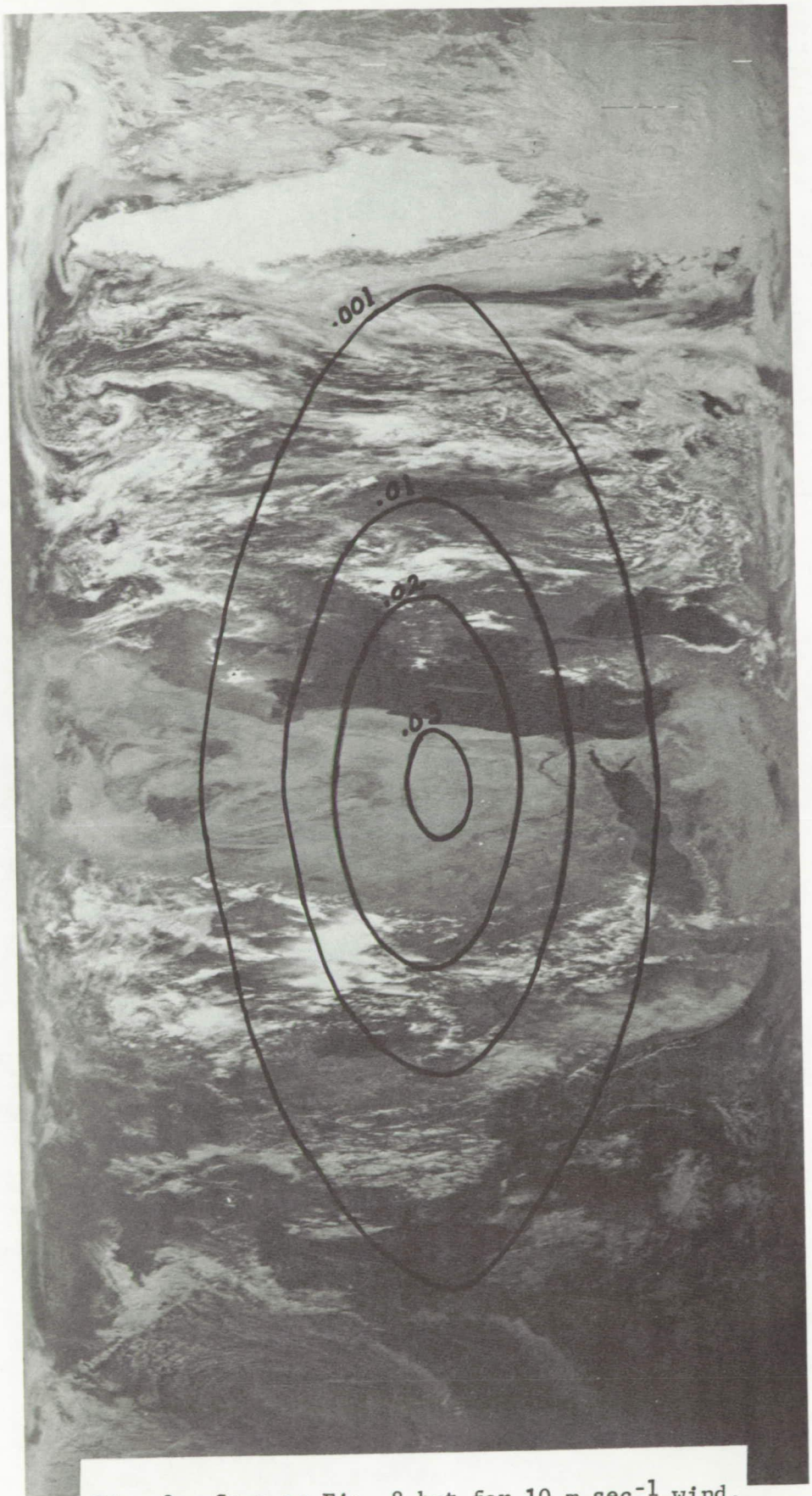

Fig. 9. Same as Fig. 8 but for 10 m sec^{-1} wind.

SPECIAL DISPLAYS OF SATELLITE INFRARED DATA FOR SEA ICE MONITORING

by

E. Paul McClain
National Oceanic & Atmospheric Administration
Washington, D. C.

INTRODUCTION

The Arctic Ocean and the fringes of the Antarctic are rather remote and inaccessible parts of the world. Furthermore, being subject to incursions of polar ice and strong storms, they are harsh environments, too. Comprehensive and repetitive oceanographic or meteorological survey by surface vessels, or even by aircraft, would be costly, difficult, and even rather hazardous. The polar-orbiting environmental Earth satellite is thus, in many ways, a suitable sensor platform for such areas.

Knowledge of sea ice distribution and condition is important to commercial and military ship movements in the Arctic and Antarctic. Much physical data on both ice buildup, movement, and decay are needed for understanding of the processes and to develop forecasting methods. Ice cover also plays an important role in the heat balance of polar regions, and this in turn influences the circulation within the atmosphere and oceans.

NOAA OPERATIONAL ENVIRONMENTAL SATELLITES

The second generation of Improved TIROS Operational Satellites was inaugerated in 1970 (Albert, 1968). Environmental satellites of this ITOS series, which are designated NOAA-1, NOAA-2, etc., carry vidicon camera systems (0.5-0.7μm), two-channel scanning radiometers (0.5-0.7μm and 10.5-12.5μm), and solar proton monitors. These satellites are put in near-polar, circular, sun-synchronous orbits at a nominal altitude of 1450 km. Equator-crossing times are 0300 and 1500 local time.

Data are received from these satellites in two modes. Global coverage on a daily basis is provided by temporary storage of information on board the spacecraft by means of tape recorders. The stored data are read out on command to complex command and data acquisition stations in Alaska and Virginia, whence they are relayed by land-line to a central facility and computer complex near Washington, D. C.

Local coverage is provided by means of a direct-readout capability known as APT (Automatic Picture Transmission), which requires only simple receiving and display equipment.

Thermal infrared imagery (9-km resolution at nadir) is used on Earth's night side to supplement the visual imagery (4-km resolution) on the day side to produce global cloud maps at 12-hour intervals. Furthermore, the IR measurements can be used to infer additional information such as cloud-top temperatures/heights (Rao, 1970) and temperatures at the surface of the sea, water or ice, day or night (Smith et al, 1970; Rao et al, 1971). Extensive computer processing of these satellite data is necessary in order to rectify them, normalize them for variable solar illumination and camera distortions or radiometer calibrations, and redisplay them on standard map projections on a regional or global basis (Bristor et al, 1966). Further manipulations of the digitized brightness or thermal values are employed to derive products such as average or composite maximum or minimum charts for selected periods (Booth & Taylor, 1969).

SEA ICE SURVEILLANCE BY SATELLITE

A major problem in the use of either visual or infrared imagery for sea ice surveys is the differentiation between sea ice and clouds, whose reflectances (or temperatures) can often be comparable. Photo-interpretation methods have proved effective, but only when applied by skilled analysts who are familiar with the meteorology/oceanography and geography of the area. Characteristic differences in form, tone, texture, and particularly of persistence and movement, are the principal interpretive tools. Changes in cloudiness from day to day are much greater than changes in the ice pack. Also clouds tend to obscure landmarks otherwise discernible.

Figure 1 is a single vidicon camera frame of the Bering Sea area taken on 14 March 1971 when the polar ice pack was near its maximum seasonal extent. The nominal grid of latitude, longitude, and coastlines is superimposed by computer during display. The boundary of the first-year ice covering the northern and eastern parts of the Bering Sea is clearly evident over most of its length. Although cloudiness is present nearby, confusion with the ice is unlikely except perhaps near the Siberian coast. There is little contrast between the ice pack and the adjacent snow-covered land. Some less reflective areas, usually indicative of the presence of some open water (i.e., less than ten/tenths concentration of ice), are discernible south of such islands as St. Lawrence, St. Matthew, and Nunivak, as well as elsewhere.

The transient nature of clouds in comparison with major ice and snow fields has enabled the development of an automated procedure for suppressing the cloudiness by compositing satellite visual data over periods of time ranging from five days upward to a month (McClain & Baker, 1969). Digitized brightness values, after rectification and normalization, are composited by saving and displaying only the minimum brightness at each grid point in the array during the period. By calibrating the composite minimum brightness (CMB) values externally with respect to the brightness of the Greenland ice cap (high reflectance) and cloudfree ocean areas (low reflectance), it has been found that distinct changes in brightness with time can be related to the concentration and physical condition of the ice, such as the presence or absence of a snow cover or melt water pools (McClain, 1972).

Lack of sufficient solar illumination, however, greatly limits the use of vidicon camera systems or scanning radiometers operating in the visible part of the spectrum for ice monitoring during much of the cold half of the year. This limitation has been overcome largely by the use of thermal infrared imagery (Barnes et al, 1970). Figure 2 is an example of thermal IR imagery obtained by direct-readout in Alaska some 12 hours after the visual image in Figure 1 was obtained. The IR image is unrectified and ungridded, and some "noise" from electrical interference is evident, but major geographic features are easily recognized. The gray-scale display employed for this image has some 32 steps corresponding to temperature intervals of about 4K and proceeding from less than 180K (white) to more than 310K (black). The coasts of Alaska and Siberia are readily seen because of the temperature contrast between the cold land and the relatively warmer ice pack covering the northern portion of the Bering Sea. This contrast is greater than the difference in reflectivity between the snow-covered land and the ice pack as seen in most vidicon pictures, when there is sufficient daylight for usuable television pictures.

SPECIAL DISPLAYS OF INFRARED DATA

Figure 2 is a standard infrared image produced for meteorological purposes. The maximum of 32 gray steps has been expended over a very large temperature range, and thus each step represents a fairly large temperature interval. In an attempt to tailor the IR display for ice analysis, several ice enhancement experiments were run. Figure 3 shows the results of using only 10 gray steps and proceeding from $\geq$ 273.5K (black) to $\leq$ 221.0K (white) with relatively large temperature intervals (see Table I). Figure 4 is the result of using 22 gray steps to cover the same temperature range with a temperature interval of about 2K (see Table II).

In both Figures 3 and 4 the southernmost boundary of the ice pack is clearly delineated by a band of relatively warm, ice-free ocean. Shallow (cool) clouds are present over much of the Bering Sea to the south of the ice pack, and deep (cold) clouds are found to the southeast and over the Aleutians, as well as to the west near northern Kamchatka. Of particular interest are the distinctly warmer areas showing up, for instance, south of the islands St. Lawrence, St. Matthew, and Nunivak, and in the eastern Gulf of Anadyr. These evidently represent areas of significantly thinner or less-concentrated ice (i.e., some open water). The enhanced ice displays facilitate the delineation of features such as these, as well as temperature contrasts associated with coastlines and cloud areas.

CONCLUDING REMARKS

Infrared measurements from Earth satellites now enable sea ice surveys and monitoring to be accomplished during the polar night, which is not possible with visual sensors. Furthermore, the use of thermal data enables additional information, such as the thickness or physical state of the ice, to be obtained or inferred. Enhancement of the IR imagery promotes the detection of significant ice boundaries, openings, thin areas, and can assist in cloud discrimination. Computer printouts of the calibrated temperature values for more quantitative studies are readily produced from the same magnetic tapes used to obtain the imagery. Experiments are being conducted to develop a multiday compositing technique for the filtering of clouds from the scene, although this is proving more difficult than it was with visual range data. The problem stems from the fact that deep temperature inversions are common at high latitudes over land in winter, resulting in some cloud tops being actually warmer than the Earth's surface in nearby cloud-free areas.

REFERENCES

1. Albert, E. G. 1968. The improved TIROS operational satellite. ESSA Technical Memorandum NESCTM-7. Dept. of Commerce, Washington, D. C., 14 pp.

2. Rao, P. K. 1970. Estimating cloud amount and height from satellite infrared radiation data. ESSA Technical Report NESCTR-54. Dept. of Commerce, Washington, D. C. 11 pp.

3. Smith, W. L., Rao, P. K., Koffler, R., & W. R. Curtis. 1970. Determination of sea-surface temperature from satellite high resolution infrared window radiation measurements. Monthly Weather Review 98:604-611.

4. Rao, P. K., Strong, A. E., & R. Koffler. 1971. Gulf Stream meanders and eddies as seen in satellite infrared imagery. Journal of Physical Oceanography 1:237-239.

5. McClain, E. P. & D. R. Baker. 1969. Experimental large-scale snow and ice mapping with composite minimum brightness charts. ESSA Technical Memorandum NESCTM-12. Dept. of Commerce, Washington, D. C., 19 pp.

6. McClain, E. P. 1972. Quantitative use of satellite vidicon data for delineating sea ice conditions. (Submitted for publication in Arctic.)

7. Bristor, C. L., Callicott, W. M., & R. E. Bradford. 1966. Operational processing of satellite pictures by computer. Monthly Weather Review 94:515-527.

8. Booth, A. L. & V. R. Taylor. 1969. Mesoscale archive and computer products of digitized video data from ESSA satellites. Bulletin of American Meteorological Society 50:431-438.

9. Barnes, J. C., Chang, D. T., & J. H. Willand. 1970. Improved techniques for mapping sea ice from satellite infrared data. Final Report to NOAA (Dept. of Commerce) on Contract No. E-67-70(N) from Allied Research Associates, Concord, Mass., 95 pp.

TABLE I.- IR ICE DISPLAY TABLE 5

Radiation Temperature Range	Gray Scale Step	Display Level
≥273.5K	1	0 (black)
268.0 - 273.0	2	10
261.5 - 267.5	3	20
255.5 - 261.5	4	27
249.5 - 255.5	5	32
243.5 - 249.0	6	37
238.0 - 243.0	7	42
231.0 - 237.0	8	47
222.0 - 230.0	9	54
≤221.0	10	63 (white)

TABLE II.- IR ICE DISPLAY TABLE 6

Radiation Temperature Range	Gray Scale Step	Display Level
≥273.5	1	0 (black)
271.0 - 273.0	2	10
268.5 - 270.5	3	14
266.0 - 268.0	4	18
263.5 - 265.5	5	22
261.0 - 263.0	6	25
↓ - ↓	↓	↓
-		
-		
-		
234.0 - 236.0	17	47
231.0 - 233.0	18	49
228.0 - 230.0	19	51
225.0 - 227.0	20	54
222.0 - 224.0	21	58
≤221.0	22	63 (white)

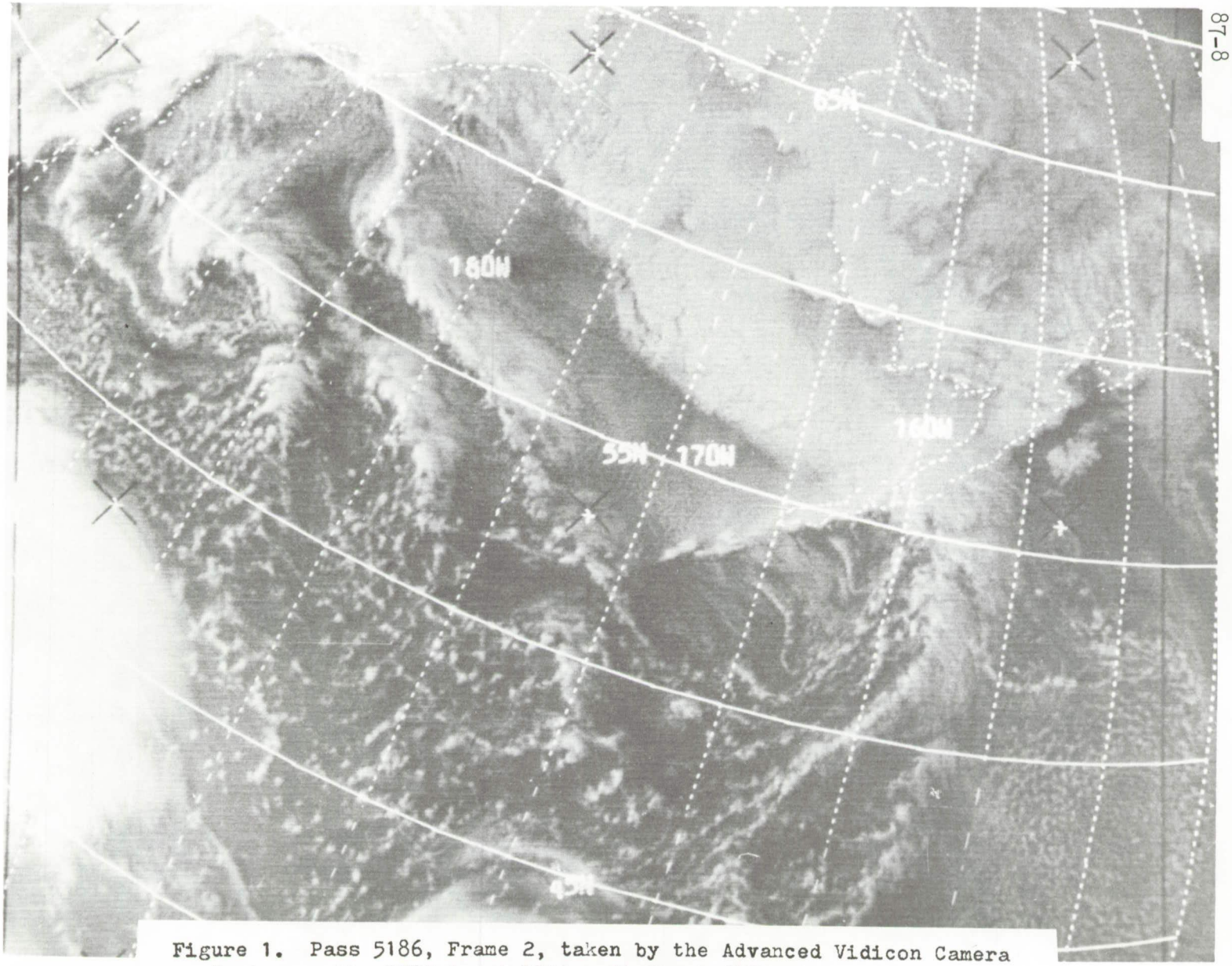

Figure 1. Pass 5186, Frame 2, taken by the Advanced Vidicon Camera System on the ITOS-1 satellite, 14 March 1971, in Bering Sea Area.

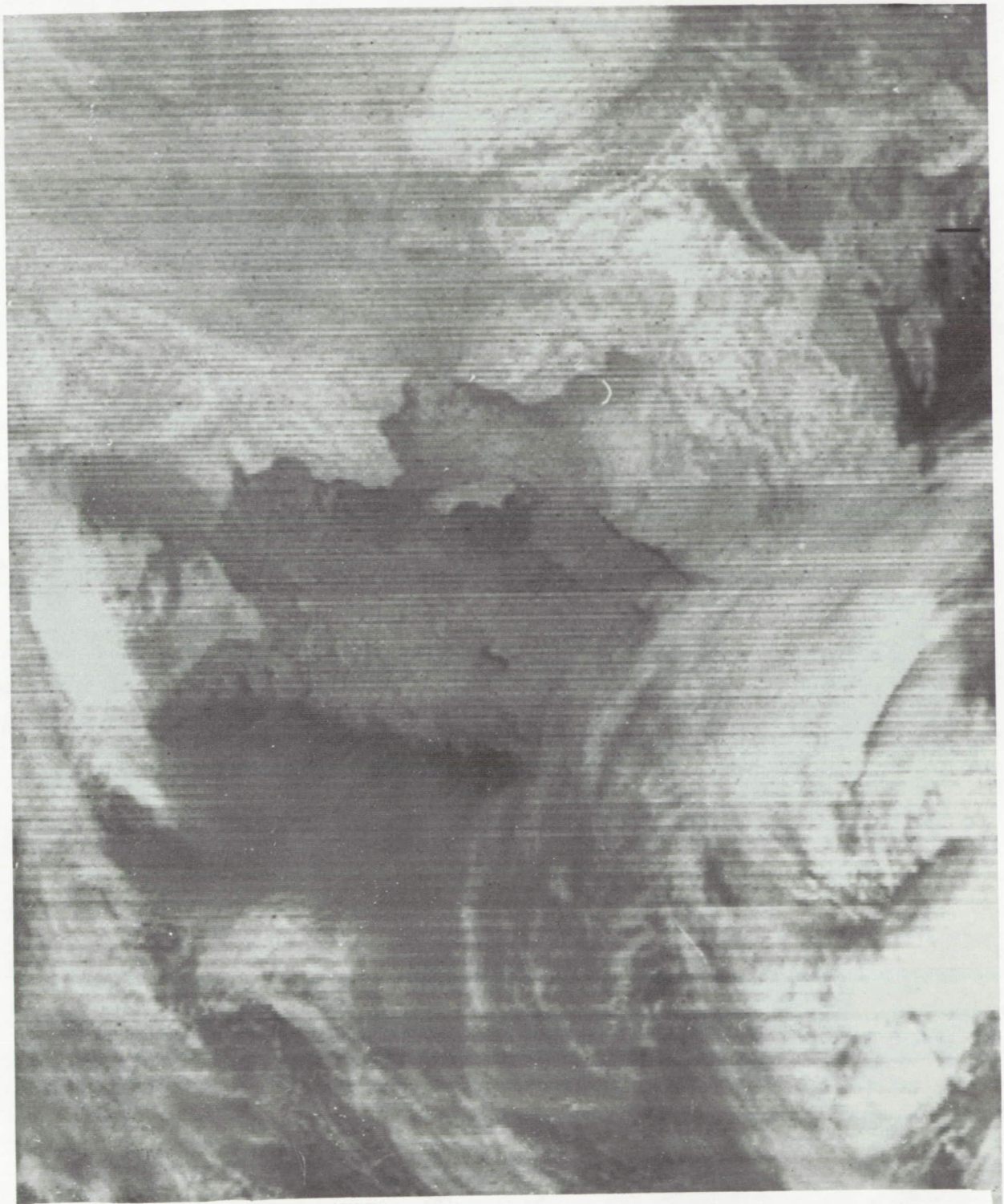

Figure 2. Direct-readout thermal infrared imagery from measurements taken by the ITOS-1 satellite on Pass 5207, 15 March 1971. This is ungridded scanner imagery of the Bering Sea area read out in Alaska.

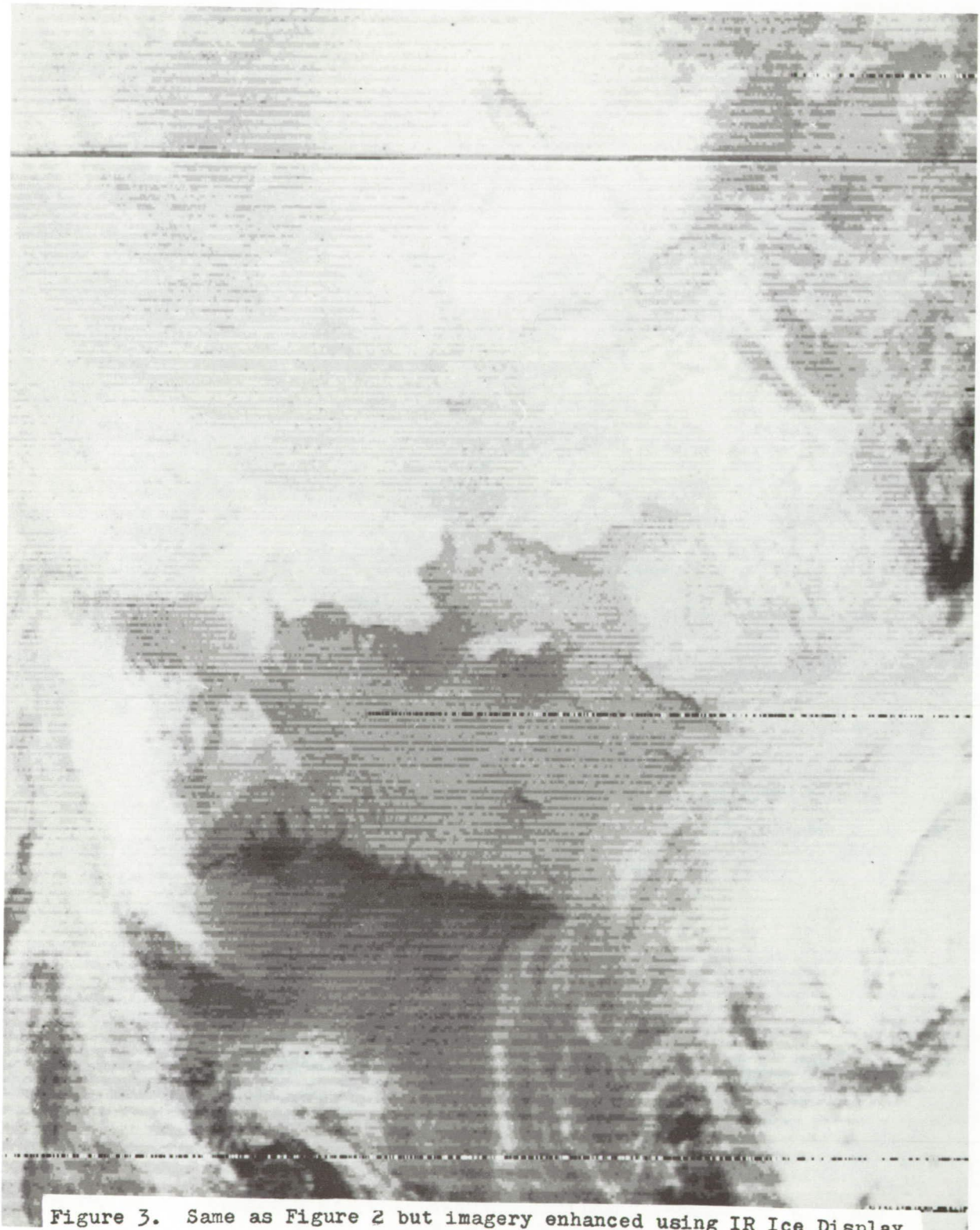

Figure 3. Same as Figure 2 but imagery enhanced using IR Ice Display Table 5 to enhance ice boundaries and other thermal contrasts.

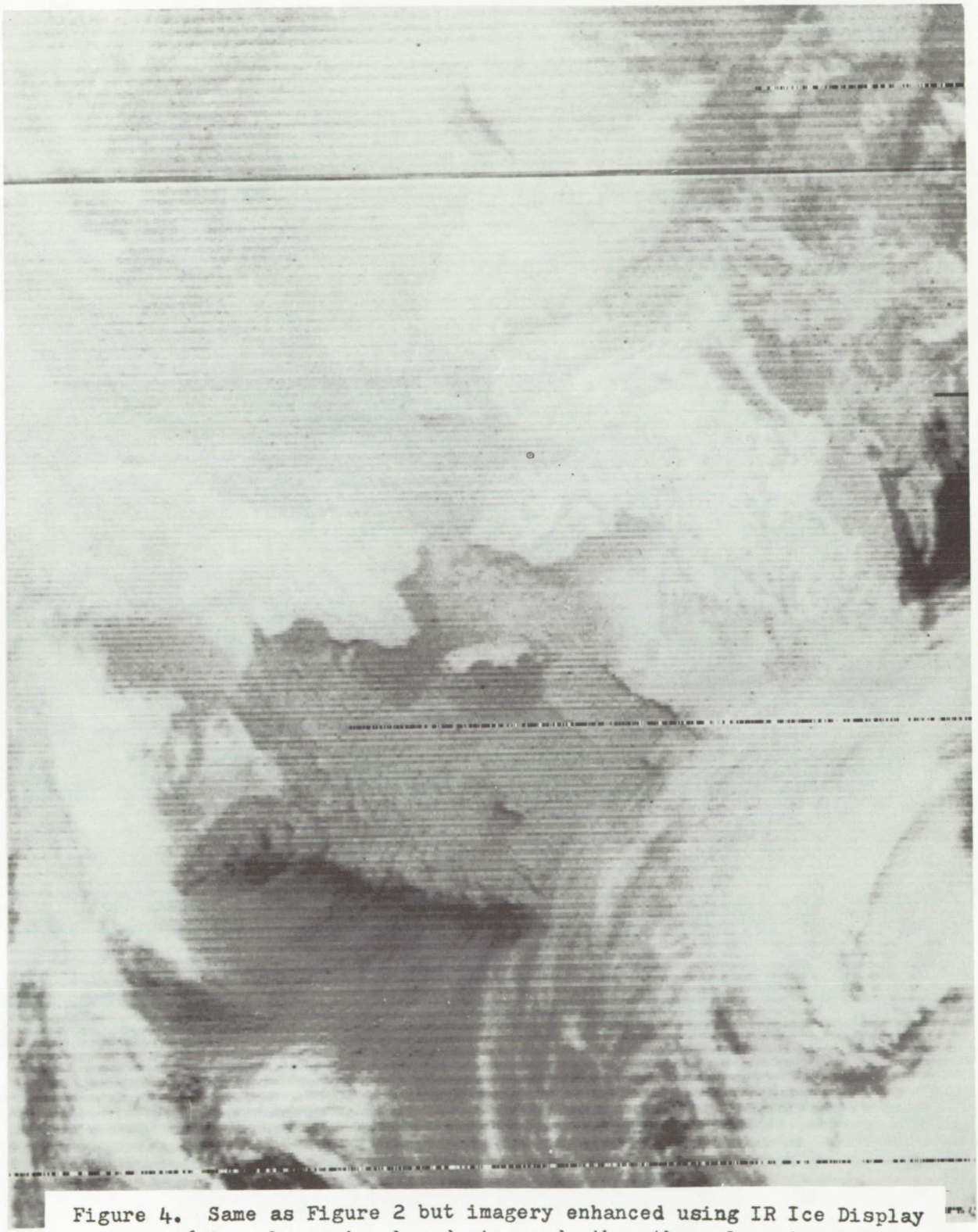

Figure 4. Same as Figure 2 but imagery enhanced using IR Ice Display Table 6 to enhance ice boundaries and other thermal contrasts.

SECTION 88

APPLICATION OF SATELLITE INFRARED MEASUREMENTS TO MAPPING SEA ICE

by

James C. Barnes*
Allied Research Associates, Inc.
Concord, Massachusetts

INTRODUCTION

This report summarizes work performed for the Environmental Sciences Group of the National Environmental Satellite Service of NOAA, under Contract No. 1-36025. The purpose of this contract is to study the application of ITOS-SR (Scanning Radiometer) Infrared measurements for mapping sea ice. The study has three principal objectives: (1) To determine whether ice distributions can be mapped from nighttime ITOS-SR data using the techniques and thresholds developed previously for Nimbus HRIR (High Resolution Infrared Radiometer) data; (2) to compare nighttime and daytime infrared measurements in the 10.5 to 12.5 μm spectral interval using ITOS and Nimbus 4 data; and (3) to perform quantitative analyses of the ITOS-SR photofacsimile data.

The work accomplished has included detailed mapping of ice features visible in the ITOS nighttime DRSR (Direct Readout SR) pictorial data and in Nimbus summertime film-strip data. Analyses of digital temperature values from computer printouts of ITOS stored data and from Nimbus data listings have also been undertaken, and densitometric measurements of both ITOS and Nimbus data have been initiated.

ANALYSIS OF PICTORIAL DATA

Detailed temperature patterns in the area of Northern Hudson Bay, Foxe Basin, and Hudson Strait were mapped from several ITOS DRSR passes during the 1971 winter season. The persistence of various areas of higher temperature indicates that these are most certainly associated with areas of lesser ice concentration near the islands and with leads and cracks in the narrow straits. The Nimbus film-strips mapped have been primarily for the purpose of comparing the film-strip patterns with digital temperature values. The techniques used to identify cloud-free areas and to map ice boundaries were those developed in earlier studies by the author and his associates using data from previous Nimbus satellites.

*The author's current affiliation is with Environmental Research & Technology, Inc., Lexington, Massachusetts 02173. The work reported in this paper is being continued at ERT, Inc.

ANALYSIS OF DIGITAL TEMPERATURE VALUES

Computer printouts for three passes of ITOS stored data over the western Canada/Alaska region during February, March, and April 1971 have been analyzed. Although cloud obscuration is evident in some areas, temperatures in the Beaufort Sea appear reasonable for ice-covered ocean. Warmer areas are evident along the northern coasts of Canada and Alaska.

Two of the ITOS passes were selected for more detailed analysis because of cloud-free conditions near Banks Island, an area previously well-documented in Nimbus 2 HRIR data. Although the values given in the ITOS data are in alphanumeric code and represent an average value of about three data spots, the orientation of the digital lines for these two passes corresponds closely to the orientation of the scan lines for a Nimbus 2 pass on 9 November 1966. A comparative analysis was performed, therefore, for these ITOS and Nimbus data.

The results of these analyses indicate that the ITOS data are not as noisy as the Nimbus 2 data, despite the fact that each of the alphanumerics used for the ITOS data represents not the actual T_{bb} value corresponding to the point, but the range of values in which the actual T_{bb} is to be found. Secondly, the ranges of temperatures corresponding to the ice ($250^{o}K$ to $260^{o}K$) and Banks Island ($240^{o}K$ to $250^{o}K$) are realistic. Thus, a tentative conclusion based on these analyses is that the ITOS digital data can depict significant ice features better than the Nimbus 2 because of the reduction in noise.

DENSITOMETRIC MEASUREMENTS

NIMBUS 4 DATA

Densitometric measurements have been made from Nimbus 4 positive transparencies for five passes over the Greenland-Baffin Bay area in April and May 1970. For these film strips, the following values were obtained for the calibration gray-scale step wedge:

Density	Gray-Scale Step Number									
	1	2	3	4	5	6	7	8	9	10
Mean	2.0	1.9	1.7	1.5	1.4	1.2	1.0	0.9	0.8	0.7
Minimum	1.9	1.6	1.4	1.3	1.1	0.9	0.8	0.7	0.6	0.6
Maximum	2.1	2.1	1.9	1.7	1.5	1.4	1.1	1.0	0.9	0.8

Using the mean densities obtained for the 10-step gray-scale wedge and the relationship between T_{bb} and the gray-scale steps given in the Nimbus 4 User's Guide, a Density-T_{bb} calibration was obtained. This "calibration" chart shows that the greatest temperature resolution, as defined by $\Delta D/\Delta T_{bb}$ is obtained at the two intervals between Steps 1 and 4,

and between Steps 5 and 7. The latter interval spans the range of temperatures significant for the identification and mapping of sea ice boundaries. In this regard, the Nimbus 4 data are similar to those of Nimbus 3 and much better than those of Nimbus 2.

A number of spot measurements were also made of representative ice features in the same passes. From the measured values and the above-mentioned Density-T_{bb} calibration chart, the following temperatures were obtained:

Feature	Mean Density	Mean T_{bb}	Maximum T_{bb}	Minimum T_{bb}
Ice Cap	0.91	234°K	256°K	196°K
Pack Ice	1.12	266°K	274°K	260°K
Water	1.26	278°K	283°K	273°K

The derived temperatures are reasonable when one considers that both Pack Ice and Open Water may contain some areas of "open pack."

ITOS-1 DRSR DATA

The ITOS data format does not include a calibration step wedge, nor is there a "nominal" gray scale calibration. Furthermore, due to the photographic processing involved, changes in the positive transparencies are to be expected from pass to pass even though the received signals may be identical. It is therefore necessary to devise some means of "normalizing" the density measurements if they are to be compared. The density of an ocean surface with temperatures at or near freezing was chosen for this "normalization."

Seven DRSR passes, each of which contained cloud-free areas in the region extending from Hudson Bay to Southern Greenland, were selected for analysis. In each pass, densities were measured at the same geographic locations. In comparing the measured values for the different passes it is evident that the density at any point can vary substantially from orbit to orbit. Since it may be assumed that for such points as those over "ice cap" areas, there should be no substantial changes in surface temperatures, the large variations in densities may be assumed to be artifact in the data processing. A second factor which substantiates this conclusion is the fact that the differences in the measurements between two passes are "systematic;" i.e., in general, the value $(D_a - D_b)$ has the same sign and approximately the same magnitude at all points, where a and b are two different passes. Furthermore, the mean values of $D_a - D_b$ for the sample points approximately equals the difference in the measured densities over the sea surface for the same orbit pairs.

Because of the systematic shift in densities between orbits, it was felt that a linear normalization technique, using the sea surface densities as reference, is justified. All measured densities were normalized by:

$$D_j^1 = D_j + kj$$

where

$$k_j = D^{sea}_{\text{orbit 4715}} - D_j^{sea}.$$

(Orbit 4715, 4 February 1971, had the smallest density value, so was selected as the base for the normalization.)

After normalization, the pass to pass differences at any point are significantly reduced, giving proof that the differences in photographic processing are linear at least through the range of densities in question. Furthermore, the results of the analysis of the ITOS densitometric measurements show that the features indicated to be "ice free," "pack ice" and "ice cap," fall into three almost unique classes of densities; that is,

$$D_{\text{ice free}} > .73$$

$$.73 \geq \overline{D}_{\text{pack ice}} \geq .61$$

$$\overline{D}_{\text{ice cap}} < .61$$

These are important findings if "objective" techniques are to be developed for field interpretation of the photographic densities.

ANALYSIS OF SUMMERTIME NIMBUS DATA

The high-resolution radiometer on the earlier Nimbus satellites measured in the 3.4 to 4.2 μm spectral interval. The resulting measurements were contaminated by reflected solar radiation during daytime hours. Thus, Nimbus 4 and ITOS-1, carrying radiometers that measure in the 10.5 to 12.5 μm interval, are the first satellites to provide infrared measurements over the arctic during the summer season.

Summertime data are in the process of being analyzed. In one instance (30 July 1970) a Nimbus 4 IDCS photograph shows an area of ice in central Baffin Bay. The ice cannot be detected in the concurrent IR film strip, in which Baffin Bay appears in a uniform gray tone.

To determine the temperature structure in more detail, digitized temperature values along several scan lines crossing the area were plotted for the same orbital pass. Two of these scan lines are shown in Figure 1,

with the temperatures plotted along the left axis and the corresponding film-strip gray levels along the right axis. These scan lines show that although the sea ice does have a lower measured IR temperature, the temperature values for both the ice and the open water fall into the same gray level. In the remainder of the study further analysis of daytime data will be undertaken to determine whether infrared measurements can provide useful ice information during the summer season.

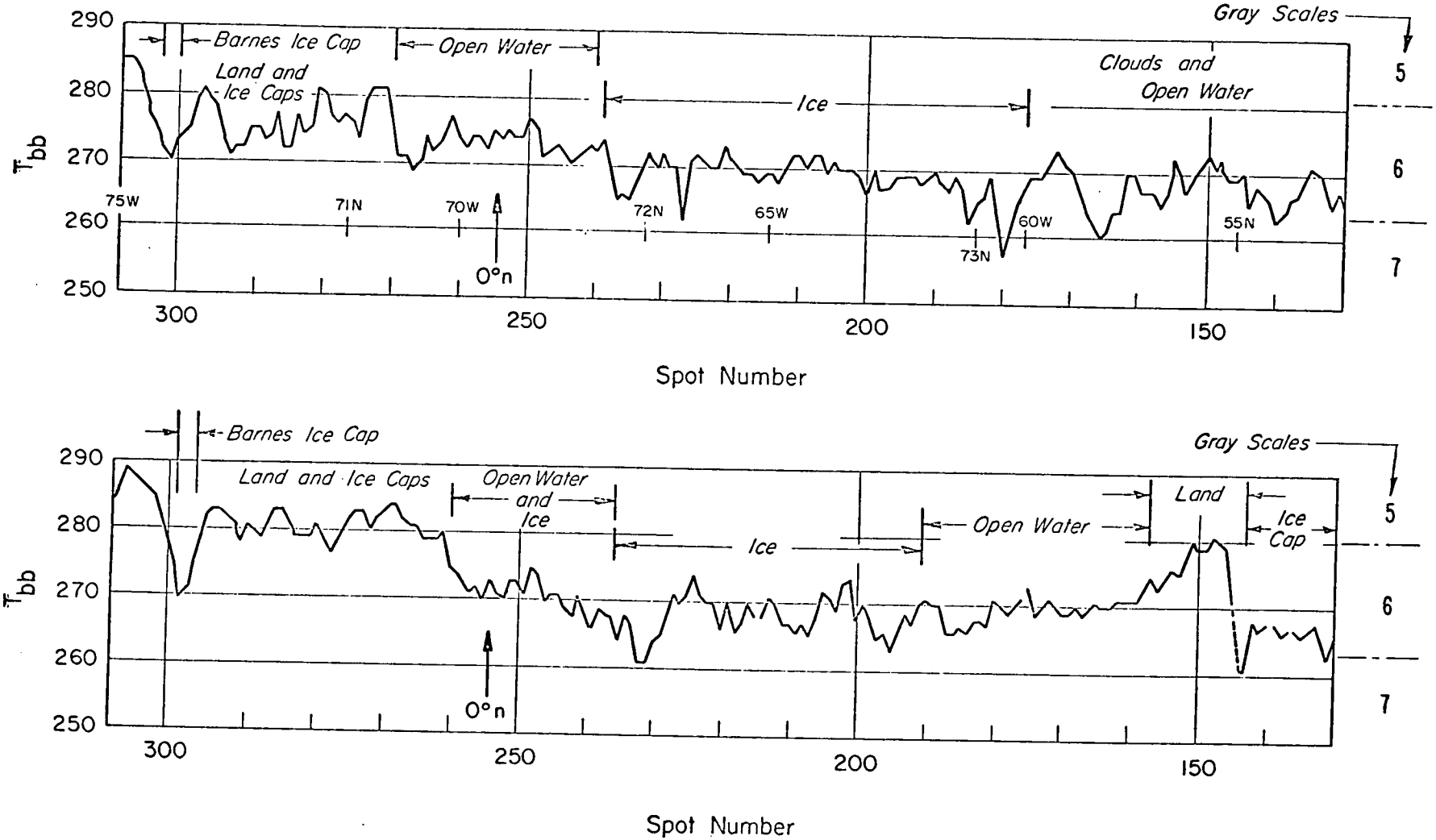

Figure 1 Analysis of digital temperature values along two scan lines crossing Baffin Bay; Nimbus 4 daytime thermal infrared, 30 July 1970.

SECTION 89

MICROWAVE EMISSION CHARACTERISTICS OF SEA ICE

by

A. T. Edgerton and G. Poe
Microwave Division
Aerojet-General Corporation
El Monte, California

ABSTRACT

The National Atmospheric and Oceanic Administration is sponsoring research concerning the microwave emission characteristics of sea ice. Initial analyses were concerned with modeling of sea ice emission and multiwavelength microwave measurements obtained north of Point Barrow, Alaska during June 1970 by Goddard Space Flight Center (GSFC). These data show that ice-water boundaries are readily discernible. A major result of this work was the general classification of sea ice brightness temperatures into categories of "high" (~240°K) and "low" (~200 - 210°K) emission corresponding to young and weathered sea ice respectively. Also, a sea ice emission model was developed which allows variations of ice salinity and temperature in directions perpendicular to the ice surface but neglects lateral variations and nonspecular surface and volume scattering effects. This model does not adequately account for the apparent bi-modal emission characteristics of sea ice.

The sea ice research has since been extended to include development of more adequate sea ice emission models and comparison of the refined models with more extensive sea ice measurements obtained by GSFC in the vicinity of the 1971 AIDJEX Camp. This work is now in progress.

INTRODUCTION

This paper describes sea ice research performed by Aerojet-General Corporation. This study, sponsored by the National Environmental Satellite Service of NOAA, is concerned with the analysis of microwave radiometric measurements of sea ice. The study was prompted, in part, by the need for an effective means of mapping sea ice conditions in the presence of the adverse arctic weather.

Specific objectives of the study include: (1) analysis of multi-frequency microwave emission characteristics of different sea ice types; (2) evaluation of attenuation (and re-radiation) at microwave frequencies of the arctic atmosphere; and (3) determination of the feasibility of mapping sea ice types and ice-water boundaries using microwave radiometry.

Experimental data used in the first phase of the sea ice study were obtained over the Beaufort Sea north of Point Barrow, Alaska during June 1970. Data were obtained by the Goddard Space Flight Center (GSFC) with instrumentation installed in a Convair 990. Instrumentation aboard the aircraft included a 1.55-cm (19.35 GHz) microwave imager, eight microwave radiometers, infrared radiometers (10 to 12 microns), various cameras, a laser geodolite, meteorological instrumentation, and various aircraft attitude and position sensors. Data were obtained at altitudes ranging from 115 m to 9 km. Data analysis was based entirely on information obtained with the aircraft.

Microwave measurements were compared with the available support data to determine the emission characteristics of the sea ice encountered during the overflight. Brightness temperature data were evaluated in terms of the dependence of microwave emission on observational wavelength, antenna viewing angle and antenna polarization.

A numerical model of microwave emission from vertically structured media was employed to evaluate the effects of variations in the brine content (neglecting volume scattering) and thermometric temperature of sea ice. A qualitative comparison of the computed and measured brightness temperatures indicates that a more complex model is needed to adequately describe microwave emission by sea ice.

The second phase of the study was initiated in January 1972. This activity is concerned with developing a more adequate sea ice emission model based, in part, on data obtained by GSFC in the vicinity of the 1971 AIDJEX Camp. Several mechanisms are presently being evaluated to explain the apparent "bi-modal" emission phenomena.

The writers wish to thank several individuals for their assistance and cooperation in this study. Drs. Nordberg, Gloersen and Wilheit of GSFC provided the aircraft data used in the study. Drs. A. Strong of NOAA and W. Campbell of the USGS were also helpful in identifying sea ice features encountered during the study. Dr. A. Strong also provided administrative and technical guidance during the study.

SEA ICE MEASUREMENTS

BACKGROUND

In June of 1970, GSFC conducted an aircraft mission to obtain microwave radiometric measurements of Arctic sea ice. The mission was carried out with Ames Research Center's Convair 990 aircraft. Multi-frequency microwave measurements were taken above a solid cloud cover at an altitude of 9 km (29,000 feet) along a flight track extending about 800 km due north of Point Barrow, Alaska, over the Beaufort Sea. On the return (southbound) leg of the flight, data were taken along the same track below the cloud cover at an altitude of approximately 125 meters (400 feet).

Microwave data derived from this flight were of good quality and correspond to a variety of sea ice features. Supporting data for the June flight include aerial photography, laser geodolite information, infrared temperature measurements (10 to 12 microns), meteorological and aircraft dynamics observations. Unfortunately, no supporting ice data (e.g., ice depth, temperature or salinity profiles, etc.) were taken along the flight track. Hence, the analysis of these data was based solely on the aircraft data.

AIRCRAFT INSTRUMENTATION

The sensor complement aboard the aircraft included a microwave imager, eight microwave radiometers, two infrared radiometers, two cameras and a laser profilometer. The infrared sensors consisted of a Barnes PRT-6 radiometer (10 to 12 microns) and an infrared temperature profile radiometer (ITPR) (10 to 11 microns). Photography was taken with a nadir-looking 70-mm camera equipped with infrared aero-ektachrome film and a 35-mm camera pointed out the left side of the aircraft 45° above nadir. Ice surface roughness data were acquired during the low level flight with a Spectra-Physics Model 3A laser geodolite.

Table I gives pertinent specifications of the microwave radiometers aboard the CV-990. The observational wavelengths of the sensors ranged from 3.2 cm (9.3 GHz) to 0.51 cm (58.8 GHz). The 1.55-cm (19.35 GHz) radiometer was the only microwave imager aboard the aircraft. The relatively large time constants utilized in the 1.35, 0.96, 0.56, 0.55, 0.51 and 2.81-cm measurements impeded detailed correlation with photographic data. The 1.55-cm imager data received primary consideration because of the excellent corresponding 70-mm downward-looking

photography. The 0.81-cm data were also of excellent quality but were difficult to correlate with surface features since the antenna beamprint (45° to the left of aircraft) was outside of the 70-mm camera's 65°30' field of view. As a result, the 0.81-cm data were correlated with visible surface variations using oblique photography from the 35-mm camera boresighted with the radiometer.

ATMOSPHERIC CONDITIONS AND DESCRIPTION OF SEA ICE ALONG FLIGHT TRACK

Point Barrow weather information for the month preceding the airborne microwave measurements was obtained from the Environmental Data Service of NOAA. During May 1970, the mean maximum and minimum temperatures were -5°C and -10°C, respectively. The extreme high temperature was +3.3°C on 30 May. The extreme low was -22.8°C on 4 May. Precipitation during May 1970 amounted to 0.03 mm, all in the form of snow. In the days just prior to the microwave measurements (6 June 1970) an intense storm of several days duration occurred over the Beaufort Sea which gave rise to subfreezing temperatures, some snowfall and presumably, renewed ice growth.

During the airborne measurements an almost solid stratus cloud deck persisted from 150 m to 600 m above the ice surface. Consequently, the supporting sea ice observations (aerial photography, surface temperature measurements, laser profiles, etc.) obtained on the high altitude (8.9 km) northbound flight had limited value in the present study. The supporting data obtained on the southbound low altitude (<150 m) return flight indicated that the air temperature ranged between -3 and -4°C (±3°C).

The available sea ice data for analyzing microwave brightness temperatures included (1) notes from sea ice observers aboard the CV990 aircraft, (2) surface temperature measurements, (3) aerial photographs and (4) laser geodolite measurements. Additional desirable (but unavailable) sea ice data include brine content, density and temperature profiles, internal ice structure and small scale surface roughness. The photographs and sea ice observer notes provided information concerning the ice types, snow cover, relative age of adjacent floes, weathering and deformation. The laser geodolite provided an uncalibrated measure of the intensity of the reflected laser signal and a direct measure of the surface relief.

The 70-mm photographs indicate that two varieties of sea ice were encountered over major portions of the flight track. These included ice of uniform appearance and conspicuously mottled (deformed) ice. The 70-mm photographs indicate that the mottled ice has experienced recent

deformation (ridging, rafting and fracturing) and is younger than the uniform textured ice. The uniform ice appears to have experienced some weathering (melting). The actual age of the two varieties of ice is uncertain, however, both types are though to be first year ice, the younger (mottled) ice being one month old or less (personal communications with W. Campbell and W. Weeks, 1970). Both varieties of ice occurred in floes ranging in size from a fraction of a kilometer to several tens of kilometers. The photographs and observer notes indicate that the uniform ice is covered with a veneer of snow of unknown thickness. The young ice also had a partial snow cover in the form of sastrugii (windblown snow ridges of about one-half meter height).

Minor occurrences of finger ice and open water were also encountered during the measurements. The finger ice occurred adjacent to polynyas and comprised a minor fraction of the flight track. The leads and polynyas were generally small and infrequent along the aircraft track.

The laser surface profile of the young sea ice floes indicate the presence of numerous angular ridges of the order of 0.5 to 1.3 meters high. The uniform floes contain low rounded, surface features of 20-cm or less height. These are believed to be weathered pressure ridges.

In summary, two distinct types of sea ice were encountered over major portions of the June 1970 mission. These will subsequently be termed (1) young ice and (2) weathered ice. The young ice was comparatively thin with extensive ridging and rafting, was probably one month old, or less, and showed no evidence of weathering (melting evidenced by rounded ridges, etc.). The weathered ice is of uniform appearance, has a generally smooth surface, and shows no signs of recent deformation.

Water and ice surface temperatures, determined with the ITPR during the low level (<150 m) measurements, ranged from 270.2 to 273.0°K and averaged about 272°K. Surface temperatures of 273°K were noted very infrequently along the flight track. Consequently, little or no liquid water should have occurred in the snow cover. At these temperatures melting can occur on the sea ice surface depending on the brine content of the ice. Unfortunately, no surface-based data are available and it is not possible to establish whether melting occurred. The sea ice was definitely not saturated (with melt water) since no melt ponds or conspicuous incipient melting were noted on the aerial photography (a few isolated ponds believed to be trapped sea water were noted on young ice floes in close proximity to buckling and rafting). Similarly, no definite statement can be made regarding the ice thickness. Estimates were attempted based on the apparent "free-board" of the floes, as determined from the geodolite observations. However, the resultant thicknesses were inconsistent and were not used in the analysis.

MICROWAVE MEASUREMENTS OF SEA ICE

General

The 1.55-cm imager data were reduced to color images and computer listings of brightness temperature versus antenna view angle (beam position). Data from the other microwave radiometers were generally reduced to computer-generated plots of brightness temperature versus time. All data (except for the 0.5 to 0.6-cm sensors) were examined collectively to determine the wavelength dependence of microwave emission by sea ice. Also, the 0.81-cm data were evaluated in terms of the polarization of sea ice emission, and the 1.55-cm data were examined in terms of emission versus view angle. Detailed comparisons between the two dominant sea ice features (young and weathered ice) were limited to the 0.81 and 1.55-cm data since these were the only data with sufficient spatial resolution.

Dual-Polarized 0.81-cm Brightness Temperatures

Dual-polarized 0.81-cm (37 GHz) microwave measurements were obtained with a side-looking radiometer oriented 45° to the left of nadir. Figure 1 presents representative data obtained in the time interval of 23:23:30 through 23:28:15. A cursory examination of Figure 1 shows that sea ice brightness temperatures are conspicuously bi-modal. Measured horizontally and vertically polarized temperatures for young (mottled) and weathered (uniform) ice are 230 and 240°K, and 180 and 190°K respectively. The sea ice data of Figure 1 exhibit approximately 10°K of polarization. These differences are somewhat greater when the radiometer calibration is taken into consideration. Also, note the substantial differences between open water (highly polarized with very low horizontally polarized brightness temperatures) and the radiometrically cool, comparatively unpolarized, weathered sea ice. These data indicate that dual-polarized measurements can be used to distinguish between the radiometrically cool weathered ice and partially beam-filling water.

Multiwavelength Brightness Temperatures

As mentioned previously, pronounced changes in low altitude 1970 Arctic microwave measurements occurred when viewing different ice types ("young" and "weathered") and when viewing ice-water boundaries. A comparison of these changes at different observational wavelengths reveals several interesting features, Figure 2. The observed contrasts in microwave emission of ice and water for a wavelength of 0.81 cm (and greater) are substantial (100 to 150°K). The greatest contrast occurs

at 2.8 cm. The reduced contrast in the vertical polarization at 0.81 cm is consistent with theoretical predictions. Also, note that the polarization differences are small when viewing the ice. These results present rather encouraging prospects for mapping ice-water boundaries with high altitude microwave measurements.

The multiwavelength contrast in observed brightness temperatures of "young" and "weathered" ice types is presented in Figure 3. The data at wavelengths greater than 0.55 cm exhibit similar responses to different ice types with the contrast increasing with decreasing wavelength. This phenomenon is presently inexplicable. The 0.81-cm data has more noise than the other odata since a shorter integration time was employed.

A graphical illustration of the contrast in emissivity of the two ice types is presented in Figure 4 as a function of observational wavelength. The change in emissivity $\Delta\epsilon$ (larger minus smaller) is presented to minimize effects of calibration errors. A surface temperature of 272°K consistent with infrared measurements has been used in computing $\Delta\epsilon$. Note that $\Delta\epsilon$ exhibits a substantial dependence on wavelength.

SEA ICE MODEL

GENERAL

Sea ice is a complex, dynamic substance. The microwave brightness temperatures of sea ice depend on such phenomena as brine content, thermometric temperature gradients, ice growth rate, internal ice structure, surface geometry as well as other physical sea ice properties. A sufficiently general theory of the microwave emission properties of sea ice which incorporates these phenomena does not presently exist. The recent theory of Stogryn[1] represents perhaps the most general treatment of the effects of basic physical phenomena on sea ice emission. The theory allows variations of the temperature and dielectric constant in the direction perpendicular to a substance's surface but neglects variations in directions parallel to the surface. Also, nonspecular surface scattering and volume scattering effects have necessarily been ignored. The necessity arises since a theory of scattering for situations in which the sizes of scattering centers or the dimensions of surface irregularities approach significant portions of the observational wavelength has not been derived at present. Thus scattering from brine pockets and possibly other structures in sea ice at microwave frequencies are presently unsolved problems.

In this section results of computations using the theory of Stogryn are given which illustrate the dependence of brightness temperature on salinity and thermal temperature of sea ice. These results are preceded by a brief outline of the theory and assumptions employed in the computations.

In the present considerations it is assumed that specifications of (1) the vertical profile of salinity and temperature and (2) the functional dependence of the dielectric constant with salinity, temperature and frequency completely determine the microwave emission of sea ice. Phenomena such as horizontal fluctuations of salinity and temperature, nonspecular scattering, and ice structure variations arising from growth history are completely ignored.

According to the theory of vertically structured media, the horizontally polarized brightness temperature at an angle of incidence θ and frequency ν is given by

$$T_h(\theta,\nu) = |R_h|^2 T_{sky}(\theta,\nu) + 4\left(\frac{2\pi\nu}{c}\right)^3 \cos\theta \int_{-\infty}^{0} dz' \, T(z') \mathrm{Im}\left[K(z',\nu)\right] |A(z')|^2 \tag{1}$$

where $T_{sky}(\theta,\nu)$ is the incident sky temperature, R_h the reflection coefficient of the surface for horizontally polarized radiation, c the free space speed of light, $T(z')$ the thermometric temperature at the depth z' below the surface, $K(z',\nu)$ the complex dielectric constant of the medium, and $A(z')$ is the value, at $z = 0$, of the solution of the differential equation

$$\frac{d^2a}{dz^2} + \left(\frac{2\pi\nu}{c}\right)^2 \left[K(z,\nu) - \sin^2\theta\right] a = -\delta(z - z') \tag{2}$$

satisfying the boundary conditions

$$\frac{da}{dz} - i\left(\frac{2\pi\nu}{c}\right) \cos\theta \; a = 0 \qquad \text{at} \quad z = 0 \tag{3a}$$

a is an outgoing wave as $z \to -\infty$ and, at the ice-water boundary $z = -E$

$$a(-E + 0) = a(-E - 0)$$

$$\left.\frac{da}{dz}\right|_{z=-E+o} = \left.\frac{da}{dz}\right|_{z=-E-o} \tag{3b}$$

The symbol Im [ ] in (1) signifies the imaginary part of the quantity enclosed in the brackets while, in (2), δ is the Dirac delta function and, in (3a), $i = \sqrt{-1}$. Similarly, the vertically polarized temperature is given by

$$T_v(\theta,\nu) = |R_v|^2 T_{sky}(\theta,\nu) + 4\left(\frac{2\pi\nu}{c}\right) \cos\theta \int dz' \, T(z') \, \mathrm{Im}\left[K(z',\nu)\right] \left[\left|\frac{dB}{dz'} + \left(\frac{dK}{dz'} \Big/ K\right) B\right|^2 + \left(\frac{2\pi\nu}{c}\right)^2 \sin^2\theta \, |B|^2\right] \quad (4)$$

where R_v is the reflection coefficient for vertically polarized radiation and B is the value, at $z = 0$, of the solution of the differential equation

$$\frac{d^2b}{dz^2} - \left(\frac{dK}{dz} \Big/ K\right) \frac{db}{dz} + \left(\frac{2\pi\nu}{c}\right)^2 \left[K(z,\nu) - \sin^2\theta\right] b = -\delta(z - z') \quad (5)$$

satisfying the boundary conditions

$$\frac{db}{dz} - i\left(\frac{2\pi\nu}{c}\right) \cos\theta \; K(0,\nu) \, b = 0 \qquad \text{at} \quad z = 0 \quad (6a)$$

b is an outgoing wave as $z \to -\infty$ and, at the ice-water boundary,

$$b(-E + 0) = b(-E - 0)$$

$$\frac{db}{dz} \Big/ K(z,\nu)\Big|_{z=-E+o} = \frac{db}{dz} \Big/ K(z,\nu)\Big|_{z=-E-o} \quad (6b)$$

A practical numerical procedure for determining R_h , R_v , A , and B when $K(z,\nu)$ is known is discussed by Stogryn. The major problems that arise in the application of (1) and (4) to the calculation of the ice brightness temperature are the specification of the temperature profile $T(z)$ and the dielectric constant $K(z,\nu)$.

The dielectric constant of salt water ice is controlled by its temperature and rate of formation. The temperature is important because the brine (liquid phase) content of salt water ice varies rapidly with temperature and does not vanish even at temperatures well below the freezing point. In addition, the brine volume is dependent on both the salinity of the water from which the ice is formed and on the rate of growth of the ice. Thus, since the dielectric properties of brine differ markedly from those of water in the solid phase, the dielectric constant of saline ice may be expected to show considerable sensitivity to environmental conditions.

Because of the complex nature of sea ice, experimental determinations of its dielectric properties at microwave frequencies would be extremely desirable. Unfortunately, these do not seem to be available. Of the measurements which are known to the authors, those of Addison[2], who determined the dielectric constant at frequencies up to 100 MHz, appear to be the most comprehensive. While Addison's measurements were conducted at frequencies which are much too low to be used for quantitative studies in the GHz region of the spectrum, his results do indicate a strong dependence of the dielectric properties of saline ice on temperature and salinity.

In the absence of measured values, it is necessary to rely on a theoretical formula for the dielectric constant. Thus, we assume that saline ice may be treated as a mixture of pure ice and brine and consider the problem of calculating the dielectric constant of the mixture. From among the available formulas, all of which must be used with caution, that of Wiener[3], which has often been used in studies of ice and snow (see, e.g., Evans[4]) was chosen. According to Wiener's formula, the dielectric constant of the mixture is

$$K = \frac{K_b\, pU + K_i(1 - p)}{pU + 1 - p} \tag{7}$$

where

$$U = \frac{K_i + f}{K_b + f} \tag{8}$$

In (7) and (8) K_b is the dielectric constant of the brine, K_i the dielectric constant of pure ice, p the brine volume (ratio of the volume occupied by the brine to the total volume of a small sample of saline ice), and f a form number which is determined by the shape of the brine cells. Since brine cells are roughly rod-like in shape, f is expected to be large. However, its precise value has not been determined previously and it must be considered to be an adjustable parameter for the purposes of this study.

The two dielectric constants, K_b and K_i, appearing in (7) and (8) have been studied in the GHz portion of the electromagnetic spectrum. According to Cumming[5], the real part of the dielectric constant of pure ice is 3.15 and independent of the temperature. Available evidence also indicates that it is independent of frequency in the GHz range. The imaginary part of the dielectric constant of the ice is temperature-dependent. However, its value is small compared to that of water and, since the present state of knowledge does not warrant a more detailed treatment, an average value of 3×10^{-3} will be used. Thus, we have

$$K_i = 3.15 + 3 \times 10^{-3} i \qquad (9)$$

The dielectric constant of brine may be computed as a function of frequency using formulas of the Debye form (Stogryn[6]) when the salinity and temperature of the brine is known. Equations for computing the brine volume p from a knowledge of salinity and temperature of sea ice are given by Stogryn[7].

RESULTS OF CALCULATIONS

On the basis of these equations and the theory presented, calculations of the brightness temperature of sea ice have been performed for a number of different models. In all cases, the models consisted of a layer of ice of uniform thickness over sea water. The ice temperature and salinity were assumed to be -1.99°C and 4°/oo respectively, at the ice-water boundary. The choice of 4°/oo for sea ice salinity at the ice-water boundary is consistent with published values. Trial calculations were also undertaken for salinity values of 8 and 12°/oo. These gave the same results, indicating that this parameter is not critical in the computations. In the various models, the temperature profile of the ice was assumed to vary linearly from the ice-water boundary to the ice-air boundary. Different salinity profiles were investigated. These included linear profiles and profiles in which the salinity varied from its surface value to a value of 12°/oo at a depth equal to one-tenth of the ice thickness, from which point it decreased linearly to its final value of 4°/oo. Calculations were also performed for total ice thicknesses of 10, 20, and 100 cm. In all cases which were investigated, the brightness temperature varied by only a fraction of a degree from that computed for a 10-cm-thick layer of ice having a linear salinity profile. This result is understandable on the basis of the large loss tangent of sea ice whose thermal temperature is close to 0°C. Hence, although the results to be presented below refer specifically to linear salinity profiles in 10-cm-thick ice, they are representative of many more complex structures.

Figures 5 and 6 show the results of calculations for frequencies of 19.4 GHz (λ = 1.55 cm) and 37 GHz (λ = 0.81 cm). In all cases it is assumed that the radiometers are close to the surface and the brightness temperatures include the effects of a model Arctic summer atmosphere which is essentially consistent with known conditions prevailing during the aircraft measurements. Computations are shown only for $\theta = 45^{\circ}$ for 37 GHz since this was the antenna viewing angle of the aircraft instrument. The 19.4 GHz plots include both $\theta = 0^{\circ}$ and $\theta = 45^{\circ}$. It is apparent from the figures that a rather large range of brightness temperatures may arise as a result of either surface temperature changes or salinity variations. These changes are especially rapid near 0°C where the brine volume of the ice increases rapidly with temperature.

Estimates of the electromagnetic power skin depth δ (depth of penetration) in sea ice were also undertaken using Equation (10) and Wiener's dielectric mixing formula. Im denotes taking the imaginary part and λ is the 5, 10 and 20 parts per thousand and temperatures of -1 through -30°C for an observational wavelength of 1.55 cm, Figure 7. Skin depth values are given in terms of free-space wavelengths. These data clearly indicate the strong dependence of microwave emission by sea ice near 0°C on near-surface phenomena.

$$\delta = \frac{\lambda}{4\pi \, \mathrm{Im}(\sqrt{K})} \qquad (10)$$

COMPARISON OF MEASUREMENTS AND THEORY

The microwave emission characteristics of sea ice are dependent on several parameters. These include (1) ice temperature, (2) salinity, (3) density, (4) ice thickness, (5) liquid water content, (6) internal structure, (7) surface roughness and (8) snow cover or surface water (if present). A model of vertically structured media has been applied with reasonable success in calculating the effects at 13.4 and 37 GHz of (1), (2), and (4) on sea water ice grown under laboratory conditions[7].

However, as noted earlier direct quantitative comparisons of measured brightness temperatures obtained during the overflights with those predicted by the above model could not be made in the present study since no information regarding the salinity and general condition of the sea ice was available. Preliminary evaluations of microwave measurements obtained during the 1971 AIDJEX Expedition where ice surface temperatures averaged about -20°C indicate that the existing vertically structured media model cannot account for the emission characteristics of weathered ice. Hence, alternate mechanisms must be examined to explain the bi-modal results.

Several alternatives are offered. First, if it is assumed that increases in nonspecular surface scattering increase the emissivity of sea ice, then the brightness temperatures of the "high" emission sea ice type may arise from the more complex surface structure of the young ice. Likewise, the temperature of the "low" emission ice type would be due to the lack of nonspecular scattering associated with the "smooth" surface of weathered ice.

A second explanation may be offered using the results noted by Addison in his dielectric constant measurements of saline ice. Although the measurements were carried out at frequencies (20 Hz to 100 MHz) lower than microwave frequencies, the phenomena observed may be applicable to microwave frequencies. Addison found in several instances that as the sea ice was subjected to changes in temperature (-10 to -22°C) the real part of the dielectric constant increased significantly (by a factor of 2 in one case). The effect was not observed in all cases but did occur often enough to be noted. Thus, if we consider weathered ice as having been recycled, the presently observed low brightness temperatures of weathered ice ("low" emission ice types) may be due to an increase in the dielectric constant. The phenomenon may be associated with drainage of brine from brine pockets in the ice.

Finally, it should be noted that although volume scattering arising from volume inhomogeneities (e.g., brine pockets, air bubbles, etc., in the ice) may explain the observed phenomenon, lack of theoretical results precludes making general intuitive statements similar to those presented above. The primary reason for considering volume scattering effects arises in the analysis of laboratory grown saline ice (Stogryn[7]) where it was found that the principal discrepancy between theory and experiment occurred at temperatures near 0°C. It was conjectured that scattering by large brine pockets in the ice invalidated the description of the dielectric constant by the simple mixing formula due to Wiener.

Preliminary analysis of acquired 1971 Arctic microwave measurements indicate that a similar bi-modal classification of sea ice emission occurred. Since the 1971 measurements were performed on ice whose temperatures were much lower than those occurring in the 1970 measurements (Nordberg[8]) (-20°C in 1971 versus 0°C in 1970), variations in brine volume as described by the existing vertically structured media model in ice appear unimportant in explaining the bi-modal emission character. Clearly a more complex model than presently available is needed to understand this phenomenon.

CONCLUSIONS AND CURRENT ACTIVITIES

CONCLUSIONS

The ultimate goal of the research reported herein is the development of a practical microwave remote sensing technique(s) for synoptic aerial and/or satellite mapping of general ice type, ice-water boundaries, ice thickness and related physical properties (e.g., salinity, temperature and density) of Arctic sea ice. An initial step toward this goal has been an integrated research program consisting of (1) numerical modeling of sea ice emission and (2) analysis of recently acquired multifrequency airborne passive microwave measurements.

In (1) the theory of vertically structured media (which incorporates subsurface salinity and temperature gradients and neglects nonspecular scattering) was employed to establish the dependence of sea ice emission on salinity and temperature for several observational wavelengths (2.81, 1.55, 1.35, 0.96, and 0.81 cm) and view angles (0 and 45 degrees from nadir). Utilizing linear distributions of salinity and temperature, it was found that a relatively large range of sea ice emissions (or brightness temperature) may arise as a result of either surface temperature or salinity changes. The computed sea ice emission exhibited the largest changes at temperatures near 0°C. (This phenomenon is due to the fact that changes in the brine volume in ice are especially rapid near 0°C.)

In (2) it was found that the observed low altitude (150 m) brightness temperatures of sea ice generally fell into two distinct ranges corresponding to "high" (240°K) and "low" (200°K). Since no "surface-truth" data were taken during the 1970 Arctic flights, photographic and laser data were utilized to identify the ice types. From all indications, the high and low brightness temperatures were respectively, young unweathered ice (thought to have formed within the past month or so) and relatively old ice which appeared to have undergone weathering (surface melting and refreezing). The contrast in brightness temperature between the two ice types decreased significantly as the observational wavelength increased. The mechanisms responsible for this phenomenon were not isolated during the first phase of this study although several possibilities were identified. A significant contrast in the brightness temperatures of ice and water was observed at all wavelengths greater than (or equal to) 0.81 cm. The contrast apparently increased with wavelength and was largest at 2.81 cm.

In summary, the present study presents rather encouraging prospects for aerial synoptic mapping of ice-water boundaries and identification of gross ice types (e.g., "young" versus "old") using passive microwave measurements.

CURRENT ACTIVITIES

Work is continuing toward development of an adequate numerical model of sea ice emission. This work is being guided by the aircraft and sea ice observations obtained during the 1971 AIDJEX Expedition. Modeling activities are focused on the effects of scattering due to brine cells, bubbles, crystal structure, surface roughness, etc.

REFERENCES

1. Stogryn, A., "The Brightness Temperature of a Vertically Structured Medium," Radio Science, Vol. 5, No. 12, pp 1397-1406, Dec. 1970.

2. Addison, J., "Electrical Properties of Saline Ice," J.A.P., Vol. 40, pp 3105-3114, 1969.

3. Wiener, O., "Leipziger Berichte," 62, p. 256, 1910.

4. Evans, S., "Dielectric Properties of Ice and Snow – A Review," J. of Glaciology, Vol. 5, pp 773-792, 1965.

5. Cumming, W., "The Dielectric Properties of Ice and Snow at 3.2 Centimeters," J.A.P., Vol. 23, pp 768-773, 1952.

6. Stogryn, A., "Equations for Calculating the Dielectric Constant of Saline Water at GHz Frequencies," IEEE Trans. MTT, Aug. 1971.

7. Stogryn, A., "The Brightness Temperature of Sea Ice," Interoffice Memo, Aerojet-General Corp., El Monte, Calif., 1970.

8. Nordberg, W., et al, "Measurements of Microwave Emission from a Foam Covered, Wind Driven Sea," NASA preprint X-650-70-384, 1970.

Table I

MICROWAVE RADIOMETERS FLOWN ON 1970 CV-990 MISSION
(all radiometers horizontally polarized unless otherwise noted)

Frequency (GHz)	Wavelength (cm)	View Angle (from Nadir)	3-dB Beamwidth (Deg)	RMS[3] (ΔT) (^{o}K)	Integ. Time (Sec)	Primary Experimentor
19.35[1]	1.55	$\pm 50^{o}$	2.8	1.40	0.025	GSFC/AGC
22.235	1.35	0^{o}	10	0.3	2	MIT/JPL
31.4	0.955	0^{o}	10	0.4	2	MIT/JPL
53.65	0.559	0^{o}	10	1.2	2	MIT/JPL
54.90	0.546	0^{o}	10	0.6	2	MIT/JPL
58.80	0.510	0^{o}	10	0.7	2	MIT/JPL
9.3	3.23	180^{o}	13	1.0	1	JPL
10.69	2.81	0^{o}	7	0.6	2	JPL
31.4	0.955	180^{o}	10	0.9	1	JPL
37.0[2]	0.811	45^{o} left	5	0.5	Variable 0.01-1.0	AGC

1. Electrically scanned radiometer.

2. 37 GHz radiometer positioned 45^{o} above nadir to the left of the aircraft, dual polarized.

3. RMS values are given for one second integration time.

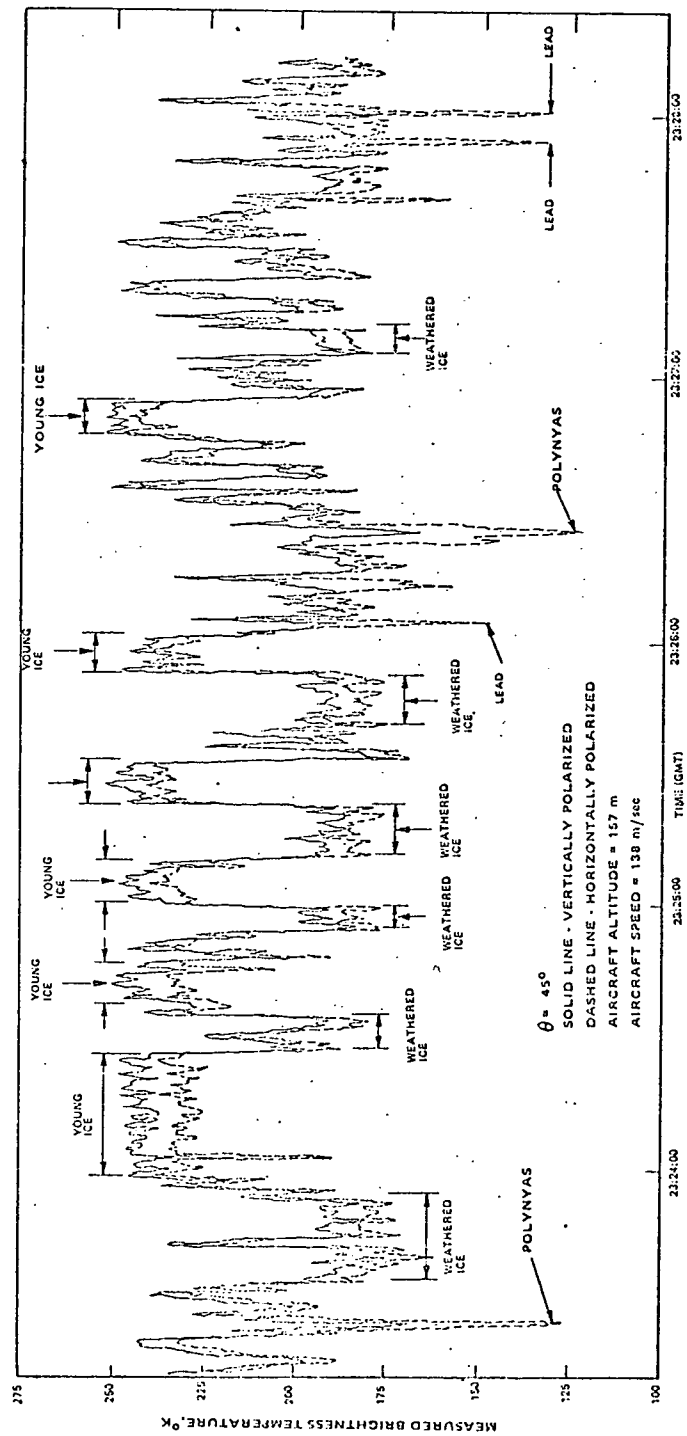

Figure 1. 8.1 mm (37 GHz) Brightness Temperature Measurements of Arctic Sea Ice, 11 June 1970

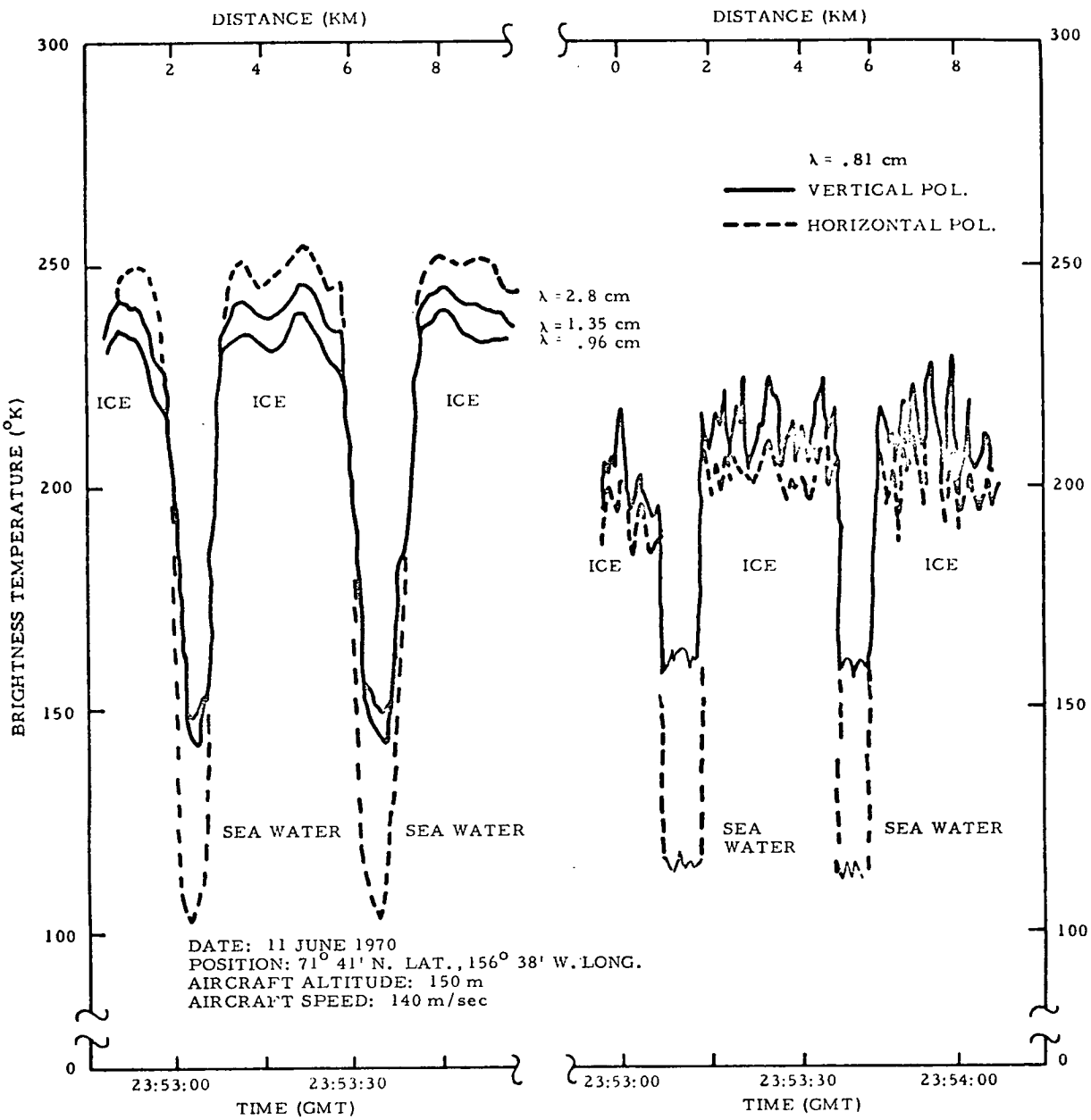

Figure 2. Typical Brightness Temperature Profile Across Ice and Sea Water.

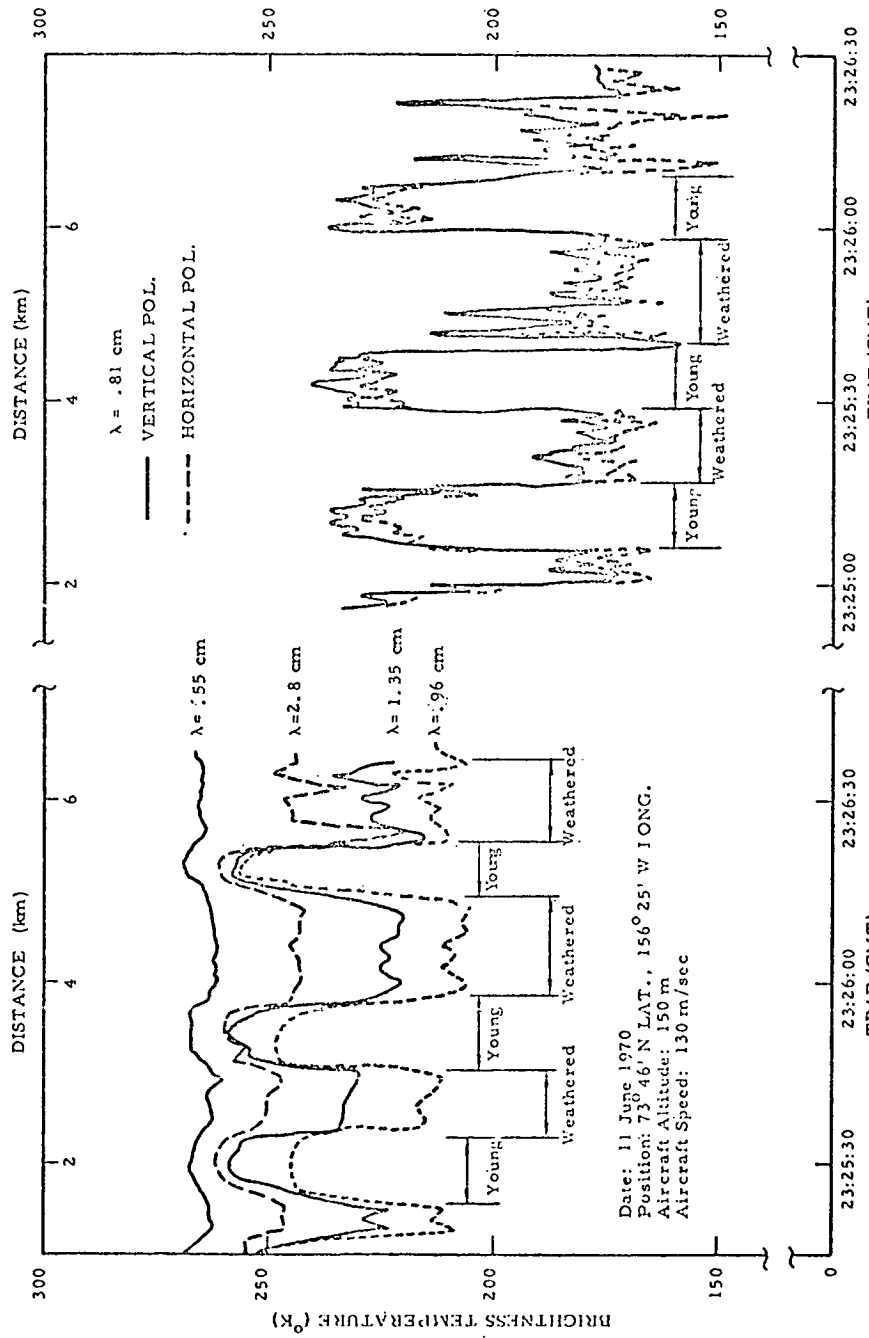

Figure 3. Typical Brightness Temperatures of "Young" and "Weathered" Ice Types

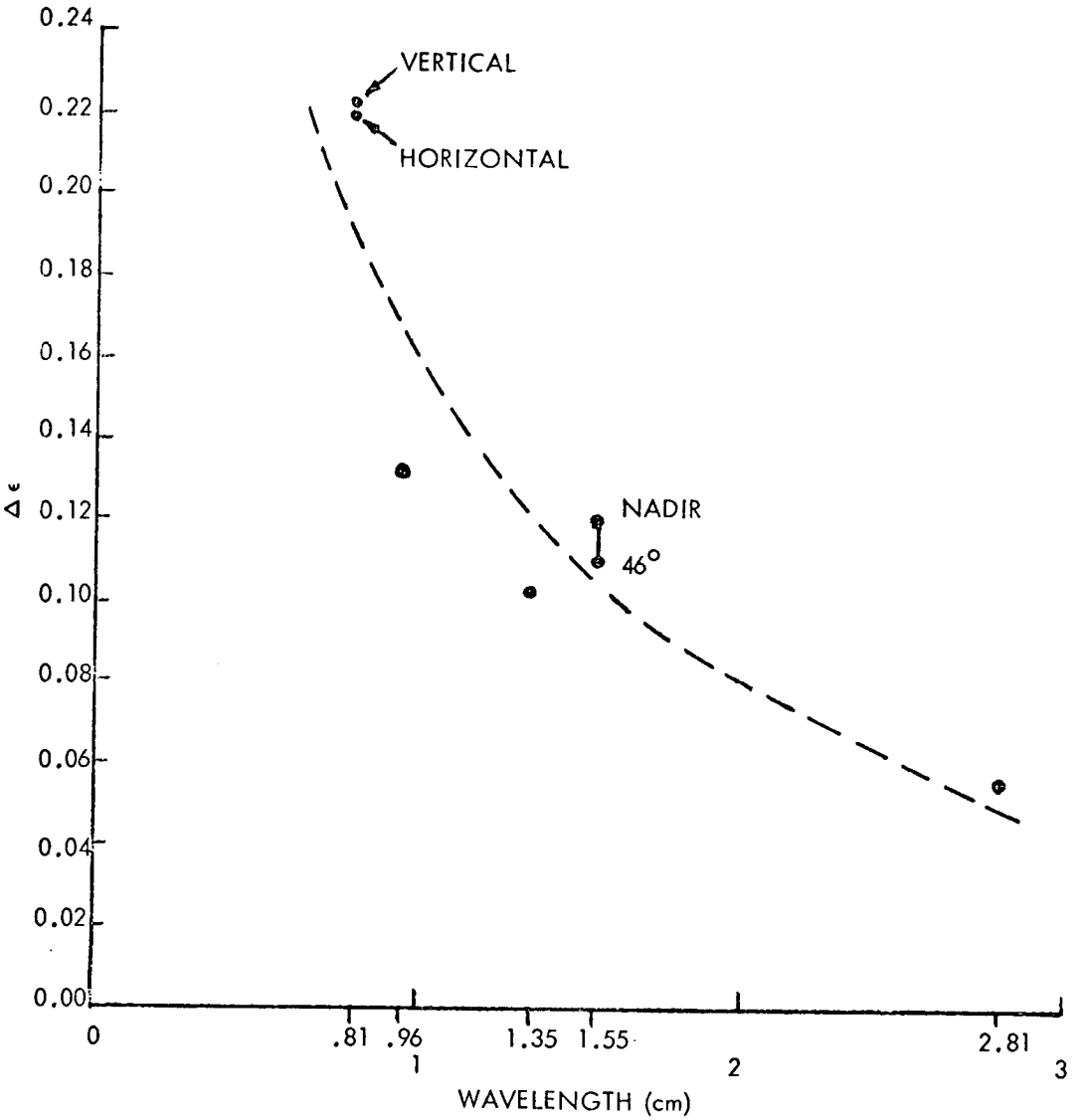

Figure 4. Change in Emissivity $\Delta\varepsilon$ for Two Ice Types Versus Observational Wavelength.

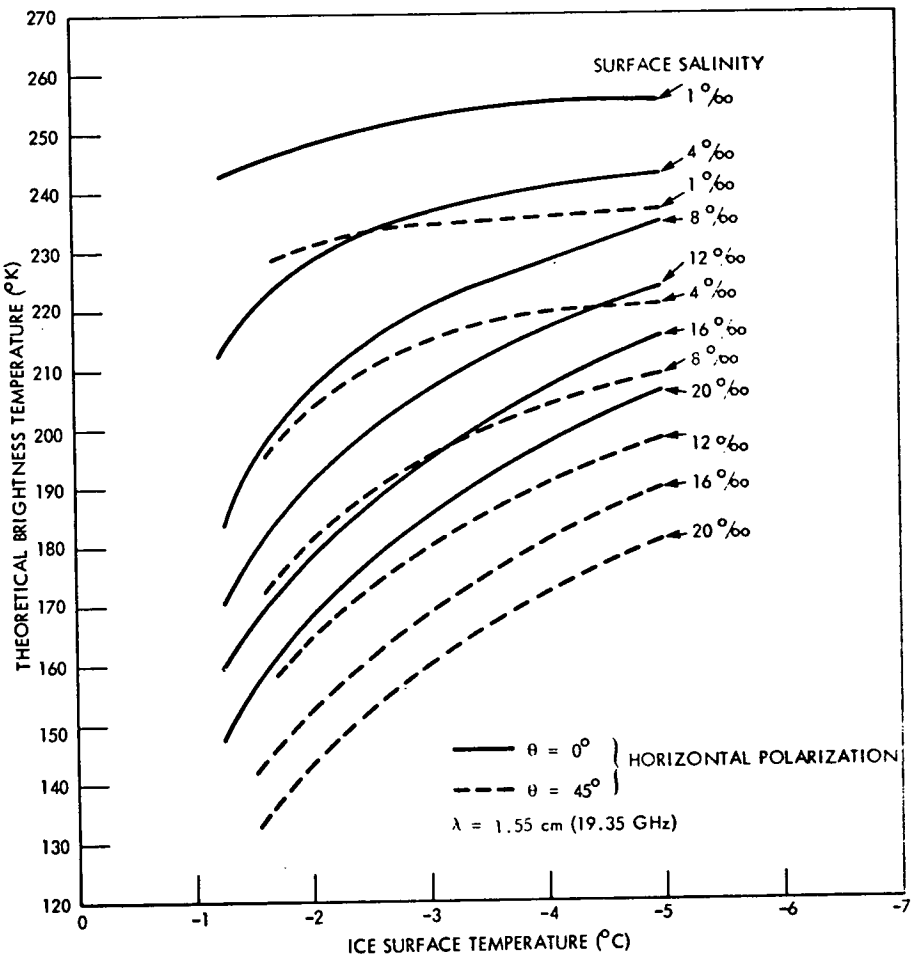

Figure 5. Brightness Temperature versus Ice Surface Temperature for Various Surface Salinities (λ = 1.55 cm)

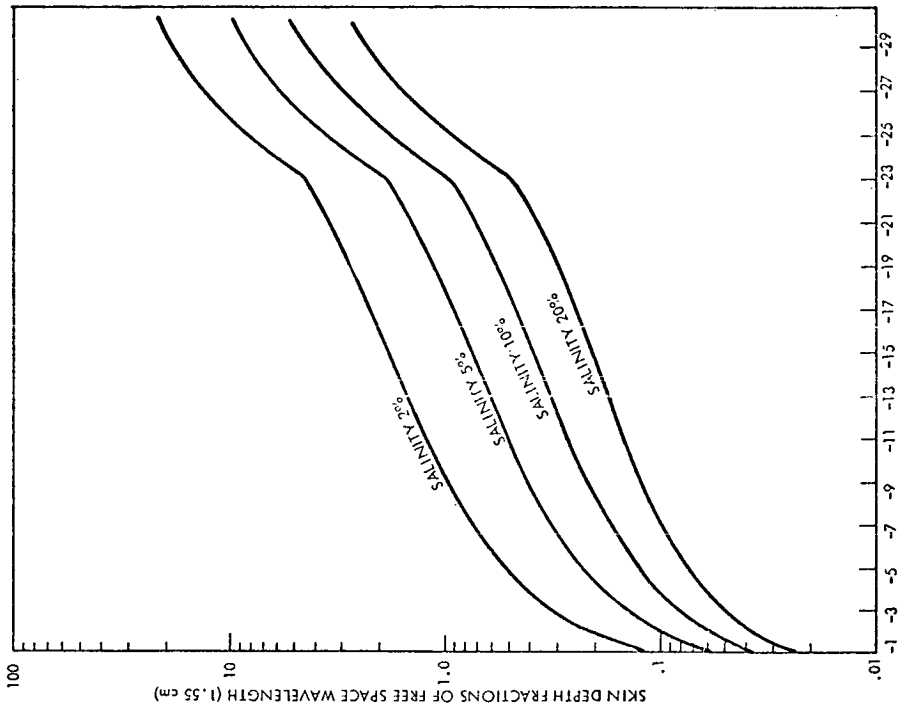

Figure 7. Skin Depth versus Sea Ice Temperature for Various Brine Concentrations, λ = 1.55 cm

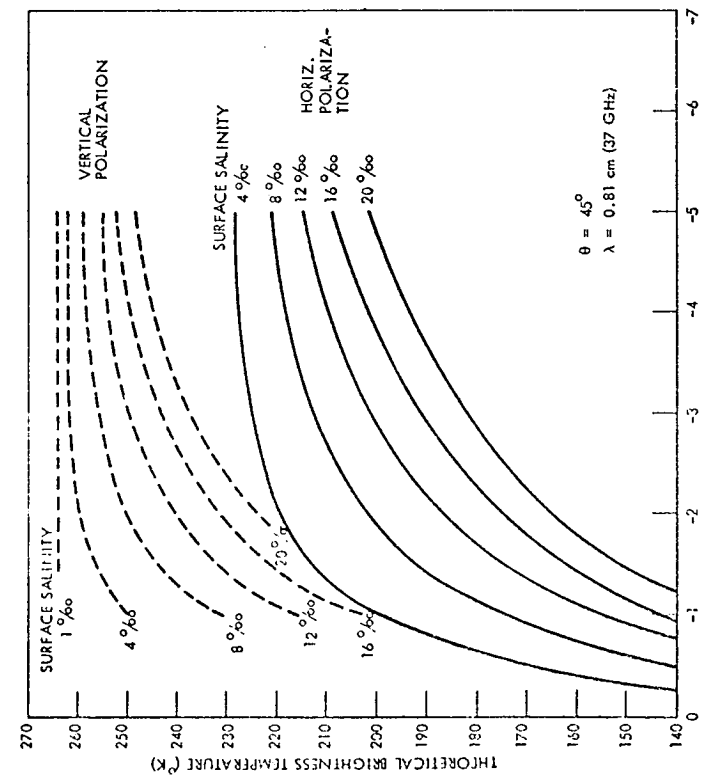

Figure 6. Brightness Temperature versus Ice Surface Temperature for Various Surface Salinities (λ = 8.1 mm)

SECTION 90

REGIONAL STUDIES USING SEA SURFACE TEMPERATURE FIELDS DERIVED FROM SATELLITE INFRARED MEASUREMENTS

by

Alan E. Strong
National Oceanic and Atmospheric Administration
Washington, D. C. 20031

INTRODUCTION

With the launching of several earth-orbiting satellites carrying infrared (IR) radiometers, it has now become possible to detect structure in sea surface temperature (Tss) distributions under relatively clear sky conditions. A number of studies (Rao, 1968; Curtis and Rao, 1969; Smith et al., 1970; Warnecke et al., 1971; Rao et al., 1971) have shown Tss distributions over both small and large areas by means of satellite IR information. This report shows three informative examples of Tss distributions over the western Atlantic which were detected by means of data from the scanning radiometer on the Improved TIROS Operational Satellite-1 (ITOS-1). This satellite series, replacing the ESSA series, became operational with NOAA's environmental satellite NOAA-1, launched in December 1970.

DIRECT READOUT INFRARED (DRIR) OCEANOGRAPHIC DISPLAY

ITOS-1, launched 23 January 1970, was designed to provide 12-hr coverage (day and night) of the entire surface of the earth, principally for meteorological purposes. The scanning radiometer (SR) has a visible and an IR channel, the latter measuring radiation in the 10.5-12.5 μm wavelength region. When the radiometer is looking straight down at the Earth's surface, the area instantaneously viewed is about 7.5 km in diameter.

These radiation measurements are temporarily stored on board the satellite for later transmission to the ground and for subsequent global mapping. For the convenience of those within transmission range of the satellite, the SR also transmits data for immediate local use directly to Automatic Picture Transmission (APT) ground stations. The IR transmission is known as Direct Readout Infrared (DRIR). Data obtained from the DRIR can be displayed on a photofacsimile recorder

to produce a continuous strip image of infrared radiance over the local area. When used properly this pictorial display can be very useful for immediate qualitative interpretation of thermal conditions. The two examples presented here have been processed to make visible the horizontal temperature gradients on the ocean surface. The gray-scale representation chosen encompasses only temperatures ranging from 0 to 30C. All cooler surfaces, such as clouds, snow and ice and much of the land surface, appear white (less radiant energy reaching the satellite), while warmer surfaces appear progressively darker. Quantitative values can be obtained by generating a calibrated gray scale wedge and comparing it with the picture, or by using a computer printout of the calibrated temperature values at grid points. In the examples presented here, each gray scale interval represents a temperature change of approximately 1C.

A GULF STREAM MEANDER OFF CAROLINAS

Figure 1 is a DRIR image obtained about 0900 GMT 15 February 1971 from ITOS-1. Some of the prominent features of this thermal image are the Florida Peninsula and the Gulf Stream. The main thermal front on the northern edge of the Gulf Stream, and the meanders along the thermal front between Charleston, S. C., and Cape Hatteras are dramatic. Three distinct gray shades, indicative of three thermal regions, can be seen as far south as the coast of Georgia. Farther south only two such regions are discernable. A similar separation in the Middle Atlantic bight region, showing three different water masses, has been shown by Rao et al. (1971), using October 1970 ITOS-1 DRIR data. The near-black area corresponds to the Gulf Stream, and the dark gray and light gray areas, just north of the Stream, correspond to the intermediate slope water mass the cooler shelf water mass, respectively. Clouds obscure the warm water of the Stream in the Florida straits. Meanders in the Gulf Stream boundary are evident just east of Cape Romain and Cape Lookout. The same features, seen in the ITOS-1 DRIR data on the following day, persisted until late February.

The analyzed Tss over a portion of the area depicted in Fig. 1 is shown in Fig. 2. Some appropriate geographic locations and gridding has been provided.

EDDIES FORM AS THE MEANDER BREAKS DOWN

Two weeks later a dramatic change occurred in the meander region of the Gulf Stream. Through breaks in overlying clouds, it was noticed in the satellite pictures that a cold eddy had started to detach from the colder water. Following the passage of a cold front the area became free of clouds on 5 March 1971. Figure 3 shows the ITOS-1

DRIR image for this day. The DRIR analysis, shown in Fig. 4, shows 18-20°C slope water being injected into 24-25°C Gulf Stream water. Three break-off eddies are visible along the northern edge of the Gulf Stream. Two, immediately east of Cape Romain and Cape Fear, are very well defined; the northernmost eddy is small and barely visible.

Because of general overcast conditions in the area, it was not possible to establish a good history on the development of these eddies during the 18-day period between the days on which these two DRIR images were acquired. Continued monitoring of ITOS-1 IR data indicated no evidence of these eddies in the same general area during a 10-day period subsequent to 5 March, nor did the meander pattern become re-established.

These eddies along the Gulf Stream boundary occur in a region of strong shearing action between the relatively slow moving slope water and the fast moving main Gulf Stream. It is possible that they are related in some way to the bottom topography or the coastline configuration. Strong, 50-kt westerly winds, associated with an intense storm that crossed the region on 4 March 1971, were reported by two ships in the vicinity of these eddies. It seems likely that these winds caused extreme stress on the ocean surface and so played a major role in the thermal structure shown in Fig. 4. The occurrence of these eddies downwind of the Carolina Capes may be more than just coincidence.

A STRONG CYCLONIC EDDY IS DISCOVERED IN THE WESTERN SARAGASSO SEA

SATELLITE OBSERVATIONS

On 12 April 1971 the NOAA-1 satellite's early morning pass (approximately 0900 GMT) viewed the Eastern United States. Much of the Eastern Seaboard was cloudfree. The scanning-radiometer provided thermal infrared imagery that revealed an intricate Gulf Stream structure, including a large meander to the north off Cape Hatteras. The DRIR data from the satellite has been displayed as above for the higher temperatures of the ocean scene in Fig. 5. The analysis of Tss accompanies the imagery in Fig. 6.

Most interesting is the meandering Gulf Stream that is present with not only a strong multi-stepped northern gradient but also a moderate thermal gradient on the Saragasso side. Another stream of warm water appears to joint (or diverge from) the Gulf Stream just southeast of Cape Hatteras. Although this structure is interesting to investigate of itself, as it may be related to the eddy, we were concerned with the cooler regions of water on the Saragasso side, primarily the cool area centered at approximately 33N, 73W.

During the following two days additional NOAA-1 DRIR data were acquired. They showed virtually an identical system. From Fig. 6 it can be seen that surface temperatures in the cooler area were near 16°C whereas the Gulf Stream to the west was running approximately 8°C warmer.

SHIP OBSERVATIONS

In May 1971 the existence of the suspected eddy was confirmed on cruise 98 of the University of Rhode Island R/V TRIDENT. This work was coordinated by Chief Scientist Philip L. Richardson. On May 11 the eddy was found 180 miles southeast of Cape Hatteras at 32° 47'N, 73° 27'W, in the area indicated by the satellite. It was characterized by a strong surface cyclonic circulation, cooler surface temperatures and a cold deep core. This feature appears similar to Gulf Stream rings that have been reported by Parker (1972). In the center of the eddy, surface temperatures were about 19°C, three degrees cooler than normally found in this location and time. Surface temperatures were warmer than the April measurements in Fig. 6. The May satellite data, however, are in agreement with this increase in temperature. The ship surface temperatures were measured with a bucket thermometer.

The surface current speeds in the eddy ranged from near zero in the central region to a maximum of 3.0 knots at a distance of 50 miles from the center. As a comparison to these note that the Gulf Stream has speeds of 4.0 knots. Thus, there was an apparent decrease in surface velocity from the time the eddy broke from the Gulf Stream.

The subsurface features of the eddy were explored by bathythermographs (BT) and hydrocast. Fig. 7 shows a BT cross-section that is a composite of March 1971 soundings along the track AB shown in Fig. 8. Although the March cross section is fortuitous, since there was no knowledge of the feature then, the cross section is similar to the more intensive survey results from the TRIDENT. These results will be published soon.

In May shape of the eddy appeared to be elliptical with the major axis at about 025° true. The ellipticity is apparent in the satellite data, the surface bucket data and from the BT data. The size of the eddy based on the location of the 15C isotherm at 500 meters was approximately 35 by 65 miles. The diameter based on the distance from the center of the eddy to the zero velocity line between the Gulf Stream and the eddy was 85 miles.

TRACKING THE EDDY

We are attempting to continue the observations of this eddy by use of satellite, plane and ship. The observations to date can be seen in Fig. 8 and indicate the eddy is moving southwest at about one mile per day. The eddy was relocated in October 1971 on the TRIDENT and again in January 1972 by the USNS WILKES. A search of all available surface temperatures and BT data is contiuing. Several cruises are scheduled during early 1972 into the eddy as it drifts onto or along the edge of the Blake Plateau.

The U. S. Naval Oceanographic Office reports one BT in the eddy in July 1971. It is suggested that all of these observations are of the same eddy and that this might possibly be the same eddy as reported near 36.5°N, 69.0W in October 1970 by the U.S. Naval Oceanographic Office (Gemmill and Gotthardt, 1971). Thus there exists the possibility that the eddy has been followed for at least ten months and perhaps as long as 15 months.

CONCLUSIONS

Gulf Stream associated eddies and meanders have been discovered and tracked through the coordinated use of satellite and ship. The concerted use of ship and satellite has provided an excellent method of studying large scale thermal features and offers a system approach to oceanographic persuits that makes for much more effective use of expensive ship operations.

REFERENCES

1. Rao, P. K., 1968: Sea surface temperature measurements from satellites. Mariners Wea. Log, 12, 152-154.

2. Curtis, W. R., and P. K. Rao, 1969: Gulf Stream thermal gradients from satellite, ship and aircraft observations. J. Geophys. Res., 74, 6984-6990.

3. Smith, W. L., P. K. Rao, R. Koffler and W. R. Curtis, 1970: The determination of sea-surface temperature from satellite high resolution infrared window radiation measurements. Mon. Wea. Rev., 98, 604-611.

4. Warnecke, G., L. J. Allison, L. McMillin and K. H. Szekielda, 1971: Remote sensing of ocean currents and sea surface temperature changes derived from the Nimbus II satellite. J. Phys. Oceanogr., 1, 45-60.

5. Rao, P. K., A. E. Strong and R. Koffler, 1971: Gulf Stream and middle Atlantic bight: Complex thermal structure as seen from an environmental satellite. Science, 173, 529-530.

6. Parker, C. E: Gulf Stream rings in the Saragasso Sea. Deep Sea Research, in press, 1972.

7. Gemmill, W., and G. A. Gotthartd: Formation and movement of a Gulf Stream meander. Paper presented at the April 1971 American Geophysical Union Meeting in Washington, D.C.

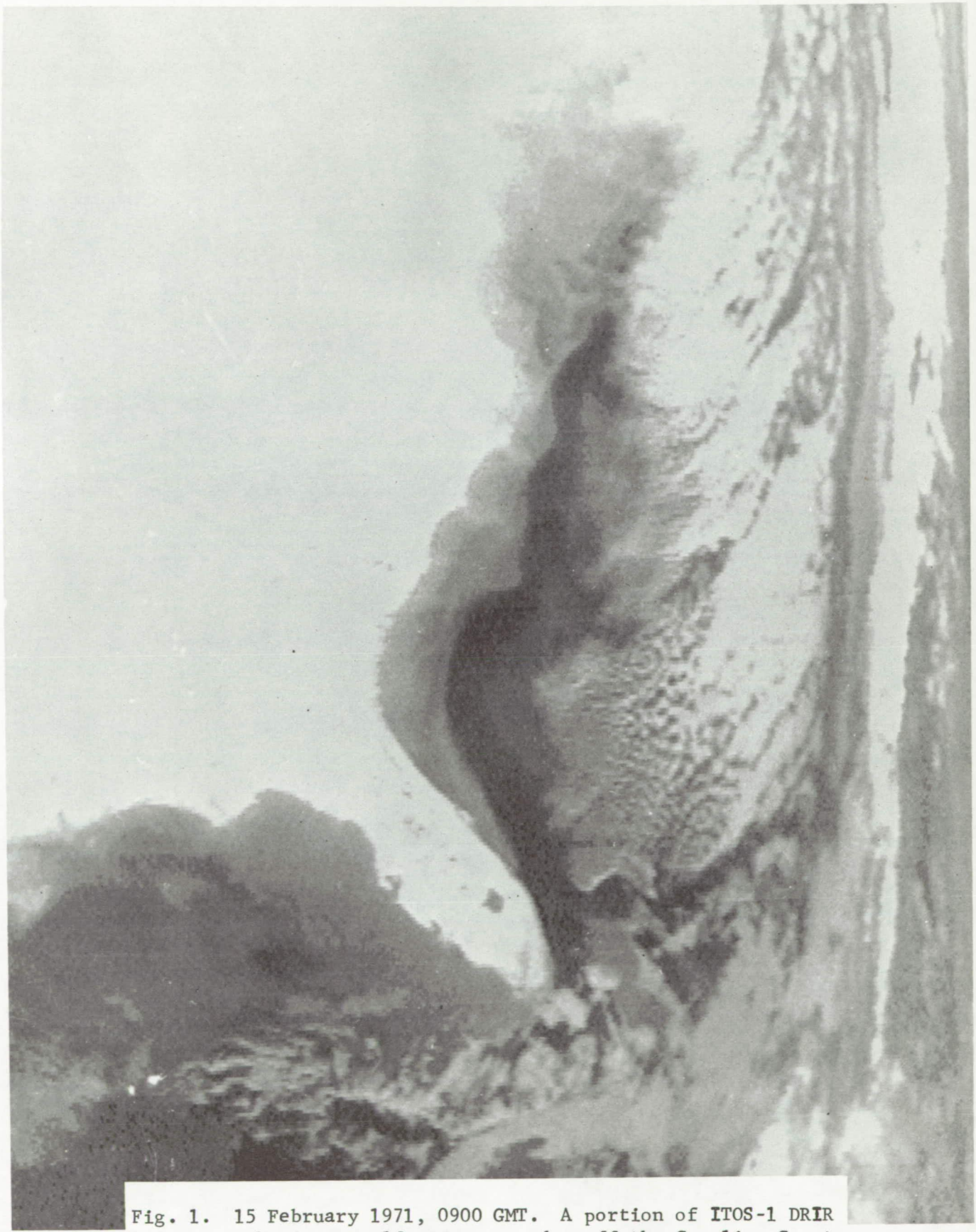

Fig. 1. 15 February 1971, 0900 GMT. A portion of ITOS-1 DRIR imagery showing a gulf stream meander off the Carolina Coast.

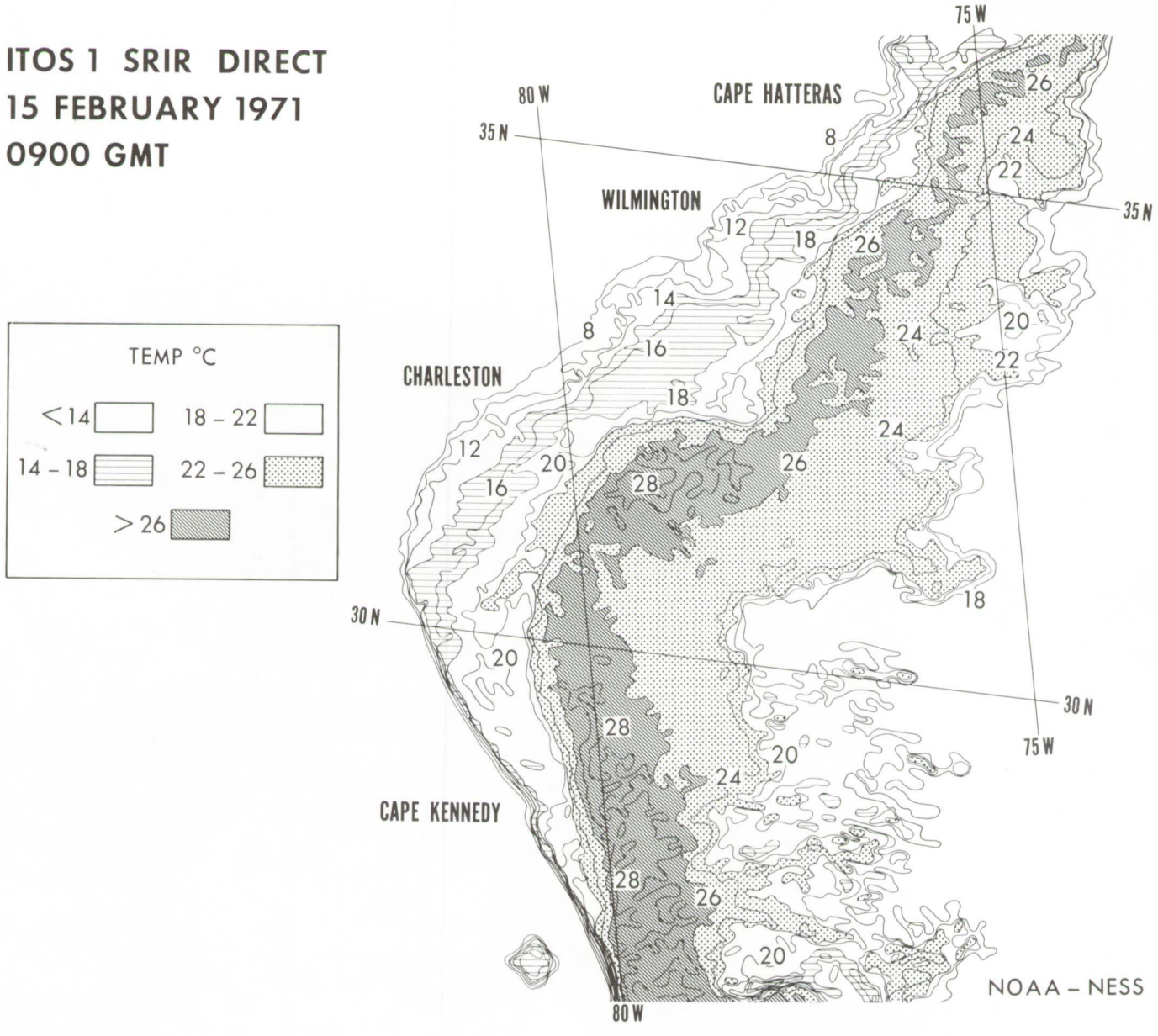

Fig. 2. T_{ss} analysis of a portion of Figure 1.

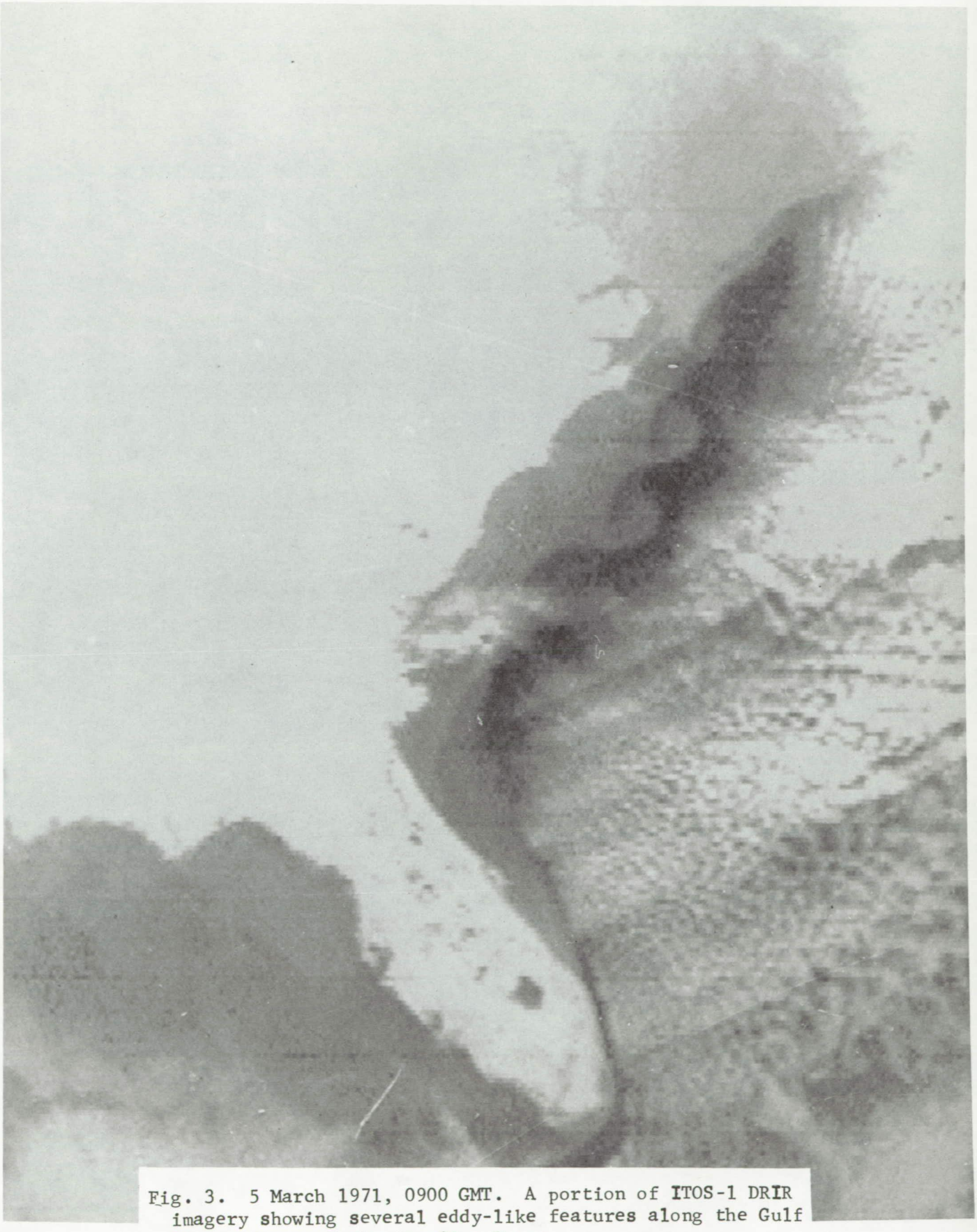

Fig. 3. 5 March 1971, 0900 GMT. A portion of ITOS-1 DRIR imagery showing several eddy-like features along the Gulf Stream front of the Carolina Coast.

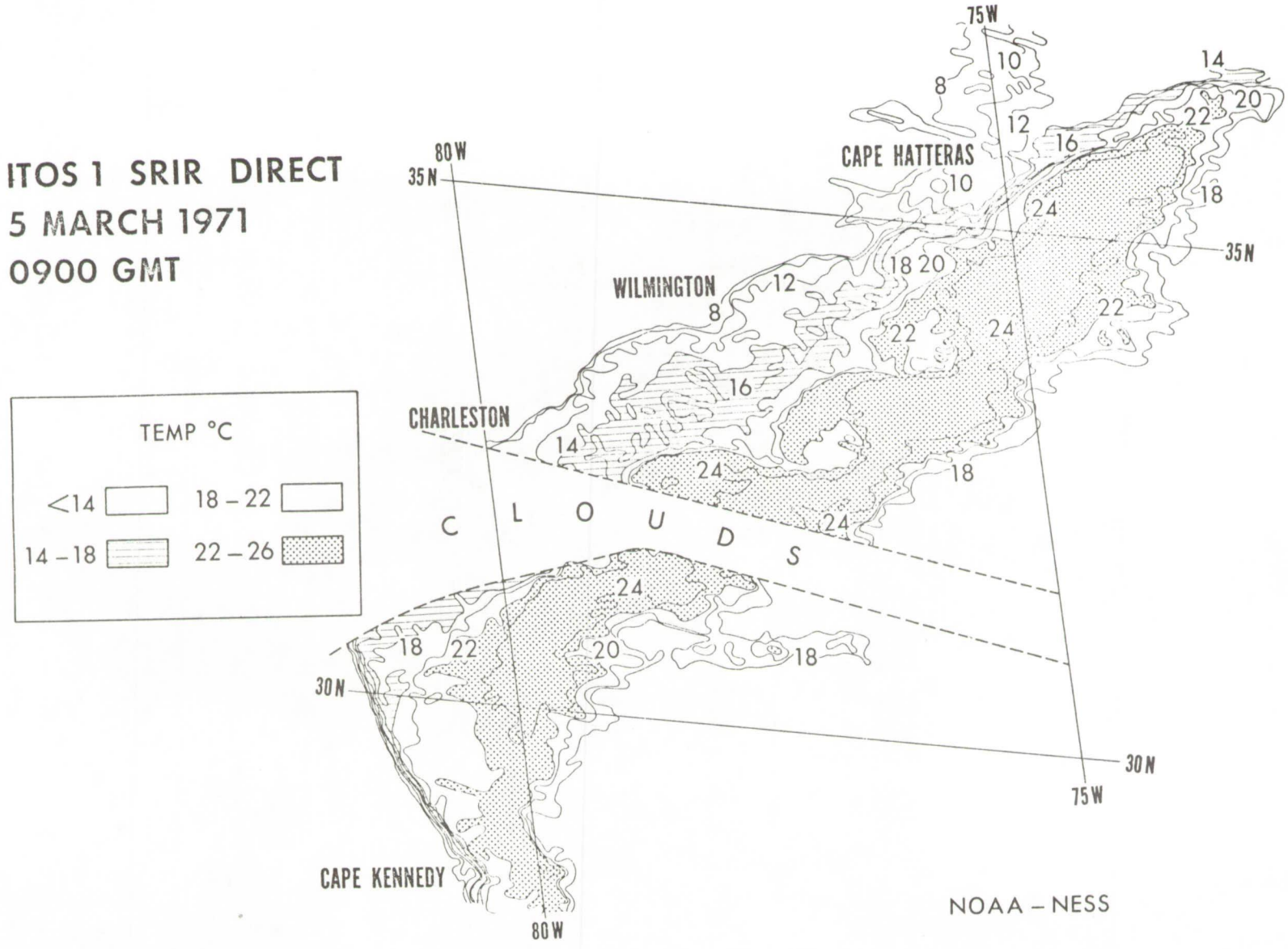

Fig. 4. T_{ss} analysis of a portion of Figure 3.

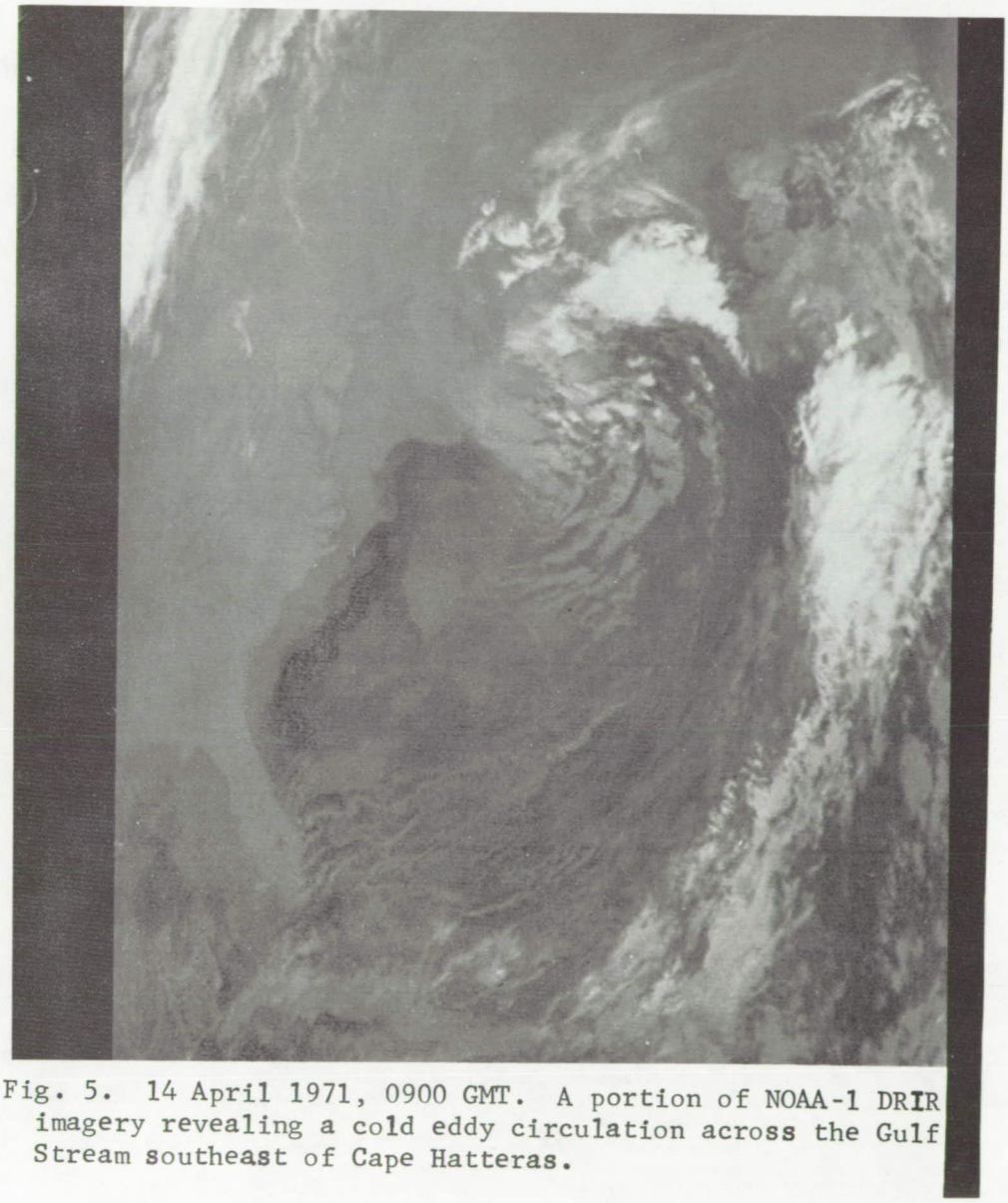

Fig. 5. 14 April 1971, 0900 GMT. A portion of NOAA-1 DRIR imagery revealing a cold eddy circulation across the Gulf Stream southeast of Cape Hatteras.

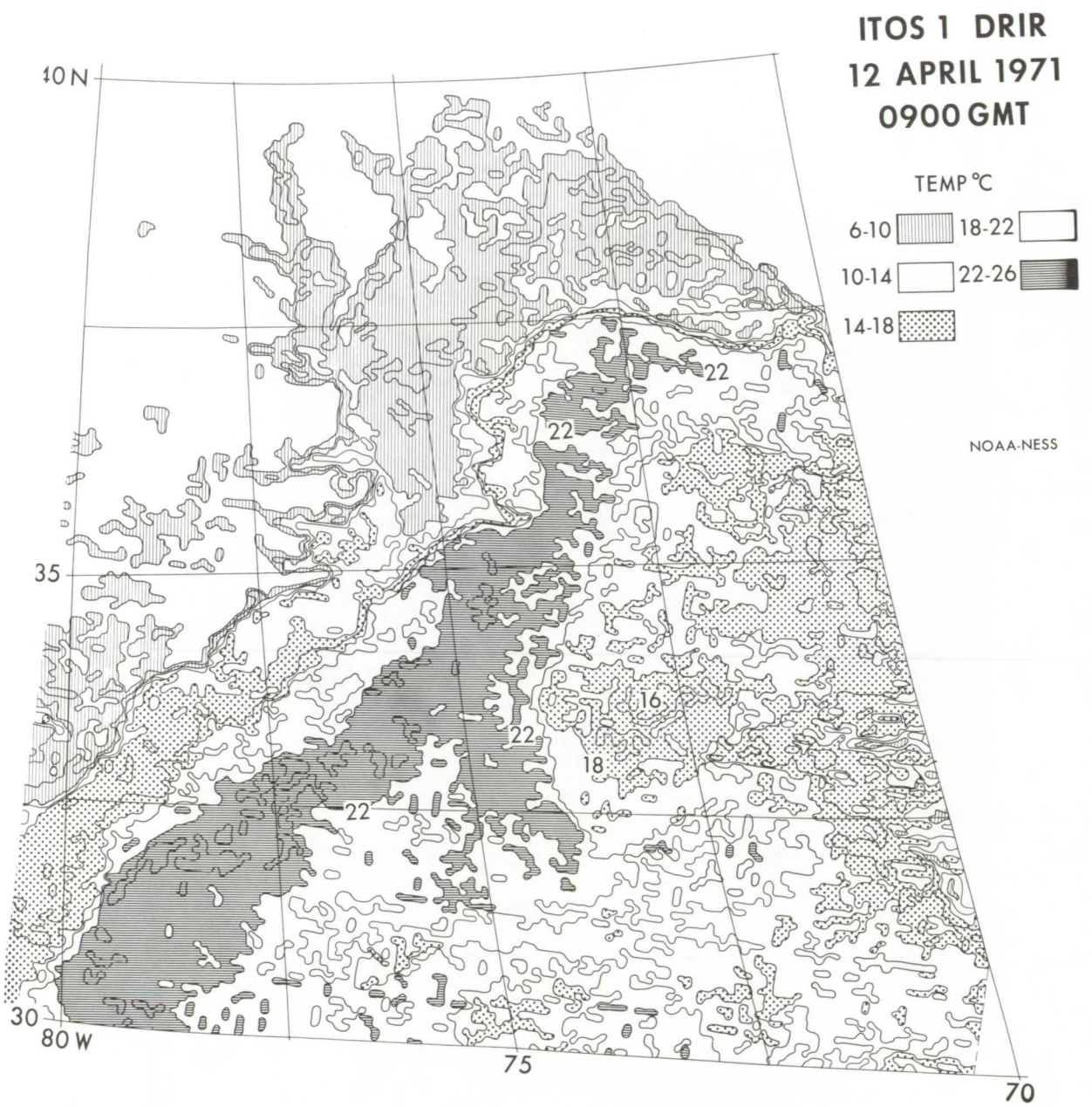

Fig. 6. T_{ss} analysis of a portion of Figure 5.

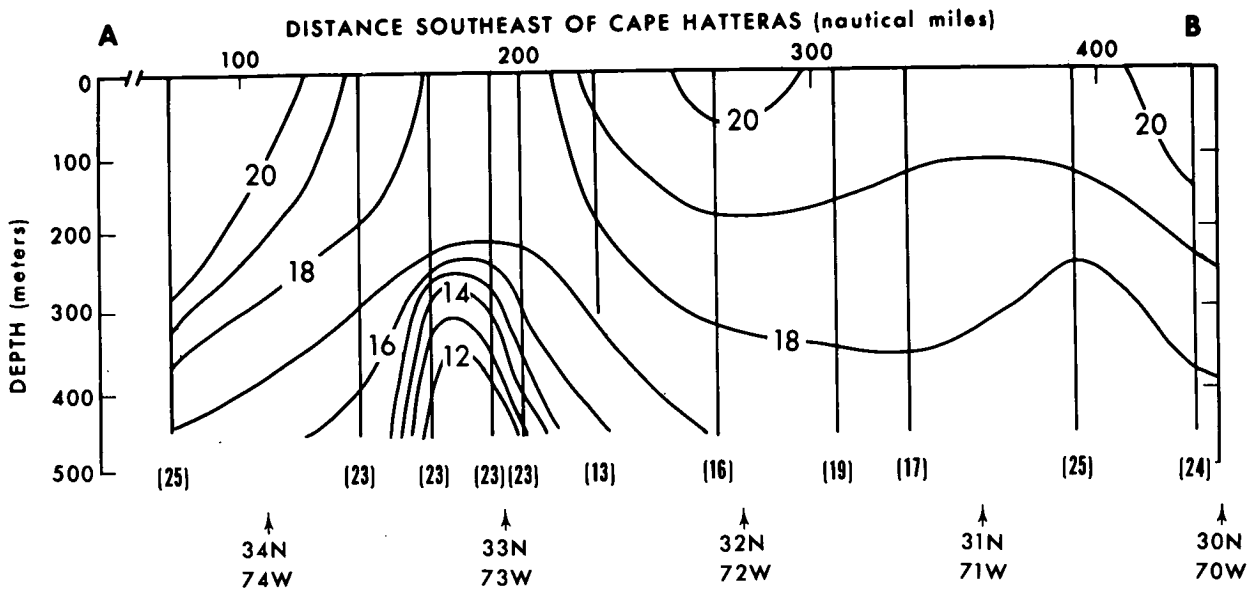

Fig. 7. BT composite cross-section for mid-March 1971 along the AB transect shown in Figure 8. BT depths are shown by vertical lines. Date for each cast is noted at bottom of sounding.

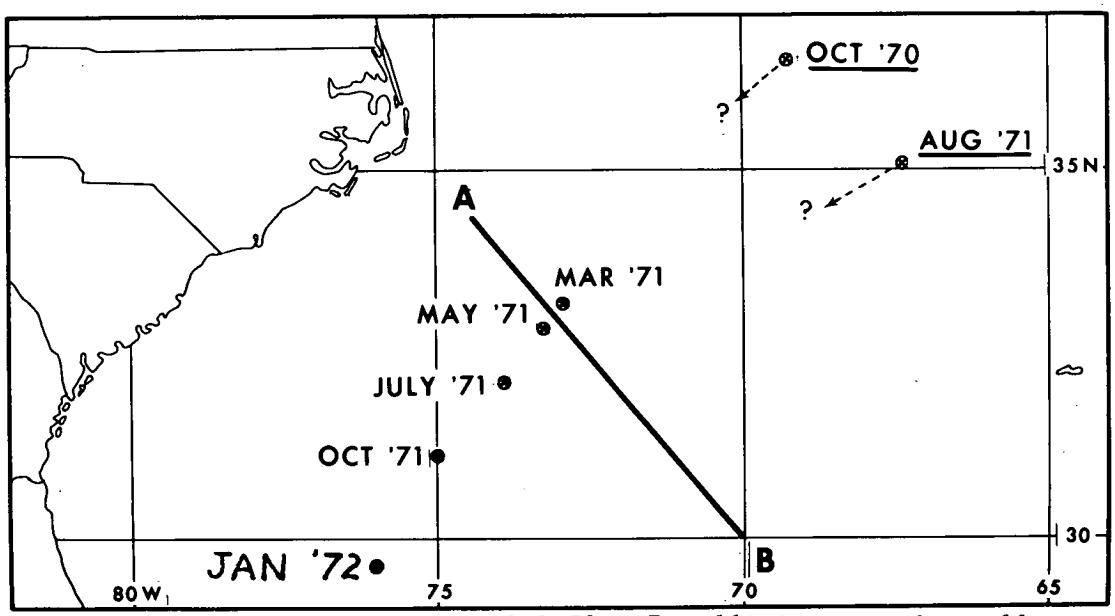

Fig. 8. Cold eddy history 1970-72. In addition, another eddy location is shown for August 1971. AB transect is shown in Figure 7.

SECTION 91

FISHERIES RESOURCE IDENTIFICATION AND ASSESSMENT STUDIES

by

William H. Stevenson
Remote Sensing Program
National Oceanic and Atmospheric Administration
National Marine Fisheries Service
Bay Saint Louis, Mississippi 39520

INTRODUCTION

With the establishment of a Fisheries Engineering Laboratory at the Mississippi Test Facility in 1970, the NMFS fisheries resource identification and assessment studies gained considerable momentum. These studies are an integral part of a broad program designed to accelerate the application of advanced technology to fisheries resource assessment, development and prediction. Program coordination activities were shifted from the Space Oceanography Program of NAVOCEANO to the National Environmental Satellite Service as part of NOAA in October 1970. Program activities in remote sensing have continued in several areas. (Figure 1). These areas are the development of low-light-level image intensifiers, spectrometers, aerial photography, and lasers for the location, identification and quantification of living marine resources at or near the sea surface. Other studies have included the development of a biologically controlled impoundment for remote sensor investigations and limited activities in fish oil film research. In addition to these remote sensing studies, the NMFS program at MTF is participating in space oceanography studies related to fisheries and in the ERTS-A and Skylab experiments. This report will deal with those aspects of the NMFS program related to fisheries resource identification and assessment during the period 1970 and 1971.

RESULTS AND DISCUSSION

FISH OIL FILM STUDY

Development of techniques to locate and identify fish oil films on the surface of the ocean were terminated in 1971 with the conclusion of a feasibility study conducted by Government Systems Division, Baird Atomic, Inc. Although these studies indicated a measurable reflectance

of the materials tested, it was considered as being impractical to continue instrumentation development until such time as the understanding of the biological structure of fish oil films was established. Up to the present time, we have been unable to collect or isolate biologically generated fish oil films on the surface of a body of water. Studies are presently being initiated at MTF to establish the feasibility of generating fish oil slicks under controlled laboratory conditions. As this technique is developed, instrumentation tests to sense these films will be reinitiated. A part of the study being conducted at MTF includes an attempt to understand the relationship, if any, between naturally formed fish oil films and the occurrence of stocks of fish.

SPECTROMETRIC FISH LOCATION

Experiments of the TRW Systems Group marine resource spectrometer were successfully concluded in November 1971. These experiments, conducted over a period of several years, strongly suggest that the location and identification of fish stocks at the surface of the water will require spectrometers of a different configuration than the one utilized in these experiments (Figure 2). As reported by TRW, "Spotting fish on an instantaneous basis using a spectrometer mounted on an airborne platform is not recommended." They continue, "If additional studies are to be pursued for the development of a stock assessment and management tool, TRW recommends an instrument utilizing a selectable differential wave band technique." The NMFS is continuing investigations in the application of spectrometers to living marine resources by conducting an inhouse investigation of the physical and biological criteria necessary to spectrometrically locate and identify fish stocks at the surface of the ocean.

PHOTOGRAPHIC IMAGERY

Investigations of the application of photographic imagery as a tool for assessing living marine resources continues at MTF in cooperation with the NMFS Pascagoula Fisheries Laboratory and the NASA Earth Resources Laboratory also located at MTF. Photographs obtained in the Northern Gulf of Mexico in the summer of 1971 are being analyzed to establish reference keys and procedures for the interpretation of aerial imagery of fish schools. This project is not attempting to advance the state of the art of aerial photography. It is being conducted to determine discrete reference keys which can be utilized in resource assessment by the evaluation of aerial photography. Photographs are being analyzed to determine optimum heights of operation and to identify unique schooling characteristics which will assist in the determination of fish school type.

REMOTE SENSING TEST FACILITY

Success in the application of remote sensing instrumentation to living marine resources has been seriously retarded by the lack of a standardized biological observation area with which to gain discrete engineering data points concerning the performance of remote sensors. In 1971, a small freshwater impoundment located in one of the buildings at MTF was utilized for this purpose in aerial photography and in spectrometer tests with TRW (Figure 3). Following a series of field operations in 1970 which had limited success, it was decided that a closed tanklike impoundment was the most practical and efficient manner in which to acquire significant engineering data. This project is continuing with the conversion of the freshwater system to saltwater, and an enlargement of the impoundment system to a size necessary for reasonable simulation of biological environments. This facility is available for the testing of any instrumentation concerning biological phenomena from above the surface of the water.

LASER FISH LOCATION

Activities in the application of laser sensing techniques have been limited to monitoring the development of systems applicable to fisheries resource assessment. Experiments under controlled conditions and field tests are being designed to take advantage of any laser system as it becomes available to the NMFS.

FISH LOCATION AT NIGHT

Low-light-level image intensification application has proceeded in an orderly fashion. Several low-light-level systems were investigated and a system manufactured by RCA was selected for initial field testing. Tests were conducted off the Oregon and Washington coasts, and in the Gulf of Mexico over naturally appearing schools of fish. In addition, controlled experiments were conducted at MTF utilizing a military type system as well as the system selected for field testing (Figure 4). Saury, anchovies, euphausid shrimp and menhaden imagery was obtained and is currently under analysis. Preliminary results indicate that a video low-light-level system will be applicable to resource assessment. Commercial potential of this technique will most likely be developed by the fishing industry utilizing a direct view system to assist in locating fish concentrations. Information gained in the field tests is considered adequate for the design of a resource assessment system utilizing low-light-level television. The system design currently under way will include optimum platform, sensor instrument, data acquisition, and data analysis techniques to produce usable information in resource assessment.

CONCLUDING REMARKS

With the development of the NMFS Marine Resource Assessment, Monitoring and Prediction Program (MARMAP) the recognition of remote sensing has taken a considerable move forward. Aerial remote sensing is an integral part of the MARMAP program and with the cooperation of NASA and other agencies is anticipated to significantly accelerate the acquisition of usable information about living marine resources over the next 5 years.

REFERENCES

_____ - Study: Fish Oil Films on the Sea Surface. Final Report Prepared for U.S. Naval Oceanographic Office. Contract No. N62306-69-C-0354. October 1970. Baird-Atomic, Inc. 125 Middlesex Turnpike, Bedford, Massachusetts.

Ramsey, R.C. - Marine Resources Spectrometer Experiment. Final Report Prepared for U.S. Naval Oceanographic Office. Contract No. N62306-71-C-0153. November 19, 1971. TRW Systems Group, Redondo Beach, California.

LEGENDS

Figure 1 - NMFS airborne remote sensing program techniques. Artistic depiction of low-light-level image intensifiers, spectrometers, aerial photography and lasers for the location, identification and quantification of living marine resources at or near the sea surface.

Figure 2 - Representative configuration of spectral signatures obtained with TRW Marine Resources Spectrometer.

Figure 3 - NMFS freshwater impoundment utilized in spectrometer and aerial photography tests. The tank is 22 ft. high and 15 ft. in diameter, and located in a building 110 ft. high at MTF. Test instruments were installed 84 ft. above the surface during tests utilizing known fish concentrations for targets.

Figure 4 - Bioluminescing targets of menhaden schools recorded by LLLTV system in Mississippi Sound October 1971. Motion of the fish school through luminescing plankton results in discrete outlines of entire fish school surface area.

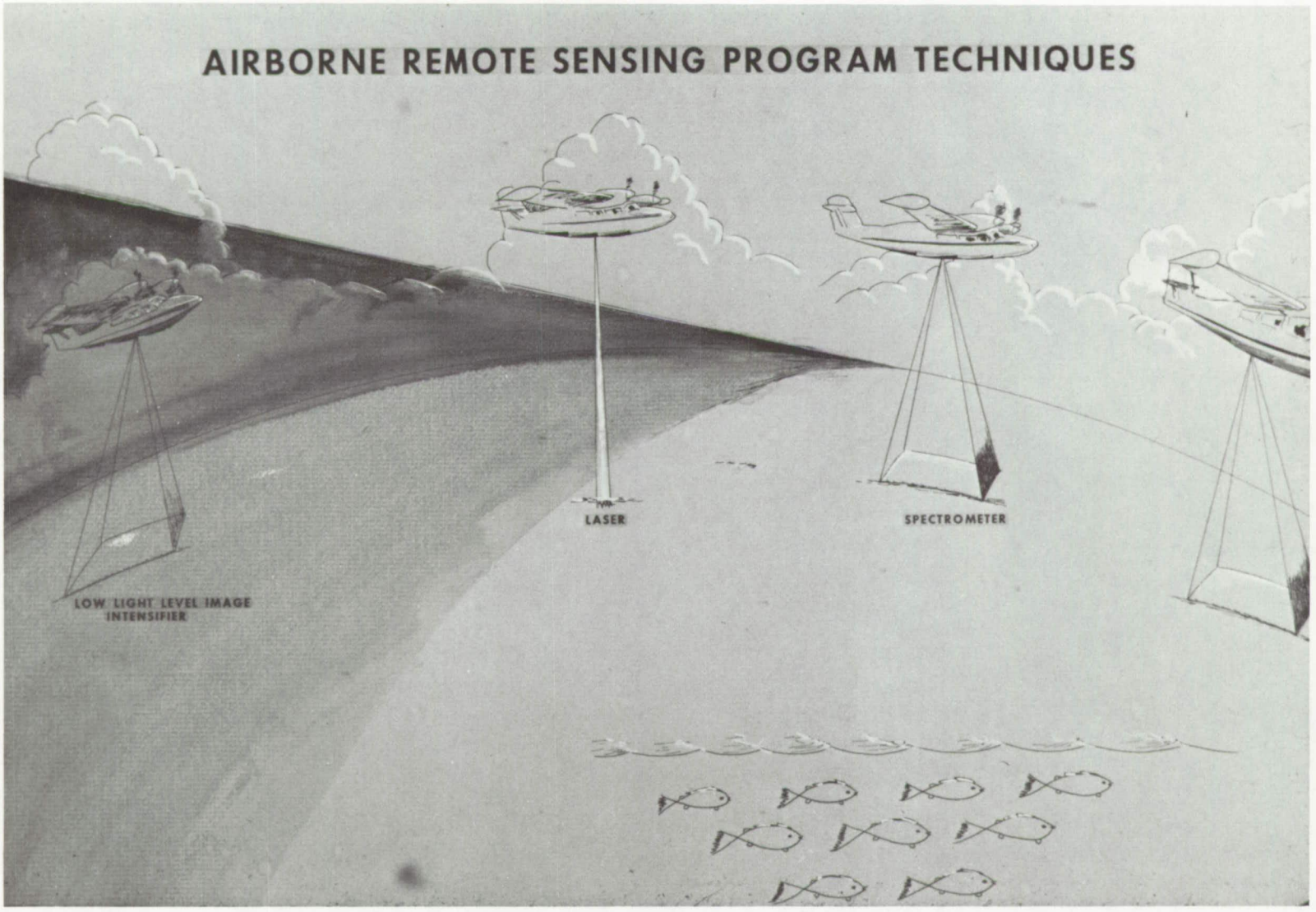

Figure 1 - NMFS airborne remote sensing techniques. Artistic depiction of low-light-level image intensifiers, spectrometers, aerial photography and lasers for the location, identification, and quantification of living marine resources at or near the sea surface.

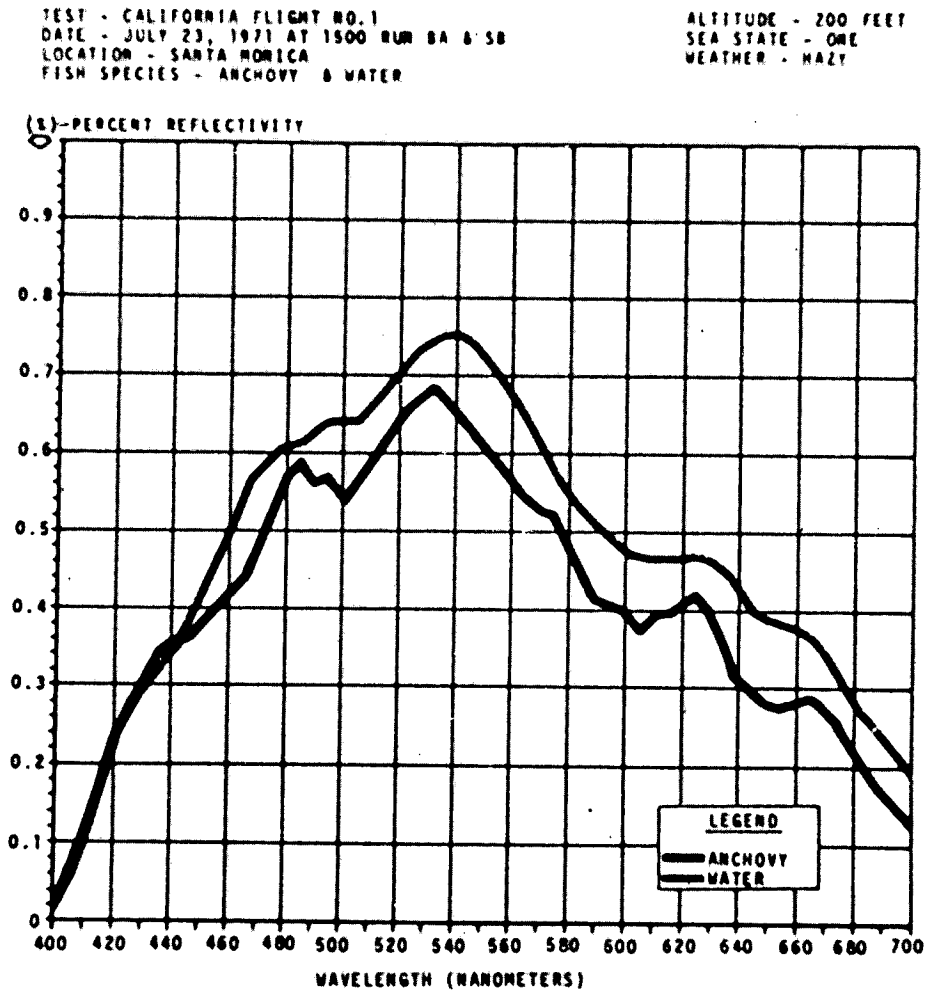

Figure 2 - Representative configuration of spectral signatures obtained with TRW Marine Resources Spectrometer.

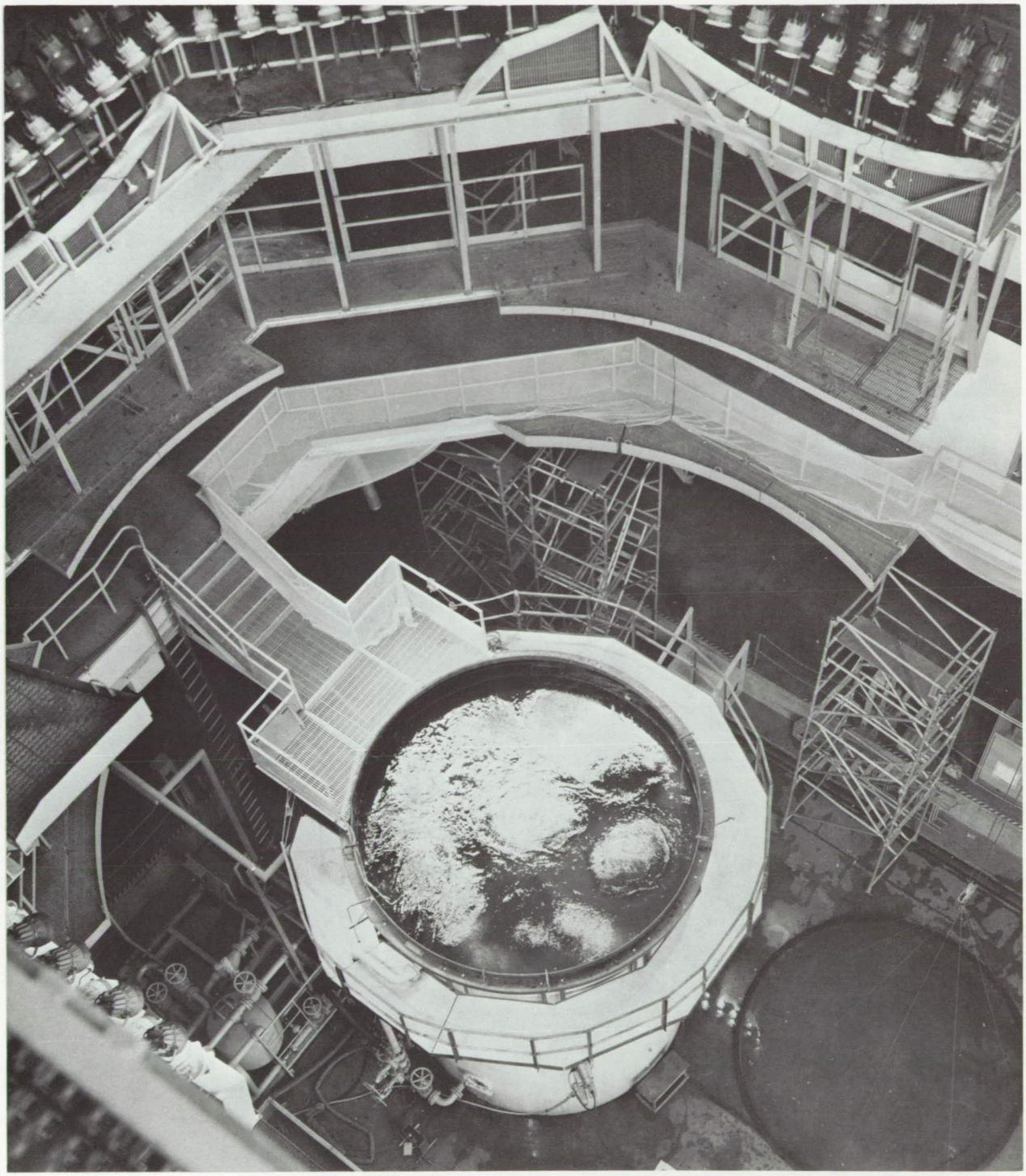

Figure 3 - NMFS freshwater impoundment utilized in spectrometer and aerial photography tests. The tank is 22 ft. high and 15 ft. in diameter, and located in a building 110 ft. high at MTF. Test instruments were installed 84 ft. above the surface during tests utilizing known fish concentrations for targets.

Figure 4 - Bioluminescing targets of menhaden schools recorded by LLLTV system in Mississippi Sound October 1971. Motion of the fish school through luminescing plankton results in discrete outlines of entire fish school surface area.

SECTION 92

COMPARISON OF REMOTE SENSORS FOR SOIL MOISTURE AND OTHER HYDROLOGIC STUDIES

by

Donald R. Wiesnet
National Oceanic and Atmospheric Administration
Washington, D. C. 20031

INTRODUCTION

NOAA's interest in aircraft and satellite hydrology is centered on, but not restricted to NOAA's statutory obligations, some of which include:

1. Flood Forecasting (NWS)
   - (a) Snow mapping
   - (b) Soil moisture
   - (c) Precipitation patterns
2. Limnology, (NOS, IFYGL, NMFS, EFL, EDS)
   - (a) Great Lakes
   - (b) Lake Ice
   - (c) Fisheries
3. Coastal Zone Hydrology (NOS, NGS, NMFS, ERL)
   - (a) Currents
   - (b) Shoreline change

In NOAA we expect that the use of satellite data and imagery will lead to improved flood and low-flow forecasts, improved water-level and ice reports for the Great Lakes, and better and faster coastal-zone storm damage assessment.

The purpose of this paper is to point out progress in lake-temperature and soil-moisture remote sensing during the past year.

MICROWAVE STUDIES OF SOIL MOISTURE

It has long been recognized that passive microwave radiation theoretically provides a means of measuring soil moisture. Inadequate microwave theory, surface scattering, the heterogeneous nature of the soil, and the unpredictability of soil-moisture distribution, are four of the many difficulties that impede progress toward this goal. A contractual study by Aerojet General funded by NOAA/NESS/ESG has moved us a step closer to that goal.

In February and March 1971, multifrequency microwave brightness temperatures of an unvegetated area near Phoenix, Arizona, were taken on the ground and by aircraft at 3000-foot and 10,000-foot altitudes. A low-level gamma-ray survey, the Aerial Radiological Measuring System (ARMS), monitored the test site at 300 and 500 feet, and a large number of ground samples were collected along the flight path. These samples were subsequently measured gravimetrically for soil moisture content.

NOAA's past efforts in the area of soil moisture studies using passive microwave techniques were aimed at carefully studying microwave emission from ground level and slightly above ground level in order to achieve a sound empirical basis for developing a theory of microwave emission that would allow a better understanding of the role played by such factors as surface and soil temperature, dielectric constant of the soil, surface roughness, soil type, and vegetation. As a result of this work, comparison of measured brightness temperatures with those computed from the recent theory of vertically structured media indicate that we now have achieved a partial understanding of the microwave emission properties of soils (Poe, Stogryn and Edgerton, 1971). Excellent agreement of computed and measured total volumes of water per unit area were obtained for all but the dry soil conditions.

Present efforts extend the previous work into aircraft levels over unvegetated fields near Phoenix, Arizona, with the simultaneous collection of ground-truth data. Briefly, 1.42 and 4.99 GH_z measured brightness temperatures along the flight lines consistently responded to measured soil moisture changes along the flight lines. Further details of this experiment are described elsewhere in this volume by A. T. Edgerton (Soil Moisture Mapping by Ground and Airborne Microwave Radiometry).

The next step in this project plan is to now move into an instrumented, vegetated test area to obtain additional aircraft microwave measurements. The Rock River Test Site in SW Minnesota is one well suited for this purpose, as a computerized hydrologic model has already been established for it, and it is monitored by special recording instruments already installed and operating.

GAMMA RAY SURVEY

One of the methods of remote sensing of areal snowpack conditions currently being investigated by the NWS Office of Hydrology in cooperation with EG&G, Inc., is the airborne measurement of passive terrestrial gamma radiation. The NWS Office of Hydrology wishes to determine the feasibility of evaluating average water equivalent of snow along selected courses. (Peck et al., 1971). Research on this subject has been conducted for several years in the Soviet Union and Norway (Kogan et al, 1965; Zotimov, 1968; Dahl and Odegaard, 1970).

Briefly, in the lowest few hundred meters of the atmosphere the gamma radiation field is largely the result of radiation from natural radioactive isotopes, normally present in the soil. Water and (or) snow attenuates the gamma radiation. This attenuation depends only on the total mass of water (Dmitriev et al., 1971) and not on the physical state of the water (snow or ice).

THE ARMS SYSTEM

The aerial radiological measuring system (ARMS) is designed and operated by EG&G, Inc. for the U. S. Atomic Energy Commission. The system is installed in a Beachcraft Twin Bonanza together with an accurate aircraft positioning system. The detector consists of 4 sodium iodide (NaI(Tl) scintillation crystals, thermally insulated and shock mounted. Its gamma-ray sensitivity is several thousand times greater than that of a common geiger counter.

PRELIMINARY RESULTS

Two legs of the survey flown minutes apart provided a measure of reliability of the system, (Fig. 1). The excellent reproducibility is readily apparent. The surveys a week apart (Fig. 2) also track well but are separated by almost a constant. This separation is caused by airborne radon daughter contributions (Fritzsche, Burson, and Burge 1971).

Figure 3 shows a relationship between the normalized net count and a moving mean of 100 soil moisture samples. Note the suppressant effect of the soil moisture on the gamma-ray emissions. These preliminary results are encouraging, and the analysis will continue. Base line flights over the Rock River test site have been completed.

It is believed that the ARMS surveys can be perfected to act as soil-moisture ground truth for the microwave overflights, by providing a kind of bulk soil moisture. If this proves to be feasible, it will greatly aid the interpretation and evaluation of airborne passive microwave data.

LAKE ONTARIO SURFACE TEMPERATURES

In spring 1970, an aerial survey of western and central Lake Ontario was flown by Bendix Aerospace Systems Division using the Bendix Thermal Mapper. The results of that survey are now available (Marshall, Hanson and Shah, 1971) and a brief synopsis of their findings follows.

Daytime infrared imagery in the 8-14 micron range was collected on May 28-29, 1970, using the Bendix LN-3 with an internal blackbody reference for temperature calibration. Altitude ranged from 11,000 ft. to 12,500 ft. during the flights. The stated ground resolution of the system is given as 30 ft. The gain was adjusted to span the 0° - 15°C range.

Marshall, Hanson and Shah, (1971) have interpreted major and minor hydrologic surface features from the mosaicked imagery. Large-scale features include:

1. The cold central zone 2.5 to 4°C
2. The Niagara River plumes, 6° - 0°C at the base, 3.5° - 4°C at the tip.
3. The midlake tongue, 4.5 to 10°C

Small-scale features described are:

1. The Toronto eddy
2. Cold shore water
3. Shear features
4. Creek plumes
5. Ships' wakes
6. Harbor features

Comparison of this aircraft survey with Canadian Dept. Transport ART surveys and ITOS HRIR data is being undertaken by NOAA/NESS in cooperation with the Canadians and with Bendix Corp. A report by Strong and others is in preparation. Additional data collection by aircraft and satellite is planned for the IFYGL data collection period.

REFERENCES

1. Peck, E. L., Bissell, V. C., Jones, E. B., and Burge, D. L., 1971, Evaluation of Snow Water Equivalent by Airborne Measurement of Passive Terrestrial Gamma Radiation, Water Resources Research, V. 7, No. 5, p. 1151-1159

2. Dmitriev, A. V., Logan, R.M., Nikiforov, M.B., and Fridman, S. D., 1971, Aircraft Gamma-Ray Survey of Snow Cover, Nordic Hydrology, V. 2, p. 47-56.

3. Kogan, R.M. et al., 1965, Determination of Water Equivalent of Snow Cover by Method of Aerial Survey. Sov. Hydrol. Selec. Pap., Engl. Transl., No. 2, p. 183-187.

4. Zotimov, N.V. 1968, Investigation of a Method of Measuring Snow Storage by Using the Gamma Radiation of the Earth, Sov. Hydrol. Secec. Pap., Engl. Transl., No. 3, p. 254-266.

5. Dahl, J. B., and Odegaard, H., 1970, Areal Measurements of Water Equivalent of Snow Deposits by Means of Natural Radioactivity in the Ground in Isotope Hydrology, 1970, p. 191-210, Internat. Atomic Energy Agency, Vienna.

6. Marshall, E. W., Hanson, D. S., and Shah, N. J., 1971, Lake Ontario Surface Temperature Features Observed in Infrared Imagery, Final Rept. BSR 3133, NOAA Contract No. 0-35245, 17 p.

7. Fritzsche, A.E., Burson, Z. G., Burge, D. L., 1971, Water Equivalent of Snow Measurements Using Natural Terrain Radiation, EGG Tech. Rept. L-1047, 53 p.

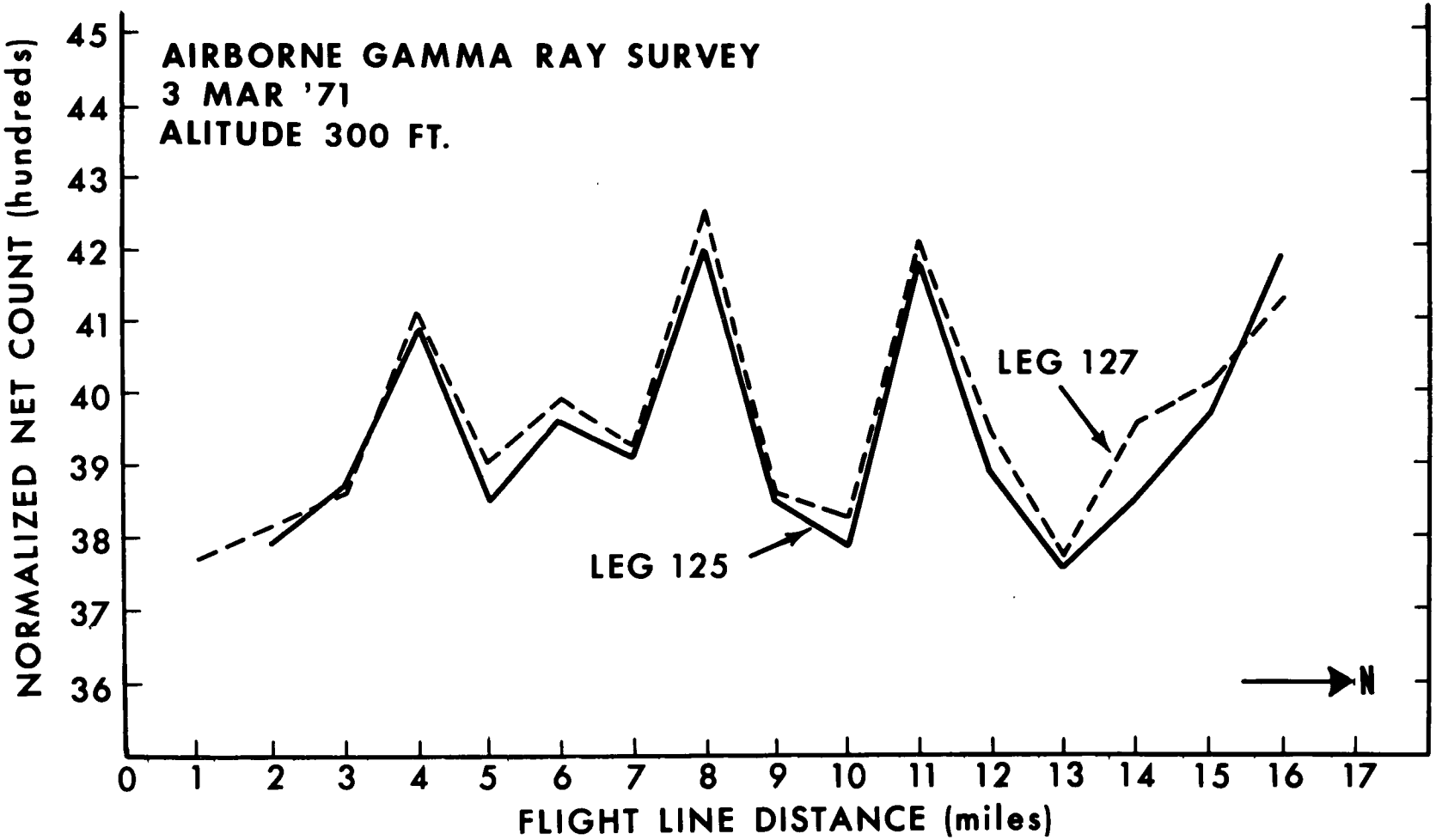

Figure 1. Comparative plot of gamma radiation vs. flight line distance shows excellent repeatibility in two legs flown only minutes apart.

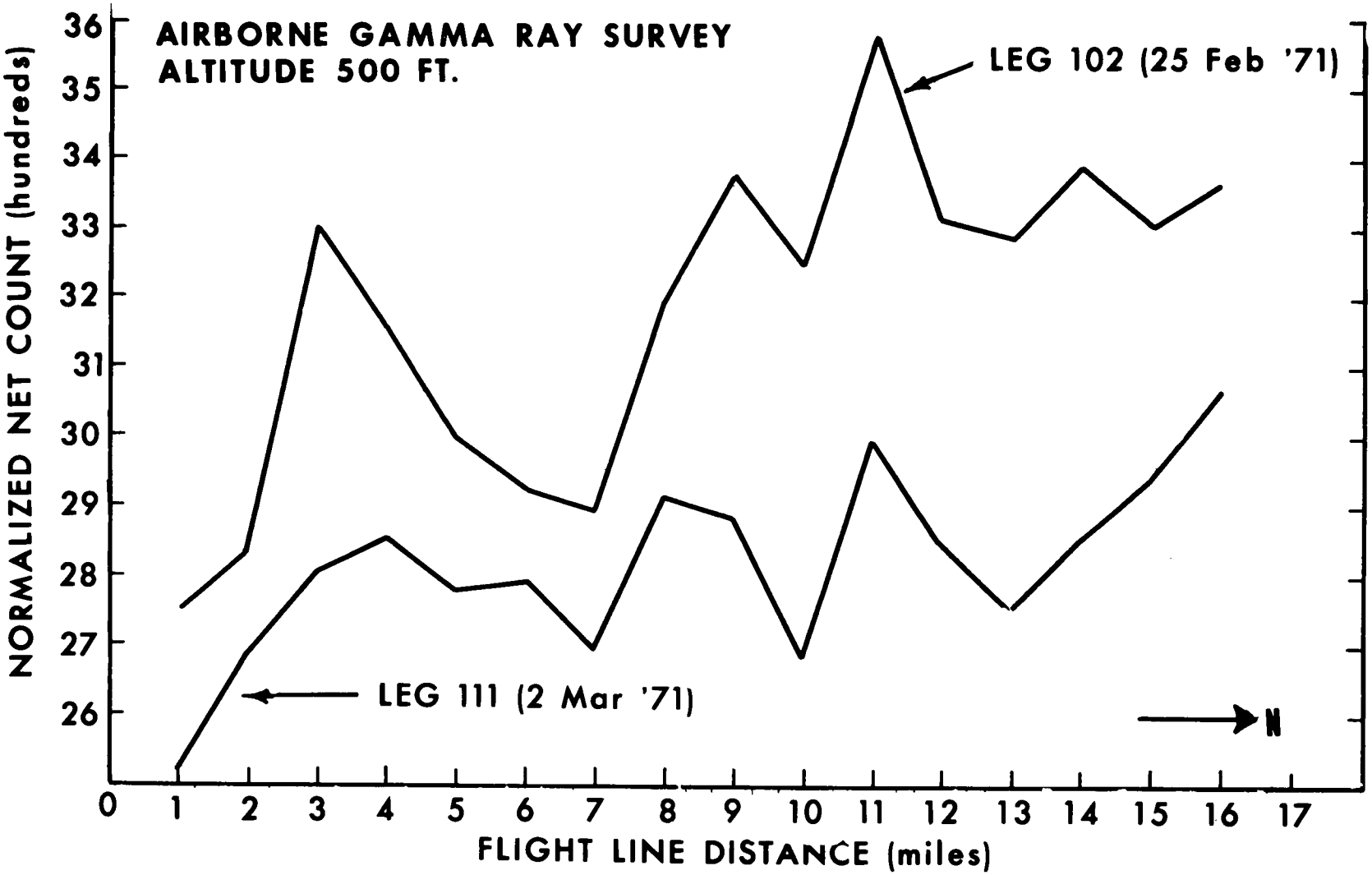

Figure 2. Plots of two aerial surveys of gamma radiation flown a week apart over the same flight line have similar trends and are separated by almost a constant.

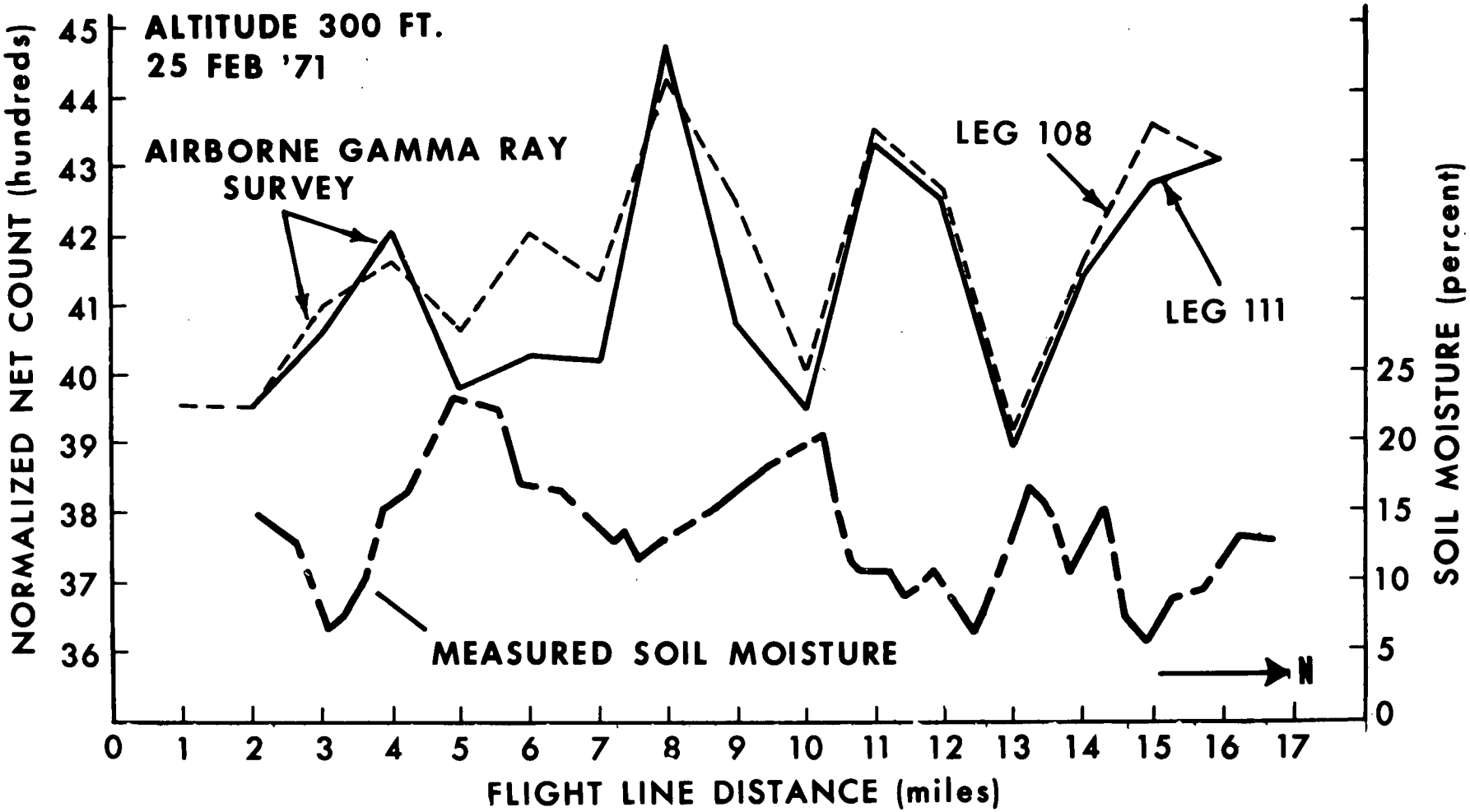

Figure 3. Running 3-point mean of measured soil moisture of 100 samples compared with ARMS gamma-ray survey. Note good repeatibility of the data and inverse relationship of soil moisture to gamma radiation.

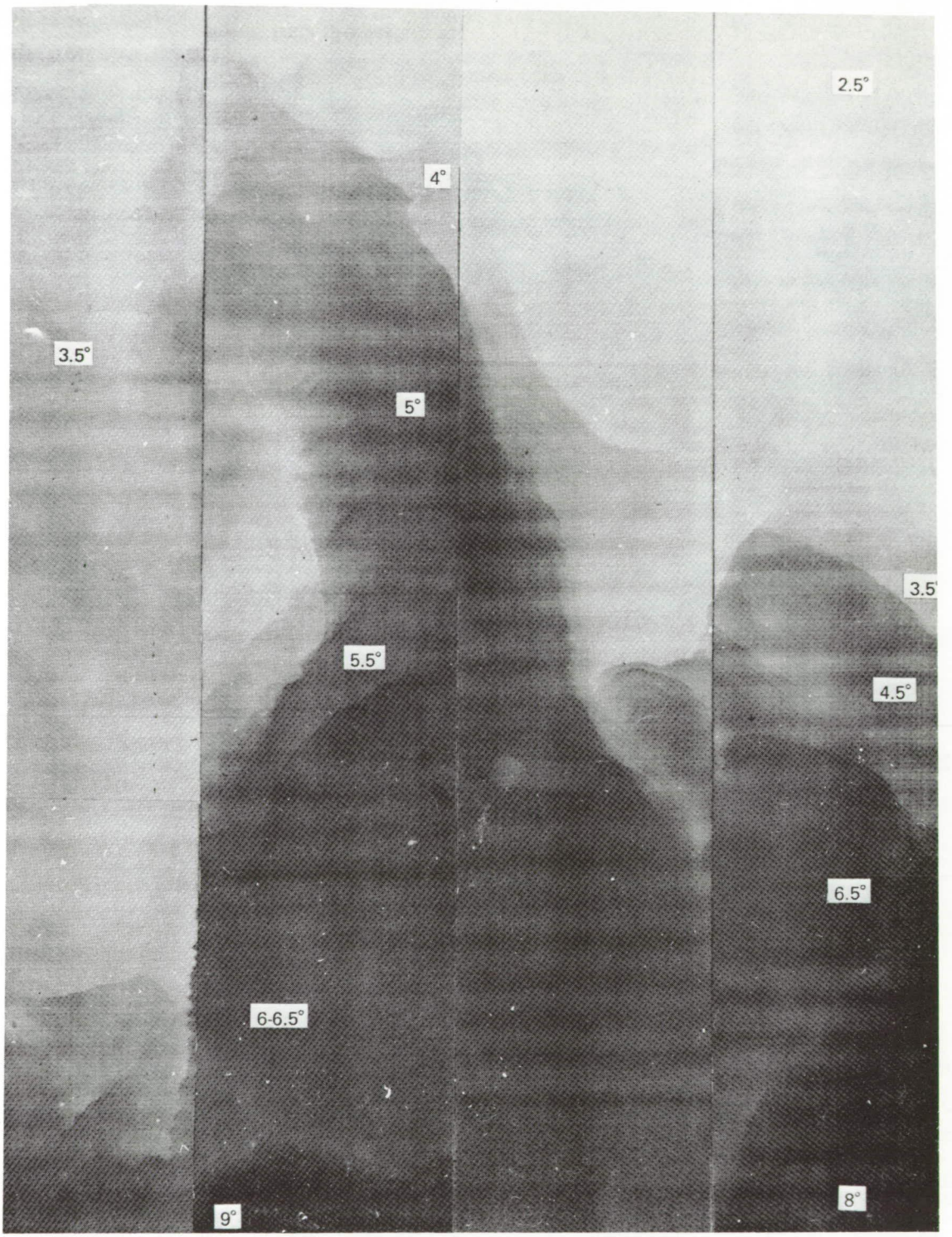

ALL TEMPERATURES ARE IN °C.

Figure 4. Aircraft infrared daytime imagery mosaic of the Niagara River plume in Lake Ontario, 28 May 1970. Dark areas are warm.

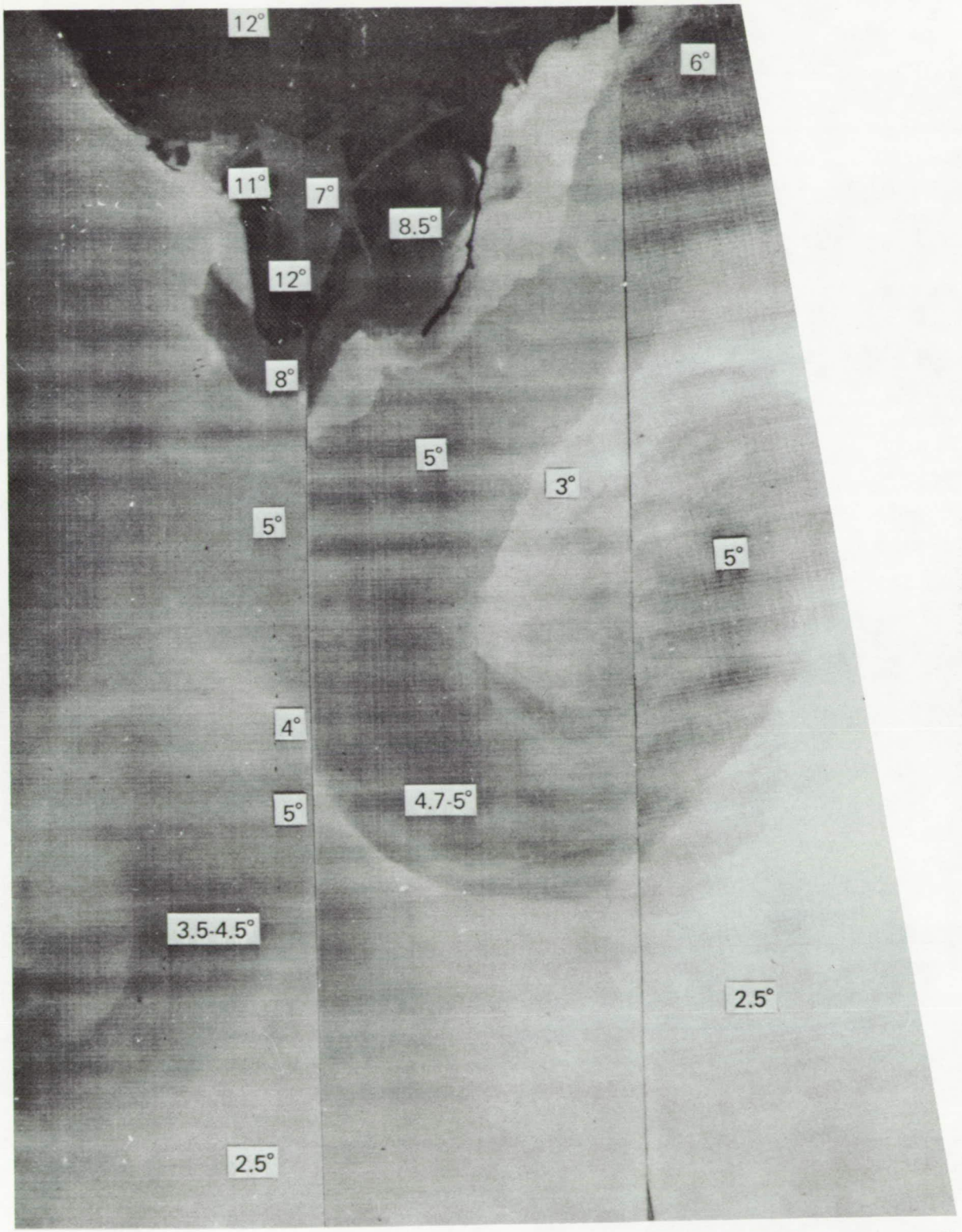

Figure 5. Aircraft infrared daytime imagery mosaic of the Toronto Eddy along north shore of Lake Ontario, 28 May 1970. Dark areas are warm.

SECTION 93

SOIL MOISTURE MAPPING BY GROUND AND AIRBORNE MICROWAVE RADIOMETRY

by

G. Poe and A. T. Edgerton
Microwave Division
Aerojet-General Corporation
El Monte, California

ABSTRACT

This paper summarizes research performed by Aerojet-General Corporation concerning remote sensing techniques for soil moisture mapping. This work, sponsored by the National Environmental Satellite Service of NOAA, is concerned with the feasibility of mapping the horizontal and vertical distribution of soil moisture with microwave radiometry. Extensive ground-based and airborne investigations were undertaken in conjunction with laboratory dielectric measurements of soils and analytical modeling. Radiometric measurements were taken in the vicinity of Phoenix, Arizona at observational wavelengths ranging from 0.81 to 21 cm. Ground experiments were conducted with the Aerojet microwave field laboratory and airborne measurements were obtained from a CV-990 aircraft operated for the Goddard Space Flight Center. Research activities have been focused on establishing basic relationships between microwave emission and the distribution of moisture. This work, including theoretical studies, laboratory and field measurements, demonstrates a basic relationship between microwave emission and soil moisture content. Although the extensive ground control data (vertical soil moisture and temperature profiles) needed to quantitatively demonstrate airborne mapping of soil moisture content were not available during the initial flights, the early results have been very encouraging.

INTRODUCTION

The moisture content of the uppermost few feet of soil directly influences (1) the productivity of large tracts of rangeland, (2) the yield of all agricultural areas, (3) the amount and rate of runoff from large portions of the Continental U. S., and (4) the engineering properties of terrain surfaces. At present, the only source of accurate soil moisture data is from laborious ground surveys which rely on detailed

coring and/or point measurements with radiation or electrical techniques which require direct contact with the soil. More qualitative estimates of soil moisture are often based on rainfall data.

Significant improvements in soil moisture survey accuracies can be achieved by monitoring soil moisture content throughout its areal extent rather than relying on limited point data. Synoptic remote sensing techniques offer this potential. Sensor requirements for this task are: (1) a direct response to soil moisture content, (2) ability to map or image soil moisture distribution with acceptable spatial resolution, (3) adverse weather capability for operation in the presence of clouds, and (4) ability to resolve the vertical distribution of moisture in upper few feet of soil. Since conventional and infrared sensors do not meet these requirements, the investigators have focused attention on the development of passive microwave soil moisture survey techniques. Natural microwave radiation from terrain surface materials penetrates clouds and can be mapped with imaging radiometers. Moreover, field investigations have demonstrated a direct and pronounced relationship between microwave emission from soils and the soil moisture content.

The following portions of this document summarize ground-based, laboratory and aircraft investigations of soil moisture determination with microwave radiometry. This work including theoretical studies, laboratory and field measurements, demonstrates a basic relationship between microwave emission and soil moisture content. These basic investigations have recently been augmented with aircraft measurements. Although the extensive ground control data (vertical soil moisture and temperature profiles) needed to quantitatively demonstrate airborne mapping of soil moisture content were not available during the initial flights, the early results have been very encouraging.

GROUND-BASED AND LABORATORY STUDIES

In the first phase of this program, a series of ground-based passive microwave measurements (1.42, 4.99, 13.4 and 37 GHz) were performed of a laboratory soil (United States Water Conservation Laboratory, Phoenix, Arizona) over a variety of moisture conditions under the auspices of the National Oceanic and Atmospheric Administration (NOAA). The experiments were designed to avoid, as much as possible, complicating features due to surface roughness (arising for example, from vegetal cover) and lateral structural variations. Extensive measurements of the near-surface (0 to 32 cm) vertical distribution of moisture and temperature accompanied the microwave measurements. Also, dielectric constant measurements of the soil as a function of the moisture concentration at ambient temperature (295°K) were performed at 37 GHz subsequent to the

passive microwave measurements. Thus, the microwave emission properties of a relatively simple physical situation consisting of an isotropic, non-magnetic semi-infinitely extended specular soil having variations of moisture and temperature only in the vertical direction was investigated. Further details which are not presented here may be found in a separate document[1].

DESCRIPTION OF EXPERIMENT

The radiometric and physical measurements taken in July 1970 of the sandy clay soil at the USWCL, Phoenix, Arizona, may conveniently be divided into twelve experiments corresponding to twelve different soil moisture conditions. Each experiment consisted essentially of obtaining dual-polarized (horizontal and vertical) multifrequency (1.42, 4.99, 13.4 and 37 GHz) brightness temperatures at 30, 40 and 50 degree antenna viewing angles (measured from nadir) together with extensive moisture profiles (total moisture content in steps of 2, 4, 8, 16 and 32 cm) over the area of observation (10 x 16 foot ellipse for a 20-foot antenna height above ground at a 50-degree angle). Temperature profile data at the surface and 2, 4, 8, 16 and 32-cm depths were taken at several locations around the area of observation during the microwave measurements. On the average 20 to 30 one-inch-diameter core moisture samples spaced 1 to 2 feet apart were taken in each experiment immediately following the microwave measurements. Variations in the moisture data at a given depth were usually less than 0.5 percent (dry weight basis) while variation in the temperature data at a given depth were less than 1 or 2°K.

The effects of lateral variations of moisture and temperature in the USWCL soil plot were minimized by positioning the radiometers so that the same area of soil was observed at each view angle. The selection of the above number of view angles and moisture measurements was made so that changes in the moisture condition due, for example, to natural evaporative processes could be minimized. Both the microwave and moisture measurements in each experiment were usually completed in less than an hour. The choice of view angles was made to exhibit polarization differences in the measurements and to keep the beam spot size within reasonable limits.

Since the method of moisture sampling involved the destruction of the soil site, each experiment was conducted on slightly different portions of the larger soil plot. However, significant lateral changes in soil properties (density or grain size) during the series of experiments were found to be negligible.

The method used to alter the soil moisture concentration consisted of inundating a relatively large soil plot and allowing natural evaporative and drainage processes to occur. Approximately two and one-half weeks were spent obtaining the microwave and moisture data as the soil conditions varied from completely saturated to relatively dry.

Model of Microwave Soil Emissions

Of the models applicable to specular substances, the recent model due to Stogryn[2] appears to be the most appropriate for analyzing the previously described experiment. In the model, variations of the dielectric constant (and hence physical properties) and temperature are allowed in the direction normal to the substance's surface and are assumed negligible in directions parallel to the substance's surface. A practical numerical scheme for computing the brightness temperature of energy propagating away from the substance is discussed elsewhere[2]. Suffice it to say, the brightness temperature of a material may be computed from a knowledge of (1) the radiation incident on the substance's surface and (2) the functional dependence of the dielectric constant and temperature with distance below the surface (only differentiable functions having a finite number of discontinuities are allowed). In general, the computed brightness temperature depends on the choice of frequency, polarization and view angle. Atmospheric attenuation can be neglected in the present situation since the radiometers in the experiment were at most 20 feet above the soil. In reality the model is a generalization of the theory of emissions by homogeneous, istropic and non-magnetic specular substances described by the well-known Fresnel reflection coefficients[3].

The computation of the radiation incident on the soil's surface was made using a standard model atmosphere for the air temperature and pressure with reasonable estimates of the cosmic noise. A typical water vapor profile of the Phoenix Valley was also used in the calculation.

DIELECTRIC CONSTANT AND MIXING FORMULAS

Dielectric constant measurements were performed on the USWCL soil using a free-space measuring system known as an ellipsometer, operating at 13.4 and 37 GHz. Details of the technique of measurement can be found elsewhere[4]. Density, temperature and moisture measurements were taken on each sample. Great care was exercised during the dielectric measurement to insure that the soil samples resembled, as closely as possible, in situ soil in both density and moisture content. Table 1 presents the results together with measurement errors. K' and K'' are the real and imaginary parts of the dielectric constant, respectively.

Uncertainty in the temperature, density and moisture content were respectively less than 1°K, 0.1 g/cm^3, and 0.5 to 2 percent. Due to the small values of K″ associated with the low loss samples, only an upper bound could be determined for small moisture contents with the ellipsometer.

Several commonly used dielectric mixing formulas were selected to compare with measured data. The formulas of Rayleigh[5], Wiener[6], Bottcher[7], and Pierce[8] were investigated. To aid in the comparisons, the dielectric constant data of von Hippel[9] at 3 and 10 GHz were used. Since the dielectric constant of solid particles is known to be relatively independent of temperature while the dielectric constant of water may be calculated accurately as a function of temperature using equations of the Debye form[10], the dielectric constant of soil is known as a function of temperature and moisture content when computed from the mixing formulas. In the computations that follow the dielectric constant of dry soil was taken to 2.55+i.001.

The formula of Wiener typically provided best agreement although the form number (appearing in the formula), F , which gave the best fit was found to vary with frequency. Thus, Wiener's mixing formula together with an appropriate range of form numbers (32-64 for 1.42 and 4.99 GHz, 16-64 for 13.4 and 16-32 for 37 GHz) was selected to relate the dielectric constant of soil with the percentage of soil moisture and temperature. The effect of density on the dielectric constant other than that occurring due to the presence of water were not pursued.

COMPARISON OF THEORY AND EXPERIMENT

A comparison of 1.42, 4.99, 13.4 and 37 GHz brightness temperatures (measured in the previously described experiment) with those computed from the theory of vertically structured media[2] using Wiener's dielectric mixing formula[6] with measured moisture-temperature profiles is presented in Figures 1 and 2. The antenna view angle is 50 degrees. Similar results were obtained at the other view angles. The range of form numbers used in Wiener's formula are indicated in the figures. The numbers in the figures refer to the twelve experiments mentioned previously. The numerous soil moisture and temperature profiles are presented elsewhere[1].

A solid line has been drawn through the measured brightness temperatures in Figures 1 and 2. As can be seen, the agreement between theory and measurements is good except for the existence of systematic differences. The lack of accurate dielectric constant information at 1.42 GHz allows an explanation of the systematic differences in Figure 1 while the lack of a completely satisfactory mixing formula fits to

measured 37 GHz dielectric constant data allows an explanation of the differences in Figure 2. In any case, the differences in vertically and horizontally polarized temperatures increase substantially with increasing moisture content and the differences are largest at lower frequencies. Also, decreases in the horizontally polarized temperatures are usually larger than the corresponding decreases in the vertically polarized temperature. This is due primarily to the Brewster angle effect associated with smooth surfaces.

MODEL FOR COMPUTING SOIL MOISTURE

Several theories of the radiometric emission characteristics of specular soils exist which may be used to compute the microwave brightness temperature of energy propagating away from soils provided information is available regarding the moisture and temperature distribution within the soil and the radiation incident on the soil surface. However, there are presently no models available which allow a computation of the moisture or temperature profiles from measured brightness temperatures. Until further theoretical and/or experimental information is available regarding the relationships between soil moisture content, dielectric constant and microwave emission (and others) empirically derived models appear appropriate.

The model described below permits a calculation of the vertical profile of the total volume of water per unit area using measured horizontally polarized brightness temperatures which have been normalized by the surface soil temperature. The model originates from the hypothesis that it is the total mass of water per unit area lying between the surface and one electromagnetic skin depth which determines the brightness temperature rather than the specific details of the distribution of moisture. The model consists of the following series of steps.

a. The measured horizontal brightness temperature (^{o}K) is divided by the surface temperature (^{o}K) of the soil. The units of the resulting numbers are defined as effective emissivities rather than emissivities since the single term emissivity can be misguiding when substantial temperature gradients occur within the soil.

b. From established curves relating effective emissivity with volume percent of water, the volume percent of water (g/cm^3) corresponding to the effective emissivity of a. is determined.

c. From established curves relating the skin depth with the volume percent of water, the skin depth (cm) corresponding to the volume percent of water of b. is determined.

d. Multiplying the skin depth (cm) of c. with the volume percent of water (g/cm^3) of b. yields the total volume of water per unit area (g/cm^2) lying beneath the soil surface and above the skin depth of c.

Thus utilizing a suitable combination of measured multifrequency horizontally polarized brightness temperatures (obtained at a particular view angle) together with the surface soil temperature, a computation of the vertical distribution of the volume of water per unit area can be made.

Several comments appear appropriate regarding the above-mentioned established curves. First, the curves in c. were obtained using Equation (1) and Wiener's mixing formula. It should be noted that the skin depth δ calculated from (1) applies to the nadir position, however, since the dielectric constant of soils having moisture contents greater than a few percent is much larger than $\sin^2\theta$ (θ is the angle from nadir) little error arises when using (1).

$$\frac{\delta}{\lambda} = \frac{1}{2\pi \mathrm{Im}(\sqrt{K})} \tag{1}$$

λ is the free-space wavelength and K is the dielectric constant calculated from Wiener's formula. Im denotes taking the imaginary part. Figures 3a, b, c, and d present skin depths for 1.42, 4.99, 13.4 and 37 GHz as functions of the volume percent of water. The skin depths were then computed from Wiener's formula with two form numbers mentioned previously (32 and 64 for 1.42 GHz, 16 and 64 for 13.4 and 16 and 32 for 37 GHz). As can be seen, modest amounts of water greatly affect the skin depths of dry soils. An average thermal temperature of $300^{\circ}K$ was used in computing K.

Second, the curves in b. were obtained as follows: horizontally polarized brightness temperature T were computed for a homogeneous, isotropic, isothermal, semi-infinitely extended, non-magnetic soil having a smooth planar surface using Equations (2) and (3). Conservation of energy and local thermodynamic equilibrium has been assumed. R is the horizontally polarized power reflection coefficient determined by the Fresnel reflection coefficients[3], T_g is the soil temperature; K is the dielectric constant; θ is the view angle from nadir; and T_s is the brightness temperature of the energy incident on the soil surface.

$$T(\theta) = (1 - R(\theta))\, T_g + R(\theta)\, T_s(\theta) \tag{2}$$

$$R(\theta) = \left| \frac{\cos\theta - \sqrt{K - \sin^2\theta}}{\cos\theta + \sqrt{K - \sin^2\theta}} \right|^2 \qquad (3)$$

T_s was assumed due to atmospheric absorption of cosmic noise. As noted earlier atmospheric attenuation of T can be neglected. T depends on the frequency through the frequency dependence of K and T_s . T_g was taken to be 297°K since the 13.4 and 37 GHz dielectric constant measurements were performed near this temperature. K was computed from Wiener's mixing formula.

Figures 4a, b, c and d present effective emissivities at 1.42, 4.99, 13.4 and 37 GHz as functions of volume percent of water for a 50-degree view angle. Similar curves were obtained for other view angles. The form numbers used in Wiener's formula are indicated in the figure. It should be noted that effects on the curves in b. and c. due to changes in the soil temperature have been neglected in the computations that follow. However, it is judged that for most soil temperatures that are encountered in situ, the effects are less than the uncertainties introduced when using Wiener's mixing formula.

COMPARISON OF CALCULATED AND MEASURED MOISTURE PROFILES

Utilizing the above model, effective emissivities were computed from the multifrequency horizontally polarized brightness temperatures and surface soil temperatures measured during the previously described experiment. The skin depths and total volumes of water per unit area corresponding to these effective emissivities were also computed. Computations were made for 30, 40, and 50 degree view angles. Figures 5 and 6 present a typical comparison of measured and computed results. A solid line has been drawn through the measured data which was linearly extrapolated beyond 32 cm. The vertical bars indicate ranges of variations associated with the moisture measurements. Wavelengths are given near the computed results. Form numbers used in Wiener's formula are indicated in the figures.

As can be seen, good agreement between measured and computed moisture contents for moderately moist to saturated soil conditions occurs at all wavelengths (Figure 5). However, there is at times relatively poor agreement for "dry" soil conditions (Figure 6). The lack of agreement for dry soils is believed due to uncertainties in the measured values of the imaginary part of the dielectric constant which in turn

introduces uncertainties in the computed skin depths. It is anticipated that additional information regarding the dependence of the imaginary part of K on the moisture content of dry soils will allow better agreement between measured and computed moisture profiles for dry soils.

AIRCRAFT MEASUREMENTS AND ANALYSIS

In the second phase of this program, multifrequency aircraft measurements of a portion of the Phoenix Valley, Arizona, were analyzed in terms of soil moisture content and compared with brightness temperature values computed with a uniform media emission model. Aircraft data were obtained by the Goddard Space Flight Center. The sensor frequencies considered in these analyses are 1.42, 4.99, 19.35, 37 and 94 GHz. Ground-control soil moisture and temperature measurements were performed by Biospheric Incorporated[11] and AGC. Results from the dielectric studies of soils as a function of moisture content are also used in the analysis.

EXPERIMENTAL DATA

The Biospherics moisture measurements were obtained from soil samples taken in the 0 to 15 cm depth interval. The temperature measurements were performed at 7.5 cm below the soil's surface. Approximately 200 soil plots (each approximately 1/4 section) were investigated by Biospherics. Soil plot locations are available in a separate report[11]. Four moisture samples were taken from each soil plot. AGC performed detailed soil moisture and temperature measurements at four locations along the north-south flight lines. Typical depth intervals at which soil moisture and temperature measurements were performed by AGC include surface to 1, 2, 4, 8, 16, and 32 cm. AGC also performed 13.4 GHz radiometric measurements on each of the sites.

The AGC soil temperature measurements showed relatively good agreement with the aircraft infrared temperatures. Fortunately, the infrared measurements did not vary significantly during the overflights, hence an average 20°C (±2°C) was used.

The correlation of the position of the aircraft (and hence radiometers) flight lines with the locations of the soil moisture measurements was made using information supplied by Goddard Space Flight Center. Although moisture measurements performed by Biospherics were taken in several hundred soil plots (each approximately 0.4 km square) along the flight lines, the number of cases in which one could state with reasonable certainty that a particular soil plot was being viewed by a

particular radiometer was not large. Moreover, the set of soil plots was different for each altitude. To minimize the effect of finite beamwidth of the antenna, only those cases in which a soil plot encompassed most of the 3-dB antenna beam spot size were considered. Although this restriction limits the number of comparisons of measured results with those computed from the model of uniform media, it did allow, for the most part, statistically meaningful analyses at 1.42, 4.99, 37 and 94 GHz.

Since only bulk moisture data were available for large portions of the Phoenix Valley, it was necessary to employ the model of uniform media to compute brightness temperatures. Computations were made of predicted airborne brightness temperatures at 1.42, 4.99, 37 and 94 GHz. Atmospheric attenuation effects were also incorporated in the calculations.

Figure 7 provides a comparison of measured and computed temperatures for 1.42 and 4.99 GHz corresponding to data taken on February 25. Average moisture contents and plot numbers (defined by Biospherics) are also shown in the figures. Descriptions of vegetal cover and general conditions of the soil are also given in the figure. Several general comments are appropriate.

First, although the vertical and horizontal polarizations of the 1.42 GHz radiometer were pointed in the nadir position, a systematic difference of the order of 10 to 15 degrees occurs between the two polarizations with the vertical component greater. A somewhat similar situation holds for measurements at 4.99 GHz for the February flight. It is reasonable to assume that the primary agent responsible for the systematic errors occurring between the two polarizations are calibration errors (due, for example, to lack of precise calibration of antenna and waveguide losses) rather than a consistent anisotropic emission of the soil. However, this explanation is not entirely satisfactory (provided antenna and waveguide losses have not changed) since airborne measurements of the Salton Sea in Southern Calibornia (February 25) show the vertically polarized temperature at 1.42 and 4.99 GHz to be less than the horizontally polarized temperature[12].

Second, somewhat systematic differences occur between measured and computed temperatures at both 1.42 and 4.99 GHz. The systematic errors may be ascribed to radiometer calibration errors, roughness effects, and/or inadequacy of Wiener's dielectric mixing formula.

Third, the correlation of measured and computed brightness temperatures was best at 1.42 and 4.99 GHz. Note that directions of changes in the computed temperatures agree, in most cases, with the directions of changes in measured temperature at 1.42 and 4.99 GHz although the changes in magnitude of measured data are usually less than changes in computed results. Of special note are cases in which changes in measured temperatures agree with computed changes even in the presence of vegetal cover

(alfalfa and wheat), see Plots 120 and 97 in Figure 7. The measurements in Plot 159 in Figure 7, however do not show the same agreement. The agreement in Plots 120 and 97 is probably related to the relatively high moisture contents (14.5 to 21 percent) while the disagreement in Plot 159 is probably related to the low moisture content (8 percent). This agrees with intuition since the contrast in emissivities between vegetal cover and dry soil is significantly less than the contrast between vegetal cover and wet soil. Carrying this conjecture slightly further, one can infer that detection of soil moisture through vegetal cover occurs when substantial amounts of water are contained in the underlying soil. Although penetration through certain forms of vegetal cover in reasonably moist soils appears possible at 1.42 and 4.99 GHz, a consistent response of 37 or 94 GHz data to soil moisture beneath vegetal cover was not apparent.

Finally, it appears that outside of systematic differences at 1.42 and 4.99 GHz, consistently better agreement occurs between measured and computed temperatures at lower frequencies (1.42 and 4.99 GHz) than at higher frequencies (37 and 94 GHz). Attributing the mechanism(s) that are responsible for this observation to small or large scale roughness effects of the soil is consistent with the intuitive feeling that what is slightly "rough" at lower frequencies is "rougher" at higher frequencies. However, a qualitative deduction of this sort really cannot be based on the above data since an equally plausible alternative can be made using the fact that the higher frequencies penetrate less in moist soils than lower frequencies. Thus, it is the near-surface moisture conditions which determine the high frequency radiometric emissions. Reasonable estimates of the depth of penetration or power skin depth δ presented earlier (Figures 3a, b, c, and d) indicate that for moisture contents greater than ten percent (by volume) the depth of penetration at 37 GHz is less than a free-space wavelength. Since relatively large changes in moisture concentration can occur between the 1 cm and 15 cm deep soil samples, it is not difficult to see that the poor agreement between measured and computed results at 37 and 94 GHz could be due to near-surface moisture variations which were not measured by the 15-cm-deep soil samples available for this study.

CORRELATION OF AIRBORNE MICROWAVE MEASUREMENTS AND SOIL MOISTURE CONTENT

As mentioned above, comparisons of presently available theory and measured airborne data reveal that a statistically meaningful dependence of measured brightness temperature on the measured soil moisture content occurs more conspicuously at the lower frequencies (1.42 and 4.99 GHz) than at the higher ones (37 and 94 GHz). In an attempt to provide quantitative information of the correlation of a set of measured brightness

temperatures $\{T_i\}$ and a corresponding set of measured soil moisture values $\{M_i\}$ a correlation $\kappa(\{T_i\},\{M_i\})$ is defined

$$\kappa\left[\{T_i\},\{M_i\}\right] = \frac{\sum_{i=1}^{N}\left(T_i-\bar{T}\right)\left(M_i-\bar{M}\right)}{\sqrt{\sum_{i=1}^{N}\left(T_i-\bar{T}\right)^2}\sqrt{\sum_{i=1}^{N}\left(M_i-\bar{M}\right)^2}} \qquad i = 1, \ldots N \qquad (4)$$

N is the number of temperature or moisture measurements and $\bar{T}$ and $\bar{M}$ are averages defined by

$$\bar{T} = \frac{1}{N}\sum_{i=1}^{N} T_i \qquad (5)$$

$$\bar{M} = \frac{1}{N}\sum_{i=1}^{N} M_i \qquad (6)$$

Computations of κ were performed for the Phoenix Valley temperature data. A qualitative illustration of the dependence of the correlation coefficient κ with frequency is shown on Figure 8. Both polarizations were averaged for each frequency. The bars in the figure indicate the range of values of κ at each frequency. The 19.35 GHz data were not used. As can be seen, a substantial decrease in κ occurs with increasing frequency for the 15-cm moisture data. It is believed that larger negative values of κ (better correlation) would have occurred at the higher frequencies had ground-based moisture measurements been taken over shallower depth intervals.

CONCLUSIONS

The ultimate goal of research reported herein is the development of a practical remote sensing technique for synoptic aerial and/or satellite mapping of the horizontal and vertical distribution of soil moisture. The initial step toward this goal has been an integrated research program consisting of numerical modeling, laboratory and field measurements and airborne data studies to establish the basic relationships between microwave emission and the hydrological properties of soil. Ground-based experiments were designed so that vegetal cover or terrain irregularities may be neglected.

Comparisons of ground-based measured brightness temperatures of a sandy soil at 21.4, 6.0, 2.2 and 0.81 cm for 30, 40 and 50 degree view angles (from nadir) with those computed from the recent theory of vertically structured media using measured vertical profiles of moisture and temperature reveal that a semi-quantitative understanding of the microwave emission properties of the soil has been achieved. Generally speaking, the agreement between measured and computed temperatures was good over a large range of moisture conditions. The major sources of uncertainties arising in the comparisons were attributed to (1) measurement errors, (2) lack of dielectric constant measurements at 21.4 and 6.0 cm and (3) lack of dielectric mixing formula to fit measured data completely satisfactorily.

A model was hypothesized to allow a computation of the vertical distribution of soil moisture (per unit area) using the ground-based measured horizontally polarized brightness temperatures and the soil surface temperature. A comparison of measured moisture profiles with those computed from 21.4, 6.0, 2.2 and 0.81 cm data for 30, 40 and 50 degree view angles shows that excellent agreement occurs for cases of reasonably damp to saturated soil conditions (8 to 30 percent moisture, dry weight basis). The agreement for "dry" soils was found to be poor. This lack of agreement is attributed to present uncertainties in the loss tangent measurements of low-loss soils since the greatest sensitivity of the soil skin depth occurs at low moisture concentrations. An interesting feature in the comparison of measured and computed moisture profiles was the fact that best agreement occurred at high moisture concentrations where uncertainties in measured brightness temperatures were apparently largest. Thus, it appears that the proposed empirical model depends more heavily on an accurate knowledge of the skin depth than on present microwave measurement uncertainties. This limitation can be removed by obtaining more precise dielectric constant data for soil and by developing improved mixing formulas.

A comparison of measured airborne brightness temperatures of the Phoenix agricultural farmlands with those computed from presently available theoretical models (uniform media and vertically structured media models) reveals that statistically meaningful agreement occurred at 1.42 and 4.99 GHz except for systematic differences listed below. Less agreement occurred between the measured and computed 37 and 94 GHz data.

The systematic differences observed in the comparisons at lower frequencies can arise from the following sources: (1) aircraft radiometer calibration errors, (2) roughness effects and (3) inadequacy of Wiener's dielectric mixing formula which is used in the computation of brightness temperatures. A check on the absolute calibration of the radiometers reveals that (1) can account for a portion but not all of the differences. Results of an earlier study indicate that (3) can account for about half of the difference. No estimates of (2) can be made at present due to the

lack of theory of the emission of diffuse substances and the lack of properly controlled experimental data.

Of special note is the apparent penetration through alfalfa and wheat (25 cm and 15 cm tall, respectively) in several cases at 1.42 and 4.99 GHz. The penetration was noted only in cases where the underlying soil had substantial amounts of moisture in excess of 14 to 21 percent (dry weight basis). Lack of detectable penetration of vegetal cover over relatively dry soil is probably due to the lack of significant contrast in the emissivities of vegetal cover and dry soil. Vegetal penetration at the higher frequencies (19.35, 37 and 94 GHz) was not observed with any discernible consistency.

The decrease in agreement of theory and measured data at 37 and 94 GHz compared with the agreement obtained at 1.42 and 4.99 GHz may be attributed to: (1) roughness effects and (2) lack of penetration into moist soils. As before, estimate of (1) cannot be made at present due to lack of experimental controlled data. Estimates of the depth of penetration indicate the emission at 37 and 94 GHz is controlled by the moisture contained in the near-surface regions of soils. (Approximately one free-space wavelength for moisture contents greater than 6.5 percent on dry weight basis.) Thus, the lack of correlation in the measured and computed 37 and 94 GHz temperatures can be due to near-surface moisture changes which were not detected in the 15-cm-deep soil samples.

An analysis of a correlation coefficient using measured and computed brightness temperatures with measured soil moisture data at all frequencies shows substantial agreement with the results mentioned above. That is, values of the correlation coefficients were consistently larger in magnitude at 1.42 and 4.99 GHz than at 37 and 94 GHz.

REFERENCES

1. Poe, G., A. Stogryn and A. T. Edgerton, "Determination of Soil Moisture Content Using Microwave Radiometry," Final Tech. Report, 1684R-1, Aerojet-General Corp., El Monte, Calif., Contract No. 0-35239, June, 1971.

2. Stogryn, A., "The Brightness Temperature of a Vertically Structured Medium," Radio Science, Vol. 5, No. 12, Dec., 1970.

3. Stratton, J., Electromagnetic Theory, McGraw-Hill Co., N. Y., 1941.

4. Poe, G., "Determination of Dielectric Properties of Natural Materials," Tech. Report No. 5, SD9016-5, Aerojet-General Corp., El Monte, Calif., Contract NOnr 4767(00)NR387-033, Feb., 1970.

5. Rayleigh, Lord (J. W. Strutt), "On the Influence of Obstacles A Arranged in Rectangular Order on the Properties of a Medium," Phil. Mag., 34, 1892.

6. Wiener, O., "leipziger Berichte," 62, 1910.

7. Bottcher, C., Theory of Electric Polarization, Elsevier, Amsterdam, 1952.

8. Pierce, C., "The Permittivity of Two Phase Mixtures," Brit. J. A. Phys., Vol. 6, Oct., 1955.

9. von Hippel, A., Dielectric Materials and Applications, MIT Press, Cambridge, Mass., 1954.

10. Stogryn, A., "Equations for Calculating the Dielectric Constant of Saline Water at GHz Frequencies," IEEE Trans. on MTT, Aug., 1971.

11. Biospherics Incorporated, "Soil Moisture Ground Truth Data for Correlation with Microwave Radiation Data," Contract No. NAS 5-21610, April 1971, Rockville, Maryland.

12. Poe, G. and A. T. Edgerton, "Determination of Soil Moisture Content with Airborne Microwave Radiometry," Final Tech. Report (to be published), 4006R-1, Aerojet-General Corp., El Monte, Calif., Contract No. 1-35378.

Table I

DIELECTRIC CONSTANT MEASUREMENTS AT 37 and 13.4 GHZ

Freq (GHz)	Temp (^{o}K)	% Moisture (Dry Wt)	Density (g/cm^3)	K′	K″
37	300	2.4	1.51	2.2 ± 0.15	<0.06
37	296	12.0	1.6	3.5 ± 0.2	1.0 ± 0.1
37	296	22.0	1.70	7.6 ± 0.4	3.5 ± 0.3
37	295	25.0	1.75	9.0 ± 0.4	5.0 ± 0.5
37	293	40.0	1.81	13.0 ± 0.5	9.0 ± 0.9
13.4	296	2.0	1.50	2.35 ± 0.15	< 0.06
13.4	294	18.0	1.75	5.8 ± 0.5	1.4 ± 0.1
13.4	293	28.0	1.80	23.0 ± 3.0	8.5 ± 1.5

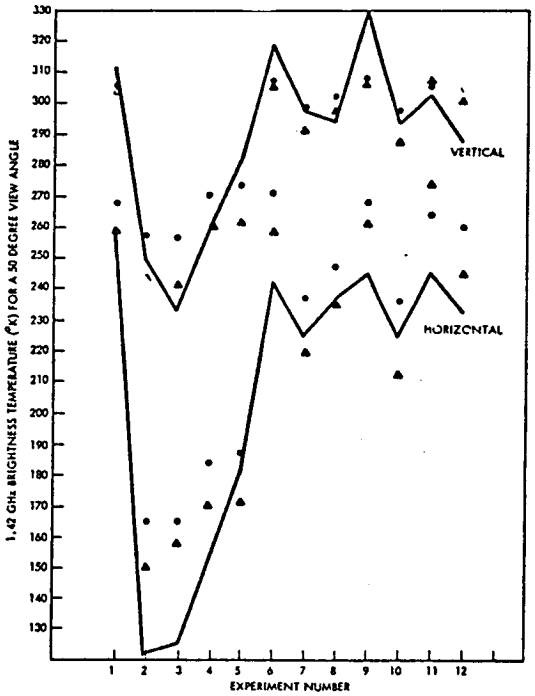

Figure 1. Comparison of measured and computed 1.42 GHz brightness temperatures. —— indicates measured temperatures while ● and ▲ indicate computed temperatures with form numbers = 32 and 64, respectively.

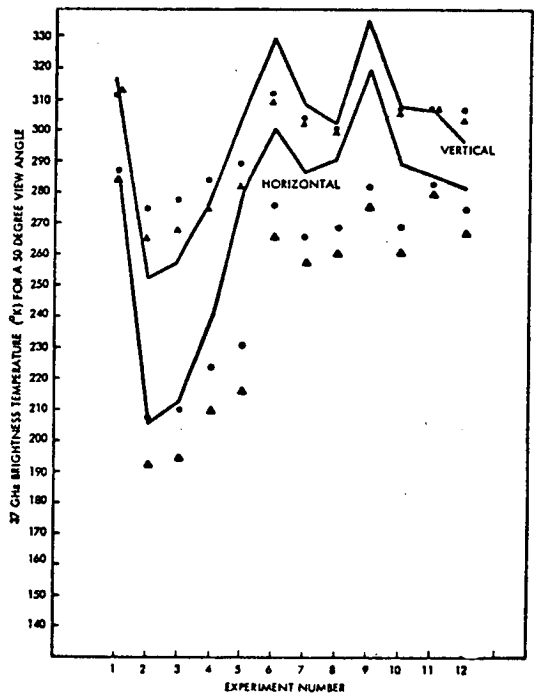

Figure 2. Comparison of measured and computed 37 GHz brightness temperatures. —— indicates measured temperatures while ● and ▲ indicate computed temperatures with form numbers = 16 and 32, respectively.

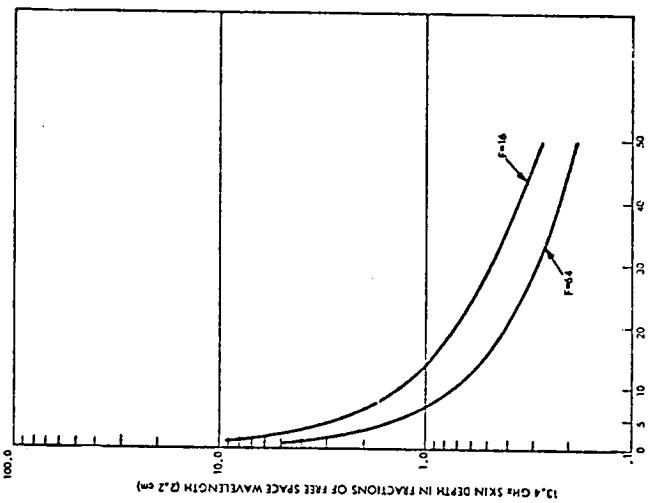

Figure 3b. Skin depth at 13.4 GHz as a function of the volume percentage of water computed from Wiener's mixing formula with form numbers 16 and 64.

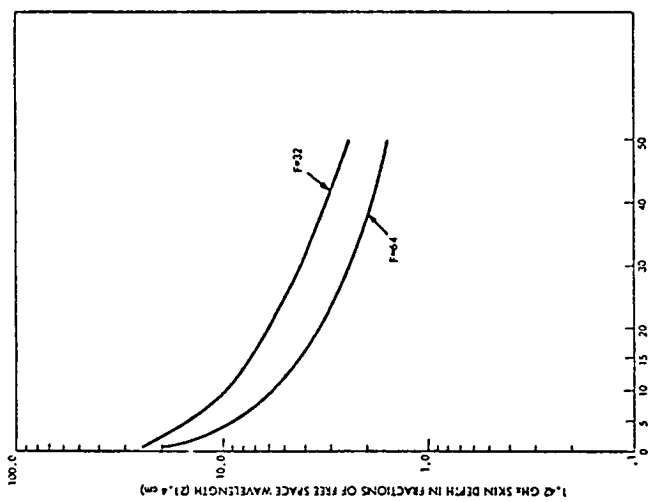

Figure 3a. Skin depth at 1.42 GHz as a function of the volume percentage of water computed from Wiener's mixing formula with form numbers 32 and 64.

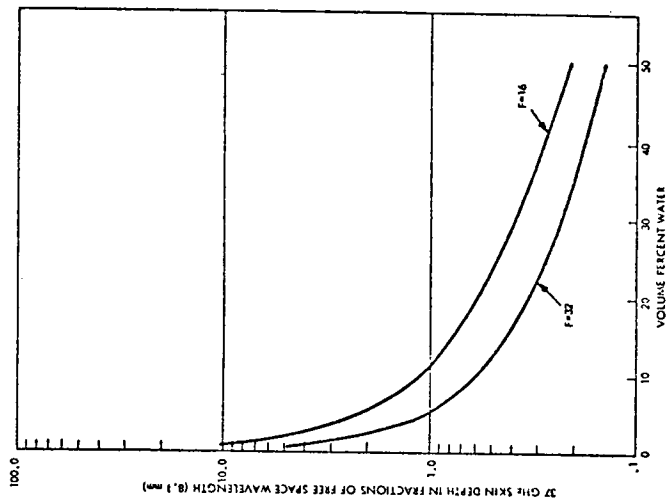

Figure 3d. Skin depth at 37 GHz as a function of the volume percentage of water computed from Wiener's mixing formula with form numbers 16 and 32.

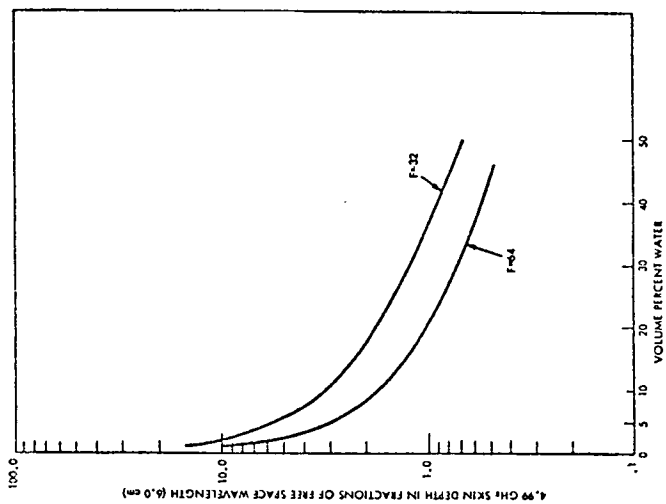

Figure 3c. Skin depth at 4.99 GHz as a function of the volume percentage of water computed from Wiener's mixing formula with form numbers 32 and 64.

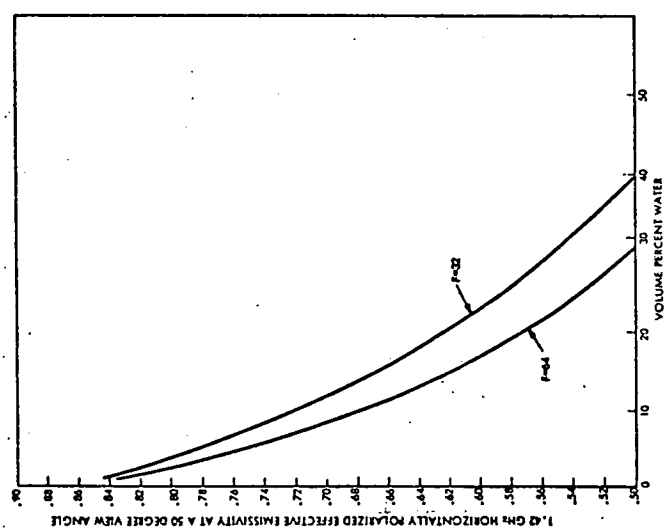

Figure 4a. Horizontally polarized 50° view angle effective emissivity at 1.42 GHz as function of the volume percentage of water computed from Wiener's mixing formula with form numbers 32 and 64.

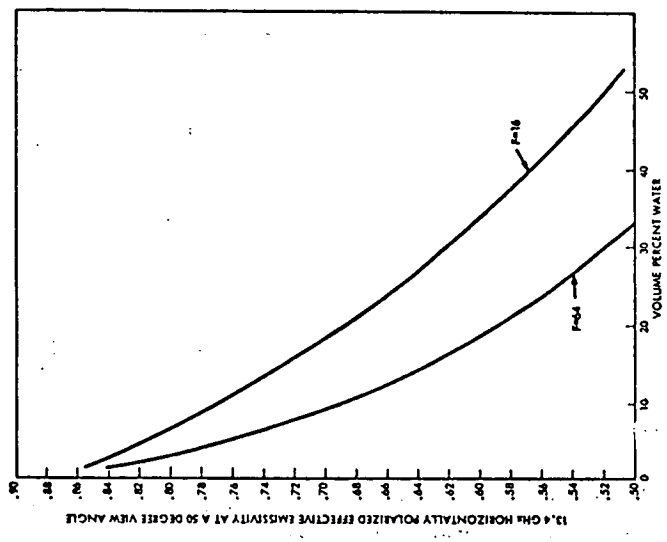

Figure 4b. Horizontally polarized 50° view angle effective emissivity at 13.4 GHz as function of the volume percentage of water computed from Wiener's mixing formula with form numbers 16 and 64.

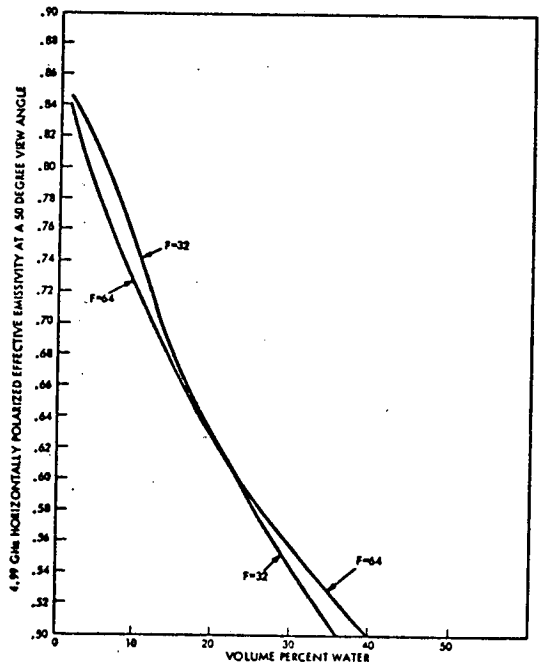

Figure 4c. Horizontally polarized 50° view angle effective emissivity at 4.99 GHz as function of the volume percentage of water computed from Wiener's mixing formula with form numbers 32 and 64.

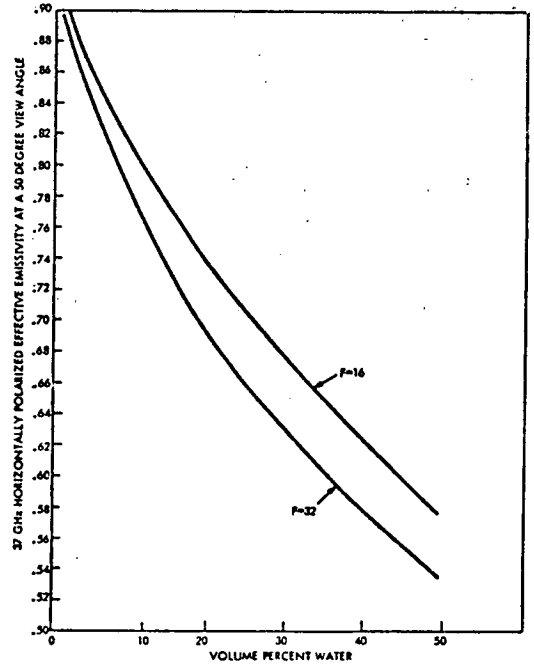

Figure 4d. Horizontally polarized 50° view angle effective emissivity at 37 GHz as function of the volume percentage of water computed from Wiener's mixing formula with form numbers 16 and 32.

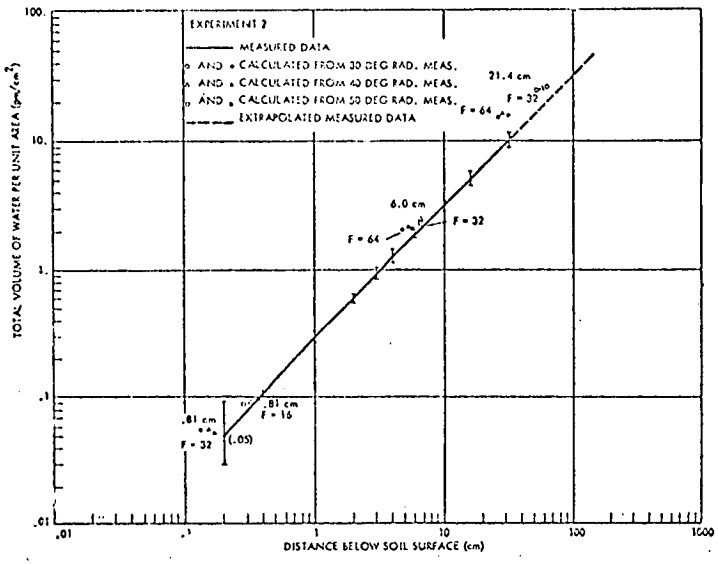

Figure 5. Comparison of measured and computed vertical moisture profiles for Experiment 2. Wavelengths are indicated near computed results with Form Numbers F.

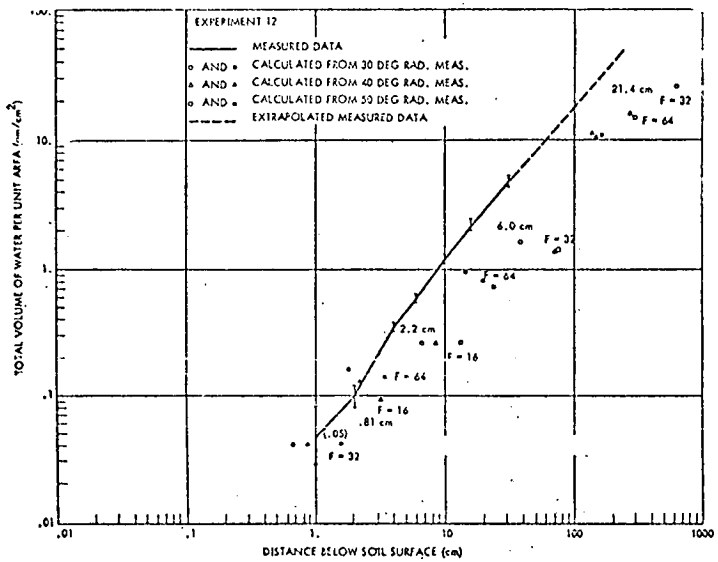

Figure 6. Comparison of measured and computed vertical moisture profiles for Experiment 12. Wavelengths are indicated near computed results with Form Numbers F.

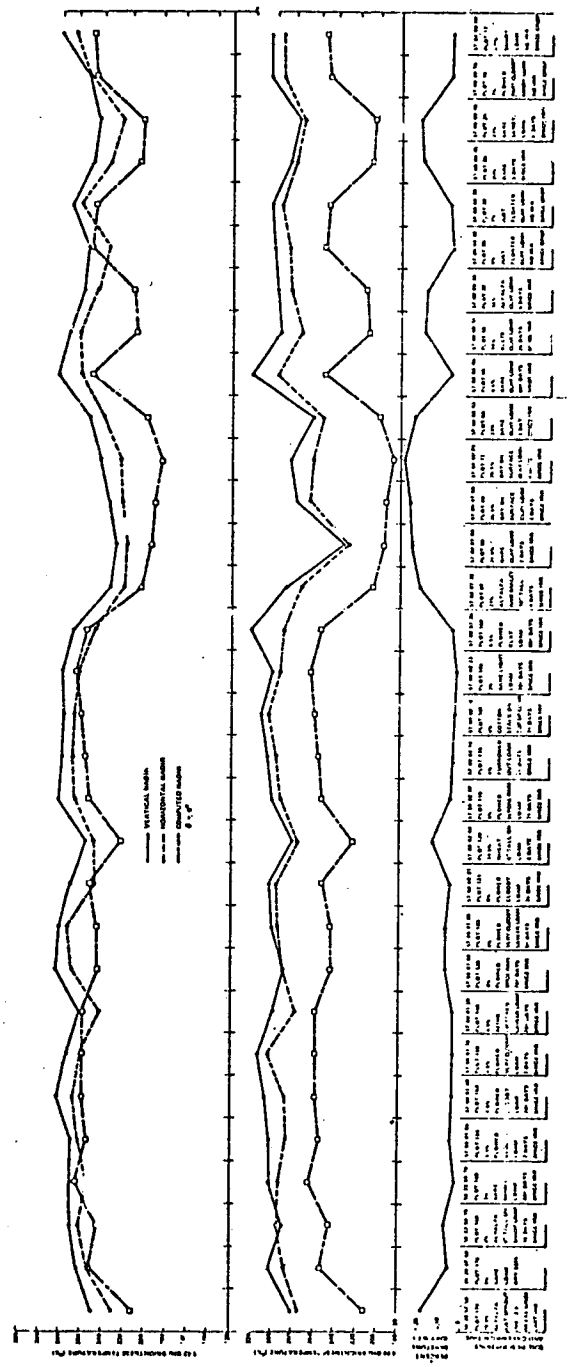

Figure 7. Comparison of airborne and computed 1.42 and 4.99 GHz brightness temperatures for the February soil moisture flight at 0.9 km altitude. Soil descriptions and integrated 15 cm deep soil moisture values are shown. Computations are based on the uniform model.

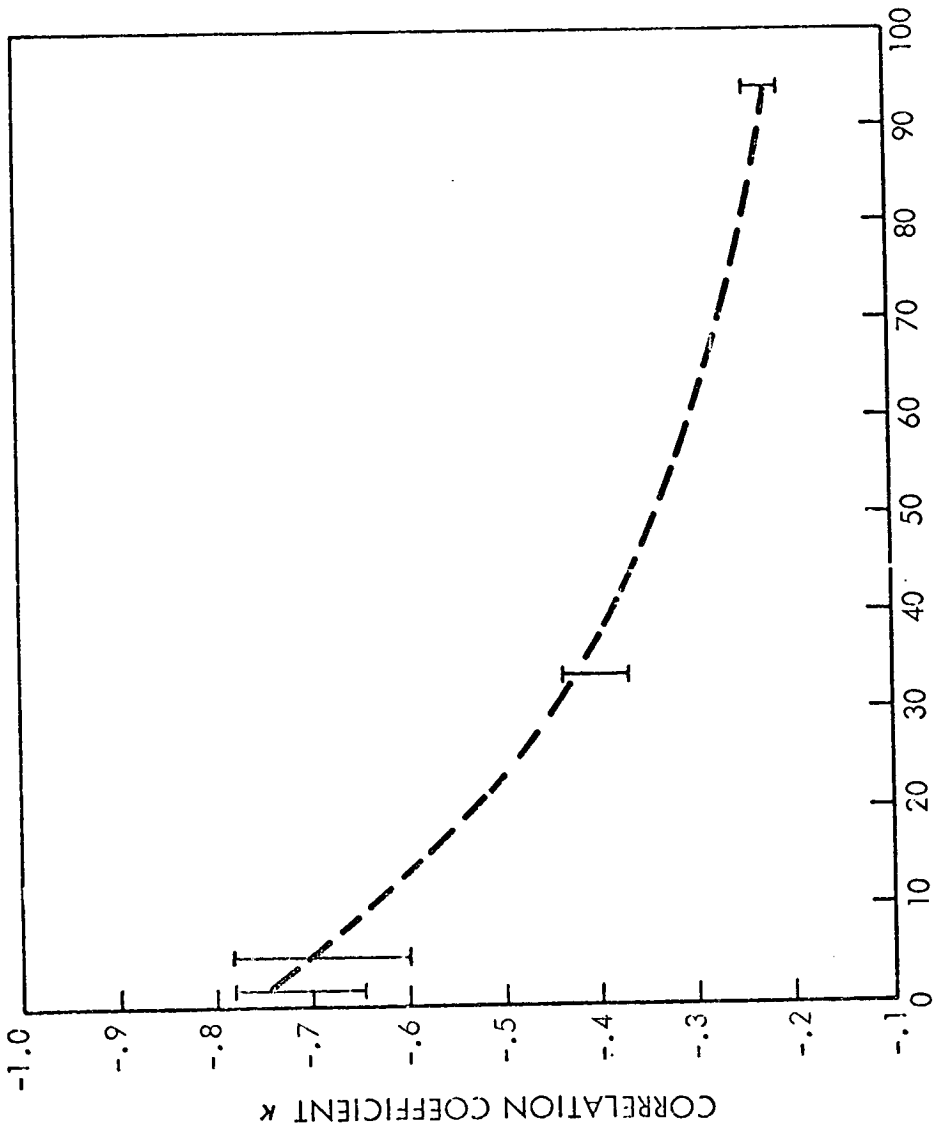

Figure 8. Correlation Coefficient versus Frequency

SECTION 94

DETERMINATION OF THAWING SNOW AND ICE SURFACES USING EARTH SATELLITE DATA

by

Donald R. Wiesnet and David F. McGinnis
National Oceanic and Atmospheric Administration
Washington, D. C. 20331

INTRODUCTION

One of the earliest proposed and perhaps least imaginative uses of environmental earth satellite systems was to map snow on continental land masses of the world. Once weather satellites, such as TIROS, Nimbus, ESSA and NOAA (as well as Gemini and Apollo missions) were up and sending back imagery of the earth to meteorologists, it became clear that snow and ice were indeed readily apparent. However, cloud cover and other problems presented obstacles to accurate snow mapping. As NOAA's satellite hydrology program developed, improved snow detection and mapping has continued to be one of its fundamental goals. Ultimately, the goal of NOAA's Satellite Hydrology Program is to provide timely, comprehensive, and repeated satellite and aircraft information on the areal distribution of hydrologic factors on a local and regional basis, and to assist in the development of applications of these data to operational and research problems in hydrology and meteorology.

The purpose of this paper is to report on the apparent differential spectral reflectance as sensed by the Imaging Dissector Camera System (IDCS) in the visible portion of the electromagnetic spectrum and by the High-Resolution-Infrared Radiometer (HRIR) in the near-IR portion of the electromagnetic spectrum . Both instruments were aboard the Nimbus 3 satellite. A paper on this phenomenon was published in November in the Monthly Weather Review (Strong, McClain, and McGinnis, 1971). Research on this differential spectral reflectance and possible applications is continuing in NOAA/NESS.

SENSORS

The experimental Nimbus 3 meteorological satellite provided for 24-hour mapping of the global cloud cover and for nighttime infrared measurements of both earth-surface and cloud-top temperatures in the 3.6 to 4.2 micron portion of the spectrum. However, during the day the HRIR was programmed to measure near infrared radiation (0.7 to 1.3

micrometers) radiation to complement the Image Dissector Camera System (0.5-0.7 micrometers). The field of view of the HRIR at nadir (8.5 km diameter) is about twice that of the IDCS (4.1 km diameter). For additional information consult the Nimbus III Users Guide (GSFC, 1969).

LAKE WINNIPEG

Figure 1 is an index map showing the location of the Nimbus 3 satellite IDCS and HRIR imagery taken simultaneously at about 1800 hours GMT (1200 hours local) on April 25, 1969. In the IDCS photograph (Figure 2A) Lake Winnipeg is clearly visible in the area between two cloud masses. The brightness of the Lake indicates the presence of ice, possibly snow-covered ice.

Compare the corresponding daytime HRIR image (Figure 2B) taken at the same time (1800 hours GMT, 1200 hours local). Cloud patterns are almost identical. The Great Lakes and parts of the Mississippi River appear darker than the adjacent land, whose vegetation is more reflective than water in the 0.7 -1.3 micron range. One would expect ice-covered Lake Winnipeg to be easily visible on the HRIR imagery, especially as the surrounding land was free of snow cover. Yet, as seen in Figure 2B, there is no trace of Lake Winnipeg on the HRIR imagery, although careful examination of the original imagery does reveal a slight darkening, suggestive of an open water surface where Lake Winnipeg ought to be.

SIERRA NEVADA SNOW COVER

Figure 1 shows the area included in Nimbus 3, simultaneous visible and near infrared imagery of California and Nevada (Figure 3) taken at 2000 GMT (1200 local) on April 25, 1969. On the visible, (Figure 3A) the snow-covered Sierra Nevada appears very bright. In the near IR (Figure 3B), the bright area is much smaller and correlates well with the high elevations. The bright band south and west of the Sierra is believed to be a band of clouds and is not snow. Why can we not see the snow that we know is the Sierra?

GROUND TRUTH

At 1200 local time the air temperature at Lake Winnipeg on April 25, 1969, ranged from 8° to 15°C. No snow was reported on the ground. In the Sierra Nevada, the air temperatures at the 1500-meter

level were about 8°C. Above the 3000-m contour, subfreezing temperatures prevailed.

DISCUSSIONS

It is postulated by Strong, McClain, and McGinnis (1971) that the melting conditions at Lake Winnipeg (8° - 15°C) caused water films to be predominant at the snow (ice) surface, thereby causing the absorption of incident solar radiation. Enough radiation was absorbed to cause the surface to appear dark on the near IR imagery. In fact, they point out that even a 1 mm layer of water would result in very high absorption of the solar radiation. In other words, the layer of water at the surface might be so thin as to be unobservable even by an experienced snow hydrologist.

The melting and breakup of lake ice has been well studied and we will repeat here the accurate description of the final stages by G. P. Williams (1966).

"The ice first starts to melt on the shore because it is thinner there and because more heat comes from the adjoining ground surface. A free water surface appears along the shoreline leaving the main body of ice floating free. At the time the ice cover still has considerable strength."

Williams (1966) also stated: "During the second stage of melting there is melt of the snow and of the snow ice on the floating ice. The melt water flows along drainage patterns on the surface and it drains to the open water at the shore line or to holes that appear to develop preferentially along old thermal cracks. When the melt water drains away, the surface has a porous, white and crumbly structure which reflects solar radiation and retards internal melting. As the melt season progresses some melt water accumulates beneath the ice surface. A typical ice-cover profile will then consist of a shallow, porous surface layer 2 to 3 inches thick, a layer of water-logged ice several inches thick and then solid unmelted ice extending to the water.

"In the final stages, the underlying entrapped water layers result in darkened surface ice and most of the incoming solar radiation is absorbed."

Despite a lengthy but not exhaustive literature search, only a few meager bits of data on spectral reflectance of snow were found: Kondrat'ev et al. (1964) found a fairly steady 90% reflectance for dry snow as wave length increased in the visible region and somewhat less -- but fairly steady -- percentage for wet snow. Mellor (1964) indicated a fairly rapid drop off for wet snow, which is more marked at the longer wave lengths. In the near IR, Montis (1951) showed a reflectance of only 25% at 1.2 micrometers, the maximum response point

of the HRIR.

NOAA/NESS is currently arranging for additional field and laboratory measurements with Goddard SFC and CRREL. Additional examples of differential spectral response have been secured and are under study.

Although the results of this study must be called preliminary, it should be pointed out that this potential 2-channel method of detecting thawing snow is of great interest to hydrologists for snowpack-runoff prediction, flood forecasting, lake navigation, and commercial shipping.

REFERENCES

1. Strong, A.E., McClain, E.P., and McGinnis, D.F., 1971, Detection of Thawing Snow and Ice Packs through the Combined Use of Visible and Near-Infrared Measurements from Earth Satellites, Monthly Weather Review, V. 99, No. 11, p. 828-830.

2. Goddard Space Flight Center, NASA, 1969, Nimbus III Users Guide, NASA, Greenbelt, Md. 238 p.

3. Williams, G.P., 1966, Freeze-up and Break-up of Fresh Water Lakes, Proc. Nat. Research Council Conf. on Ice Pressures Against Structures. Tech. Man. 92, p. 203-215.

4. Mellor, Malcom, 1964, Properties of Snow, Cold Regions Science and Engineering, Pt. III, Sec. A., U.S. Cold Regions Res. and Eng. Lab., Hanover, N. H., 105 p.

5. Mantis, H.T., 1951, Review of the properties of Snow and Ice, vs. Cold Regions Res. and Eng. Lab., Hanover, N. H.

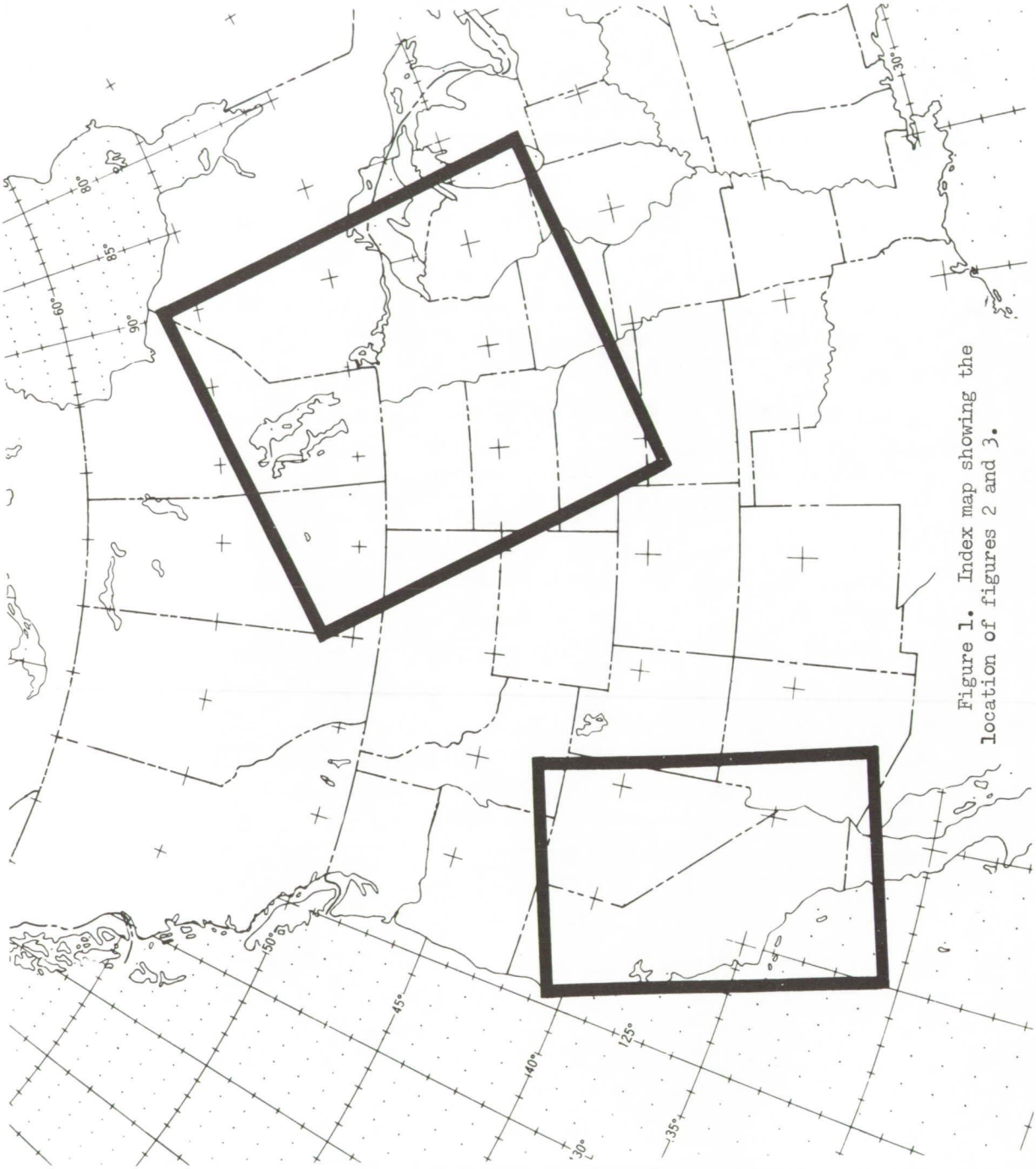

Figure 1. Index map showing the location of figures 2 and 3.

(a) IDCS

λ = 0.5 to 0.7 μm

(b) HRIR

λ = 0.7 to 1.3 μm

Figure 2. Simultaneous daytime visible (a) and near IR (b) images of the Lake Winnipeg area, showing detection of melting lake ice in the visible but no reflectance of the melting ice in the IR. Air temperature, 8°C; 1800 hours GMT.

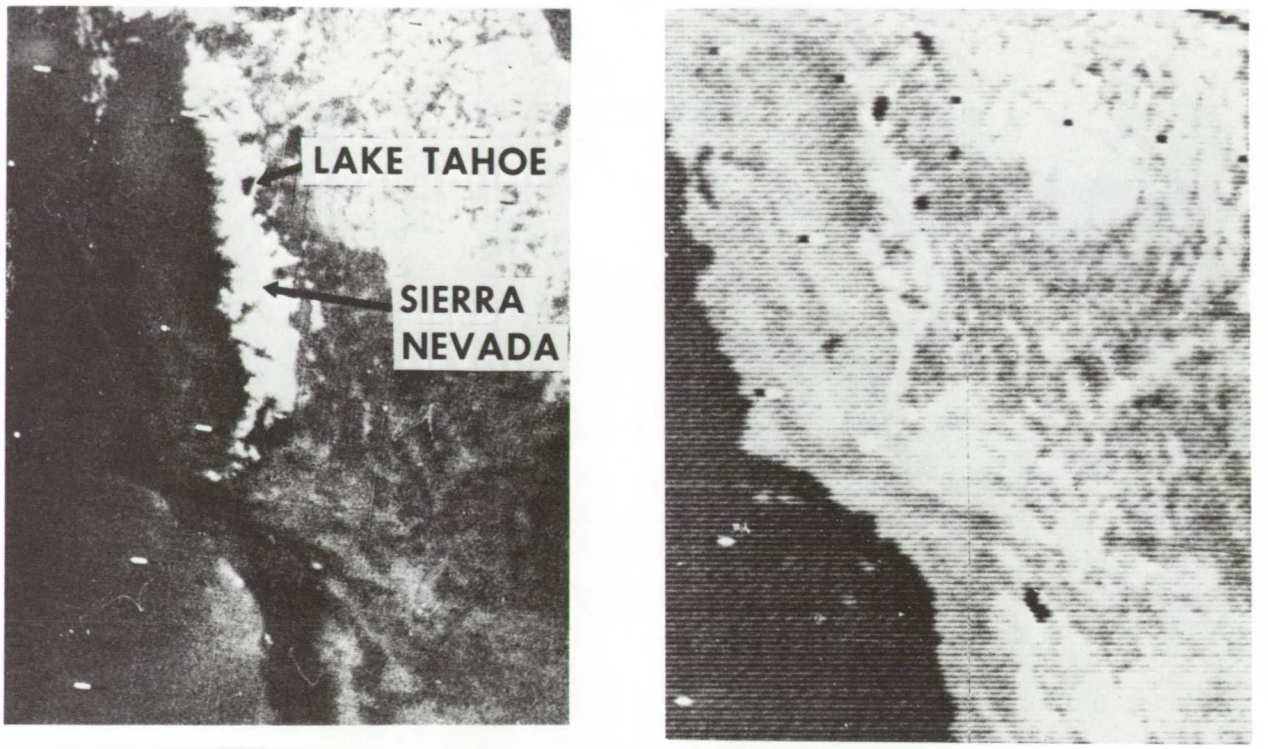

Figure 3. Simultaneous daytime visible (a) and near IR (b) images over the Sierra Nevada showing non-reflectance in the near IR of melting snow in the lower areas of the Sierra Nevada. April 25, 1969 at 2000 GMT.

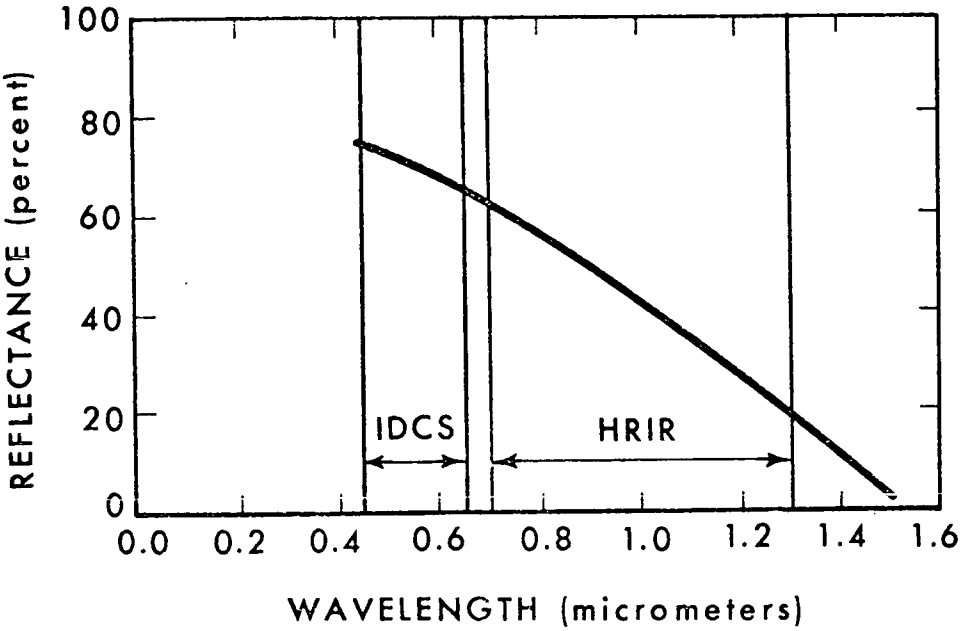

Figure 4. Spectral Reflectance of melting snow (Mantis, 1951).

SECTION 95

SNOW STUDIES USING THERMAL INFRARED OBSERVATIONS FROM EARTH SATELLITES

by

James C. Barnes*
Allied Research Associates, Inc.
Concord, Massachusetts

INTRODUCTION

This report summarizes work performed for the Environmental Sciences Group of the National Environmental Satellite Service of NOAA, under Contract No. 1-35350. The purpose of this contract is to study the application of satellite high resolution infrared data for mapping snow cover. The study has two objectives: (1) to determine whether existing radiometers onboard the Nimbus and ITOS satellites can provide hydrologically useful snow information, and (2) to develop analysis techniques applicable to future IR sensor systems on earth satellites. The IR measurements are being analyzed in conjunction with concurrent satellite photographs and conventional snow cover data.

DATA SAMPLE

Infrared measurements from the Nimbus 4 and ITOS-1 satellites are being analyzed in this study. The Nimbus 4 THIR (Temperature Humidity Infrared Radiometer) system was in operation from early April 1970 until 8 April 1971, except for a brief period during January. ITOS-1 was launched in February 1970 and operated until June 1971. The most usable data from the ITOS SR (Scanning Radiometer) system were during the period from December 1970 through April 1971.

The infrared channels of the THIR and SR sensors measure in the same spectral interval (10.5 to 12.5 μm) and are similar in spatial resolution (approximately 8 km). Thus, measurements from the two sensors can be considered compatible. Since these were the first high-resolution radiometers to measure in the 10.5 to 12.5 μm channel, the Nimbus 4 and ITOS-1 satellites have provided for the first time both nighttime and daytime thermal infrared data.

*The author's current affiliation is with Environmental Research & Technology, Inc., Lexington, Massachusetts 02173. The work reported in this paper is being continued at ERT, Inc.

Data have been analyzed for three primary geographic areas: (1) the Northeastern United States, including New England and New York; (2) the Upper Mississippi-Missouri River Basin region; and (3) the Sierra Nevada in California. Infrared measurements during periods of snow cover and snow cover change are available for all three of these areas, each of which has different terrain and vegetation characteristics. A few analyses have been extended into the south-central part of the country and into other mountain areas, principally the Colorado Rockies and the Pacific Northwest.

ANALYSIS OF FILM STRIP DATA

For the geographic areas described above, the temperature patterns evident in Nimbus THIR and ITOS SR film strip data have been mapped onto base maps and have been correlated with snow distributions mapped from satellite photographs, snow reports obtained from climatological data summaries, and other information derived from elevation and forest cover charts. These analyses are described in the following paragraphs.

NORTHEASTERN UNITED STATES

Nimbus 4 THIR

Very good quality data were available over the Northeast during April and May 1970, early in the operation of Nimbus 4. Primarily through identification of land features, the region was determined to be cloud-free in passes on six dates during this period. Snow distributions evident on concurrent Nimbus IDCS (Image Dissector Camera System) photographs were also mapped for these dates and overlayed on the mapped IR temperature patterns.

The period from 14 April to 5 May 1970 was a period of rapid snow melt in New England and New York. Snow reports indicate that most of the higher terrain was snow covered in early April, whereas by the end of the month little snow cover remained. The decrease in snow extent is clearly evident in the IDCS photographs. On 14 April, the IR film strip displays an area of distinctly lower temperature that correlates very closely with the area of snow cover mapped from the photograph. On the other dates analyzed the agreement is also good; on 5 May, when the photograph shows little or no snow cover, the IR temperatures are uniformly higher over the entire area. In these film strips, no variation in gray tone can be detected within the snow-covered areas; these areas simply appear uniformly colder than the lower elevation, non-snow covered terrain such as the Hudson, Mohawk, and St. Lawrence Valleys.

ITOS-1 DRSR

Temperature patterns were also mapped from a sample of ITOS-1 nighttime DRSR film strips from February and March 1971. In each case sufficient identification of land features, such as coastlines, lakes and river valleys, was evident in the IR imagery to determine the cloud-free regions. These data also show good agreement in most instances between areas of lower DRSR temperatures and snow cover. In one February case distinct variations in gray tone are evident within areas such as the Adirondack Mountains of New York; more detailed analysis is currently being carried out to determine whether these variations can be related to differences in elevation and vegetation, since the area is thought to be uniformly snow-covered at that time.

A DRSR pass on 9 February shows particularly distinct gray-tone patterns over the eastern and central United States. Three bright bands of significantly lower temperature exist: one across Southern Missouri and northern Arkansas into Oklahoma; another from Ohio and western Pennsylvania, southward across Kentucky and Tennessee to northern Mississippi; and the other along the Appalachians. The colder bands correlate very well with areas of recent snowfall (on 7 and 8 February, snow fell as far south as Mississippi). Snow reports indicate from 1 to 6 inches of snow within the areas of lower temperature; no snow was reported outside these areas.

UPPER MISSISSIPPI-MISSOURI RIVER BASIN REGION

Nimbus 4 daytime THIR film strips over the Upper Mississippi and Missouri River Basins region have been analyzed for several dates during December 1970. For the data analyzed areas of lower temperature are generally in good agreement with the actual limit of the snow cover as mapped from concurrent IDCS photographs. In most cases, in fact, a narrow band of less than one inch of snow cover through central Minnesota and the Dakotas appears as an area of slightly higher temperature than does the surrounding snow-covered terrain.

SIERRA NEVADA

Similar analyses have also been performed for some 15 Nimbus 4 daytime passes over the Sierras during the runoff period of April, May, and June 1970. In many of the film strips, two distinct gray levels are evident in the area of the southern Sierras. The maximum brightness (lowest temperatures) varies considerably from day to day, however, indicating that quantitative evaluation of IR film strips on a day to day basis is difficult. In comparative analyses with the snow extent mapped

from concurrent photographs, the area of brighter tone appears to be associated with the higher terrain in general rather than with the snow-covered areas. The brightest tone occurs within the snow-covered area, but even the extent of this tone does not correlate exactly with the extent of snow cover. The area of lowest temperatures in one nighttime pass analyzed (24 April) is more limited in extent than the corresponding brightest tone in the daytime pass on the same date. Since this is an isolated case, however, it is difficult to draw any conclusions from it regarding differences in daytime and nighttime IR measurements.

ANALYSIS OF DIGITIZED DATA

In order to obtain a more quantitative evaluation of relationships between measured IR temperatures and snow cover, digitized data are being analyzed. Digitized data are available from Nimbus in the form of 1:1 million scale Mercator maps with nearly full-resolution temperatures printed; ITOS computer printouts also provide close to full resolution data, although ranges of temperature, in approximately 2^{o} intervals, are given rather than actual values.

COMPLETED ANALYSES

The initial analysis of the digitized data has consisted of mapping the temperature distribution (at approximately $10^{o}K$ intervals) and correlating these distributions with geographic features and with the snow extent mapped from the IR film strips and the Nimbus IDCS photographs.

NORTHEASTERN USA

The results of the initial analysis for the Northeast indicate the IR temperatures over snow-covered terrain to be several degrees higher than would be anticipated. For three representative passes, the IR temperature values that provide the best fit with the snow line mapped from the IDCS photographs (and with the snow line mapped from the IR film strips, which as stated earlier was found to be in close agreement with the IDCS snow line) are as follows: (14 April) T = $285^{o}K$, (16 April) T = $290^{o}K$, (26 April) T = 289^{o} K. For these same dates, the average temperatures for the nonsnow-covered areas of southern New England are about 292, 296, and $296^{o}K$, respectively. The temperatures for representative ocean areas just east of New England remain about 274 to $276^{o}K$ throughout the period. Thus, the sensor system seems to be relatively stable and the snow-covered areas are consistently 6 to $7^{o}K$ colder than the nonsnow-covered areas. However, even with a melting snow surface, one would expect the sensor to measure a temperature of near $273^{o}K$ over the snow; the actual measured temperatures are some 10 to 15^{o} K higher than the expected value.

FAR WEST

Nimbus daytime passes over the Sierras on 5 and 31 May 1970 also display temperatures somewhat higher than anticipated. On 5 May the temperature that appears to be associated with the boundary of the brightest tone in the film strip is 290°K; on this date, the lowest temperatures measured over the Sierras are about 276°K. On 31 May, the temperatures are some 10° higher than on 5 May.

Analysis of the daytime and nighttime maps on 24 April 1970 indicates that the nighttime temperatures over the snow-covered Sierras region are some 10 to 15° lower than the daytime values. The nighttime minimum values are between 260° and 265°K and the maximum values near 275°; these are closer to the temperatures anticipated for snow surfaces.

The ITOS computer printouts also show temperatures closer to those anticipated, especially during nighttime. For the three dates for which data were available, the mean temperatures over the Sierras are as follows: (7 February) T(day) = 276°K, T(night) = 264°K; (18 March) T(day) = 272°K, T(night) = 260°K; (15 April) T(day) = 276°K, T(night) = 264°K. It is seen, therefore, that despite the advance in season the overall temperatures remain similar.

The nighttime IR temperatures are also seen to be some 10 to 15°K lower than the daytime. However, it has been noted that despite the lower temperatures, the definition of the higher mountains is obscured in the nighttime measurements. This is apparently due to the fact that the lower terrain, particularly over the Great Basin, cools considerably at night. The result is a uniformly low temperature over the entire area, regardless of elevation.

UPPER MISSISSIPPI-MISSOURI RIVER BASIN REGION

Three Nimbus passes over the Midwest have been analyzed. In two daytime passes, on 17 and 29 December 1970, the snow line as mapped from IDCS photographs is associated with IR temperatures of 270 to 275°K. In nighttime data on 29 December, the corresponding temperature is about 260°K. Thus, in this geographic area also, the difference between daytime and nighttime IR measurements over snow cover is 10 to 15°K. Overall, the temperatures are considerably lower than those measured in the spring over the Northeast, but are in the same range as those measured by ITOS over the Sierras.

ANALYSES IN PROGRESS

Further investigations are currently in progress to determine in more detail the structure of the IR temperature measurements across snow fields. For each of the above geographic areas, analyses using both the data on hand and additional data will include: (1) Determination of the temperatures that best fit the apparent snow line mapped from the IR film strips and from satellite photographs, and the average temperatures over snow-covered and nonsnow-covered areas; (2) for selected climatological stations representative of both lower and higher elevations in the regions of interest, determination of the mean value and the range of measured IR temperatures for that immediate area; and (3) for each observation date, plotting of snow depth and the maximum and minimum surface temperatures for each climatological station, along with station elevations and profiles of the general elevation of each area. The results of these analyses will be evaluated with regard to the satellite system (Nimbus or ITOS), the season of observation (some passes are midwinter whereas others are in spring during snow melt periods), snow amount, terrain elevation, and vegetation characteristics.

In addition to the above analyses, investigations are underway to determine the effects of variations in emissivity and surface temperature that might result from partially snow-covered ground. Preliminary calculations have indicated that during daytime, even a relatively small amount of bare rock (say, 2/10 rock and 8/10 snow within the field of view of the radiometer) might have a significant effect on the measured temperature.

SUMMARY OF PRELIMINARY RESULTS

ANALYSIS OF FILM STRIP DATA

1. The ITOS-1 direct readout data (DRSR) are less noisy than the Nimbus 4 THIR film strips. Small temperature variations are, therefore, more clearly depicted in the ITOS data.

2. In the Northeast (New England and New York) during April 1970, areas of distinctly lower temperature (brighter tone) are displayed in several Nimbus film strips. The limits of these areas are in close agreement with the limits of snow cover mapped from Nimbus photographic data and from snow reports.

3. Although the snow-covered areas appear in a uniform gray tone in the above-mentioned Nimbus data, considerable variation in the temperatures measured over snow cover is detectable in an ITOS nighttime DRSR

pass across the Northeast in February 1971. Later in the same month, new snowfall of from 1 to 6 inches across parts of the south-central USA is clearly depicted in ITOS nighttime DRSR data.

4. In the Upper Mississippi-Missouri River Basins region, snow-covered areas during December 1970 appear colder than nonsnow-covered areas in Nimbus film strips. In fact, an area in the Missouri Basin, in which an inch or less of snow depth is reported, appears noticeably warmer than the surrounding areas of several inches snow depth. The forested area near Lake Superior, which in photographic data always appears in a darker tone than the adjacent nonforested areas when snow covered, cannot be detected in the IR film strips.

5. In Nimbus daytime film strips over the West, the Sierra Nevada and other mountain ranges appear distinctly colder than the lower elevations. However, the extent of the coldest patterns appears to be associated with the higher elevation terrain rather than with snow extent.

ANALYSIS OF DIGITIZED DATA

1. In the Nimbus daytime data over the Northeast during April 1970, the snow-covered areas are at least 6 to 7°K colder than the non-snow-covered areas. However, temperatures within snow-covered areas are as high as 285 to 290°K, some 10 to 15° higher than would be anticipated. These measurements were made on relatively warm days, with the reported maximum air temperatures at stations within the snow-covered areas being as high as 290°K.

2. In Nimbus daytime data over the Sierras during May 1970, the measured temperatures are also as high as 290-300°K, considerably higher than would be anticipated even over a melting snow surface.

3. ITOS data during February, March, and April 1970 depict daytime temperatures over the Sierras of 272 to 276°K and nighttime temperatures of 260 to 264°K. During nighttime, however, definition of the mountain ranges is greatly reduced because of the cooling of the lower elevation terrain.

4. In a limited sample of Nimbus data over the Midwest during December 1970, the snow line mapped from photographic and film strip data is associated with an IR temperature of 270 to 275°K in the daytime measurements and about 260°K in the nighttime measurements.

LABORATORY INVESTIGATIONS RELATED TO MICROWAVES

by

Omar H. Shemdin
Department of Coastal and Oceanographic Engineering
University of Florida
Gainesville, Florida

INTRODUCTION

Research continues on the detection of the ocean surface properties by remote methods. Two frequently used microwave instruments are the radar and the radiometer. The radar backscatter cross section and the brightness temperature sensed by the radiometer are intimately related to the microstructure of the ocean surface. The exact nature of the dependence is not completely understood yet. An extensive study by Porter and Wentz (1971) explored the factors which influence the use of the radiometer for detection of ocean surface temperatures. Hollinger (1971) found that the brightness temperature increased with wind speed which suggests the possible use of the radiometer as an instrument for remote sensing of wind speed. The use of radar as a remote anemometer has received considerable attention by the Naval Research Laboratory and a number of their publications on this matter are available. A parallel investigation is conducted jointly by the University of Kansas and New York University and their results are documented in a series of publications. Complete agreement between the results of available investigations is not in hand yet and is perhaps the primary motivation for the initiation of the controlled laboratory investigation described herein.

An alternate method for estimating the wind speed is by evaluating the percentage of whitecaps area in aerial photographs of the ocean surface, and by correlating with wind speed. This method was explored by Ross, Cardone and Conway (1970). The available whitecaps data at different wind speeds exhibit an increasing trend although the large scatter in the data shown by Monahan (1969, 1971) cannot be ignored. The possibility of other factors which influence the whitecaps area such as sea state or swell need to be considered.

The present investigation was authorized by the Spacecraft Oceanography Project of the Naval Research Laboratory under Contract No. N62306-71-C0033 to study in a laboratory controlled environment the structure of the water surface and the immediate layers above and below the surface. The scope includes (i) the investigation of the capillary

waves and their interaction with gravity waves, (ii) the formation of whitecaps at different wind speeds and the influence of gravity waves on whitecaps, and (iii) the wind generated spray under different wind and wave conditions. The comprehensive laboratory investigation was facilitated by the participation of Dr. R. J. Lai and Messrs. A. M. Reece and G. Tober. Only a brief description of the total study is described here and for more details the reader is referred to a report by Shemdin, Lai, Reece and Tober (1972).

DESCRIPTION AND APPARATUS

Wind and Wave Facility. - The wind and wave facility at the University of Florida was described in detail by Shemdin (1969). Briefly, the wave channel is 1.83 meters wide and 45.7 meters long, and is divided into two bays of equal width. The height of the facility is 1.93 meters. One bay is provided with a roof and is used as a wind channel. The water depth is maintained at 91.5 cm by a small water pump. The air intake is modified to simulate rough turbulent air flow in the wind channel as shown in Figure 1. The facility is equipped with a mechanical wave generator which can generate simple and random waves. A wave absorber beach is provided at the downwind end of the facility and is made of baskets filled with stainless steel turnings. The baskets absorb approximately 95% of the incoming wave energy of waves with frequencies greater than 0.8 HZ.

The velocity profiles above the water surface were investigated and found to follow a logarithmic distribution as shown by Lai and Shemdin (1971). These measurements were repeated for the present investigation to obtain a complete description of the wind field corresponding to the measured whitecaps area and spray.

Experiments were conducted in the wind and wave facility with both fresh well water and a prepared salt water solution with salt concentration equal to 35 parts per thousand. The surface tension of the well water was measured and compared to that of ordinary tap water. The surface tension of the prepared salt water was measured and compared to that of the ocean water. Figure 2 shows a comparison between the surface tension values of different samples. It was concluded that the prepared salt water solution was similar in physical properties to that of the ocean water.

Hot-film Anemometer System for Measuring Spray. - A technique using a hot-film anemometer was developed to measure spray above the water surface. A hot-film is cooled when hit by a drop which produces a change in the film resistence and consequently generates a voltage

pulse. A calibration procedure was followed in which uniform droplets were generated and their diameters were recorded photographically. The droplets were allowed to hit the hot-film and the corresponding voltage heights were recorded. It was found that the height of the voltage pulse increased with increasing droplet diameter. The hot-film anemometer and calibration system is shown in Figure 3. The hot-film was placed in the air stream above the water surface and the calibration curve was used to determine the droplets size distribution under given wind conditions.

Laser-Optical Gage for Measuring Capillary Waves. - Capacitance gages are limited in studying the structure of high frequency waves because of the finite draining time of water along an insulated wire. Cox (1958) developed an optical gage to measure slopes of capillary waves. His technique, however, produces significant errors when the water surface displacements are large. A laser-optical gage was developed to study slopes of capillary waves in the presence of gravity waves. The gage is insensitive to the surface displacements produced by gravity waves generated in the wind and wave facility to within tolerable limits. A schematic of the facility cross-section and position of the laser and optical detector is shown in Figure 4. Details of the optical detector are shown in Figure 5. Simultaneous slope measurement in the downwind and crosswind directions are obtained by a beam splitter, two wedges filled with ink to produce spacial gradients of light intensities and two photo multiplier tubes. Changes in the surface slope correspond to variations in the voltage output from the photo multiplier tubes. A procedure was developed to linearize the voltage-spectral computations of capillary waves.

Whitecaps Area Measurement. - An overhead camera was used to obtain photographs of the water surface. The camera was mounted at an angle facing upwind. The distortion in the surface area was calibrated and used to obtain accurate estimates of the whitecaps area. For each wind, fetch and wave condition five photographs were averaged to arrive at an average whitecaps area.

Other Miscellaneous Equipment. - A Beckman Instruments salinometer, Model RS5-3, was used to detect salinity changes in the facility. A pitot static tube and sensitive pressure transducer were used to measure the wind velocity. A thermister probe and readout device, Model 431J, manufactured by Yellow Springs Instrument Company was used to measure the air and water temperatures. The humidity was obtained by measuring the wet and dry bulb temperatures with the same instrument.

EXPERIMENTAL PROCEDURE AND METHOD OF ANALYSIS

Two major experiments were conducted, one with fresh water and the other with salt water. In each case measurements of spray and capillary waves were obtained at three different wind speeds and at fetch 24.36 (i.e. 24.36 meters downwind of the air intake). At each wind speed measurements were obtained both in the presence and absence of mechanically generated gravity waves. The whitecaps areas were obtained under the above conditions and at two other fetches 9.15 and 15.3 meters to investigate their fetch limited properties. Spray and capillary wave measurements could only be obtained at one fetch in the available time. The scopes of the fresh-water experiment is shown in Table 1 and the saltwater experiment is shown in Table 2. A comprehensive description of tests, calibration and procedures is given in the report by Shemdin, et al (1972).

RESULTS AND DISCUSSIONS

Whitecaps Area. - The increase in whitecaps area with wind speed is shown in Figure 6 for both the fresh-water and salt-water. The whitecaps area increased from zero at 10 m/sec to approximately 10% at 15 m/sec and was consistant with the upper limit of field measurements given by Ross et al (1970). For a given wind speed the whitecaps area increased with fetch up to saturation at fetch 15.3. The whitecaps area remained constant thereafter.

A significant reduction in whitecaps area was effected by mechanically generated gravity waves as shown in Figure 7. Small amplitude gravity waves produced the highest reduction in whitecaps area for a given wind speed. The whitecaps area increased with increasing gravity wave amplitude up to an unstable amplitude whence the breaking of gravity waves increased the whitecaps area up to 45%. The influence of swell in the ocean, neglected by previous investigators, may well be the major reason for the data scatter shown by Monahan (1969, 1971).

Spray. - The drop size distribution was obtained by statistical analysis of pulse heights recorded on oscillograph paper. Drop size distributions are shown in Figure 8 from measurements at three elevations above the mean water level. The ordinate represents the number of drops per unit volume within a given drop diameter band width. The integral under a distribution curve represents the total number of drops per unit volume. The d^{-3} line is shown for comparison. An analysis of the relationship between drop size distribution and the surface shear stress is given by Shemdin et al (1972).

The total number of drops passing a unit vertical area per unit time, P, is found to decrease logarithmically with height as shown in Figure 9. Such a distribution is convenient and allows the construction of a simple analytical model for drops. The droplet factor P_* is a characteristic parameter similar in nature to the shear velocity U_* obtained from the logarithmic velocity distributions of rough turbulent shear flows. It is found from the experimental results that P_* increases exponentially with U_*.

Capillary Waves. - Slope records of the down-wind and cross-wind components of capillary waves are shown in Figure 10 and compared with a simultaneous water surface displacement record obtained by a capacitance gage. The optical records exhibit the presence of capillary waves up to 50 HZ whereas the capacitance gage does not respond to such frequencies. It can be observed that the capillary waves persist on the down-wind slope of the longer wind waves which demonstrates the importance of capillary waves and their interactions with longer waves.

In the presence of a long mechanically generated gravity wave the capillary wave records are shown in Figure 11 and exhibit an uneven distribution of capillary waves along the gravity wave profile. More capillary waves appear on the crests of the gravity waves compared to the troughs and are consistent with strong nonlinear interactions between the capillary and the gravity waves. Energy spectra of the gravity and capillary are given by Shemdin et al (1972).

The strong interaction between the capillary and the gravity waves offers an explanation for the decrease in the whitecaps area produced by the mechanically generated gravity wave. It is seen that the capillary waves transfer part of their excess energy to the gravity waves by nonlinear interaction.

The results of the present investigation amplify the importance of the capillary-gravity waves interactions in influencing the whitecaps area and in determining the ocean surface microstructure, both of which influence the radar backscatter and the brightness temperature sensed by a radiometer.

CONCLUSIONS AND RECOMMENDATIONS

The following conclusions are derived from the present laboratory study:

1. Capillary waves generated by wind interact strongly with gravity waves generated mechanically.

2. The whitecaps area increases with wind speed from zero at 10 m/sec to approximately 10% at 15 m/sec. The long gravity waves reduce the whitecaps area significantly.

3. The size distribution of drops above the water surface has spectral features similar to field observations. The long gravity waves increase the total number of drops at a given elevation above the water surface. The total number of drops decrease with height according to a logarithmic distribution.

The effort up to date in this investigation was to develop the instrumentation and techniques to measure the capillary wave structure, whitecaps area and spray. With these objectives already accomplished and with sufficient experimental data in hand to asses the nature of the air-sea phenomena related to remote sensing the following recommendations are proposed:

1. Power spectra of capillary wave slopes need to be investigated under different wind, fetch and gravity wave conditions.

2. A radar mounted on the wind and wave facility can provide valuable information which can be interpreted in light of the measured microstructure of the water surface.

3. A radiometer mounted on the wind and wave facility can provide information on brightness temperature which can be related to the measured whitecaps area, surface temperature and microstructure of the surface.

4. Laboratory investigations of the radar and the radiometer as potential instruments for measuring, remotely, the wind speed is strongly recommended.

REFERENCES

1. Cox, C. S. (1958) Measurements of Slopes of High-frequency Wind Waves, J. Marine Res., 16, 199-225.

2. Hollinger, J. P. (1971) Passive Microwave Measurements of Sea Surface Roughness, IEEE Trans., GE-9, 165-169.

3. Lai, R. J. and Shemdin, O. H. (1971) Laboratory Investigation of Air Turbulence Above Simple Water Waves, J. Geophys. Res., 76, 7334-7350.

4. Monahan, E. C. (1968) Sea Spray as a Function of Low Elevation Wind Speed, J. Geophys. Res., 73, 1127-1137.

5. Monahan, E. C. (1969) Fresh Water Whitecaps, J. Atmos. Sciences, 26, 1026-1029.

6. Monahan, E. C. (1971) Oceanic Whitecaps, J. Phys. Oceanog. 1, 139-144.

7. Porter, R. A. and Wentz, III, F. J. (1971) Microwave Radiometric Study of Ocean Surface Characteristics, Radiometric Technology, Inc. Tech. Report No. 1-35140, Wakefield, Mass.

8. Ross, D. B., Cardone, V. J. and Conway Jr., T.W. (1970) Laser and Microwave Observations of Sea-Surface Condition for Fetch-Limited 17 - to 25 - m/sec Winds, IEEE Transactions, GE-8, 326-336.

9. Shemdin, O. H. (1969) Air-Sea Interaction Laboratory Facility, Department of Coastal and Oceanographic Engineering Tech. Report No. 3, Univ. of Fla., Gainesville.

10. Shemdin, O. H., Lai, R. J., Reece, A.M., and Tober G. (1972) Laboratory Investigations of Whitecaps, Spray and Capillary Waves, Department of Coastal and Oceanographic Engineering Tech. Report No. 11, University of Florida, Gainesville.

TABLE I

SCOPE OF FRESH-WATER EXPERIMENT
AT FETCH 24.36 m

Wave Conditions	Wind speed (m/sec)			
	10	15	17	18.7
Wind waves	3	4	5	6
f = 1.0 Hz, H = 5 cm	9	10	11	12
f = 1.0 Hz, H = 15 cm	15	16	17	18
f = 0.7 Hz, H = 10.5 cm	21	22	23	24

Whitecaps - Runs - 3 - 6, 10 - 12, 15 - 18, 21 - 24

Spray - Runs 3 - 6, 9 - 12, 15 - 18, 21 - 24

TABLE II

SCOPE OF SALT-WATER EXPERIMENT

Wave Conditions	Wind Speed (m/sec)				
	5	10	15	16.7	18.1
Wind Waves	1	2	3	4	5
f= 1.0Hz, H = 5 cm F= 24.36 m	6	7	8	9	10
f= 1.0Hz, H = 15 cm F= 24.36 m	11	12	13	14	15
f= 1.0Hz, H = 20 cm F= 24.36 m	16	17	18	19	20
f= 1.0Hz, H = 25 cm F= 24.36 m	21	22	23	24	25
Wind Waves F = 15.3 m	26	27	28	29	30
Wind Waves F = 9.15 m	31	32	33	34	35

Whitecaps - Runs	2 - 5, 7 - 10, 12 - 15, 17 - 20, 22 - 25, 27 - 30, 32 - 35.
Spray - Runs	2 - 5, 7 - 10, 12 - 15, 17 - 20, 22 - 25.
Capillary Waves - Runs	1 - 3, 6 - 7, 11 - 13, 16 - 18, 21 - 23, 26 - 28, 31 - 33.

LIST OF FIGURES

Figure 1 - Side View of Air Intake of Wind and Wave Facility.

Figure 2 - Surface Tension Measurement of Salt-water and Fresh-water.

Figure 3 - Hot-film Anemometer System for Measuring Spray.

Figure 4 - Schematic Cross View of Laser-optical System for Measuring Surface Slopes.

Figure 5 - Schematic Breakdown of Optical Sensor to Measure Surface Slopes.

Figure 6 - Whitecaps Area Vs. Wind Speed at Fetch 24.36 for Fresh-Water (light points) and Salt-Water (solid points) At Fetch 24.36.

Figure 7 - Influence of Mechanical Waves on Whitecaps Area at Different Wind Speeds.

Figure 8 - Drop Size Distributions at Three Elevations Above Mean Water Level When Windspeed = 15.0 m/sec. ∇ - 13 cm, Δ - 15.5 cm, $\circ$ - 18.0 cm.

Figure 9 - Logarithmic Distribution of Spray With Height Above Mean Water Level.

Figure 10 - Downwind (top) and Crosswind (bottom) Slope Records of Wind Waves Obtained by Optical Gage Compared to Water Surface Displacement Record (middle) Obtained by Capacitance Gage.

Figure 11 - Downwind (top) and Crosswind (bottom) Slopes of Wind and Mechanical Waves Obtained by Optional Gage Compared to Water Surface Displacement Obtained by Capacitance Gage.

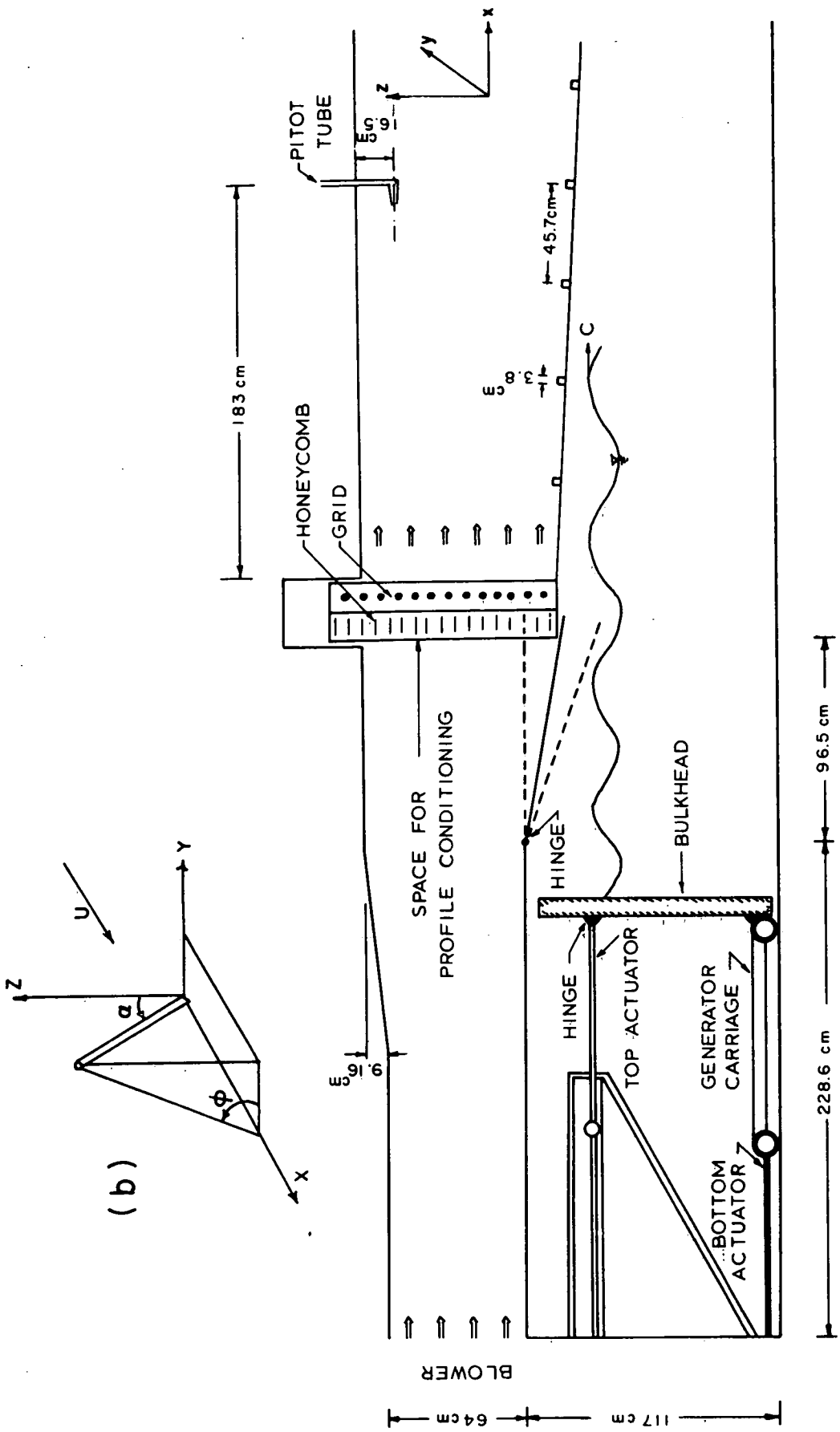
PITOT TUBE
6.5 cm
z
y
x
45.7cm
3.8 cm
C
183 cm
HONEYCOMB
GRID
SPACE FOR PROFILE CONDITIONING
9.6 cm
HINGE
BULKHEAD
HINGE
TOP ACTUATOR
GENERATOR CARRIAGE
BOTTOM ACTUATOR
BLOWER
64 cm
117 cm
96.5 cm
228.6 cm
(a)
U
Y
Z
X
α
φ
(b)

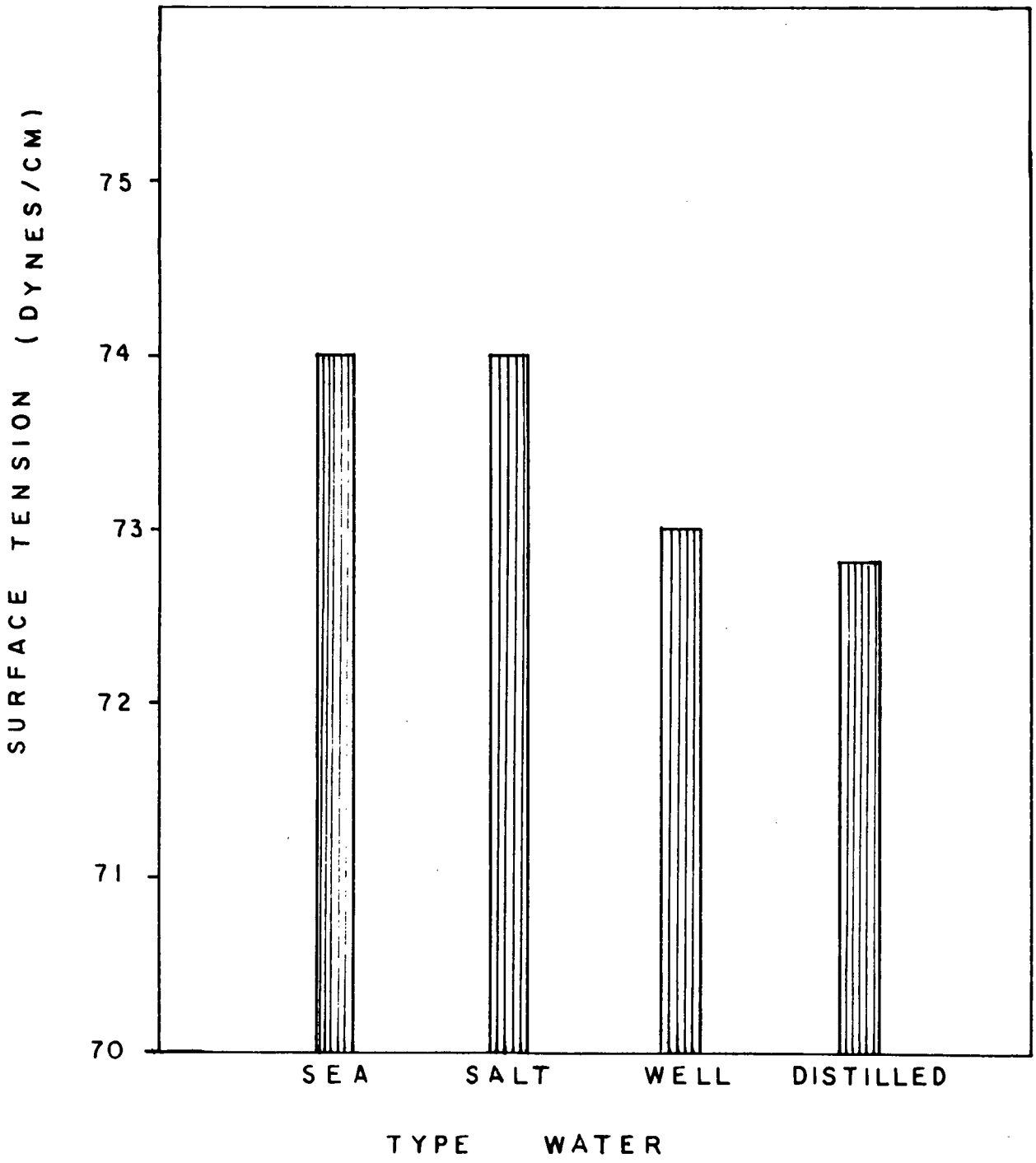
SURFACE TENSION (DYNES/CM)
75
74
73
72
71
70
SEA
SALT
WELL
DISTILLED
TYPE WATER

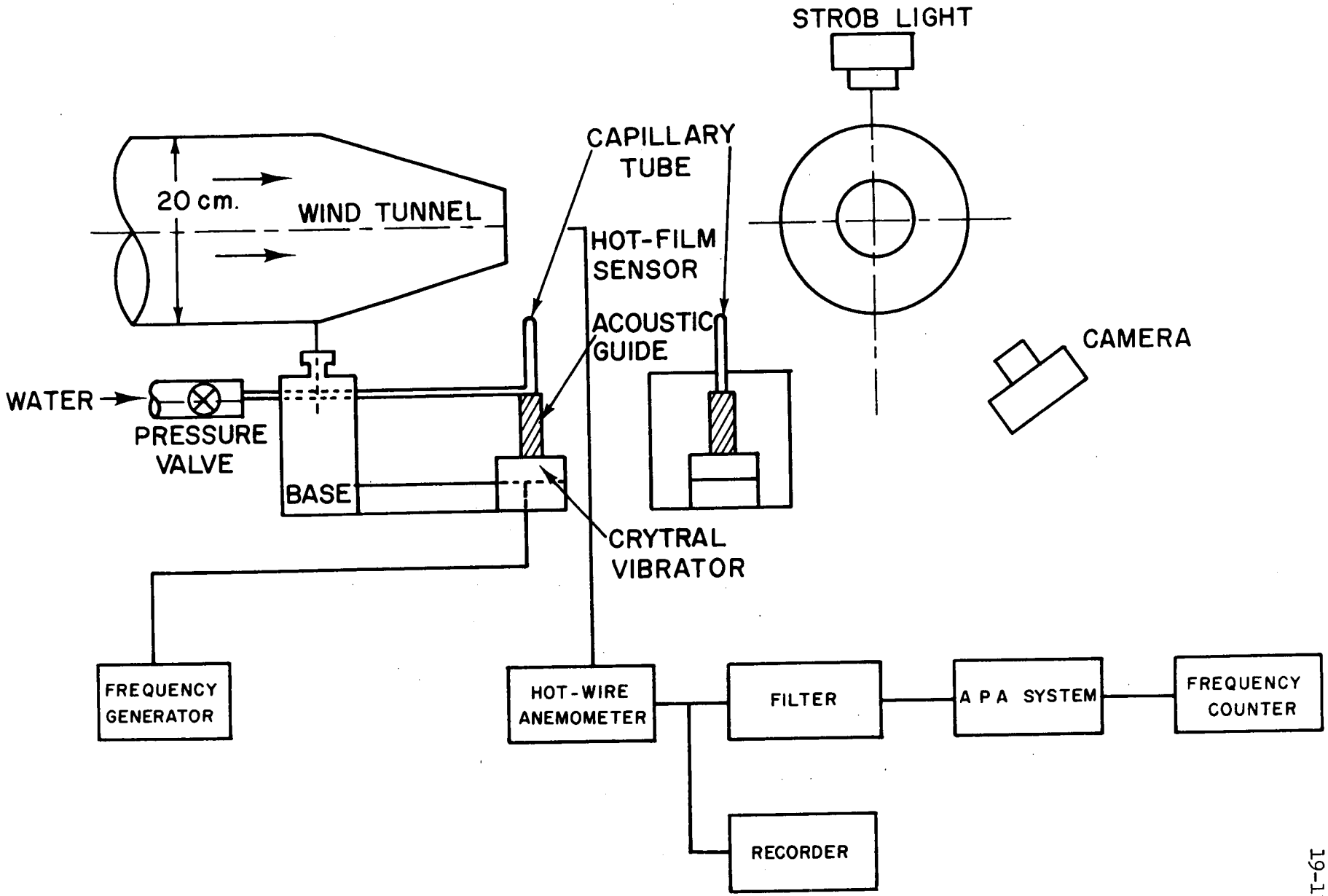
STROB LIGHT
CAPILLARY TUBE
20 cm.
WIND TUNNEL
HOT-FILM SENSOR
ACOUSTIC GUIDE
CAMERA
WATER
PRESSURE VALVE
BASE
CRYTRAL VIBRATOR
FREQUENCY GENERATOR
HOT-WIRE ANEMOMETER
FILTER
A P A SYSTEM
FREQUENCY COUNTER
RECORDER

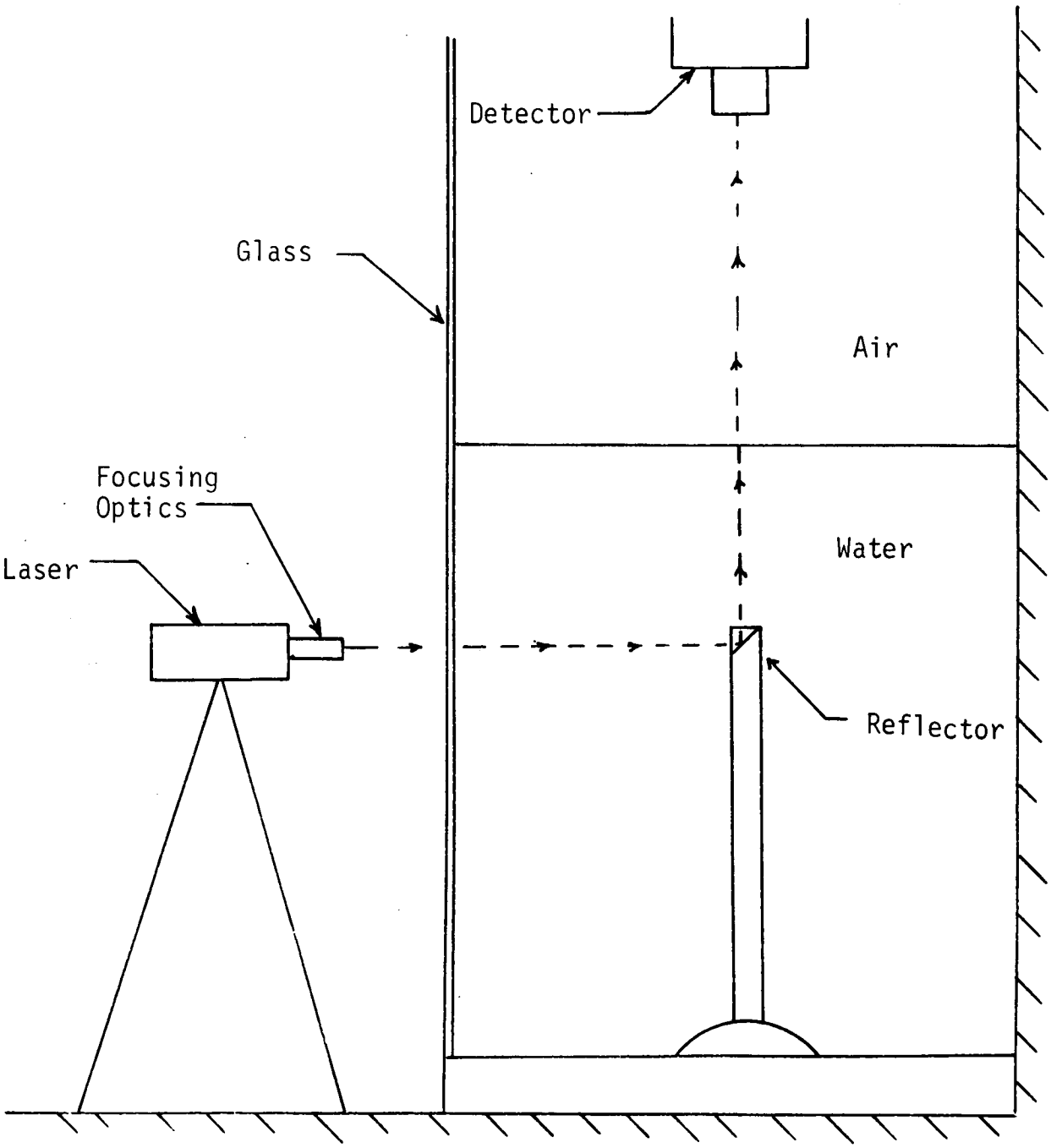
Detector
Glass
Air
Focusing
Optics
Laser
Water
Reflector

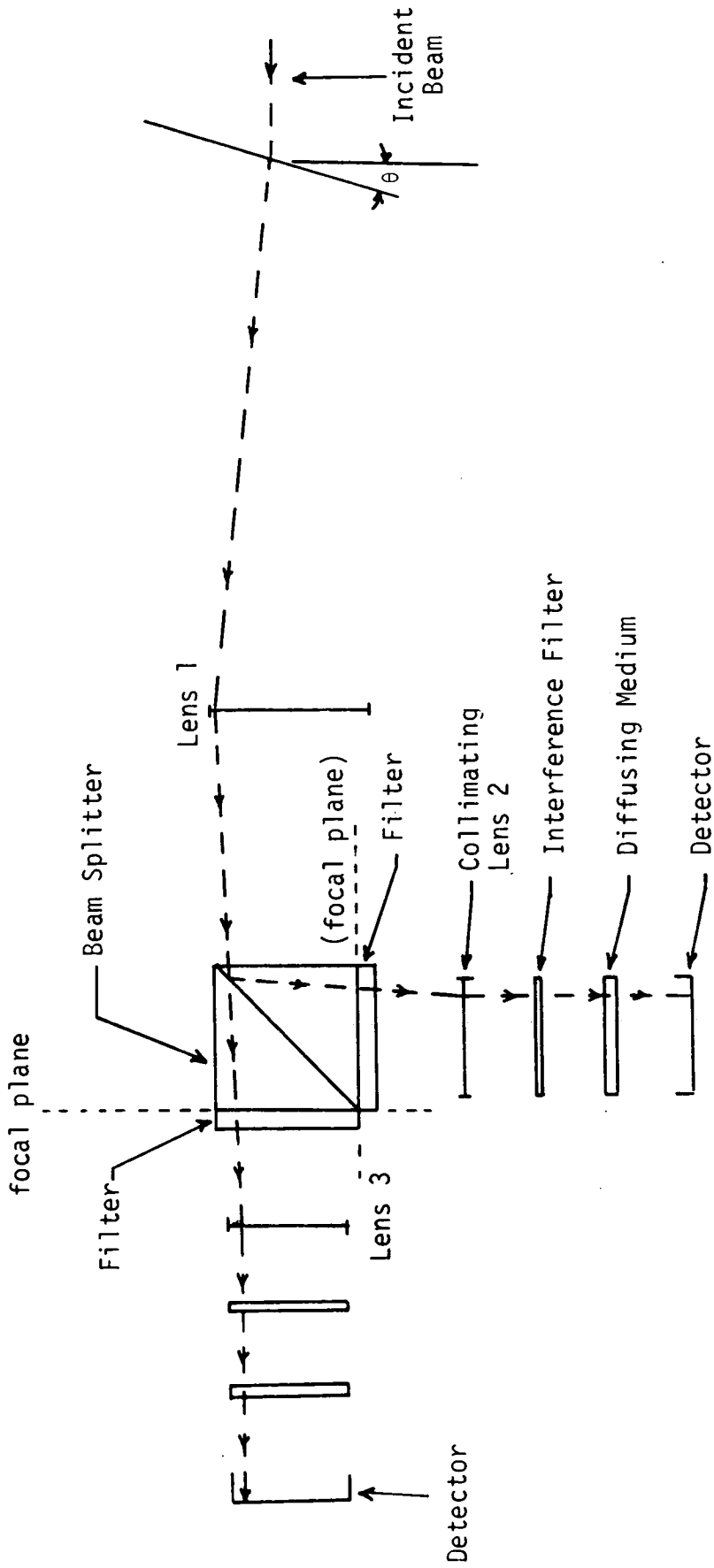
Incident Beam
θ
Lens 1
Beam Splitter
(focal plane)
Filter
Collimating Lens 2
Interference Filter
Diffusing Medium
Detector
focal plane
Filter
Lens 3
Detector

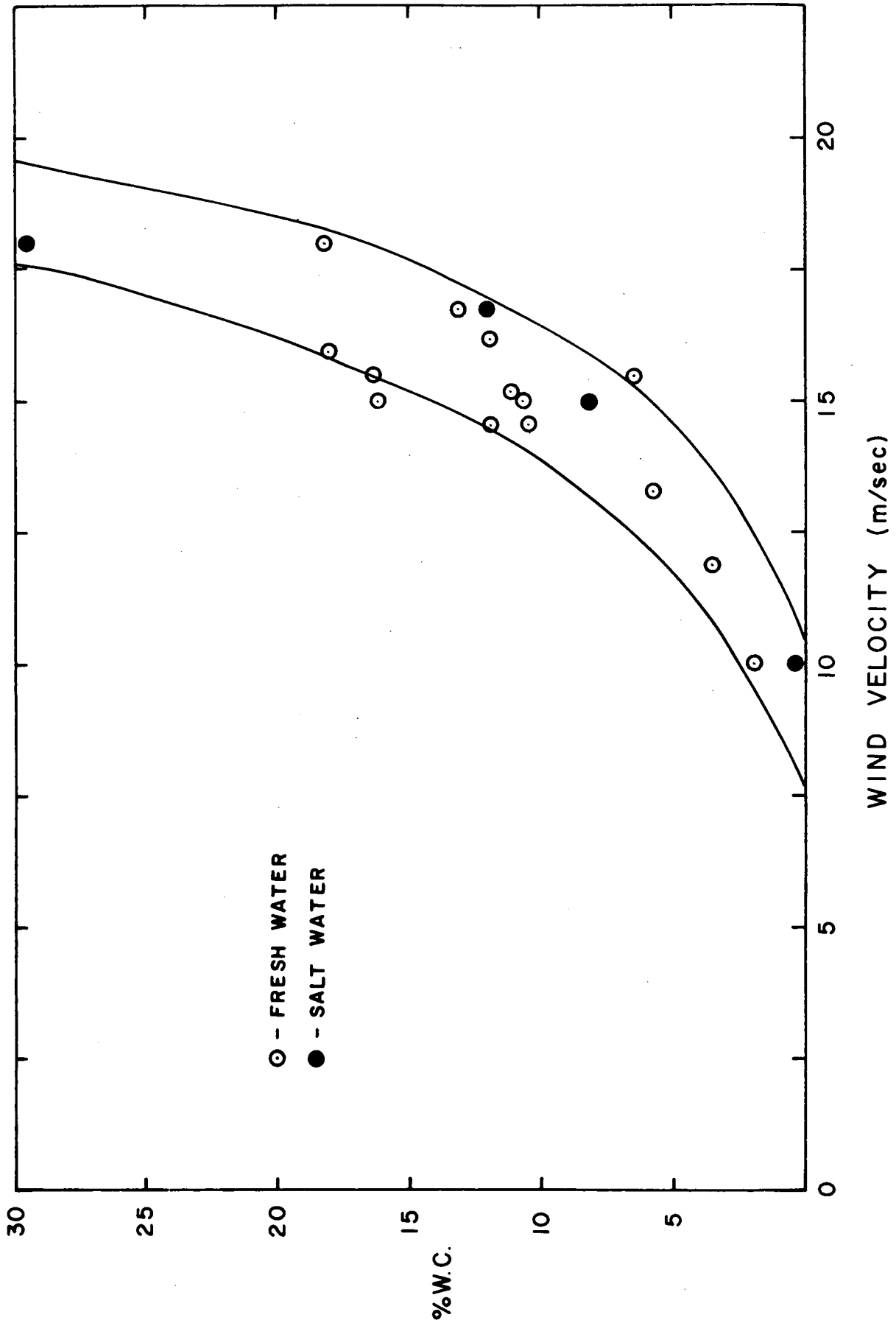
30
25
20
15
10
5
%W.C.
0
5
10
15
20
WIND VELOCITY (m/sec)
⊙ - FRESH WATER
● - SALT WATER

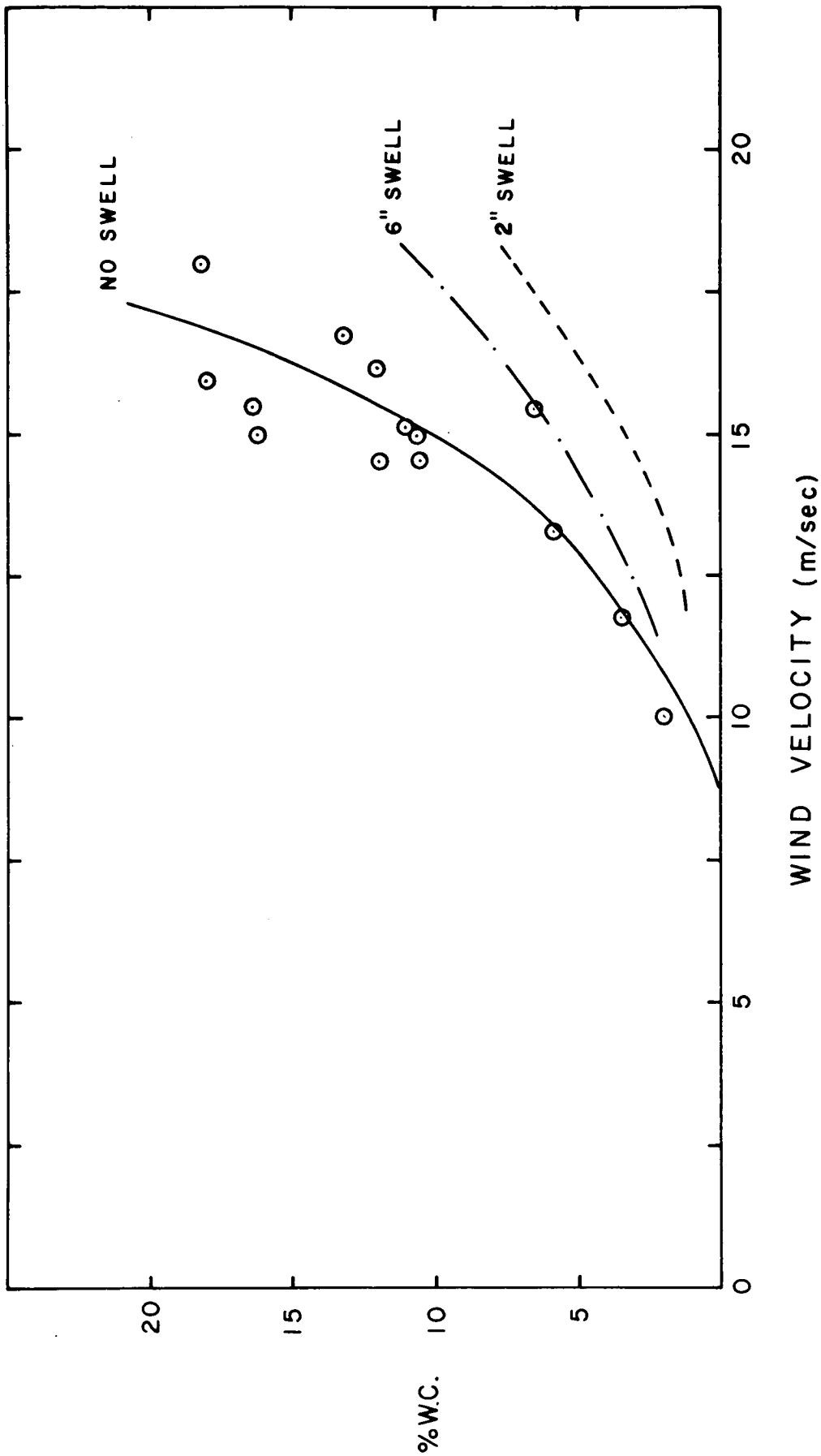
NO SWELL
6" SWELL
2" SWELL
%W.C.
WIND VELOCITY (m/sec)
0
5
10
15
20

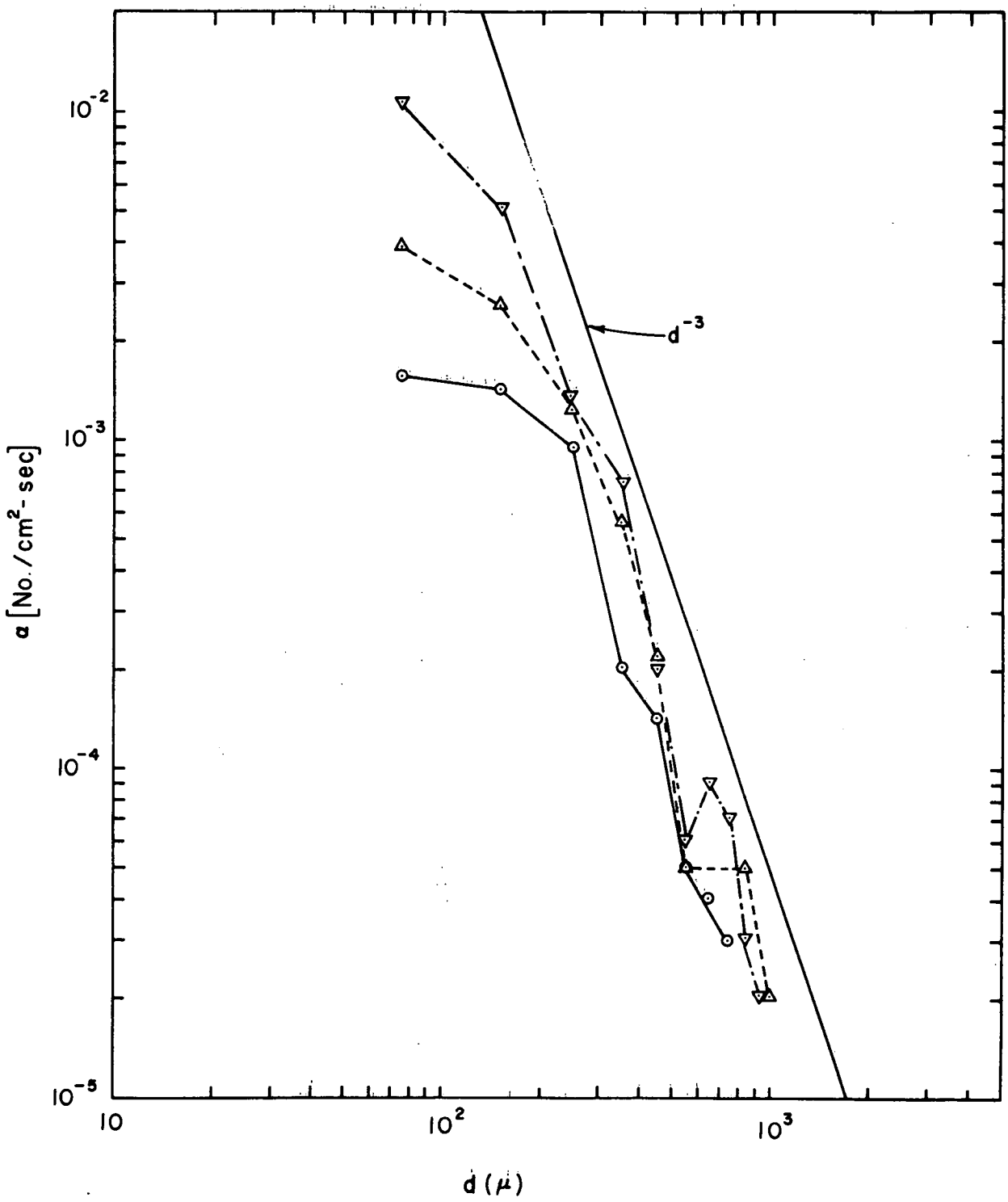
10^{-2}
10^{-3}
10^{-4}
10^{-5}
d^{-3}
a [No./cm^2- sec]
10
10^2
10^3
d (μ)

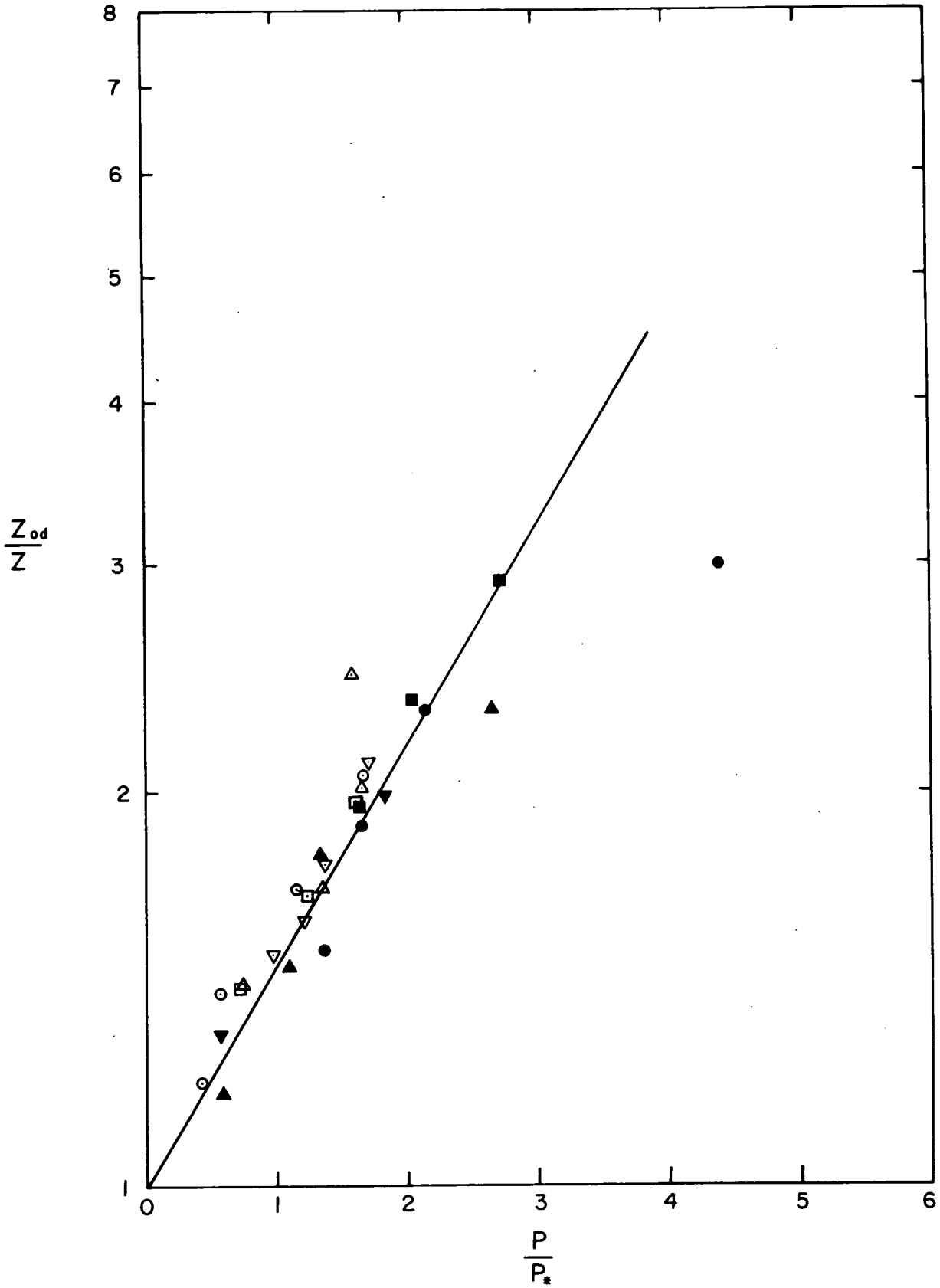
8
7
6
5
4
3
2
1
0
1
2
3
4
5
6
$\frac{Z_{od}}{Z}$
$\frac{P}{P_*}$

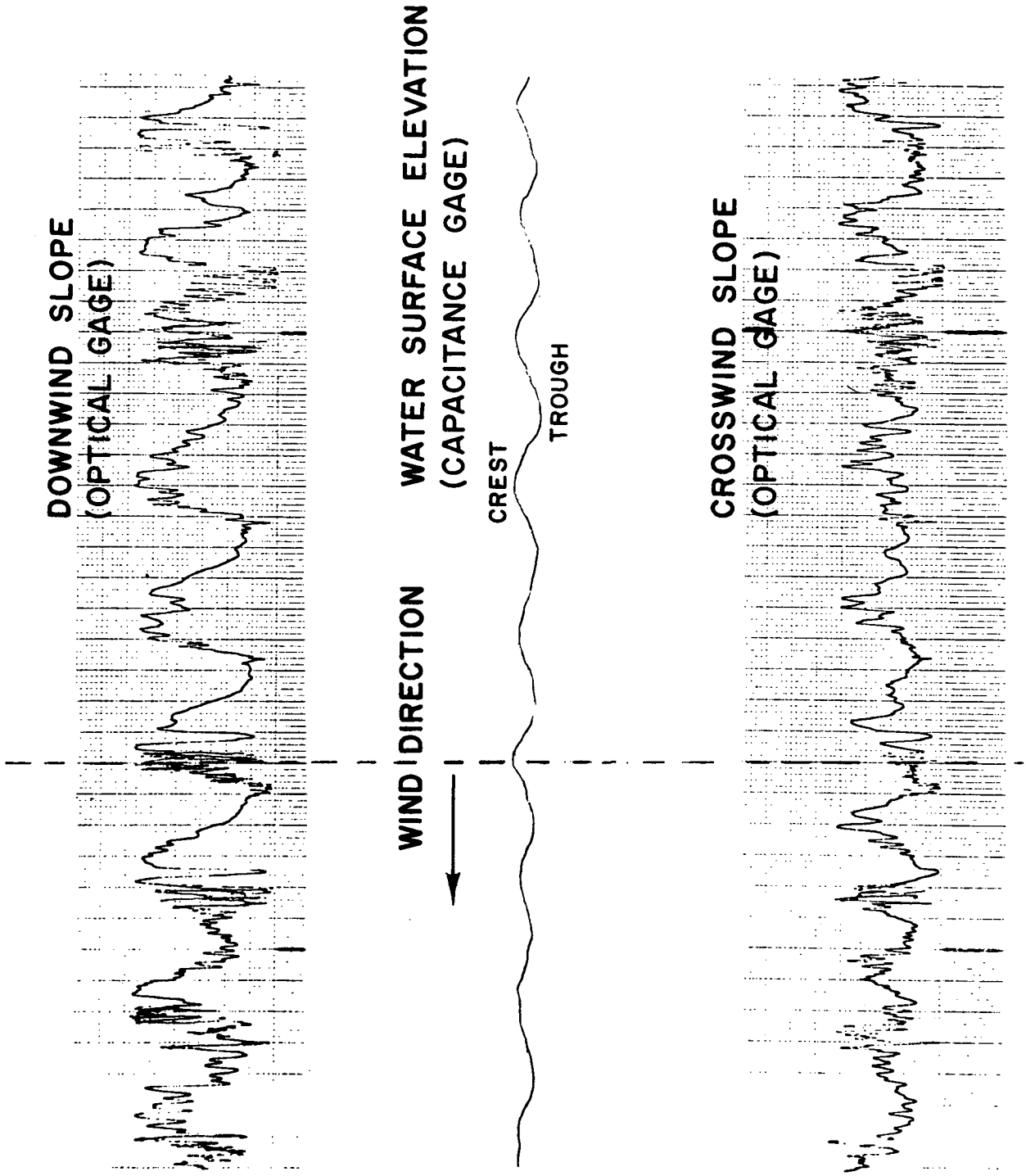
DOWNWIND SLOPE
(OPTICAL GAGE)
WATER SURFACE ELEVATION
(CAPACITANCE GAGE)
WIND DIRECTION
CREST
TROUGH
CROSSWIND SLOPE
(OPTICAL GAGE)

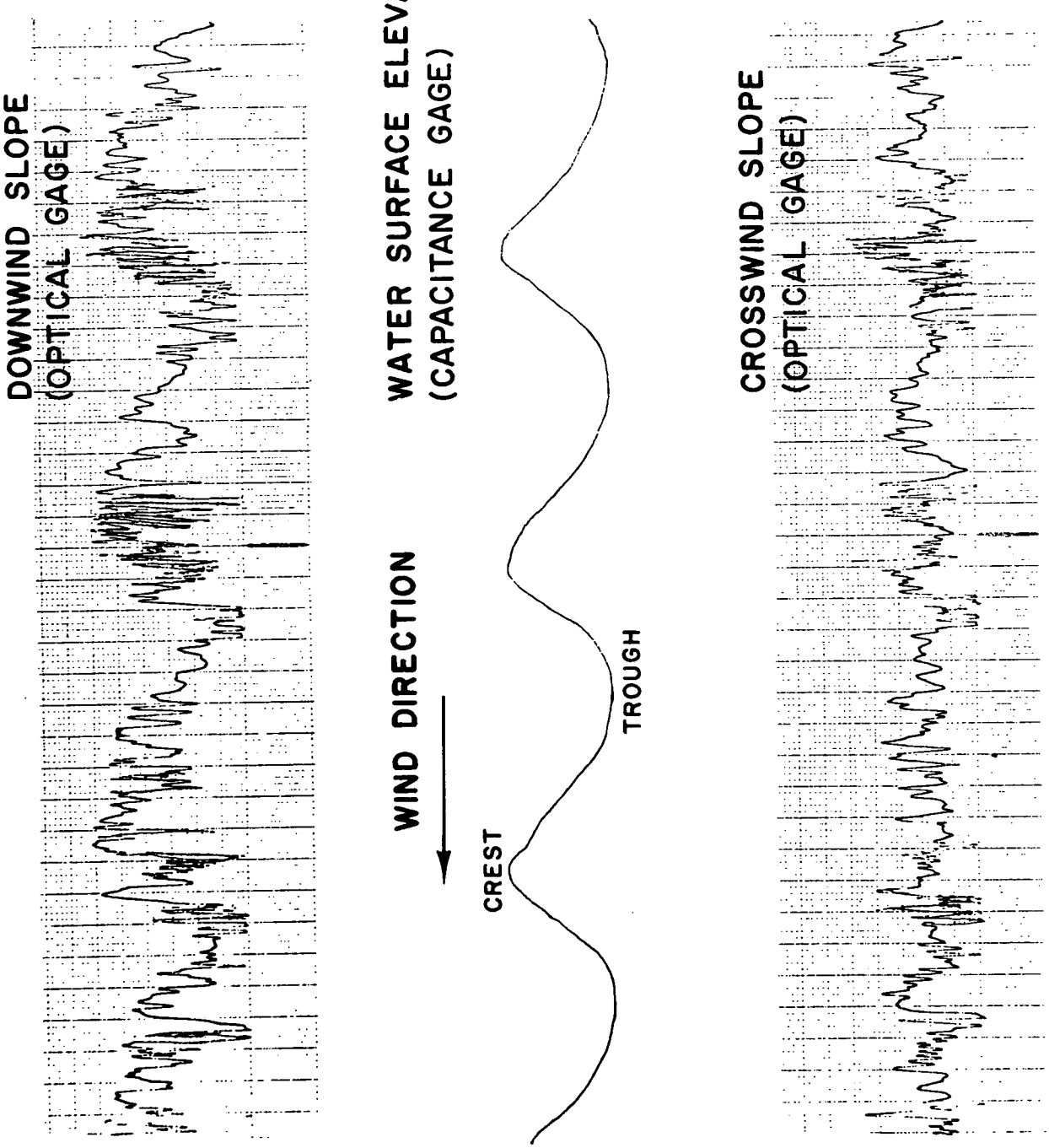
DOWNWIND SLOPE
(OPTICAL GAGE)
WATER SURFACE ELEVATION
(CAPACITANCE GAGE)
WIND DIRECTION
CREST
TROUGH
CROSSWIND SLOPE
(OPTICAL GAGE)

SECTION 97

THE EXTRAPOLATION OF LABORATORY AND AIRCRAFT RADAR SEA RETURN DATA TO SPACECRAFT ALTITUDES

by

Willard J. Pierson
Department of Meteorology and Oceanography
School of Engineering and Science
New York University

and

Richard K. Moore
Remote Sensing Laboratory
University of Kansas

ABSTRACT

Laboratory measurements show that the spectra of the capillary waves grow with wind speed over six orders of magnitude. Measurements in a wind-water tunnel show a simple one to one relationship between σ^{o}_{VV} and wind speed. The laboratory data for both waves and backscatter have negligible scatter because the wind for each measurement was constant and the radar return and wave spectra were averaged over a long enough time. Other conditions did not change.

Regression analyses of upwind and crosswind values of $10 \log_{10} (\overline{\sigma}^{o}(\theta)/\overline{\sigma}^{o}(10°))$ from aircraft data show linear relationships with the logarithm of the wind speed at 15°, 25° and 35°. The data have substantial scatter in part because both the average wind speed and average sea return values had to be estimated from relatively short samples. The scatter can be partially understood and predicted from a combination of turbulence theory, radar theory, and the small sampling theory of statistical inference. The scatter is caused in part by two effects; the turbulence of the wind over the water and the "fading" characteristics of the radar return.

When these results are applied to a prediction of the sea return values to be obtained by S193 on Skylab, it can be shown that the size of the illuminated patch effectively averages out the horizontal scales of gustiness so that the measurement will correspond to the synoptic scale wind. The effect of "fading" will introduce a scatter of less than six percent for angles greater than 15°.

There will still be some difficult problems to be solved for S193. These problems are described, and methods for their solution are reviewed.

INTRODUCTION

Both laboratory and aircraft measurements over the ocean increasingly support a strong correlation between radar sea return and wind velocity. It is dangerous to oversimplify the results obtained in the laboratory, and apply them directly to the open ocean without first accounting for differences between laboratory and open ocean conditions. However, once these differences are accounted for, the combined information obtained from the laboratory and from aircraft measurements makes it possible to understand some of the reasons for the scatter in the aircraft data and to calculate what these effects will be in the measurements to be made by S193 on Skylab. Such an analysis also reveals that only part of the scatter in the aircraft data is caused by sampling variability in the data. Reasons for this additional scatter are postulated. Many of these other sources of scatter will not be present in S193, and still others can be removed with the larger data base to be made available when Skylab is flown.

LABORATORY DATA

Laboratory data on the form of the capillary wave spectrum have been combined to show that the capillary spectrum in a wind-water tunnel varies over six orders of magnitude as shown by Pierson, Jackson, et al. (1971). In Figure 1, the capillary waves are very low below a friction velocity, u_*, of 10 or 12 cm/sec. Then the waves grow by more than four orders of magnitude as the friction velocity changes by just a few cm/sec. The spectrum still grows with increasing wind speed all the way to friction velocities of 150 cm/sec, but more slowly. Photographic data also support the conclusion that the spectrum grows with increasing wind speed in the capillary frequency range.

Wright has measured σ^{o}_{VV} at 60° off the vertical in a wind-water tunnel for a wide range of wind speeds. These values are the exact unnormalized values for the scattering cross section. Some of the preliminary results are shown in Figure 2. The backscatter from the capillary waves clearly increases with increasing wind speed. The change from a very steep slope to a less steep slope in this plot corresponds to the value D equals one in Figure 1. Wind speeds in the free air section of the tunnel are given in feet/min. An auxiliary scale gives

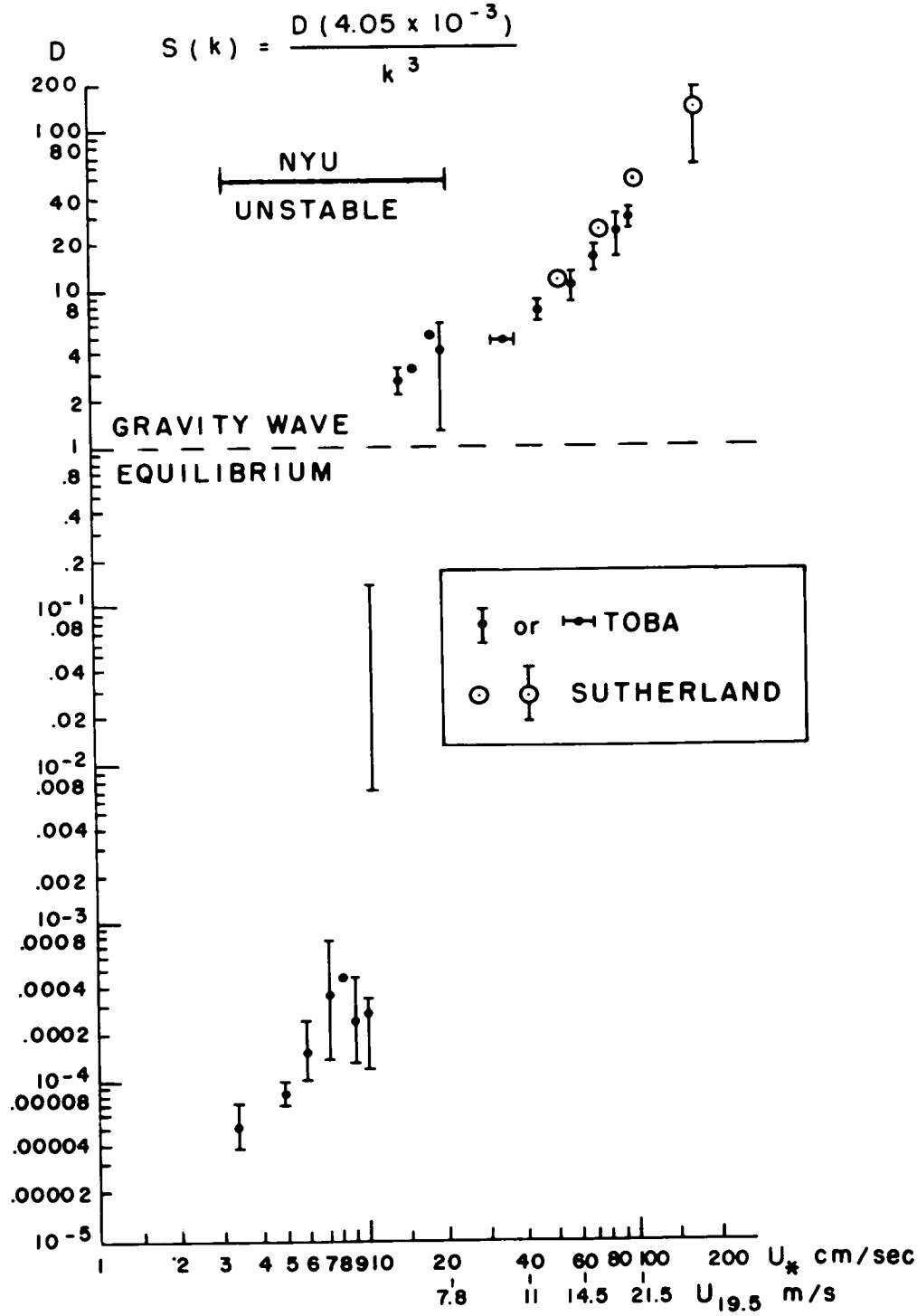

FIG. 1. VARIATION OF D AS A FUNCTION OF U_* IN THE CAPILLARY WAVE SPECTRUM.

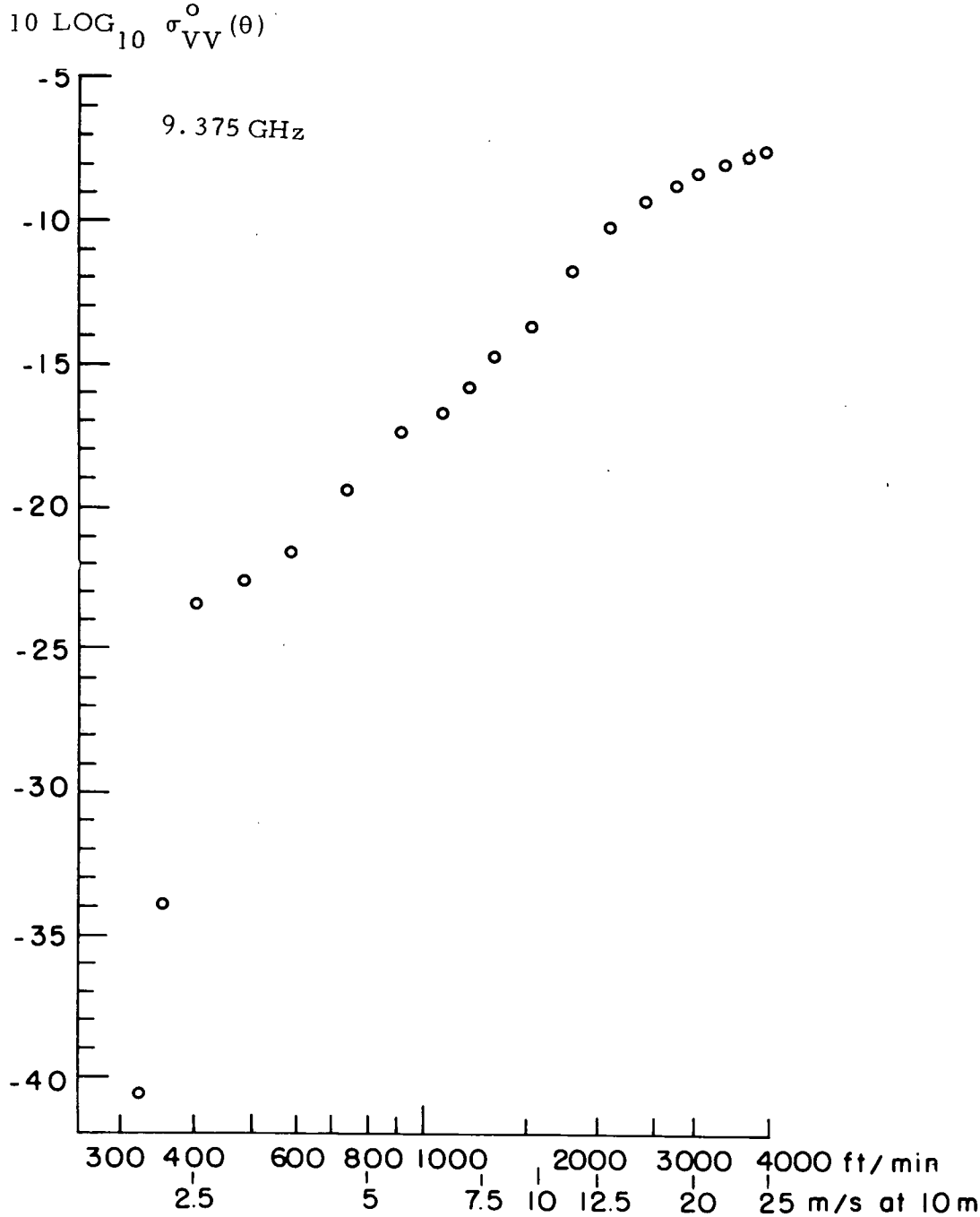

FIG. 2 RADAR BACKSCATTER AS A FUNCTION OF WIND SPEED IN A WIND-WATER TUNNEL. DATA COURTESY OF DR. JOHN WRIGHT.

the approximate equivalent wind at 10 meters over the ocean.

In experiments in wind-water tunnels, it is possible to keep conditions relatively simple compared to the open ocean. Measurements can be averaged over a sufficiently long time so as to ensure the elimination of sampling variability. Near the surface of the open ocean, wind speeds of the values shown would produce much larger waves, with a spectrum extending to much lower frequencies. Moreover, the winds over the ocean are not as steady as the winds in a wind-water tunnel.

ATMOSPHERIC TURBULENCE

The atmosphere is turbulent; its many scales of motion can be assigned to three categories; the microscale, the mesoscale and the macroscale, or the planetary scale. A wind vane and an anemometer respond to the frequencies in the microscale with some damping. The mesoscale is often unimportant over the oceans, but it is important for the study of, for example, mountain-valley winds, thunderstorms, and heat islands over cities.

Lumley and Panofsky (1964) cite an important paper by Van der Hoven (1957) that first attempted to study the full range of motions for the horizontal wind. A figure from Lumley and Panofsky (1964) which is redrawn from Van der Hoven (1957) is repeated here as Figure 3.

This figure is an oversimplification of the problem; yet the oversimplification provides an important insight into the nature of turbulence. The vertical scale is $n\,S(n)$ where n is the frequency and $S(n)$ is the variance spectrum of the wind with dimensions of $(\text{velocity})^2$ times time so that the vertical axis has the dimensions of $m^2\ sec^{-2}$. The horizontal scale is a logarithmic scale in n where n is in cycles per hour.

The graph has the property that

$$\int_{n_1}^{n_2} n\,S(n)\,d\log n = \int_{n_1}^{n_2} n\,S(n)\,\frac{dn}{n} = \int_{n_1}^{n_2} S(n)\,dn \qquad (1)$$

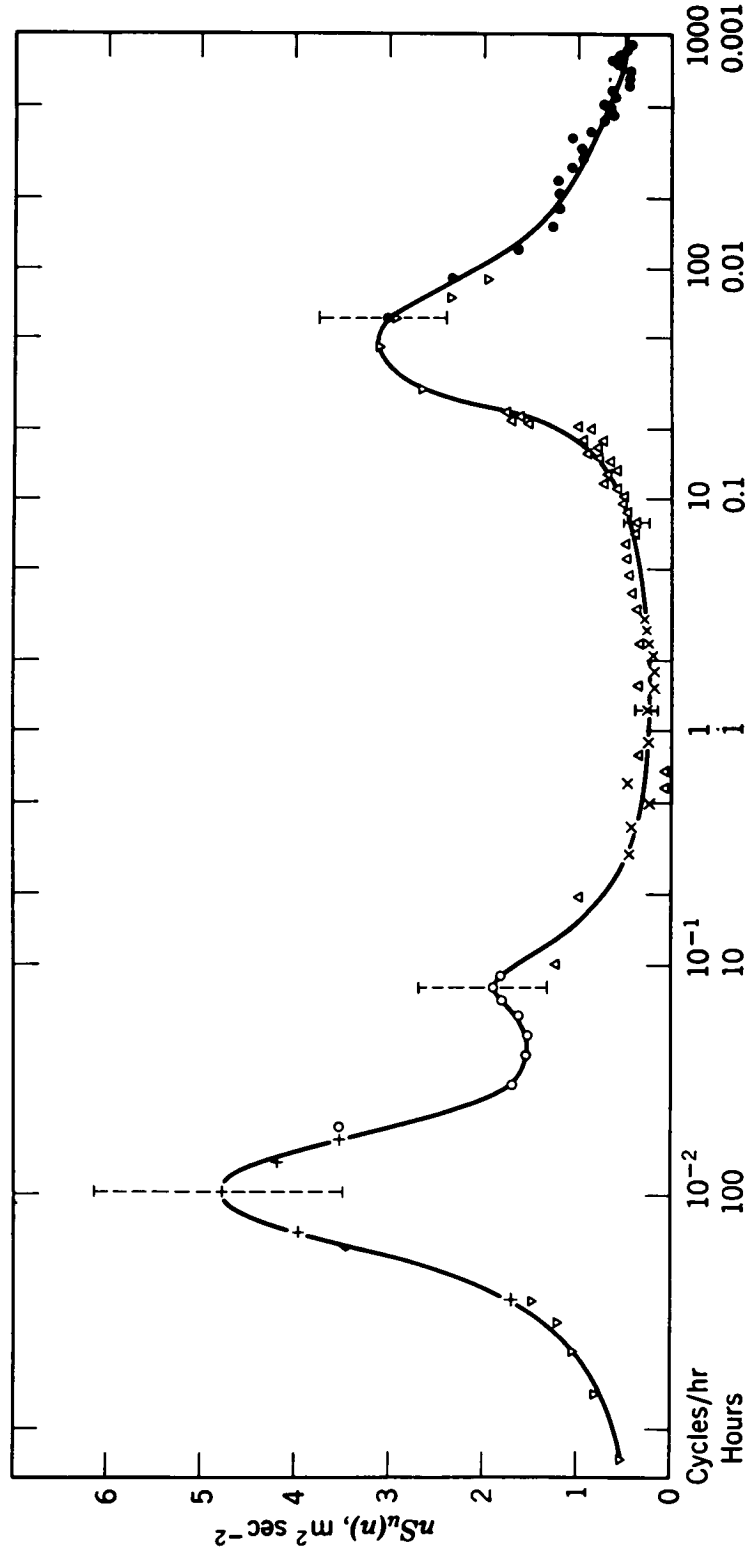

FIG. 3. Schematic spectrum of wind speed near the ground estimated from a study of Van der Hoven (1957).

(FROM LUMLEY AND PANOFSKY (1964), INTERSCIENCE, JOHN WILEY AND SONS).

so that this form preserves area in contrast to one where the logarithm of S(n) is plotted against the logarithm of n.

Figure 3 has three relative maxima; one near 50 cycles per hour, one near one cycle per twelve hours and one near one cycle per four days. The part on the left is typical of what might be computed for S(n) if say, the winds were recorded by an anemometer near the ground once an hour as one hour averages for a year or so and then the variance spectrum was computed. The part on the left would vary considerably from one place in the world to another.

The part on the right represents the spectrum of the gusts and lulls of the horizontal wind. It really depends to a very large extent on the speed and direction of the average planetary wind during the time the record was obtained from which the spectrum on the right side was computed. If the synoptic scale wind is high, the spectrum on the right will be high. If the wind is low, the spectrum will be low.

The usual anemometer installation is hardly the optimum instrumentation for the study of turbulence, but studies of turbulence with faster response instrumentation by Phelps and Pond (1971) and DeLeonibus (1971) show that simple anemometers yield useful information on the important scales of turbulence in the wind. Much of what was known through 1964 is summarized by Lumley and Panofsky (1964).

The important point about Figure 3 is not the three peaks in the spectrum, which fluctuate in amplitude and position, but the low region in the spectrum extending from about .05 to 10 cycles per hour. The area under the curve to the left of this band is five to six times greater than the area under the curve in the band. The area to the right is four to five times greater.

The low region in this spectrum justifies the fundamental hypothesis of numerical weather prediction; namely that the turbulent high frequency part of atmospheric motions can be filtered out of the synoptic scales, and parameterized as "eddy Austausch" coefficients so that numerical weather predictions can be carried out on a grid with spacings large compared to the scales of the eddies in the spectra on the right hand side. The numerical weather prediction schemes use functions of the synoptic scale winds that depend on a parameterization of the turbulence. The synoptic scale winds are nearly horizontal with the vertical components of the motion being 10^{-4} times the horizontal components.

If $\vec{V}(x, y, z, t)$ is the horizontal wind in the planetary boundary layer over the ocean, then

$$\bar{\vec{V}}(x, y, x, t) = \frac{1}{T} \int_{t-T/2}^{t+T/2} \vec{V}(x, y, z, t_o)\ dt_o \qquad (2)$$

and

$$\vec{V}(x, y, z, t) = \bar{\vec{V}}(x, y, z, t) + \vec{V}'(x, y, z, t) \qquad (3)$$

where

$$\vec{V}'(x, y, z, t) = \vec{V}(x, y, z, t) - \bar{\vec{V}}(x, y, z, t) \qquad (4)$$

The turbulence, that is the fluctuations in the wind to the right of, say, one cycle per half hour, is now in the $\vec{V}'$. The synoptic scale wind, in the absence of any important mesoscale perturbation, such as thunderstorms, is now the V.

Equally well, one could write equation 5 instead of equation 2 and substitute a space average for a time average where A is some area over the ocean surface.

$$\bar{\vec{V}}(x, y, z, t) = \frac{1}{A} \int_A \int \vec{V}(x_o, y_o, z, t)\ dx_o\ dy_o \qquad (5)$$

These concepts have been applied to a study of the best way to process anemometer data to be obtained by the National Data Buoy System of NOAA by Baer and Withee (1972a, 1972b). Numerous spectra similar to the one shown in Figure 3 for Argus Island, Keflavik, Iceland, and a site in the Pacific Ocean are shown that have the same properties as Figure 3. A report by Millard (1968) is cited that also show a similar spectrum.

The problem addressed in this study is to provide the best estimate of the horizontal vector wind for numerical forecasting purposes and for synoptic meteorological purposes. It is shown that the best that can be done is to give the wind, for a homogeneous area of flow, to within a

standard deviation of about one knot.

Equation 2 represents the simplest way to estimate a synoptic scale wind. It corresponds to the so-called "box-car" or rectangular weight function in which the limits of integration are set from $-\infty$ to $+\infty$ and a function $G(t - t_o)$ equal to $1/T$ for $t - T/2 < t_o < t + T/2$ is inserted after the integral sign. This weight function is not too good in its effect on the spectrum of the wind because it does not act like a sharp low pass filter. Frequencies both below $2\pi/T$ and above $2\pi/T$ are passed in varying amounts by the filter. A properly normalized weight function of the form $\cos \pi(t - t_o)/T$ can be shown to improve the filter characteristics, for example.

It is to be expected that improved ways to process anemometer data will result from further work in this problem area. For example, Baer and Withee (1972b), have studied how to locate and report the sudden changes, as a function of time, in wind direction and speed that occur during frontal passages.

For the purposes of this study of the aircraft program and of the results to be expected from S193, it should be noted first of all, that a scattering of data buoys over the ocean comparable to the scattering of ships in the results of Druyan(1971) could provide calibration points for a radar-radiometer system on a spacecraft in the form of properly averaged vector winds good to about 1 knot standard deviation in speed and a few degrees in direction.

It should also be noted that there is room for improvement in the area average indicated by equation (5). The average need not be restricted in concept to an average of weight one inside a certain area and zero outside the area. A properly chosen weight function can filter the wave number spectrum of the horizontal wind for numerical prediction purposes very efficiently.

Taylor's Hypothesis. - Taylor's hypothesis provides a means to relate measurements of the wind at a point as a function of time to measurements of the wind along a line (usually in the upwind downwind direction) as a function of distance. One way of describing the hypothesis is to say that it assumes that the pattern of turbulence is "frozen" and is advected past a point by the mean wind. This is equivalent to the assumption that the length of an eddy in space is given by multiplying the period of an eddy in time by the mean wind speed.

Lumley and Panofsky (1964) state that "Lappe, Davidson and Notess (1959) show by a comparison between tower measurements and airplane measurements at 90 and 120 m high, respectively, (the higher speed airplane measurements are almost sure to be satisfactory) that the hypothesis appears to be valid for horizontal wind fluctuation but that the vertical fluctuation measured by airplanes contains more low-frequency energy than the tower measurements. The authors ascribe this discrepancy to the effect of wind shear described by Lin. On the other hand, however, the terrain is not homogeneous, and flow patterns fixed relative to the ground contributing to the airplane, but not to tower measurements, may be responsible for the discrepancy".

"In summary, the very limited information seems to indicate that Taylor's hypothesis is generally applicable except for the low wave number components of vertical velocity fluctuations. Therefore all time spectra and correlation functions observed at a fixed point or from airplanes will, in what follows, be interpreted as space spectra and correlation functions along the direction of mean motion".

More recently, multiple arrays of wind sensors seem to suggest that eddies are dispersive. Typically, eddies can travel about six times their own length before they die out as shown by McDonald and Herrin (1971). The use of the Taylor's hypothesis in what follows is conservative. The additional decorrelation that is observed would increase the estimates of the number of degrees of freedom.

Argus Island Anemometer Data. - Figure 4 shows a small segment of an anemometer record obtained at Argus Island during Mission 119 (1970). This particular segment is a portion of the record obtained during the time near Flight 7, Run 1, Line 1. It shows the winds fluctuating from 12 knots to 21 knots in 60 seconds. A total of 2000 values of this Argus Island anemometer record were read every 4 seconds 1000 values before the Flight 7, Run 1, Line 1 measurements and for 1000 values after.

The covariance function for the anemometer record is shown in Figure 5. The variance spectrum is shown in Figure 6 as plotted on a relative scale. The covariance function shows a quasi-exponential non-oscillatory decay out to 144 seconds as plotted. At 400 seconds, the covariance is still equal to 0.28 or about 7% of the value at the origin.

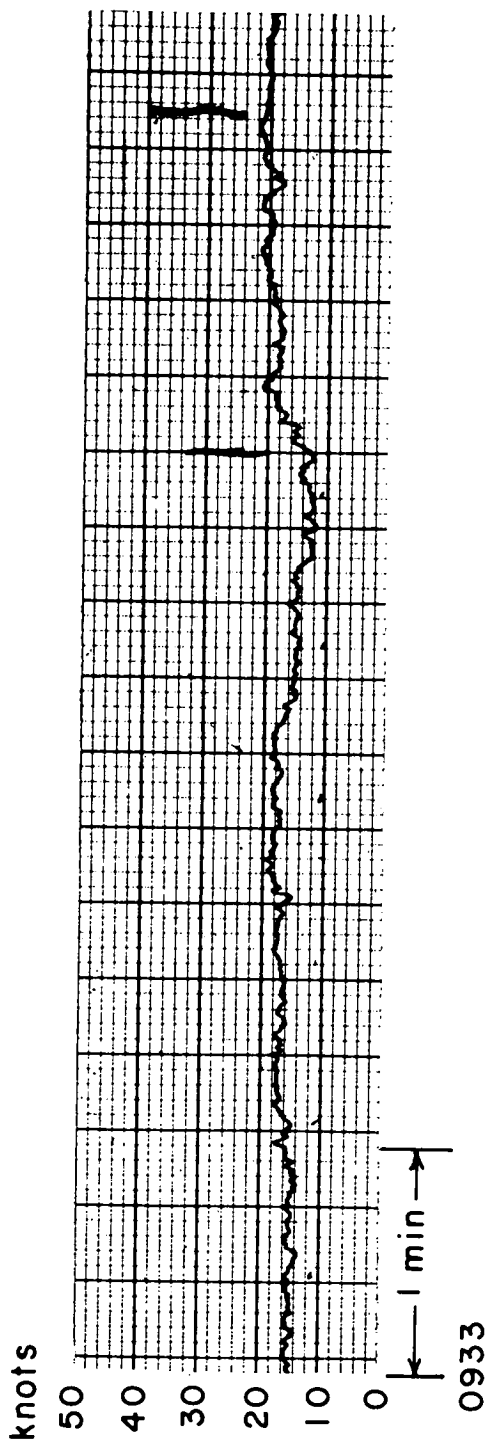

ARGUS ISLAND WIND RECORD

FIG. 4

Each spectral estimate has about 40 degrees of freedom according to Blackman and Tukey (1958). The spectrum shows that the major portion of the variability is concentrated in the low frequencies, corresponding to periods of 50 seconds and higher.

A well-known problem in statistics, is that of estimating the mean and variance of a normal population given a sample of N independent observations from a given population and of determining the variance and standard deviation of the estimate of the mean. For a sample of N independent observations the variance of the sample mean is given by the estimate of the variance $(SD_v)^2$ of the population divided by N as in equation 6.

$$\sigma^2_{\overline{V}} = \frac{(SD_v)^2}{N} \tag{6}$$

The 2000 points in the anemometer record are not independent and therefore equation 6 cannot be used with N equal to 2000. There are several ways to account for the correlation between points in such a time series. An equation given in Neumann and Pierson (1966) as given originally in Blackman and Tukey (1958) accounts for the decorrelations at different lags and provides for an effective number of degrees of freedom N^* as in

$$N^* = \frac{N}{m} \frac{[\Sigma S^*]^2}{\Sigma (S^*)^2} \tag{7}$$

where m is the number of smoothed spectral estimates available and the S* are the hanned spectral estimates. This equation holds best for spectra that do not depart too much from a white noise spectrum.

For this particular anemometer record, the effective number of degrees of freedom may be only about 178. The 2000 point autocorrelated record is perhaps the equivalent of a totally uncorrelated sample of 178 values from a normal population. The standard deviation of the sample mean is thus quite a bit larger than it would be for the same variance if the sample had consisted of 2000 independent points.

If the 178 independent points were thought to be equally spaced over the 2000 point time history, they would be located at about every 11th point, or every 44 seconds. This statement needs to be interpreted properly. Clearly from Figure 5 the covariance is still fairly high at

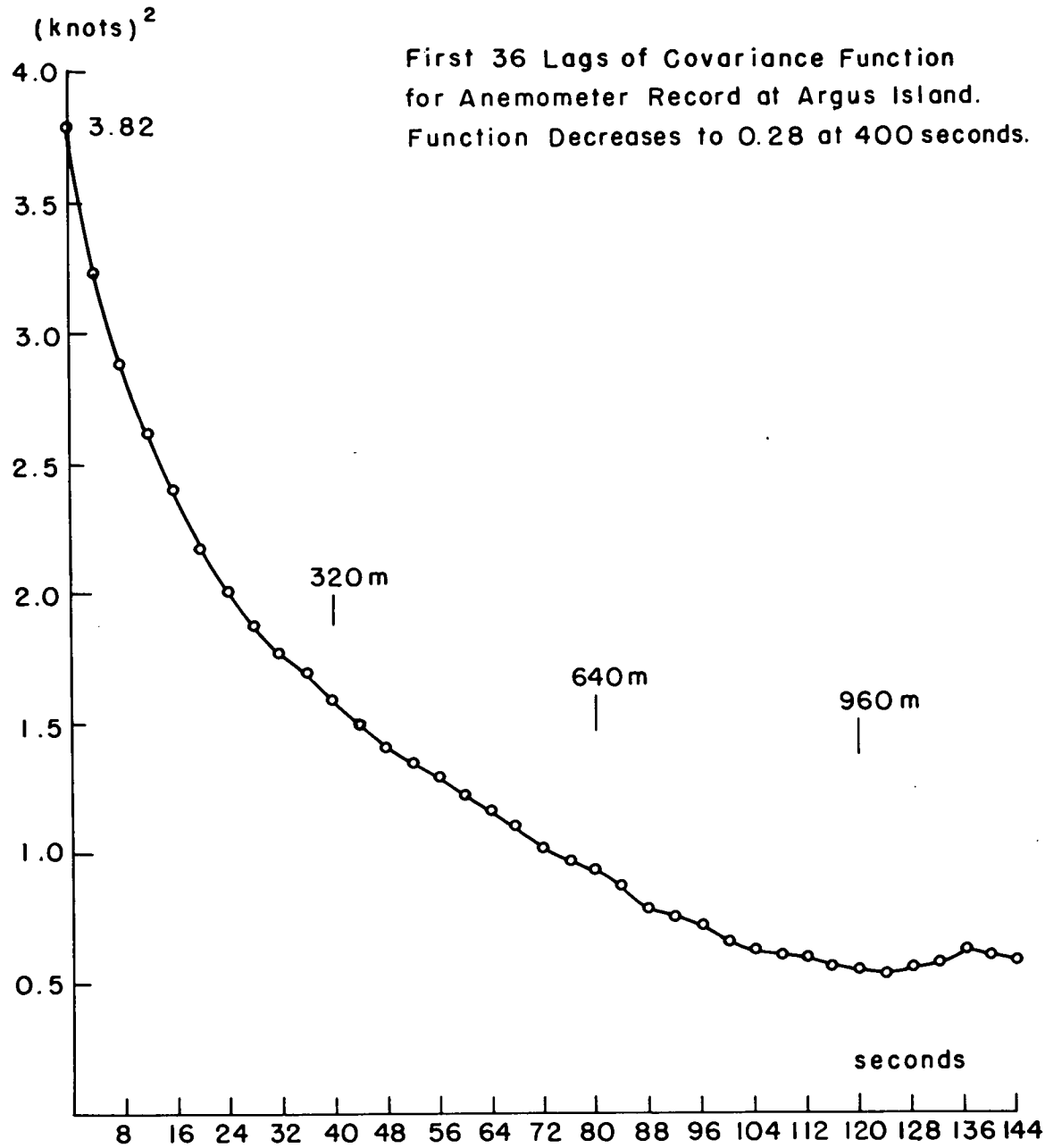
(knots)²
First 36 Lags of Covariance Function
for Anemometer Record at Argus Island.
Function Decreases to 0.28 at 400 seconds.
4.0
3.82
3.5
3.0
2.5
2.0
1.5
1.0
0.5
320m
640m
960m
seconds
8 16 24 32 40 48 56 64 72 80 88 96 104 112 120 128 136 144

FIG. 5

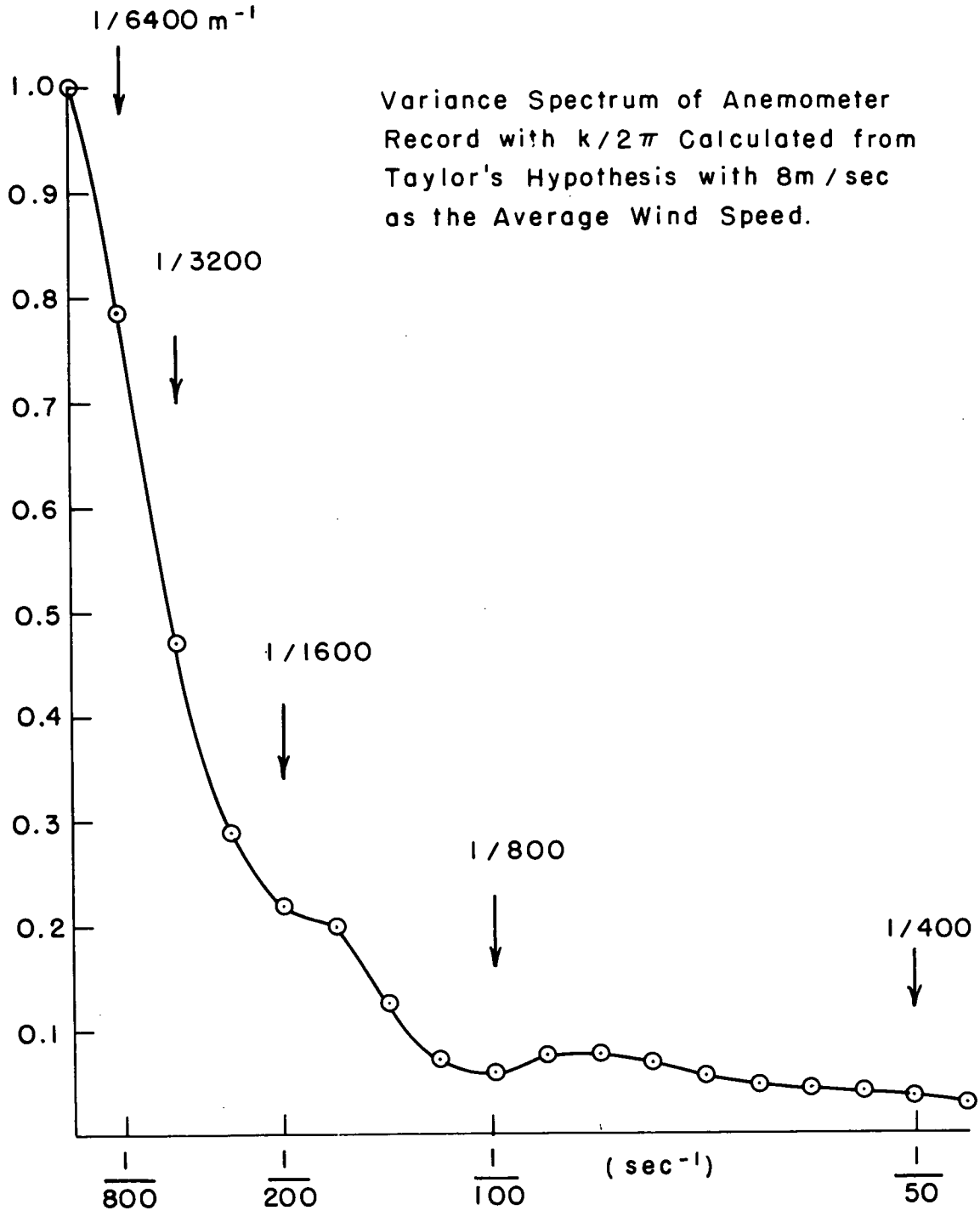
1/6400 m⁻¹
1.0
0.9
1/3200
0.8
0.7
0.6
0.5
1/1600
0.4
0.3
1/800
0.2
1/400
0.1
Variance Spectrum of Anemometer Record with k/2π Calculated from Taylor's Hypothesis with 8m/sec as the Average Wind Speed.
1/800
1/200
1/100
(sec⁻¹)
1/50

FIG. 6

44 seconds. The real point is that this complicated, non-independent time series of points contains enough information on the variance of the process and its frequency content to make it possible to replace it by an equivalent N^* independent points for the purpose of determining confidence intervals on $\overline{V}$. The 44 second apart effectively independent points in the anemometer record, if advected at a speed of 8 meters per second, implies that points 350 meters apart along an upwind line in space would be effectively independent in this same sense.

General Properties of the Turbulent Wind. - It is just as difficult to get a reliable estimate of the mean wind when a radar measurement is made over the ocean as it is to get a reliable estimate of the radar scattering cross section. In the plots and tables to follow, the scatter is caused just as much by inadequacies in the wind speed measurements as it is caused by the possible errors in the radar measurements.

In working with the turbulent wind, meteorologists study both the spectra and cross spectra of the $\vec{V}'$ components as described above and the vertical velocity fluctuations, w'. They also study the variation of the mean wind as a function of elevation above the ocean surface, $\vec{V}(z)$.

The variation of mean wind with height above the ocean surface depends on the stability of the layer of air over the water, which in turn is controlled by the air-sea temperature difference. If the air-sea temperature difference is small, the lapse rate in the atmosphere is adiabatic and the wind varies with height according a logarithmic wind profile. If the air is colder than the water the atmosphere is unstable, and, for the same wind above the surface there will be a greater stress on the surface. Conversely, with the air warmer than the water the atmosphere is stable and for a given wind above the surface, it will be less.

All of these factors were taken into account by Cardone (1969) in developing a computer based procedure for studying the winds in the planetary boundary layer. They are also taken into account in the interpretation of the winds for the various missions. The winds reported and used in these studies are the "equivalent" winds for a neutrally stratified atmosphere referred to 19.5 meters above the ocean surface. They would produce the same stress at the surface as the measured wind at some other elevation with some known air sea temperature difference according to the available theories on the subject. In general, the effect of air-sea temperature difference is relatively unimportant for high winds.

The fluctuations in wind speed recorded by a cup anemometer are more or less the equivalent of the fluctuations of the vector component of the wind in the direction of the mean wind. The spectrum shown in Figure 6 is typical of such spectra in that a record 8000 seconds long does not resolve the maximum away from the origin.

In general, according to Lumley and Panofsky (1964), the variance of this turbulent spectrum grows as the square of the mean wind as in equation 8

$$VAR = (SD_v)^2 = \int_0^\infty S(n)\, dn \cong K \overline{V}^2 \qquad (8)$$

when the wind is measured at a fixed height.

The value of SD_v is relatively constant with height so that, since the mean wind increases with height, the "relative gustiness" $SD_v/\overline{V}$ decreases with height. For a fixed height $SD_v/\overline{V}$ is also dependent on the air-sea temperature difference. In general, $SD_v/\overline{V}$ can be considered to range from about 0.10 to 0.30 with high values reserved for unstable air and light winds.

For the anemometer record being studied the mean wind was 17.0 knots before correction for height above the surface and stability effects and the standard deviation was 1.95 knots so that, at anemometer height,

$$\frac{SD_v}{\overline{V}} = 0.114 \qquad (9)$$

THE AIRCRAFT PROGRAM

Radar Sea Return Measurements and Wind Speed. - The scatterometer used to measure sea return was a continuous wave radar with a vertically polarized fan beam that differentiated the angle θ off the vertical by means of Doppler shifts in the backscattered radiation. Bradley (1971) has carried out an extensive analysis of this system. This study relies heavily upon his analysis, differing however, in some important points.

A typical upwind data run would be obtained by flying for about five minutes in a direction chosen visually to be perpendicular to the direction of the oncoming waves at the sea surface. The backscattered signal from ahead is upshifted in frequency, while that from behind is downshifted. Appropriate signal processing techniques yield measurements of σ^o in the vertical transmit vertical receive mode for various angles off the vertical.

The largest slice of recorded data that could be handled by the available computer at MSC was 0.3275 seconds long, and every fourth one of these data slices (spaced consequently 1.31 seconds apart) was chosen for analysis. Each 0.3275 second data slice yielded a measurement of σ^o at all desired angles. A four minute data run would yield about 180 separate measurements of σ^o for each angle. For such a run, a single average value of σ^o obtained from the individual values computed from each 0.3275 second sample was obtained for comparison with the average measured, or estimated, wind speed. Data processed for the different runs varied in duration, so the number 180 is appropriate only for a 4 minute run.

Bradley (1971) has given the result of a regression analysis of σ^o on $\overline{V}$ for the data obtained during Missions 119 and 156.

The values of A and B in equation (10) were determined for upwind and cross wind conditions for 35°, 25°, and 15° as a least square regression of log $\overline{V}$ on $\overline{\sigma}^o_N$. The values of A and B are given in Table 1.

$$10 \log_{10} \frac{\overline{\sigma}^o(\theta)}{\overline{\sigma}^o(10°)} = A + B \log_{10} \overline{V} \qquad (10)$$

TABLE I.- RESULTS OF CURVE FITTING BY BRADLEY (1971) FOR MISSIONS 119 AND 156

Wind Direction	θ	A	B	RMS Error
upwind	15°	- 7.51	3.30	0.717 db
	25°	-25.56	11.21	0.892
	35°	-34.42	14.93	0.882
crosswind	15°	- 6.68	2.13	0.748
	25°	-22.84	7.51	1.196
	35°	-35.51	12.62	1.355

The use of equation 10 to study the individual values of σ^o provides a great amount of information on the nature of the return. Denote $\overline{\sigma}^o(\theta)/\overline{\sigma}^o(10°)$ by $\overline{\sigma}^o_N(\theta)$ in equation 10 so that

$$10 \log_{10} (\overline{\sigma}^o_N(\theta)) = A + B \log_{10} \overline{V} \qquad (11)$$

A change of $\Delta\sigma^o_N$ in $\overline{\sigma}^o_N$ must produce a corresponding change of ΔV in V as in equation 12.

$$10 \log_{10} (\overline{\sigma}^o_N + \Delta\sigma^o_N) = A + B \log_{10} (\overline{V} + \Delta V)$$

$$= A + B \log_{10} \overline{V} + B \log_{10} \left(1 + \frac{\Delta V}{\overline{V}}\right) \qquad (12)$$

If equation 11 is subtracted from equation 12, the result is equation 13.

$$1 + \frac{\Delta\sigma^o_N}{\sigma^o_N} = \left(1 + \frac{\Delta V}{V}\right)^{B/10} \qquad (13)$$

Changes in $\Delta\sigma^o_N$ (one of the individual values observed as a time series during a particular flight line) are caused by two effects: (1) the radar backscatter is a random variable because of the noiselike character of the fading and (2) the backscattered signal strength changes because of actual changes in the roughness of the surface.

The variability of the measurements of σ^o due to fading depends on the total number of independent samples in the return signal. Bradley (1971) has given the formula for this source of variability and from it, it is possible to compute SD_σ, the standard deviation of σ^o_N.

From equation 13, $1 + \Delta V/\overline{V}$ and $1 - \Delta V/\overline{V}$ can then be computed as in Table II.

TABLE II. - VARIATION OF APPARENT WIND SPEED DUE TO FADING FOR A 0.3275 SECOND MEASUREMENT FOR AN UNDERLYING SURFACE WITH CONSTANT ROUGHNESS.

θ	$1 + \frac{\Delta\sigma^o_N}{\sigma_N}$	$1 + \frac{\Delta V}{V}$	$1 - \frac{\Delta V}{V}$
15°	1.12	1.41	0.71
25°	1.13	1.12	0.89
35°	1.15	1.10	0.91

The equivalent values in db for $1 + \Delta\bar{\sigma}^o_N / \bar{\sigma}_N$ in Table II are 0.49, 0.53 and 0.62 db.

Fading for this particular instrument over a uniformly rough surface amounting to 12% thus causes 41% apparent wind fluctuations at θ equal to 15°. At 35°, in contrast, fading produces only 10% apparent fluctuations in the wind. For example, if the true wind had been 30 knots, a value of σ^o at 15° could have been obtained that would indicate a wind as high as 42 knots or as low as 21 knots for about one-third of the values. At 35°, the wind could be computed to be as high as 33 knots and as low as 27 knots.

The scattering cross section will also vary if the roughness of the underlying surface varies. This roughness is dominantly controlled by the capillary wave structure, and as shown in Figure 1, the roughness increases with increasing wind speed. The capillary waves respond very quickly to variations in the wind speed so that if the wind is, say, 20% higher than the mean over a particular illuminated cell, σ^o will increase accordingly. The amount of this change is shown in Table III. Possible values for the ratio of the standard deviation of the wind speed to the mean wind speed are listed across the top of the table. The body of the table contains the resulting change of $1 + \Delta\bar{\sigma}^o_N / \bar{\sigma}_N$ and the equivalent value in db.

TABLE III. - VARIATION OF $1 + \Delta\sigma^o/\sigma^o$ IN TERMS OF FLUCTUATIONS OF THE WIND ABOUT THE MEAN WIND SPEED AS EXPRESSED BY $SD_v/\bar{V}$

	$SD_v/\bar{V}$ = 0.15		0.20		0.30	
	$1+\Delta\bar{\sigma}^o/\bar{\sigma}^o$	db	$1+\Delta\bar{\sigma}^o/\bar{\sigma}^o$	db	$1+\Delta\bar{\sigma}^o/\bar{\sigma}^o$	
15°	1.05	0.20	1.06	0.26	1.09	0.38
25°	1.18	0.73	1.23	0.89	1.34	1.28
35°	1.23	0.91	1.31	1.18	1.48	1.70

For example, if $SD_v/\bar{V}$ is 0.20 and the mean wind is say 30 knots, there will be patches over the ocean where the wind gusts will be 36 knots, and at 35°, σ^o would increase by 1.18 db if the average value of σ^o for a 36 knot wind were recorded.

Of course, these two effects occur together. A high gust will produce sea return that scatters about the expected value for that high wind according to the values in Table II. For example, a 30 knot average wind could have a local gust of 36 knots where the expected sea return would be 1.18 db higher because of the gust. However, sampling variability due to fading would produce fluctuations of ± 0.62 db about this value.

It is important to note that the fading effect is large for small θ and small for large θ whereas the variation in wind speed produces a large effect for large θ and a small effect for small θ.

For future study, the bar over $\bar{\sigma}^o(\theta)$ and over V can be removed and equation 10 can be written as equation 14.

$$10 \log_{10} \frac{\sigma^o(\theta)}{\bar{\sigma}^o(10°)} = A + B \log_{10} V$$

$$= 10 \log_{10} a + B \log_{10} V \quad (14)$$

Now, for example $\sigma^o(\theta)$ represents the individual values determined by 0.3275 second averages obtained every 1.31 seconds during an upwind flight at, say, 35° and V represents the wind speed that would be computed by solving for V in equation 14 as in equation 15.

$$V(\sigma^o(\theta)) = 10^{\frac{10}{B}\log_{10}\frac{\sigma^o(\theta)}{a\,\bar{\sigma}(10°)}} = \left[\frac{1}{a}\frac{\sigma^o(\theta)}{\bar{\sigma}(10°)}\right]^{\frac{10}{B}} \qquad (15)$$

Segments of the graphs that result from treating the successive values of σ^o as a time series and computing $V(\sigma^o(\theta))$ for 35°, 25°, and 15° for Flight 7, Run 1, Line 1 (an upwind run) are shown in Figure 7.

The aircraft ground speed should be added to the mean wind speed to obtain the speed of the aircraft relative to the "frozen" field of turbulence. The measurements of σ^o, 1.31 seconds apart are effectively 127 meters apart in the turbulence pattern. Were the pattern advected by the mean wind at, say, 8 meters per second, equivalent measurements by an anemometer would be about 16 seconds apart. A four minute long aircraft flight is thus the equivalent of a $(16/1.31) \times 4 \cong 49$ minute anemometer record.

These three functions do not look very much like the anemometer record of the wind shown in Figure 4. The one for 35° looks the most like an anemometer record, and the one for 15° has fluctuations in it for an excess of what could be expected in an anemometer record.

The analysis of these three space histories (after the use of Taylor's hypothesis) is shown in the next six figures. Figures 8 and 9 show the covariance function and the spectrum for $V(\sigma^o(35°))$. Figures 10 and 11 show these functions for 25°, and Figures 12 and 13, for 15°. The spectral estimates as computed from formulas given by Blackman and Tukey (1958) have only seven degrees of freedom so that the confidence intervals are quite broad as shown in the figures.

The curves for 35° show that this record has a standard deviation of 2.75 knots and therefore a variance of 7.56 $(\text{knots})^2$. The covariance function in Figure 8 drops off to about one-half the value at zero at the first lag. It does not really get to zero until just short of 1 kilometer. The spectrum has a large contribution to the total variance in the wave number range below $1/2036\ m^{-1}$ and substantial contributions on to $1/508\ m^{-1}$.

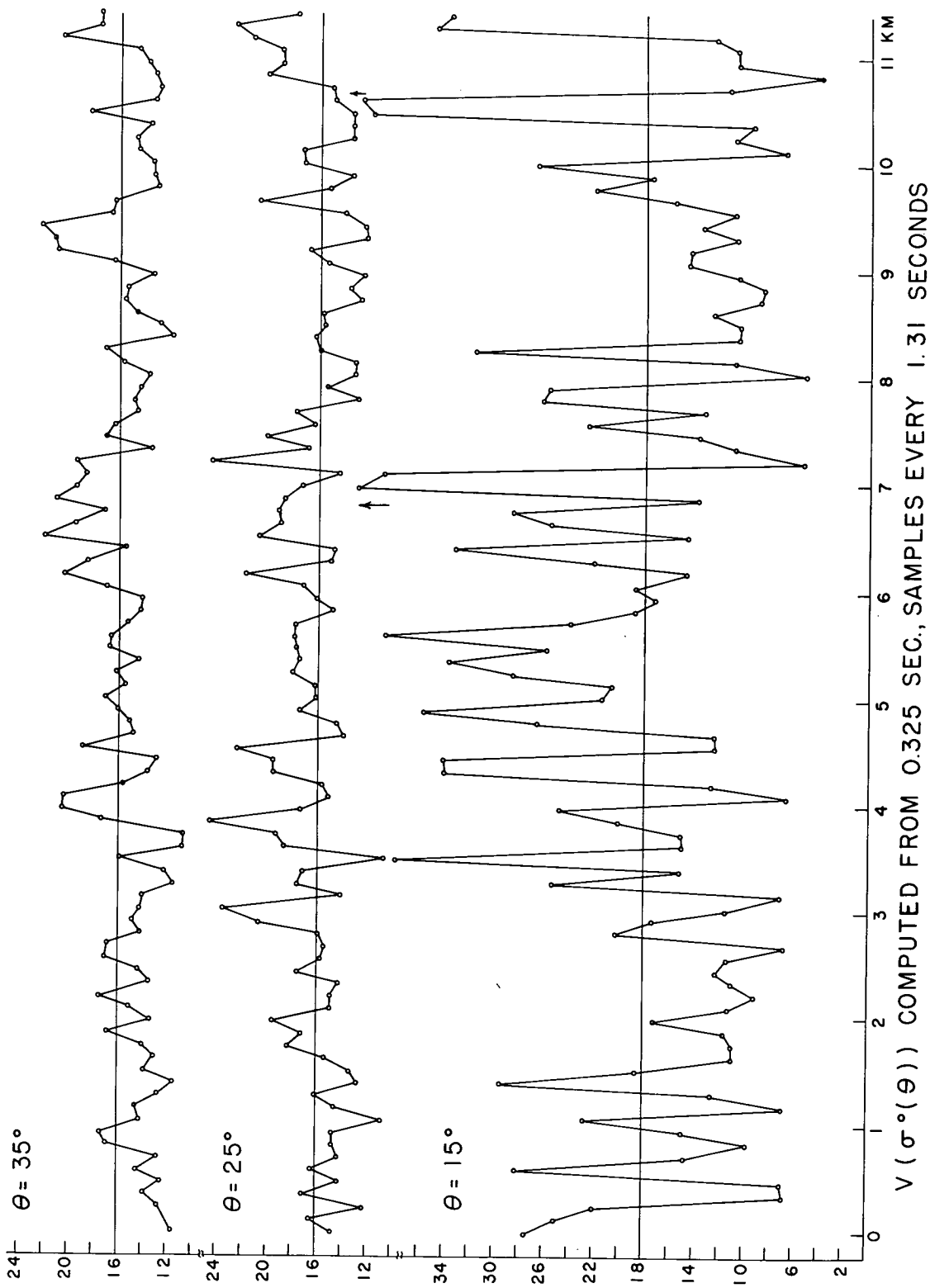

V (σ°(θ)) COMPUTED FROM 0.325 SEC., SAMPLES EVERY 1.31 SECONDS
FIG. 7

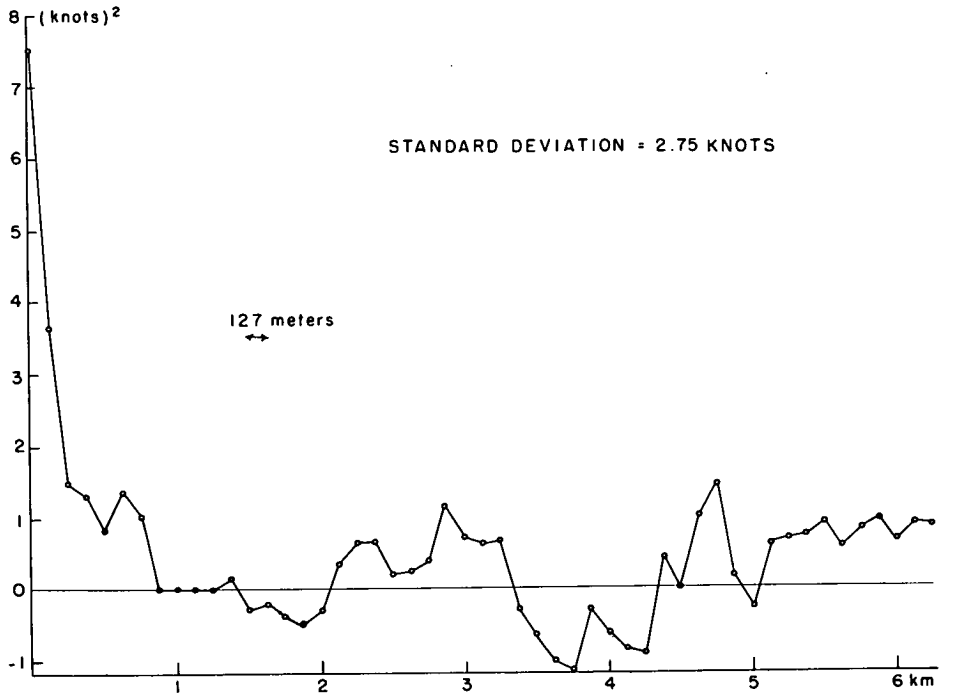

FIG. 8 COVARIANCE FUNCTION V [$\sigma°(35°)$]

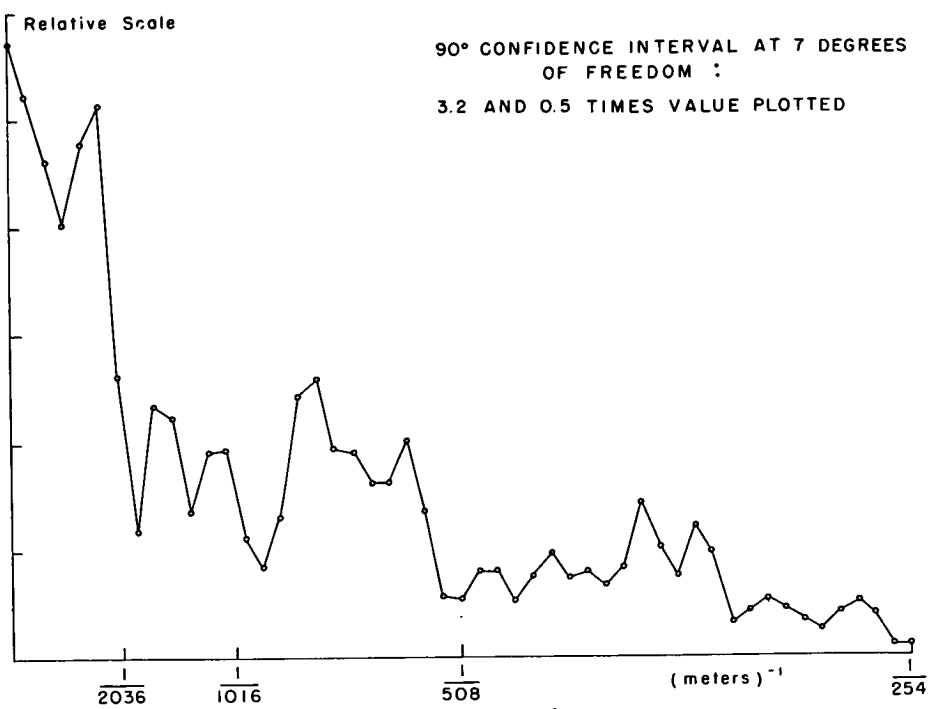

FIG. 9 $S(k/2\pi)$ for $\theta = 35°$

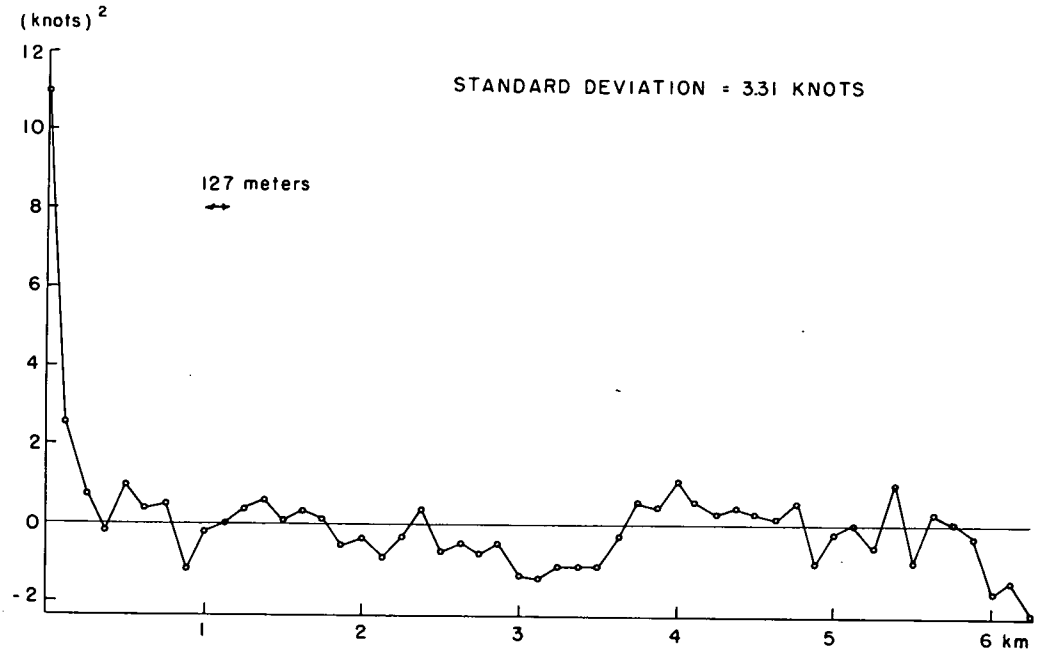

FIG. 10 COVARIANCE FUNCTION V [$\sigma°(25°)$]

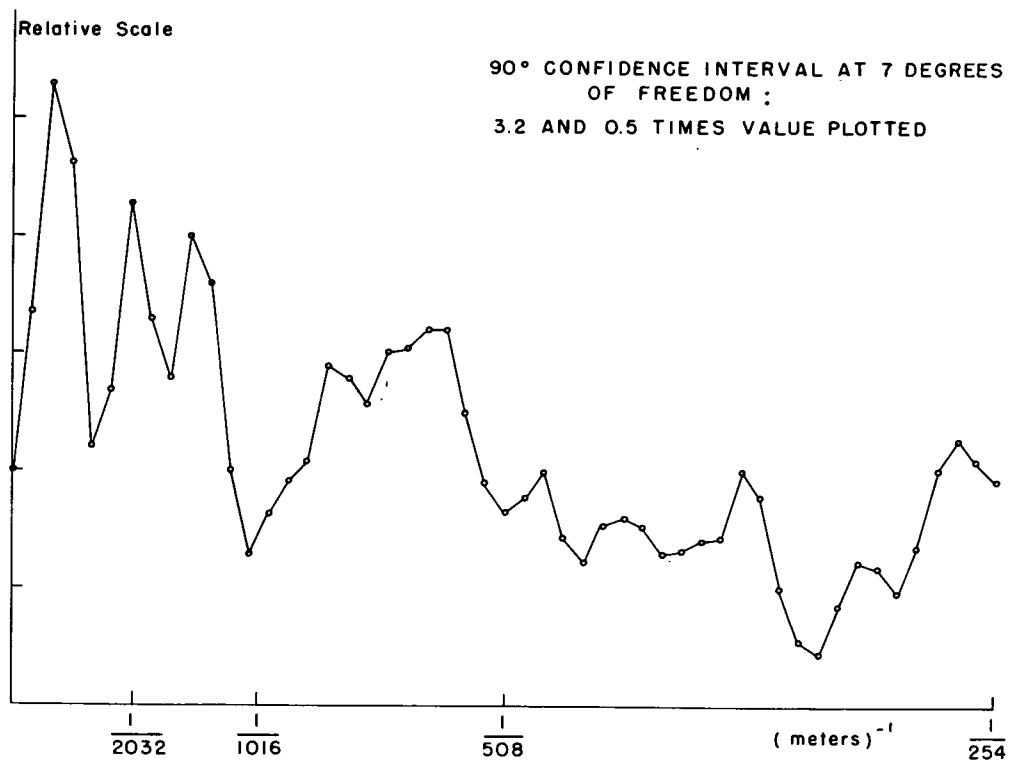

FIG. 11 S (k / 2π) for $\theta = 25°$

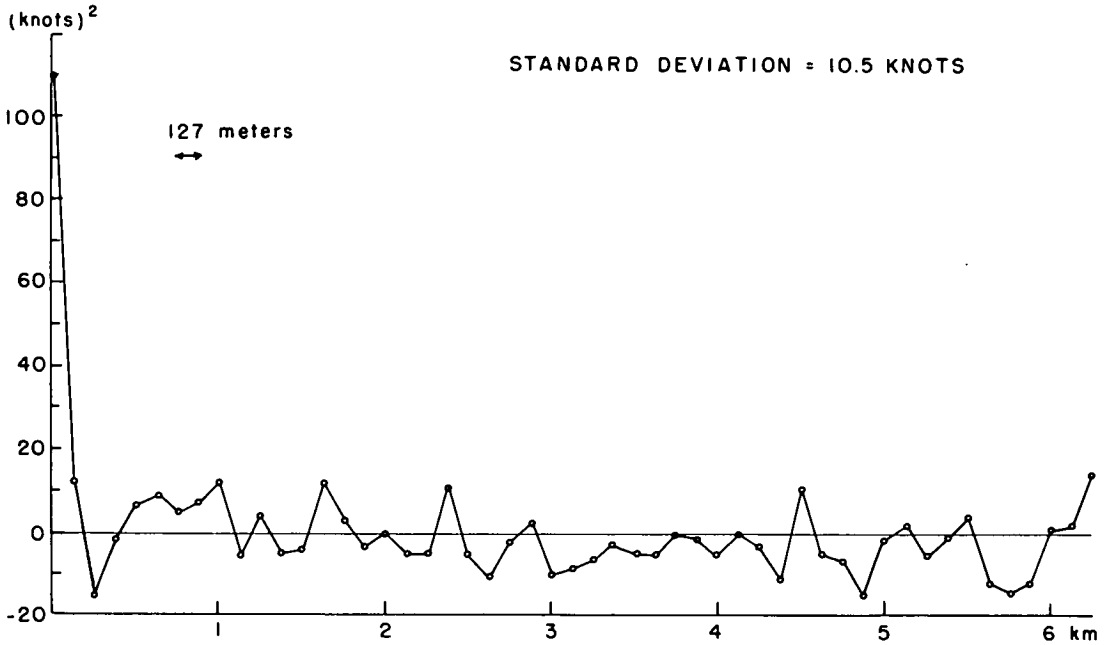

FIG. 12 COVARIANCE FUNCTION V [σ°(15°)]

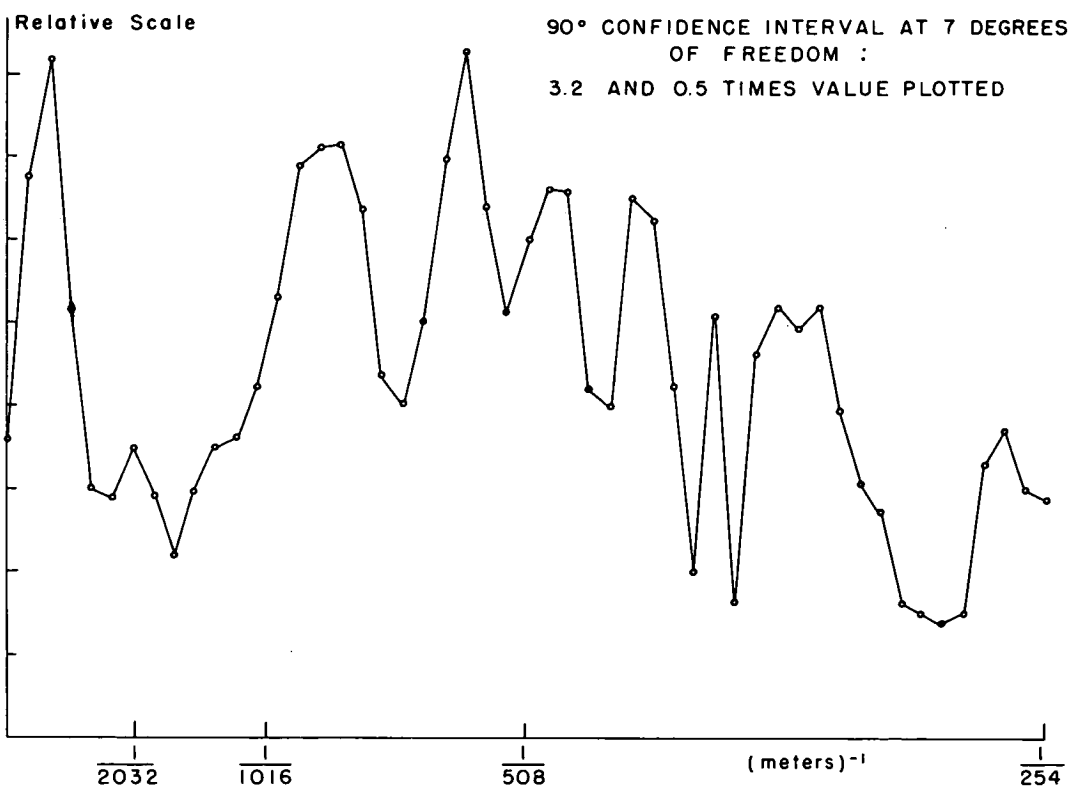

FIG. 13 $S(k/2\pi)$ for $\theta = 15°$

Figures 8 and 9 should be compared with Figures 5 and 6 from the anemometer record. The variance of the anemometer record was 3.82 (knots)^2, and the variance of $V(\sigma^o(35°))$ is 7.56 (knots)^2. The record graphed as $V(\sigma(35°))$ is thus a combination of the true fluctuations of the wind over the water and fading as described by Tables II and III. The peak at the left represents the anemometer fluctuations, which contribute 3.82 (knots)^2 to the variance, and the nearly flat part on the right, represents the superimposed white noise effect of the uncorrelated fading fluctuations which contribute 3.74 (knots)^2 to the variance. They happen to be approximately equal for this particular set of circumstances.

For 25°, the corresponding figures are Figures 10 and 11. The variance is 10.96 (knots)^2 so that 7.12 (knots)^2 are due to radar white noise effects (fading) and the rest to actual wind fluctuations. The relative peak in the spectrum at low frequencies despite the fact that almost 70% of the variability in the series is uncorrelated noise is notable.

For 15°, the corresponding figures are Figures 12 and 13. The variance is 110 (knots)^2 and less than 3% of the variability would be attributable to actual fluctuations in the wind over the water. The covariance function oscillates in a random way above and below zero, and the spectrum, since each point has only seven degrees of freedom is essentially a white noise spectrum.

The most important feature of the preceeding analysis is that the radar sea return has been shown to be responsive to one, two and three knot fluctuations about the average wind speed over distances of about 127 meters on the sea surface for large θ. The hypothesis that a large part of radar sea return is in practically instantaneous equilibrium with the local wind is substantiaed by this analysis. The result of the analysis of these three time (or space) series are perfectly predictable from Tables II and III. Wind variability is large enough to be at least as important as fading at 35°, whereas at 15°, fading completely submerges any wind variability.

These same time series techniques can also be applied to the series of original values of σ^o at 10°, 15°, 25° and 35°. The spectra and covariance functions are remarkably like the ones for the transformed wind speeds despite the exponential transformation. From these spectra by means of equation 7, the effective number of degrees of freedom in the sample of 189 values of σ^o can be found.

It now becomes possible to put one standard deviation confidence intervals on the estimates of the mean values of such quantities as

$$10 \log_{10} \frac{\bar{\sigma}^{o}(35°)}{\bar{\sigma}^{o}(10°)}$$

as given in Table IV. The effective number of independent points instead of being 189 has been reduced to the values shown, but the loss of degrees of freedom is much less than in the anemometer record in which 2000 data points were equivalent to 178 independent points. It has been assumed that $\sigma^{o}(10°)$ is independent of the other σ^{o} values so the variances have been added and the lowest applicable degrees of freedom has been used.

TABLE IV. - ANALYSIS OF FLIGHT 7, RUN 1, LINE 1.

				189 data points	
θ	$10 \log_{10} \bar{\sigma}^{o}$	SD_{σ} (db)	VAR	N^{*}	$\sqrt{N^{*}}$
10°	10.28	0.823	0.68	152	12
15°	9.100	0.807	0.65	143	12
25°	1.596	0.975	0.95	142	12
35°	-7.056	1.081	1.18	95	10
35°-10°	-17.34	1.36	1.86		
25°-10°	- 8.68	1.28	1.63		
15°-10°	- 1.18	1.15	1.33		

$$10 \log_{10} \left(\bar{\sigma}(35°) / \bar{\sigma}(10°) \right) = -17.34 \pm 0.136$$

$$10 \log_{10} \left(\bar{\sigma}(25°) / \bar{\sigma}(10°) \right) = -8.68 \pm 0.107$$

$$10 \log_{10} \left(\bar{\sigma}(15°) / \bar{\sigma}(10°) \right) = -1.18 \pm 0.096$$

The normalized average σ_{N}^{o} values for 35°, 25°, and 15° have been estimated to within ± 0.136, ± 0.107, and ± 0.096 db respectively.

It will be recalled that the mean of the anemometer record was

17 knots the standard deviation was 1.95 knots. The degrees of freedom were estimated by one procedure to be 178 for an 8000 second (133 minute) record. The flight line was shown to be the equivalent of a 49 minute anemometer record so that the sampling variability in the estimate of the mean would have (49/133) × 178, or about 65 degrees of freedom. This results in an estimate of the one standard deviation confidence interval on the mean wind of $\bar{v} = 17 \pm 0.24$ knots.

This estimate of the variability of the mean wind is suspect because of the shape of the wind spectrum. It was checked by a further study of the anemometer record at Argus Island. Actual 49 minute overlapping samples of three portions of the record were averaged for times near Flights 9 and 7. The actual standard deviations of these averages were 0.33 knots, 0.38 knots and 0.55 knots. The range in the averages was 1.24 knots, 1.41 knots and 2.25 knots. The values of 0.38 knots and 1.41 knots apply to Flight 7, Line 1, Run 1.

Similar results have been given by Bradley (1971) for other data runs as well as this one. The method he used to estimate the standard deviation of the sample mean of σ^o was more conservative so that broader confidence intervals were obtained. The estimated variability of the winds is comparable. Nevertheless, even these confidence intervals are quite narrow.

All of these results have to be corrected for atmospheric stability and the elevation of the anemometer and for variations in the antenna pattern both within missions and from one mission to another.

For $\theta = 35°$, the results are summarized for most of the data obtained on Missions 119 and 156, after all appropriate corrections, in Table V. There are 20 data sets identified by flight and mission. The meteorologist's estimate of the wind is given by V_M, good to ± 0.5 knots. The value of σ_N^o is also given along with the wind computed from this radar measurement, V_R, as tabulated. The difference to one-tenth of a knot is also tabulated, and the root mean square value of the difference in 2.6 knots.

A scatter plot of V_R versus V_M is shown in Figure 14. The scatter is really not very large and is due to both the difficulties of specifying the wind from the meteorological point of view and the scattering cross section from a radar point of view.

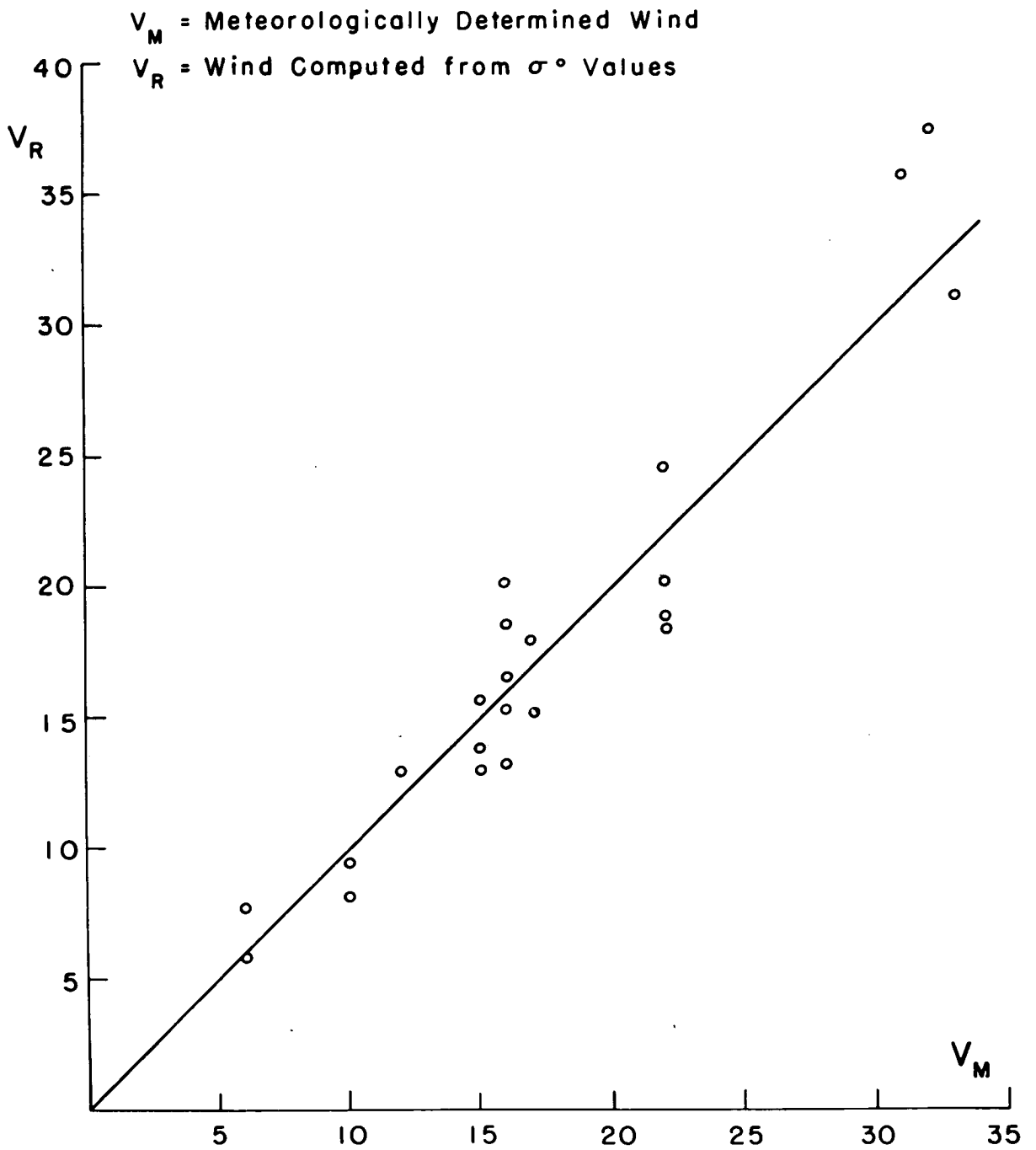

FIG. 14. SCATTER DIAGRAM OF WIND SPEED DETERMINED METEOROLOGICALLY VERSUS WIND SPEED DETERMINED BY RADAR.

TABLE V.- METEOROLOGICAL WIND ESTIMATES, σ^o VALUES AND WIND SPEED COMPUTED FROM σ^o VALUES FOR UP-WIND 35° INCIDENCE ANGLE FOR DATA FROM MISSIONS 119 AND 156.

Set	Mission	Flight	V_M	$\bar{\sigma}^o$(db)	V_R	Differences
1	119	9-3-3	6	-23.17	5.7	0.3
2	119	9-2-2*	6	-21.23	7.6	-1.6
3	156	3-4-5	10	-20.02	9.2	0.8
4	156	3-4-6*	10	-21.04	7.9	2.1
5	119	5-1-2	12	-18.02	12.6	-0.6
6	156	5-4-5	15	-16.65	15.5	-0.5
7	156	5-4-6*	15	-17.47	13.7	1.3
8	119	7-1-1	16	-16.25	16.5	-0.5
9	119	7-1-2*	16	-15.01	20.0	4
10	119	9-1-1	16	-16.88	15.0	1
11	119	9-1-2*	16	-15.5	18.5	-2.5
12	119	7-1-7	17	-15.70	17.9	-0.9
13	119	9-1-3	17	-16.85	15.0	2
14	156	7-8-5	22	-13.67	24.5	-2.5
15	156	7-8-6	22	-14.97	20.0	2
16	119	2-1-1	22	-15.69	18.0	4
17	119	2-1-2*	22	-15.52	18.5	3.5
18	156	2-8-1	31	-11.23	35.7	-4.7
19	119	3-1-2*	32	-10.96	37.3	-5.3
20	119	3-1-1	33	-12.15	31.0	2
				RMS ERROR		2.6 knots

An Inconsistency. - The data on Flight 7-1-1 show that the scatter in the measurement of a particular average scattering cross section is small. The scatter in the measurement of the average wind is also small. Moreover, the data show that the measurements of σ^o are actually responding to the gusts and lulls in the wind over the ocean surface along the path scanned by the beam.

On the other hand, the data in Table V and Figure 14 show a much larger scatter between the sea return and the wind, or the wind computed from the sea return and the meteorological wind, than can be explained on the basis of measurements made on a particular flight line

and run. Even if these estimates are off so that $\overline{\sigma}_o$ scatters by ± 0.3 db and $\overline{V}$ by $\pm$ 1 knot, the scatter in the full data set is still too large.

The greater scatter in the total set of data with rms errors of 0.7 db and 2.6 knots, or so, must be explainable in terms of factors other than the duration of the flight line and the concurrent measurement of the wind, especially for the Argus Island, Mission 119 results. These sources of scatter can be instrumental and meteorological and, or, oceanographic.

For example, the starred values for the flights in Table V were obtained with the aircraft flying downwind looking upwind with the aft pointing beam. Many of these values go with a corresponding set of values with the aircraft flying upwind looking upwind with the forward pointing beam. These pairs of measurements were made within just a few minutes of each other. Although Bradley (1971) attempted to calibrate out fore beam-aft beam antenna pattern differences, these values suggest the possibility of a residual error in this effect.

In processing the scatterometry data, one important part of the calculation is the ground speed of the aircraft, which is used in determining the Doppler shift. This in turn is used to calculate the backscatter for each angle. A study of the determination of the ground speed for Mission 119 lead to the conclusion that the ground speed was not determined with complete accuracy. Revised values of the ground speed are given by Pierson and Cardone (1971). The use of an incorrect value for the ground speed has two effects. It shifts the measured value to a value of θ different from the one desired, and it gives a value that needs to be corrected for by a different angle in the antenna gain correction. The combined effect is rather difficult to account for fully, but it can surely introduce additional scatter.

Other sources of residual error can be meteorological and/or oceanographic. The form of the wind profile with height and the drag coefficient must be known to be able to compute the variation of wind with height and the friction velocity. The scatter in such a basic quantity as the drag coefficient has been documented for Argus Island observations by DeLeonibus (1971).

There is also the problem of the effect of the Argus Island Platform and supporting structure on the wind flow past the anemometer on the tower. This effect was studied by Thornthwaite et al (1965) at Argus Island and by Mollo-Christenson and Seesholtz (1967) for a similar,

but smaller tower in a wind tunnel. For a south wind, the speed measured by the anemometer could be 4 or 5% too high. However, not enough information is available to make corrections for tower effects for the variety of wind directions encountered during Mission 119. Hence, no correction for this effect was attempted. The variation of this effect with wind direction could easily account for another $\frac{1}{2}$ to 1 knot scatter in the estimate of the average wind.

There is one oceanographic source of scatter that has not been removed from the data. The high frequency part of the wave spectrum is in equilibrium with the local wind but the lower frequency gravity wave portion need not be in equilibrium, as a fully developed sea, with the wind. Preliminary models of radar sea return show a dependence of σ^o on the longer higher waves in the spectrum and the present relationship can eventually be corrected for this variation in more complicated systems by means of both theory and multiple regression techniques. At the present level of development of the theory of sea return this added refinement is probably premature.

It is our opinion that much of this scatter has to do with meteorological, aircraft and radar instrument difficulties. With scanning pencil beam radars such as the one built under the AAFE Radscat program and for S193 on Skylab, a good part of this scatter may not be present. Under the AAFE Langley Radscat program, plans are being made to minimize the problems of estimating the average wind.

To study this problem further, the two sources of variability identified in the preceding sections will be extrapolated to spacecraft altitudes for S193. The result will be predictions of the capabilities of S193 in clear air to determine the wind speed and direction over the oceans under the assumption that the scatter in the data will be caused by the combination of fading and a turbulent wind over the water.

EXTRAPOLATION TO S193

The two sources of scatter in the measurement of σ^o obtained with aircraft that were identified in this report have their counterpart for S193 and the effects of both fading and turbulence can be taken into account for measurements to be made by S193. Both of these effects result in a very small scatter in the measurements.

Skylab S193 Scanning Patterns. - Three typical orbit segments for Skylab during which S193 might be turned on are illustrated in Figure 15. The wind field near the surface of the ocean as deduced from ship reports is illustrated in Figure 16 and the cloud cover that was present is shown in Figure 17.

Orbit segment A in Figure 15 shows the cross-track non-contiguous scanning mode. The antenna points straight down and at angles of 15.6°, 29.4°, 40.1 and 48° off of the vertical at the spacecraft. Because of the curvature of the earth the appropriate θ values will be larger than these angles.

The illuminated areas shown by the open circles are not drawn to scale. They are larger as the angle increases. At each cell, six different measurements will be made; σ^o_{VV}, σ^o_{HH}, σ^o_{HV}, and σ^o_{VH} and the passive microwave temperature for two polarizations. The pass shown would obtain 870 separate measurements in about seven minutes.

Orbit segment B shows a northbound pass and orbit segment C shows a southbound pass on the non-contiguous forward scanning mode. Each black ellipse represents a series of six measurements at each of the five different angles at nearly the same place on the ocean surface for a total of 30 measurements.

Figure 16 shows a wind field analysis such as might occur during a Skylab pass. The various scanning modes would scan cells on the ocean surface in which the wind speed varied all the way from 5 knots, or so, to perhaps 50 or 70 knots, depending on the scanning mode and the exact location of the radar illuminated areas on the sea surface.

The "radar scatter" or "fading variability" of S193. - S193 measurements have a source of scatter analogous to the fading that results from the 0.3275 second averages in the aircraft data. Each of the four S193 radar measurements are averaged over about 0.6 seconds and the bandwidth of the system is such that the received power is measured to within 7% for each measurement. Thus within one standard deviation the radar scattering cross section is good to within 1 ± 0.07 of the expected value. In fact, the averaging time is a function of the antenna angle and has been chosen so that this value is an upper bound for all scan angles.

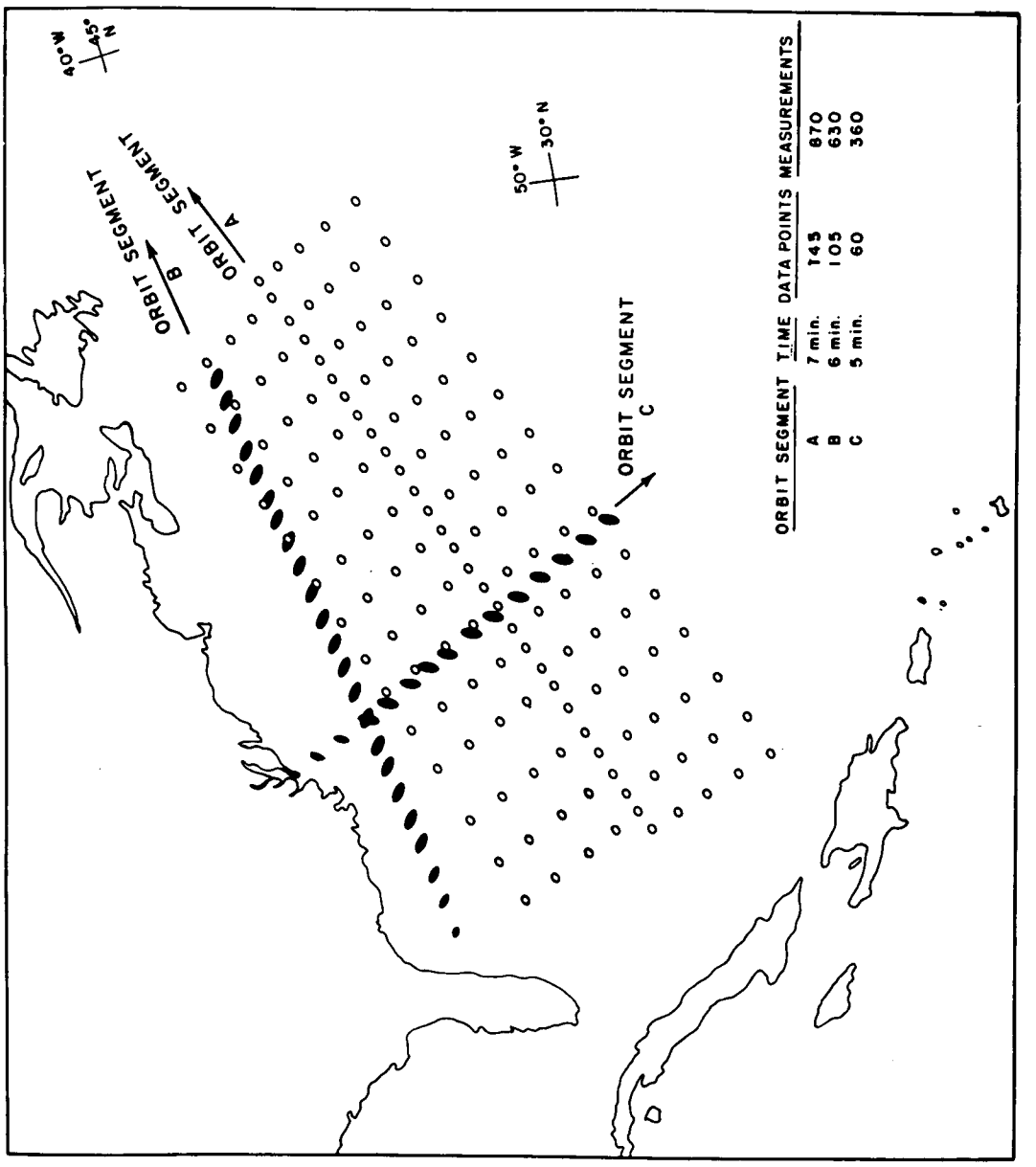

FIG. 15. CROSS TRACK AND ALONG TRACK SCANNING PATTERNS FOR S193 ON SKYLAB.

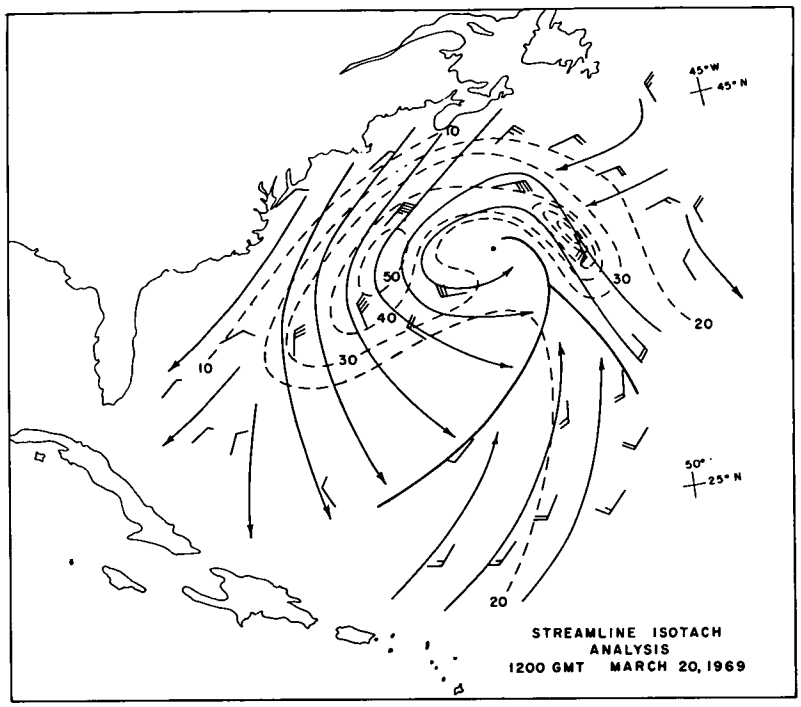
45°W
45°N
10
50
40
30
30
20
10
30
50°
25°N
20
STREAMLINE ISOTACH
ANALYSIS
1200 GMT MARCH 20, 1969

FIG. 16

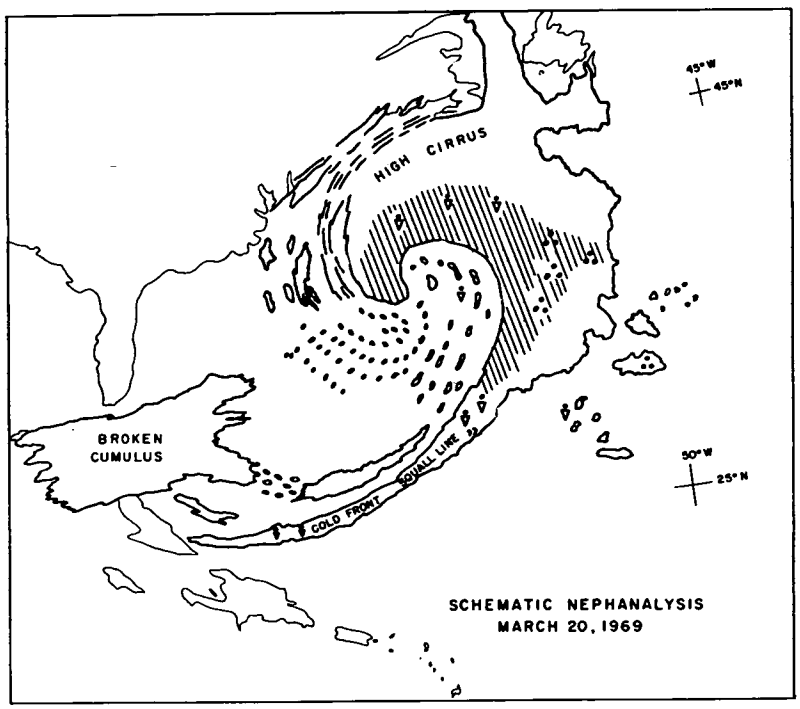
45°W
45°N
HIGH CIRRUS
BROKEN
CUMULUS
COLD FRONT
SQUALL LINE
50°W
25°N
SCHEMATIC NEPHANALYSIS
MARCH 20, 1969

FIG. 17

This design fact yields the standard deviation of measurements of σ^o which is $\pm$ 0.3 db. Table VI shows the results using this value for SD_σ in equation 13 for the off-vertical values of θ and the values of B found by Bradley (1971). The upwind B for 15° was used for 15.6°, the B for 25° was used for 29.4° and the B for 35° was used for both 40.1° and 48°. In actuality, the values for B for these angles are likely to be higher, which in turn implies a lower percentage variability in the wind estimates.

It also must be assumed that the same kind of equation as equation 11 will also be valid for non-normalized measurements of σ^o at these various values of θ. Since the transmitted power is monitored in S193, the values of σ^o should be primary measurements that will not have to be normalized to 10° as in the aircraft flights. The constant, A, will be different for the S193 measurements but the equation should still be of the same form. Results similar to Table VI can also be computed for cross wind conditions and somewhat larger percentages of scatter would result.

TABLE VI. - CONSERVATIVE ESTIMATES OF PER POINT VARIABILITY DUE TO FADING OF UPWIND WIND SPEED MEASUREMENTS BASED ON SINGLE MEASUREMENT OF σ^o BY S193.

log 1.07 = 0.030	SD_σ = 0.3 db	
θ	$\log_{10}(1 + \Delta v/v)$	$1 + \Delta V/V$
15.6°	0.0909	1.23
29.4°	0.0266	1.06
40.1°	0.0201	1.05
48°	0.0201	1.05

In essence for angles of 29.4° and greater, the wind speed estimate for a single measurement of σ^o_{VV} will scatter by about $\pm$ 6% about the true value due to this source of variability. All theoretical and observational data to date suggest that σ^o_{HH}, σ^o_{HV} and σ^o_{VH} will all provide additional equally independent estimates of the wind-speed and that the scatter will be comparable. The average of four such estimates, since each one will be independent, will produce a final estimate within 3% of the expected value.

The available data on $\sigma^{o}_{VV}(\theta)$ as a function of wind speed all suggest that at $\theta = 0$, $\sigma^{o}_{VV}(0)$ decreases with increasing wind speed and that at an angle near 10°, or so, $\sigma^{o}_{VV}(\theta)$ does not depend strongly on wind speed. This is why the normalized measurements at 15° are relatively insensitive to wind speed and why the values for $1 + \Delta V/V$ and $1 - \Delta V/V$ are large for 15°. An operational instrument could avoid this problem by tilting the antenna forward as described by Moore and Pierson (1971). The values given for 15° in Tables I, II, III, IV, and VI are all a natural consequence of the shape of the scattering cross section curve and are therefore to be expected.

S193 also measures passive microwave temperature in two polarizations. Moore et al (1971) have combined the data obtained by Nordberg and Hollinger in a plot that shows that, given the sea surface temperature, ΔT_B(°K), increases at 0.96 ± 0.16 °K/(m/s) for 19 GHz as the wind varies from zero to 30 meters per second.

The variation of ΔT_{BHH}(°K) for 13.9 GHz will not be as strong as that at 19 GHz, but through cloudless skies after correction for atmospheric temperature and water vapor and without obvious corrections for fetch and duration, which change the amount of foam, a similar dependence about 75% as strong could lead to the dependence given by equation 16

$$V \cong (0.78 \pm 0.16)\, \Delta T_{BHH}(°K) \qquad (16)$$

It may then be possible to estimate the wind speed at 15° to within about 20% by a passive measurement. Refinements in calculating the amount of foam could reduce this scatter substantially. At 0°, there will again be a wind speed dependence for σ^{c}, which can be combined with the passive microwave to determine the wind.

Moreover, the passive microwave measurements appear to be independent of wind direction. It should be possible to devise a proceedure in which all six measurements for a θ greater than 15° can be used to determine both wind speed and direction to within a choice of four possible angles, $\pm X$ and $\pm X + 180°$, at each cell through cloudless skies. Three of these four angles can often be eliminated by synoptic considerations.

Effects of Turbulent Wind Field on Measurements Made with S193. - The patch of ocean illuminated by the radar beam on S193 varies in area and dimensions as a function of the angle of the beam off the vertical. The area of the patch is 95 km^2 for 0° and increases to 385 km^2 at 48° as shown in Table VII.

The area given in this table is computed on the assumption that the main lobe of the antenna pattern illuminates the sea surface with constant power over the entire given area and that there is zero power outside the area. It is also an instantaneous value. The time required to make the measurement spreads out the illuminated area and applies a trapezoidal weight function to a broadened pattern. This incremental area is also tabulated for the cross track mode, but it was not used in the rest of the calculations. This incremental area actually increases the value of N by an amount equivalent to adding about half the incremental area to the values tabulated under "area". The rest of the entries in the table are therefore conservative.

The analysis of the Argus Island anemometer record led to the conclusion that for a wind speed near 16 knots the anemometer record would be the equivalent of measurements of wind speed every 350 meters along a line on the ocean surface in the wind direction. Lumley and Panofsky (1964) show that the horizontal wind decorrelates in the cross wind direction at least as fast as in the upwind-downwind direction so that points on a square grid 350 meters on a side over the area illuminated by the radar beam could represent the equivalent number of independent observations of the wind. The wind at each of these points, and in fact over the entire area, is fluctuating above and below the desired average value as represented by equation 5 in much the same way that anemometer records fluctuate.

A square 350 meters on a side has an area of $(0.35)^2 = 0.123$ square kilometers so that there are effectively 8 independent points per square kilometer of illuminated area for a 16 knot wind.

The number of effectively independent points for a 16 knot wind is shown in Table VII for each antenna angle. These values have to be reduced by a factor of four when the wind speed is doubled and by a factor of nine when the wind is tripled because of the scaling laws for turbulence. Even for a 48 knot wind, there are at least 84 degrees of freedom in the vertical.

TABLE VII. - CONSERVATIVE DEGREES OF FREEDOM (N) IN ESTIMATES OF VARIANCE OF THE AVERAGE WIND OVER THE RADAR ILLUMINATED PATCH, AND 95% CONFIDENCE INTERVAL ON $\bar{V}$ FOR $SD_v/V = 0.20$ AS GIVEN BY $\bar{V} \pm (2SD_v/\sqrt{N})$.

Angle	0°	15.6°	29.4°	40.1°	48°
Area $(KM)^2$	95	108	151	236	385
Incremental Area $(KM)^2$	21	39	68	97	142
$N(\bar{V} = 16$ knots)	760	864	1208	1888	3080
$N(\bar{V} = 32$ knots)	190	216	302	472	770
$N(\bar{V} = 48$ knots)	84	96	134	209	347
$1/\sqrt{N}$ (16)	.036	.033	.028	.023	.018
$1/\sqrt{N}$ (32)	.072	.066	.056	.046	.036
$1/\sqrt{N}$ (48)	.109	.102	.086	.069	.054
95% Confidence Interval					
16 knots	16.24	16.20	16.18	16.14	16.11
	15.76	15.80	15.82	15.86	15.89
32 knots	32.92	32.85	32.72	32.59	32.46
	31.08	31.15	31.28	31.41	31.54
48 knots	50.09	49.96	49.65	49.32	49.03
	45.91	46.04	46.35	46.68	46.97

If the standard deviation of the wind is 20% of the mean wind, 95% confidence intervals on the mean wind can be found by computing as in Table VII.

These confidence intervals are delightfully narrow. For intercomparison with other numbers in this paper, they should be halved. The 95% confidence intervals are plus or minus less than 1 knot for all entries in the table except 48 knots. The largest percentage variation for 0° and a 48 knot wind is 4.4%. It can be concluded that the illuminated patch is large enough to provide a truly stable estimate of the average wind for the purposes of synoptic meteorology.

The dimensions of the spot illuminated by the radar beam are given in Table VIII. The spot at 48° is roughly elliptical with the doubled major axis distance equal to 29 km and the doubled minor axis distance equal to 17 km as an example from the table.

Here again the spot is actually stretched in one direction due to spacecraft motion. The stretching makes the values in the table conservative.

TABLE VIII. DIMENSIONS OF PATCH OF OCEAN ILLUMINATED BY S193 RADAR BEAM AND FREQUENCIES IN AN ANEMOMETER RECORD THAT CORRESPOND TO THESE DIMENSIONS.

Angle	0°	15.6°	29.4°	40.1°	48°
Area $(KM)^2$	95	108	151	236	385
Approximate Length (KM)	11	12	15	21	29
Approximate Width (KM)	11	12	13	15	17
Equivalent Time Minutes					
8 meters/sec	23	25	31	44	60
	23	25	27	31	35
16 meters/sec	11	12	15	22	30
	11	12	13	15	17
24 meters/sec	7	8	10	15	20
	7	8	9	10	12
Approximate Cycles/Hour					
8 meters/sec	2.6	2.4	1.9	1.4	1.0
	2.6	2.4	2.2	1.9	1.7
16 meters/sec	5.5	5.0	4.0	2.7	2.0
	5.5	5.0	4.6	4.0	3.5
24 meters/sec	8.6	7.5	6.0	4.0	3.0
	8.6	7.5	6.7	6.0	5.0

Consider a sinusoidal perturbation in the wind with a length in space given by these tabulated dimensions and assume that it is advected by the mean wind. Such a perturbation moving at 8 meters per second would take 60 minutes, as tabulated, to travel 29 km across the beam. The 29 km ocean distance is thus the equivalent of a perturbation with a period of 60 minutes in an anemomber record when the mean wind is 8 meters/sec.

The periods that result for each antenna angle and for the two distances across each patch are all given in Table VIII. They range from 7 minutes to 60 minutes. The reciprocals of these numbers converted to cycles per hour are given as the last set of entries. The values range from 1.0 to 8.6 cycles per hour. Either way, when these periods, or frequencies, are located on the spectrum in Figure 3, they all fall in the valley between the microscale turbulent fluctuations and the synoptic scale winds. The illuminated patch of sea surface from the scanning pencil beam on S193 acts as a very efficient way to obtain the quantity shown in equation 5 by acting as a low pass filter to suppress the microscale fluctuations and provide a very stable scattering cross section measurement representative of the desired synoptic scale wind.

The two dimensional "box-car", or square sided, weight function assumed for the antenna pattern is an over simplification of the problem. The power illuminating the surface decreases in a radial direction from some center spot whose location depends on geometry and the movement of the spacecraft during the time required for one measurement. To account for 96% of the total power involved, the dimensions of instantaneous pattern must be increased by a factor of 1.65 so that the area is increased by a factor of about 2.6. The exact form of the weight function will depend on many factors. It will, however, be a smoothly varying function that builds from zero to a unimodel peak, perhaps with roughly elliptical lines of equal power.

Such a weight function when used in equation 5 would produce a filter in vector wave number space that would act like a fairly sharp low pass filter and provide a good measurement of the synoptic scale wind. Work on the antenna pattern is in progress at the University of Kansas, and it will be possible to refine these calculations for application during Skylab.

In summary, two of the sources of variability in estimates of the mean wind for synoptic scale purposes, namely fading in the scattered signal and turbulent fluctuations in the wind over the water are both adequately averaged in the design of S193. The two sources of scatter combined produce a total scatter of, at most, 7%, except at 15°, so that two-thirds of the time a 30 knot wind would be estimated to be between 28 and 32 knots and a 40 knot wind would be estimated to be between 37 and 43 knots.

Additional Sources of Scatter for S193 Data. - The root mean square error for σ^o in db found by Bradley (1971) as given in Table I, and the scatter in Table V and Figure 14 was not all explained by fading effects and the turbulence in the wind. For both S193 and the airborne AAFE Langley Radscat, the instrumental problems due to the use of the fan beam Doppler system will not be present. There remains the problem of determining the wind velocity accurately for the areas of the ocean to be sampled by these instruments.

Unfortunately, the improved design of these two new instruments cannot be matched by an improvement in the accuracy with which the wind speed can be determined meteorologically, especially for S193. Some improvement can be obtained for experiments with the airborne instrument.

The problem of the adequate determination of the synoptic scale wind for patterns scanned by S193 as in Figure 15 has been treated in a proposal to NASA by McClain, Moore, Pierson and Talwani (1971) and by an amended proposal in which a concurrent aircraft program is described. The wind field as shown in Figure 16 ought to be smoothly varying over synoptic scale distances. Computer based procedures such as those developed by Cardone (1969) and described by Pierson (1970) can be used to smooth the wind field given by ship reports and surface atmospheric measurements so as to determine the wind. It is to be expected however that these estimates of the wind velocity will introduce considerable scatter in the regressions of σ^o values on wind velocity. Not only will the upwind and crosswind situations have to be treated, but also all possible angles between the beam and the wind direction. The data base for these studies will, however, be much greater so that the scatter will be more easily understood.

The use of S193 on Skylab has converted an instrument system, which when used on an aircraft, would be responsive to microscale effects and

therefore have concurrent measurement and sampling problems, to a true synoptic scale instrument in which the microscale is averaged out. The result may even be that winds determined by S193 will be so good that other wind measurement systems such as ship reports and anemometers on buoys will be calibrated against S193 instead of the other way around.

Other Problems of S193. - The preceding considerations have all been carried out under the assumption that the beam passes through clear air to the sea surface. There is the additional problem of determining the wind velocity through clouds and precipitation as illustrated by Figure 17. This problem has to be treated by Moore et al (1971). The essential points are that passive measurements lose contact with the sea surface when clouds are present long before the radar measurements and that the passive measurements can be used to correct the radar measurements for atmospheric cloud effects and find the wind at the surface.

Also there is the possibility that variations in radar backscatter can be caused by variations in sea surface temperature, salinity, and surface properties which produce changes in the dielectric properties of the water. These effects may have to be calibrated out. Finally, theories of radar sea return show that it depends on the entire wave spectrum and not on just the high wave number part of the spectrum. The dominant effect is from the short waves, but corrections for that part of the spectrum not in local equilibrium with the wind will have to be developed. These corrections are expected to be small, but necessary.

CONCLUSIONS

The extrapolation of laboratory and aircraft radar sea return data to spacecraft altitudes has shown, for S193 on Skylab, that fading effects will contribute very little scatter to the measurements and that the microscale turbulent fluctuations in the wind will be averaged out. The result should be very stable estimates of the synoptic scale winds.

Additional sources of scatter in the aircraft program were identified as being instrumental, associated with the fan beam Doppler radar that was used and the anemometer location on Argus Island, and meteorological and oceanographic. The radar problems will not be present for S193. There will still be problems in defining the wind by means of meteorological measurements to comparable accuracies.

Other problems, unique to a space instrument, such as making measurements through clouds and precipitation were identified. Methods for their solution were given.

The volume, and the improved quality, of the data from S193 should make it possible to meet the scientific objective for S193 which is to prove conclusively that simultaneous measured values of the radar scattering cross section matrix and the microwave temperature for two different polarizations at 13.9 GHz will provide data from which the winds in the planetary boundary layer over the oceans can be inferred.

ACKNOWLEDGEMENTS

The research upon which this report is based was supported by the Remote Sensing Oceanography Group of the Naval Research Laboratory under Contract N62306-70-A-0075.0007 at New York University and by generous support from several contracts and grants from NASA at the University of Kansas. The authors wish to acknowledge the contributions to this paper of many of their co-workers at Kansas and New York Universitites as indicated by their names as authors and co-authors of reports and papers cited in the references. Our thanks are also due to Mr. Duncan Ross who checked the Argus Island anemometer and obtained the anemometer data continuously during Mission 119.

Contribution No. 125, Geophysical Sciences Laboratory, New York University, Department of Meteorology and Oceanography.

REFERENCES

Baer, L. and G.W. Withee, 1971a: A methodology for defining an operational synoptic temporal oceanic sampling system I stationary conditions. J. Appl. Meteor., Vol. 10, No. 6, pp. 1053-1060.

_____, 1971b: A methodology for defining an operational synoptic temporal oceanic sampling system II non-stationary conditions. J. Appl. Meteor., Vol.10, No. 6, pp. 1061-1065.

Blackman, R.B. and J.W. Tukey, 1958: The measurement of power spectra from the point of view of communications engineering. Bell System Tech. Journ., January and March, Vol. 37, [also in book form, Dover, New York].

Bradley, G.A., 1971: Remote sensing of ocean winds using a radar scatterometer. Tech. Report 177-22, The University of Kansas Center for Research, 191 pp.

Cardone, V.J., 1969: Specification of the wind field distribution in the marine boundary layer for wave forecasting. Geophysical Sciences Lab. Report TR-69-1, New York University.

DeLeonibus, P.S., 1971: Momentum flux and wave spectra observations from an ocean tower. J. Geophys. Res. Oceans and Atmospheres, Vol. 76, No. 27, pp. 6506-6527.

Druyan, L.M., 1971: Objective analysis of sea level winds and pressures derived from simulated observations of a satellite radar radiometer and actual conventional data. Geophysical Sciences Lab. Report TR-71-7, New York University.

Lumley, J.L. and H.A. Panofsky, 1964: The structure of atmospheric turbulence. Monographs and Texts in Physics and Astronomy, Vol. XII, Interscience Publishers, John Wiley and Sons.

Lappe, U.O., B. Davidson and C.B. Notess, 1959: Analysis of atmospheric turbulence spectra obtained from concurrent airplane and tower measurements. Inst. Aero. Sci. Report No. 59-44.

McClain, E.P., R.K. Moore, W.J. Pierson and M. Talwani, 1971: A joint meteorological oceanographic geodetic and sensor evaluation program for experiment S193 on Skylab. Proposal submitted to NASA.

McDonald, J.A. and E. Herrin, 1971: The nature of turbulence. Dallas Geophysical Lab., Southern Methodist University, Dallas, Texas, August 1971, 73 pp.

Millard, R.C., Jr., 1968: Wind measurement from buoys: a sampling scheme. Unpublished manuscript, Woods Hole Oceanographic Institution, Contract ONR NR 083-004.

Mollo-Christensen, E.L. and J.R. Seesholtz, 1967: Wind tunnel measurements of the wind disturbance field of a model of the Buzzard's Bay entrance light tower. J.Geophys. Res., Vol. 72, pp. 3549-3556.

Moore, R.K. and W.J. Pierson, 1971: Worldwide oceanic wind and wave predictions using a satellite radar radiometer. J. of Hydronaut., Vol.5, No. 2, pp. 52-60.

Moore, R.K., J.P. Claassen, A.K. Fung, S. Wu and H.L. Chan, 1971: Toward RADSCAT measurements over the sea and their interpretation, in Advanced Applications Flight Experiments Principal Investigators' Review. NASA Langley Research Center, pp. 115-140.

Neumann, G. and W.J. Pierson, 1966: Principles of Physical Oceanography. Prentice-Hall Book Co., 545 pp.

Phelps, G.T. and S. Pond, 1971: Spectra of the temperature and humidity fluctuations and of the fluxes of moisture and sensible heat in the marine boundary layer. J. Atmos. Sci., Vol. 28, No. 6, pp.918-928.

Pierson, W.J., 1970: The integration of remote sensing data into global weather prediction, wave forecasting, and ocean circulation computer based systems, in Hydrology and Oceanography Third Annual Earth Resources Review, Vol. III, pp. 70-1 to 70-27.

Pierson, W.J. and V.J. Cardone, 1971: Radar satellite oceanography and ocean dynamics, (Final Report on Contract N62306-70-A-0075, Task Order .0005 with supplemental material on Task Order .0007 for the period 1 July 1970 to 1 December 1971), New York University, School of Engineering and Science.

Pierson, W.J., F.C. Jackson, R.A. Stacy, and E. Mehr, 1971: Research on the problem of the radar return from a wind roughened sea, Advanced Applications Flight Experiments Principal Investigators' Review, October 5-6, 1971, NASA Langley Research Center, pp. 83-114.

Pond, S., G.T. Phelps, J.E. Paquin, G. McBean, and R.W. Stewart, 1971: Measurement of the turbulent fluxes of momentum, moisture, and sensible heat over the ocean. J. Atmos. Sci., Vol. 28, No. 6, pp. 901-917.

Thornthwaite, C.W., W.J. Superior, and R.T. Field, 1965: Disturbance of air flow around Argus Island Tower near Bermuda. J. Geophys. Res., Vol. 70, No. 24, pp. 6047-6052.

Van der Hoven, I., 1957: Power spectrum of horizontal wind speed in the frequency range from 0.0007 to 900 cycles per hour. J. Meteorol., Vol. 14, pg. 160.

SECTION 98

MISSION 119 PASSIVE MICROWAVE RESULTS

by

J. P. Hollinger and R. A. Mennella
E. O. Hulburt Center for Space Research
Naval Research Laboratory
Washington, D. C.

INTRODUCTION

Passive microwave measurements of the sea surface for the purpose of determining surface wind speeds were made from the NP3A aircraft (NASA-927). Observations were made at frequencies of 1.4, 10.6, and 31.4 GHz during NASA Mission 119 undertaken off Bermuda in the vicinity of Argus Island sea tower during January 1970.

The microwave brightness temperature dependence on sea surface wind speeds arises from two effects (1). The first effect results from increasing roughness of the compact water surface with wind speed and the second effect from the increasing coverage of white caps and sea foam with increasing wind speed. Although both are roughness effects, the first is referred to as the surface roughness effect and the second as the foam effect.

Passive microwave observations from Argus Island ocean tower (1) have shown that the surface roughness effect, besides being dependent on the wind speed, is also dependent on observational frequency, increasing with increasing frequency. The surface roughness effect is closely coupled to the local wind fields, rapidly responding to changes in local wind, and appears relatively insensitive to the energy content of the low frequency gravity waves. In addition the surface roughness effect is a function of the angle of observation and the polarization of the radiation received. The wind speed dependence is greatest at larger incidence angles of horizontal polarization. The roughness effect appears to be dominant for wind speeds less than 30 to 40 knots (2).

The sea foam effect is expected to be dominant at the higher wind speeds (> 30 knots) when the surface is covered with a high percentage of sea foam. Unfortunately the

percentage of foam-covered surface as a function of wind speed is not a unique relationship but is greatly influenced by the fetch and duration of the wind, the air-sea temperature differences and the salinity (3). The microwave brightness temperature of sea foam is known to be on the order of 100°K higher than the radiometric temperature of the surrounding sea water (1), (2), (4), (5), (6), (7). The sea foam effect, as compared to the surface roughness effect, appears to be relatively independent of polarization and incidence angle. It is also expected that the brightness temperature of foam should decrease with decreasing observational frequency for foam layers having thicknesses of only a fraction of the observational wavelength. The data available at present is, however, insufficient to describe in detail the microwave characteristics of foam as a function of frequency, polarization, and incidence angle.

Most airborne passive microwave measurements of sea surface conditions have been performed by the NASA/GSFC 19.4 GHz scanning radiometer which is a single polarization device that scans in incidence angle ± 50 degrees (5), (6), (7), (8). A lesser amount of airborne measurements have been made either with fixed angle or calibration limited systems or were made over a limited range of sea surface conditions (4), (6), (9). Further airborne multifrequency passive microwave measurements are required to unequivocally demonstrate that an airborne radiometer system can indeed provide radiometric brightness temperature changes that can be quantitatively correlated with wind induced sea surface roughness and foam effects.

The ability of airborne radiometers to quantitatively and accurately measure surface wind fields over a wide range of wind and sea conditions may best be tested by using a multifrequency airborne system having dual polarization, and observing at multiple look angles over a wide variety of sea surface conditions. Accordingly, Mission 119 was conducted using the NASA NP3A multifrequency radiometers in a locale expected to provide the required categories of sea surface variations.

DESCRIPTION OF EQUIPMENT

The radiometers, mounted behind the radome in the nose of the P3A, are conventional Dicke-type radiometers using

crystal mixers and klystron local oscillators. Argon noise generators are used for inflight calibrations for the 10.6 and 31.4 GHz systems, and a solid-state noise generator is used for the 1.42 GHz radiometer. The basic system parameters are listed in the following table. A full description of the systems operation, calibration, data collection, and recording is contained in LEC/HASD Technical Report 649D.21.017C (10).

TABLE

Frequency (GHz)	ΔT_{rms}* (°K)	Half-Power Beam Width (Degrees)	Typical Radome Loss Value (dB)	Antenna Loss (dB)
1.4	1.6	16	0.30	2.10
10.6	1.0	5	0.45	0.45
31.4	0.8	5	1.20	0.25

*referenced to outside of the radome for a one-second time constant.

GROUND TRUTH

Primary ground truth was recorded at the Argus Island tower and consisted of wind speed, wind direction, significant wave height, and maximum wave height as provided by D. B. Ross of NAVOCEANO (11). All airborne data used in analysis were runs starting or stopping within the vicinity of the tower. The wind speeds correlated with the airborne measurements ranged from six to thirty-six knots and were obtained by averaging over ten second intervals the wind speed data recorded at a height of 43.3 meters above the sea surface. The sea temperature measured by the PRT-5 infrared radiometer during the measurements was 290°K ± 1°K; the salinity has been measured at 35 o/oo ± 1 o/oo.

DATA COLLECTION AND PROBLEMS

During the nine flights, forty-five data sets were collected. A data set consisted of either horizontal or

vertical polarization observations at nine incidence angles between nadir and 80 degrees. Evidences of long and short term instabilities in the radiometer systems necessitated using more than thirty percent of the flight time for in-flight calibrations. Large, obvious instabilities appearing during and after operations at high altitudes resulted in all the data (40 %) taken above 1500 feet to be excluded from analysis.

Absence of identification data on magnetic tape recordings prevented a timely, efficient reduction of all aircraft tape recorded data. The main radiometer output data was obtained from manual reduction of the on-board analog strip charts although supplementary data required in the reduction program was derived from the magnetic tape. The raw data, plotted as a function of look angle, was used to evaluate the stability of each set and to rectify obvious discrepancies in the radome loss values that had been provided by MSC as a function of frequency, incidence angle, and polarization. The uncertainties in radome losses and instabilities of the system precluded the derivation of accurate absolute brightness temperatures. However, the system is considered capable of providing useful relative measurements for comparison between frequencies and for comparison with the Argus Island tower based measurements.

1.4 GHZ RADIOMETER

Large day-to-day shifts were observed in the radiometer output levels such as might be caused by a variable lossy element in the antenna line or to a varying inflight calibration temperature. A study of the performance of the in-flight reference generator during the mission dismissed this as a source of trouble. Several months after the mission, the 1.4 GHz phased array antenna exhibited a loss greater than 3 dB, was dismantled, found to have defective elements, and was refurbished. Consequently, the 1.4 GHz results cannot be presented until a valid level adjustment, if one is possible, can be performed upon the data.

10.6 GHZ AND 31.4 GHZ RADIOMETERS

The data presented here is the average for a specific wind speed on a given day. The raw data was converted to antenna temperatures by using the inflight calibrations, the temperatures of the Dicke-load, waveguide, antenna, and

radome, and the loss values of the radome and waveguides. Normally, data at nadir is independent of polarization and may simply be averaged together; however, the radome losses were different for each polarization and had different errors. Consequently, a bias level existed between the data collected at nadir horizontal polarization and nadir vertical polarization. The two polarization components were averaged together after a multiplicative correction factor, based on the calm sea data, was applied to all nadir data.

A "first-order" correction for reflected sky radiation was made by using a calculated emissivity to obtain a sea reflectivity and assuming specular reflection of the sky radiation

$$[1 - e(\theta)]\,[1 - e^{\tau \sec \theta}]\,T_{sky} \quad .$$

$e(\theta)$ = calculated emissivity as a function of angle and polarization for smooth sea water at 18°C.

τ = optical depth was determined from an NRL clean air atmospheric model which required an absolute humidity input which in turn was determined from aircraft measurements of relative humidity and temperature recorded at 200 to 500 feet altitude.

θ = incidence angle of observation.

T_o = temperature of atmosphere ± 295°K.

This correction removes the bulk of the reflected sky radiation. However, the corrected data still contains a small residual reflected sky component which is dependent upon the atmospheric opacity and sea surface roughness (1).

As all the antennas have high beam efficiencies (90%), a correction for the antenna beam pattern was made by using the beam efficiency factor of 0.9 for all three frequencies and making a constant correction for the sidelobes and backlobes contributions, independent of angle. No further correction or data treatment was considered justified in light of the operational instabilities and unknowns in the system parameters. The relative errors in the derived brightness temperatures are estimated to be ± 3°K.

RESULTS

Figure 1 presents the nadir and 50 degree incidence angle observations for both polarizations at 10.6 and 31.4 GHz. The solid lines are linear least-square solutions fitted to the data. A wind speed dependence is apparent in all of the measurements. However the dependence is at least twice as large at 50 degrees horizontal polarization than at nadir or 50 degrees vertical polarization. The wind speed sensitivity is comparable, within the error of measurement, at nadir and at 50 degrees vertical polarization. In addition the wind speed dependence is larger at 31.4 GHz than at 10.6 GHz.

As mentioned previously, the radiometric temperature contributions associated with the foam effect are relatively insensitive to polarization and incidence angle; whereas surface roughness effects are greatest for the horizontal component at large incidence angles (2). The larger wind speed dependence at 50 degrees horizontal polarization is attributed to a combination of surface roughness and sea foam effects. Whereas, the smaller dependence for vertical polarization and at nadir look angles is considered to be due principally to sea foam.

The presence of such a relatively low percentage of sea foam suggested by the data was substantiated by the ground truth; even for the 33 to 36 knot wind case, Williams (12) estimated a foam coverage of five and a half percent. The potential of using the 50 degree horizontal polarization (Ka band) as an indicator of surface wind fields is demonstrated here even on a relative measurement basis.

OBSERVATIONAL-FREQUENCY DEPENDENCE OF THE SURFACE ROUGHNESS EFFECT

It is desirable to combine both the Argus Island tower measurements (1) at 1.4, 8.4, and 19.3 GHz and the aircraft measurements at 10.6 and 31.4 GHz for analysis of the wind speed dependence of the surface roughness effect on observational frequency. In order to effect this comparison, the sea foam contributions must be removed from the aircraft measurements. The aircraft data may be modified to remove the foam effects by adopting the 5.5% foam coverage value

reported by Williams (12) for 33 to 36 knot winds. A value of 100°K temperature increase for 100% foam coverage has been reported (2), (5). Assuming a linear approximation for percentage of foam versus increase in brightness temperature, a foam-induced contribution of 0.16°K/knot will result using a 5.5% foam coverage over a 35 knot range. Note that the magnitude of this foam contribution is consistent, within the stated error, with the wind speed dependence observed at nadir and 50 degrees for vertical polarization at both the 10.6 GHz and 31.4 GHz. Such a modification applied to the nadir and 50 degree vertical polarization data virtually removes the wind speed dependence as would be expected if the dependence were due primarily to foam effects. Furthermore, subtracting this foam contribution from the 50 degree horizontal polarization data yields results which indicate a sensitivity due to the surface roughness effect alone that is 1.8 times greater at 31.4 GHz than at 10.6 GHz.

The aircraft results with the sea foam contribution removed may be compared with the results from Argus Island tower (1) to examine the frequency dependence of the surface roughness effect. The wind speed dependence at 50 degrees incidence angle for horizontal polarization is presented as a function of frequency in figure 2. The present results are indicated by x's and the Argus Island results at 1.4, 8.4, and 19.4 GHz are represented by O's. The aircraft results agree well with the tower measurements and indicate a wind speed dependence which increases with frequency. Although the data is well represented by the dotted line, which indicates a wind speed dependence proportional to the square root of the frequency, we have no compelling explanation for such a relationship.

CONCLUSIONS

Mission 119 airborne passive microwave measurements definitely demonstrated that the microwave brightness temperature of the sea is significantly dependent on the surface wind fields. The measurements show that the wind speed dependence for the 50 degree incidence angle horizontal polarization component is greater than the dependence either for the vertically polarized component at 50 degrees incidence angle or for nadir. Further, the greater wind speed dependence for the 31.4 GHz than for the 10.6 GHz radiometers demonstrates, in agreement with the Argus Tower results, that the sensitivity to wind speed increases with increasing

observational frequency.

All of the increase of brightness temperature with wind speed at nadir and at 50 degree vertical polarization was readily accounted for in total by the foam effects. The horizontal polarization component at 50 degrees incidence angle had a major wind-speed dependent residual component even after removal of the foam effect. This residual is due to the surface roughness effect and is also in agreement with the Argus Tower measurements. Indeed, these airborne measurements support the contention that there are two effects, roughness and foam, that are responsible for the dependence of the microwave brightness temperature on surface wind speeds.

These measurements, along with the Argus Tower measurements, indicate the significant potential of using passive microwave radiometers as a means of remotely sensing wind from calm to 50 knots and above. Because foam effects are relatively small below 25 knots, observations at large incidence angles must be made to take advantage of the roughness effect predominant at the lower wind speeds.

REFERENCES

(1) Hollinger, J. P., "Passive Microwave Measurements of Sea Surface Roughness," IEEE Trans. Geoscience Electronics, GE-9(3), July 1971, pp. 165-169.

(2) Hollinger, J. P., "Remote Passive Microwave Sensing of the Ocean Surface," Proc. of the Seventh International Symposium on Remote Sensing of Environment, Vol. III, 17-21 May 1971, University of Michigan, Ann Arbor, Michigan, pp. 1807-1817.

(3) Monahan, E. C., "Oceanic Whitecaps," Journal of Physical Oceanography, Vol. 1, No. 2, April 1971, pp. 139-144.

(4) Williams, G. F., "Microwave Radiometry of the Ocean and the Possibility of Marine Wind Velocity Determination from Satellite Observations," Journal of Geophys. Res., Vol. 74, No. 18, August 20, 1969, pp. 4591-4594.

(5) Nordberg, W., J. Conaway, and P. Thaddeus, "Microwave Observations of Sea State from Aircraft," Quarterly Journal Royal Meteorological Society, Vol. 95, No. 404,

April 1969, pp. 408-413.

(6) Nordberg, W., J. Conaway, D. B. Ross, and T. Wilheit, "Measurements of Microwave Emission from a Foam-Covered Wind Driven Sea," J. Atmosphere Science, Vol. 28, April 1971, pp. 429-435.

(7) Ross, D. B., V. J. Cardone, and J. W. Conaway, "Laser and Microwave Observations of Sea Surface Conditions for Fetch-Limited 17 to 25-m/s Winds," IEEE Trans. on Geoscience Electronics, Vol. GE-8, No. 4, October 1970, pp. 326-336.

(8) Strong, A. E., "Mapping Sea-Surface Roughness Using Microwave Radiometry," Journal of Geophysical Research, Vol. 76, No. 36, December 20, 1971, pp. 8641-8648.

(9) Edgerton, A. T., et al. "Microwave Emission Characteristics of Natural Materials and the Environment," Aerojet General Corporation under Office of Naval Research Contract N000 14-70C-0351, February 1971, pp. 3/29-3/33.

(10) Mennella, R. A., "Operation and Calibration of the Multifrequency Passive Microwave Radiometer," March 1970 LEC/HASD Technical Report No. 649D.21.017C. Prepared for NASA/MSC Earth Observations Division Contract, NAS 9-5191.

(11) Ross, D. B., "Argus Island JOSS Ground Truth," NAVOCEANO Memorandum of 8 July 1970.

(12) Williams, G. F., Jr. "Microwave Radiometry of the Ocean," Final Report for Contract N62306-69-C-0301, Rosenstiel School of Marine and Atmospheric Science, Univ. of Miami, (August Quarterly Report) pp. 6-8, June 1961.

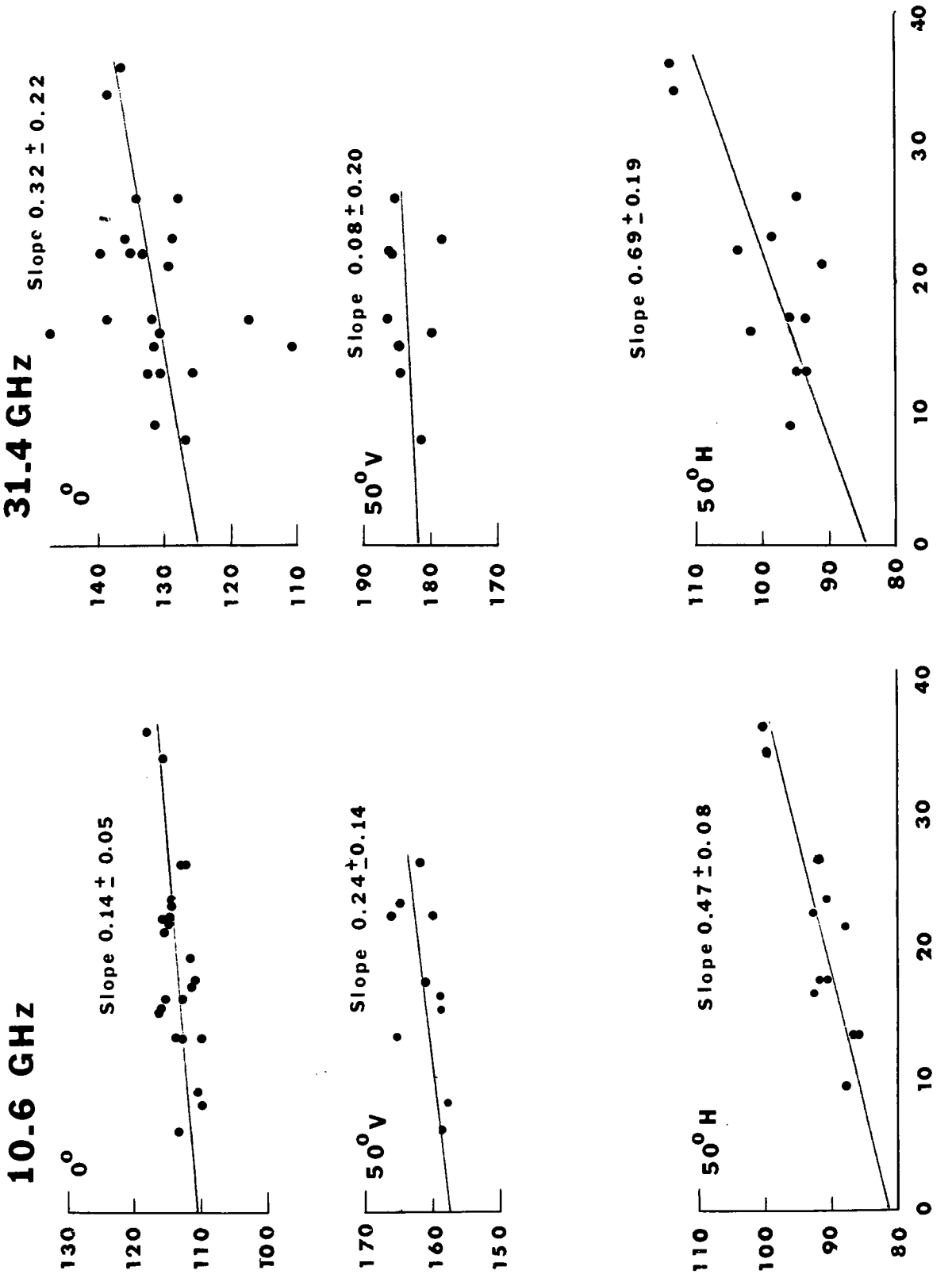
31.4 GHz
10.6 GHz
0°
50°V
50°H
Slope 0.32 ± 0.22
Slope 0.08 ± 0.20
Slope 0.69 ± 0.19
Slope 0.14 ± 0.05
Slope 0.24 ± 0.14
Slope 0.47 ± 0.08
CORRECTED ANTENNA TEMPERATURE (°K)
WIND SPEED (Knots)

Figure 1

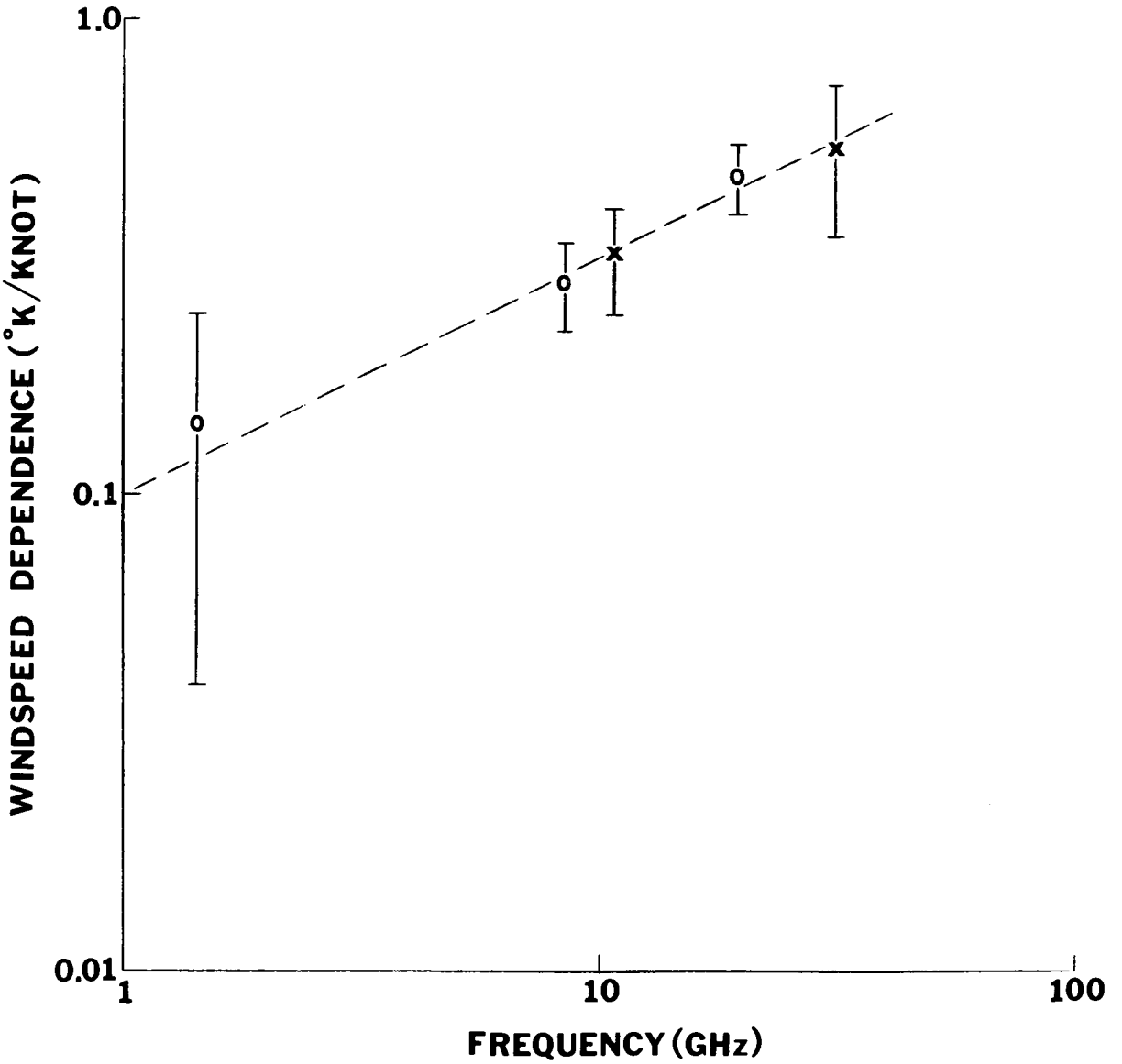

Figure 2

(PAPER NOT SUBMITTED FOR PUBLICATION)

SECTION 99

GROUND TRUTH INVESTIGATIONS FOR AIDJEX 71

by William Campbell

ABSTRACT

(Not available)

SECTION 100

APPLICATION OF THERMAL RADIATION DATA TO FISHERY OCEANOGRAPHY

by

Merritt Stevenson and Forrest Miller
Inter-American Tropical Tuna Commission
c/o Scripps Institution of Oceanography
La Jolla, California

INTRODUCTION

Work on the varied aspects of research related to our SPOC contract has continued since our last report (April - September) in the areas of: Project Little Window-1 and -2, DRIR data conversion, improvements on the APT receiver, equatorial upwelling and the new topic of thermal fronts. Since the Objectives of our contract are noted in the contract they will not be repeated in this report. The Tasks however, represent the means of reaching our goals and because our work is designed around the 4 Task areas they are repeated below:

Task I - Complete studies relating analyses of sea surface temperatures as derived from APT and other satellite data to similar analyses using conventional data as related to Project Little Window.

Task II - Prepare analyses of processed satellite, oceanographic, and meteorological data for selected periods to be determined by investigator.

Task III - Begin preliminary studies on procedures for monitoring oceanographic environmental conditions for fisheries by combining satellite data with conventional sea surface data.

Task IV - Evaluate the results of Task I, II, and III and prepare reports on these results and progress during the one year contract period as set forth in Section 6.0 DOCUMENTATION AND REPORTS of the Contract.

RESEARCH ACTIVITIES

PROJECT LITTLE WINDOW-1

Final preparations were made several months ago on a data report containing the oceanographic and meteorological observations made during LW-1 (14-23 March, 1970) and the report was published as part of the IATTC Data Report (Stevenson and Miller, 1971) in December. Copies of the report for use by interested scientists may be obtained from Commission headquarters in La Jolla.

PROJECT LITTLE WINDOW-2

Much of our effort during the past three months on this particular study has been to make the final preparations on figures and tables of oceanographic and meteorological information collected aboard the R/V DAVID STARR JORDAN (National Marine Fisheries Service, NOAA) and the ALEJANDRO VON HUMBOLDT (National Fisheries Institute, Mexico). These materials along with an explanation, will form the basis for a second data report. Present plans call for the addition of data from research aircraft and HRIR and DRIR data from satellites. Because these data have only recently become available, the additional compilation is expected to take another 2 months of time.

Preliminary Meteorological Results

During Project Little Window-2 (LW-2) meteorological observations were made to determine: 1) the effect of surface winds on ocean mixing; 2) the vertical heat and moisture flux between ocean and atmosphere by measuring the vertical profiles of moisture and temperature and; 3) thermal stability in the marine layer of the atmosphere and its effect on the ocean surface temperature. To accomplish these objectives detailed surface and upper air (radiosonde) observations were made at frequent intervals, particularly during the times of satellite passages overhead. The data taken aboard the R/V JORDAN and 4 Mexican research vessels are being prepared for a data report in tables and horizontal charts.

From May 1 to 4, surface winds became light and variable in direction over the LW-2 area in the Gulf between 24° N and 25.5° N. Over most of this area the surface air and sea surface temperatures were initially in equilibrium; as the winds became lighter (less than 5 kts) the surface water temperatures warmed up creating a highly stratified

condition. Because the air in the marine layer was warm and moist (high humidity) during this period, the air-sea exchange of heat was minimal; the winds were too light to induce much mixing of the surface layer in the Gulf. Periodically, high thin cirrus clouds obscured the sun or moon, but the clouds were either absent or very thin during times of satellite passages over the JORDAN.

By May 5 the winds shifted to the south and strengthened and as a weak weather front passed, a narrow band of middle and high clouds moved over the LW-2 area. Fortunately, this happened between a day and night pass of the NOAA-1 satellite. Thereafter, winds shifted to the northwest and strengthened. Significant wind mixing of the surface layers of the Gulf began early on May 5. In addition, colder and drier air from the west was advected over the area creating a condition favorable for an upward flux of heat from the sea surface. Sky conditions remained quite clear after May 5 with only small patches of thin cirrus moving over the area.

Throughout most of the LW-2 Project, the radiosonde data revealed a dry atmosphere (except during frontal passage) with an average integrated water vapor content of 1.5 cm in the air column above the Gulf. Apparently the small amount of water vapor in the atmosphere caused only a slight attenuation of the radiance received by the 11 micron infrared sensor on the spacecraft. Preliminary plots of the thermal infrared data showing sea surface temperatures only slightly colder than those observed seem to confirm this.

Preliminary Oceanographic Results

Information about oceanographic conditions during LW-2 was obtained from temperature measurements made continuously with a towed thermistor (HST), infrared radiation thermometer (PRT), thermo-salinograph and at individual stations with expendable bathythermographs (XBT's) and an in-situ salinometer (STD). Since each of these methods differs from the other methods, an inter-comparison was made of the various data. A check of the bucket thermometer readings with the other data suggests that the bucket temperatures showed more "scatter" than the other methods and may have been due to the presence of a shallow layer of stratified surface water. Under such conditions the manner and location of taking the sample measurements from a vessel is very important. A comparison of the bucket values and the STD data was fairly good ($r = .89$, $p < 0.5\%$) although the bucket temperatures were about 0.2°C above the STD readings. Because the PRT operates on the same principles as the HRIR spacecraft sensors and could serve as a primary means of collecting ground-truth information, data from the PRT were compared with STD and HST temperatures. The resulting relation between the PRT and STD data was good

($r = .93$, $P < 0.5\%$), though the PRT values were about 1.2°C low. The correlation between the HST and the PRT was also good ($r = .93$, $P < 0.5\%$) with the PRT readings about 1.3°C low. From such inter-comparisons then, it appears that about 1.2°C should be added to PRT readings from LW-2 to bring them into agreement with the other measurements. The high degree of correlation between the towed thermistor and the shipboard PRT (during LW-2) provides encouragement for future use of a shipboard PRT in future calibration studies.

Surface temperatures obtained from the towed thermistor (HST) tended to be low on both the east and west sides of the Gulf, with slightly higher values in the central part of the Gulf. Temperatures on the east side of the Gulf increased from 19.9°C on May 1, by about 0.6°C, on May 2. On May 3-5 atmospheric conditions were clear and calm and the temperature increased up to 25.2°C on the east side. By May 6, however, the changing weather brought about a marked decrease in temperature so that surface temperatures were reduced to May 1 values. During the same period the central and western parts of the Gulf underwent similar changes in temperature. The time series collected by the 3 Mexican naval vessels at their anchor stations also show a gradual warming trend from May 1 through May 4, after which increased winds brought about a cooling interval from May 4 through May 6. In addition to the warming and cooling trends, diurnal heating occurred in the surface layer and caused water temperatures to vary by about $\pm$1.2°C. Because this diurnal change is about equal in magnitude to gradients across the Gulf, it appears that a correction for diurnal change may need to be applied to shipboard observations to bring them into alignment with measurements made with airborne sensors and those made from spacecraft instruments.

DIGITIZATION OF INFRARED DATA

During the past several months a number of infrared images on 35 mm and 70 mm film negatives have been photo-scanned on the micro-densitometer* located at the S.I.O. Vis. Lab. Considerable flexibility of the system is provided by an IBM 360/44 interfaced to the densitometer. The 50 micron aperture was used during the scanning operation with 2 exceptions when the 100 and 200 micron window was used to compare aperture induced noise from apertures of different size. The arrays of digital values (8 bit; 0-255 range) resulting from the digitizing process, if contoured at 10 unit intervals, provide maps quite similar to those obtained if the same data were digitized directly by electronic means. Although a contoured map of digitized units can provide considerable information about warm and cool regions, there is a need to convert these

* (Model Photoscan P1000, Optronics Int., Inc., 7 Stuart Rd. Chelmsford, Mass. 01824)

values into meaningful temperatures. Several schemes are available for converting an array of digitized values into temperatures.

The first method for calibration utilizes the step wedge, a part of every scan line and the bolometer reading (measures the ambient temperature within the spacecraft). The bolometer is used to determine a small correction to the HRIR sensor output because the sensor's voltage varies not only with the incoming radiation but also with the temperature of the sensor. The step wedge is used to provide several reference points for a scan line so that a conversion can be affected between sensor voltage and infrared temperature.

When the infrared image is digitized from a photographic negative, the wedge is also digitized so that a similar relationship of wedge to scan line can be obtained. A different type of problem is added when the incoming signal from a satellite is received by the APT receiver and is passed through a waveform remodulation unit to enhance the "warm part" of the photograph. Whereas the digitization of regular infrared images is linearized with a logarithmic amplifier and the resulting distribution of steps are approximately linear (e.g. the Vis. Lab. densitometer), care must be taken when the signals are processed with the waveform remodulation unit.

After the data have been converted to temperature values, corrections to account for the water and carbon dioxide vapor in the atmosphere, non-blackness of the water and non-zero nadir viewing angle need to be applied. The following section describes some aspects of this scheme for applying corrections to infrared data from NIMBUS IV.

THE NIMBUS IV (THIR) DATA OVER THE EASTERN TROPICAL PACIFIC

In September we began a new phase of our research in which thermal-humidity infrared (THIR) data, received from NASA, are being examined and compared to sea surface temperatures recorded by the NMFS research vessel DAVID STARR JORDAN. Accurate surface temperatures are seldom obtained in the equatorial part of the eastern tropical Pacific because of the limited research cruises in that area; but during March, 1971 the JORDAN, on the SKIPJACK fishery research cruise (March-April, 1971) obtained accurate and detailed oceanographic and meteorological observations (including upper air soundings) from 5°S to 10°N, between 118°W and 120°W an important area of upwelling and marine productivity. Fortunately, the NIMBUS IV satellite passed over the eastern tropical Pacific once each day; and the THIR data was recorded and archived at the Goddard Space Flight Center in formats useful for research.

Analysis of Infrared Data

For the period of February and March, 1971, the NIMBUS Users Group at the Goddard Space Flight Center selected for us several day and night orbits of thermal infrared data covering the eastern tropical Pacific, from 110°W to 140°W and between 30°N and 10°S, when there was 30% or less cloud cover. After the infrared data had been screened from the archived data file they were converted into temperatures (°K) and were plotted on a 1:1 million mercator map projection. At this projection scale each data point consisted of two to five infrared scan points, representing a resolution slightly greater than the resolution of the radiometer.

Initially, we selected two periods, March 11-12 and March 19-20, when sufficient sea surface temperatures were available from the R/V JORDAN in an equatorial area which was relatively free of clouds. The thermal infrared data for March 11 (daytime orbit #4532) have been analyzed in detail; and as soon as maps of the other days have been received from NASA, they will be analyzed to provide continuity in time and space.

Although the temperature patterns revealed by the infrared data for March 11 do not resemble closely those obtained from conventional ship data, the warmer temperatures were located where the NIMBUS IV video (IDCS) photographs showed that the minimum cloudiness occured. In contrast, the cold infrared temperatures corresponded geographically to the cloudy areas of the intertropical convergence zone. Similar results have been observed many times before; but over the eastern torpical Pacific, where research in tuna ecology is carried out extensively, the ability of spacecraft infrared sensors to detect sea surface temperatures will greatly enhance our ability to monitor a region where water temperatures may be outside the range in which tunas may be found in commercial quantities.

Three significant, but not surprising, features evolved from the analysis of the March 11 infrared data. First, sea surface temperatures derived from the daytime THIR data were approximately 11.5°C colder than those observed by the R/V JORDAN or other commercial vessels sailing between 4°S and 4°N along 119°W. A deep, warm and moist marine layer in the atmosphere apparently attributed to a strong attenuation of the radiation received by the infrared sensor. Second, a statistical comparison of sea surface temperatures based on THIR data and observed surface temperatures gave a high correlation coefficient ($r = .85$) and a least-squares fit according to:

$$T_J = .45T_S + 19.13$$

where T_J = sensor temperature referenced to the R/V JORDAN and

T_S = sensor temperature

A third noticeable feature revealed a recognizable pattern of noise superimposed over the thermal radiation received as the satellite passed over. The spurious noise was apparently caused by the spacecraft tape recorder.

Since NASA had not filtered (smoothed) or corrected the THIR data in any way, part of it was processed through the computer with a 2-D filter program which had been successfully used before. The result shown in figure 1a was a more coherent isotherm pattern which retained the essential features displayed in the unsmoothed and uncorrected sea surface temperature analysis (Fig. 1b)

Because extensive cloud cover obstructs the satellite's view of the ocean surface, it was important to accurately outline areas more than half covered by clouds (the resolution of video cameras will not permit the recording of scattered cumulus clouds). From enlargements of video (IDCS) and infrared (THIR) data gridded by computer and recorded on 70 mm film, we transferred recognized cloud patterns and types to the 1:1 million mercator projection with the use of an engineering pantograph. Thus, we were able to superimpose the cloud patterns onto the infrared temperature charts and determine more accurately which areas had minimum cloud cover.

It was possible to recognize cloud types in the eastern tropical Pacific when NIMBUS IV passed over during the daytime. With simultaneous coverage of an area by the video (IDCS) camera and the THIR (11 micron) sensor, we have been able to differentiate low stratus clouds from middle and high cirrus clouds. Over areas covered extensively by low stratus it has been difficult to determine from infrared data alone where the stratus clouds begin or ended and the sea surface was visible to the satellite sensors. This has been particularly true to the west of Baja California and to some degree in the equatorial regions between 5°N and 10°N. The daytime IDCS cloud photographs have been very useful in this respect; but to completely evaluate the thermal temperature field derived from infrared data, it was necessary to process the vertical temperature and moisture profiles of the atmosphere from radiosonde data.

During the SKIPJACK cruise, personnel from the National Weather

Service were aboard the R/V JORDAN to make radiosonde observations. Balloons were released at least once a day in order to obtain representative profiles of moisture and temperature from the ocean surface to heights up to 18 km. Copies of the radiosonde data for this period have been obtained from the National Data Center, Asheville, North Carolina.

From the radiosonde data, temperature and water vapor content have been interpolated at 50 mb. (pressure-altitude)intervals. The preliminary results revealed that the atmosphere in the equatorial region was much warmer and considerably more moist than the atmosphere over the Gulf of California. By comparison, temperatures in the lower half of the atmosphere within 5° latitude of the equator are about 3°C higher in the marine layer than over the Gulf; and the total precipitation near the equator exceeds that in the dry Gulf by a factor of 3 to 4. Thus, the optical path was quite opaque to the NIMBUS IV, THIR sensor; and atmospheric attenuation of outgoing thermal radiation was computed to be nearly the maximum expected for a deep tropical atmosphere.

As mentioned earlier, sea surface temperatures derived from THIR data were about 11.5°C lower than observed by the R/V JORDAN along 119°W. (Fig. 2). Until the radiosonde data had been examined closely, these temperatures seemed to be colder than expected. However, the theoretical, atmospheric attenuation curves computed for NIMBUS III and a moist atmosphere during project Little Window-1 indicate that data from the infrared sensor (11 micron channel) would require corrections greater than 7°C for data in the nadir angle range of 0° to 30°. We are presently attempting to work out a computer program for the radiative transfer equations described by Kunde (1967). When this task is completed we will be able to compute accurate atmospheric attenuation curves for infrared sensors used on either NIMBUS or ITOS satellites. For the present, it appears that the available corrections for NIMBUS III HRIR data are not greatly different than those we will derive from NIMBUS IV data.

If adequate sea surface temperatures were available from ships over the oceans, limb darkening (atmospheric attenuation and ocean surface non-blackness) corrections could be obtained by merely applying the temperature difference between satellite infrared data and ship observations. Unfortunately, this will seldom be possible over large areas; and this direct means of calibrating thermal infrared data can be accomplished only on special projects similar to Little Window 2.

Because most of the eastern tropical Pacific has a moist warm atmosphere throughout the year, it is essential to establish a means of correcting satellite infrared data for atmospheric attenuation. Future satellites will obtain continuous moisture and temperature profiles along the optical and orbital paths. The first IRIS sensor experiment on NIMBUS IV has established this potential. In the meantime, radio-

sonde data will provide the needed data to determine from the ocean upward the opaqueness of the atmospheric window in the 10.5 to 12.5 micron region.

An important task of our research is to determine the limb darkening corrections over the eastern tropical Pacific where the fishery-oceanography is being conducted. If after applying these corrections to the infrared data over cloud free areas, the surface temperatures agree closely with the ground truth data, we can complete the evaluation of remote sensing of sea surface temperatures. Although it has been established that prominent features such as the Gulf Stream can be detected by remote sensing, there remains much research to be conducted over areas where ocean fronts and upwelling concentrates food for the tuna fishery.

In the introduction to this section we outlined an indirect approach to deriving digital values of sea surface temperatures by scanning photographs of infrared data with a microdensitometer. The principal drawback of this method is related to the large variations in film emulsions or densities and film processing procedures. However, it is possible with an APT satellite receiver to record on the same film strip both the calibration (step) wedge in the sensor housing and the earth scan of infrared data. It is possible also to maintain precise controls in the film processing and apply known calibration step wedge temperatures to corresponding gray-tones in the film which have been converted to numbers with the densitometer. Although this procedure has little ultimate value in working with stored infrared data that has been digitized at data acquisition centers, it is providing us with another approach to evaluating the NIMBUS IV data over the equatorial tropical Pacific.

NASA provides 70 mm film strips of infrared data and corresponding video photographs for daytime orbits to accompany the grid prints of digitized thermal infrared data. Each film strip of earth scanned infrared data is followed by a 10-step, calibration gray scale which is put on the film electronically to show the dynamic (equivalent blackbody temperature) range used to represent radiance from clouds or earth. However, this gray scale is not accurate enough to assign specific temperatures because of variations in film density and emulsions during film processing. Therefore, it is necessary to obtain accurate sensor temperature readings from the original analog data files. Upon request NASA also makes available analog records from the original spacecraft interrogation tape records. The analog data consist of Visicorder oscillograph records of each full (360°) scan with corresponding time/date markings below the analog trace. Selected areas of the infrared

films, where ground truth data were available for March 11, 12, 19 and 20, 1971, have been scanned with the micro-densitometer at the Visibility Laboratory, S.I.O. Also the 10-step calibration wedge was scanned from the same strip of film so that the emulsion density characteristics should be known over the entire strip.

Because the individual steps are not exactly uniform, each step can be characterized by a mean value and a standard deviation about the mean (see Fig. 5). Mean values of the steps indicate that the steps are not uniformly spaced, but are compressed at either end of the wedge. In addition, the distribution of observations about each mean value becomes progressively larger with increase in optical density (darkest gray tones).

From selected analog records we have been able to extract equivalent black body temperatures for scan lines which correspond to those on the infrared photographs which have been digitized. Thus, we have been able to assign temperatures to the 10-step calibration gray scale which has also been digitized from the 70 mm film. Finally, working from the step wedge temperatures to the digitized infrared photographs we will be able to convert film density counts to equivalent black body temperatures representing clouds or sea surface. We are presently evaluating this technique by comparing sea surface temperature charts derived by this indirect method with those obtained by the more conventional method described in previous sections.

ALTERNATE METHOD FOR CALIBRATION OF INFRARED DATA

An alternate and more empirical scheme for converting digital values derived from photo-scanned negatives into realistic temperatures requires the use of ground (sea surface) temperature values in a cloud free area within the general region of interest. In order to obtain a reasonable least squares equation from the 2 data sets, it appears necessary to have the digitized density units corresponding to surface temperatures extend over a range of 30 density units or more, to insure a useful conversion over a range of several degrees C. Implicit in the constant of this equation are the several individual correction factors. For most accurate results a variable correction factor resulting from changes in the nadir angle needs to be added after the other correction has been applied.

An example of this statistical conversion is seen in figure 3. The spatial correlation ($r = .92$, $P < 0.5\%$) resulted in a relatively accurate conversion of digital units off southwest Baja California and within the Gulf of California but somewhat low temperatures over land and cloudy regions. If the wedge is used in conjunction with the least squares fit, the calibration can be extended over a considerably larger portion of the thermal range of the instrument.

THERMAL FRONTS

Thermal fronts are usually associated with ocean current boundaries and where two dissimilar water types are in juxtaposition. These boundary regions are either convergent or divergent, depending upon whether the surface layers are approaching or receeding from the zone. Considerable biomass may be concentrated along a convergent frontal zone and this accumulation of forage appears to attract large fish that can then be harvested by fishermen. Also pelagic fish such as tunas may well use thermal fronts for reference in traveling along their migratory routes.

While the average seasonal position of the major surface fronts in the world oceans have been outlined, relatively little is known of the extent and nature of short period displacements of these fronts. Local fronts by comparison are largely unmapped and will remain so until greater use is made of data collected from satellites and oceanographic vessels to make synoptic studies of these features. Because there will probably never be an adequate number of research vessels available to provide the detailed coverage over large regions, the ability of the high resolution infrared sensors to rapidly scan large portions of an ocean in a synoptic fashion provides a method of obtaining these data when atmospheric conditions permit.

Various methods have been developed in the fields of meteorology and oceanography for enhancing frontal zones such as Clarke and Laevastu (1967). Our initial approach has been to evaluate the method of Clarke and Laevastu and to determine how effective it would be in the present situation. In practice a computer program was first written to determine the absolute value of the gradient of the temperature ($|\nabla T|$) and then an array of surface DRIR temperature data was used with the program and the results were compared with the initial temperature field (Fig. 4). This technique produces maximum values corresponding to the central region where the gradient is a maximum. A second program was then written for determining the gradient of the gradient function previously determined ($-\nabla|\nabla T|$). This time by not taking the absolute value of the new function we have three important reference points for a

frontal zone; a maximum negative value corresponding to the cold side of the front; a zero value corresponding to the maximum gradient in the zone and a maximum positive value corresponding to the warm side of the front. Further improvements on this method may consist of the addition of a smoothing procedure to be used after the gradient fields have been determined.

REFERENCES

1. Stevenson, M. R. and F. R. Miller. 1971. Oceanographic and meteorological observations for Project Little Window: March 1970. Inter-Amer. Trop. Tuna Comm. Data Report No. 4. [in English and Spanish]. 324 p.

2. Kunde, V.G. 1967. Theoretical computations of the outgoing infrared radiance from a planetary atmosphere. NASA Techn. Note, TN D-4045, NASA, Washington, D. C.

3. Clarke, L. C. and T. Laevastu. 1967. Numerical Methods for Synoptic Computation of Oceanic Fronts and Water Type Boundaries. Int. J. Oc. & Limn. Vol. 1 (1):28-45.

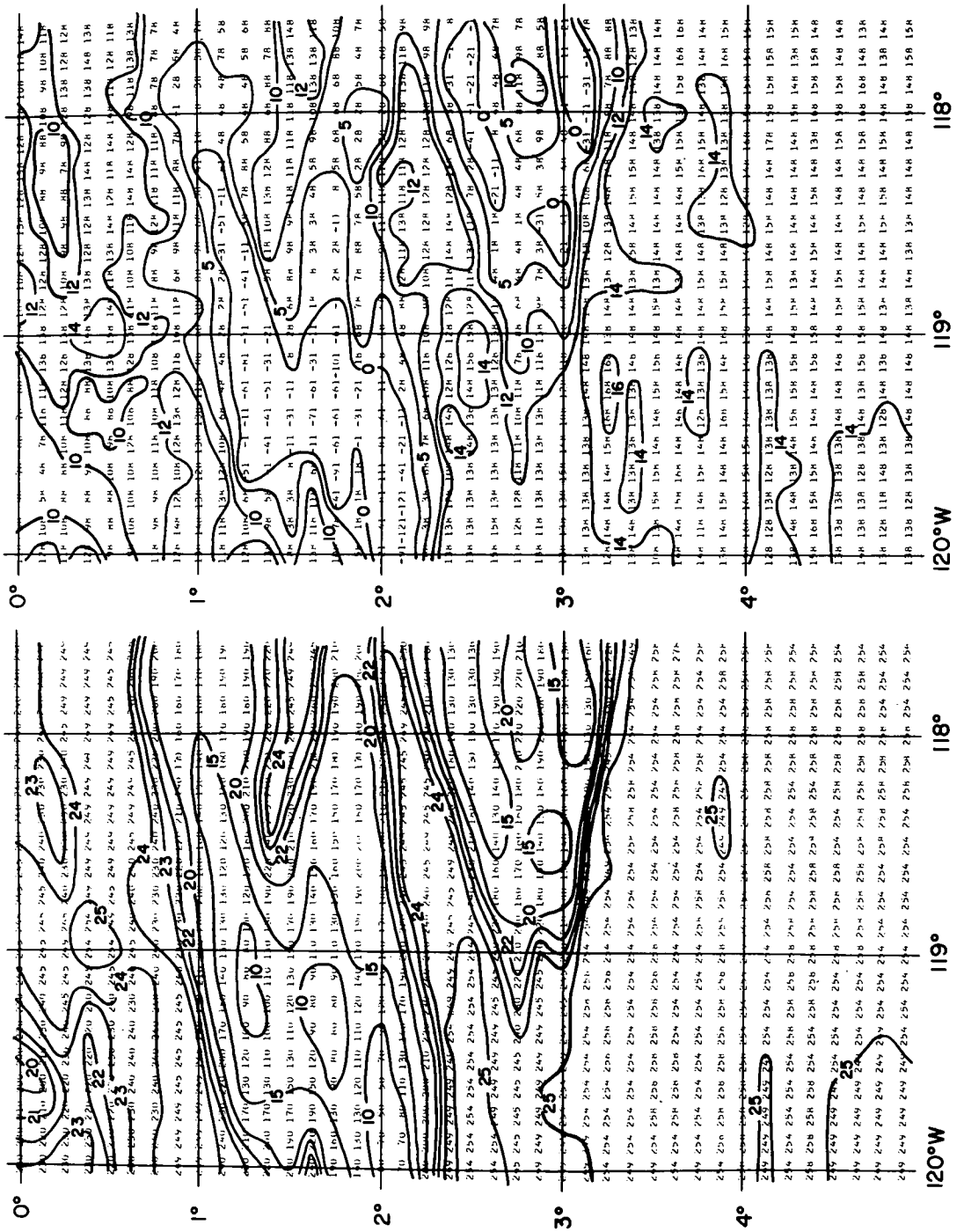

Figure 1. A. Smoothed THIR data (in °C) corrected for ground turth from NIMBUS IV (orbit #4532) for March 11, 1971.
B. Unfiltered THIR data (in °C) uncorrected for ground truth for the same orbit.

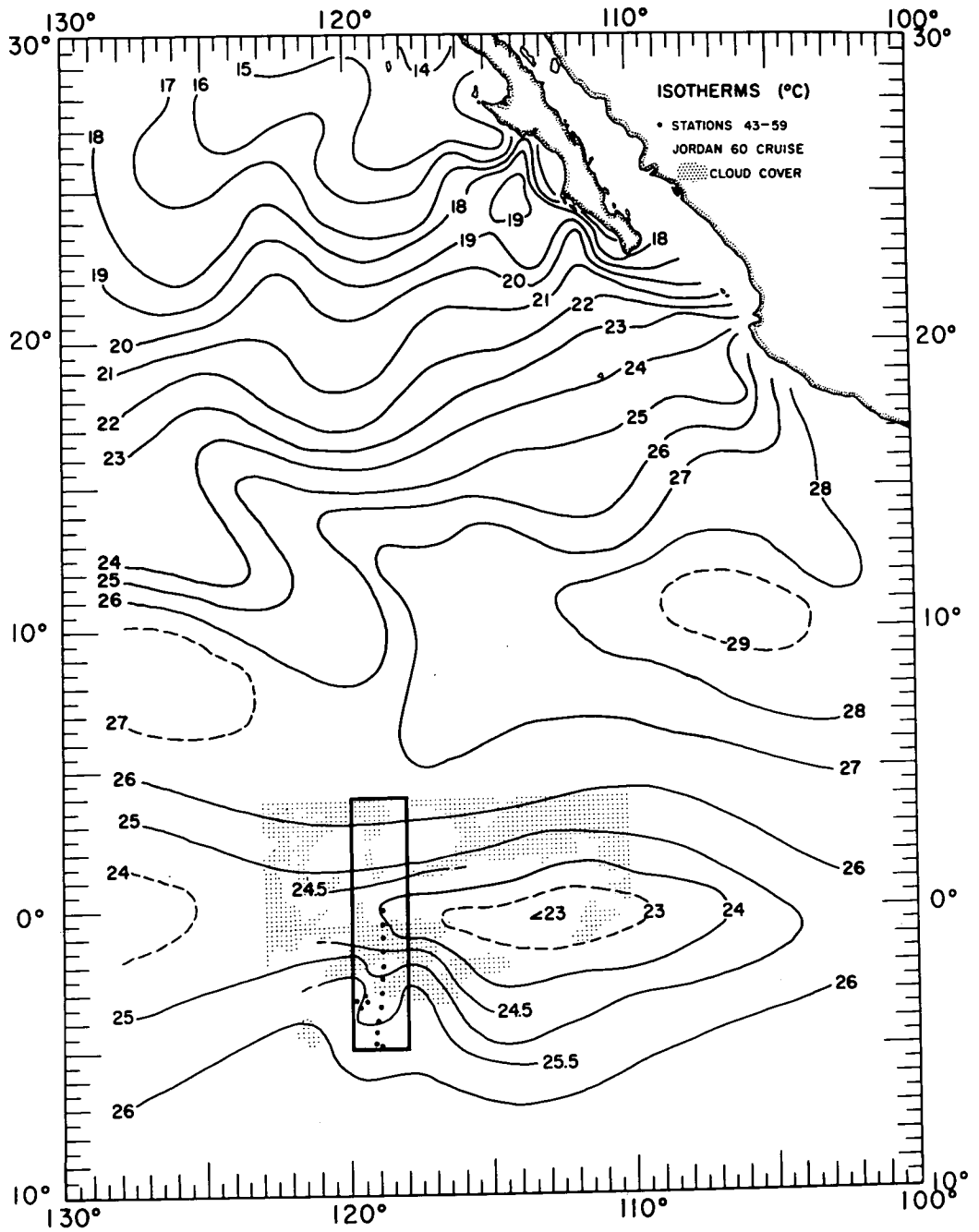

Figure 2. Sea surface temperature (in °C) based on data from R/V JORDAN and other vessels in the ETP for the period March 10-12, 1971. Note that cloud boundaries have been added in the transequatorial area to indicate those areas causing additional attenuation of infrared radiation. The enclosed area (4°N - 5°S) corresponds to the area shown in figure 1a-b.

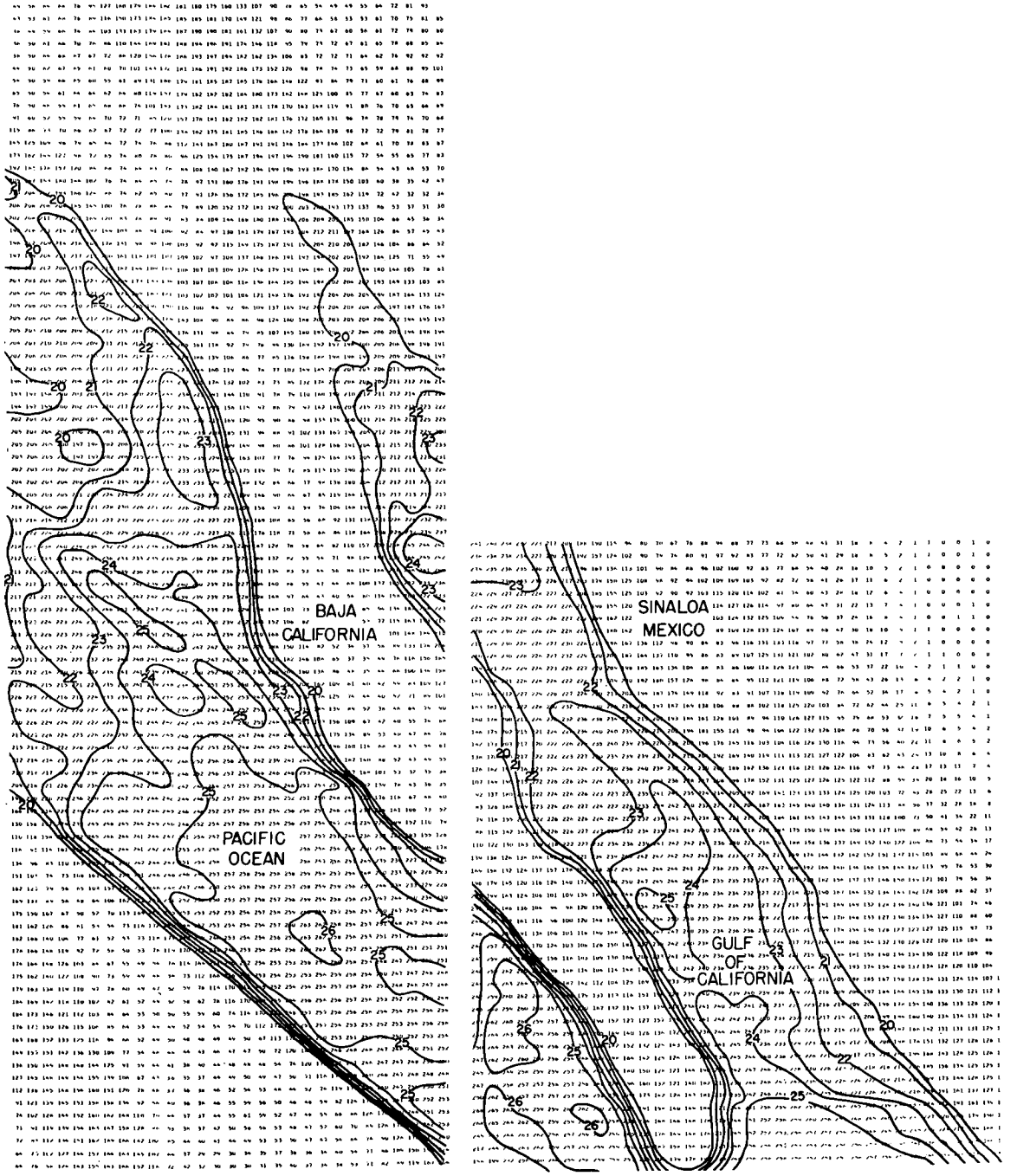

Figure 3. Digitization of DRIR information by photo-scanning and subsequent conversion to temperature (in °C) using a least-squares relation.

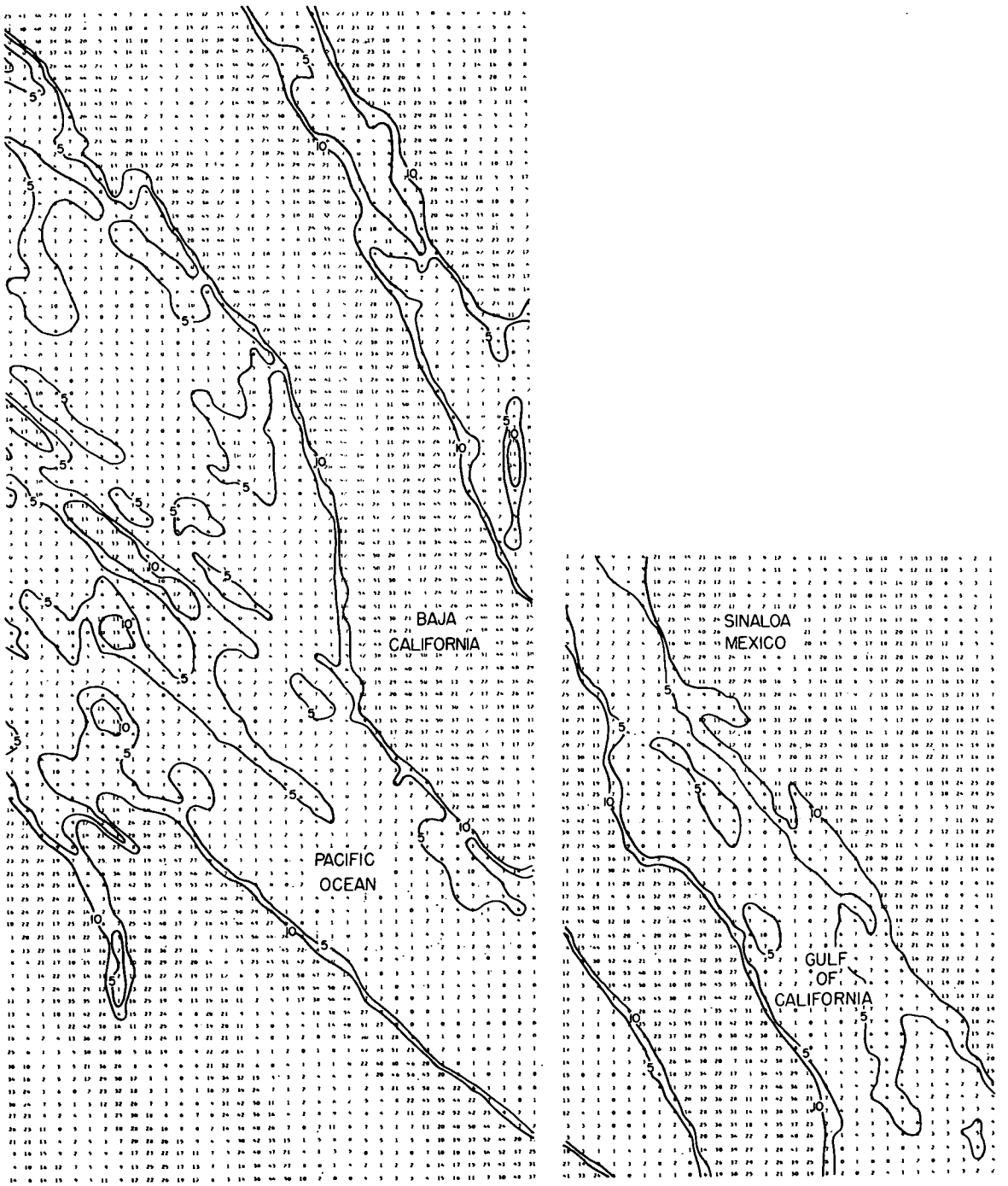

Figure 4. Frontal enhancement of sea surface temperature (in °C, times 0.1); same data sources as for figure 3.

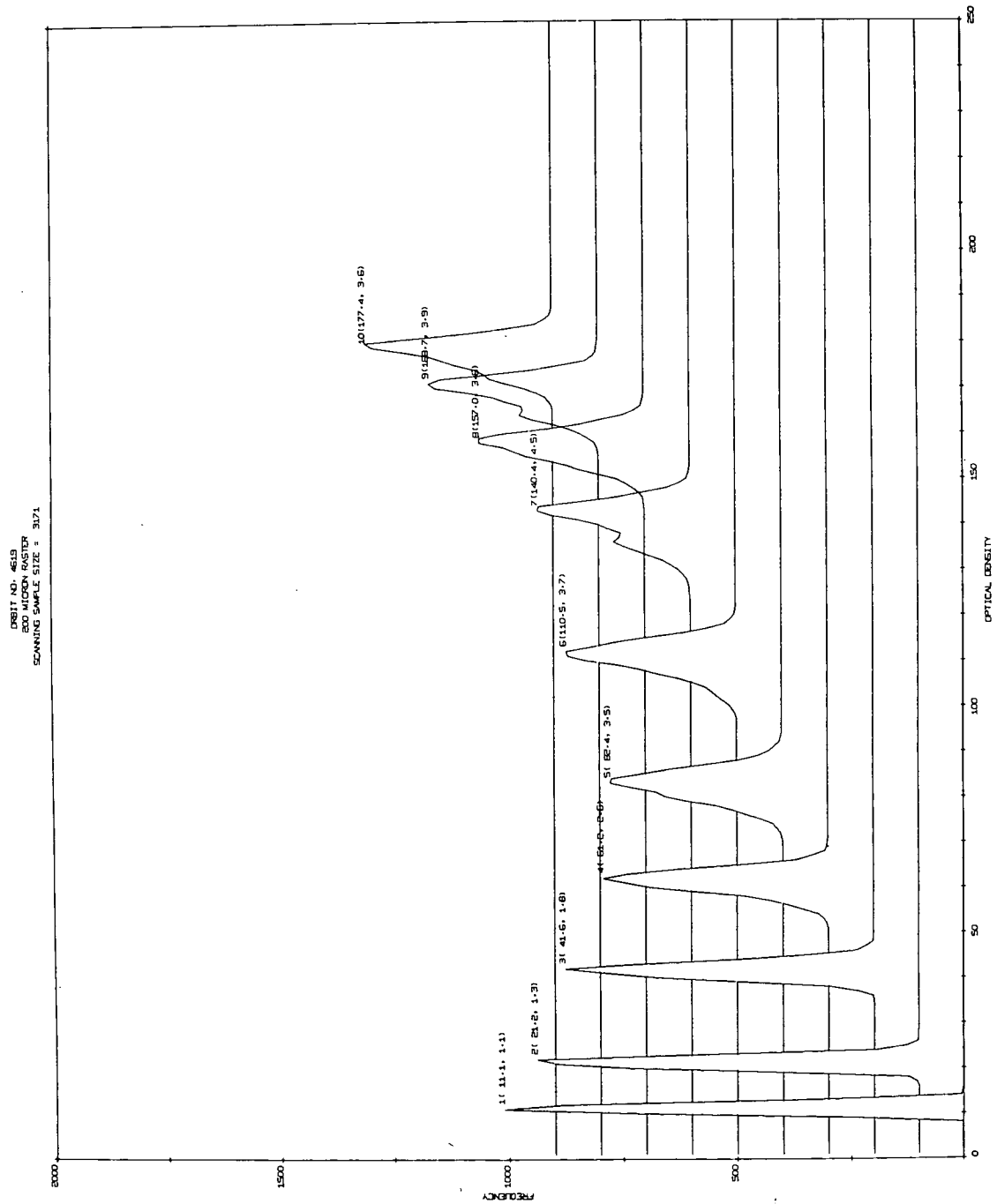

Figure 5. Frequency histogram of individual steps of 10-step reference wedge. Wedge was scanned by a densitometer using a 200-micron raster. Numbers in brackets are the means and standard deviations for each step, respectively. Number of counts per step is given at the top of the figure.

SECTION 101

THE CASE FOR OCEAN COLOR

by

Henry J. Yotko
Remote Sensing Oceanography Project
Naval Research Laboratory
Washington, D. C. 20390

INTRODUCTION

The potential for providing world-wide, repeatable ocean color data affords, for the first time, a means for the oceanographer to assess water mass properties and productivity in meaningful terms. Color together with surface temperature can define water masses, delineate upwelling areas, determine regions of productivity and detect certain other constituents in in the water. Most of the emphasis has been on productivity on developing a means of determining the condition of fisheries based on monitoring the first link in the food chain in the sea. This paper, however, attempts to introduce the concept that monitoring the plankton producing areas of the world is important to assessing the exchange of $CO_2/02$ on a world-wide basis as a part of a lift-support system.

DISCUSSION

People who have seen both the major oceans of the world usually contend that the Atlantic is green and the Pacific is blue. Visual impression of characteristic or dominant colors of the various seas is acknowledged by the names such as Red Sea, Yellow Sea, Black Sea which were assigned by ancient observers. Color variations also played an important part in assisting early navigators to traverse the unmapped expanse of the oceans by locating familiar water masses.

The usually subtle contrasts in color are generally emphasized when viewed at some level above the surface. Some of these variations have been reported visually from aircraft altitudes and occasionally recorded on film

or by spectrometers. In fact, Colonel John Glenn (reference 1) reported seeing the Gulf Stream on the first manned Mercury flight in 1961. Large scale ocean fronts have also been noted on imagery obtained from satellites as high as geosynchromons altitudes.

The color of the oceans is determined by the reflective, absorptive and scattering properties of the water as well as the atmosphere above. Light irradiating the sea surface undergoes reflection and refraction. The reflected portion is characterized by properties which permit its use for describing the shape of the reflecting surface, i.e., the use of glitter for describing the sea or wind conditions at the surface. The refracted portion penetrates the sea and, in the absence of scattering, is eventually extinguished by absorption. Actually, the light is subjected to scattering by particles of all sizes from molecules through collodial particles to large bubbles, or in the shallow water, even the bottom. About 50% of the incident light is backscattered upward on the high seas.

Of importance is that in many cases the absorption is selective and the scattering is spectral so that the backscattered light differs markedly from "white light" giving the upwelling light characteristics which can be utilized to describe the bulk properties and constituents of the water.

In clearest ocean water the effective path length is quite long and the upward scattered light is strongly blue. Where the water contains many absorbers and scatterers (particularly in coastal regions and upwelling areas) the shift is toward the green portion of the spectrum. In some areas with heavy concentrations of suspended material washed in from the shore, reds, browns and yellows may predominate.

Significant absorvers and scatters in certain portions of the oceans are minute plants and animals termed plankton. Plankton consists of three categories: Diatoms (plants), Dinoflagellates, and a miscellany of minute forms termed Nanoplankton.

A good deal of emphasis has been placed on assessment and monitoring areas of productivity on plankton growth of the basis that they constitute the fundamental initial linking the chain of life in the sea. It is essential to monitor these areas of potential productivity for the purposes of concluding as to the "health" of the biological matter in the area.However, a significant characteristic of these plankton is that they have a capability of transforming light energy to glucose through the process of photosynthesis. During the photosynthesis process, carbon dioxide is absorbed and oxygen is released. This process is shown in very simplified form below:

(from the air) (solar radiation) (to the air)

$H_2O + CO_2$ + light energy $1/6\ (C_6H_{12}O_6) + O_2$

(derived from reference 2)

Of course, in respiration the opposite basic effect results. Nevertheless, this process is an important link in maintaining the oxygen and carbon dioxide levels; in essence a fundamental component of the life support system of earth. The importance of the oceans and the planktons within the oceans in the oxygen carbon dioxide cycle is acknowledged. The largest amount of CO_2 exchange involves the oceans. Data have shown a seasonal variation and indicate that considerably more CO_2 exchange takes place in the southern hemisphere than in the north. Data, however, are obtained only sporadically and piecemeal.

A system is required to make assessments on a global basis and monitor conditions with sufficient frequency to note changes of significance to the life support system.

Since plankters play an important part of the O_2/CO_2 cycle, assessment of their health and extent can provide information to assist in interpreting world O_2/CO_2 conditions.

Currently, data on biological activity is collected in small samples in certain selected areas, principally in the spring of the year. Efforts are then made to project the data samples to make judgements on conditions of the whole population. These estimates can be off by several orders of magnitude (reference 3).

Similarly, although conventional oceanographic observations include color determinations the samples are obtained at single points at infrequent intervals to make more than broad generalizations or categorizations of world ocean colors (reference 4). The dynamics are completely lost in the technique. In fact, measurements involve subjective judgements of an observer on the color which prevails.

Experiments (reference 5) have indicated a potential for remote sensing of ocean color which would provide large area (or world wide) coverage at a high enough repeat time to furnish needed information for making judgements on conditions of chlorophyll producing areas of the world. Considerable work still continues to be required in this area but the payoff of creating a capability for monitoring world wide extent and change of parameters which constitute an important part of the world life support system appears large.

CONCLUSION

The world oceans are an important segment of the O_2 and CO_2 cycle. The pytoplankton with the properties of photosynthesis (chlorophyll production) absorb CO_2 and produce oxygen. The greatest exchange takes place between the atmosphere and the ocean. The use of remote sensing and unique facilities afforded by satellite coverage provide for acquiring data which can be used to develop a base map of chlorophyll producing areas and monitoring changes which may be significant to the balance of CO_2 and O_2 production in the world. In essence the technique could be considered equivalent to a guage providing information on life support systems aboard spacecraft.

REFERENCES

(1) Glenn, J.H. Jr., "Pilot's Flight Report", Results of the First Manned Orbital Space Flight, February 1962.

(2) Watt, A.D., "Placing Atmospheric CO_2 in Perspective", IEEE Spectrarium, November 1971.

(3) Fraser, J.H., "Plankton Resources", Encyclopedia of Marine Resources, pp. 533-539, Frank E. Firth Editor, 1969.

(4) Lepley, L.K. "Coastal Water Clarity from Space Photographs", Photogrammetric Engineering, Vol. 34, No. 7, July 1968.

(5) Clarke, G.C.; Ewing, G.C.; Lorenzen, C.L.,"Spectra of Back-scattered Light from the Sea Obtained from Aircraft as a Measure of Cholorphyll Concentration", Science,Vol. 167, No. 3921, February 1970.

SECTION 102

DETECTION OF OCEAN CHLOROPHYLL FROM EARTH ORBIT

by

Seibert Q. Duntley
Visibility Laboratory
Scripps Institution of Oceanography
University of California, San Diego

Calculations have been made of the magnitude of the optical signature of ocean chlorophyll available to any remote sensor in earth orbit. The study had several goals, and all of them were achieved. First, it was desired to ascertain whether commercially significant concentrations of chlorophyll-A pigments in the ocean would produce a sufficient optical signal at orbital altitudes to operate optical remote sensors, such as those being planned for the Earth Observatory Satellite, on clear and hazy days. Second, it was desired to explore the effect of solar altitude on these optical signals, because this is an important matter in choosing the best orbit for an oceanographic satellite. Third, it was desired to find the best orientation for the field of view for a remote sensor in orbit in order to optimize its ability to detect ocean chlorophyll.

We avoided many uncertainties by using only atmospheric, oceanographic, and lighting data. These were obtained on board ships and from aircraft. The only use we made of mathematical modeling concerned the enrichment of chlorophyll above the concentration found in the ocean water that was measured. Richer waters were simulated by using laboratory spectrophotometric measurements of living cultures of ocean phytoplankton in radiative transfer calculations which predicted the optical properties of ocean waters containing concentrations of chlorophyll-A pigments covering the entire range of commercial importance beginning with arid water, where the concentration is 0.1 mg/m^3 or less, and extending to a concentration of 10 mg/m^3, which characterizes richly productive ocean water.

One of my colleagues at Scripps, John E. Tyler, has a submersible, double-grating, double-channel photoelectric spectroradiometer which he and another colleague, Dr. Raymond C. Smith, have taken on many oceanographic expeditions. Some of their data is recorded in a comparatively new book published by Gordon and Breach, which is entitled "Measurements of Spectral Irradiance Underwater." (1) My first two figures are plotted from tables which begin on page 66 in that volume. These data were obtained in clear, blue, arid ocean water in the southern part of the Gulf of California near Islas Tres Marias. A biologist on board the vessel collected water samples at various depths and measured the concentration of chlorophyll-A pigments by the extraction process; he characterized the water as having a concentration of 0.112 mg/m^3. This ocean location represented, therefore, the upper boundary of commercially arid waters from the standpoint of chlorophyll concentration.

Figure 1 represents the spectral reflectance of deep ocean water as measured beneath the water surface. Figure 2 shows diffuse attenuation coefficients for spectral irradiance in water; they are the slopes of log-linear depth profiles of measured spectral irradiance and are tabulated by Tyler and Smith in their book referenced above. All of our results are based on this pair of spectral curves. Two data are necessary at each wavelength because two independent phenomena, scattering and absorption, govern the spectral properties of water.

From Figures 1 and 2 it was possible to calculate spectral diffuse backscattering coefficients and the spectral diffuse absorption coefficients of the ocean water at Islas Tres Marias by a previously published method. (2) The results are shown in Figures 3 and 4. These coefficients are linearly related to the concentration of chlorophyll-A pigments. Thus, corresponding coefficients for known concentrations of laboratory cultures of ocean phytoplankton can be added to those in Figures 3 and 4 in order to predict the optical properties of ocean water containing any arbitrary concentration of chlorophyll-A pigments.

Our colleagues in marine biology at the Scripps Institution of Oceanography supplied us with laboratory cultures of the most important classes of ocean phytoplankton and measured the concentration of chlorophyll-A pigments in each of them. The collaboration of marine biologist Dale A. Kiefer is very gratefully acknowledged. Together we measured the spectral diffuse reflectance and the spectral diffuse optical density of one centimeter thicknesses of living cultures of typical coccolithophorids, dinoflagelattes, and diatoms. We used the original Hardy recording spectrophotometer for this purpose. (3) Many details of the spectrophotometric technique are in the 1942 paper. (2) The laboratory data are shown in Figures 5 and 6.

Spectral diffuse backscattering coefficients and spectral diffuse absorption coefficients were calculated from Figures 5 and 6 for unit concentrations of each species of phytoplankton, and they are plotted in Figures 7 and 8.

Phytoplankton in commercial fishing grounds are always a mixture of the principal species. We were advised by our colleagues at Scripps who specialize in food-chain marine biology that in commercial fishing grounds the most common mixture contains 12 % coccolithophorids, 38 % dinoflagellates, and 50 % diatoms. Coefficients for the separate cultures were combined in these proportions to produce the curves marked MIXTURE in Figures 7 and 8. The coefficients for that MIXTURE were then added in appropriate concentrations to the corresponding optical coefficients for the arid ocean water measured at Islas Tres Marias. This procedure enabled the spectral reflectance of ocean waters containing chlorophyll-A pigment concentrations from .1 to 10 mg/m^3 to be calculated. Figure 9

illustrates one of these results by means of the curve marked "10 mg/m^3;" the other curve, marked 0.1 mg/m^3, is identical with Figure 1 and represents the measurements of Tyler and Smith at Islas Tres Marias. From the standpoint of ocean color, the curve for 0.1 mg/m^3 depicts blue water, whereas that for 10 mg/m^3 indicates a strong green.

The cholrophyll-A pigments contained in phytoplankton have strong spectral absorption in the blue and in the far red region of the spectrum. The red absorption is probably of little use for remote sensing because the water molecule itself absorbs red light so strongly that daylight does not penetrate deeply. Addition of phytoplankton to arid ocean water causes the reflectance of the ocean to be diminished in the blue region of the spectrum where chlorophyll absorbs strongly. At the same time, however, the reflectance increases in the yellow-green region of the spectrum. This increase in reflectance may seem surprising until it is remembered that ocean phytoplankton both scatter and absorb light. The scattering is due to the fact that they are armored; that is, they have thin cases or shells of calcaceous, silacaceous, or cellulose-like materials. In the blue, absorption due to chlorophyll dominates the optical properties of the phytoplankton, but in the yellowish green (around 560 nm) chlorophyll absorbs very little and scattering predominates. The spectral reflectance of clear ocean water is roughly proportional to the ratio of the spectral back-scattering coefficient to the spectral absorption coefficient.

The way in which the spectral reflectance of ocean water at 450 nm and 560 nm varies with concentration of chlorophyll-A pigments is shown by Figure 10. Interestingly, in terms of green light at 523 nm the ratio of the back-scattering coefficient to absorption coefficient for the mixture of ocean phytoplankton used in this study has the same value as the corresponding ratio of back-scattering to absorption coefficients for the water measured by Tyler and Smith at Islas Tres Marias. Therefore, addition of phytoplankton to this ocean water causes almost no change in the spectral reflectance at 523, although it does diminish the water clarity slightly. This fact causes reflectance curves like those in Figure 9 to exhibit a hinge point at 523 nm.

Having predicted the spectral reflectance characteristics for ocean waters containing the complete range of chlorophyll concentrations that are of importance to ocean food chain productivity it remained to use this information to predict the chlorophyll signal that will reach remote sensors in orbit. Fortunately, my colleagues and I have, for many years, engaged in a data collection program to obtain exactly the type of information that is needed to accomplish this. Our measurements have been made from aircraft, spacecraft, ships, and ground stations. Figures 11 and 12 show the facilities we employed to collect the data that were used in the calculations described in this paper. Figure 11 is a photograph of the specially instrumented C-130 aircraft which is used in the atmospheric

data collection program we conduct under the auspices of the Air Force Cambridge Research Laboratories. This airplane has been extensively modified, both inside and out, for the determination of optical and meteorological parameters. It is equipped, for example, with scanners which map the skies above and below the airplane. At low altitude over the ocean our lower scanner maps the water surface and records the manner in which sunlight and skylight are reflected. All of the optical sensors in the aircraft combine to measure contrast attenuation by the lower atmosphere along any path of sight, inclined upward or downward. This information is supplemented by data taken at sea level with the instrument shown in Figure 12, which we call a contrast reduction meter. It has the capability of determining from a ground station the reduction of contrast throughout the total atmosphere, that is to say, from the surface of the earth to orbital altitude.

The ground based and airborne facilities have been used on hundreds of days in many parts of the world. Our data banks and computer programs for their use were established many years ago and are continually updated. It was a simple matter, therefore, to select measured data representing real days when the path of sight from sea surface to orbit was cloud-free and to combine those data with the ocean reflectance curves in this paper to ascertain the chlorophyll signal available to any orbiting remote sensor.

A typical result is shown in Figure 13. It is a polar plot of the field of view directly beneath an orbiting spacecraft. The nadir is at center. The outer circle represents a circular field of view 50° in angular radius as seen from the spacecraft. On the occasion depicted by this figure, the solar zenith angle was 30.9° and therefore the solar reflection point in the ocean surface is seen 30.9° from the nadir, near the top of the figure on the radial marked zero.

The ocean color sensors planned by NASA for the Earth Observatory Satellite are expected to have a sensitivity sufficient to detect a change in optical input of 0.001 when a sensor element passes from arid water to water containing significant chlorophyll-A pigments. The bold contour in this figure is a locus of points in the field of view where the optical signal changes by 0.001 in passing from arid water to water containing 0.30 mg/m^3 of chlorophyll-A pigments. Within and above this contour the signal level is too small to be detected by the sensor. Throughout the entire remainder of the field of view, however, there is more than enough signal. The figure has been computed for green light at 560 nm and for a surface wind speed of 10 knots, a value below that required to produce whitecaps. The calculation has been based on data for a cloud-free, clear day that was measured in the vicinity of San Diego on 2 September 1964. The air mass was unstable, continental, tropical. The U.S. Weather Bureau reported "visibility" 10 to 20 miles, temperature 72°F to 76°F, relative humidity 0.50 to 0.64. Local meteorologists described it as a "mild Santa Ana condition."

On that day optical data were taken from soon after sunrise until nearly sunset. From our data bank we have selected six solar altitudes ranging from a high solar zenith angle of 24.3° to a low sun with a solar zenith angle of 70.6°. These six solar zenith angles are compared by the curves in Figure 14. They represent orbital signal levels in the plane of the sun for a chlorophyll concentration of 0.30 mg/m^3. The second curve from the top is for the solar zenith angle 30.9° and corresponds with the polar plot in Figure 13. The left point on the curve represents the optical signal available to the sensor at the top of the diagram. It is less than the sensor threshold, 0.001. Progressing to the right, the curve passes through the solar reflection point and climbs to the 0.001 threshold near 11° from the nadir. From there on there is ample signal for the sensor.

Several conclusions can be drawn from Figure 14. The available optical signal was greatest in the case of the curve representing a solar zenith angle of 30.9°. The signal level and its angular extent is almost but not quite as good when the sun is at 24.3°, but it is badly degraded when the solar zenith angle is 42.0°. Virtually none of the field of view is available for lower heights of sun. It is clear that, for the conditions which these curves represent, the solar altitude should be 30° or less.

The field of view planned for the sensors on the Earth Observatory Satellite is not 100° in angular diameter but half that amount. It is clear from Figure 13 that it would be better to place the field of view off the nadir, away from the sun. For example, the 50° field of view might be chosen to extend from 5° toward the sun to 45° away from the sun. Studies of similar curves for other azimuths and different atmospheric and windspeed conditions seem to make this choice of field of view appear to be wise for many circumstances.

Not all fair weather is as clear as was the day represented by Figures 13 and 14. A more common, hazier, blue-sky occasion was measured near San Diego on 30 July 1964. It is represented by Figures 15 and 16. There was a stable maritime polar air-mass over the sea that day and the sky contained 0.2 to 0.3 broken clouds. The "visibility" was officially reported as 10 miles. The sea-level temperature was 71° to 73°F. and the relative humidity was 60 to 68 percent. Although the sky was blue overhead the horizon appeared gray because of low-level atmospheric haze.

Figure 15 shows that the 560 nm optical signal reaching orbital altitude from an ocean chlorophyll concentration of 0.3 mg/m^3 was virtually undetectable on the "hazy" day just described. Only in a tiny region just below the center of the diagram is there a small part of the field of view in which the sensor can perform its task successfully. This is too small a field to be very useful. That is not to say that the sensor is useless on this occasion. It is merely unable to detect a low

chlorophyll-A pigment concentration that is only three times greater than the arid water threshold. Figure 16, on the other hand, shows that the same sensor can detect a concentration of 0.7 mg/m^3 throughout the entire field of view under these conditions.

Figures 13 through 17 relate to chlorophyll detection by means of green light at 560 nm. Figure 9 shows, however, that in terms of the sub-surface reflectance of ocean water the magnitude of the optical signal for a given chlorophyll-A pigment concentration is greater in the blue region of the spectrum than it is in the green. Scattering of light by the atmosphere, on the other hand, ordinarily attenuates the blue optical signal to a greater extent than it does the green. There has been considerable speculation, therefore, concerning whether the blue signal can be used at orbital altitudes. One result of our study is that on both the clear and the hazy days the blue signal at orbit was greater than the green signal. Even on the hazy day the blue signal was, on the average, 40 percent greater than the green signal. This is illustrated by Figures 17 and 18. The former shows signal contour for green light, a chlorophyll-A pigment concentration of 0.3 mg/m^3, the hazy day, a wind speed of 14 knots when the sea is sprinkled with whitecaps, and a solar zenith angle of 32.4°. Under these circumstances an optical sensor having a threshold at 0.001 will detect the chlorophyll in only two tiny areas near the nadir. Almost the entire field of view is denied to the sensor in terms of green light. Figure 18, however, shows that under essentially identical conditions a blue sensor having the same contrast threshold can perform the detection throughout the entire field of view.

Orbital remote sensors should measure the apparent spectral radiance of the ocean surface throughout most of the visible spectrum in order to differentiate the presence of chlorophyll from other ocean colorants. Any scattering material, such as suspended sediments, can cause the reflectance of the ocean to increase. Therefore, a sensor operating only in terms of 560 nm green light would have no way to distinguish between the presence of sediment and the presence of chlorophyll. Correspondingly, a blue sensor operating only at 450 nm can not distinguish between chlorophyll and other blue-absorbing substances in ocean water. It is probable, however, that only ocean phytoplankton cause the sub-surface reflectance to rise at 560 nm, remain fixed at 523 nm, and diminish at 450 nm. That unique spectral signature is detectable at orbital altitude on the clear and hazy days to which this study applies.

REFERENCES

1. J. E. Tyler and R. C. Smith, Measurements of Spectral Irradiance Underwater (Gordon and Breach Science Publishers, New York, 1970).

2. S. Q. Duntley, J. Opt. Soc. Am. 32, 61 (1942).

3. A. C. Hardy, J. Opt. Soc. Am. 25, 305 (1935).

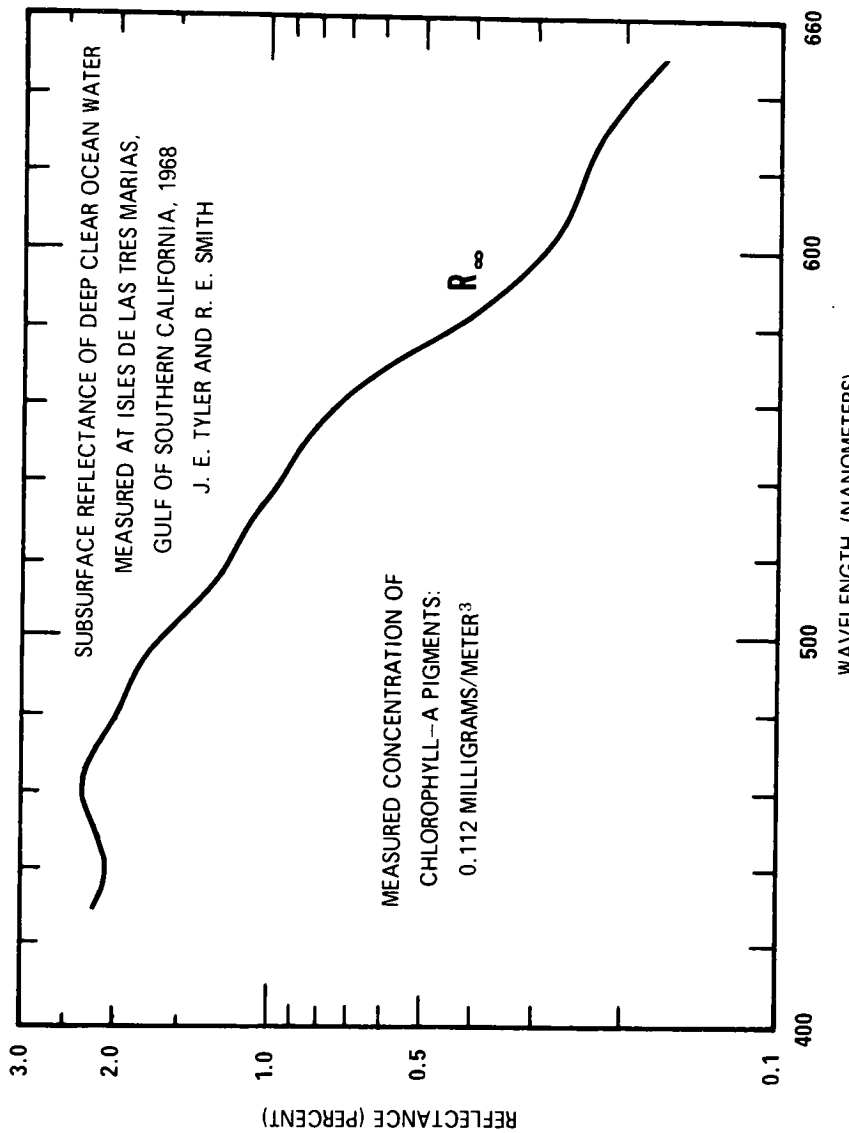
SUBSURFACE REFLECTANCE OF DEEP CLEAR OCEAN WATER
MEASURED AT ISLES DE LAS TRES MARIAS,
GULF OF SOUTHERN CALIFORNIA, 1968
J. E. TYLER AND R. E. SMITH
MEASURED CONCENTRATION OF
CHLOROPHYLL–A PIGMENTS:
0.112 MILLIGRAMS/METER³
R_∞
REFLECTANCE (PERCENT)
3.0
2.0
1.0
0.5
0.1
400
500
600
660
WAVELENGTH (NANOMETERS)

Figure 1

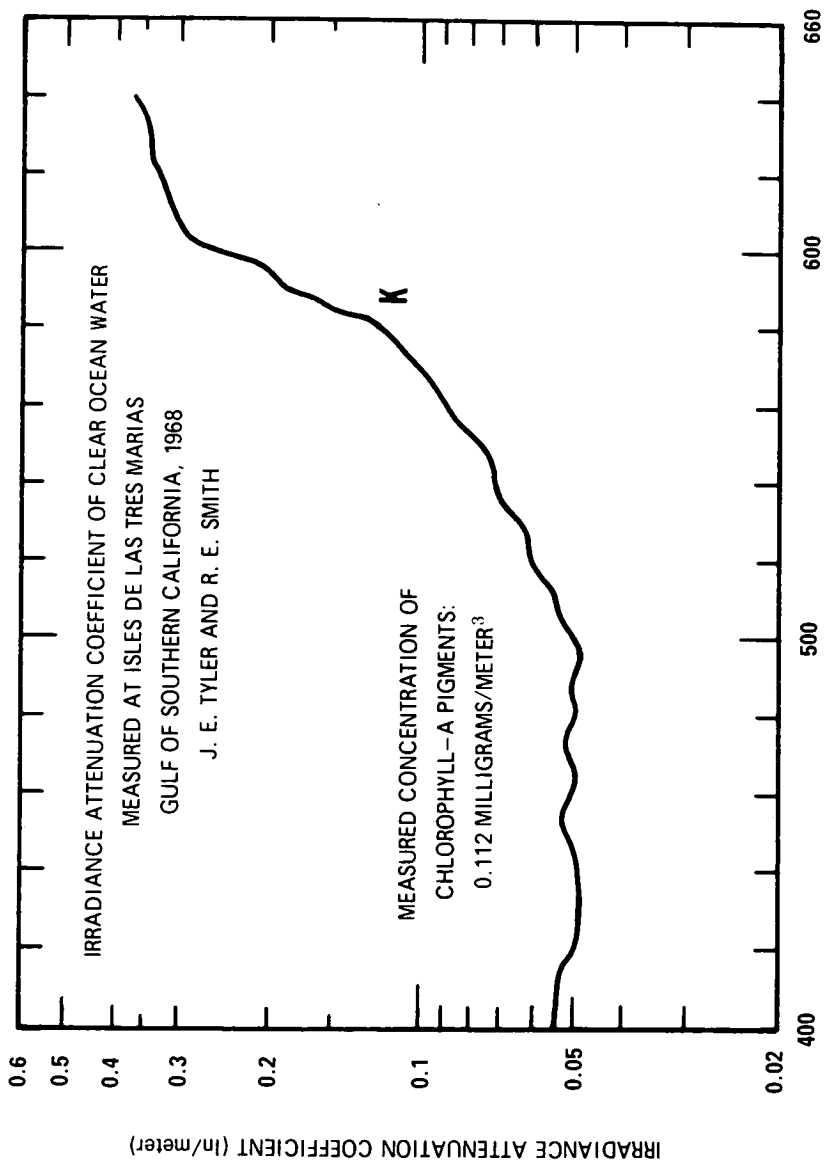
IRRADIANCE ATTENUATION COEFFICIENT OF CLEAR OCEAN WATER
MEASURED AT ISLES DE LAS TRES MARIAS
GULF OF SOUTHERN CALIFORNIA, 1968
J. E. TYLER AND R. E. SMITH
MEASURED CONCENTRATION OF
CHLOROPHYLL-A PIGMENTS:
0.112 MILLIGRAMS/METER3
K
IRRADIANCE ATTENUATION COEFFICIENT (In/meter)
0.6
0.5
0.4
0.3
0.2
0.1
0.05
0.02
400
500
600
660
WAVELENGTH (NANOMETERS)

Figure 2

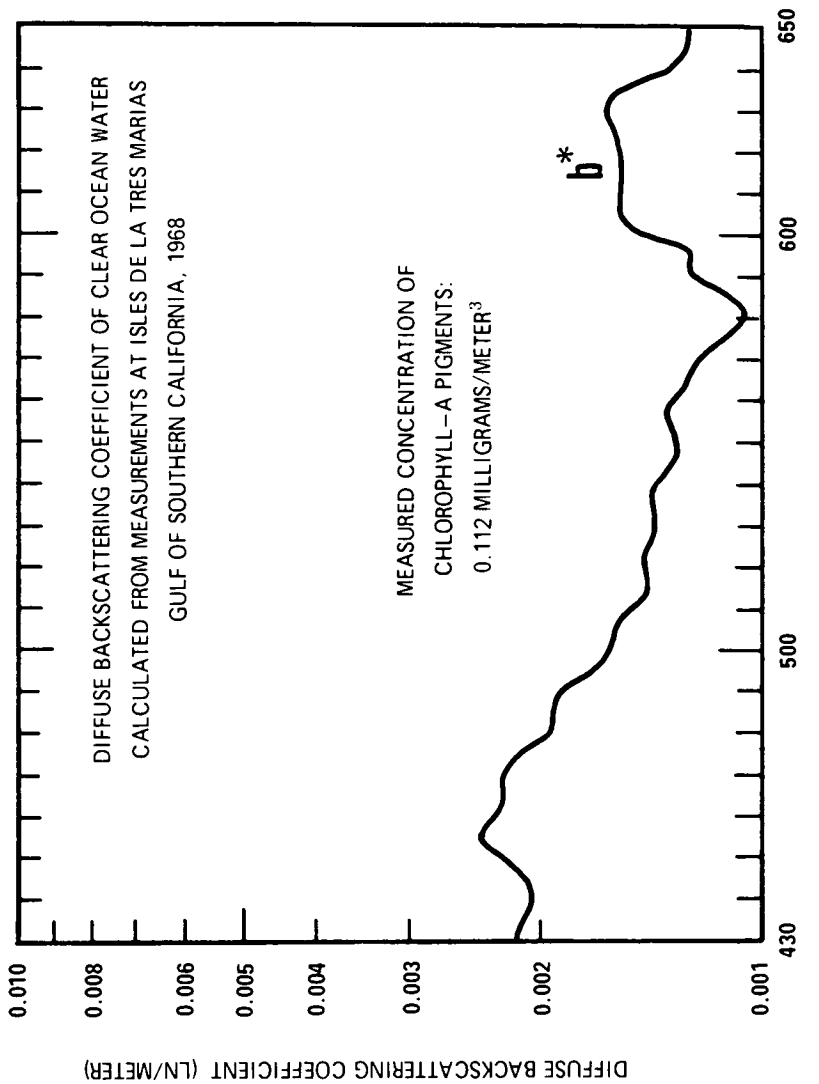
DIFFUSE BACKSCATTERING COEFFICIENT OF CLEAR OCEAN WATER
CALCULATED FROM MEASUREMENTS AT ISLES DE LA TRES MARIAS
GULF OF SOUTHERN CALIFORNIA, 1968
MEASURED CONCENTRATION OF
CHLOROPHYLL-A PIGMENTS:
0.112 MILLIGRAMS/METER3
b*
DIFFUSE BACKSCATTERING COEFFICIENT (LN/METER)
0.010
0.008
0.006
0.005
0.004
0.003
0.002
0.001
430
500
600
650
WAVELENGTH (NANOMETERS)

Figure 3

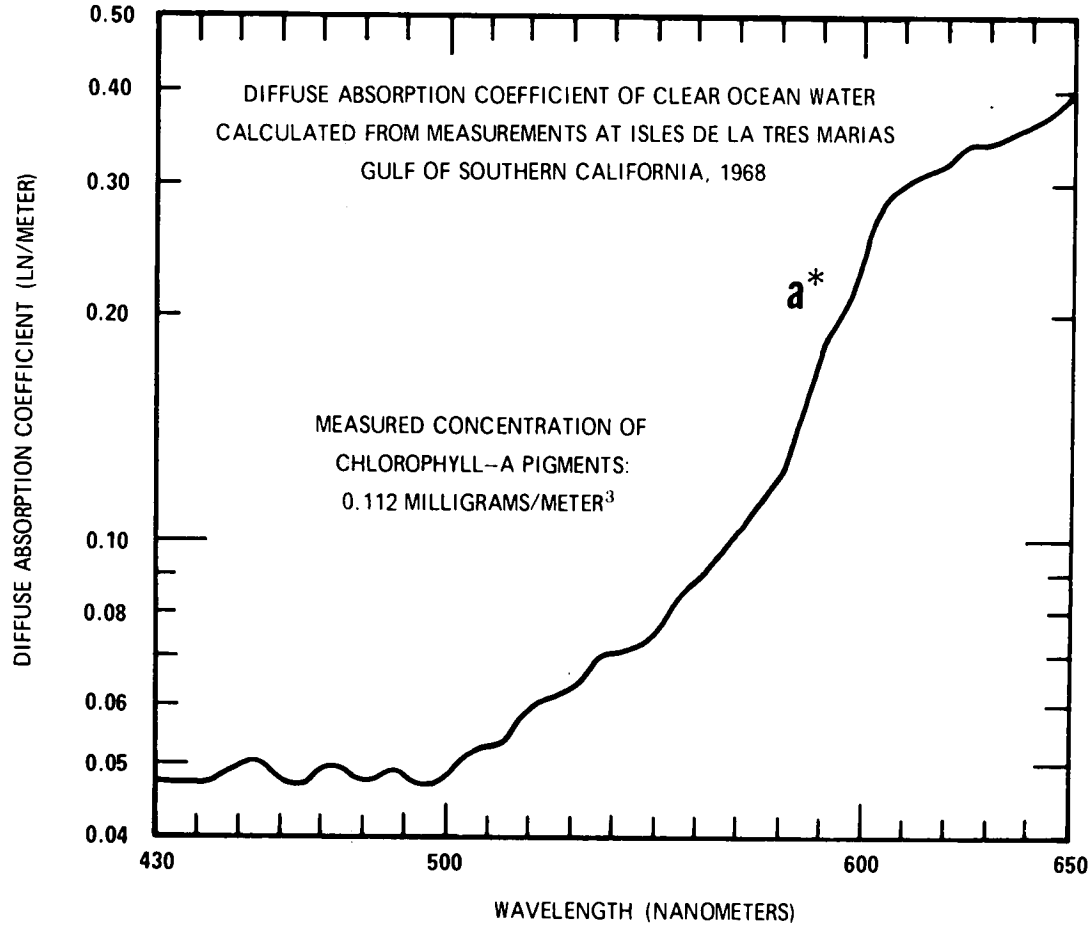
DIFFUSE ABSORPTION COEFFICIENT OF CLEAR OCEAN WATER
CALCULATED FROM MEASUREMENTS AT ISLES DE LA TRES MARIAS
GULF OF SOUTHERN CALIFORNIA, 1968
a*
MEASURED CONCENTRATION OF
CHLOROPHYLL-A PIGMENTS:
0.112 MILLIGRAMS/METER3
DIFFUSE ABSORPTION COEFFICIENT (LN/METER)
0.50
0.40
0.30
0.20
0.10
0.08
0.06
0.05
0.04
430
500
600
650
WAVELENGTH (NANOMETERS)

Figure 4

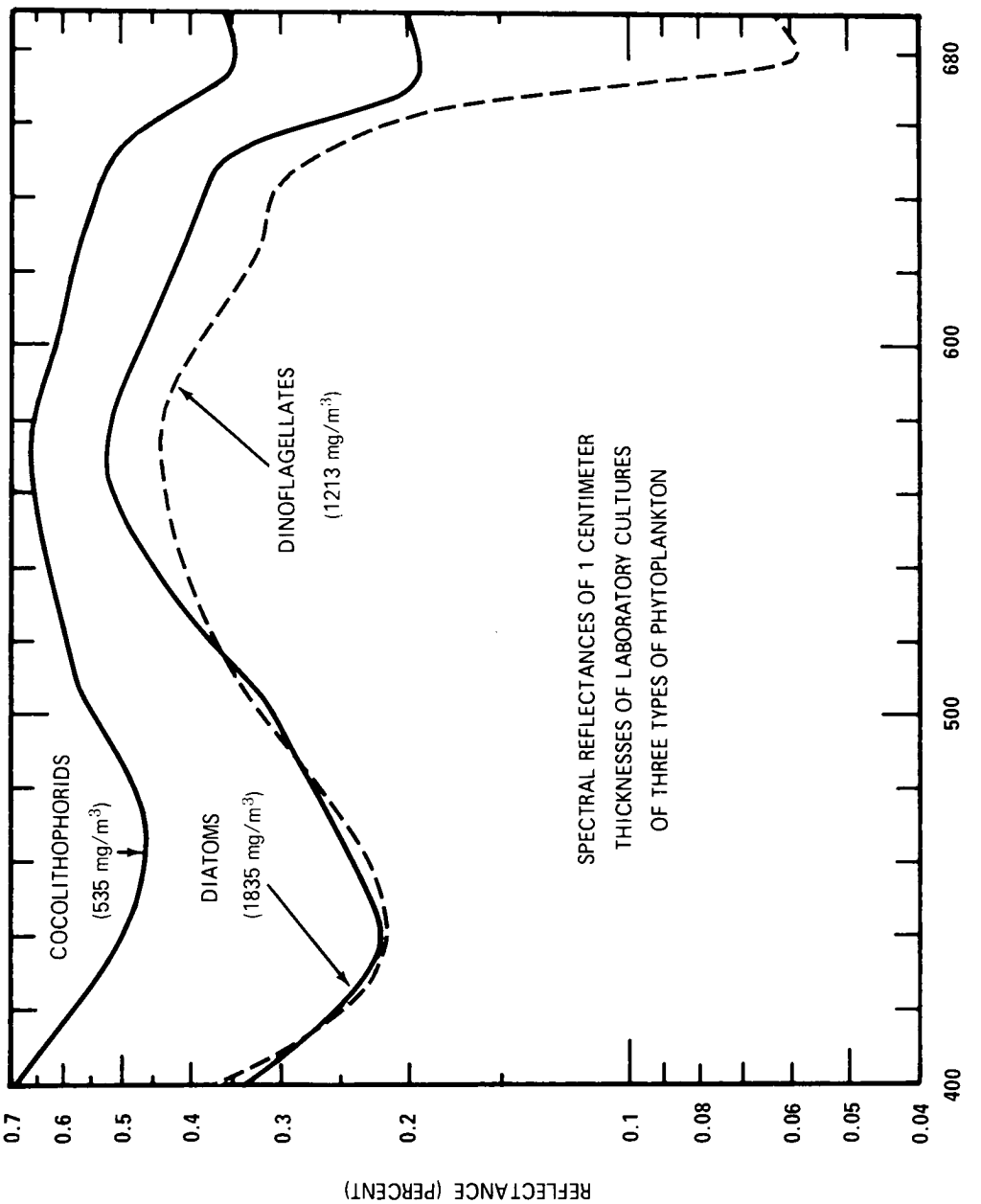
SPECTRAL REFLECTANCES OF 1 CENTIMETER
THICKNESSES OF LABORATORY CULTURES
OF THREE TYPES OF PHYTOPLANKTON
COCOLITHOPHORIDS
(535 mg/m³)
DIATOMS
(1835 mg/m³)
DINOFLAGELLATES
(1213 mg/m³)
REFLECTANCE (PERCENT)
0.7
0.6
0.5
0.4
0.3
0.2
0.1
0.08
0.06
0.05
0.04
400
500
600
680
WAVELENGTH (NANOMETERS)

Figure 5

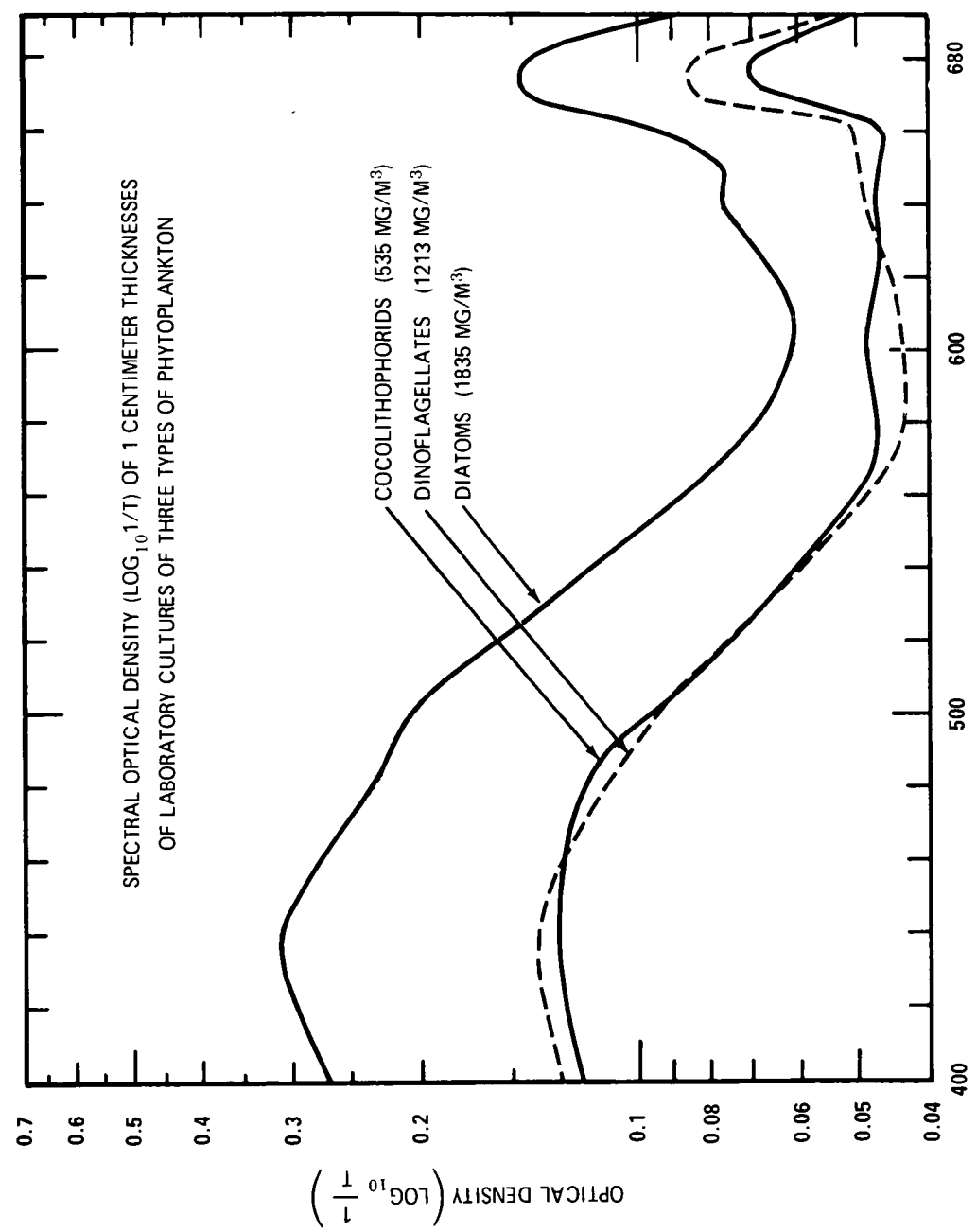
SPECTRAL OPTICAL DENSITY ($LOG_{10}1/T$) OF 1 CENTIMETER THICKNESSES
OF LABORATORY CULTURES OF THREE TYPES OF PHYTOPLANKTON
COCOLITHOPHORIDS (535 MG/M^3)
DINOFLAGELLATES (1213 MG/M^3)
DIATOMS (1835 MG/M^3)
OPTICAL DENSITY $\left(LOG_{10}\frac{1}{T}\right)$
0.7
0.6
0.5
0.4
0.3
0.2
0.1
0.08
0.06
0.05
0.04
400
500
600
680
WAVELENGTH (NANOMETERS)

Figure 6

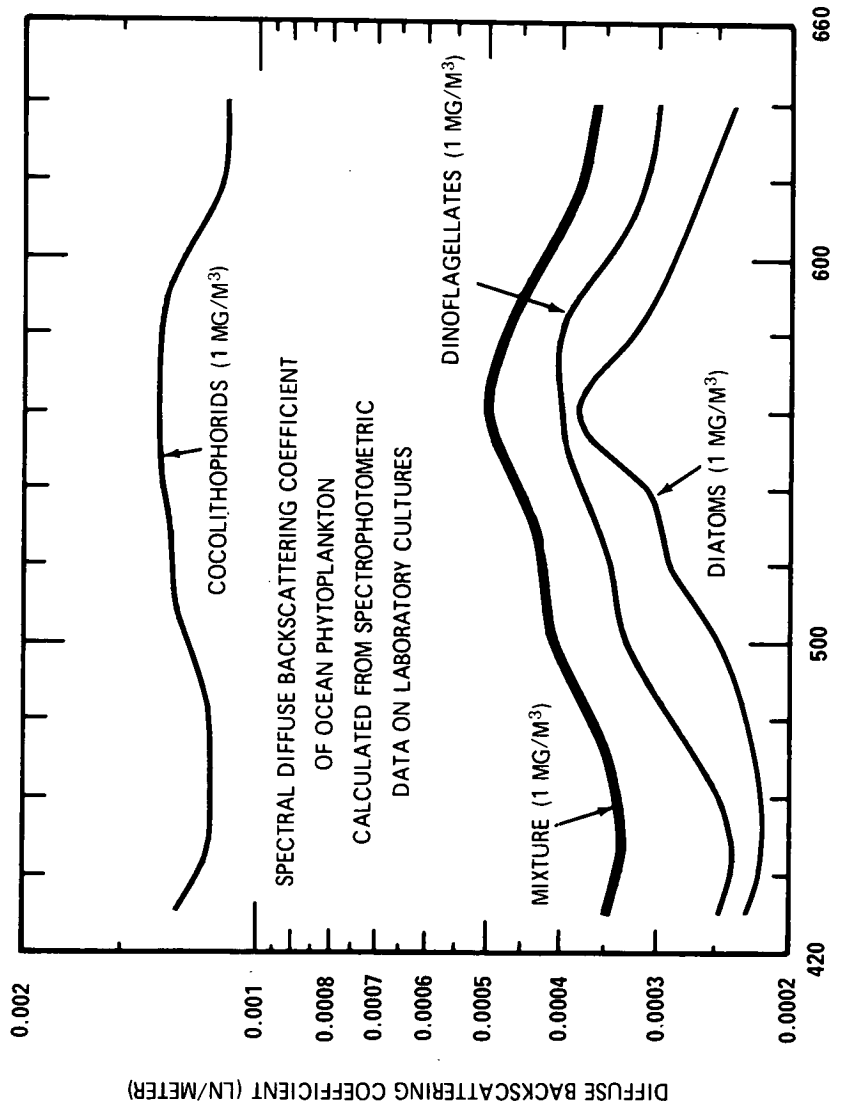
SPECTRAL DIFFUSE BACKSCATTERING COEFFICIENT
OF OCEAN PHYTOPLANKTON
CALCULATED FROM SPECTROPHOTOMETRIC
DATA ON LABORATORY CULTURES
COCOLITHOPHORIDS (1 MG/M3)
DINOFLAGELLATES (1 MG/M3)
MIXTURE (1 MG/M3)
DIATOMS (1 MG/M3)
DIFFUSE BACKSCATTERING COEFFICIENT (LN/METER)
0.002
0.001
0.0008
0.0007
0.0006
0.0005
0.0004
0.0003
0.0002
420
500
600
660
WAVELENGTH (NANOMETERS)

Figure 7

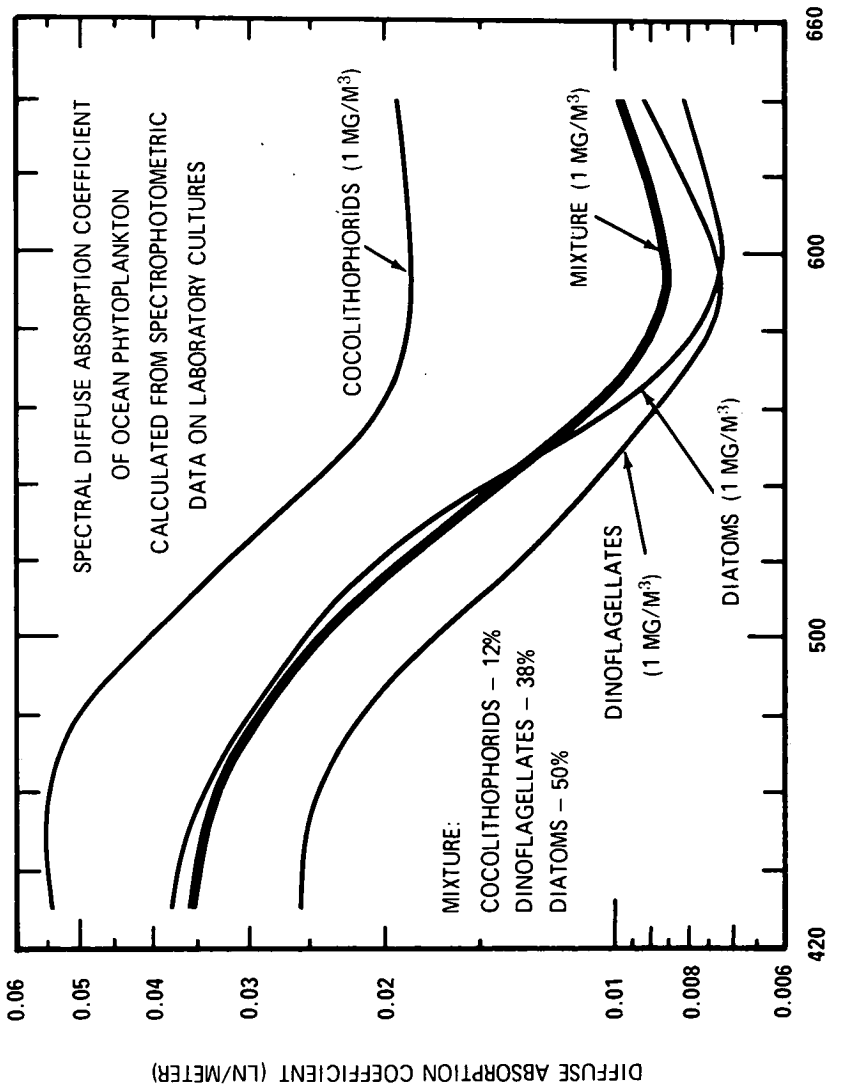
SPECTRAL DIFFUSE ABSORPTION COEFFICIENT
OF OCEAN PHYTOPLANKTON
CALCULATED FROM SPECTROPHOTOMETRIC
DATA ON LABORATORY CULTURES
COCOLITHOPHORIDS (1 MG/M3)
MIXTURE (1 MG/M3)
DINOFLAGELLATES
(1 MG/M3)
DIATOMS (1 MG/M3)
MIXTURE:
COCOLITHOPHORIDS – 12%
DINOFLAGELLATES – 38%
DIATOMS – 50%
DIFFUSE ABSORPTION COEFFICIENT (LN/METER)
0.06
0.05
0.04
0.03
0.02
0.01
0.008
0.006
420
500
600
660
WAVELENGTH (NANOMETERS)

Figure 8

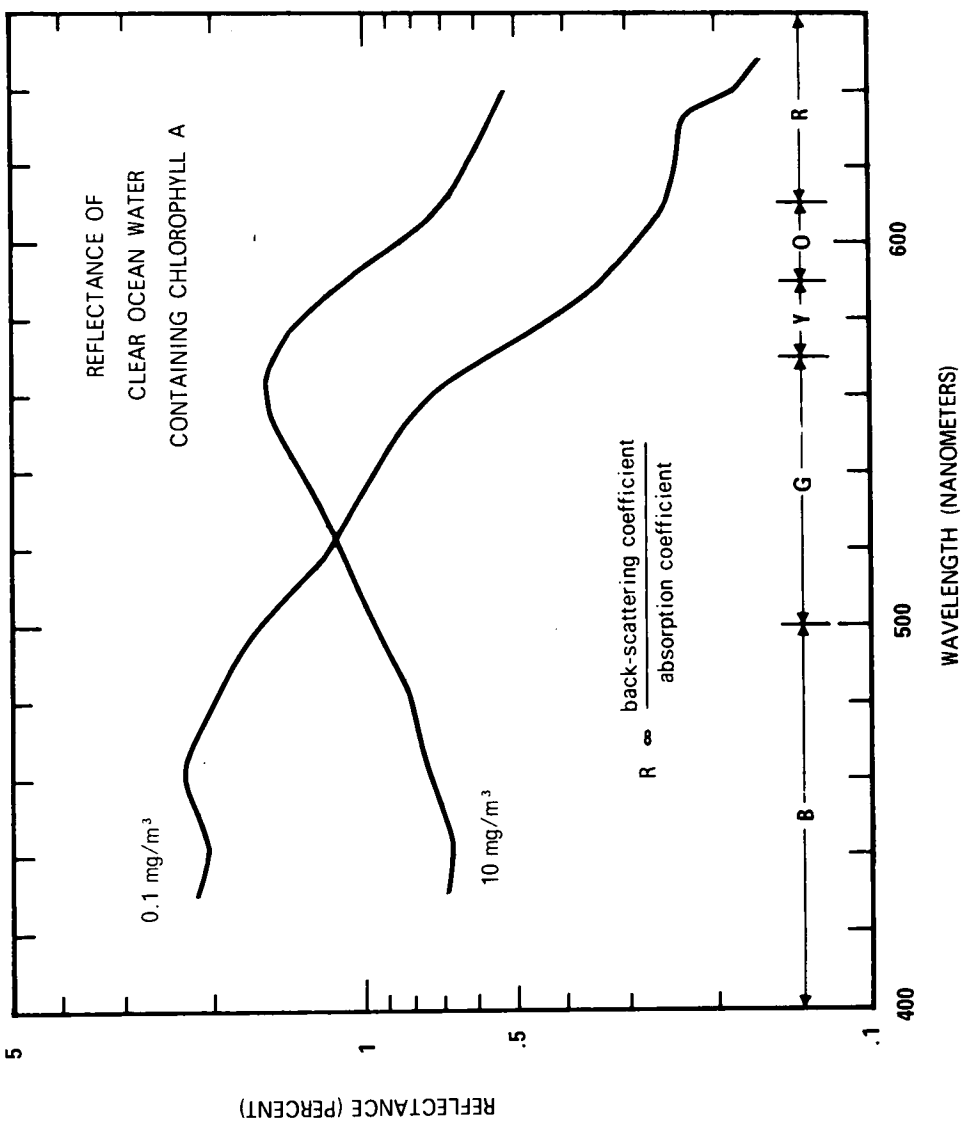
REFLECTANCE OF
CLEAR OCEAN WATER
CONTAINING CHLOROPHYLL A
0.1 mg/m³
10 mg/m³
R ∞ back-scattering coefficient / absorption coefficient
B
G
Y
O
R
5
1
.5
.1
400
500
600
WAVELENGTH (NANOMETERS)
REFLECTANCE (PERCENT)

Figure 9

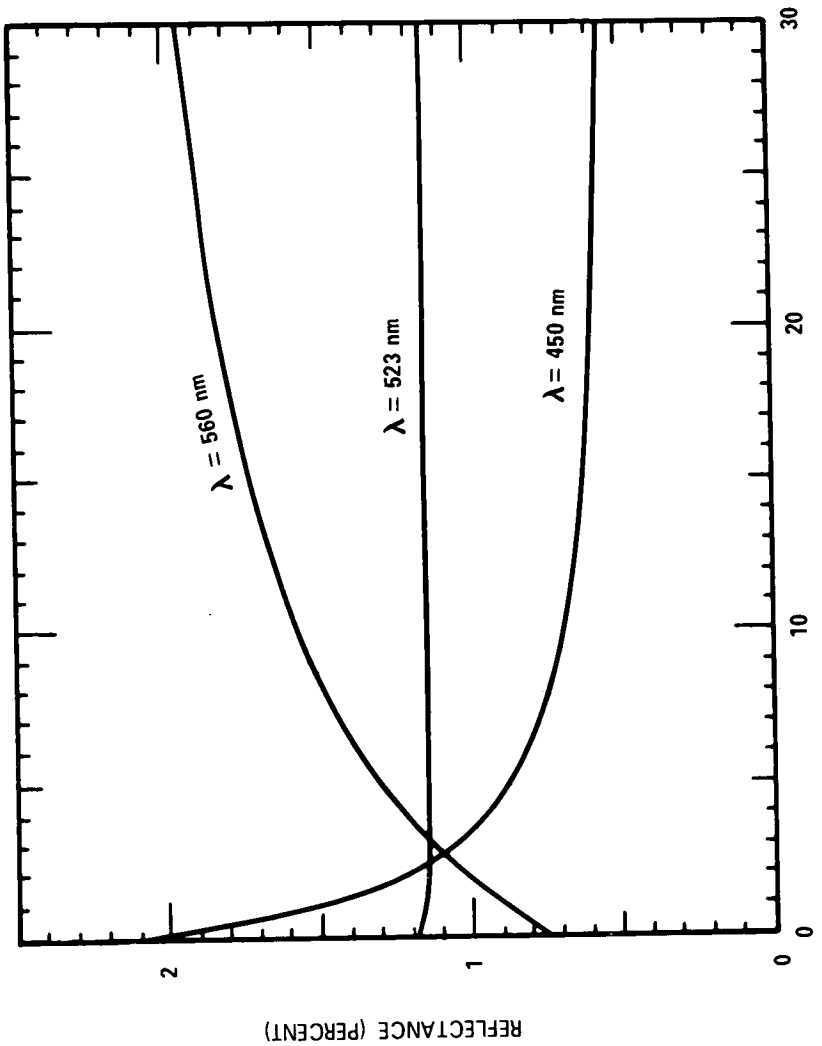
λ = 560 nm
λ = 523 nm
λ = 450 nm
REFLECTANCE (PERCENT)
0
1
2
0
10
20
30
CONCENTRATION OF CHLOROPHYLL-A PIGMENTS IN CLEAR OCEAN WATER
(MILLIGRAMS/METER^3)

Figure 10

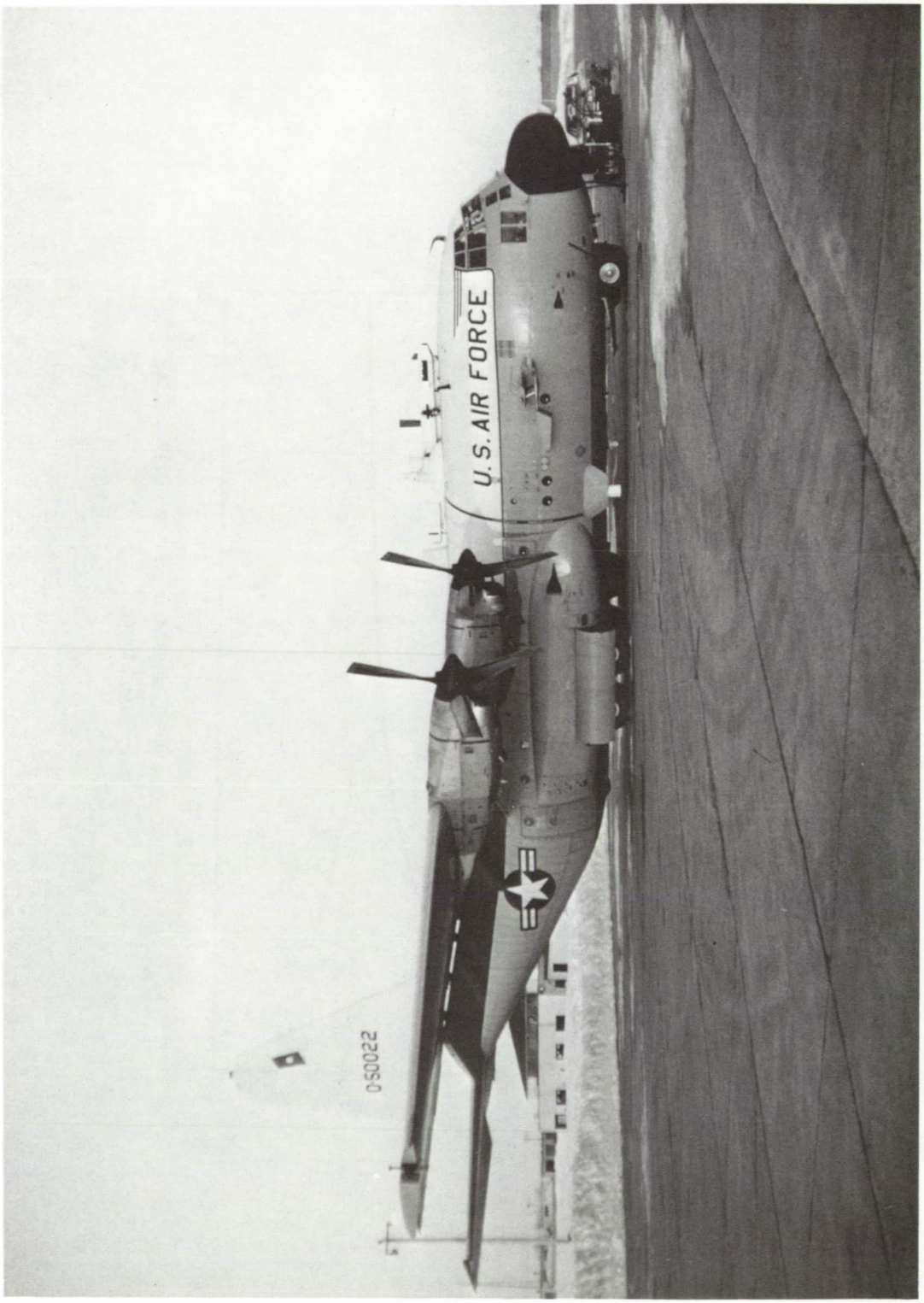

Figure 11. Instrumented C-130 Aircraft

Figure 12. Contrast Reduction Meter

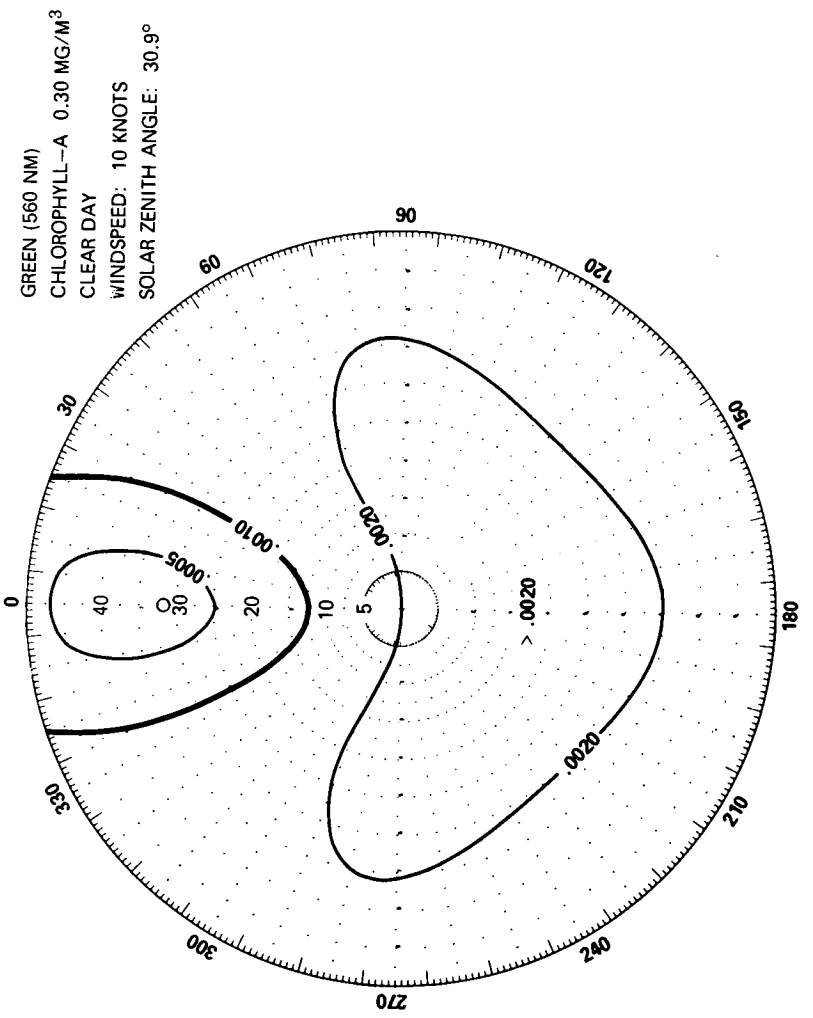
GREEN (560 NM)
CHLOROPHYLL–A 0.30 MG/M3
CLEAR DAY
WINDSPEED: 10 KNOTS
SOLAR ZENITH ANGLE: 30.9°
0
30
60
90
120
150
180
210
240
270
300
330
40
30
20
10
5
.0005
.0010
.0020
.0020
> .0020

Figure 13

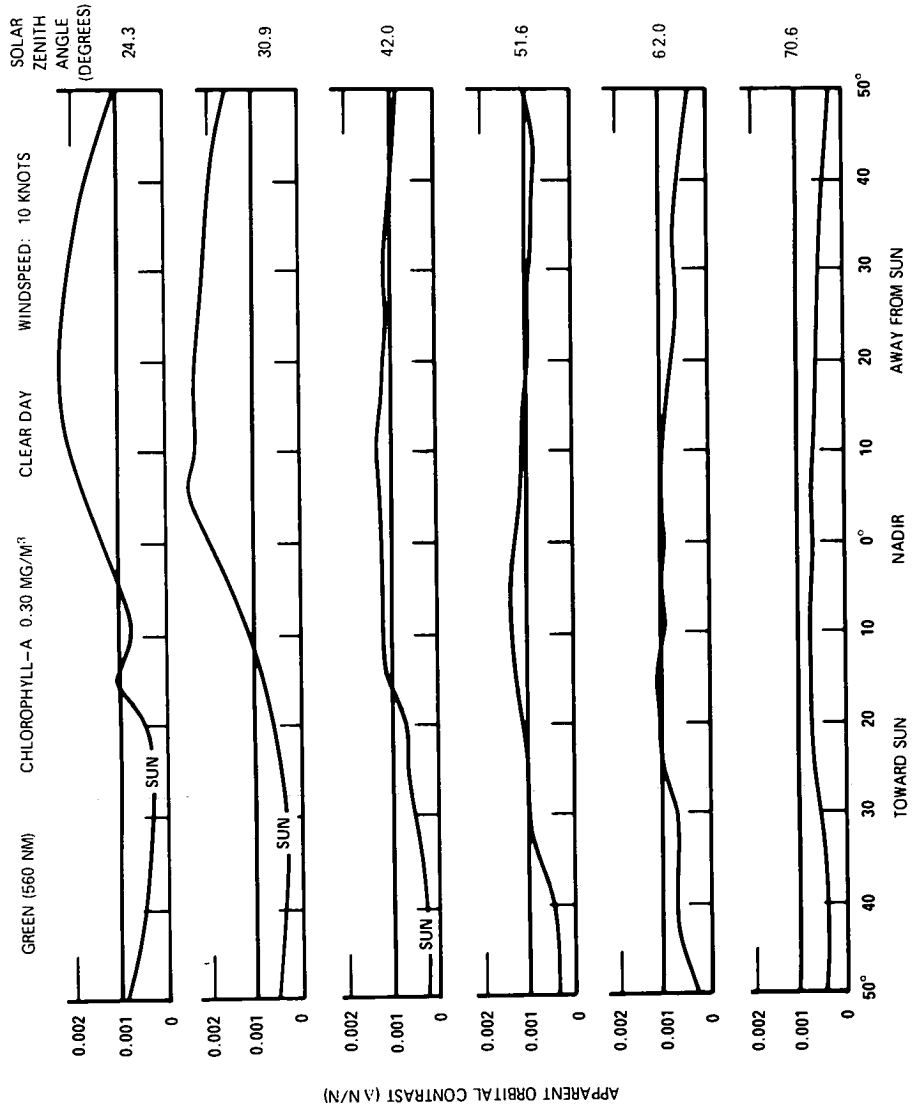
GREEN (560 NM) CHLOROPHYLL-A 0.30 MG/M³ CLEAR DAY WINDSPEED: 10 KNOTS
SOLAR ZENITH ANGLE (DEGREES)
24.3
30.9
42.0
51.6
62.0
70.6
SUN
0.002
0.001
0
APPARENT ORBITAL CONTRAST (Δ N/N)
TOWARD SUN
NADIR
AWAY FROM SUN
50°
40
30
20
10
0°

Figure 14

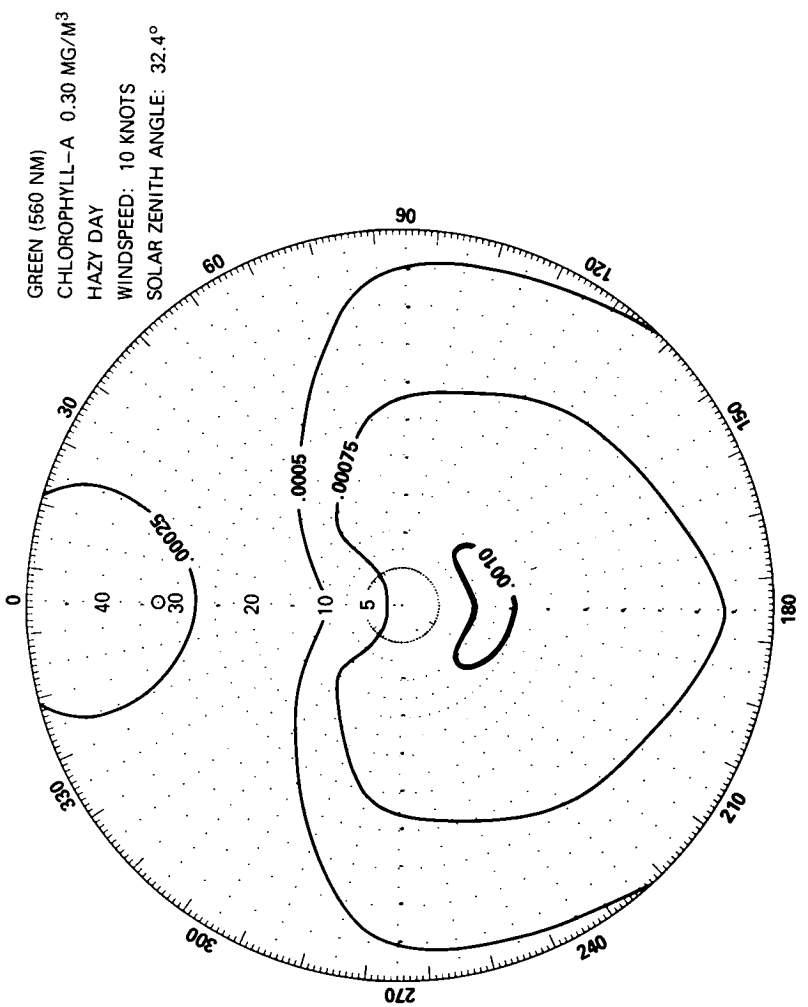
GREEN (560 NM)
CHLOROPHYLL-A 0.30 MG/M3
HAZY DAY
WINDSPEED: 10 KNOTS
SOLAR ZENITH ANGLE: 32.4°
0
30
60
90
120
150
180
210
240
270
300
330
40
30
20
10
5
.00025
.0005
.00075
.0010

Figure 15

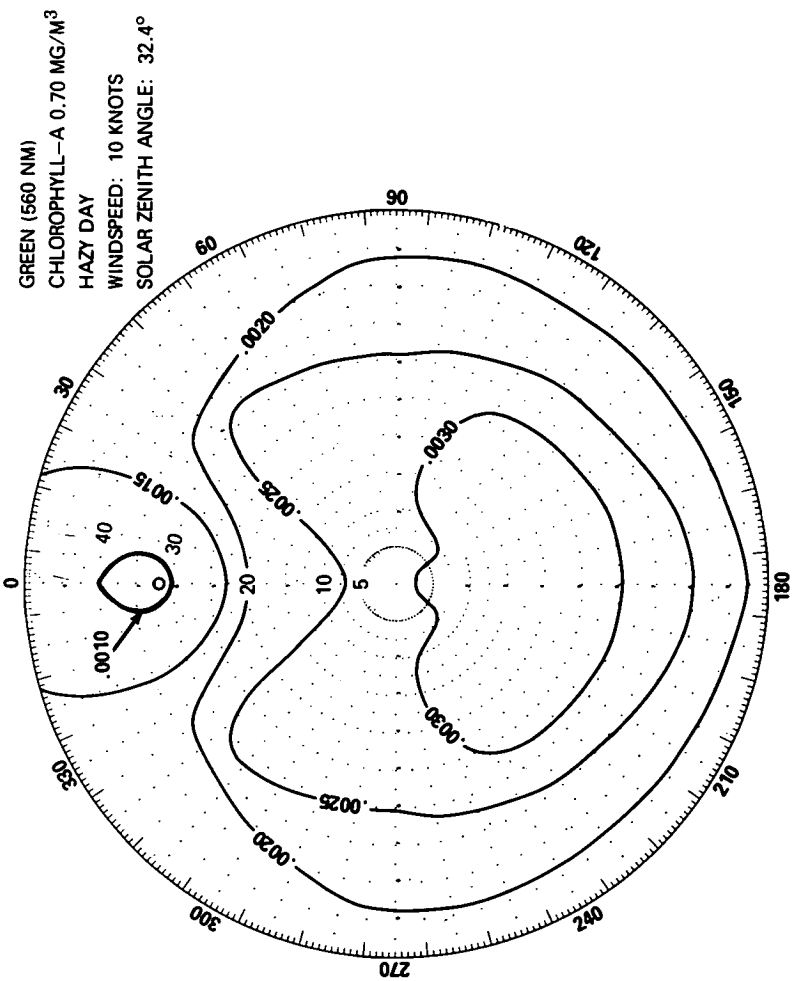
GREEN (560 NM)
CHLOROPHYLL–A 0.70 MG/M3
HAZY DAY
WINDSPEED: 10 KNOTS
SOLAR ZENITH ANGLE: 32.4°
0
30
60
90
120
150
180
210
240
270
300
330
.0010
.0015
.0020
.0025
.0030
40
30
20
10
5

Figure 16

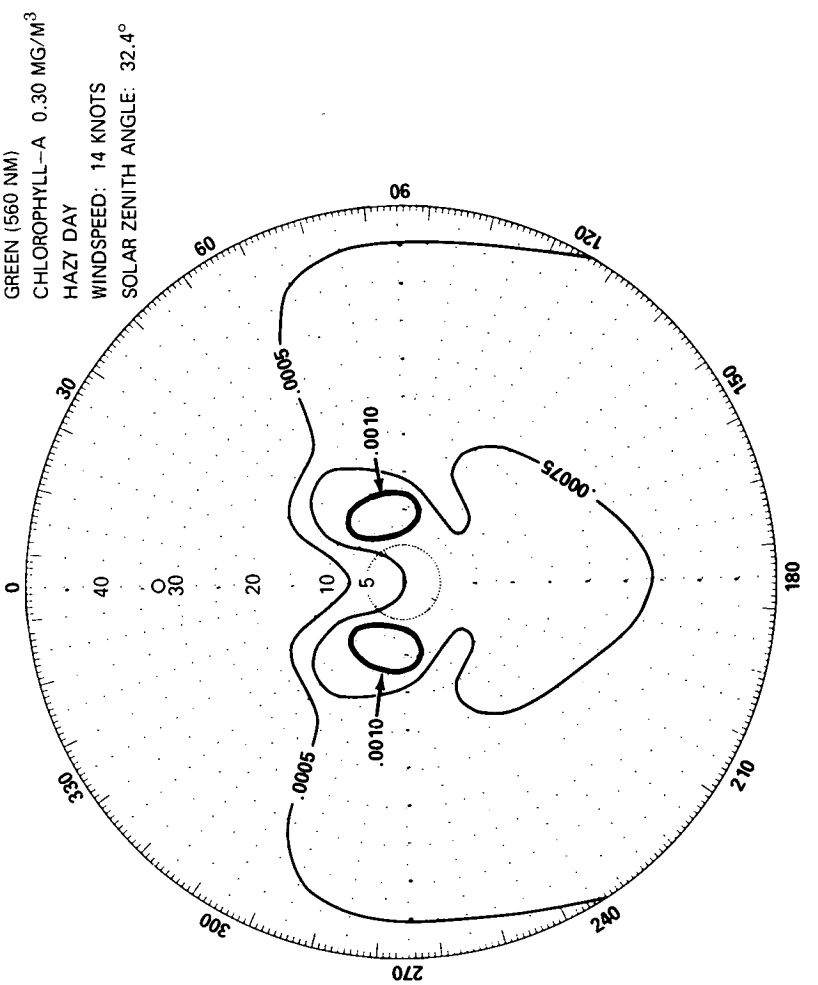
GREEN (560 NM)
CHLOROPHYLL-A 0.30 MG/M3
HAZY DAY
WINDSPEED: 14 KNOTS
SOLAR ZENITH ANGLE: 32.4°
0
30
60
90
120
150
180
210
240
270
300
330
40
30
20
10
5
.0005
.0010
.00075
.0005
.0010

Figure 17

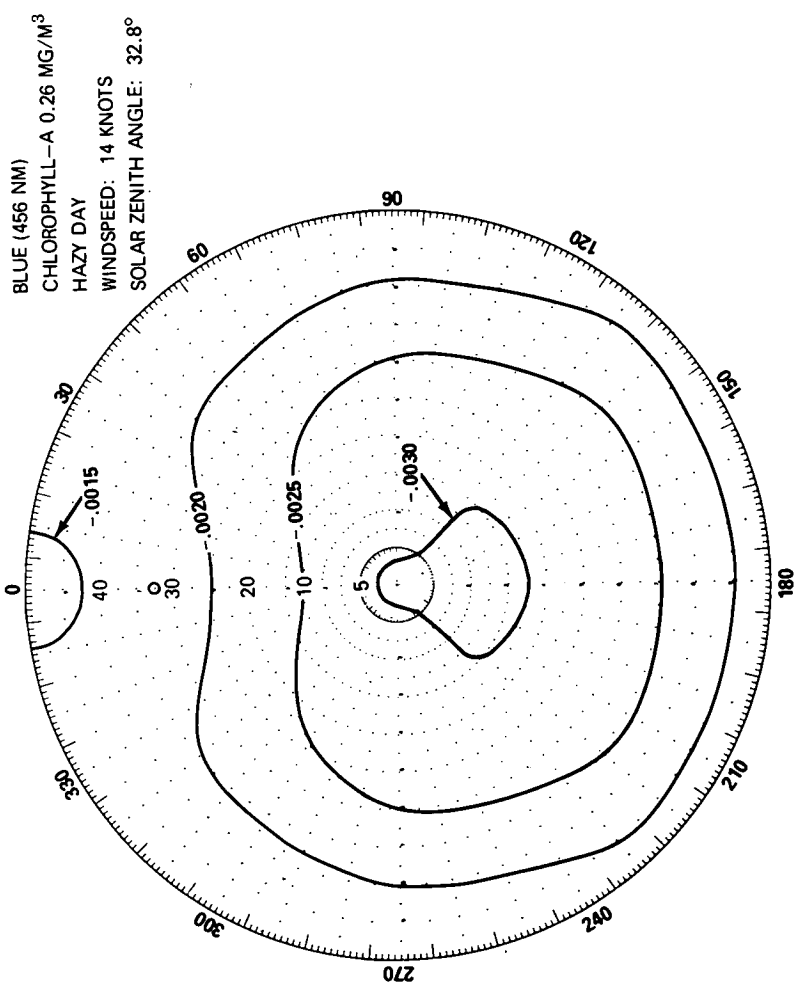
BLUE (456 NM)
CHLOROPHYLL–A 0.26 MG/M3
HAZY DAY
WINDSPEED: 14 KNOTS
SOLAR ZENITH ANGLE: 32.8°
0
30
60
90
120
150
180
210
240
270
300
330
-.0015
-.0020
-.0025
-.0030
40
30
20
10
5

Figure 18

SECTION 103

A TECHNIQUE FOR THE REDUCTION AND ANALYSIS OF OCEAN SPECTRAL DATA

By

Peter G. White
TRW Systems Group
Redondo Beach, Calif.

INTRODUCTION

One of the most difficult problems associated with the interpretation of remote spectral measurements of the ocean is the separation of atmospheric effects from the signal which originates in the water. The total signal received by a high altitude aircraft or spacecraft contains information originating in both the water itself and the atmosphere, with the latter predominating.

Because the user of these data is interested in the difference between the spectral radiance of various bodies of water, he finds it necessary to measure small percentage differences in radiance, even though the basic differences in the signal from the water bodies may be substantial. This is illustrated by the following:

$$S_T = S_A + S_W$$

where S_T, S_A and S_W are the signal received at the sensor, and the individual components from the atmosphere and the water, respectively. S_A is large compared to S_W; typically larger by a factor of 10 in the case of a spacecraft measurement. Thus an uncertainty of 1% in S_T can result in an uncertainty of 10% in deriving S_W. This imposes severe accuracy and sensitivity requirements on the measurement of S_T and on the calibration of the instrument which makes these measurements.

The following paragraphs describe some initial investigations of a method of reducing and analyzing raw ocean spectral data which avoids most of the problems associated with atmospheric effects, and which requires the application of little if any calibration information to the data.

ANALYSIS OF RAW SPECTRAL DATA

Figure 1 shows unreduced spectral curves of two bodies of water as sensed from 1,000 ft. altitude. The data are in arbitrary units and are described by the following:

$$S_\lambda = [IR(\rho_W \tau + \rho_A)]_\lambda G$$

where

S_λ is the ordinate of Figure 1

I is the solar spectral irradiance at the ocean surface

R is the spectral response of the measuring instrument

ρ_W is the spectral reflectivity of the ocean

ρ_A is the effective spectral reflectivity of the atmosphere

τ is the spectral transmission of the atmosphere from the surface to the measurement altitude

G is an instrument conversion factor.

The data were taken with a rapid scanning spectrometer and the curves of Figure 1 represent the analog output of the instrument. The spectrometer has a spectral resolution of 10 nm. Figure 2 shows spectral curves of the same two water bodies as measured from 25,000 ft. altitude.

A comparison of the two figures shows that differences between the two water bodies are much more apparent at the lower altitude (Figure 1). At higher altitude (Figure 2) the additive light backscattered by the atmosphere significantly reduces the percentage differences between the curves. In spite of this, features due to differences between the two types of water may be distinguished on Figure 2 as well as Figure 1.

In order to enhance these differences and at the same time reject the information contained in the general shape of the curve (spectral response of the instrument, spectral irradiance of the sun, and atmospheric radiance) the second derivative of each of the four curves has been calculated and plotted in Figures 3 and 4.

Note that certain features of the derivative curves appear to be relatively independent of altitude.

In order to identify spectral regions which are most sensitive to changes in water color and least sensitive to atmospheric effects, the following technique has been used to isolate the relative effects of each.

Figure 5 is a plot of the difference in second derivatives ($S''_B - S''_A$) of the two types of water (identified as A and B for convenience). Note that the curves are strikingly similar regardless of altitude. Similarly Figure 6 is a plot of the difference of the second derivatives of the two altitudes ($S''_{1000} - S''_{25,000}$). The similarity between the curves here is even more marked, indicating that we have successfully isolated the effects on the second derivative of water color (Figure 5) and atmosphere (Figure 6).

In order to determine the spectral regions in which water color effects on the second derivative predominate over atmospheric effects, Figure 7 has been prepared showing the subtractive difference between the curves of

Figures 5 and 6. Those portions of the curve below zero (atmospheric effect greater than water color effect) have not been plotted. Regions of maximum difference are centered at 486, 570, 604, and 655 nanometers. It is suggested that second derivatives of raw spectral curves be evaluated at these wavelengths in order to minimize atmospheric effects and give maximum information about the water type. However it is probable that other types of water will yield additional wavelengths well suited for discrimination.

PRACTICAL CONSIDERATIONS IN USING THE TECHNIQUE

As stated earlier, the spectral resolution of the raw data is 10 nm. In order to determine the effect of spectral resolution on the technique, the raw data was degraded to 30 nm resolution by passing a "moving window" numerical filter of 30 nm width over the data and then again calculating the second derivatives. Figure 8 is an example of the 30 nm raw data compared to the 10 nm data. There is a general smoothing of the curve at 30 nm.

Figure 9 shows the second derivatives of the Figure 8 (30 nm resolution) data. A measure of the information lost by degrading the resolution from 10 to 30 nm is the difference in amplitude of the curve from 570 to 604 nm. On this basis the information lost (amplitude reduction) is 21%.

In calculating the second derivative, another spectral filter is used in the calculation as follows:

$$S''_{\lambda+\beta/2} = (S_{\lambda}-S_{\lambda+\beta}) - (S_{\lambda+\Delta\lambda}-S_{\lambda+\Delta\lambda+\beta})$$

where β is the spectral bandpass of the filter and $\Delta\lambda$ is wavelength interval between calculations (5 nm in the examples given). All of the previous examples have used a β of 30 nm. This appears to be approximately optimum to maximize differences between the curves, but for comparison, Figure 10 shows the effect of reducing β to 10 nm. Considerably more structure is apparent in the curve, but it is not clear at this time how much is due to Fraunhoffer lines, atmospheric absorptions and noise as opposed to water color information.

The effect of increasing $\Delta\lambda$ to 15 nm from 5 nm (decreasing sampling rate by a factor of 3) is shown in the second derivative plots of Figure 11. The advantage of maintaining $\Delta\lambda$ at 5 nm is obvious.

Another important factor in using this method is the need for data which has been acquired in a "moving window" type of spectral scan as opposed to individual detectors located in each of the spectral bands. A moving window scan is one in which an aperture, whose width defines the spectral resolution is moved at a constant velocity over the spectrum to be analyzed. If this is not done (i.e., if separate detectors are located in different regions of the spectrum) then it is necessary to mathematically fit a curve from point to point through the spectrum to reduce $\Delta\lambda$. The characteristics of the equation used to fit the curve will then have a strong undesirable influence on the second derivative.

MEASUREMENT SENSITIVITY

The potential sensitivity of the second derivative technique can be illustrated by comparing data from the two bodies of water shown in Figure 2 as measured from 25,000 ft. altitude. Although the actual content of plankton in each type of water is not known exactly, surface truth measurements established that the type A water contained approximately ten times the plankton of type B. If we consider the excursion of the second derivative from 570 to 604 nanometers to be an indicator of plankton content, then the value of this indicator increased by 3.7 times from type B to type A. This suggests a non-linear relationship between the indicator and the plankton content, and/or a positive value of the indicator when the plankton count is zero. However, the maximum apparent noise or scatter on the derivative curves is less than one part in 50 of the range of the indicator which implies that the water may be categorized into some 25 levels between the limits shown. It is not expected that the clarity or haze content of the atmosphere will have an appreciable effect on these accuracies for sun zenith angles of less than 40° and viewing angles less than 10° off the nadir.[1]

CONCLUSIONS

1. The analysis technique described is capable of distinguishing fairly subtle differences in water color from data which has been measured through an atmosphere with at least half the optical density of the earth's total atmosphere.

2. The technique does not require the application of calibrations to the raw data, other than a simple correction for solar elevation angle.

3. Data obtained at 30 nm spectral resolution has about 20% less information content than data with 10 nm resolution.

4. Data should be obtained with a single "moving window" type spectral scan, with individual digitized samples about 5 nm apart.

---

[1] R. S. Fraser and R. C. Ramsey, "Nadir Spectral Radiance of the Sunlit Earth as Viewed from above the Atmosphere," TRW Internal Publication.

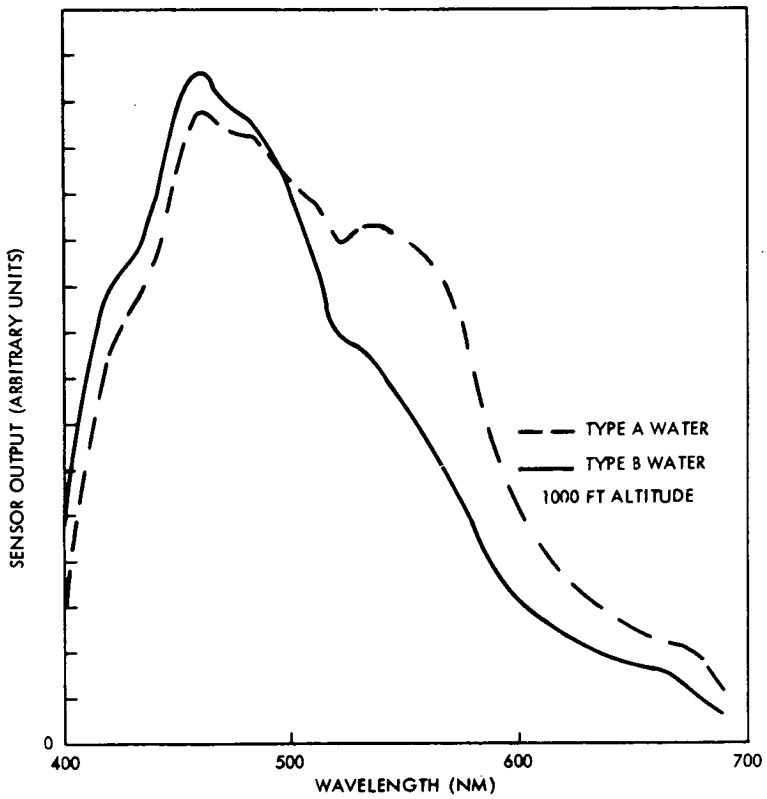

FIGURE 1. UNREDUCED SENSOR OUTPUT SIGNAL - 1000 FT ALTITUDE

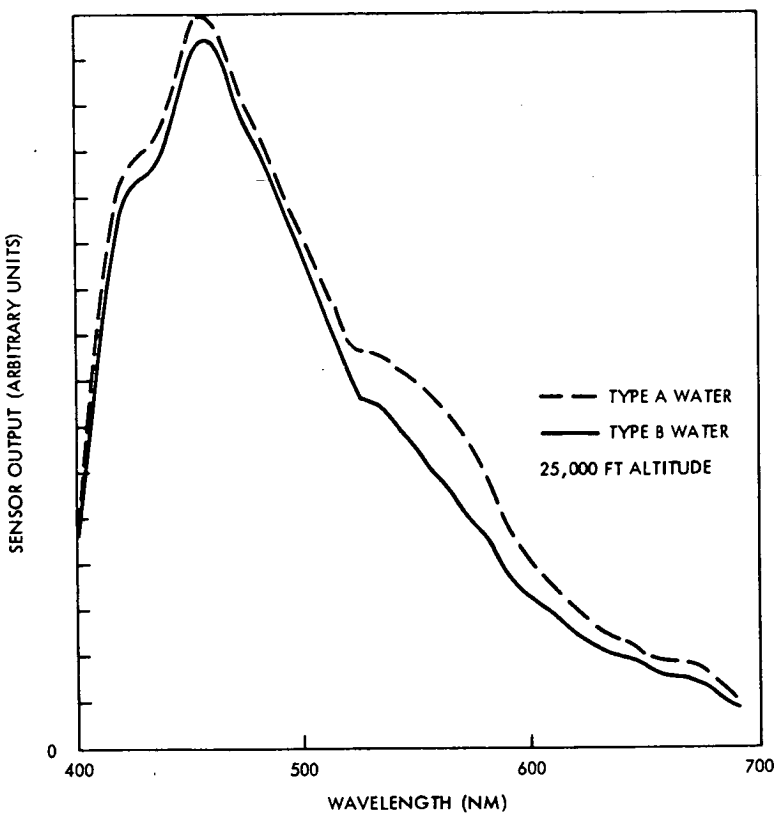

FIGURE 2. UNREDUCED SENSOR OUTPUT SIGNAL - 25,000 FT ALTITUDE

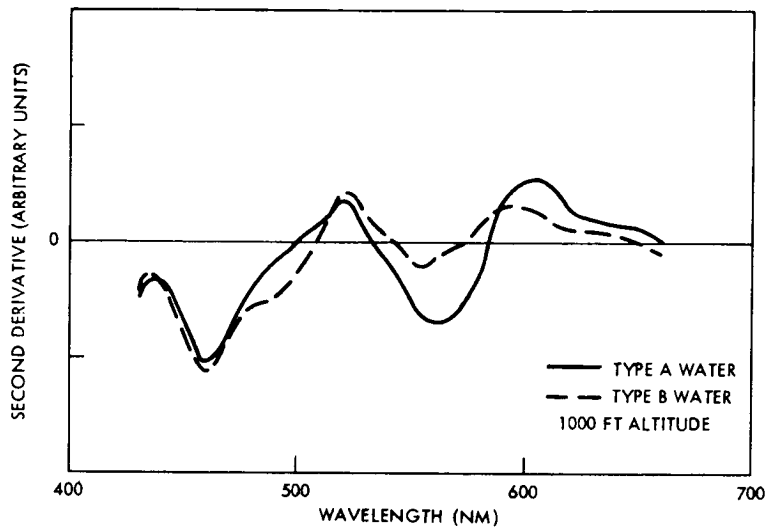

FIGURE 3. SECOND DERIVATIVES - 1000 FT ALTITUDE

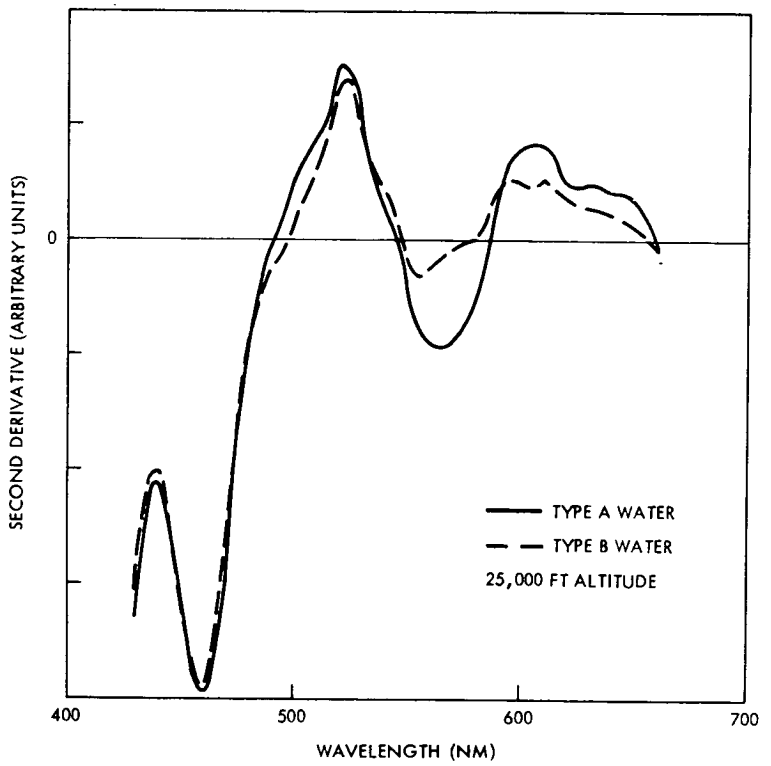

FIGURE 4. SECOND DERIVATIVES - 25,000 FT ALTITUDE

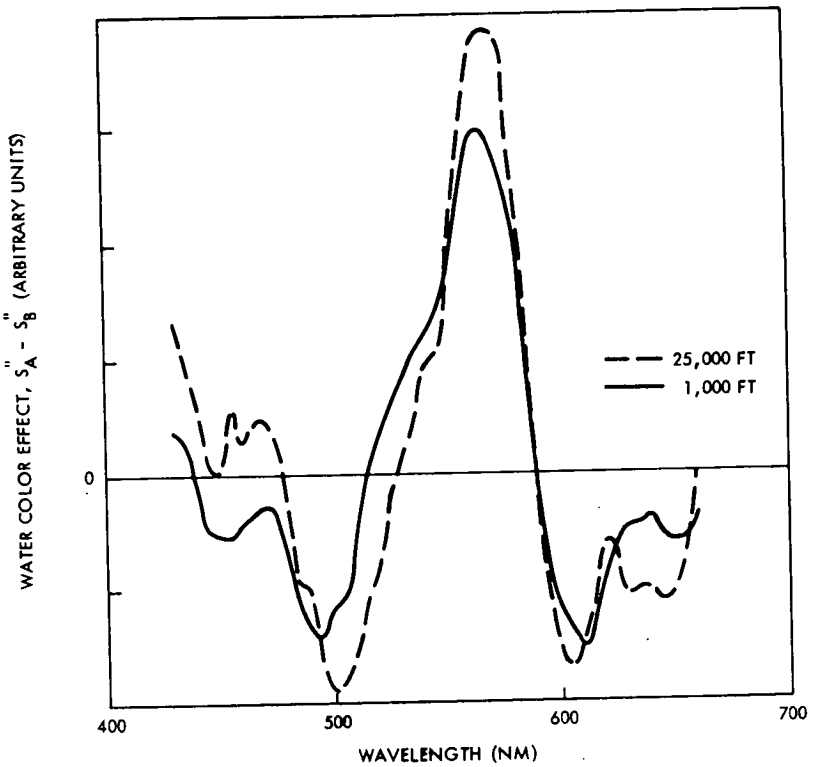

FIGURE 5. WATERCOLOR EFFECT ON SECOND DERIVATIVE

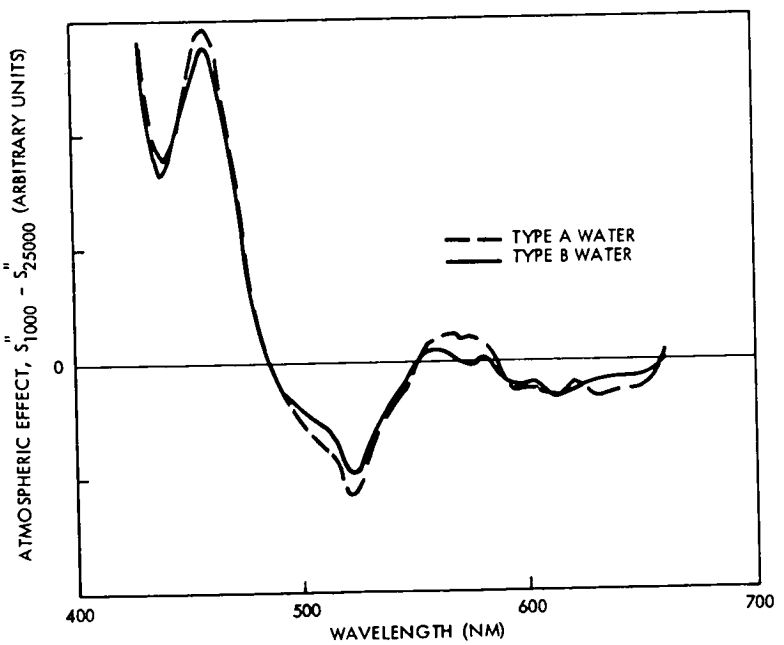

FIGURE 6. ATMOSPHERIC EFFECT ON SECOND DERIVATIVE

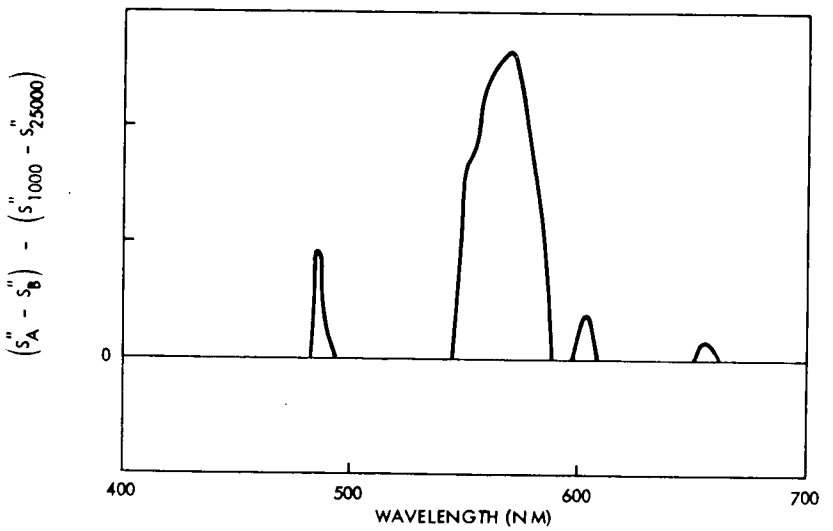

FIGURE 7. SPECTRAL REGIONS WHERE WATERCOLOR EFFECTS PREDOMINATE OVER ATMOSPHERIC EFFECTS

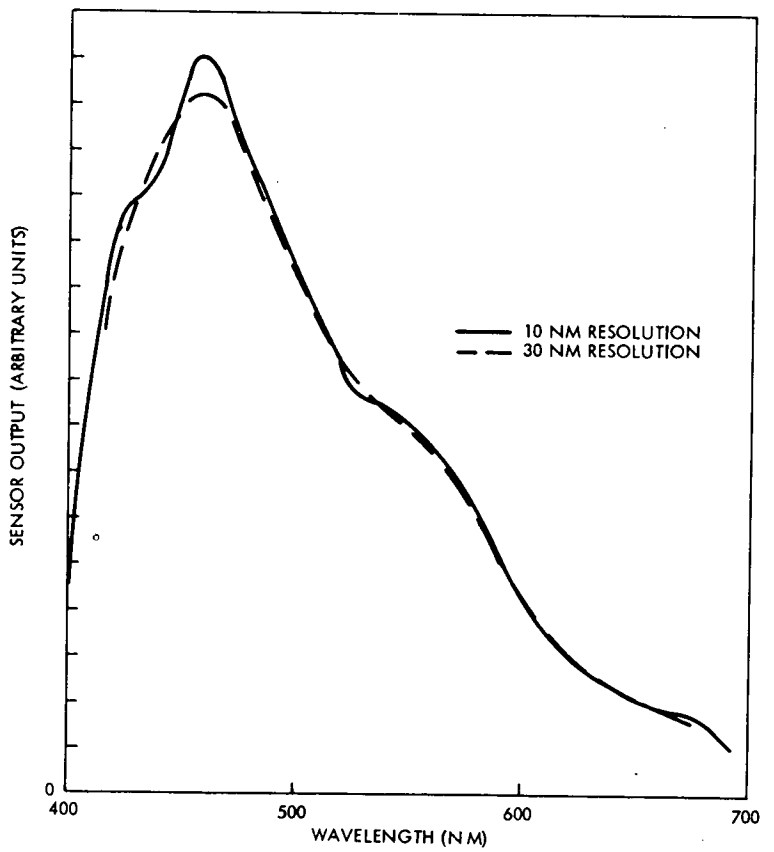

FIGURE 8. EFFECT OF SENSOR SPECTRAL RESOLUTION ON RAW DATA

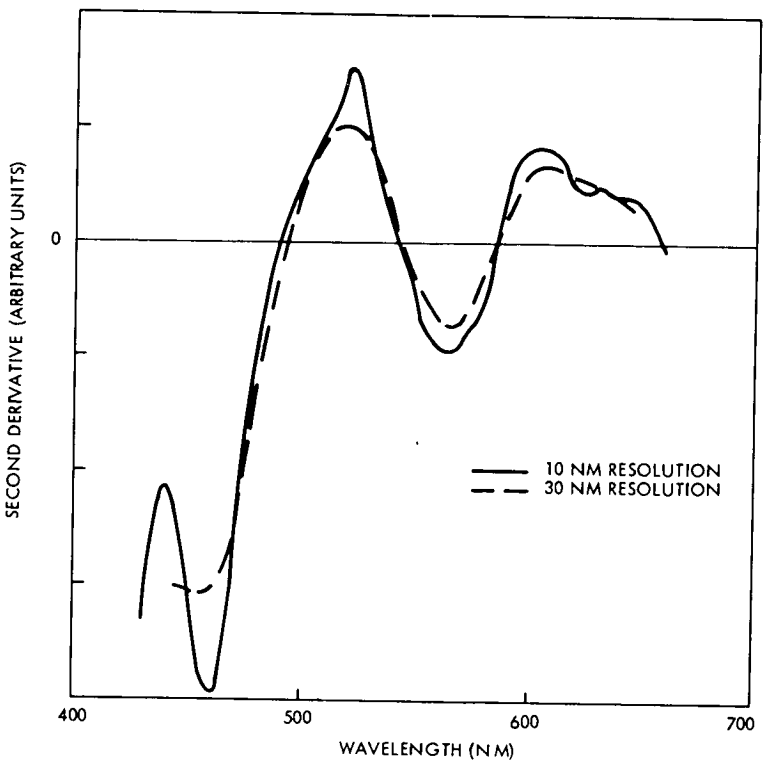

FIGURE 9. EFFECT OF SENSOR SPECTRAL RESOLUTION ON SECOND DERIVATIVE

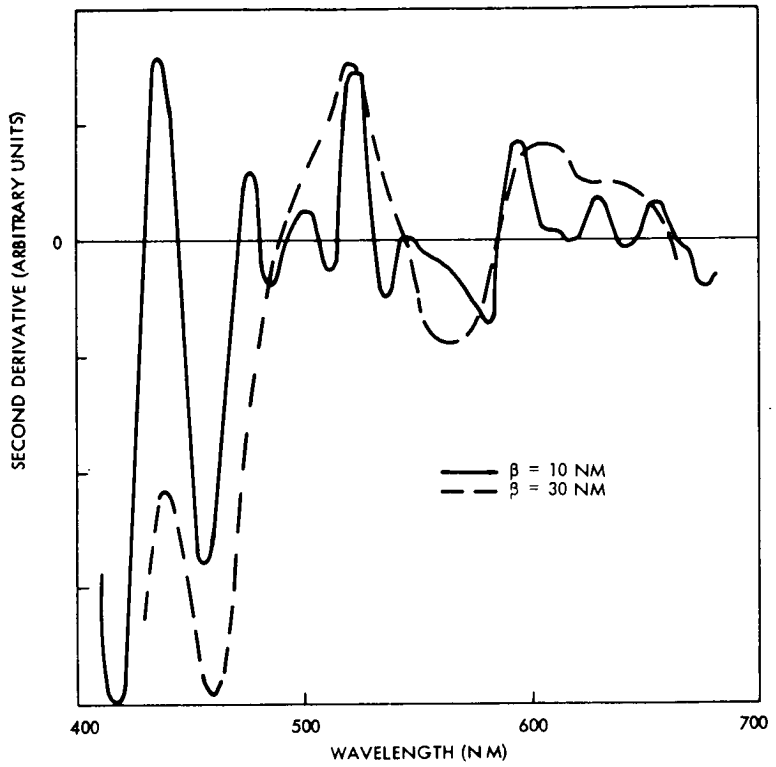

FIGURE 10. EFFECT OF FILTER PARAMETER β ON SECOND DERIVATIVE

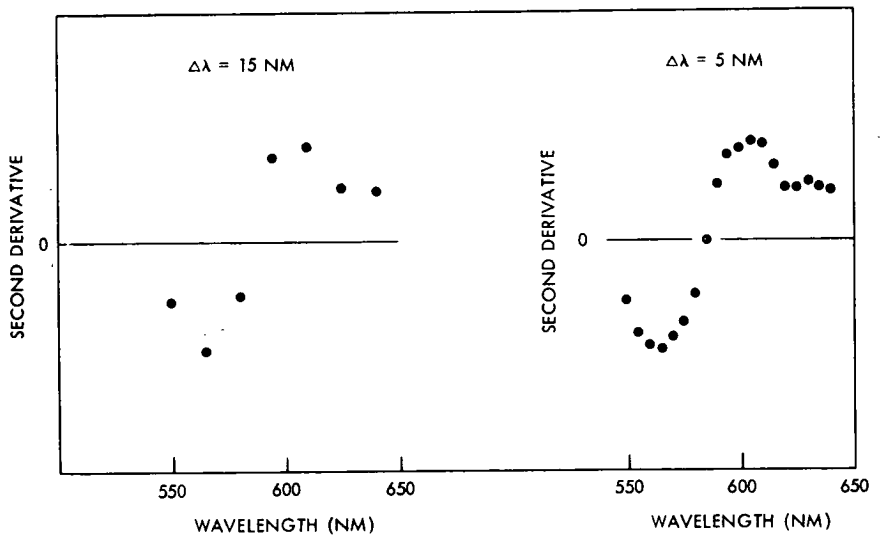

FIGURE 11. EFFECT OF SAMPLING RATE ON SECOND DERIVATIVE CURVE

(PAPER NOT SUBMITTED FOR PUBLICATION)

SECTION 104

AIRBORNE DIFFERENTIAL RADIOMETER MEASUREMENTS OF CHLOROPHYLL IN WATER

By John C. Arvesen

NASA-Ames Research Center
Moffett Field, California 94035

ABSTRACT

An airborne differential radiometer has been developed to detect chlorophyll in water bodies. Remote measurements during overflights have been correlated with laboratory analyses of water samples obtained coincident with the flights. All phytoplankton possess chlorophyll a as one of the chromophores which absorb solar energy. The presence of chlorophyll a modifies upwelling sunlight from water bodies at characteristic wavelengths corresponding to its absorption maxima and minima. Absorption maxima occur near 440 and 680 nm with an absorption minimum in the region 500 to 600 nm. The characteristics of spectral absorptance of chlorophyll a and the spectral absorptance of water are criteria used to select two wavelength regions for intercomparison. The differential radiometer continuously subtracts the intensity at a sample wavelength (443 nm), located near the chlorophyll absorption maximum, from the intensity at a reference wavelength (525 nm), located outside the absorption region. The two wavelength regions are symmetrical with the absorptance minimum of water to equalize scattering effects due to suspended particles in the water. The upwelling intensity at the reference wavelength primarily represents the background for the measurement while the intensity at the sample wavelength is due to both background and the presence of chlorophyll. Changes in light intensity, variations in water surface roughness, or scattering within the water body have a similar effect on the intensity at both wavelengths and are corrected by an automatic gain control. Variations in the concentration of chlorophyll, however, primarily affects the intensity at the sample wavelength, resulting in a signal output from the differential radiometer.

Flights have been performed to evaluate the application of the instrumentation over selected water bodies. The water bodies were selected to include freshwater lakes at high and low eutrophic levels, marine waters of high and low productivity and estuaries with both high sediment content and high chlorophyll content. The results show that the instrumentation is able to provide a continuous measurement of chlorophyll concentrations along the flight path from less than 0.02 mg/m^3 to greater than 10 mg/m^3. There exists a linear correlation between the output signal of the differential radiometer and the logarithm of chlorophyll concentration. This character of the measurement is very important because it means that small changes in chlorophyll concentration can be detected in water bodies

possessing low chlorophyll. This makes the instrumentation particularly suitable for ocean surveys where areas of higher productivity can be located against the relatively sterile background of the global ocean system. The ability to quickly cover large areas and to have the results immediately available for real-time analysis makes the instrumentation and techniques especially adapted to survey work.

SECTION 105

REMOTE MEASUREMENT OF CHLOROPHYLL CONCENTRATION AND SECCHI-DEPTH USING THE PRINCIPAL COMPONENTS OF THE OCEAN'S COLOR SPECTRUM

by

James L. Mueller
Oceanography Department
Oregon State University
Corvallis, Oregon

INTRODUCTION

Several investigators have published data and theoretical arguments which suggest that a correlation exists between oceanic chlorophyll concentration and the ocean's color spectrum. There is a need however, for a more quantitative description of the nature and variability of the relationship. In this paper are presented some statistical results and conclusions, based on direct comparisons of the ocean's color and chlorophyll concentration, which may help to fill this gap.

The ocean color and ground-truth data for this analysis were collected during Mission 140 of NASA's NP3A earth resources aircraft over the period from 6 through 14 August 1970. During this experiment, chlorophyll and light attenuation data were collected by Oregon State University's R/V CAYUSE and the chartered R/V JUDY K. All sets of comparative observations are simultaneous in the sense that the ship began sampling when the aircraft came overhead.

This investigation is supported by the U. S. Naval Oceanographic Office (Spacecraft Oceanography Project) contract number N62306-70-C-041.

The use of a spectrometer and the valuable services of Mr. Richard Ramsey were provided, under subcontract, by TRW Systems Group, TRW INC., Redondo Beach, California.

DESCRIPTION OF APPARATUS

Ocean color spectra were observed with an off-plane,Ebert type, blazed diffraction grating spectrometer designed and built by TRW Inc. The spectral resolution of the spectrometer is between 5 and 7.5 nannometers. Approximately one second is required to observe one spectrum between 750 and 400 nannometers, and approximately 3 seconds elapse after the start of one spectrum until the start of the next.

The output from the TRW spectrometer was recorded both on a Sanborn strip chart recorder and on analog magnetic tape. The strip chart records were used for the present investigation.

Pigment samples were collected by filtering water from Van Dorn sampling bottles, with subsequent handling as described in Strickland and Parsons (1965,pp117-127).

Light attenuation data were observed aboard the ships both using a submersible photometer (flat-plate detector) and a standard white secchi-disk.

PROCEDURES AND METHODS OF ANALYSIS

Water samples were taken, and light attenuation measured by the crew of each research vessel simultaneously with the NP3A aircraft's arrival overhead for a station. Aboard the aircraft, the TRW spectrometer was directed away from the sun's azimuth and tilted 15° from nadir to avoid the sun glitter pattern. On each station the aircraft flew two or more data runs, each ideally being about two miles in length centered about the ship's position.

CHLOROPHYLL DATA PROCESSING

Filtered pigment samples were frozen and subsequently analysed for chlorophylls a, b, and c concentrations by the methods described in Strickland and Parsons (1965, pp117-127). The samples were also analysed for plant and animal caratenoid concentrations, but since these were uniformly less than 1 mg/m^3 we have ignored caratenoids in this first analysis.

The blue absorption bands of the three chlorophylls overlap considerably, and their distinctive red bands are overwhelmingly masked by water's aborption of red light. Therefore, we have assumed that the effect of a given concentration of total chlorophyll (a + b + c) on water color will not depend on the proportions of a, b, and c in a first approximation.

The effect of water and its contents on the daylight spectrum is a function of the pathlength followed by the light, i.e. upon some color producing depth to which light penetrates and is backscattered up into the atmosphere. It is intuitively reasonable to assume that a spectrometer responds to light backscattered from a color-producing depth about the same as the depth which a human eye can see. On this reasoning then, we have assumed color-producing depth to equal secchi-depth. Secchi-depth is the depth at which a large white disk may barely be seen by an observer above the water surface.

Hence, the measure of chlorophyll concentration which we have attempted to relate to the ocean's color spectrum is Chlorophyll (a + b + c) averaged over secchi-depth. In the sequel we will refer to this quantity simply as "chlorophyll concentration".

Our chlorophyll data were collected at discrete depths, making it necessary for us to approximate a continuous distribution by assuming a linear trend between observations. This profile was then truncated at secchi-depth and averaged as though the data had been collected continuously.

OCEAN COLOR SPECTRA PROCESSING

The strip charts from the TRW spectrometer system were calibrated for wavelength, and then digitized on-line to Oregon State University's CDC3300 computer. A program was developed to convert each spectrum into a vector of 70 irradiance components, each representing a 5-nm band between 400 and 750 nm. The same program corrected each spectrum for amplifier gain setting, dark-voltage error (a function of wavelength and slit number), variations in slit width, and calibrated photomultiplier response (a function of wavelength).

Data Smoothing

During the one second required to observe a single spectrum, the aircraft's forward motion caused the spectrometer to scan a strip of water about 100 meters long. This phenomenon caused each component of each spectrum to represent a distinctly different area on the ocean's surface. So if whitecaps are randomly distributed on the sea surface, or if small-scale random fluctuations in cloud cover cause fluctuations in incident irradiance, fluctuations will occur randomly in wavelength in the observed upwelled light spectra. This process is illustrated in Figure I.

Random fluctuations in cloud densities can, of course, occur on scales larger than 100 meters. This causes a variation in overall irradiance levels, but individual spectra are not contaminated internally. Variations in irradiance level make it impossible to directly compare different spectra though.

The second noise effect is routinely compensated for by normalizing each spectrum with respect to irradiance observed at some reference wavelength, e.g. 570 nm. This practice is risky in the presence of small scale fluctuations, however, for we have no assurance that the normalization wavelength is not contaminated in some non-average way. To avoid this difficulty, we departed from custom and normalized each spectrum with respect to its own mean irradiance.

Small scale whitecap and cloud induced noise is not so easily smoothed over, but we have developed a satisfactory method of doing so. If we average within each wavelength band over several spectra, then each component of the average spectrum should contain an average amount of small scale noise.

Occasionally the spectrometer viewed an unusually large whitecap, or a ship. Any such occurrence caused an anomalously large fluctuation that was not representative of the average conditions for the set of spectra being considered. The filtering problem we faced was to identify these anomalous fluctuations, and then to remove their effects from the smoothed data.

An "outlier" is an observation determined by some statistical criterion to belong to a population different from that to which the rest of the observations in the sample belong. Anomalously large fluctuations in our data were regarded as outliers, and the following iterative smoothing procedure was adopted:

1. After each spectral component was expressed as a fraction of the mean for that spectrum, natural logarithms were taken of the data to improve the normality of distribution. After this transformation, the variance behaved linearly as a function of wavelength over the regions 420-580nm and 580-700nm.

2. For each wavelength band, the variances from all data runs for a given station were pooled. Then a least squares linear regression was performed to relate variance to wavelength. The regression estimates of s^2 (sample variance) were then used to compute, for each wavelength band, the statistic:

$$O_{\pm} = \frac{\max |I - \bar{I}|}{s}$$

where I is relative irradiance for a particular wavelength band and spectrum, and $\bar{I}$ is the mean for that wavelength band and data run. Critical values of this statistic are tabulated in Halperin, et al (1955). For simplicity we assumed 25 degrees of freedom for the regression estimate of s, even though we might argue for a larger number on the strength of the large effective sample size.

3. When for any band $O_{\pm}$ exceeded the tabulated critical value, the rejected component was examined in the original, untransformed data matrix. The anomalous fluctuation associated with that outlier was then removed by substitution of values which made the offending spectrum behave locally in a manner consistent with the behavior of the rest of the spectra in the sample. This usually involved adjustment of a few data points adjacent to the outlier, even though these were not rejected on the basis of their own magnitudes.

4. The entire process was repeated iteratively until no outliers were detected. The successive smoothing of background noise allowed discovery of outliers in secondary iterations that were undetectable against the noise level of the earlier iteration(s).

The final step in smoothing the ocean color spectra was to examine each data run for linear trends which might be attributable to horizontal gradients of chlorophyll concentration. Least squares regression coefficients were calculated for each wavelength band in each data run, and then these coefficients were smoothed by taking a simple moving average over wavelength. The smoothed regression coefficients were used, finally, to adjust the smoothed mean spectrum to correspond to the position in the data run occupied by the research vessel.

Principal Component Analysis

For any sample of N-component vectors, the N N-component eigenvectors of the sample covariance matrix for the bases of an orthogonal coordinate system into which the original observations may be transformed without any loss of information. When extracted, this eigensystem will always be aligned so that the first eigenvector, e_{1j} $(j = 1,2,...N)$, defines the direction of maximum sample variance. Further, e_{2j} defines the direction of the next largest amount of sample variance orthogonal to e_{1j}, and so forth with each successive eigenvector representing a direction of lesser variance than any of its predecessors. Because of this property, if the sample variations occur in definite modes, i.e. if the original N-variables vary together in definable ways, then most of the variation may be accounted for in terms of only the first few eigenvectors.

An original observation vector X_j $(j = 1,2,....,N)$, may be transformed into its eigensystem representation through the k equations:

$$Y_i = e_{ij} (X_j - E_j); \text{ where } j = 1,2,....,N; \; i = 1,2,....,k \qquad (1)$$

and where E_j is the sample mean vector, e_{ij} is the i^{th} eigenvector, and Y_i is called the i^{th} principal component of X_j. Thus we effect the transformation:

$$(X_1,X_2,.....,X_N) \longrightarrow (Y_1,Y_2,.....,Y_k)$$

where k is selected less than or equal to N to retain the desired proportion of sample variance. When k is considerably less than N, we gain a significant reduction in the number of variables in exchange for a defined, and presumably acceptable, loss of sample variation.

Any original vector X_j may be recovered from its principal component representation Y_i through the N equations

$$X_j = E_j + Y_1 e_{1j} + Y_2 e_{2j} + ...+ Y_k e_{kj} \qquad (2)$$

where $j = 1,2,.....,N$.

Morrison (1967) gives a thorough, yet readable, introduction to principal component analysis. Simonds (1963) and Church (1966) discuss examples similar to the present application, i.e. analysis of data recorded in the form of a curve. This method is alternativel referred to as "principal component analysis", "eigenvector analysis", or "characteristic vector analysis" in the literature.

It is possible to apply regression results obtained using the principal components of one sample to subsequently observed samples. Simply regard the mean vector of the original sample (E_j) as the origin of the coordinate

system and apply equation (1), using the eigenvectors (e_{ij}) obtained from the original sample. For example, to estimate chlorophyll concentration, using equation (3) below, from any observed ocean color spectrum, use the values of E_j, e_{1j}, and e_{2j} given in Figure II. With these values determine Y_1 and Y_2 from equation (1) and substitute into equation (3).

Multiple Regression Analysis

Linear least squares multiple regression analyses were performed using standard methods. The first "k" principal components Y_i were treated as independent variables, with alternatively chlorophyll concentration (C) or secchi-depth (Z_s) as dependent variable, yielding equations of the form

$$C = A + B_1Y_1 + B_2Y_2 + \ldots\ldots + B_kY_k$$

The squared multiple correlation coefficient (R^2) was calculated to estimate the percentage of variability in the dependent variable accounted for by the regression equation.

We also calculated, as a measure of precision, the residual standard deviation

$$S_{c.y} = \left[\frac{\sum_{m=1}^{n}(C - \overset{*}{C})_m^2}{n - q}\right]^{\frac{1}{2}}$$

where C and $\overset{*}{C}$ are respectively the observed value and regression estimate of the dependent variable, n is the number of observations, and $q = k + 1$ is the total number of variables in the regression equation.

Finally, simultaneous confidence limits were calculated for the regression coefficients. When such a confidence interval contained zero, it was regarded as strong evidence of no significant correlation between the associated independent variable and the dependent variable, allowing that term to be dropped from the equation.

DISCUSSION OF RESULTS

A principal component analysis was performed on the sample of 31 trend-adjusted mean color spectra, each having 55-components between 420 and 695nm. The mean vector (E_j) and first two eigenvectors (e_{ij}; i = 1,2; j = 1,2,.....,55) are given in Figure II.

The first eigenvector (e_{1j}) accounts for 75% of sample variance, and the second eigenvector (e_{2j}) accounts for an additional 20%. Thus, 95% of the total variance in the sample of 31 55-component color vectors ($X_1, X_2, \ldots\ldots, X_{55}$) is contained in 31 pairs (Y_1, Y_2).

CHLOROPHYLL CONCENTRATION

A regression analysis was performed using $\ln(0.508 + C)$ as the dependent variable, and Y_1 and Y_2 as independent variables, with the result

$$\ln (0.508 + C) = 1.0085 - 0.5149\ Y_1 + 1.2790\ Y_2 \qquad (3)$$

where C is chlorophyll concentration in mg/m^3, and the arbitrary constant 0.508 is the ratio of the average specific absorption coefficients of water and chlorophyll. Equation (3) is significant at the 0.005 level and accounts for 77% of the variability in the observed chlorophyll data (over the range from 0.00 mg/m^3 to 8.43 mg/m^3). The residual standard deviation was ± 1.62 mg/m^3. These results are collected in Table I and illustrated in the scatter diagrams of Figure III. In Figure III note that residual deviation is measured from the plane of the two regression lines; a glance at only one marginal distribution can be misleading.

SECCHI-DEPTH

Ocean color is produced by wavelength selective processes acting over color producing depth, which we have assumed to be equal to secchi-depth. Therefore we expect a strong correlation between secchi-depth and the ocean color spectrum.

As a first step we plotted the scatter diagrams shown in Figure IV. These graphs suggest a partitioning of the sample, with classification according to which research vessel collected the ground truth data. This distinction is a result of the different ocean environments in which the two vessels operated. The JUDY K operated exclusively within a few miles of the mouht of the Columbia River, where we may assume uniformly high densities of suspended particles. The CAYUSE on the other hand, operated in a more oceanic regime well away from the river mouth, where we may assume relatively low densities of suspended particles. We have tentatively and arbitrarily described the two environments as respectively a particle-scattering dominated and an absorption dominated ocean color system.

A multiple regression analysis of secchi-depth (Z_s) versus Y_1 and Y_2 for the particle-scattering dominated subsample yielded

$$Z_{s(p)} = 5.483 + 1.768\ Y_1 \qquad \text{meters} \qquad (4)$$

where the regression coefficient of Y_2 was shown to not be significantly different from zero by simultaneous confidence intervals. Equation (4) accounts for only 55% of the variability in secchi-depth, but the sample range was very narrow (2.5 to 6.5 meters). The residual standard deviation is only $\pm$ 1 meter. These results are collected in Table IIa and illustrated in Figure IVa.

A similar analysis of the absorption dominated subsample yielded

$$Z_{s(a)} = 9.214 - 7.833\ Y_2 \qquad \text{meters} \qquad (5)$$

where the regression coefficient of Y_1 was shown to be not significantly different from zero by simultaneous confidence intervals. Equation (5) accounts for 82% of the variability in secchi-depth over a range from 6 to 20 meters. Residual standard deviation is $\pm$ 2.16 meters. These results are collected in Table IIb and depicted in Figure IVb.

INTERPRETATION AND APPLICATION

Through joint use of equations 3 through 5 it is possible to estimate chlorophyll concentration averaged over secchi-depth, estimate secchi-depth (i.e. the depth of the layer in which we are estimating chlorophyll), and say somethingabout particle concentrations (at least qualitatively).

For routine application of these results, it should be possible to estimate Y_1 and Y_2 from irradiance measurements in three narrow wavelength bands (I_1, I_2, I_3).[2] By solving the three equations

$$\ln I_j = \ln \bar{I} + E_j + Y_1 e_{1j} + Y_2 e_{2j}$$

for Y_1 and Y_2 ($\ln \bar{I}$ is also unknown, but it need not be solved for explicitly), estimates may be obtained for substitution in equations (3) through (5). Values for E_j, e_{1j} and e_{2j} are to be taken from Figure II for the appropriate wavelengths.

For example, if irradiances are measured in 3 10nm-wide wavelength bands centered on 495nm (j=1), 547.5nm (j = 2) and 602.5nm (j=3), then

$$Y_1 = \frac{1}{0.300}\left\{\ln\left(\frac{I_1}{I_2}\right) + 0.475\right\}$$

$$Y_2 = \frac{1}{0.208}\left\{\ln\left[\left(\frac{I_2}{I_1}\right)\left(\frac{I_1}{I_3}\right)^{\frac{1}{2}}\right] - 0.330\right\}$$

which is nearly as simple as attempting to measure chlorophyll from only a single measured ratio of irradiances.

CONCLUDING REMARKS

We have shown by empirical means that it is possible to measure chlorophyll concentration in the ocean as a linear function of the first two principal

components of the ocean's color spectrum. The residual standard deviation of the estimate is about $\pm$ 1.6 mg/m^3.

The chlorophyll concentration estimated is the average over secchi-depth, which may also be estimated: a) within about 25% in very turbid waters as a linear function of Y_1, and b) within about 15% in relatively clear ocean waters as a linear function of Y_2.

For routine application of these results, Y_1 and Y_2 may be estimated easily from irradiance measurements in only three narrow wavelength bands. A 3-channel measurement will not suffice for future investigations aimed at broadening or improving these results, however. A full spectrum analysis by methods similar to those presented here is recommended for that task.

The relatively poor fit to the chlorophyll data ($\pm$ 1.6 mg/m^3) suggests that we next conduct a covariance analysis to examine the joint effects of chlorophyll, particle scattering and secchi-depth on ocean color.

REFERENCES

Church, Alonzo Jr. (1966). Analysis of data when the response is a curve. TECHNOMETRICS, Vol 8 No 2 pp 229-246

Halperin, M., S.W. Greenhouse, J. Cornfield, and J. Zalokar (1955) Tables of percentage points for the studentized maximum absolute deviate in normal samples. AMER. STATIST. ASSN. JOUR. March 1955, pp185-195

Morrison, D. F. MULTIVARIATE STATISTICAL METHODS McGraw Hill, New York (1967) 338p

Simonds, J. L. (1963) Application of characteristic vector analysis to photographic and optical response data. JOUR. OPT. SOC. AM. Vol 53 No. 6 pp 968-974

Strickland, J.D.H., and Parsons, T.R. (1965). A manual of sea water analysis. FISH RES. BD. CANADA BULL. No. 122, 172p

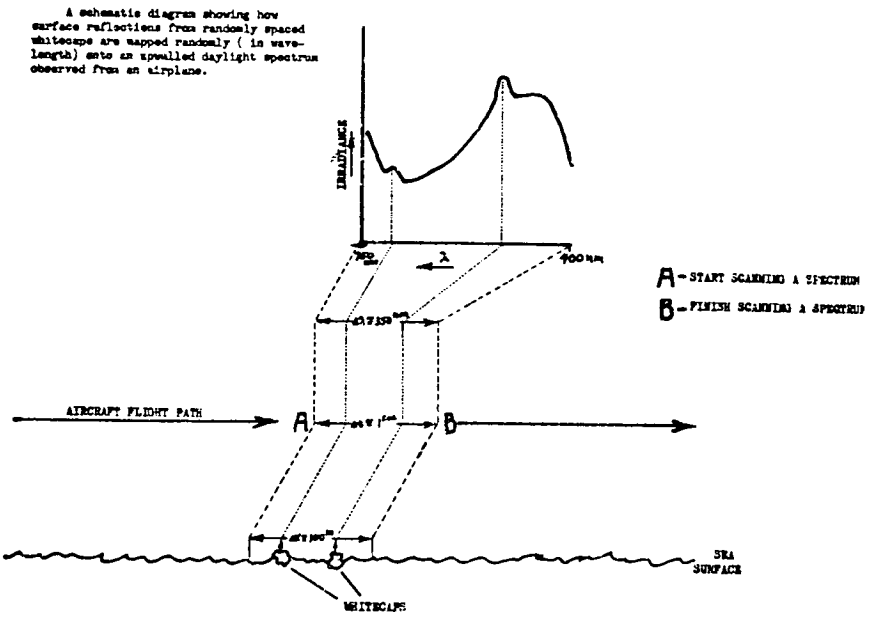
A schematic diagram showing how surface reflections from randomly spaced whitecaps are mapped randomly (in wavelength) onto an upwelled daylight spectrum observed from an airplane.
IRRADIANCE
λ
A - START SCANNING A SPECTRUM
B - FINISH SCANNING A SPECTRUM
AIRCRAFT FLIGHT PATH
A
B
SEA SURFACE
WHITECAPS

FIGURE I.

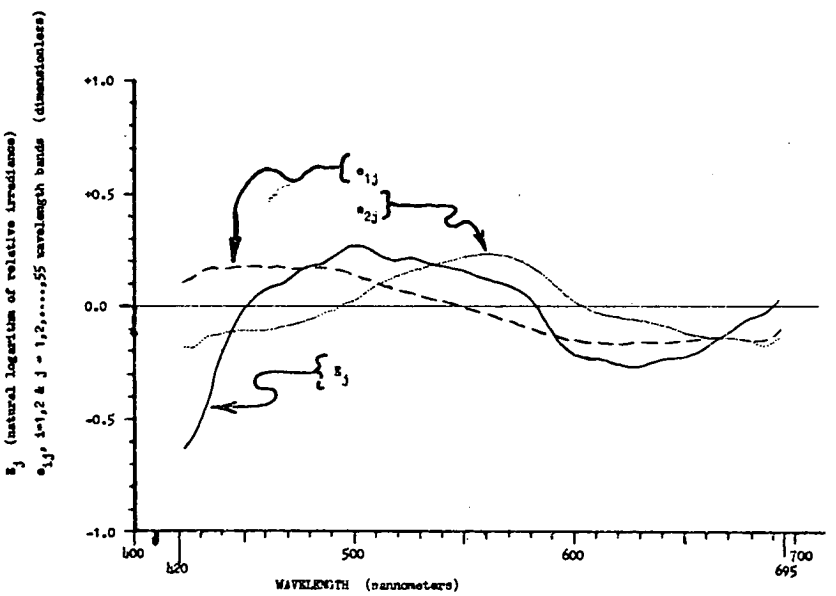

THE EIGENSTRUCTURE OF OCEAN COLOR, as determined from a sample of 31 mean spectra.

E_j = EIGENSYSTEM ORIGIN, taken to be the SAMPLE MEAN VECTOR

e_{ij} = FIRST (i = 1) & SECOND ORTHONORMAL BASIS VECTORS of the EIGENSYSTEM, computed as the first two EIGENVECTORS OF THE SAMPLE COVARIANCE MATRIX

FIGURE II.

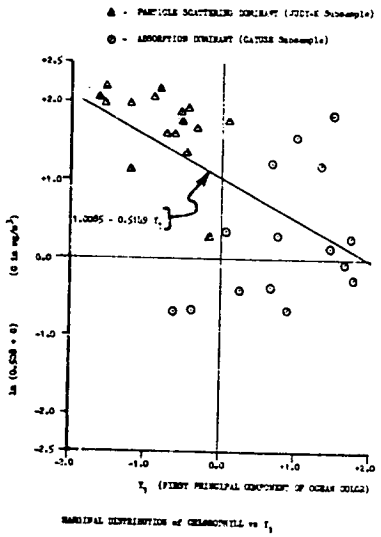

FIGURE III(a)

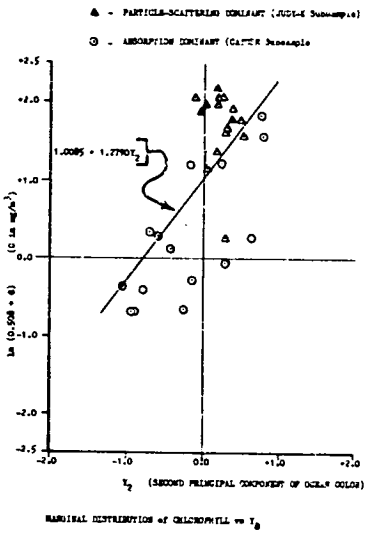

FIGURE III (b)

TABLE I

CHLOROPHYLL CONCENTRATION and the PRINCIPAL COMPONENTS OF OCEAN COLOR

MULTIPLE REGRESSION ANALYSIS RESULTS

$\ln (0.508 + C) = 1.0085 - 0.5149\ Y_1 + 1.2790\ Y_2$

Significant at the 0.005 level.

$R^2 = 0.77$ (percent of variance in chlorophyll concentration accounted for by the regression equation)

$R = 0.88$

$S_{c.y} = \pm 1.62$ mg-chl/m^3 (standard deviation from regression plane)

$S_{c.y} = 19\%$ of sample range.

Simultaneous Confidence Limits on Regression Coefficients:

97.5% CI on β_1 : $-0.9487 \leq \beta_1 \leq -0.0811$

97.5% CI on β_2 : $0.4487 \leq \beta_2 \leq 2.1093$

C = Sum of chlorophylls a, b, and c averaged over secchi depth, which is assumed equal to color producing depth.

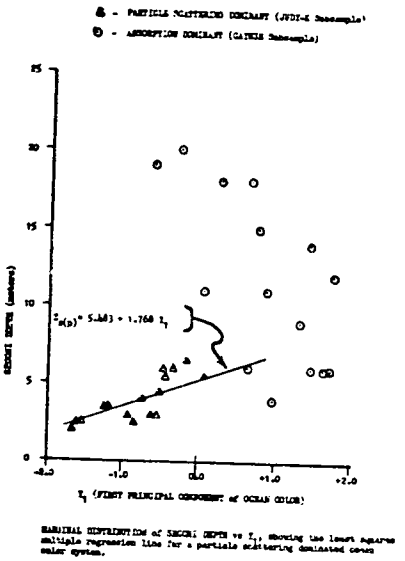

MARGINAL DISTRIBUTION of SECCHI DEPTH vs Y_1, showing the least squares multiple regression line for a particle scattering dominated ocean color system.

FIGURE IVa

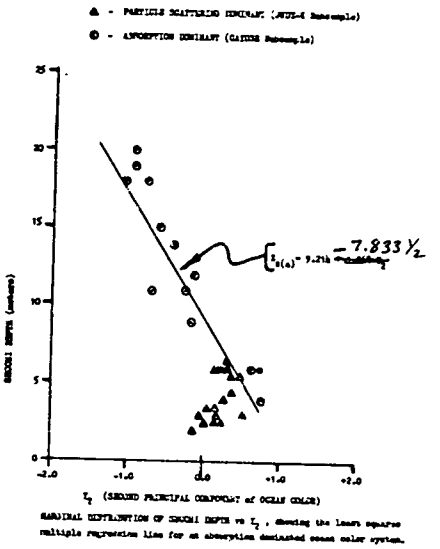

MARGINAL DISTRIBUTION OF SECCHI DEPTH vs Y_2, showing the least squares multiple regression line for an absorption dominated ocean color system.

FIGURE IVb

TABLE II

(a)

MULTIPLE REGRESSION ANALYSIS RESULTS

$Z_{s(p)} = 5.883 + 1.768\ Y_1$ (meters)

Significant at the 0.01 level.

$R^2 = 0.55$ (percent of sample variance in $Z_{s(p)}$ accounted for by the regression equation)

$R = 0.74$

$S_{o.y} = \pm 0.98$ meters (standard deviation from regression line)
$S_{o.y} = 25\%$ of sample range.

Simultaneous Confidence Limits on Regression Coefficients:

90% on β_1: $0.341 \leq \beta_1 \leq 3.195$

90% CI on β_0 included zero, indicating that secchi depth is not significantly correlated with Y_1 in a particle scattering dominated ocean color system.

(b)

MULTIPLE REGRESSION ANALYSIS RESULTS

$Z_{s(a)} = 9.214 - 7.833\ Y_2$

Significant at the 0.005 level.

$R^2 = 0.82$ (percent of variance in $Z_{s(a)}$ accounted for by the regression equation.)

$R = 0.90$

$S_{o.y} = \pm 2.152$ meters (standard deviation from regression line.)
$S_{o.y} = 13\%$ of sample range

Simultaneous Confidence Limits on Regression Coefficients:

90% CI on β_1 included zero, indicating that secchi depth is not significantly correlated with Y_1 in an absorption dominated ocean color system.

95% on β_2: $-11.991 \leq \beta_2 \leq -1.675$

SECTION 106

SURFACE TRUTH MEASUREMENTS OF OPTICAL PROPERTIES OF THE WATERS IN THE NORTHERN GULF OF CALIFORNIA

by

Roswell W. Austin
Visibility Laboratory
Scripps Institution of Oceanography
University of California, San Diego

ABSTRACT

Due to the clear, cloud-free atmosphere which prevails over the southwestern United States and northwestern Mexico, many excellent photographs of this area have been obtained from Gemini and Apollo space flights. Several of these show the delta of the Colorado River and the northwestern Gulf of California with remarkable clarity. The clearly discernible water coloration in the imagery has led to the suggestion that remote sensing techniques may be usefully applied in such areas to determine bathymetric information.

Measurements of the optical properties of the water in this region obtained on the Fresnel II cruise of the SIO R/V ELLEN B. SCRIPPS in March 1971 showed that generally low transmissivities prevailed and at no station did the beam transmittance for the total water column exceed 2.5×10^{-8}. In such water, no significant portion of the surface light can be attributed to bottom reflection and any correlation between water depth and spectral radiance at the surface must result from secondarily related phenomena.

INTRODUCTION

The availability of space photography of coastal waters has prompted numerous investigators to examine the possibilities of using such imagery to gather information about the near-shore bottom topography and about the coastal water itself. There are many excellent examples of Gemini and Apollo photography where bottom features are clearly and unmistakably discernible. Demarcations between deep water and shoal water areas can be readily determined. Features

visible within the shoal water areas can be located for subsequent investigation from surface vessels. Other space photography of coastal areas has shown marked water coloration features which can be interpreted as being due to turbid water effluent from rivers and harbors. From such photography, much can be learned about the areal extent of sedimentation from river systems and an excellent synoptic insight can be gained into coastwise currents, insight which could probably never be obtained from a surface-vessel survey. However, one cannot always, in a photograph obtained from orbital altitude, differentiate simply between those variations in image density which are caused by bottom effects and those caused by water effects.

A case in point might be the Gemini 5 and Apollo 9 photographs which have been obtained of the northwestern Gulf of California and the delta of the Colorado River. Excellent photography of this area has been acquired because of the high frequency of orbital coverage and because of the unusually high incidence of clear, cloudless days which the region enjoys. The possibility of using such imagery to obtain bathymetric information directly, or as an aid in acquiring such information, has occurred to numerous investigators. Ross (1) using a density slicing scheme, found some interesting correlations between isodensity contours and reported water depths for this area. Yost (2) also examined the Apollo 9 SO65 experiment imagery of this region and found a correlation between image density and water depths up to about 12 meters.

Unfortunately, the spatial variations in the radiance of the ocean surface, which after modification by the atmosphere are responsible for the image density pattern in the space photograph, are not solely dependent on water depth. Obviously variation in bottom reflectance and in the transmission and reflectance properties of the overlying water will also affect the radiance exiting the water surface. It is, therefore, necessary to demonstrate that these properties are essentially invariant over the region of interest in order to relate uniquely the radiance at the water surface to water depth. We will show that in the northwestern Gulf of California the water properties were not only highly nonuniform but the optical transmittance of the total water column was so low at all locations for which measurements are available that no significant portion of the surface radiance was attributable to light leaving the bottom.

DESCRIPTION OF REGION

The Gulf of California is roughly 600 nautical miles long and averages less than 100 miles in width. In the south, depths as great as 3700 meters are found, while in the north above Tiburon Island, depths are mainly less than 200 meters. In the extreme northern end, sediments from the Colorado River have reduced the depth to less than 40 meters over extensive areas (3). The Colorado River no longer transports any significant quantities of river detritus into the Gulf, however. Since 1935, the formerly large river detrital load has been trapped in Lake Mead. Much of the river water below Hoover Dam has been diverted to agricultural uses for many years and only a minor portion of the total river flow now reaches the Gulf of California (4).

The size and shape of the Gulf provides a resonant system to the semi-diurnal tidal cycle with the result that an 8 to 10 meter tidal range is found in the northern reaches of the Gulf. When the river was still active, spring tides were accompanied by a tidal bore 2 to 3 meters high that swept up the river estuary at speeds of 6 to 8 knots (4). Now, this tidal action on the silted bottom and mud flats of the estuary serves to keep a tremendous sediment load in continual circulation. Tongues of turbid water appear near the surface at the river mouth and farther south flow on the bottom or at intermediate depths with clearer water overlying them.

SURFACE TRUTH MEASUREMENTS

In March 1971 the Visibility Laboratory of the Scripps Institution of Oceanography (SIO) conducted a program of measurements of the optical properties in the waters of the Gulf of California. This cruise, named Fresnel II, was conducted on the SIO R/V ELLEN B. SCRIPPS. The track for the complete cruise is shown in Fig. 1. Stations 8, 9 and 10 were located at the northern end of the Gulf. Two transects were made across the Gulf on successive days, the first at 31° North and the second at 31° 20' North. Stations were made at approximately 30-minute intervals along each of the transects (Fig. 2). Individual stations were designated 8A through 8S and 9A through 9P.

At each station, a vertical profile of the water transmissivity at a wavelength of 530 nanometers was obtained with the Visibility Laboratory transmissometer (5). This instrument provides an output on an

"x-y" plotter of the transmittance per meter for image-forming light as a function of depth. A thermistor sensor and a second pen provide a simultaneous record of the temperature profile. At each location, a subjective color determination was made against a Munsell color scale. At noon on each day, a longer station, 8-I and 9-I, was maintained while transmittance profiles were obtained at five discrete wavelengths from 450 nanometers to 611 nanometers. At these noontime stations, the Scripps submersible spectroradiometer (6) was used to determine the downwelling spectral irradiance at two depths and the upwelling spectral irradiance at two depths over the wavelength range from 350 to 700 nanometers. While transiting between stations, a continuous record was obtained of the water depth with a precision depth recorder. Station locations were determined by radar fixes on Rocas Consag in the middle of the Gulf and on prominent shore features.

Figure 3 shows a vertical section along the track at 31° North latitude. The solid bottom contour between stations A and S represents our determination of bottom depth. The dotted line is bathymetry which was presented by Thompson in 1965 (4).

Figure 4 is a transmissometer profile showing the transmittance per meter as the ordinate plotted against depth for Station 8-C. Note that the surface transmission is 70 per cent per meter, but that below 4 meters the transmission drops abruptly to less than 1 per cent per meter at 10 meters and continues at essentially zero transmission until the bottom is found at 23-1/2 meters. Only 2×10^{-6} of the image-forming light starting up from a depth of 10 meters will reach the surface without scattering or absorption. The transmission of the remaining 13-1/2 meters is below the measuring capability of our instrumentation. We can state without equivocation, however, that no sensible image-forming light was reaching the surface under this circumstance. The implication of this curve is that there is a moderately clear layer of water overlying a heavy, silt-laden tidal current. The same types of profiles were found at the western stations on both days. The surface water on this station, No. 8-C, was clearer than the ones to the west and north, however. The next profile, Fig. 5, obtained at Station 8-K, shows much more structure in the vertical column, but again we have clear water at the surface overlying layers of varying turbidity and a second layer of relatively clear water between 55 and 65 meters. An image of a feature on the bottom here would be attenuated by about 5×10^{-33} before reaching the surface.

Figure 6 shows the vertical section at 31° 20' North, along the track of the northernmost transect on March 23. The transmittance

profiles on the east shore showed evidence of more vertical mixing, as they had relatively uniform transmittances all the way to the bottom. Transmissivities were generally between only 10 and 30 per cent per meter in this area. Station 9-D was somewhat clearer, however, with transmittances upward of 54 per cent per meter near the surface (Fig 7). This station had the highest total path transmission of any of the stations on the two transects. The total vertical column transmittance for an image at this station was still only 2.5×10^{-8}.

The profile in Figure 8 was obtained at Station 9-J and again shows a reasonably clear layer at the surface with an underlying layer of very turbid water at a depth of about 10 meters. Such a layer not only attenuates bottom images being transmitted through it, but because of its sediment content, it has a higher reflectivity than the overlying water and it might well give a radiometric signal that could be misinterpreted ascoming from the bottom.

DISCUSSION

In order to remotely sense water depth, the change in the sensed signal resulting from a depth change equal to the required resolution of the measurement must be larger than those signal changes caused by variations in bottom reflectance or water properties. The effective reflectance of the bottom will change with the type of sands, silts, rocks, etc.; with the roughness and general morphology of the area; and very markedly with the presence or absence of bottom vegetation. The primary water properties involved are the volume absorption coefficient and the volume scattering coefficient. Changes in these will affect both the amount of light reaching the bottom and the attenuation of the reflected light on its return passage to the surface. Additionally, changes in the scattering properties will result in changes in the reflectance of the water as suggested in the previous section.

Information about the bottom reflectance of this region of the Gulf is quite limited. The bottom is composed of sands, silts, and clays in various combinations. They are mostly of terrigenous origin with only a small fraction of biogenous material. The color of those bottom samples reported by Thompson (4) and of the four samples obtained on the Fresnel II cruise were all very similar. The reflectance of all samples as determined by comparison with the Munsell color scale, and for one sample by measurement with a reflectometer, was between 12 and 13 per cent. The incidence of rocks is undoubtedly very small because of the deep layers of sediment deposited by the

Colorado River. The continued scrubbing action of the strong tidal currents prevents extensive growth of bottom vegetation.

Separate absorption and scattering data for the 36 stations in the northern Gulf were not obtained, as such measurements would have been difficult and too time-consuming. Instead, the beam transmittance profiles discussed under "Surface Truth Measurements" were obtained, from which the total volume attenuation coefficient may be computed.

This attenuation coefficient is the sum of the absorption and scattering coefficients and with it one may compute the transmittance of image-forming light through the water column. This is the transmittance for those portions of an image subtending small angles, i.e., for the high spatial frequencies. To compute the transmittance for the general or average radiance level of its bottom, i.e., for the low spatial frequencies in the image, the attenuation coefficient for the diffuse light field must be used. This was determined from the measurements of ambient spectral irradiance versus depth obtained with the submersible spectroradiometer at the two noontime stations. It was found that the attenuation coefficient for irradiance determined by this method was one-fifth the attenuation coefficient for image-forming light, as determined from the transmissometer data, when computed for the same wavelength and over the same water path. It will be assumed that this ratio prevailed at all depths and for all stations in this region.

The need for scattering coefficient data can be eliminated by a direct determination of the water reflectance. This may be accomplished by taking the ratio of the upwelling spectral irradiance to the downwelling spectral irradiance as measured at a single depth by the spectroradiometer. Using the irradiances measured at about 5 meters the reflectances at 530 nanometers were between 1.3 and 1.5 per cent for the two noontime stations.

The above concepts are shown in analytical form in the following. Reference should be made to Fig. 9 for explanation of the terminology. The daylight irradiance, $H_{-}(0)$, incident on a plane just below the water surface is transmitted to the bottom at depth Z_b with a transmittance for the total path ${}_{*}T$. The resulting irradiance on the bottom is

$$H_{-}(Z_b) = {}_{*}T \times H_{-}(0).$$

This is reflected upward by the bottom reflectance ${}_{b}R$, resulting in an upwelling irradiance at the bottom of $H_{+}(Z_b)$ which may be written as

$$H_{+}(Z_b) = {}_{*}T \times {}_{b}R \times H_{-}(0).$$

Now the parameter of interest is the upwelling bottom radiance,

$$ {}_bN_+(Z_b). $$

As the bottom will approximate a diffuse or lambert reflector, this radiance may be written as

$$ {}_bN_+(Z_b) = \frac{H_+(Z_b)}{\pi} = {}_*T \times {}_bR \frac{H_-(0)}{\pi} . $$

If the bottom is essentially featureless so that the average radiance level of the bottom rather than image details of high spatial frequencies is to be transmitted, then the bottom radiance will be transmitted upward with the same diffuse transmittance ${}_*T$ used to determine the transmission of irradiance to the bottom. Therefore we may write

$$ {}_bN_+(0) = {}_*T^2 \, {}_bR \quad \frac{H_-(0)}{\pi} $$

for the component of the radiance just below the surface due to the bottom.

Added to this will be the upwelling radiance contributed by the water ${}_wN_+(0)$. Here also we can make the assumption that the angular reflectance properties of the water are such that we can treat it as a diffuse reflector and therefore write

$$ {}_wN_+(0) = {}_wR \frac{H_-(0)}{\pi} . $$

Fortunately ${}_wR$ is not strongly dependent upon depth so that we may use the values computed from irradiance measurements at 5 meters to approximate the reflectance just below the surface.[1]

Summing the contributions from the water and the bottom, the total upwelling radiance at the surface is

$$ {}_tN_+(0) = {}_bN_+(0) + {}_wN_+(0) $$
$$ = \left[{}_*T \, {}_bR + {}_wR \right] \frac{H_-(0)}{\pi} . $$

---

[1] It should be noted that the effect of interreflection of the upwelling light at the surface is neglected in this development for simplification. Although this effect is not trivial in general, its neglect here does not affect the conclusions.

The radiance ${}_tN_+(0)$ is the signal which, after passage through the atmosphere, is remotely sensed and therefore must be functionally related to depth. The diffuse transmittance, ${}_*T$ is, of course, the variable which is depth dependent. Using the five to one ratio found between the attenuation coefficients for image forming and diffuse light the transmissometer profile data was used to compute diffuse transmittances for the total water column, ${}_*T$ at all stations. The highly nonuniform nature of the transmittance profiles as shown in the examples given in Figs. 4, 5, 7 and 8 results in ${}_*T$ values for the various stations which are more dependent on water properties at the particular location than on water depth. Moreover the ${}_*T^2$ term at all stations was so small that radiance resulting from the water reflectance was overwhelmingly larger than that from the bottom, i.e.

$$ {}_wN_+(0) >> {}_bN_+(0). $$

We have placed the requirement that the horizontal variability in ${}_*T$, ${}_bR$, ${}_wR$ and $H_-(0)$ must result in smaller changes in ${}_tN_+(0)$ than the change which results from a depth increment equal to the resolution of the measurement. It is patently clear that at the 36 stations where surface truth data was obtained the requirement cannot be met.

If we define a ratio F such that

$$ F = \frac{{}_bN_+(0)}{{}_tN_+(0)} , $$

then

$$ F = \frac{{}_bR \times {}_*T}{{}_bR \times T^2 + {}_wR} . $$

For the cases where ${}_wN_+(0) >> {}_bN_+(0)$

$$ F = \frac{{}_bR \times {}_*T^2}{{}_wR} $$

The ratio, F, was calculated for all stations. It was never larger than .01, meaning that at no station on the track did the bottom irradiance signal contribute as much as 1 per cent to the total signal available from the water surface. Thus 99 per cent of this radiance had its genesis in the backscatter from the water itself. Under these circumstances the remote sensing technique may be useful for delineating and tracing turbid water but is unlikely to be of significant value for bathymetric purposes.

One additional interesting computation was performed which illustrates the problem of estimating depth in water with variable transmittance properties. Assuming a bottom with uniform 13 per cent reflectance and a water mass with uniform 1.3 per cent reflectance the depth was computed at each station such that F = 0.01. Actual beam transmittance profile data was used with the five to one coefficient conversion mentioned earlier. If the water were uniform in transmittance--which is the assumption which must be made for remote sensing--the depth would be constant. Figs. 10 and 11 show how this imaginary bottom varied in depth due to the water variability.

CONCLUSIONS

Only under circumstances where the variability in bottom reflectance, water reflectance and water transmittance is small over the area of interest can water depth be effectively sensed remotely. Under most situations the signal at the surface which originated at ocean floor must be much larger than that component of the signal generated by backscatter from the water.

In areas such as the delta of the Colorado River, where tidal currents carry tremendous sediment loads rendering the water essentially opaque, any correlation between the sensible variations in the image of the water area and bottom topography must be attributed to secondary relationships as, for example, the proximity to the surface of a reflective, silt-laden tidal current.

REFERENCES

(1) Ross, Donald S., Image-Tone Enhancement, Technical Papers from the 35th Annual Meeting of the American Society of Photogrammetry, March 1969, p. 319.

(2) Yost, Edward, R. Anderson and S. Wenderoth, Co-Investigator Report: NASA Apollo 9 S065 Experiment Multispectral Terrain Photography, Long Island University, Science Engineering Research Group, C. W. Post Center, Greenvale, New York, Jan. 1970, pp. 162-185.

(3) Rusnak, Gene A., Fisher, R. L., Shepard, F. P., Bathymetry and Faults of Gulf of California, Marine Geology of the Gulf of California - A Symposium, Memoir No. 3, The American Association of Petroleum Geologists, 1964.

(4) Thompson, Robert W., Tidal Flat Sedimentation on the Colorado River Delta, Northwestern Gulf of California (Ph. D. dissertations), SIO, UCSD, 1965.

(5) Petzold, T. J., and R. W. Austin, An Underwater Transmissometer for Ocean Survey Work, Scripps Institution of Oceanography, SIO Ref. 68-9, April 1968.

(6) Tyler, John E., and R. C. Smith, Measurements of Spectral Radiance Underwater, Gorden and Breach Science Publishers, New York, 1970.

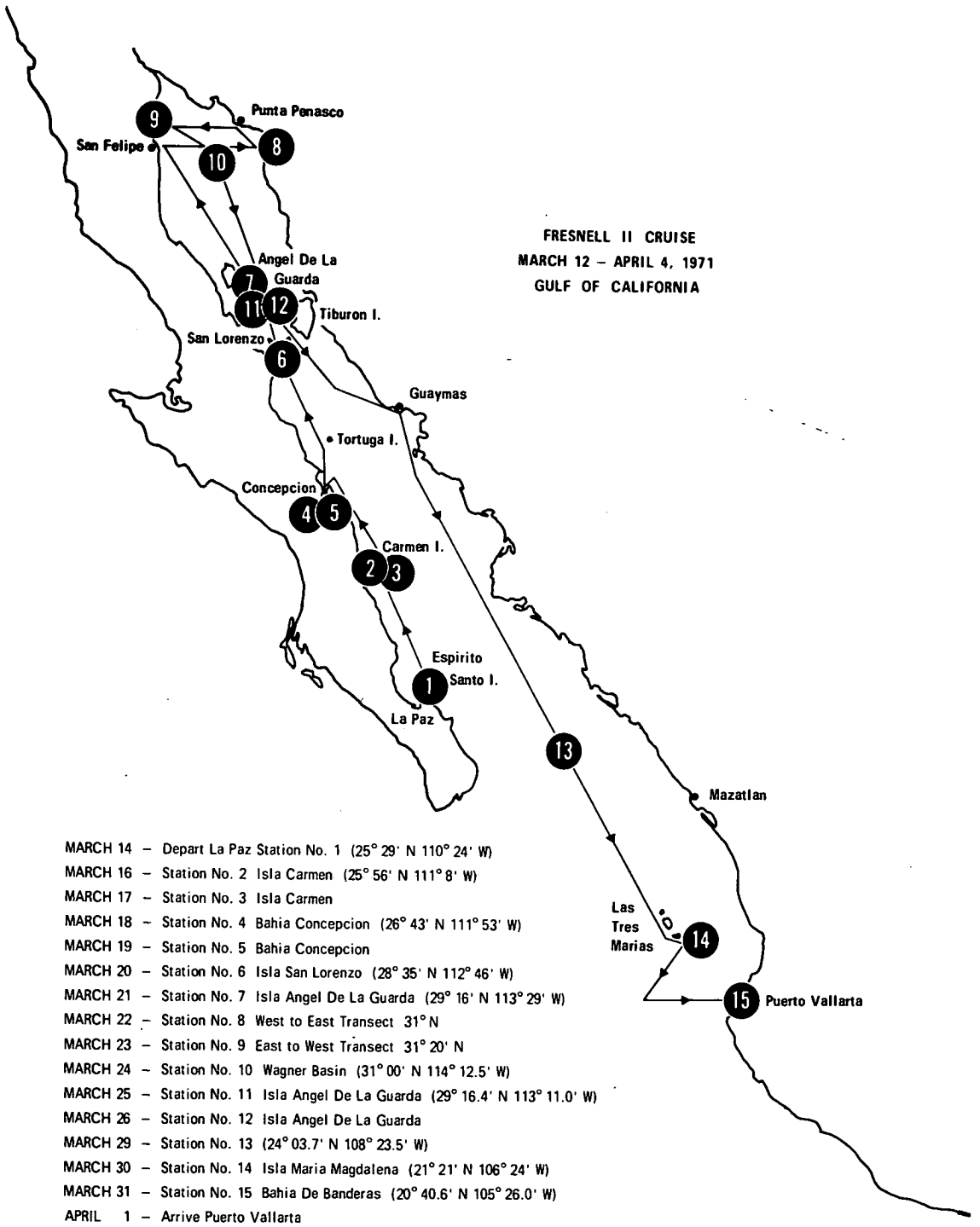

MARCH 14 – Depart La Paz Station No. 1 (25° 29' N 110° 24' W)
MARCH 16 – Station No. 2 Isla Carmen (25° 56' N 111° 8' W)
MARCH 17 – Station No. 3 Isla Carmen
MARCH 18 – Station No. 4 Bahia Concepcion (26° 43' N 111° 53' W)
MARCH 19 – Station No. 5 Bahia Concepcion
MARCH 20 – Station No. 6 Isla San Lorenzo (28° 35' N 112° 46' W)
MARCH 21 – Station No. 7 Isla Angel De La Guarda (29° 16' N 113° 29' W)
MARCH 22 – Station No. 8 West to East Transect 31° N
MARCH 23 – Station No. 9 East to West Transect 31° 20' N
MARCH 24 – Station No. 10 Wagner Basin (31° 00' N 114° 12.5' W)
MARCH 25 – Station No. 11 Isla Angel De La Guarda (29° 16.4' N 113° 11.0' W)
MARCH 26 – Station No. 12 Isla Angel De La Guarda
MARCH 29 – Station No. 13 (24° 03.7' N 108° 23.5' W)
MARCH 30 – Station No. 14 Isla Maria Magdalena (21° 21' N 106° 24' W)
MARCH 31 – Station No. 15 Bahia De Banderas (20° 40.6' N 105° 26.0' W)
APRIL 1 – Arrive Puerto Vallarta

Figure 1. – Track of Fresnell II Cruise.

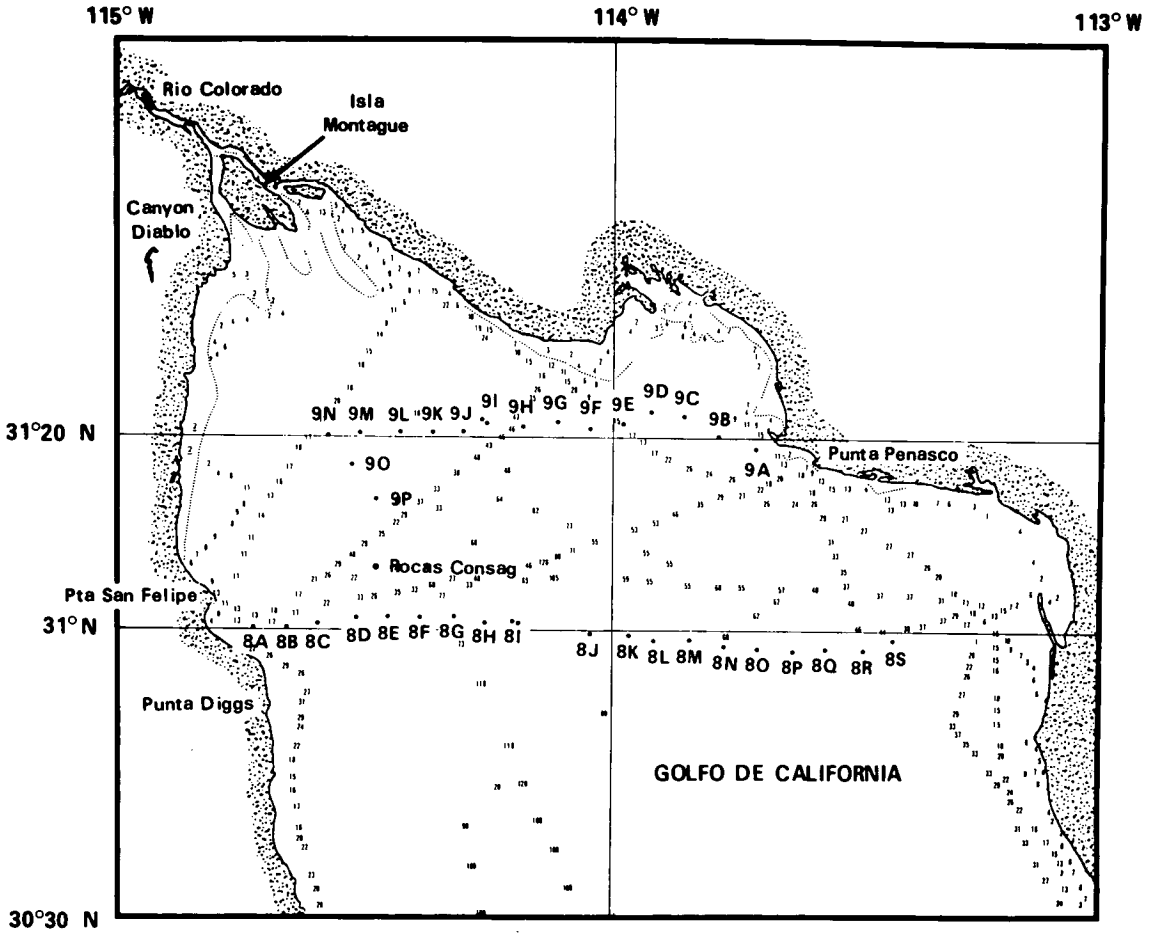

Figure 2. – Locations for Stations 8 and 9 at the northern end of the Gulf of California.

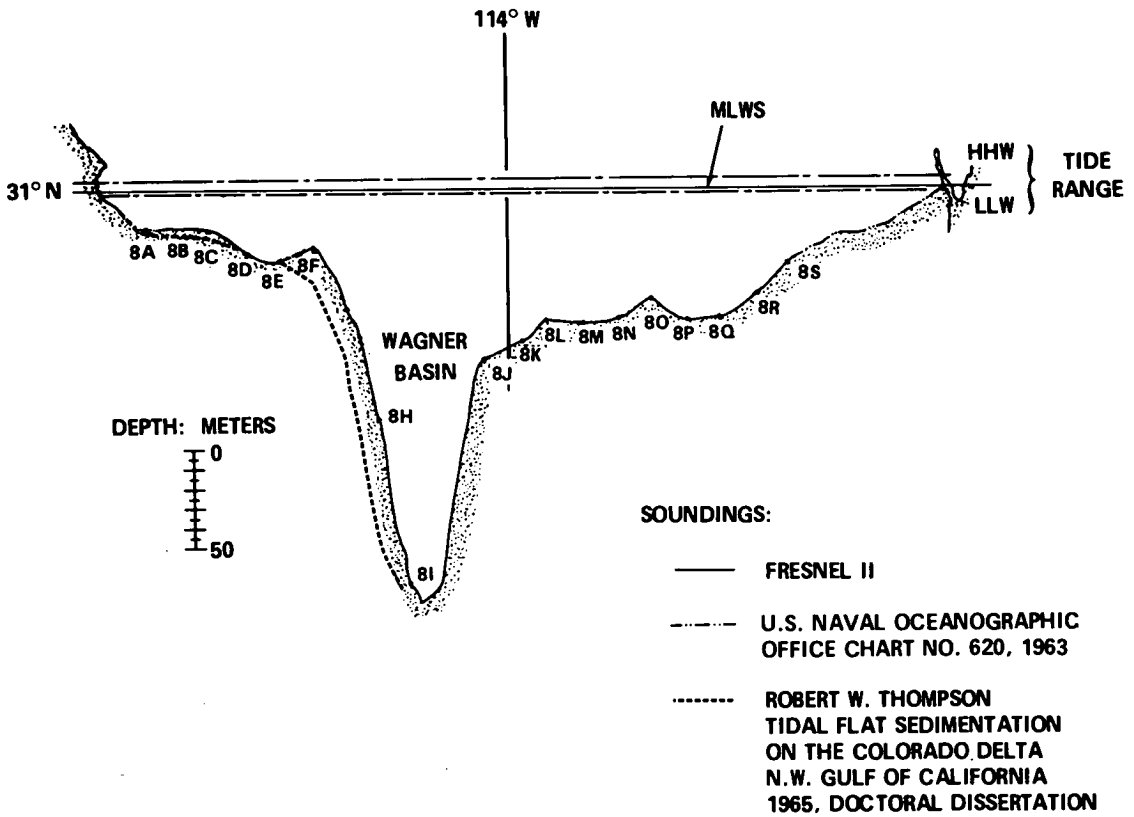

Figure 3. – Depth profile of a section through the Gulf of California at 31° North latitude. Stations 8A – 8S, March 22, 1971.

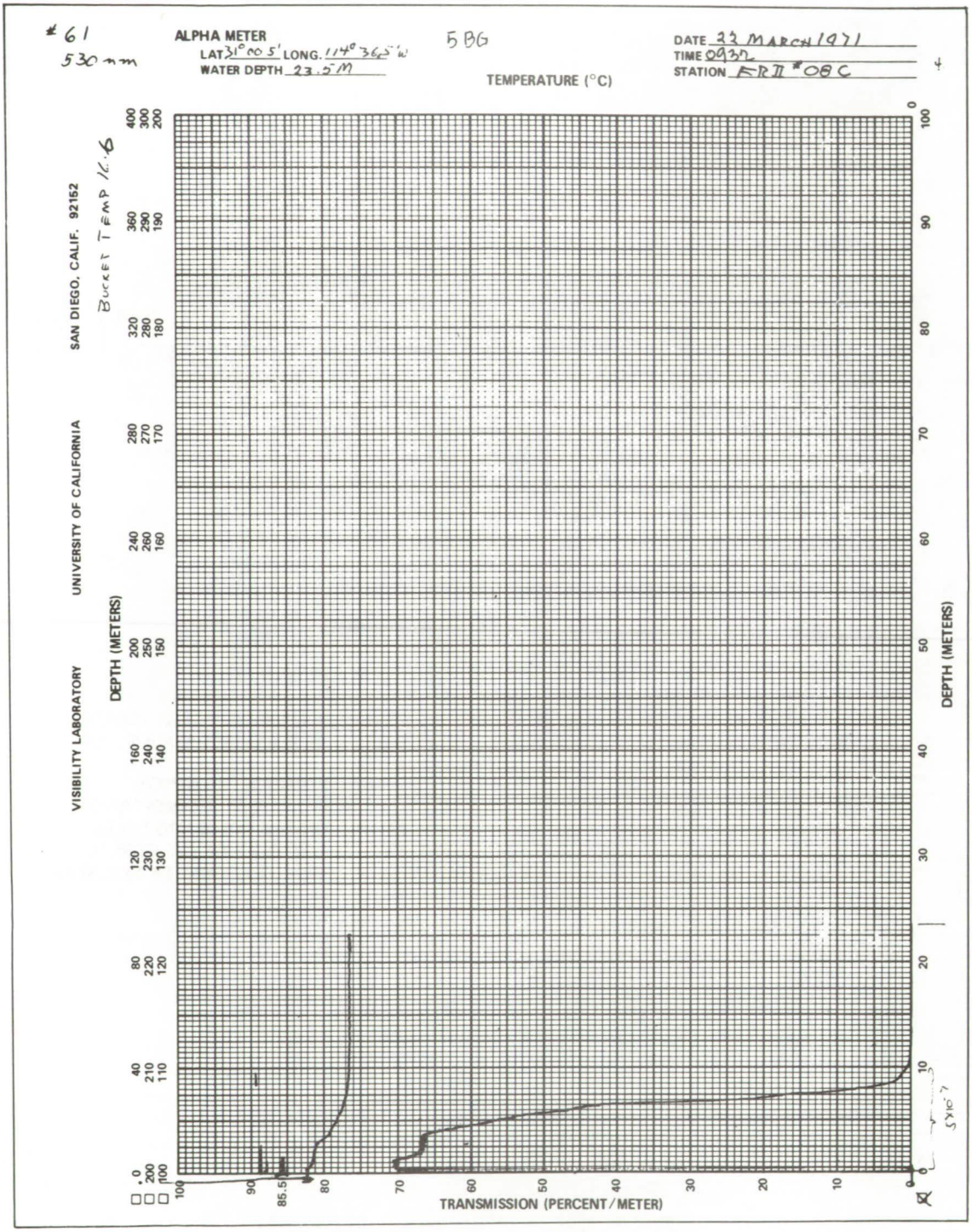

Figure 4. – Profile of transmittance and temperature versus depth at Station 8C.

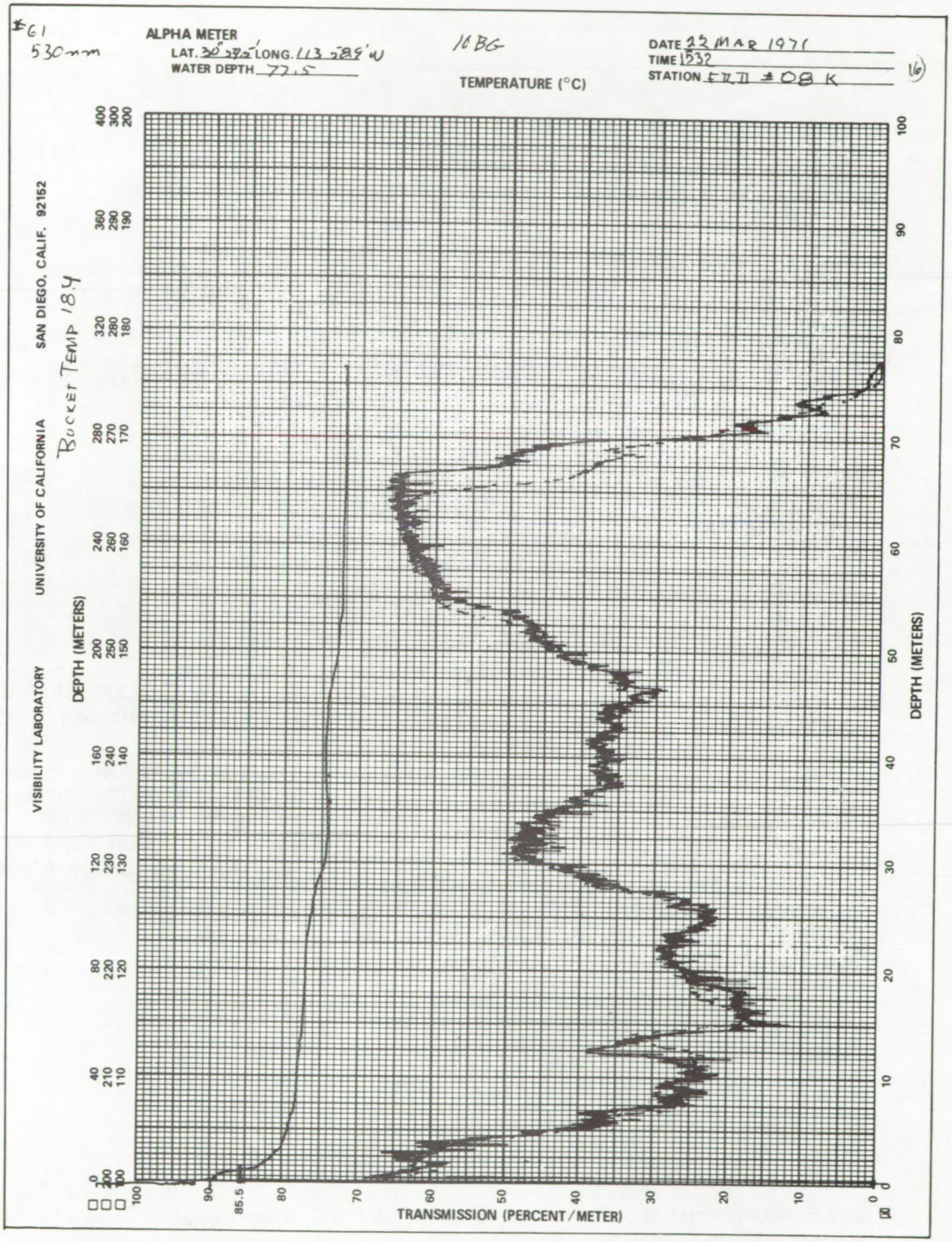

Figure 5. – Profile of transmittance and temperature versus depth at Station 8K.

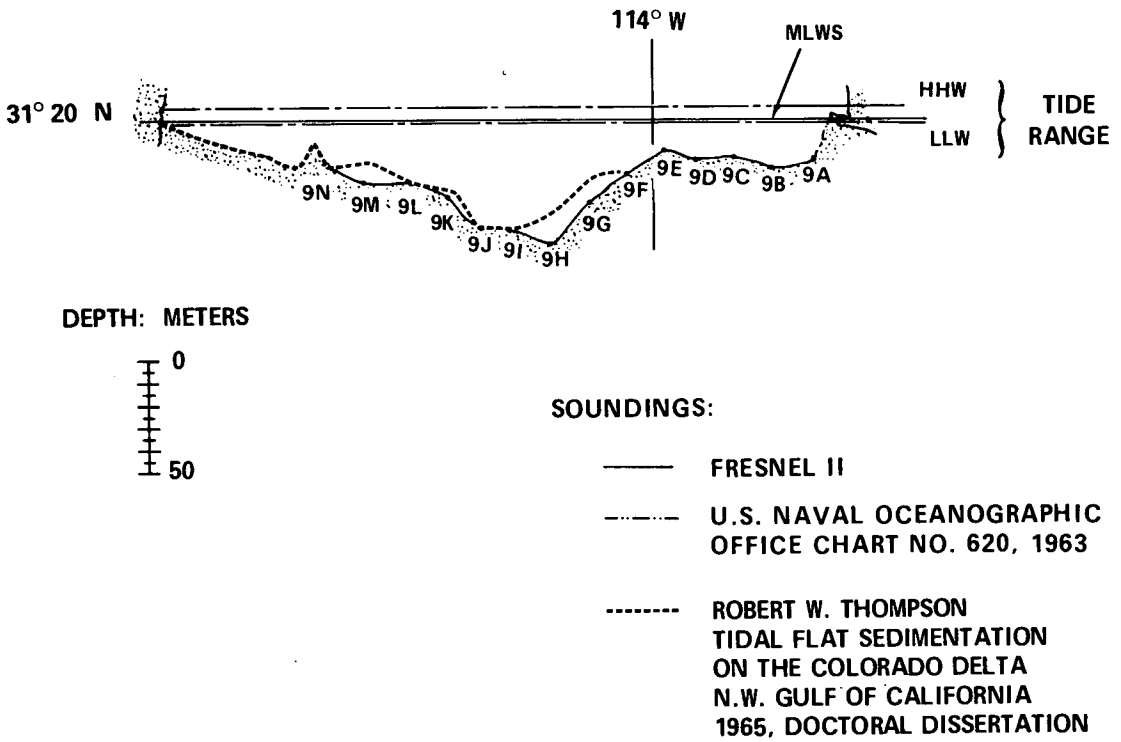

Figure 6. – Depth profile of a section through the Gulf of California at 31° 20' North latitude. Stations 9A – 9N, March 23, 1971.

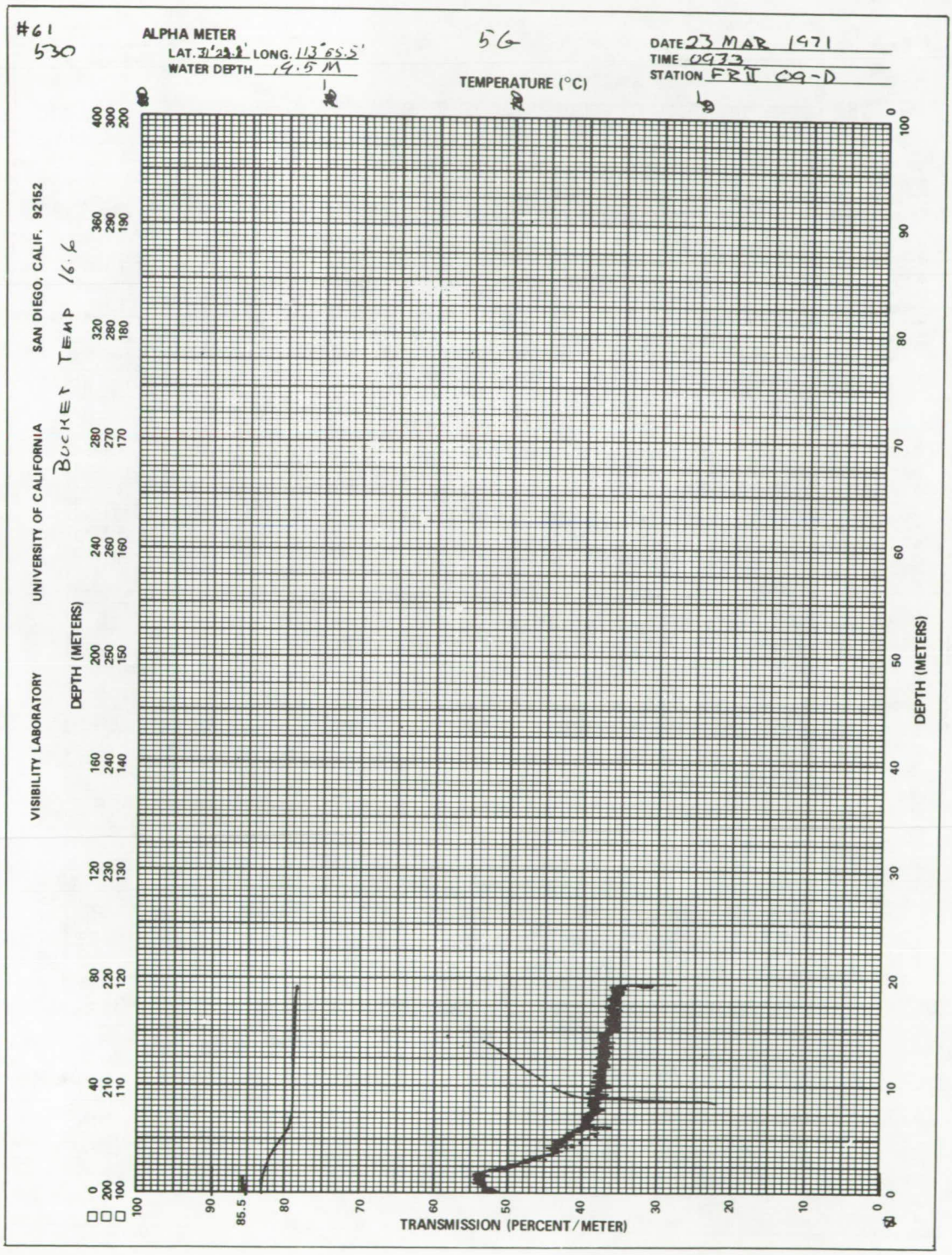

Figure 7. – Profile of transmittance and temperature versus depth at Station 9D.

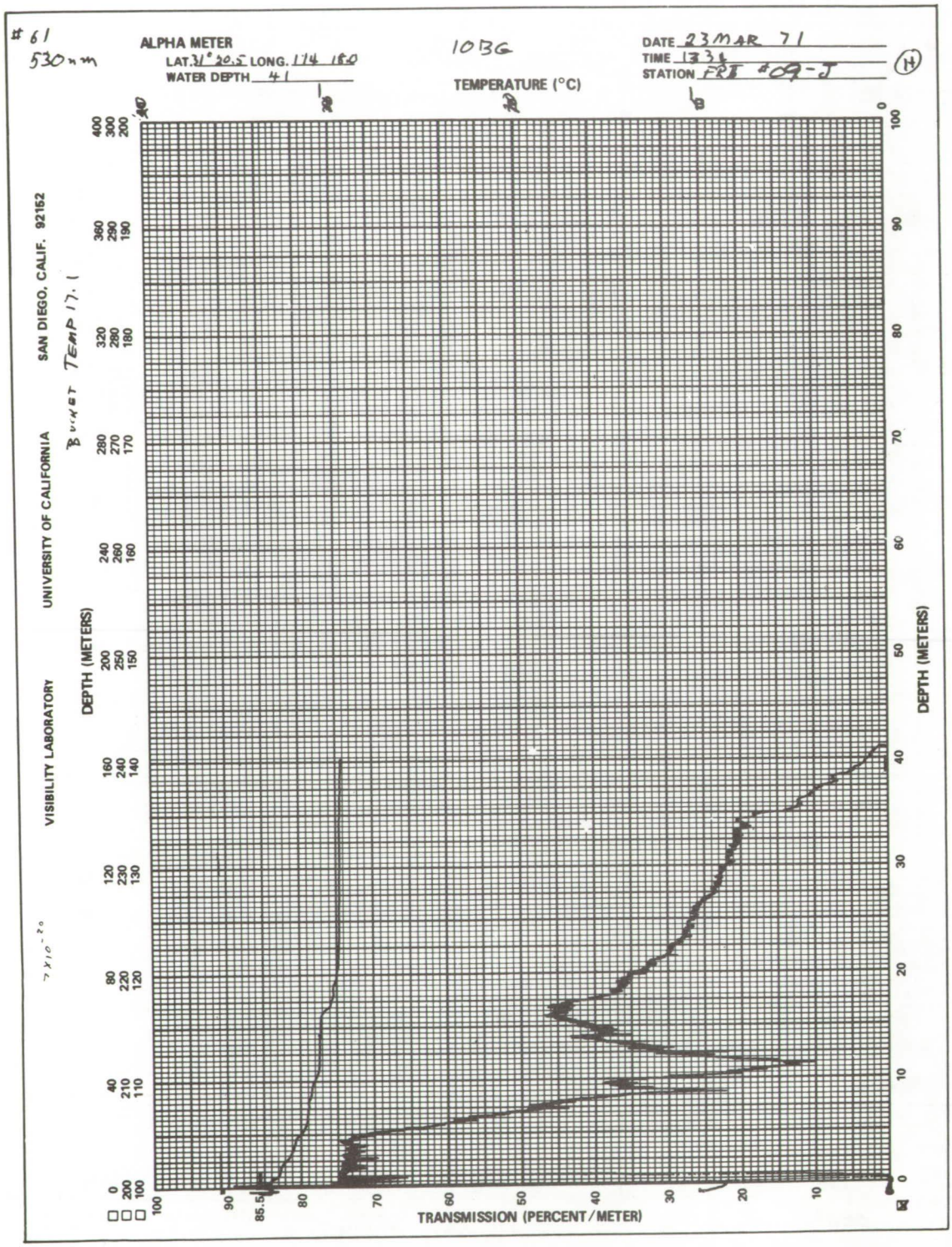

Figure 8. – Profile of transmittance and temperature versus depth at Station 9J.

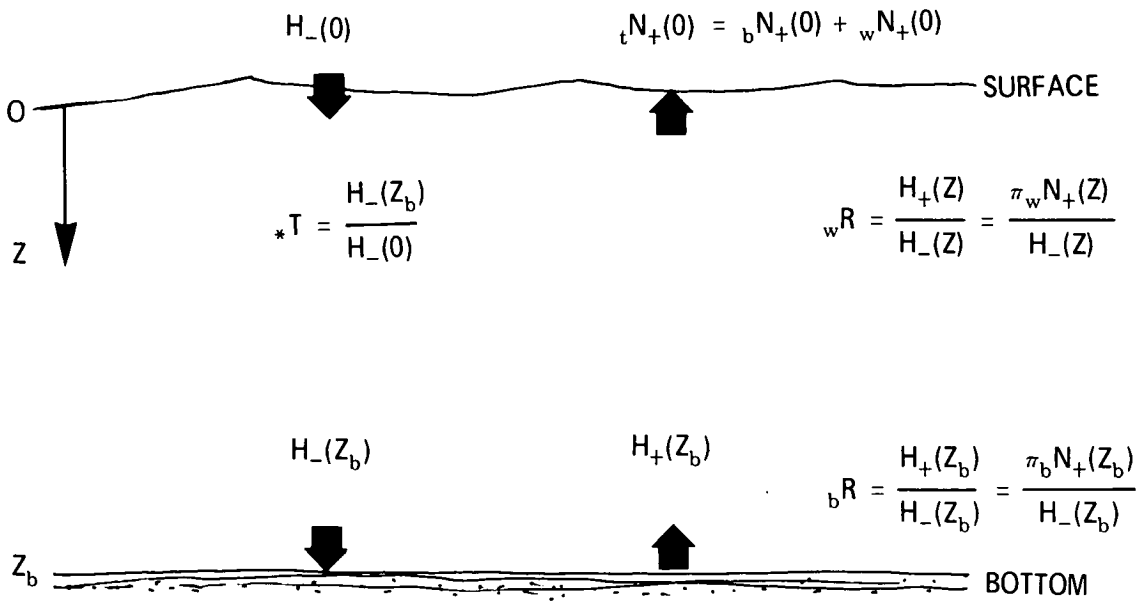

Z	Depth, O-Surface, Z_b Bottom Depth
$H_-(Z)$	Downwelling Irradiance at Depth Z
$H_+(Z)$	Upwelling Irradiance at Depth Z
$N_+(Z)$	Upwelling Radiance at Depth Z
$*T$	Irradiance (or Diffuse Light) Transmittance for Z_b
$_wR$	Water Reflectance
$_bR$	Bottom Reflectance

Figure 9. – Definitions and Symbology.

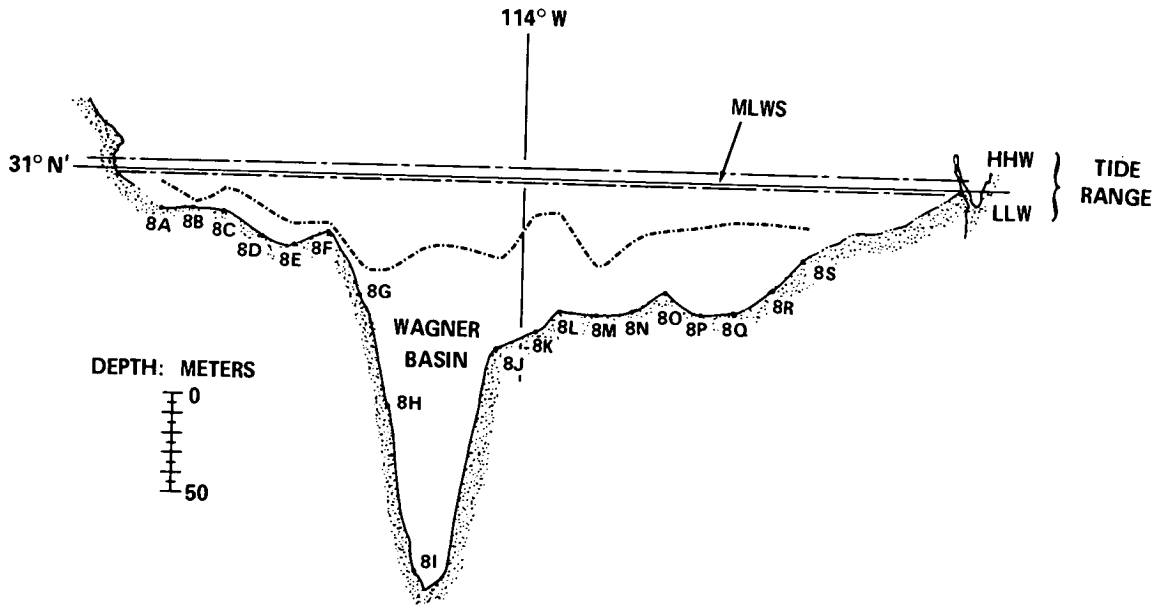

Figure 10. – Section through the Gulf of California at 31° North latitude. Dotted line shows bottom contour necessary in order for bottom to contribute 1 percent to the total upwelling radiance.

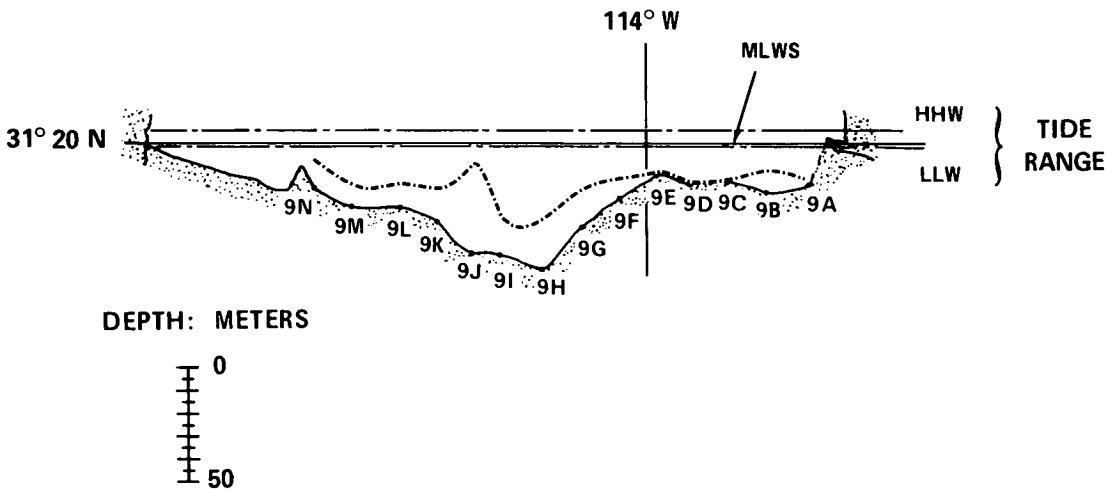

Figure 11. – Section through the Gulf of California at 31° 20' North latitude. Dotted line shows bottom contour necessary in order for bottom to contribute 1 percent to the total upwelling radiance.

SECTION 107

PRACTICAL UTILITY OF THE BLUE SPECTRAL REGION

by

Donald S. Ross
Vice President
International Imaging Systems
Mountain View, California

INTRODUCTION

Optical filters have been used in aerial photography to reduce the effects of atmospheric luminance (haze), thereby improving contrast and apparent spatial resolution in images intended for visual interpretation. Unfortunately, such filters also prevent the recording of scene radiances in the blue spectral region below 500nm.

Interpretation is, however, no longer dependent on visual methods, and many devices and techniques are now available for detecting image data which are below the threshold of visual recognition.(1)

In oceanography, information of vital scientific and economic importance is in the 400-500nm band; information on water clarity, color, biological activity, depth, bottom composition and topography, currents, sediment transport and many other features is found in the blue region.

It had been thought that atmospheric effects would completely degrade scene radiance values in blue spectral records taken from altitudes above 50,000 feet, particularly from space platforms. Gemini, Apollo and NASA/Ames U-2 photography show this is not invariably the case.

Some aspects of multispectral photography in the blue region are discussed briefly, and sample images from past and present work are submitted to demonstrate the potential utility of the blue multispectral record for oceanography.

Much of the work reported herein has been supported by past contracts with NAVOCEANO, Spacecraft Oceanography Program, and by the successor organization, NRL Remote Sensing Oceanography Project, on Contract N62306-71-C-0045.

FILTER BANDS, AND LIGHT IN AIR AND WATER

The behavior of light in air and water is a complex subject, touched on briefly here as a reminder of some salient factors affecting remote sensing of ocean subjects. Comprehensive treatments are given in references (2) and (3).

Light in the Atmosphere.- Sunlight incident on the scene, and image light reflected by it toward the camera is scattered and absorbed by atmospheric gasses and aerosols throughout the whole photographic spectrum, including the infrared. Rayleigh scattering is wavelength dependent, is worst in the blue region, and can be predicted. Mie scattering and absorption by aerosol particles which vary widely in size, mixture and concentration on a diurnal and seasonal basis, is seldom predictable, or even measureable in most operational situations. Depending on the aerosol condition, Mie effects can be as serious in the green as in the blue region. Mie scattering is normally the most important contributor to atmospheric haze, and the consequent degradation of image contrast in photography, and depressed S/N ratios in direct radiometric sensing. Limited evidence(4) suggests lower concentrations of aerosols may predominate over open ocean areas. Highest concentrations are probably worst over humid tropical forests, and are least over desert and arid landmasses. Mie scattering is usually restricted to altitudes below 50,000 feet.

In summary, image-forming light in the air is subject to spectral absorption, and scattering; and is embedded in non-image haze-light on its passage to the camera. Degrading effects vary widely in the blue and green regions, but are usually more serious in the former.

Light Transmission in the Water.- Light is attenuated and scattered in the water by process similar to those in the atmosphere, but to a much greater extent.

The water acts as an optical filter, and the spectral passband changes with turbidity. The marked difference between mean oceanic and coastal waters is shown in Figure 1. As turbidity increases attenuation rises sharply and peak transmission shifts toward the longer-wavelength green or yellow region.

Light from the Water.- Where turbidity and scattered light in the water are sufficient to deny deep penetration, the spectrum of light from the water can often be associated with and form part of water color assessment, sediment transporting mechanisms, flow and discharge patterns, upwelling, biological activity and similar phenomena; in this case scattered light can provide useful information.

A calm water surface reflects about 3 to 6% of the diffuse skylight toward the camera at sun altitudes of 30° or above, throughout the visible spectrum. Waves complicate the situation, and also optically refract subsurface detail; hardly of consequence in small-scale imagery.

To recapitulate, light from the subsurface is characterized by low radiance levels viewed through surface effects which lessen an already low subject contrast. The spectral window in average clear water is in the 450-470nm region, and in more turbid water around 530-550nm.

Filter Bands.- Practical experience has shown that red filters which block light below 600nm limit subsurface photographic penetration to a few feet. Useful penetration is obtained in the green region, and filters which transmit in the 500-570nm band are optimum. Light admitted in the 580-600 nm band dilutes green chromatic contrast in additive color analysis by adding yellow, and should be excluded.

Relating these practical considerations to Figure 1, the attenuation coefficients for coastal and ocean waters at 570nm in the green are nominally 0.0032 and 0.001, respectively on the scale illustrated. The same orders of attenuation are found at 490nm for coastal, and 410nm for oceanic waters. A green record acquired in the 500-570nm band would thus be optimum for both water types.

If the same attenuation factors are used to select an equivalent blue band between 400 and 500nm, little if any penetration could be expected in coastal water, but would be at a maximum in clear water between 410 and 500nm, with a peak near 460nm, where the worst atmospheric effects occur.

Lepley[5] analyzed large amounts of Secchi disk data on worldwide coastal water clarity available at the Naval Oceanographic Office and estimated the following:

Percent Transmission per Meter	Secchi Depth	Percentage of World Coastlines
0 - 70%	0 - 5m	15%
70% - 92%	5 - 20m	50%
More than 92%	Over 20m	35%
(More than 95%	Over 30m	10%)

Thus, a large percentage of coastal waters appear to have significant transmission in the blue region.

In any case, where a synoptic image may include 10,000 square miles of ocean, many water classes will be found, and a blue spectral record is required if water color assessment is to be attempted.

NATURAL COLOR AND MULTISPECTRAL OCEAN PHOTOGRAPHY

In view of the behavior of light in the water and air, it would seem doubtful that a useable image for oceanography could be obtained in the blue band. However, there are available hundreds of images taken from space and from high altitude aircraft in NASA files which permit an evaluation of feasibility.

Gemini and Apollo Photography.- Many 70mm images of ocean subjects were made with natural color film on these missions. Figure 2 shows color sensitivity curves for a typical Kodak Ektachrome film and the spectral transmission of a lens of the type used. On some, but not all, missions haze filters were used. These do not substantially reduce the blue passband below 400nm; only the transmission. For example, Wratten haze filters HF-3 and HF-5 combined permit 10%T at 400nm, 40%T at 430nm and 60%T at 490nm. The sensitivity of the blue layer in the color films integrated with lens and filter transmission factors thus permitted a peak response at 430-450nm in the Gemini and Apollo photography, where the worst effects of atmospheric haze should occur.

While natural color film does not record spectral information as accurately as is possible with multispectral systems, its response in the blue, green and red regions can each be separated in the laboratory by simple methods to determine relative spectral scene brightnesses.

Color Separation of Images.- The information potential of the blue spectral region in remote ocean sensing was first reported in 1967[6]. A third generation Gemini V image of the Tongue of the Ocean was color-separated by narrow-band interference filters and control sensitometry, using cloud as the density reference. The photograph is an oblique, taken through more than one air mass. The center of the image is about 140 nautical miles from the camera, and maximum haze effects could be anticipated. Four bands were extracted and were reproduced at the same gamma in Figures 3A (450nm), 3B (500nm), 3C (550nm) and 3D (650nm).

The original separations show that better clear water penetration is obtained at 450nm than at 500nm, and at 500nm than at 550nm, while in the 650nm record only the shallowest or above-water features remain. This is consistent with the known spectral transmission of clear water of this kind, as shown in Figure 1. Also, as expected, the visual contrast is least in the blue and improves with each longer wavelength spectral separation.

The most important point is that, as Figure 3A clearly demonstrates, a great deal of subsurface information was recorded in the blue-sensitive layer of the colorfilm, through the atmosphere. Since 1967, dozens of other ocean images taken from space have been color-separated and similar results have been obtained in the blue band. A few enlarged images are illustrated in Figures 4, 5, and 6.

NASA/Ames U-2 Multispectral Photography.- During 1971, in support of NASA/Ames earth resources photographic operations, an I^2S Mark I Multispectral Camera was flown at 65,000 feet in a U-2 on several occasions over California coastal waters. Considerable haze is normally found in this area. The black-and-white Wratten filter spectral bands were 47B-blue, 57A-green, 25-red, and 88A-infrared. A set of these images is shown in Figure 7. The dominant wavelength of the blue filter is 449.4nm for daylight.

The gammas of the original blue, green and red images are matched within a 1.60 - 1.70 range, preserving the relative scene brightness ratios between the three spectral bands, as received at the camera station. Non-image-forming light in the atmosphere has veiled the blue record, and reduced the contrast of detail to the point where visual interpretation is difficult; this has been rectified in Figure 8 by increasing reproduction contrast to show variations in water radiance which the image actually contains.

Image Pre-Processing. As atmospheric effects seriously reduce ocean scene contrast in the blue and green bands, it is usually necessary to "enhance" the images for maximum utilization during analysis, whether this be by visual, electronic or photographic density-slicing, additive color or other methods now available. The simplest means of pre-processing is to reproduce the image at higher contrast on photographic materials used in process line copy work. A tone reproduction cycle of this kind is shown in Figure 9.

At the lower right (A) the sensitometric spectral response of the blue layer in a positive color transparency has been plotted from a NASA/MSC control tablet. The density positions of two points of interest, shallow and deep water as measured in the image, are noted on the curve, the difference being 0.22. In the first stage of contrast enhancement, the blue image was color-separated from the original on a process film (B) and the density difference between the two water areas was increased to 0.80. The separation negative was then reproduced, again on high-contrast film, to provide a workprint in which the 0.22 density difference of the original is now 1.77; or eight times as great. Density differences as small as 0.01 have become 0.08, and more readily detectible for any method of analysis.(C)

The original film recorded this part of the scene at a gamma of 2.0, that is at twice the scene contrast apparent at the camera station. The workprint has an effective scene gamma of 16.0.(D)

Contrast and Haze: Haze affects the recording of low scene radiances more than higher values with all sensors, causing non-linear distortions in the reproduction(7). While this cannot be corrected unless haze factors are known accurately, increasing contrast in the photographic image in effect improves the ratio significantly between the background noise (haze) and the low radiance levels common in ocean photography.

BLUE SPECTRAL IMAGE ANALYSIS

It is not the purpose of this paper to detail the many specific ways in which a blue spectral record contributes to the analysis of ocean phenomena, but only to show that it is possible to obtain useful imagery in this region from orbital altitudes. Interpretation is a matter for the oceanographer. However, a few practical applications are discussed below.

Water Color Assessment.- The color of water is a key indicator to many ocean phenomena and energy processes. Clear water, barren of biota and inert suspended material, appears deep blue; the degree to which color shifts toward the green indicates an increasing content of plankton, sediment or similar materials. Apparent color may vary with the type of bottom and water depth, mixing of water masses and many other causes. A blue spectral record, which by various methods can be compared with the green record, is required for assessing water color (In coastal waters a red record is also needed for determining the red and brown contributions from estuaries and rivers).

Although the blue image may not be a faithful linear representation of scene radiances, accuracy is not essential if differences between the blue and green bands can be detected; these indicate variations in the water mass from whatever source. In small-scale images, many areas of color variation can be detected rapidly by additive color viewing with high-contrast images. The degree of contrast enhancement depends on the quality of the original, and no set rule can be offered; but contrast should be sufficient for accentuating chromatic differences. The green image suffers from atmospheric distortion effects less than the blue, and usually can be reproduced at a lower contrast.

In additive viewing, false color modes aid detection of color changes. The green record can be projected as red and the blue as blue or green as shown in Figure 10, to more clearly show the patterns of water color change for qualitative evaluation.

Image digitizing and computer processing promise methods for improved quantitative analysis of the blue-green color ratios where atmospheric radiance corrections can be applied from models or direct measurements.

Bathymetry.- In areas of clear water and homogeneously reflecting bottom, water depth contours which agree with hydrographic charts have been derived from space photographs by density-slicing techniques[6][8]. As the blue sensitive layer in the colorfilm records in the region of highest transmission in the water, the deepest penetration is obtained, and blue color separations are frequently used for this work. Clear water also has substantial green transmission, and a 44A separation filter is often used to include color information from 420nm to 560nm.

In several cases correlation of charted depths with density slices at 120 and 180 feet appear to be valid. An example is shown in Figure 11. Since the bottom can be seen in standard, un-enhanced color photography at depths of 140 feet, taken from 60,000 feet in the Bahamas, there is no reason to doubt that similar results can be obtained from space with appropriate blue region sensors, and that in many areas bathymetric contours can be derived with minimal ground truth spot checking. There are hundreds of "doubtful soundings" where much lesser depths are reported, and which may be examined by this method in future.

Chlorophyll Detection.- The concentration of phytoplankton in the ocean is related to commercial fishing areas, and is usually associated with upwelling, currents, water chemistry and other features of interest in physical oceanography. Experimental scanning radiometers flown in aircraft have been successful in detecting and measuring chlorophyll concentrations[9][10].

One method of data reduction electronically differentiates the green and blue water radiances to detect a chlorophyll absorption band around 440nm[10]. By comparing the blue measurements with reference data taken simultaneously at 525nm where chlorophyll is transparent, as shown in Figure 12, radiance data from surface effects and scattered light similar to both channels can be cancelled. The remaining relative radiance values in the blue channel are then attributable to chlorophyll absorption and concentration.

There are analogous photographic processes where positive and negative images are combined to mask out similar reflectance values of the same scene taken in two spectral bands, permitting only that which is different to be printed[8]. Whether this can be used for detecting chlorophyll remains to be tested, but some data are available which show promise. Figure 13 is of red, green and blue multispectral images

taken from an altitude of 1500 feet near La Jolla, California, during an experiment for Scripps Visibility Laboratory in December 1970. The negative images are reproduced at normal contrast, and the positives at high contrast. The red band (25 filter) clearly shows a "red tide" phytoplankton bloom as the white areas in the positive, while the absorption of light by chlorophyll in the blue band makes the same areas appear dark. In this instance, the green band (57A filter)* is not suitable for masking the blue record, as its transmission (Figure 12) overlaps part of the chlorophyll absorption band and would tend to mask useful data. Enlarged sections of images taken of the same area from 12,000 feet are compared in Figure 14, where the strong absorption effect is still seen and relative chlorophyll concentration can be estimated within the image. Under these atmospheric conditions there is little question that this bloom would have been detected from 60,000 feet or higher.

Intense phytoplankton blooms of this kind contain much higher concentrations of chlorophyll than normal. Experiments supported by ground truth will be required to determine the lower limits of detection with multispectral photography from higher altitudes, by applying masking processes and other more refined methods of analysis and display.

Coastal Processes.- In the analysis of the Apollo IX image AS9-20-3128, Pamlico Sound and the North Carolina Coast, Mairs[11] provides a classical example of what it is possible to infer about coastal and ocean processes from a space image. Using the natural color photograph and red, green and blue color separations as an aid in determining the probable depth and concentration of sediments, and their sinking, mixing and diffusion rates, he was able to develop a model which incorporated jet theory, surface temperatures, currents, climatological factors, color differences, tidal cycles and other phenomena to account for the form, distribution and juxtaposition of the water-borne sediment masses and their apparent radiance.

---

*The experiment was to record the submerged target near the boats with a 57A filter, which has a passband closely resembling the response of the ERTS Return Beam Vidicon "green" camera. The red tide bloom was fortuitous.

At a later date, a color separation of this image was density-sliced, Figure 15. Each density level could be separated from those adjacent, in effect contouring the sediment depth by luminosity levels; a distinct aid in analyzing images of this type for examining similar coastal processes which occur on a worldwide basis, related directly to beach building, erosion, current flow and many other factors which bear not only on scientific studies, but on shipping traffic, fisheries, coastal utilization, pollution detection and other practical applications.

Water Pollution.- Experimental data are available from radiometric sensors and multispectral photography to show that the blue is one of the best spectral regions in which oil spills can be detected. Oils modify surface characteristics, affecting the reflectance of skylight in the blue band. Samples from high altitudes are not yet available. As in the case of chlorophyll detection, the possibility of monitoring such disasters from orbital altitudes needs investigation.

Industrial water pollution detection and control will be aided by using a blue record as one of the primary bands for assessing water colors which deviate from the norm. Excessive algal growth encouraged by phosphate or other pollutants provide one example.

BLUE RECORD OF LAND AREAS

Enhanced ocean blue records show marked improvement in the contrast of adjacent land areas, aiding interpretation of coastal processes. Features related to geology, agriculture, forestry, land use and many other applications are displayed in an improved form. A blue record is of particular value in geological interpretation, and many man-made features are emphasized in this spectral region. Oceanography is, therefore, not the only earth science which can use a blue image to advantage.

The recording problem is minimized in arid areas, but even in the tropics it is possible to make a blue record of useful quality. Two examples are given in Figure 16. The duplicate 70mm color films from which the enlarged sections were made were chosen as examples of severe tropical blue haze, which masks land form and detail almost completely.

It was necessary to enhance both the green and blue color separations to show the amount of detail actually present in images of this poor quality.

CONCLUSIONS

Sufficient practical evidence is on hand to prove the feasibility of making a blue spectral record from aerospace altitudes which is not only useful, but essential for obtaining vital oceanographic information. The problems of atmospheric luminance in degrading the image cannot be overlooked, but means for significantly enhancing the blue record are available. Electronic and photo-optical image enhancement techniques are necessary for extracting maximum information from blue (and green) multispectral photographs, and should be applied as standard analytical procedures.

While haze effects vary, the probability of securing a useful image is likely to be as good as the probability of having suitable cloud-free conditions; possibly better.

A minimum passband of 460 to 500nm is required, but photographic evidence suggests cut-on could begin as low as 440nm to provide additional information.

REFERENCES

1 - Ross, D. S. - Enhancing Aerospace Imagery for Visual Interpretation - SPIE 15th Annual Technical Symposium Proceedings, Vol. 3, Sep. 1970

2 - Duntley, S. Q. - Light in the Sea, JOSA, 53, (2), Feb 1963

3 - Turner, R. E., et al - Importance of Atmospheric Scattering in Remote Sensing - Proceedings Seventh International Symposium on Remote Sensing of Environment, U of Michigan, Vol III, May 1971

4 - Junge, C. E. - Atmospheric Chemistry, Advances in Geophysics, Vol 4, 1958

5 - Lepley, L. K. - Coastal Water Clarity from Space Photographs, Photogrammetric Engineering, Vol XXXVI, No. 7, Jul 1968

6 - Ross, D. S. - Color Enhancement for Ocean Cartography, Ocean from Space Symposium, Am. Soc. for Oceanography, Houston, April 1967

7 - Brock, G. C. - The Physical Aspects of Aerial Photography, Dover ed. 1967

8 - Ross, D. S. - Image Tone Enhancement, Papers, 36th Annual Meeting, American Society of Photogrammetry, Mar 1970

9 - Clark, G. L., Ewing, G. C. & Lorenzen, C. J. - Spectra of Backscattered Light from the Sea Obtained from Aircraft as a Measure of Chlorophyll Concentration, Science, 167, 1119-1121 (1970)

10 - Arveson, J., Millard, J. P., Weaver, E. C. - Remote Sensing of Chlorophyll and Temperature in Marine and Fresh Waters, Proceedings XXII International Astronautics Congress, Brussels, Sept 20-25, 1971

11 - Mairs, R. L. - Coastal & Sedimentologic Interpretation of Apollo IX Space Photography; Carolina's Continental Shelf, USA, Photogrammetric Engineering, Vol XXXVI, No. 10, Oct 1970

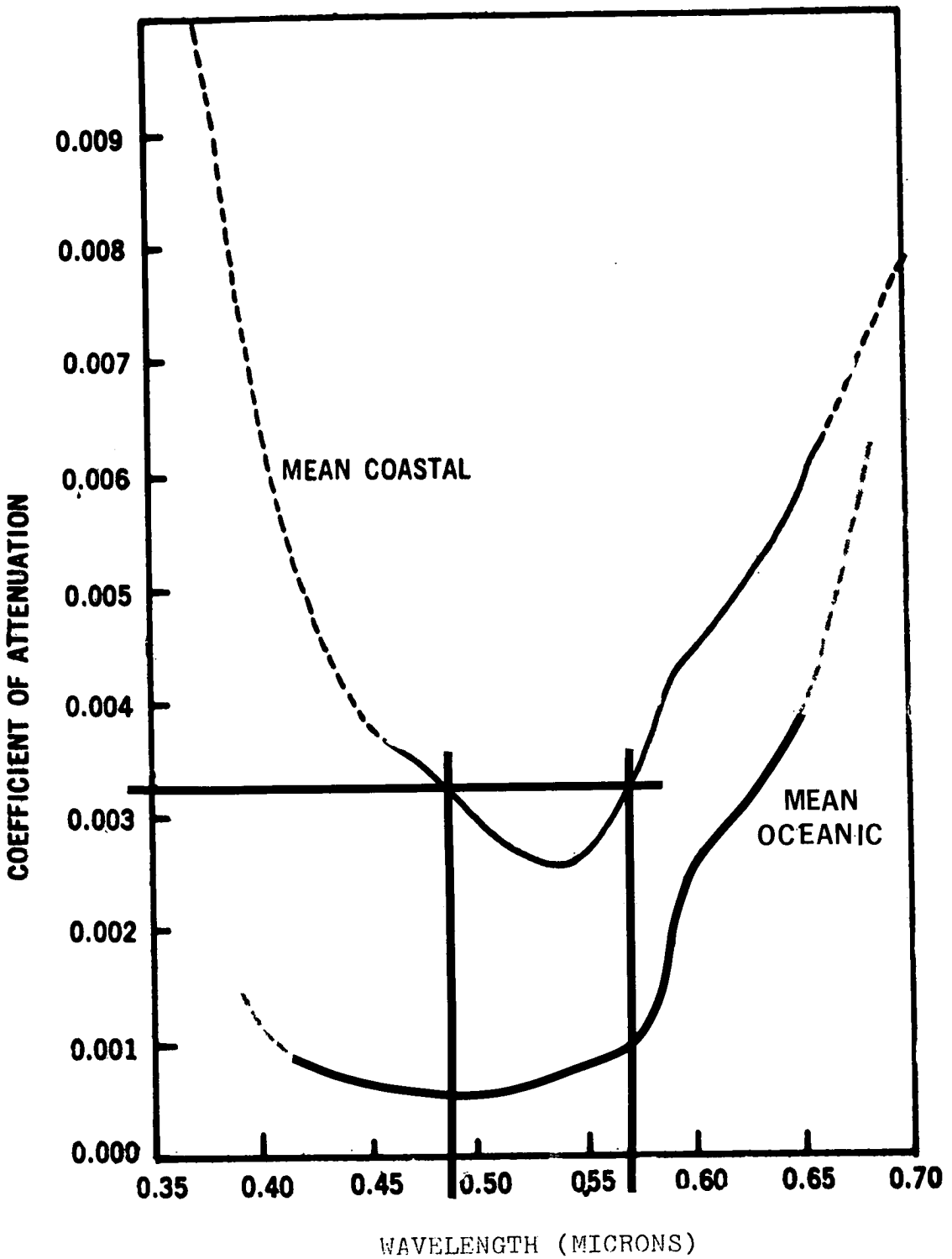

Figure 1.- Attenuation of Light in Seawater

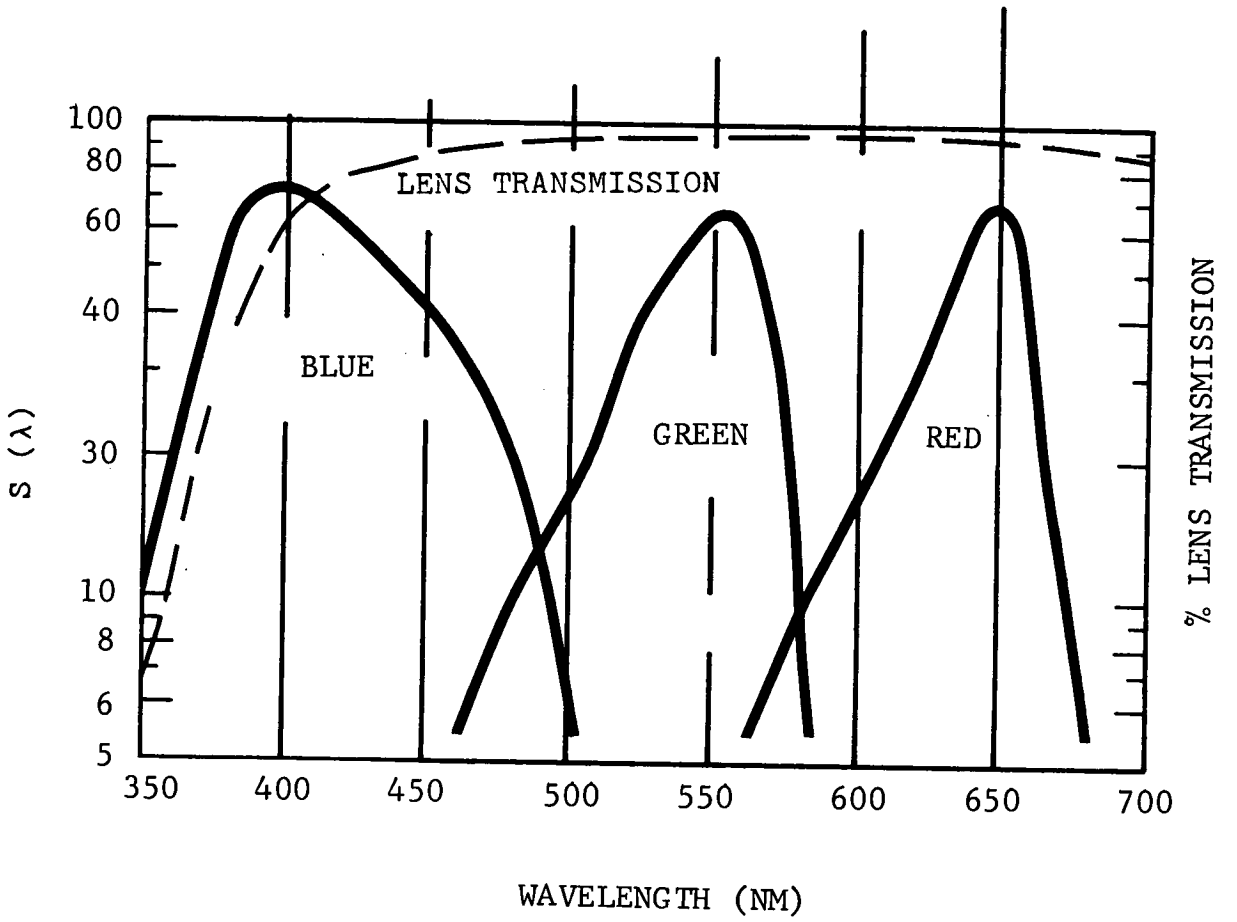

Figure 2.- Relative Sensitivities of blue, green and red layers in an Ektachrome natural color film, compared with spectral transmission of a Feiss Planar 80mm focal length lens. Note peak blue film response at 400 nm.

A. 450 mμ

B. 500 mμ

Figure 3 Color Separation Prints

C. 550 mμ

D. 650 mμ

Figure 3 Color Separation Prints (Continued)

BLUE GREEN

Figure 4.- Enlarged portions of color separations, AS9-20-3127, Cape Lookout, S. Carolina. Note visible water difference in blue image.

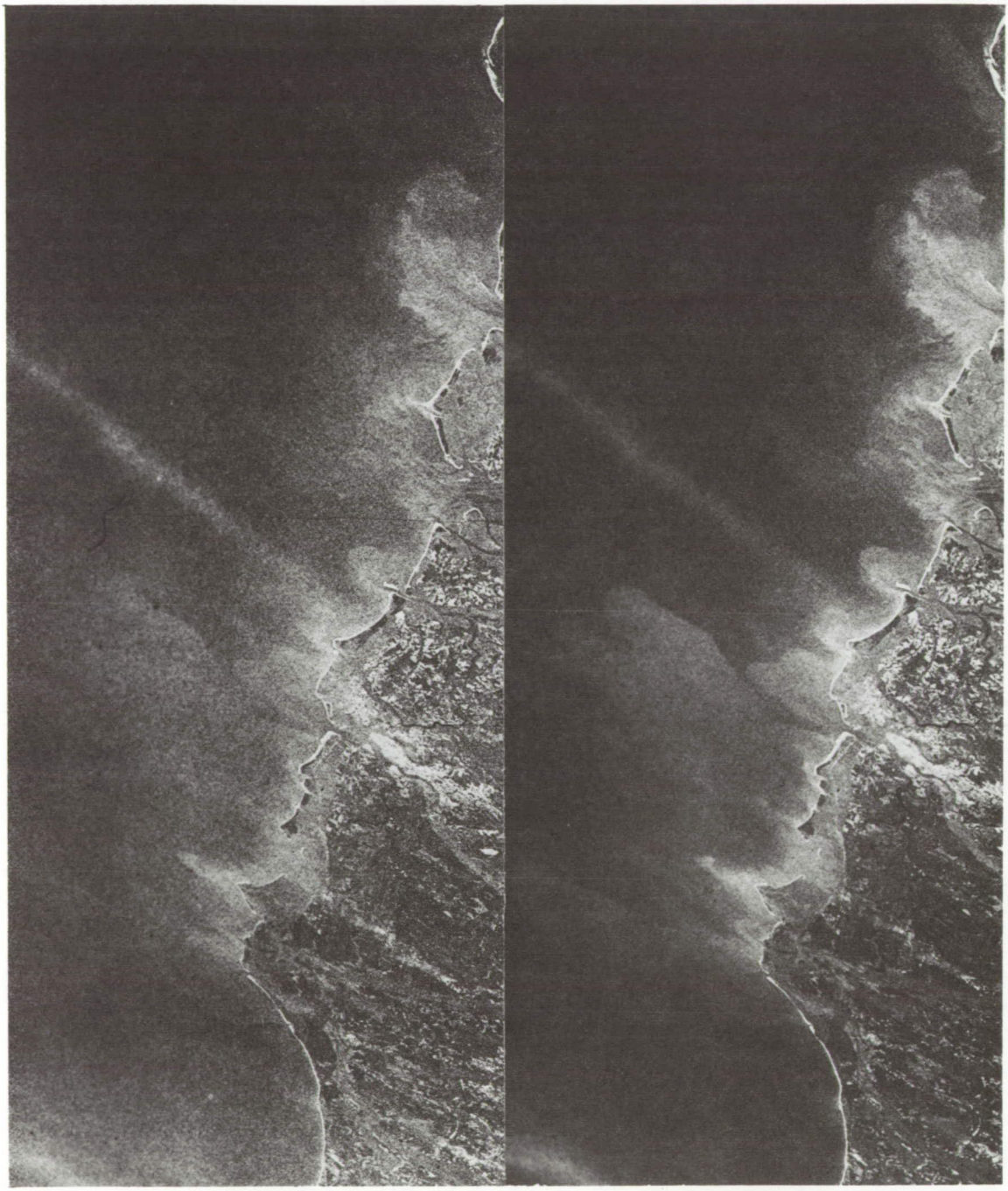

BLUE GREEN

Figure 5.- AS9-20-3148, coast of Georgia, S. Carolina. Differences in light absorption and scattering in the water show clearly.

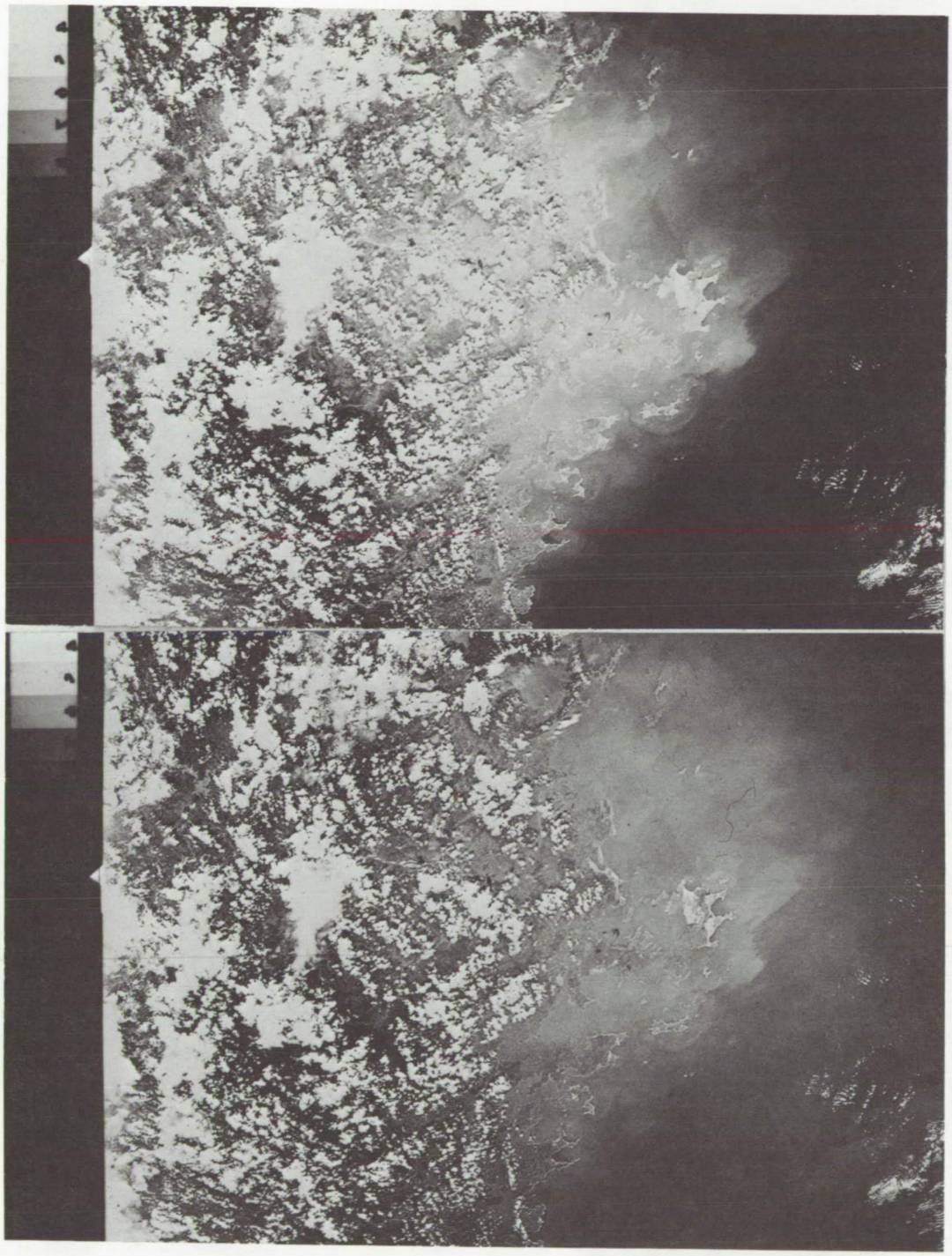

Figure 6.- GT X, S66-45953. Formosa Strait. Green separation (upper) compared with blue record.

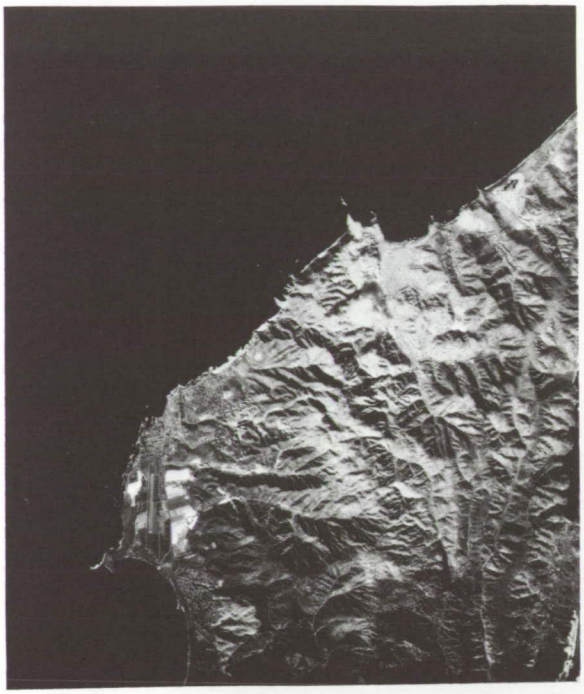

A - Infrared Record (88A)

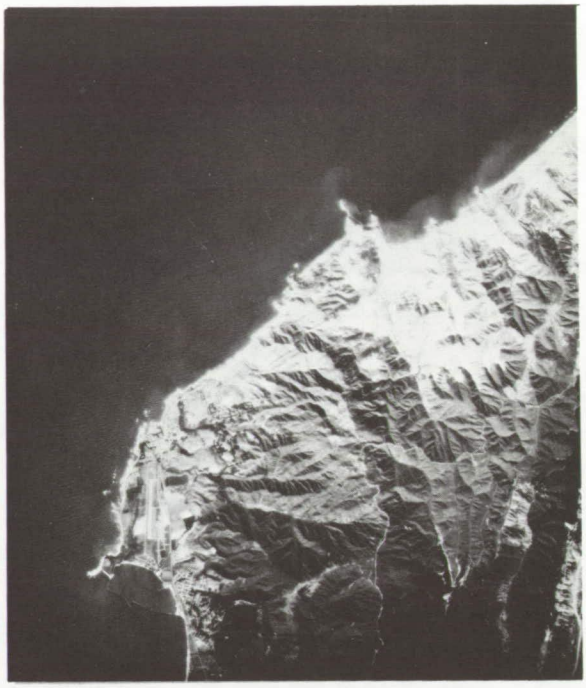

B - Red Record (25)

C - Green Record (57A)

D - Blue Record (47B)

Figure 7 .- Moss Beach, Ca. from 65,000 ft., 6-inch lenses I^2S Multispectral Camera. NASA/Ames. Sections of 3.5-inch square images at contact scale.

Figure 8.- Enlarged section of I^2S Blue Record shown in Figure 7(D). Contrast enhanced to emphasize variations in light in water.

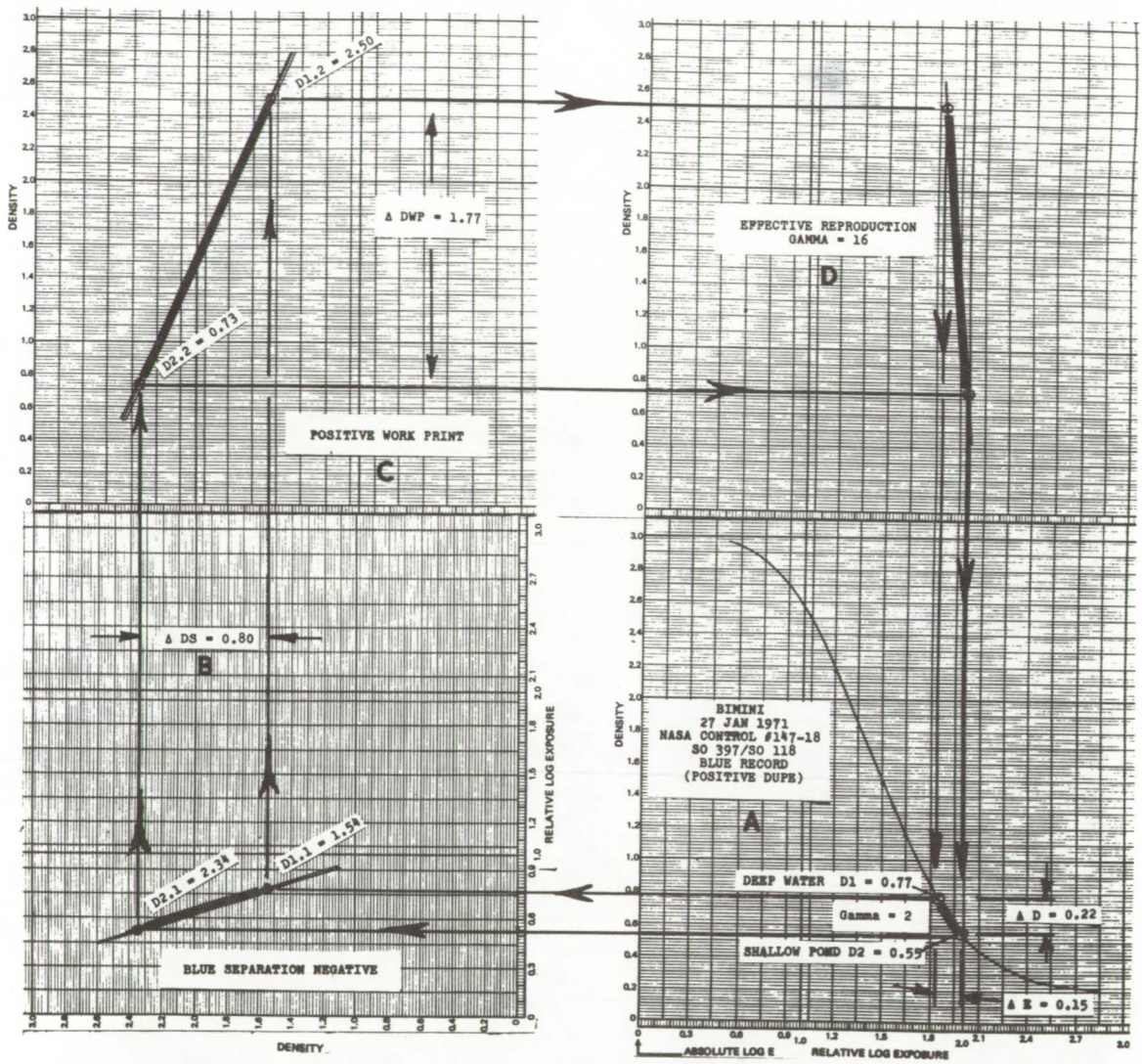

Figure 9. - High contrast photographic color separation and reproduction greatly increase small density differences and scene contrast for improved visual interpretation, as well as for other enhancement techniques. Density differences in the original at (A) have been converted from 0.22 to 1.77 in the workprint in the tone reproduction cycle illustrated above.

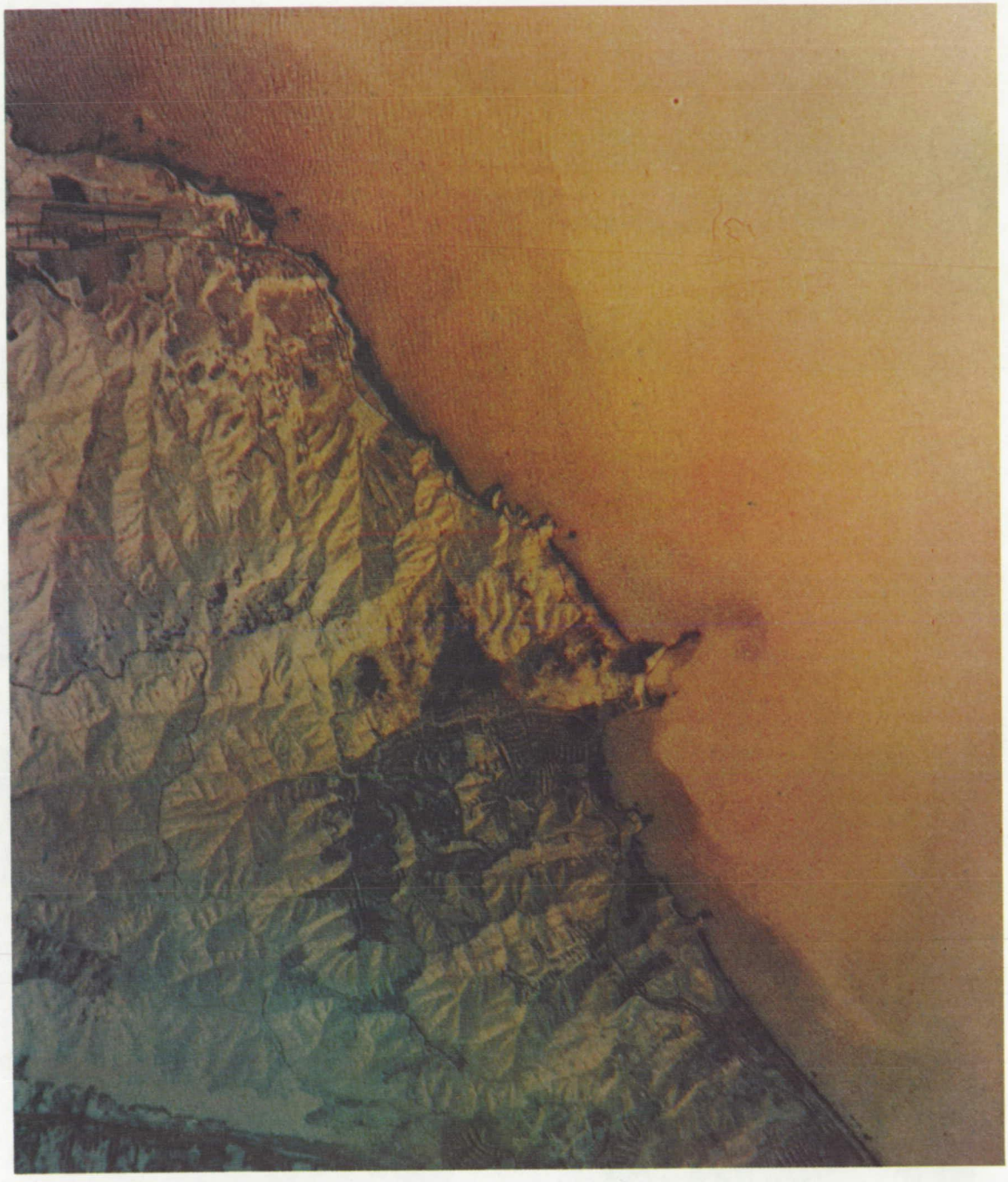

Figure 10 - Moss Beach, Ca. NASA/Ames U-2 photograph from 65,000 ft. ASL, I^2S Mark I Multispectral Camera. Additive color projection of blue and green negatives on screen of Mini-Addcol Viewer. Blue record projected as blue, and green as red. See also Figure 7.

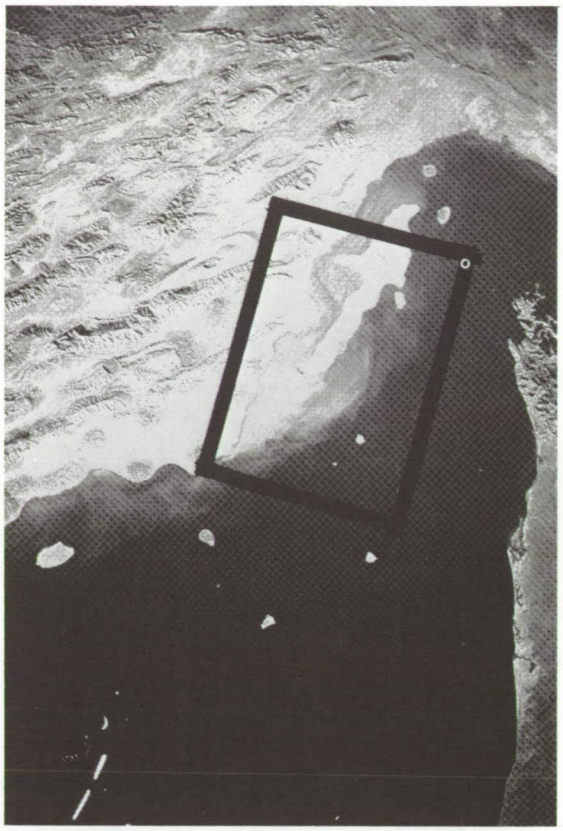

Figure 11A NASA/MSC No. S66-63485 Iran – Trucial Coast, Persian Gulf; Qeshm Island, Astronauts Lovell and Aldrin, Gemini XII, November 1966, Hasselblad Camera, 38 mm, Zeiss Biogon Lens. Altitude about 110 NM. Original scale about 1:8,000,000.

(U. S. NAVAL OCEANOGRAPHIC OFFICE - SPACECRAFT OCEANOGRAPHY PROJECT)

Figure 11B Enlarged, enhanced section of Figure 11A; density levels at 10-20 fathoms

Figure 11C Density levels at approximately 20-30 fathoms

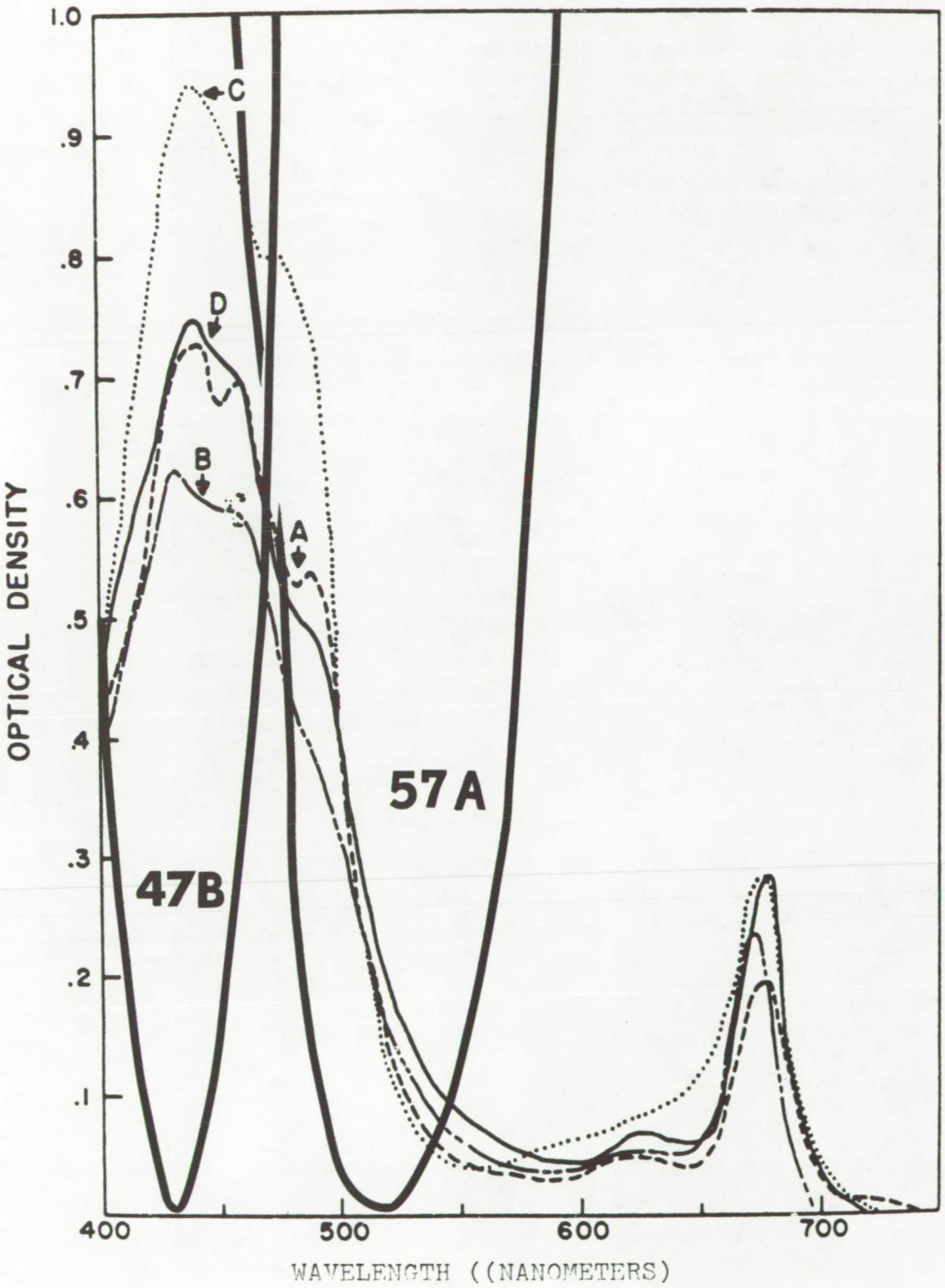

Figure 12 - Absorption spectra of extracts of several plankton species, (A),(B),(C);(D) is from a natural population sample, Woods Hole waters (Yentsch, 1960), Compared with normalized densities of Wratten filters 47B-blue and 57A-green.

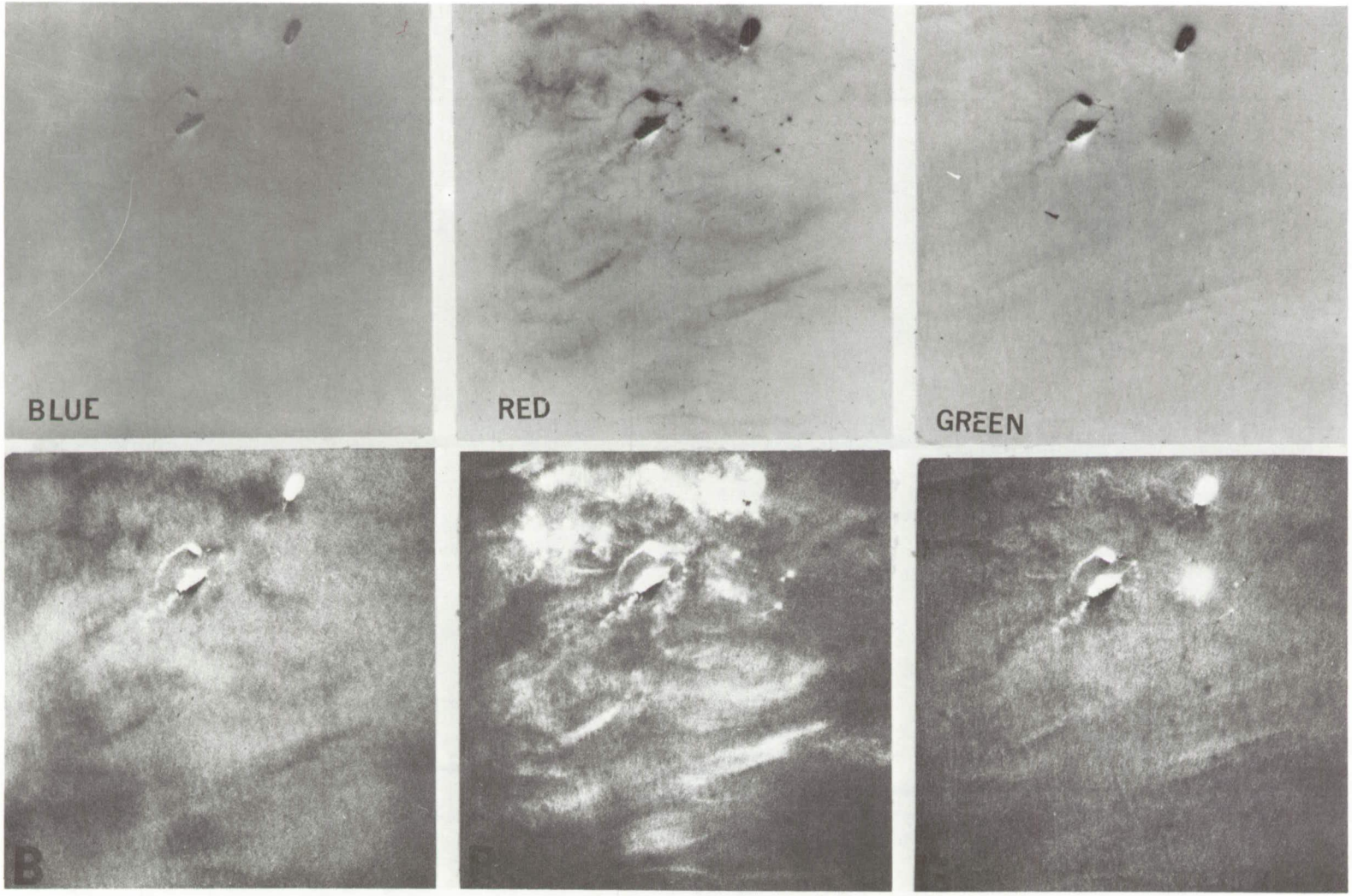

Figure 13. - Normal contrast multispectral negatives and high contrast positives of red tide bloom, 1500 ft. ASL. Chlorophyll absorption shows strongly in the blue image.

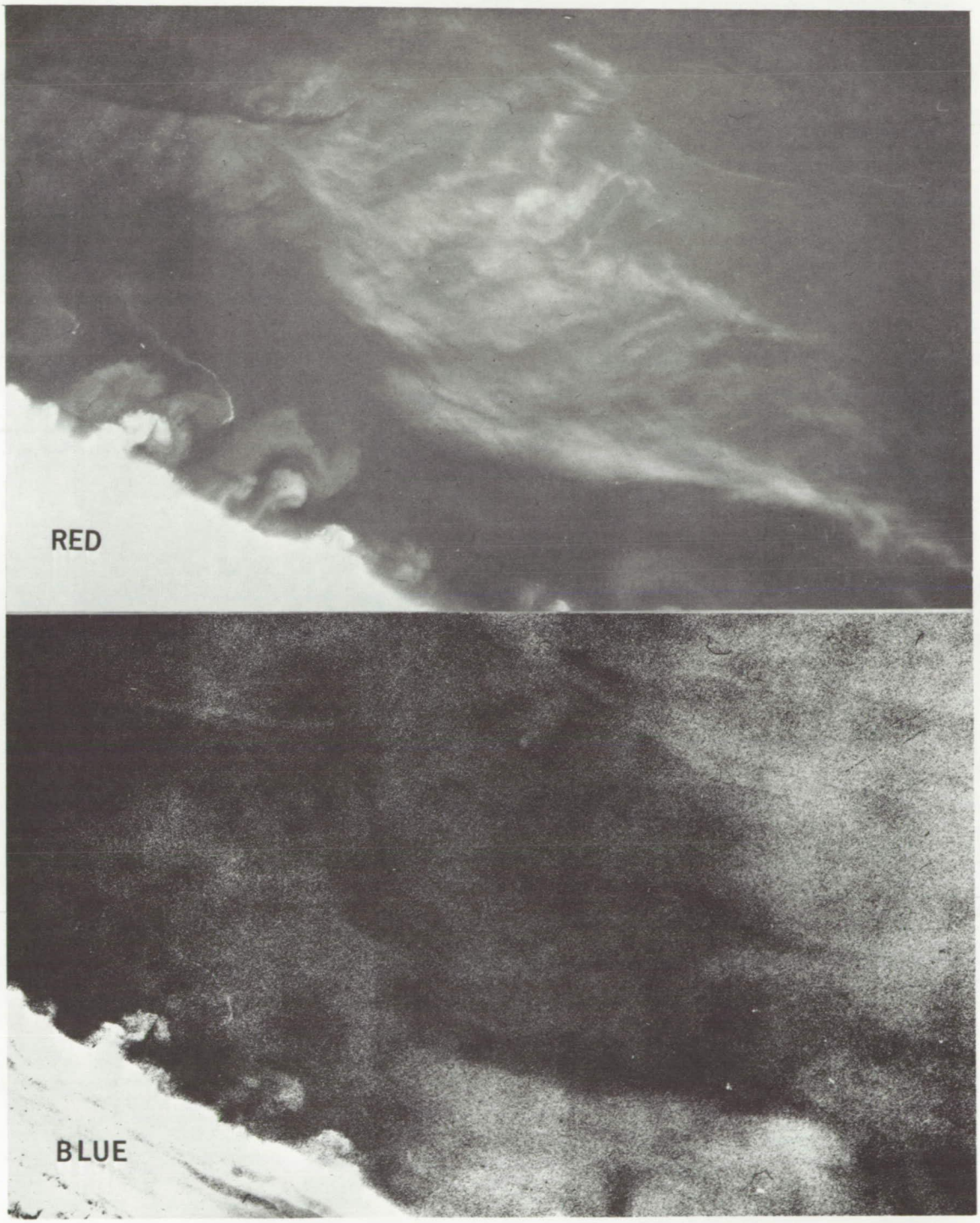

Figure 14. - Area of red tide bloom shown in Figure 13 as recorded from 12,000 ft. ASL.

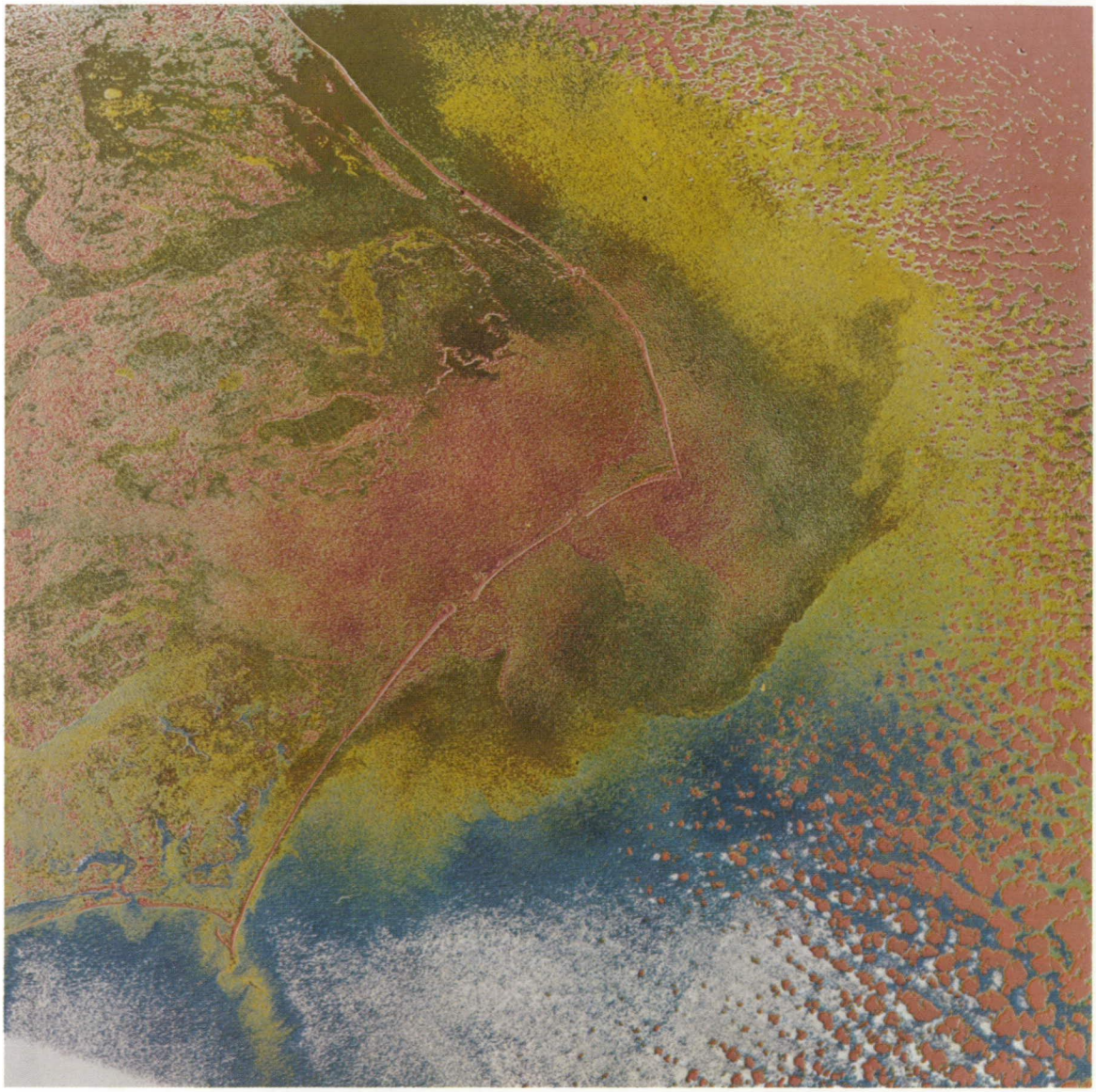

Figure 15.- AS9-20-3128. Pamlico Sound, Cape Hatteras, N. Carolina Coast. Photo-Optical false color density slicing. Colors peel apart in the original to show ten separate brightness contours in the water area.

BLUE

GREEN

AS9-20-3165 - Peru, 12°S, March 1969

BLUE

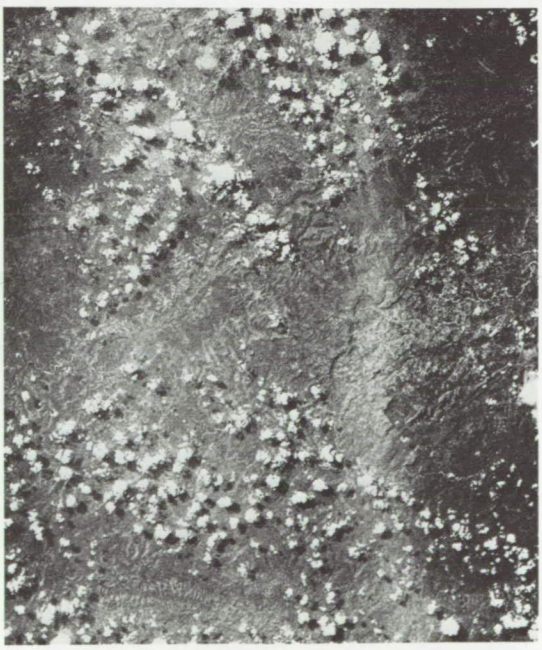

GREEN

GT VII, S65-63934, 15°S, Brazil, Mato Grosso, Dec. 1965

Figure 16. - High-Contrast Color Separations of Land

SECTION 108

EVALUATION OF FACTORS AFFECTING RESOLUTION OF SHALLOW-WATER BOTTOM FEATURES

BY:

Curtis C. Mason, Dean R. Norris, and I. Dale Browne
NASA Manned Spacecraft Center
Houston, Texas 77058

INTRODUCTION

Interest in studying the shallow-water areas of the world and the affects of man's activities on these areas is increasing. As a result, aerial photography is becoming important as a means of improving the effectiveness of these shallow-water studies. To ensure good photography, the effects that factors such as submergence depth, sun angle, film and filter type, exposure, aircraft altitude, and polarization have on the photographic resolution of an underwater object must be determined.

Previous aerial photographic studies over water have either concentrated on the attenuation of light or have not considered the full range of variables. Recent work in this field has been performed photographing various subjects such as the deck of small submersible (1), colored and gray scale panels (2,3), and natural bottom features (4,5,6). In none of this work has an underwater resolution target been used.

TEST PROGRAM

To study the affects different factors have on aerial photography of underwater objects, a test program was carried out in the vicinity of the Tektite II habitat in Lameshur Bay of St. John Island in the Virgin Islands. The water in this area is very clear. A specially designed target (fig. 1) with resolution-bar dimensions of 4 by 12 feet, 2 by 6 feet, 1 by 3 feet, and 1/2 by 1-1/2 feet was used to evaluate the affects that the parameters mentioned previously have on underwater resolution. Divers from the Tektite project were used to develop the deployment technique for the target. During actual data collection, divers from the Cape Fear Technical Institute Research Vessel Advance II were used to position the target at depths ranging from 5 to 60 feet below the surface.

The 12- by 24-foot target was made buoyant, was positioned at the proper depth by four winches mounted at the corners of the target, and was fastened by cables to weights positioned on the bottom of Lameshur

Bay. This target was photographed from the selected altitude of 2000 feet for all parameters examined, with the exception of altitude variations, by a P3A aircraft. The aircraft was equipped with a 6-inch-focal-length RC-8 camera, four 3-inch-focal-length KA62 cameras, and four 80-millimeter-focal-length electric Hasselblad cameras. The RC-8 camera used a clear antivignetting filter and was loaded with a specially manufactured Ansco D500 color film that did not have the blue sensitive layer. One of the KA62 cameras used Kodak SO-397 color Ektachrome film, the other three KA62 cameras used Kodak 2405 highspeed Panchromatic film with Wratten 57, 47, and 25A filters. The camera equipped with the Wratten 47 filter malfunctioned during the mission. Three of the Hasselblad cameras used Kodak 2405 film with Wratten 2E and 47, Wratten 45, and Wratten 21 and 57 filters. The fourth Hasselblad camera used Kodak 2424 black and white infrared film and a Wratten 89B filter. The nominal transmittance of the filters used with the Kodak 2405 film is shown in figure 2. On one flight, the four Hasselblad cameras were replaced with a second RC-8 camera that was loaded with specially manufactured Kodak SO-397 color Ektachrome film without the blue sensitive layer. The submerged target was overflown with the aircraft heading north. For control, a duplicate resolution target was laid out on the beach so that the submerged target and then the beach target would be photographed.

AFFECTS OF VARIOUS FACTORS ON RESOLUTION

As expected, submergence depth was the most important factor affecting resolution. A careful examination of the original 2405 film with a 57 filter determined that for the target on the beach, the light-gray 1- by 3-foot bars, as well as the black 1- by 3-foot bars, were visible; but the black 1/2- by 1-1/2-foot bars were barely discernable. At a 5-foot submergence depth, the black 1- by 3-foot bars were visible; however, the light-gray 1- by 3-foot bars were not visible, the light-gray 2- by 6-foot bars were barely visible, and the black 1/2- by 1-1/2-foot bars were poorly defined. At a 15-foot submergence depth, the black 2- by 6-foot bars were visible, and the black 1- by 3-foot bars were poorly defined. At a 30-foot submergence depth, one of the black 2- by 6-foot bars is visible, but no trace of the black 1- by 3-foot bars could be seen. At a 45-foot submergence depth, the black 4- by 12-foot bar is still clearly visible. At a 60-foot depth, the target is barely visible, and there is only an indication of the black 4- by 12-foot bar.

A comparison of the affect that filters and color film have on resolution is given in Table 1. Except for the view taken with the Wratten 25A filter, it is difficult to discern any appreciable difference in the target resolution. Using the Wratten 25A filter, the target at the 30-foot submergence depth could not be imaged, although it

was clearly visible at the 15-foot submergence depth. A more critical comparison of the filter performance by viewing the original negatives for all submergence depths (see Table 1) indicated that images obtained with the Ektachrome film (SO-397) were slightly superior to all the others. Those obtained with the 2405 film and following Wratten filters; 2E & 47, 57, and 21 & 57; were next and of equal quality. Images obtained with the 2405 film and Wratten 45 filter were slightly poorer still.

The images obtained with the specially manufactured Ansco D500 film, the specially manufactured Kodak SO-397 color Ektachrome film, and the Kodak SO-397 Ektachrome film were compared with the target submerged to 30 feet. Comparison of the two films without the blue sensitive layer as opposed to standard color film is hampered by the standard color film being exposed in a camera with a 3-inch rather than a 6-inch focal length. Even so, it was difficult to determine visually any significant difference in resolution.

With the target submerged 40 feet it was difficult to determine visually any difference in resolution due to sun angle changes as long as the target is not in the sunglint area. The main affect of varying sun angle is to increase the area of the frame covered by sunglint. The photographs in figure 3 were obtained with a 3-inch-focal-length camera. This figure shows the portion that was affected by sunglint. At the 56° and 71° sun angles, the photographs taken with the 80-millimeter-focal-length Hasselblad camera and a 56-millimeter film format were almost entirely covered by sunglint.

The affect that exposure has on resolution was determined with the target at a depth of 40 feet and the camera set for one-stop underexposure, normal exposure, and one- and two-stop overexposure on four successive overpasses. What was considered normal exposure had been determined by a sequence of test exposures made one month prior to the actual test program. The exposure that gave the best contrast for bottom features was chosen for normal exposure. (This was about two stops over normal land exposure.) Although the total film density varies for the one-stop underexposure, normal exposure, and one-stop overexposure, the resolution of the 4- by 12-foot bars on the target did not change. For the two-stop overexposure, little can be seen other than the boat on the surface.

The affect that aircraft altitude has on resolution is illustrated in figure 4. These photographs were taken with the target submerged 40 feet and the aircraft flying at 2000-, 4000-, and 12,000-foot altitudes. The examples used in figure 4 were taken with Kodak 2405 film and a Wratten 57 filter. The target can be readily identified in both the 2000- and the 4000-foot-altitude photography, but not in the 12,000-foot

altitude photography, as a result of the low contrast between the target and the water so that the target is lost in the grain of the image. The 4- by 12-foot bar is distinguishable in the 2000-foot-altitude photograph but is difficult to distinguish in the 4000-foot-altitude photograph.

The effect of using a polarizing filter was determined with the target submerged to a 30-foot depth. A polarizing filter was oriented so as to cause a maximum reduction of glare from the water surface. The camera was opened up two stops to compensate for the polarizing filter. In both cases, the 4- by 12-foot bar is clearly visible in the photographs. There is a slight indication of the 2- by 6-foot bars in the photograph obtained without the polarizing filter.

DENSITOMETRIC ANALYSIS

To avoid subjectivity that may be inherent in the visual analysis of the film density tracings were made over the target using the original Kodak 2405 film exposed with the Wratten 57 filter. All readings made on the underwater target were normalized to readings made on the shore target using the following procedures: (1) For each photographic run density tracings were made of both the underwater and shore target, (2) from these tracing density values for the 4 x 12 foot white and the second 4 x 12 foot black bar were determined for the shore and underwater targets, (3) a relative density versus log exposure (E) curve (figure 5), made from density readings of a step wedge placed on the film before developing, was used to determine the relative log exposure values for both the black and the white bar, (4) a log contrast ratio was computed by subtracting the log E values of the white bar from the black bar, and (5) a normalized contrast ratio was then computed by dividing the underwater target contrast ratio by the shore water target contrast ratio. Results of these densitometer measurements are given in table II.

An indication of the amount of variability in the data is obtained by examining the contrast ratios for the four runs over the target at 40 ft. depth with the camera set for one stop overexposure. These contrast ratio varied from 0.047 to 0.100, a factor of two. However, two of the values were essentially the same, 0.070 versus 0.073 and bracketed the average value of 0.072 for the four measurements. Consistency of this contrast ratio with varying conditions other than depth can be evaluated by examining the remaining data for the 40 foot submergence depth. From this data it is seen that for one stop under exposure and two normal exposures at 34° and 46° sun angles contrast ratios were within the error brackets for the one stop overexposure data. The normal exposure values were very near the average of the one stop overexposure. It is apparent that conditions other than submergence depth have very

little influence on the contrast ratio.

Changes of contrast ratio with submergence depth is shown in figure 6. In this figure all readings made at a particular depth were used regardless of the photographic conditions under which they were made. The circles indicate the average values while the error bars indicate the maximum and minimum values for that depth. From 5 ft. depth to 30 ft. depth there was a rapid decrease in contrast ratio. From 40 ft. depth to 60 ft. depth there was little change in the contrast ratio with this change only poorly correlating with depth. A smooth curve could be drawn through the error bar region showing a monotonic decrease in contrast ratio with depth.

Using a polarizing filter did not appear to improve the resolution of the underwater target as its contrast ratio was only 0.072 versus 0.140 for the un-polarized exposure made under the same conditions. A second contrast ratio value of 0.264 for a target at 30 ft. depth and no polarizing filter may be in error as the contrast value for the shore target was considerably lower than all other shore target contrast values.

Due to the large variations in the normalized contrast ratios for targets submerged at 40 ft. depth and the failure of the average contrast ratio to decrease monotonically from the 40 ft. depth to the 60 ft. depth it appears that the densitometric analysis of the photography is no more sensitive than the visual analysis.

CONCLUSIONS

As expected, the most important factors affecting resolution of bottom features are submergence depth and image scale on the original film. Small-sized bars or low contrast features (or both) disappeared quickly with submergence. As long as the film and filters recorded adequate energy in the 410- to 600-millimicron wavelength region, water depth penetration was not seriously affected. Resolution of bottom features was relatively independent of sun angle and exposure as long as sunglint was avoided and exposure was within plus or minus one stop of optimum. Use of a polarizing filter did not improve target resolution.

REFERENCES

1. Ross, D. S. and R. C. Jensen 1969. Experiments in oceanographic aerospace photography. BEN FRANKLIN spectral filter tests. Philco Ford TF-DA2108, 29 August 1969.

2. Vary, Willard E. 1969. Remote Sensing by aerial color photography for water depth penetration and ocean bottom detail, presented at the Proceedings of the Sixth International Symposium on Remote Sensing of Environment, University of Michigan, Ann Arbor, Michigan, October 13-16, 1969.

3. Yost, Edward and Wenderoth, Sondra, 1970. Remote sensing of coastal waters using multispectral photographic techniques. Science Engineering Research Group, Long Island University, Technical Report SERG-TR-10, January 1, 1970.

4. Conrod, A., M. Kelly, and A. Boersma 1968. Aerial photography for shallow water studies on the west edge of the Bahama Banks. Experimental Astronomy Laboratory, Massachusetts Institute of Technology, RE-42, November, 1968.

5. Kelly, Mahlon G. 1969. Applications of remote photography to the study of coastal ecology in Biscayne Bay, Florida. Contribution of the Department of Biology, University of Miami, Coral Gables, Florida, July, 1969.

6. Kelly, Mahlon G. and Alfred Conrod 1969. Aerial photographic studies of shallow water benthic ecology. In: Remote Sensing in Ecology. University of Georgia Press, Athens. pp 173-184.

TABLE I. ABILITY TO RESOLVE BARS ON RESOLUTION TARGET

SUBMERGENCE DEPTH FT.	WRATTEN FILTER TYPE WITH 2405 B&W FILM					EKTACHROME
	45	2E + 47	25A	57	21 + 57	
60	TARGET	TARGET	NOTHING	TARGET	4 X 12-	4 X 12-
45	4 X 12	4 X 12	NOTHING	4 X 12	4 X 12	4 X 12
30	2 X 6-	2 X 6	NOTHING	2 X 6	2 X 6	2 X 6
15	2 X 6+	1 X 3-	1 X 3-	1 X 3-	2 X 6+	1 X 3-
5	1 X 3-	1 X 3+	1 X 3+	1 X 3+	1 X 3+	$\frac{1}{2}$ X $1\frac{1}{2}$

CODE 1 X 3 SMALLEST SIZED RESOLUTION BAR VISIBLE

1 X 3- BAR JUST BARELY VISIBLE

1 X 3+ BAR VERY CLEARLY VISIBLE

TABLE II. DATA FROM DENSITOMETER READINGS, 2405 FILM WITH W-57 FILTER, 2000 FEET ALTITUDE.

TARGET DEPTH (ft.)	FRAME NO.		DENSITY READINGS				CONTRAST RATIOS		NORMALIZED CONTRAST RATIOS	COMMENTS
			SHORE		UNDERW.					
	SHORE	UNDERW.	BLACK	WHITE	BLACK	WHITE	SHORE	UNDERW.		
5	169	168	1.62	2.77	1.27	2.53	4.74	4.63	0.980	
5	175	173	1.48	2.86	1.62	2.92	5.54	5.41	0.980	
15	179	177	1.43	2.70	1.43	1.81	4.95	1.14	0.230	
15	225	224	1.23	2.51	1.50	2.12	4.65	2.14	0.460	Clouds(?)
30	220	219	1.28	2.58	0.62	0.86	4.83	0.66	0.140	
30	230	229	1.67	2.74	0.89	1.07	4.70	0.34	0.072	Polarized
30	233	232	1.70	2.40	1.58	1.85	2.84	0.75	0.264	
40	003	003	1.65	2.67	1.47	1.59	4.20	0.30	0.071	34° sun angle
40	007	007	0.88	2.45	0.89	1.00	5.40	0.30	0.056	1 under exposed
40	015	015	2.00	3.30	1.59	1.70	6.40	0.30	0.047	1 over exposed
40	011	011	1.97	2.87	1.04	1.15	4.10	0.30	0.073	1 over exposed
40	023	023	2.00	3.01	1.31	1.48	4.60	0.46	0.100	1 over exposed
40	027	027	1.97	3.06	1.25	1.38	5.00	0.35	0.070	1 over exposed
40	031	031	1.13	2.53	1.55	1.65	5.10	0.30	0.059	
40	035	035	1.50	2.77	1.50	1.62	5.10	0.33	0.065	46° sun angle
45	213	212	1.32	2.61	1.24	1.37	4.85	0.36	0.074	Clouds (?)
45	216	215	1.35	2.67	1.15	1.34	5.05	0.50	0.099	
60	208	207	1.76	2.78	1.17	1.29	4.40	0.32	0.073	

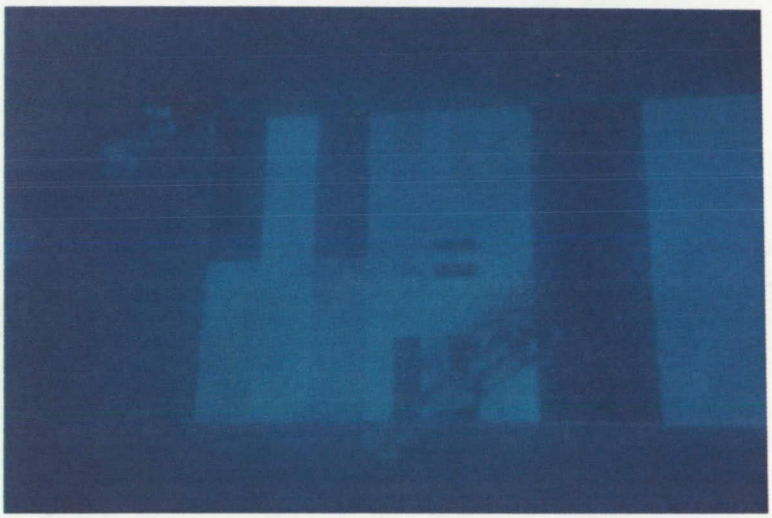

Figure 1. Target used in the test program.

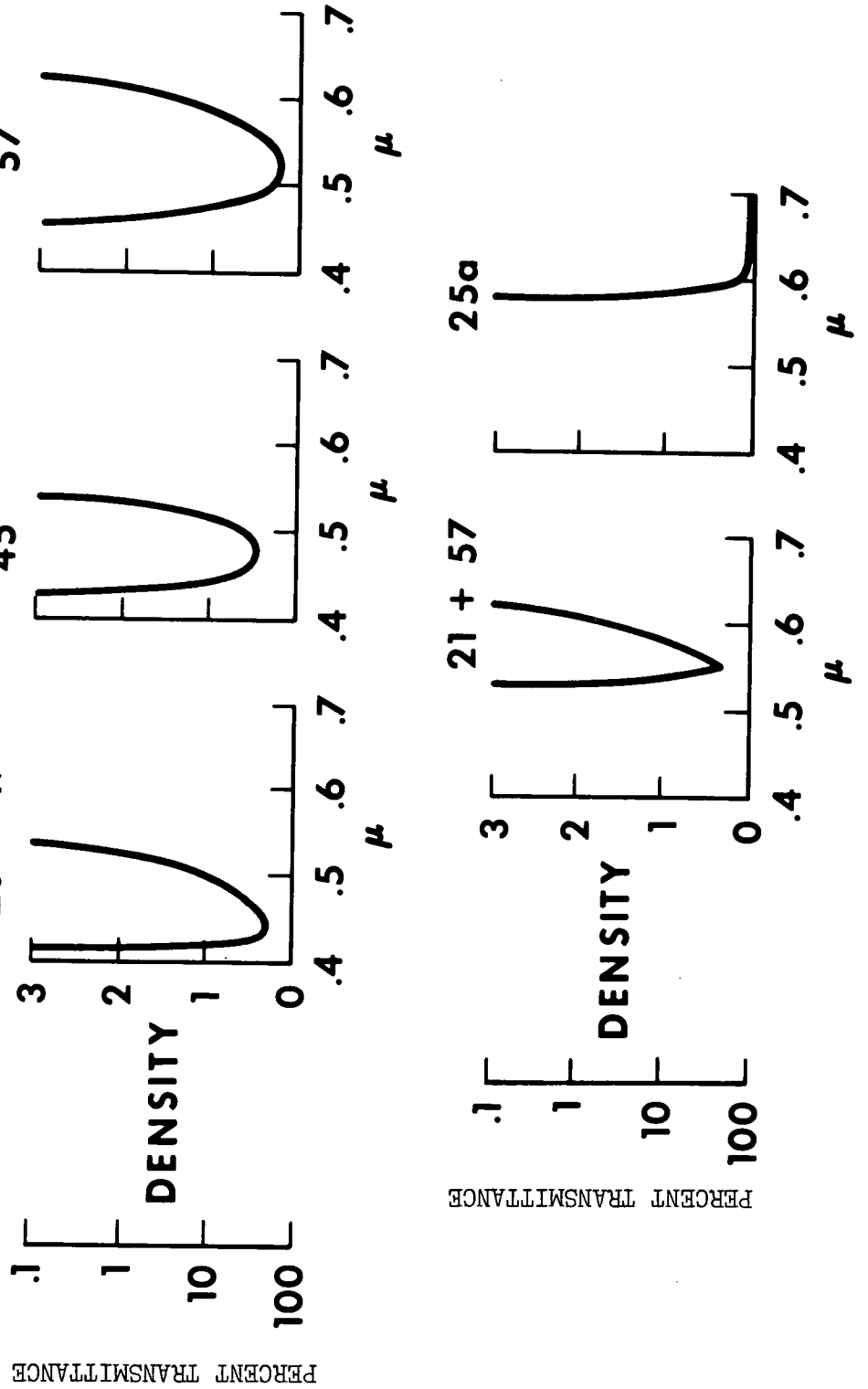

Fugure 2. Filters used in the test program. Kodak 2405 Panchromatic film used in all views.

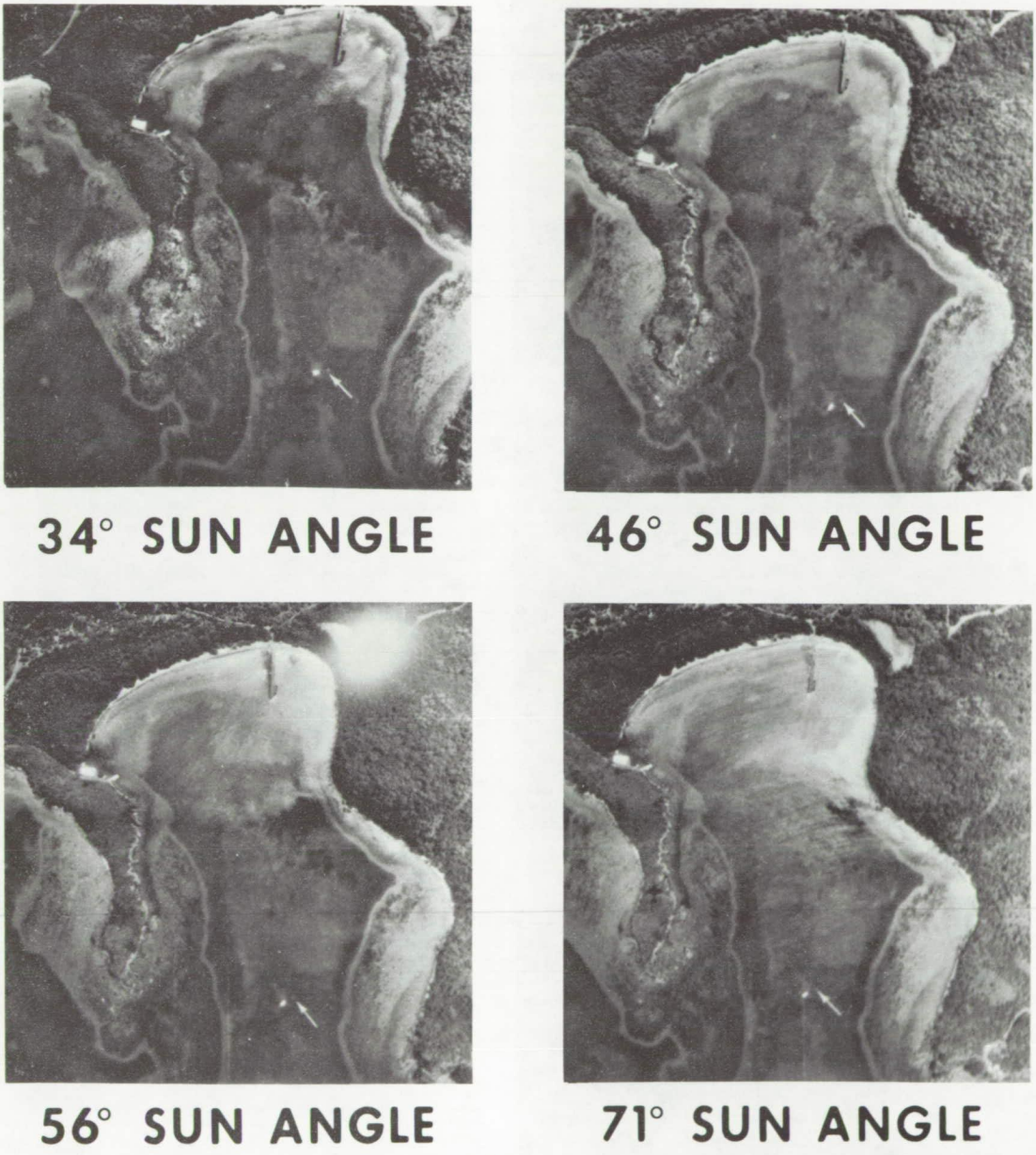

Figure 3. Portion of 4-1/2 inch frame covered by sunglint with the sun at variuos angles.

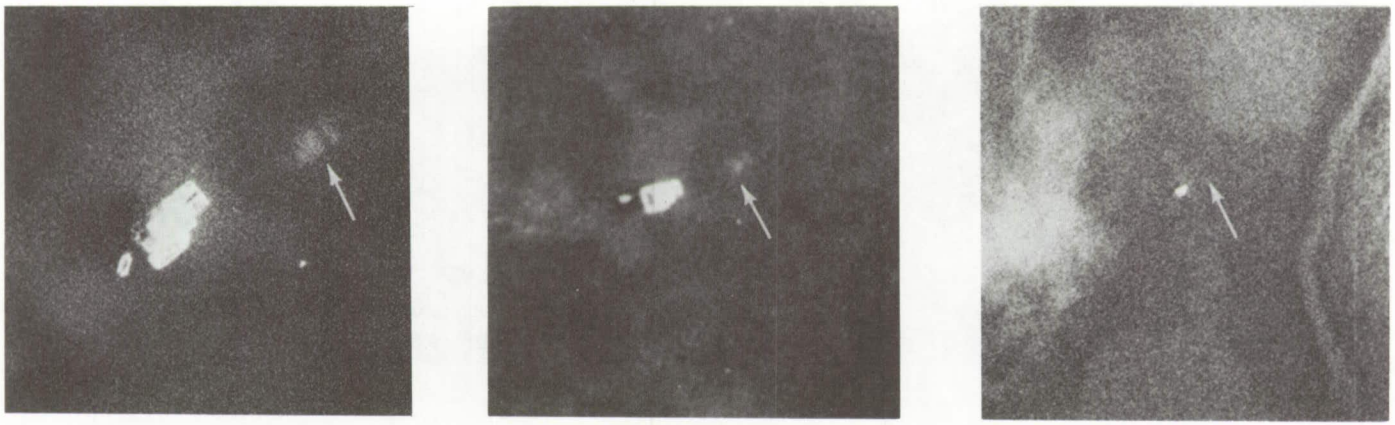

Figure 4. Effect that altitude has on resolution. The target is at 40 ft. submergence depth.

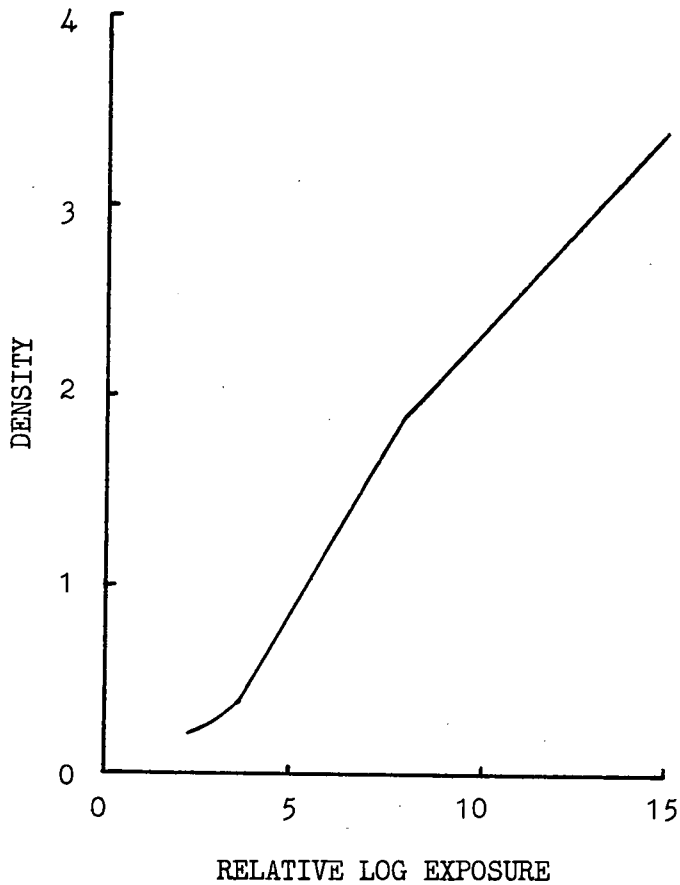

Figure 5. Density versus relative log exposure curve.

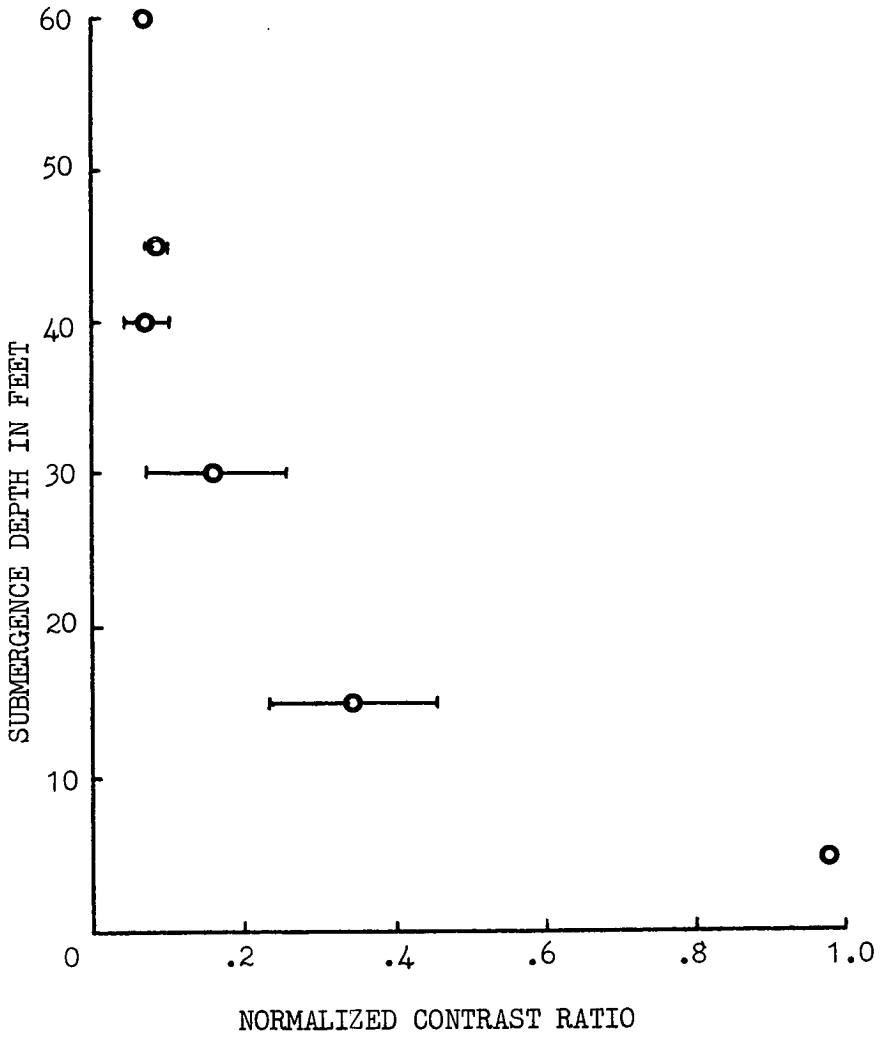

Figure 6. Depth of submergence versus normalized contrast ratio.

SECTION 109

MULTISPECTRAL OBSERVATIONS OF MARINE ENVIRONMENTS

by

Fabian C. Polcyn
University of Michigan
Ann Arbor, Michigan

In previous reports (Ref. 1, 2) we have seen how the multispectral scanner has been used to map various features of the land and vegetation. In this paper we wish to demonstrate how the concept of the multispectral scanner, using multiple channels in registry and recorded on magnetic tape, can be used in variety of applications in the marine environment. In Fig. 1 we observe how the multiple bands spanning the ultraviolet through the visible and into the thermal infrared has been used, not only to detect the presence of the oil slick but also to permit its discrimination and possibly its thickness. Four test oil slicks were flown in cooperation with the U. S. Coast Guard (Ref. 3) and resulting tonal patterns can be observed. The different intensities across the four bands demonstrate clearly how the four oil types of different specific gravities can be discriminated.

A second application area is demonstrated in Fig. 2 where the results of mapping the benthic vegetation communities in the lower part of Biscayne Bay, Florida is shown. Originally the figure was in color and each color was used to isolate the particular vegetation community or bottom type i.e., sand or clay. The black represents the shoreline near Turkey Point. This work was done in cooperation with the U. S. Geological Survey (Ref. 4). These benthic communities were submerged under water at some 6 to 8 feet deep.

In the area of pollution monitoring, Fig. 3 is an example in three bands of a pollutant from a steel processing plant, and in this case we note that there is no contrast of the pollutant in the .55-.58 micrometer band, whereas the pollutant has a darker tone than the receiving waters in the .40-.44 μm, and it has a lighter tone than the receiving waters in the red band at .62-.66 μm. This variation of tone with wavelength can be emphasized by displaying the results on a graph of apparent reflectance vs. wavelength is shown in Fig. 4. In this case we see the result of a number of different effluents from different industries along the Detroit River, and we note how each has its own characteristic reflectance curve , thus suggesting the possibility of identification of a pollutant from its reflectance signature.

In a fifth area of application we have found that different light penetration capabilities into water at different wavelengths can be used to measure water depth. We constructed a model that will use ratios of spectral channels and with the proper auxillary information produce a depth

chart as illustrated in Fig. 5 (Ref. 5). The accuracies for such an example is shown in Fig. 6 where we compare the computed depth made with data from a multispectral scanner with depth soundings made for the same region. One can note that for depths down to 20 feet there is good agreement and as the depth increases resulting in smaller signal to noise ratios the uncertainties in the depth measurement becomes greater. This chart is for the test site 167 in the Lake Michigan beach areas in contrast to the previous example taken in the Florida Keys area.

The model that relates multispectral information to water depth has been developed using the geometry shown in the next figure (Fig. 7) where sunlight is the source of energy and the reflected radiation from the bottom is detected by the sensor. Ultimately the scanner should be operated with a laser ranging device on board the same aircraft that would supply an independent measure of sample depths thus allowing for the calculation of extinction coefficients of light in water and the ratio of bottom reflectances, removing the need for using average values.

When there is scattering of light in the water a modification is necessary before depths are calculated. In the next figure (Fig. 8) are the equations that were developed for relating the apparent reflectance developed from the scanner in terms of a bottom reflection modified by the effects of scattering, s, and absorption, α. Angles θ and ϕ are merely the angles of observation and incidence as shown in Fig. 7.

We have found that for best results in depth calculations between inshore and offshore waters in the Lake Michigan area, the scattering term must be taken into account. For a test area in this region, Fig. 9, we have calculated the relative attenuation coefficient for two areas, 80 feet from shore and 200 feet from shore where the depth goes down to 7-1/2 feet. There are differences in the attenuation coefficient due to the effects of suspended sediments and the increased scattering of light. Once this correction is made the accuracies in depth measurements for both inshore waters and offshore waters becomes greatly increased. This ability of the model to handle a scattering term is expected to be useful when we wish to begin calculations of the total quantities of pollutant or suspended sediments in a given outfall. Figure 10 is an illustration of why we think the spectra carries this quantity of information. The spectra taken directly at the outfall of one of the industrial discharges is compared to the sample taken 100 feet downstream and that in turn is compared to the spectrum from the Detroit River itself. The spectral shape demonstrates the dillution of the pollutant mixing with the river water. With a new model being developed we expect to take into account this dillution through the spectrum information and with the proper control points sampled from a boat, estimates on mass in suspension should be possible. As a minimum, calculation of concentration gradients should be possible even without having the control points, but for maximum utility some ground truth is needed.

Further application areas are illustrated by using high altitude photography supplied by NASA and taken on Mission 103. They also illustrate what may be possible with a satellite multispectral system in mapping the extent of shore currents, and beach erosion, and lake pollution on a wide area basis. Figure 11 is a black and white reproduction of a color photograph that shows evidence of complicated patterns of suspension in Lake Michigan near Frankfort, Michigan. The right hand portion of Crystal Lake, shown in the middle of the picture, shows a turbidity pattern which appears to be related to water quality degradation reported in this end of the lake by residents. In the top part of the picture we see the formation of a beach area through deposition of sand and formed by the coastal currents in this area. The higher altitude photography suggests that we can begin to understand the complicated circulation patterns involved in these coastal formations.

In another area of application, Fig. 12, we again see a photo taken at 60,000 feet by the NASA RB-57 of the ports of Muskegon and Grand Haven, Michigan. There is the outfall of a paper plant in Muskegon Lake and the distinct outline of the Grand River and Muskegon River discharges into Lake Michigan can be seen. Here shore currents are preventing these pollution laden waters from mixing completely with the deeper lake waters and in some cases the shore currents force the plumes inward along the beaches.

These shore currents are set up by prevailing winds and we believe they play a major role in the movement and deposition of sand along the Lake Michigan shores. In Fig. 13, we see this shore current, covering an area of one to two miles, by the sharp demarcation line representing different currents and the increase in turbidity associated with the transport of sand. Land protrusions into the lake upset these shore currents producing the eddy patterns shown in the figure. We can emphasize this offshore current formation again by referring to Fig. 14. Here the sharp boundaries between the current inshore and the lake can be seen by the discontinuity in the sun glitter pattern. Two different wave directions must be involved across the discontinuity. The dimensions of these shore currents should now be measureable with the use of such remotely sensed data.

In some cases these currents will trap the pollutant outfall from the rivers inshore. In Fig. 15 a river plume outline is actually trapped and brought into shore by the formation of this offshore current through wind processes. This is a phenomena that can happen any time during the spring, fall and summer, in contrast to the "thermal bar" effect which is essentially a spring phenomena. This particular thermal feature can be mapped using thermal infrared data. In Fig. 16 are the results of a flight line 14-1/2 miles in length along the Michigan shore between Muskegon and Port Sheldon. Depending on the wind condition, the thermal water masses from the Grand River, as well as from a power generating plant can be seen relative to the warm water created along the shore in spring due to the higher temperature of the land. In the April 22nd data, the "thermal bar" has not been formed

and most of the lighter tone (warmer temperature) areas are due to the outfalls of the Grand River. By the 30th of April we see a distinct boundary along the entire 14 mile strip, which by May 7 has moved farther offshore completing the annual cycle. The natural warming of these waters and the mixing of temperature zones can be seen in Fig. 17. Here for the 30th of April different temperatures slices are displayed for each temperature range. Through such analysis an understanding of the temperature regimes and the area distribution, as well as the order of magnitude of the various radiances from both rivers and power plants, can be observed which should lead to a better definition of temperature standards and site placement of power plants.

Associated with these temperature patterns are color patterns due to the different algal communities and sand suspensions. With a multispectral scanner we can map the distribution of water masses by their spectral signatures. This is illustrated in Fig. 18 where the different tones correspond to different water masses inshore and offshore. In some cases, eddy features are enhanced and the possibility of relating chlorophyll patterns to temperature patterns is now possible with multispectral sensors.

We have seen in the figures shown the potential for multispectral remote sensing to provide the type of information that is needed in understanding some very complicated problems in the marine environment. As NASA develops further capabilities with spaceborne multispectral sensors, we expect these examples to be important in other parts of the U.S. and to play their role in helping to manage our environment.

REFERENCES

1. Nalepka, R. F. 1970. "Investigation of Multispectral Discrimination Techniques." Infrared and Optics Laboratory, Willow Run Laboratories Institute of Science and Technology, The University of Michigan, Ann Arbor, Michigan, January 1970.

2. Burge, W. G. and W. L. Brown. 1970. "A Study of Waterfowl Habitat in North Dakota Using Remote Sensing Techniques." Final Report 1 May 1969 - 31 January 1970. Report # 2771-7-F, Infrared and Optics Laboratory, Willow Run Laboratories, Institute of Science and Technology, The University of Michigan, Ann Arbor, Michigan, July 1970.

3. Horvath, R., W. L. Morgan, and S. R. Stewart. 1971. "Optical Remote Sensing of Oil Slicks: Signature Analysis and Systems Evaluation." Final Report on Project 724104.2/1. Prepared for: U. S. Coast Guard Headquarters, prepared by: Willow Run Laboratories, Institute of Science and Technology, The University of Michigan, Ann Arbor, Michigan. October 1971.

4. Higer, A. L., M. C. Kolipinski, N. S. Thomson, and L. Purkerson. 1971. "Use of Processed Multispectral Scanner Data With a Digital Simulation Model for Forecasting Thermally Induced Changes In Benthic Vegetation in Biscayne Bay, Florida." In the Proceedings of the Seventh International Symposium on Remote Sensing of Environment, Ann Arbor, Michigan. p. 2055, May 1971.

5. Brown, W. L., F. C. Polcyn, A. N. Sellman, and S. R. Stewart. 1971. "Water Depth Measurement by Wave Refraction and Multispectral Techniques." Infrared and Optics Laboratory, Willow Run Laboratories, Institute of Science and Technology, University of Michigan, Ann Arbor, Michigan. Prepared for: NASA Manned Spacecraft Center, Technical Report 03165-31-T, August 1971.

a) .32 – .38 µm

b) .45 – .47 µm

c) .55 – .58 µm

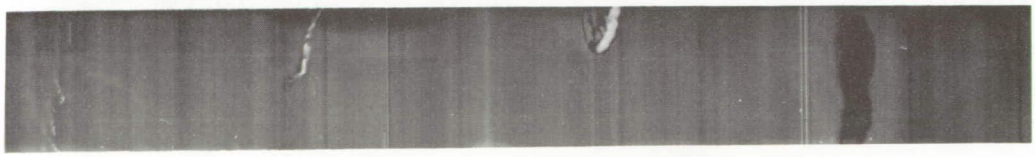

d) 9.3 – 11.7 µm

MULTISPECTRAL IMAGERY OF FOUR OILS

ALTITUDE: 2000 ft. DATE: 10/28/70 TIME: 1212

FROM L. to R.: 9.7 gravity fuel oil, 21.6 gravity crude oil, 26.1 gravity crude oil, diesel fuel

FIGURE 1

FIGURE 2

UNDERWATER VEGETATION MAPPING IN BISCAYNE BAY USING ANALOG COMPUTER PROCESSING OF MULTI-SPECTRAL DATA (Black represents coastlines; original map was in color.)

0.40 to 0.44 μ

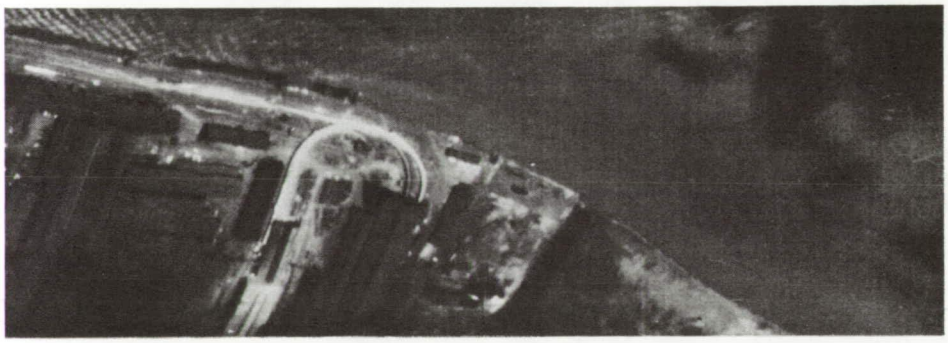

0.55 to 0.58 μ

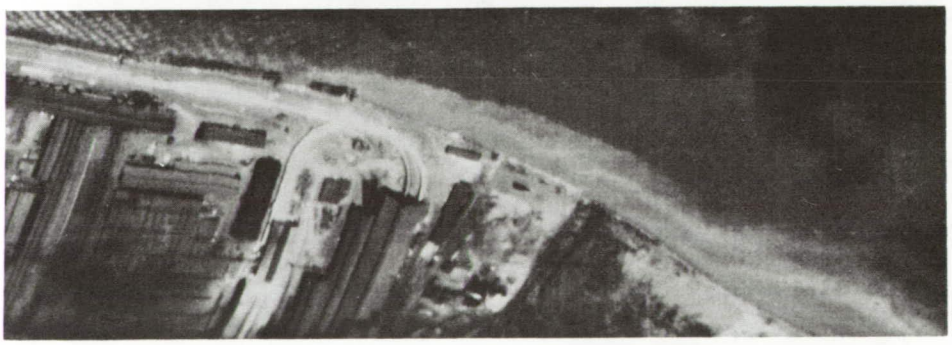

0.62 to 0.66 μ

Multispectral Comparison of Effluent Contrast

Infrared and Optics Laboratory

Willow Run Laboratories

THE INSTITUTE OF SCIENCE AND TECHNOLOGY
THE UNIVERSITY OF MICHIGAN

FIGURE 3

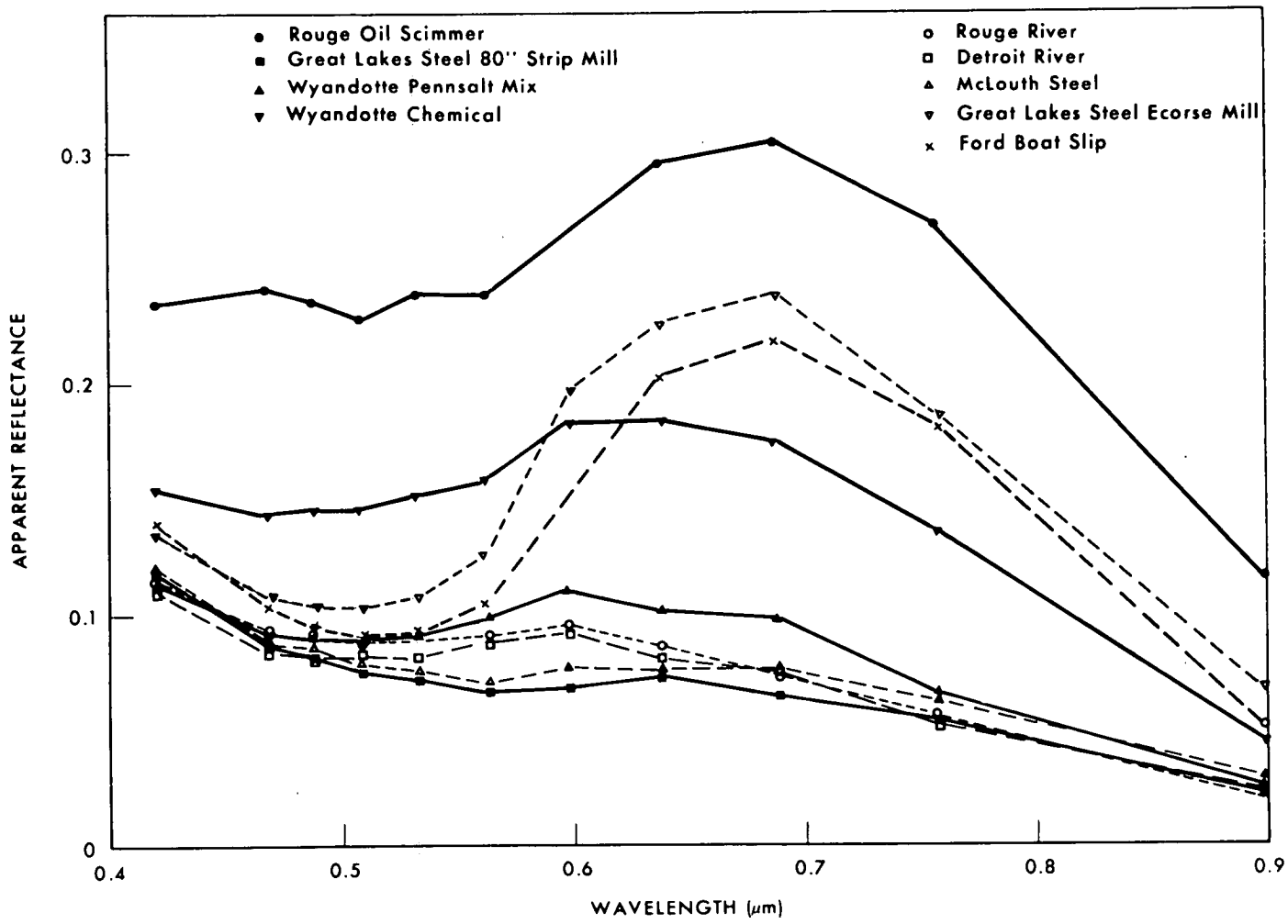

COMPARISON OF SPECTRA OF MAJOR POLLUTANTS IN ROUGE AND DETROIT RIVERS

Infrared and Optics Laboratory — Willow Run Laboratories — THE INSTITUTE OF SCIENCE AND TECHNOLOGY, THE UNIVERSITY OF MICHIGAN

FIGURE 4

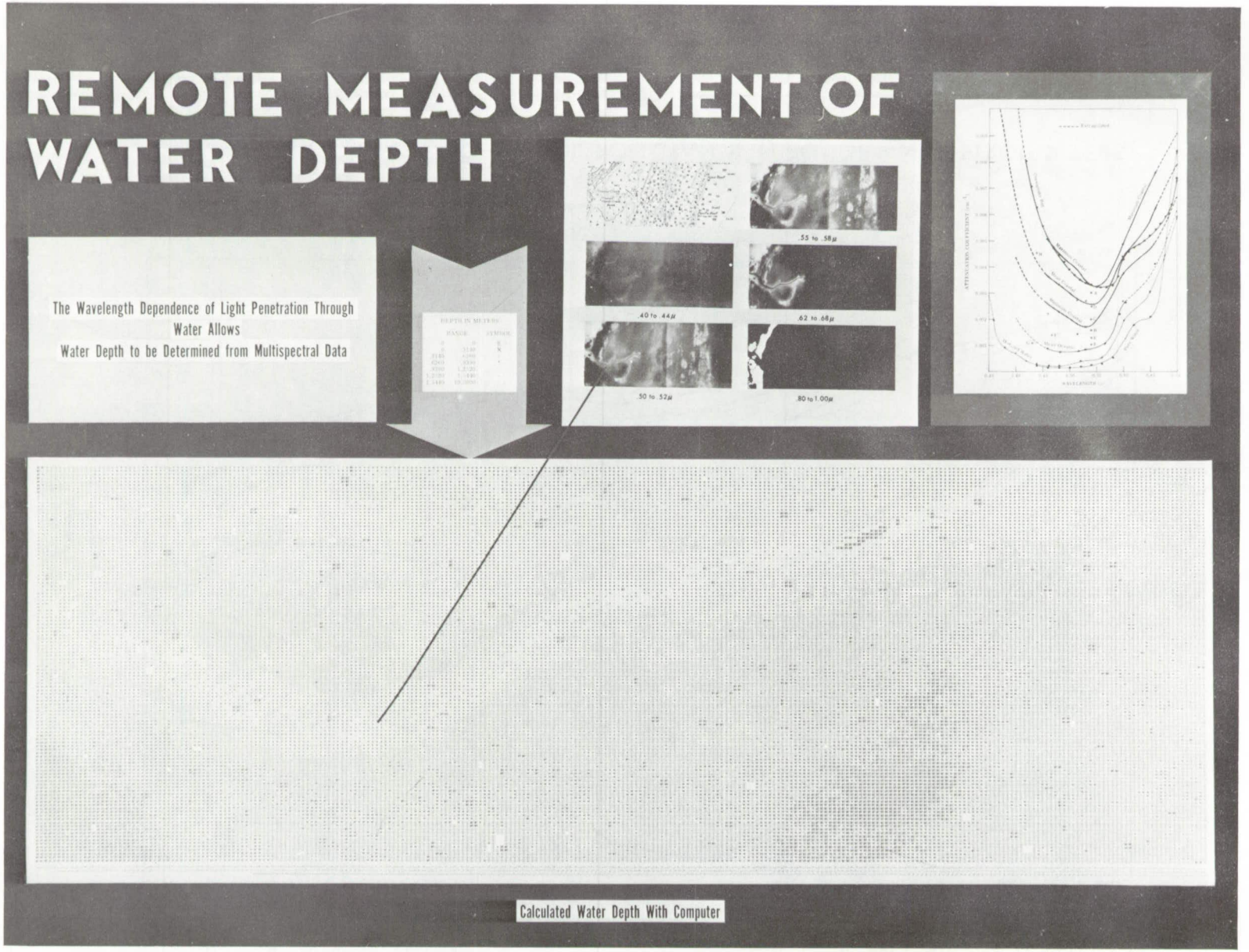
REMOTE MEASUREMENT OF WATER DEPTH
The Wavelength Dependence of Light Penetration Through Water Allows
Water Depth to be Determined from Multispectral Data
.55 to .58μ
.40 to .44μ
.62 to .68μ
.50 to .52μ
.80 to 1.00μ
Calculated Water Depth With Computer

FIGURE 5

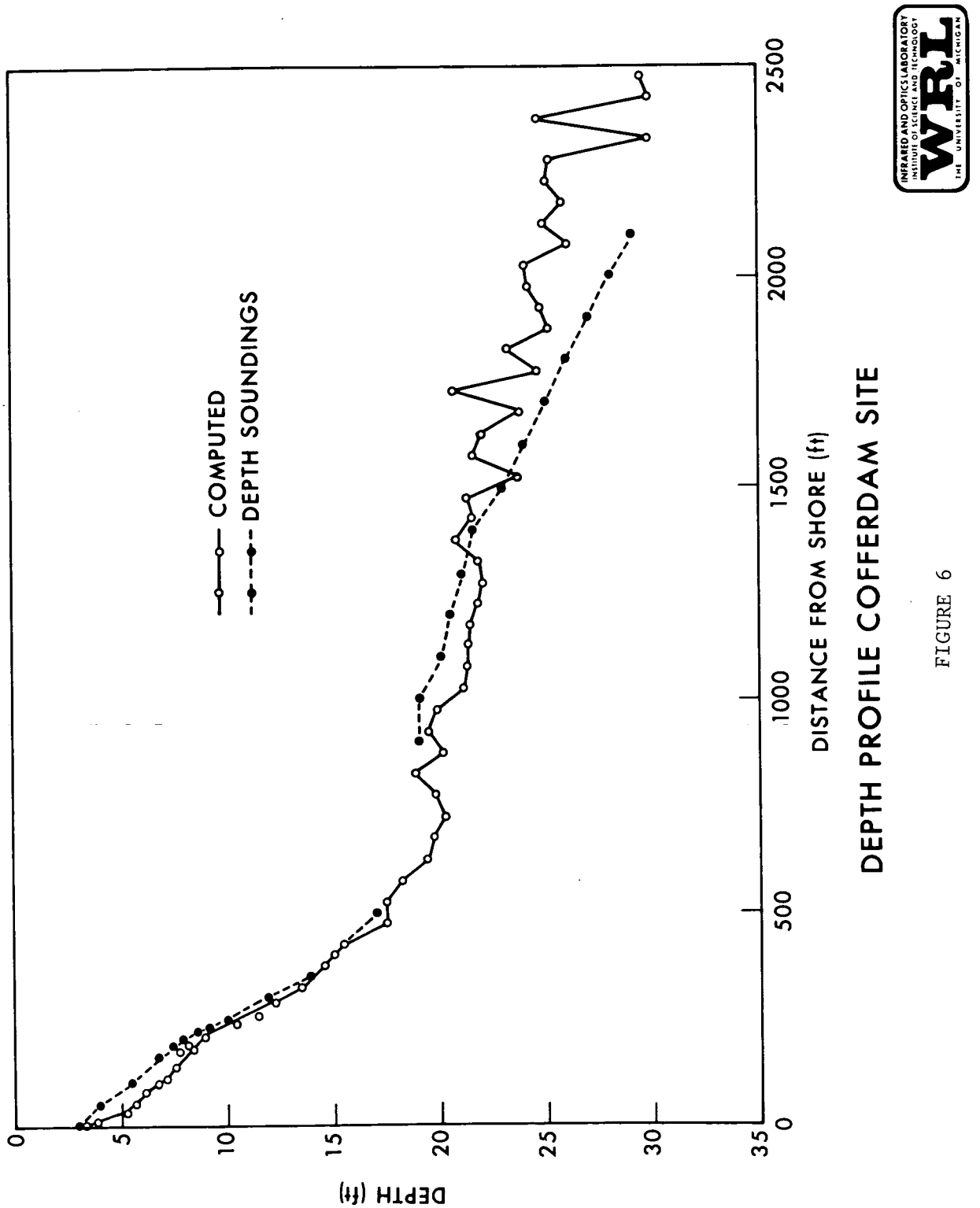
COMPUTED
DEPTH SOUNDINGS
DEPTH (ft)
0
5
10
15
20
25
30
35
0
500
1000
1500
2000
2500
DISTANCE FROM SHORE (ft)
DEPTH PROFILE COFFERDAM SITE
INFRARED AND OPTICS LABORATORY
INSTITUTE OF SCIENCE AND TECHNOLOGY
WRL
THE UNIVERSITY OF MICHIGAN

FIGURE 6

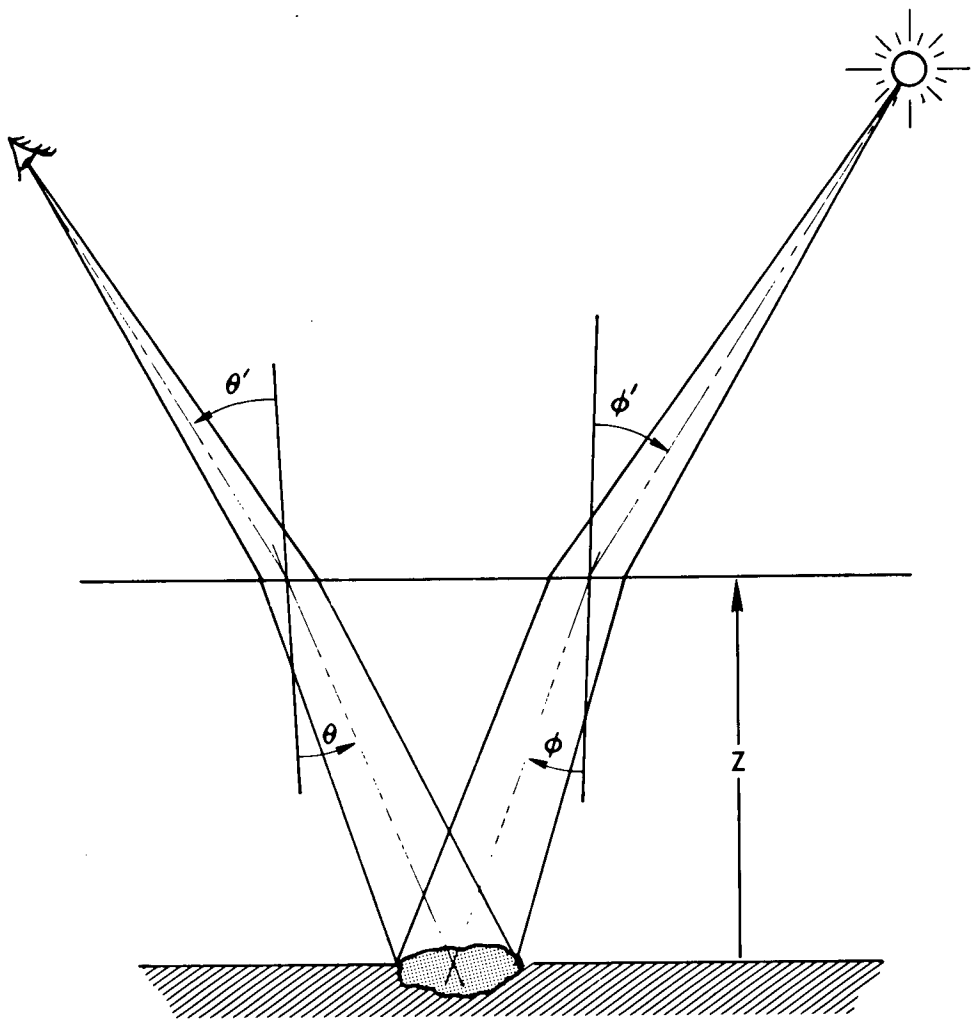

SCHEMATIC REPRESENTATION OF THE OBERVATION OF REFLECTED SUNLIGHT BY A REMOTE SENSOR

FIGURE 7

INFRARED AND OPTICS LABORATORY
INSTITUTE OF SCIENCE AND TECHNOLOGY
WRL
THE UNIVERSITY OF MICHIGAN

$$V_i(z) = \left(\frac{V_{ss}}{\rho_{ss}}\right)_i \rho_i e^{-\alpha f(\theta,\phi) z}$$

where

$$\rho_i = \rho_b - \frac{s}{\alpha} \frac{1}{4\pi \cos\phi f(\theta, \phi)}$$

FIGURE 8

CALCULATION OF REFLECTANCE ρ_i IN PRESENCE OF SCATTERING, s, AND BOTTOM REFLECTION ρ_B

z = depth of water

V_{ss}, ρ_{ss} are sun sensor voltage response and reflectance

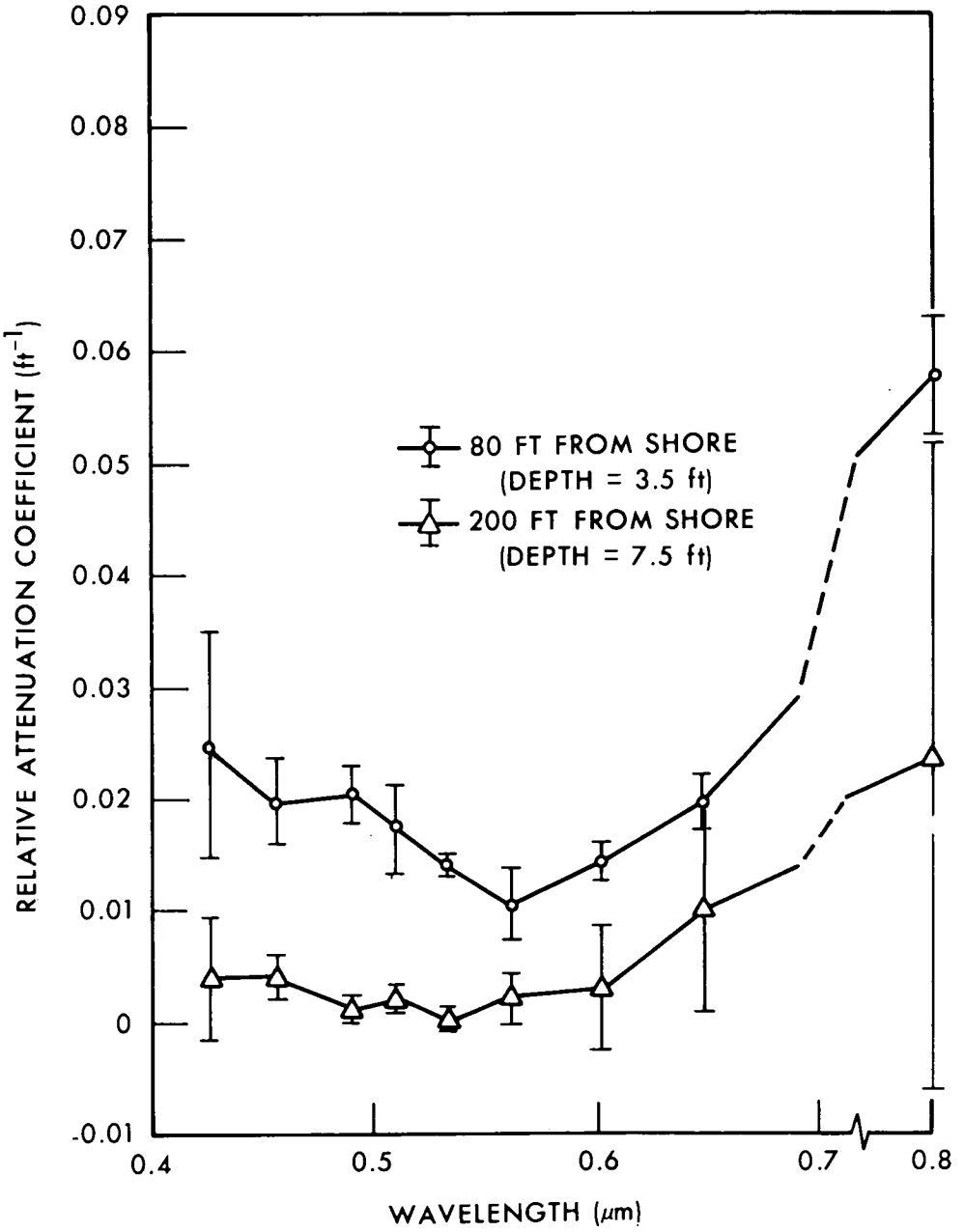

ATTENUATION COEFFICIENTS (COMPUTED) COFFERDAM SITE

FIGURE 9

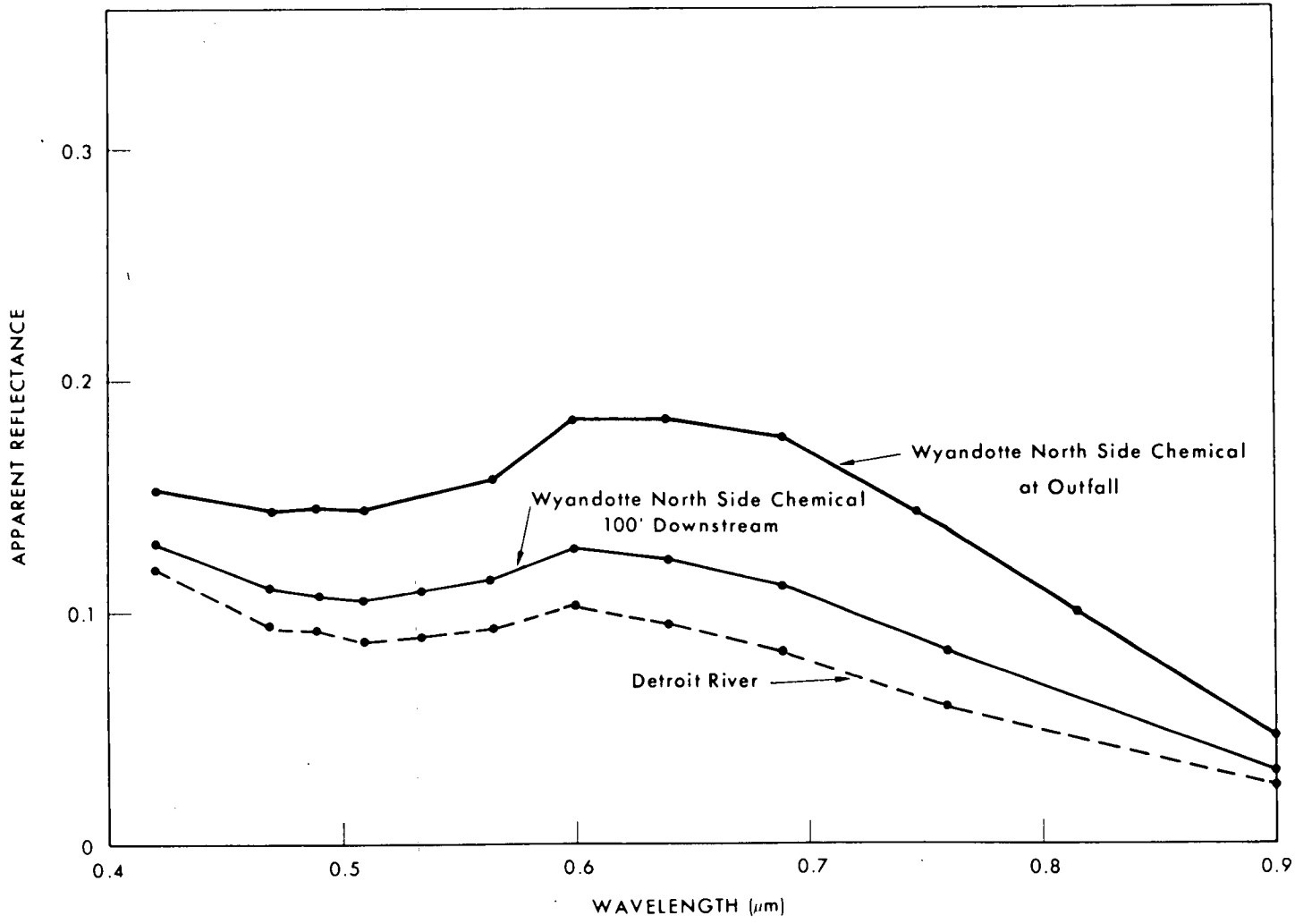

SPECTRA OF WYANDOTTE NORTH SIDE CHEMICAL SHOWING CONCENTRATION DIFFERENCES

FIGURE 10

FIGURE 11

HIGH ALTITUDE PHOTOGRAPH OF
MICHIGAN COASTLINE NEAR FRANKFORT,
MICHIGAN (Mission 103)

FIGURE 12

HIGH ALTITUDE PHOTOGRAPH OF
OUTFALLS OF THE MUSKEGON AND GRAND
RIVERS INTO LAKE MICHIGAN

FIGURE 13

EVIDENCE OF BEACH EROSION BY SHORE CURRENTS NEAR BIG SABLE PT.

FIGURE 14

SUN GLITTER DISCONTINUITY GIVING
EVIDENCE OF SHORE CURRENT

FIGURE 15

ENTRAPMENT OF RIVER OUTFALL BY
NEARSHORE CURRENT PREVENTS MIXING
WITH DEEPER LAKE WATERS

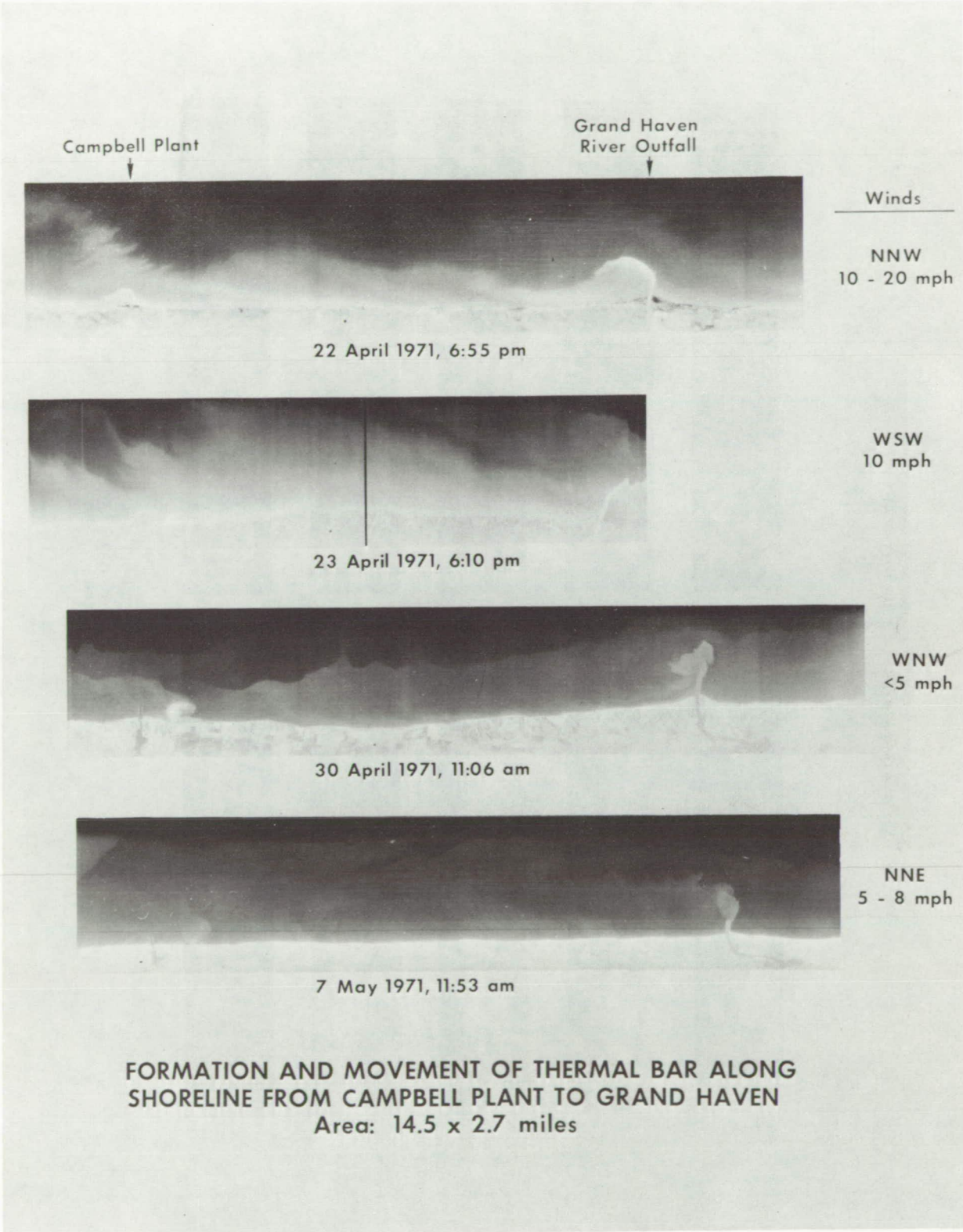
Campbell Plant
Grand Haven
River Outfall
Winds
NNW
10 - 20 mph
22 April 1971, 6:55 pm
WSW
10 mph
23 April 1971, 6:10 pm
WNW
<5 mph
30 April 1971, 11:06 am
NNE
5 - 8 mph
7 May 1971, 11:53 am
FORMATION AND MOVEMENT OF THERMAL BAR ALONG
SHORELINE FROM CAMPBELL PLANT TO GRAND HAVEN
Area: 14.5 x 2.7 miles

FIGURE 16

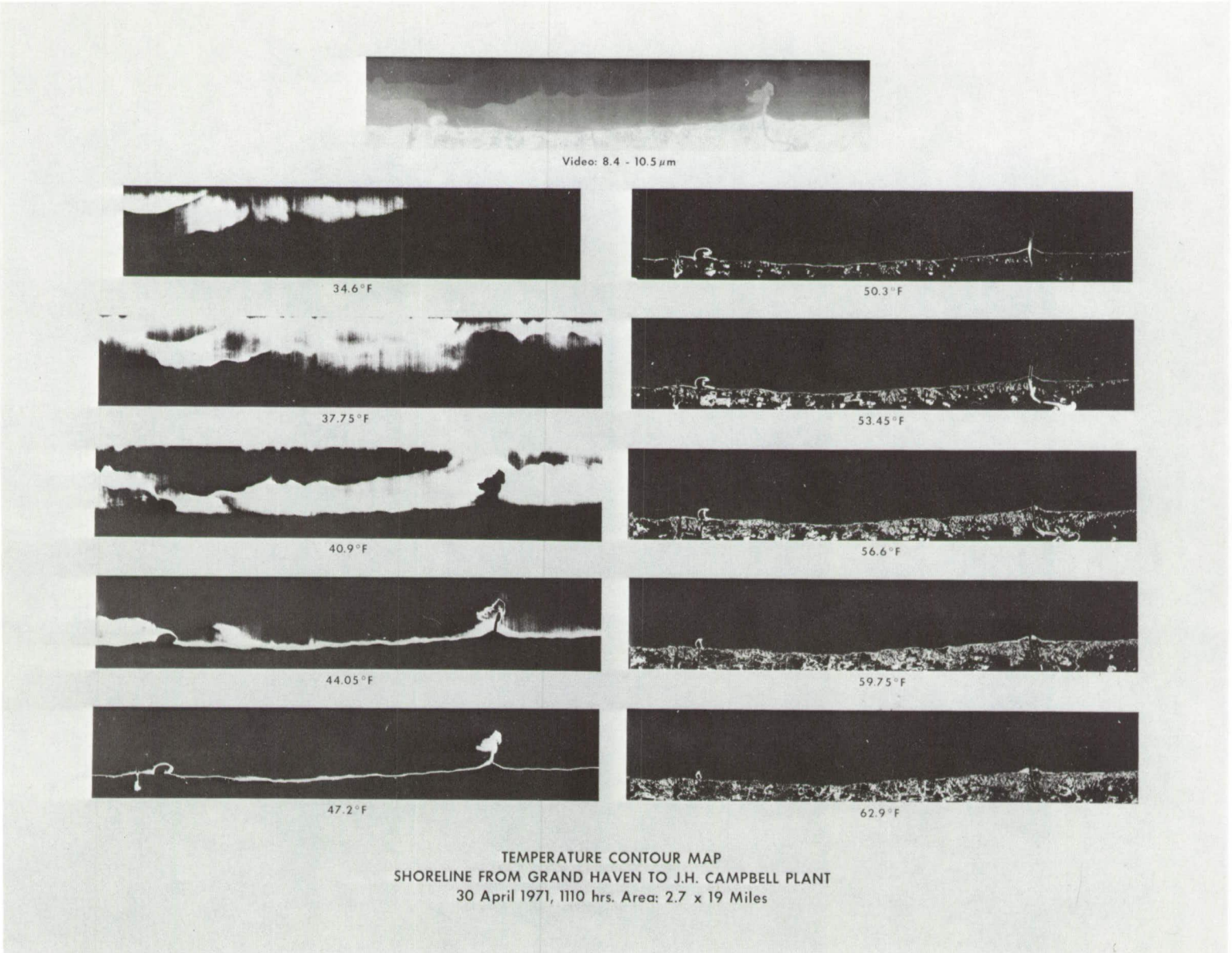

TEMPERATURE CONTOUR MAP
SHORELINE FROM GRAND HAVEN TO J.H. CAMPBELL PLANT
30 April 1971, 1110 hrs. Area: 2.7 x 19 Miles

FIGURE 17

FIGURE 18

ZONES OF WATER MASSES ALONG
MICHIGAN SHORELINE ENHANCED BY
MULTISPECTRAL PROCESSING

SECTION 110

COASTAL AND ESTUARINE APPLICATIONS OF MULTISPECTRAL PHOTOGRAPHY

by

Edward Yost
Sondra Wenderoth
Science Engineering Research Group
Long Island University
Greenvale, New York 11548

ABSTRACT

An evaluation of multispectral photographic techniques for optical penetration of water in northeastern United States and Gulf of Mexico coastal waters is made. Spectral bands to maximize the detectability of underwater objects is a function of the type of particulant matter in suspension, as well as the size and quantity of the particles. The spectral band (493-543 nm), when exposed to place the water mass at about unity density on the photographic emulsion, was found to give the best water penetration independent of altitude or time of day as long as solar glitter from the surface of the water was avoided.

When optimally exposed, the images of surface and underwater objects showed greater chromatic enhancement in multispectral color renditions than on conventional aerial Ektachrome color films. Multispectral negative color renditions were found to be equally as good as positive color images for achieving color differences between the water mass and submerged objects.

An isoluminous color technique has been perfected. This photographic process eliminates the dimension of brightness from a multispectral color presentation. By this method, objects exhibiting subtle spectral differences which are normally obscured by the comparatively large brightness present in coastal waters can be detected. Colorimetric measurements of isoluminous images showed that they provided vivid color differences of underwater targets. The isoluminous technique should be quite useful in detecting subtle color differences in coastal waters which result from phytoplankton concentrations, suspended particulant matter, oil and pollutants, as well as for the identification of sub-surface objects.

INTRODUCTION

The results of a two-part experiment to evaluate multispectral photographic techniques for remote sensing of coastal environments are discussed herein. The research was conducted during the last half of 1967 and during 1968, with analysis extending through 1969.

The Long Island University four-lens multispectral camera was used to obtain spectral photography of both a northeastern coastal site at Montauk Point, Long Island, New York and the Gulf of Mexico coastal site off Santa Rosa Island (Pensacola), Florida. Photo interpretation, densitometric and colorimetric analyses of the imagery obtained were performed using the multispectral additive color viewer and auxiliary equipment. Simultaneous aerial Ektachrome photography was also taken during both parts of the experiment. Five different spectral bands were used to obtain spectral photography. At the northeastern coastal side, the spectral bands were chosen to match the bands of the spectrum to which the color film was sensitive. At the Gulf Coast site, filters especially designed for coastal water penetration were used.

Throughout the experiment extensive environmental measurements were made. These environmental "controls" included: (1) surface and submerged gray scale and color targets, (2) measurements of the intensity and spectral distribution of solar radiation incident upon the water surface and "downwelling" at various depths, (3) spectroradiometric measurement of solar energy reflected by surface and underwater targets, as well as the "natural" upwelling irradiance of the water; (4) colorimetric measurements of the surface targets, and (5) biological-physical analysis of the samples of the water in which the targets were embedded.

FUNDAMENTAL PROBLEMS

Prior to performance of the experiment, two fundamental problems were distinguished as being of critical importance in obtaining precision multispectral photography of coastal waters. These problems are not unique to photographic sensors and, in fact, generally apply to any remote sensing technique in the .26 to 3 micron part of the electromagnetic spectrum where reflection rather than emission phenomenon is encountered.

The first problem relates to the lack of accuracy and precision in the structure of the image due to instrumentation errors. These arise from three sources: (1) sensor errors in formation of the spectral image, (2) photographic errors in transforming the image energy to density in the photograph subsequently used in data reduction, (3) errors in the viewing apparatus which constructs the color image for qualitative viewing by the interpreter and for quantitative colorimetric analysis.

Psycho-physiological variables in viewing color images are not treated in this report, although such considerations are critical in the qualitative interpretation of aerial photography. All the data presented herein are in terms of analytical color measurement and thus psychological variables such as simultaneous contrast enhancement do not appear in this analysis.

The second problem centers on the environment. In this case, three variables are distinguished: (1) the intensity and spectral distribution of the solar illuminant (a fractional part of which is reflected into the camera and thus forms the image) changes as a function of the solar angle, atmospheric conditions, secondary reflectance, and the relative composition of direct sunlight and diffuse skylight, (2) the in situ spectral reflectance of surface objects is known to vary dynamically at least as a function of the non-lambertian (directional) spectral reflectance of such objects (due to their orientation with respect to both the angle of incidence and angle of reflection), as well as due to temporal changes in the absorption and transmission of the object itself, and (3) the atmosphere and water media between the object and the sensor which scatters and absorbs the radiation reflected by the object.

OBJECTIVES

The primary objectives of the research were as follows:

-- To establish the factors which affect the detection and identification of man-made objects embedded in coastal waters using multispectral techniques.

-- To evaluate to what degree subtle differences between underwater objects and the water in which they are embedded can be used for detection and identification without special knowledge of their spectral reflectance characteristics.

-- To compare the characteristics of images formed by multispectral additive color photography with conventional subtractive color film.

-- To measure the environmental variables which affect the multispectral technique of remote sensing and to correlate these environmental variables with the imagery.

-- To obtain upwelling and downwelling irradiance measurements of coastal waters in order to indicate the optimum spectral bands for optical penetration.

-- To improve techniques for imaging and analysis of subtle surface and sub-surface phenomena peculiar to coastal waters.

PROCEDURES

The general procedures used throughout the experiment are discussed below with reference to the objectives of the experiment and the fundamental problems to be overcome when using the multispectral photographic technique for remote sensing.

The multispectral camera was equipped with filters which passed radiation in the desired bands of the spectrum (Yost and Wenderoth, 1967). The film used was both black-and-white Plus-X (8401) or Tri-X (8403). An auxiliary K-24 camera, with a lens identical to those used in the multispectral camera, was loaded with Aero Ektachrome (8442) color film. The two cameras were aligned in a common mount such that the optical axes were parallel. All cameras were activated by a common intervalometer so that exposures were taken at the same time (within the shutter tolerances of the two cameras). A range of exposures was used in both the multispectral camera and color camera to insure the best possible exposure of the scene on the film.

The negative film was processed in a continuous Versamat processor using D-19 developer. Sensitometric control was maintained throughout the processing. In general, a medium-to-high contrast was obtained on the negative although this varied depending on the conditions encountered at a particular test site. Positive transparencies were obtained by duplicating on Kodak Aerial duplicating film (5427) using a Niagara printer and processed in a Versamat using MX 641-1 developer. Sensitometric control was, of course, maintained. Color films were processed using the rewind method, control strips being used to insure the best possible development within the state of the technology.

Densitometric measurements were made of water, the surface, and underwater target images on the black-and-white spectral negatives. The positive images were placed in the additive color viewer. Numerous color spaces were experimentally formed in order to establish those which gave the greatest color differentiation of the images from each other and from the water. These additive color renditions on the viewer screen were photographed using color film. The surface and underwater target images and the images of the coastal waters were measured on the color reproduction using a color densitometer. An analytical chromaticity coordinate determination was made from the color densities using a special computer program. This data was compared with surface measurements of the target colors and spectra made close to the time the photography was taken. A similar analysis was performed on the subtractive color film (aerial Ektachrome)

Environmental measurements of the indident and reflected solar radiation were made. Analyses were performed comparing the percent directional reflectance of surface and underwater targets and the spectral irradiance of the water in which the targets were embedded.

DISCUSSION

An experimental methodology was developed for measuring the performance of various exposures and film/filter combinations for multispectral remote sensing of coastal waters. This quantitative process involved computing the underwater exposure latitude of standard gray scale targets in relation to the exposure latitude of surface targets. At the same time the incident solar radiation and "downwelling" radiation impinging on the sub-surface target array was measured. The methodology included densitometric and colorimetric measurements of the spectral images formed on the multispectral additive color viewer and on aerial Ektachrome film.

A 120-foot by 15-foot hydrodynamically stable structure was designed and oonstructed to submerge the target array below the surface to any desired depth up to 100 feet (see Figure 1). This structure held the targets parallel to the surface and taut without ripples in the cloth (which would cast shadows on the targets, thereby reducing their brightness). The target array was recovered and used repeatedly. The spectral reflectance and colorimetric characteristics of the subsurface and an identical surface gray scale and color target array were calibrated (see Figure 2). In situ measurements of spectral reflectance were made when imagery was obtained (see Figure 3).

Techniques for colorimetric analysis of color imagery were perfected and methods for processing to compensate for the effects of the radiation passed by the filters established. The effects of gamma and the density of the images were also determined as shown in Figure 4.

Spectral measurements of the optical properties of water obtained both independently and jointly with the spectral photography showed the existence of great variation in both the percent of incident light which is downwelling at various depths and the percent upwelling to the surface (see Figure 5). The clearest coastal waters (in which objects can be photographed at depths of 150 feet) were measured to have a peak percent downwelling light at 480 nm, 97 percent reaching a depth of 10 feet and 70 percent reaching a depth of 42 feet. At lower depths radiation at wavelengths greater than 625 nm was absorbed (see Figure 6). High backscatter was measured to exist in the clearest coastal waters at 450 nm. In "dirty" inshore coastal waters, both in the Gulf of Mexico and in the northeast, the peak percent upwelling

light was at 560 nm, demonstrating the absorption of both blue and red light (see Figure 7). Off-shore measurements showed peak upwelling light at 525 nm.

The exposure latitude of targets submerged in northeastern coastal waters recorded by spectral photography using blue (397-512 nm), green (491-585 nm), and red (597-715 nm) filters was determined (see Figure 8). These waters contain large quantities of suspended particulant matter. Quantitative measurement of the comparative penetration capability of the filtration demonstrated that the log exposure latitude of the green spectral band was twice that of the red and three times that of the blue band (see Figure 9). The optimum exposure of underwater objects for all spectral bands was found to occur when the surface was overexposed to place that ambient water illumination at unity density on the recording emulsion.

A series of experiments to reduce solar glitter from the water surface by using polarizing filters was conducted. Various orientations of the plane of polarization were used with respect to the angle of the incident solar radiation impinging on the water surface. No improvement in water penetration capability was found. In fact, the reduction in exposure produced by these filters made them of dubious value.

A set of filters specially designed for coastal water penetration were used in the second phase of the experiment conducted in the Gulf of Mexico. The detectability of underwater objects was found to be best in the 493-543 nm band and almost as good in the 491-595 nm band. The detection of underwater objects was found to be considerably reduced in the 552-604 nm band and unuseable in the 593-658 nm band. It was found that the time of day produced no measurable change in underwater detectability of objects as long as solar angles which cause surface glitter are avoided. However, the relative exposure in each spectral band was measurably affected by time of day. The lens apertures of each spectral band must be adjusted to compensate for this effect in the manner discussed in the text. A decrease in aperture opening of 1 f/stop is necessary when increasing altitude from 1000 feet to 10,000 feet above sea level. In addition, it was found that objects darker than the water in which they were embedded were often as detectable as brighter objects, a condition which persisted to the extinction depth. The overriding consideration in detection of sub-surface objects was found to be the amount of organic and non-organic particulant in suspension in the water. This is the major factor which affects the detection of underwater objects next to wave deformation of the water surface.

CONCLUSIONS

Colorimetric analyses of surface and underwater target images in various multispectral additive color renditions and in aerial Ektachrome photographs were performed on the images obtained at the northeastern test site near Montauk Point, Long Island, New York. These results are summarized as follows:

-- Color of surface images can be greatly enhanced in multispectral color photography by increasing the saturation of these images. To achieve this enhanced color effect the multispectral photographs must be optimally exposed for surface detail which obscures most underwater objects. However, the colorimetric measurements made indicate that improved identification of surface objects by their color is undoubtedly possible.

-- The detection and identification of underwater targets by image color differences is superior on multispectral color renditions compared to color film (aerial Ektachrome) when both are optimally exposed for underwater detail. However, surface detail is lost in the multispectral image due to over-exposure.

-- By using multispectral negative black-and-white transparencies for additive color projection, it is possible to get equally as good color enhancement of underwater targets without incurring the added time and expense in making positive transparencies.

-- Bright underwater detail was detectable in conventional color film (aerial Ektachrome), but all color differences were lost with the exception of the yellow and white targets which were visible although greatly desaturated.

A multispectral photographic technique previously developed by the authors and used in detecting subtle surface differences in coastal waters (Life magazine, 1966) has been brought along to a point where it can be used as a precision tool for detecting subtle color (spectral) differences in water masses. A color image of surface and underwater targets using this isoluminous technique is shown in Figure 10.

This photographic technique eliminates all brightness differences from the scene and shows as a color image only those objects which have a spectral difference. In this manner, both very bright detail such as color targets and objects of low brightness (underwater color targets) are both well imaged as vivid colors. The color differences between identical color surface and underwater targets is due solely to the

water between them unaffected by their relative brightness.

All chromatic (colorless) objects such as the surface and underwater gray scale targets are shown as images of equal brightness. The reader should notice that variations in brightness do not offset isoluminous image characteristics. The shadow of a building over the yellow target does not affect the image color. The reader should compare this to conventional color film image (Figure 10) where the target can only be seen in the shadow area. It is anticipated that this technique will be quite useful for detecting very subtle differences in water color such as are cuased by chlorophyll. Such small changes in color are often masked by large brightness differences from the water surface.

REFERENCES

Yost, Edward and Sondra Wenderoth (1971): "Multispectral Photographic Remote Sensing of Coastal Environments", Science Engineering Research Group Technical Report TR-11, Long Island University, New York.

_____ (1970): "Remote Sensing of Coastal Waters Using Multispectral Photographic Techniques", Science Engineering Research Group Technical Report TR-10, Long Island University, New York.

_____ (1970): "Remote Sensing of Coastal Environments Using Multispectral Photographic Techniques", Proceedings of the Symposium on Hydrobiology, Miami Beach, Florida, pp. 274-302.

_____ (1967): "Multispectral Color Aerial Photography", Photogrammetric Engineering, pp. 1021-1033.

Figure 1. Underwater target array showing buoy arrangement with target submerged.

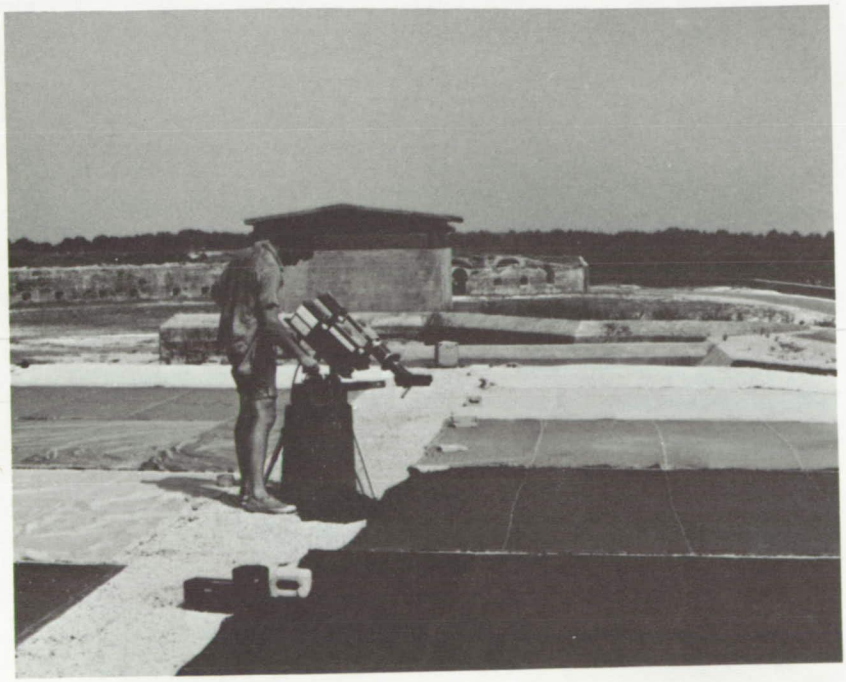

Figure 2. Measurement of the reflectance spectra of surface targets.

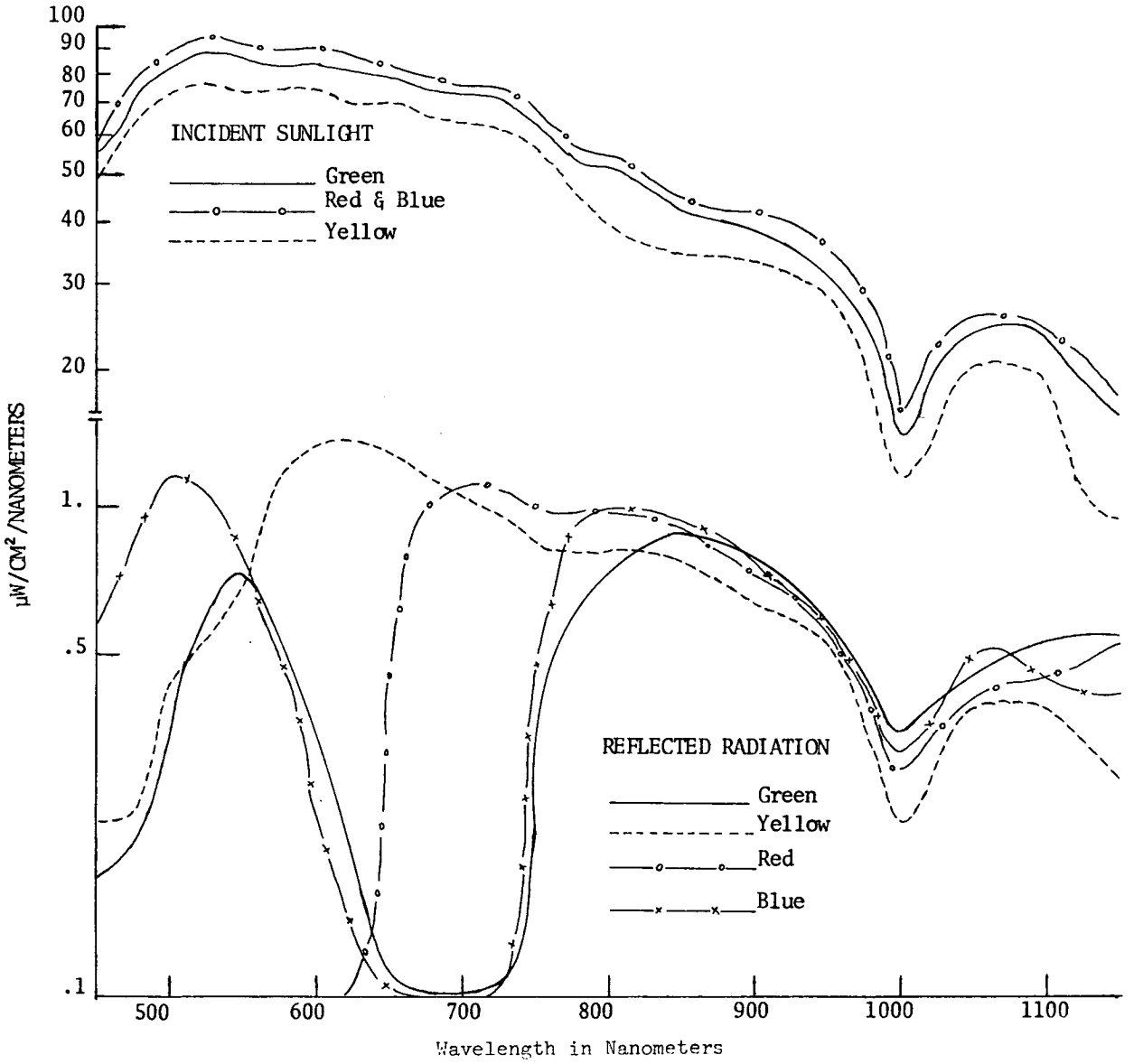

Figure 3. Incident solar radiation and radiation reflected from dacron targets used in second phase of experiment.

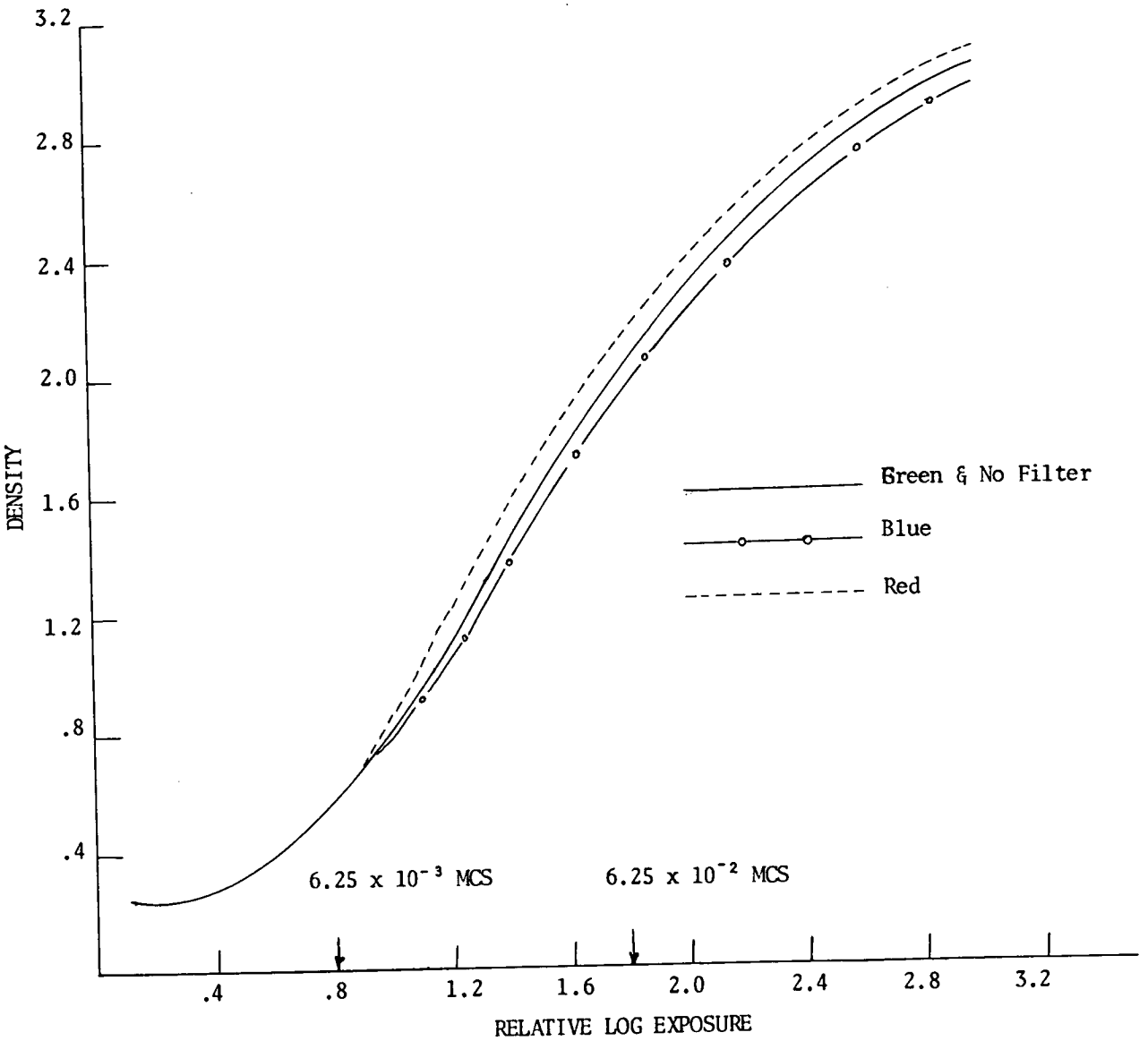

Figure 4. Characteristic curves of multispectral imagery. Ektachrome film (8401), MX 641 developer, five minutes at 80°F.

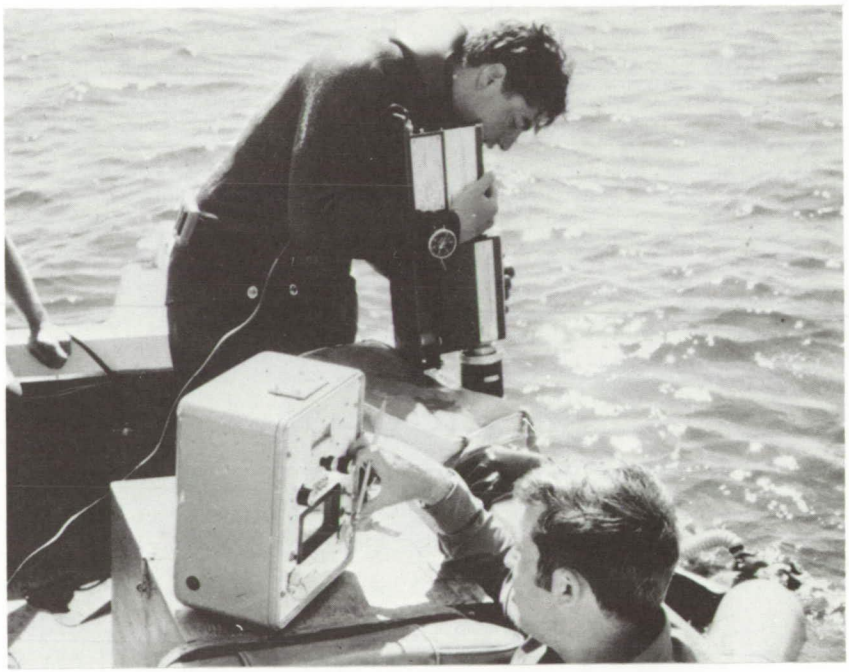

Figure 5. Surface measurements of incident sunlight and upwelling irradiance.

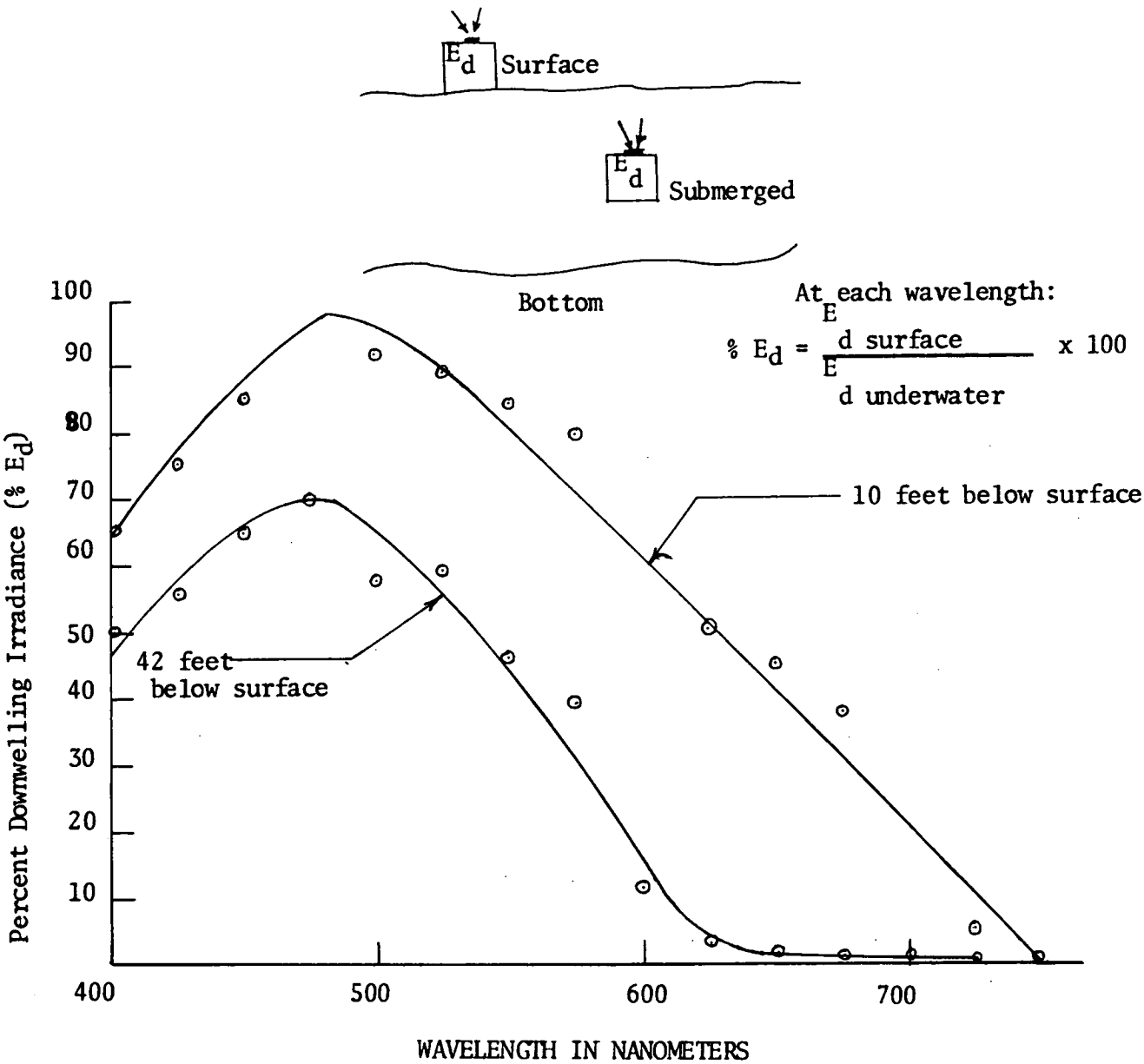

Figure 6. Downwelling reference: Percent downwelling irradiance at 10 and 42 feet below the surface, Tongue of the Ocean, Andros Island, Bahamas.

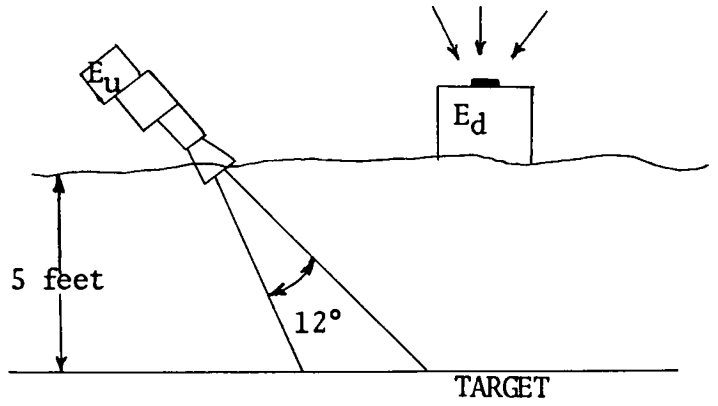

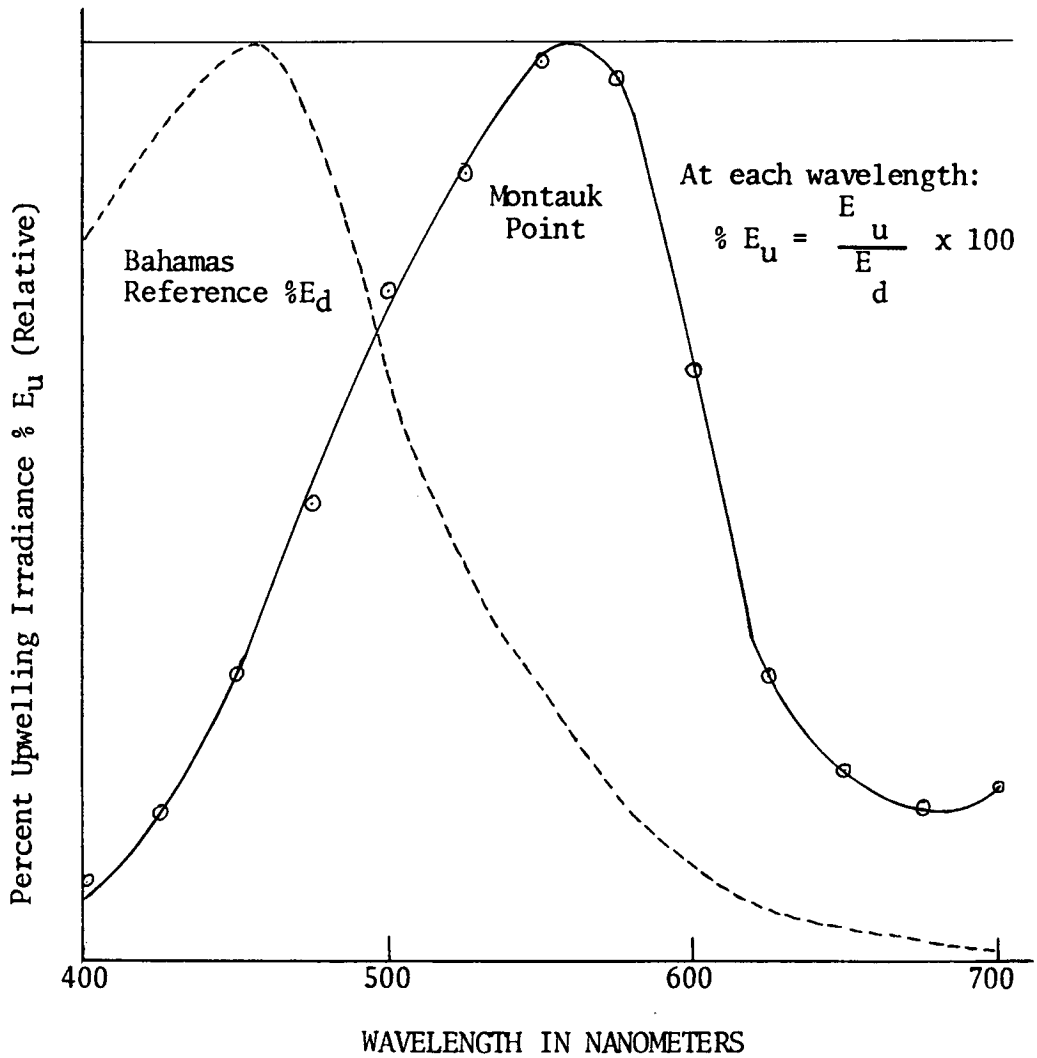

Figure 7. Percent upwelling irradiance of water mass with white target five feet below the surface, Fort Pond Bay, Montauk Point, Long Island, New York. Average of four readings 1722 to 1747 GMT, October 7, 1967.

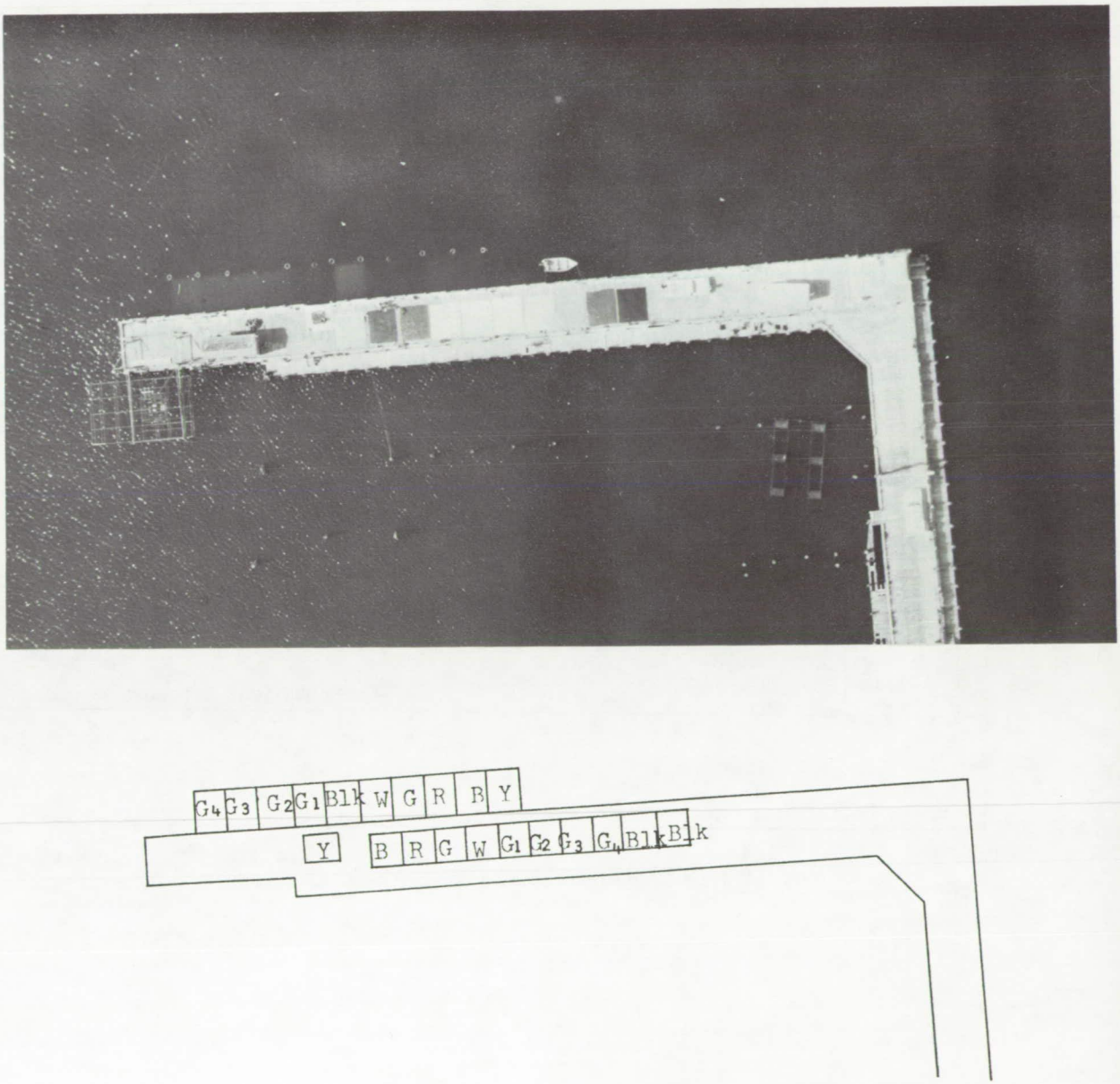

Figure 8. Details of the target area, Fort Pond Bay, Montauk Point, Long Island, New York.

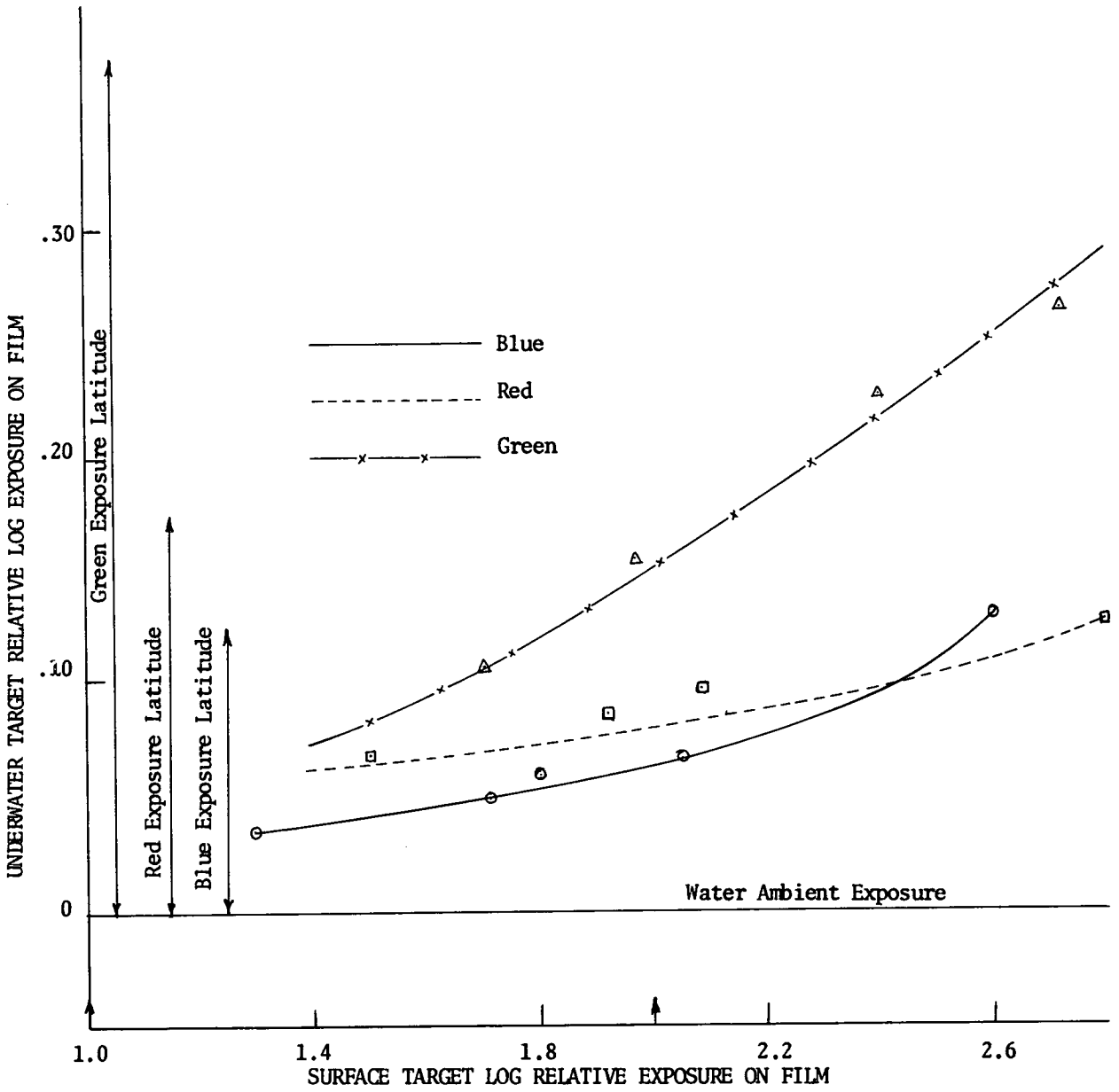

Figure 9. Underwater target relative log exposure in green spectral band, Montauk Point, October 1967.

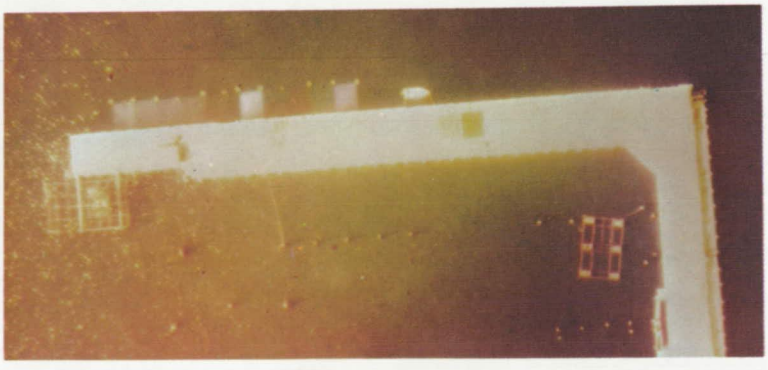

Figure 10. Photographic reproductions of surface underwater target arrays on isoluminous and conventional color multispectral renditions, as well as on aerial Ektachrome color film. Underwater target array submerged 12 feet in murky northeastern coastal waters.

(PAPER NOT SUBMITTED FOR PUBLICATION

SECTION 111

EFFLUENT MIXING IN THE MISSISSIPPI REGION DELTA, LOUISIANA

by James Coleman, Lyn Wright, and
Ronald Becker

ABSTRACT

(Not available)

SECTION 112

A STUDY OF TEMPORAL ESTUARINE FLOW DYNAMICS

by

Robert L. Mairs
Naval Research Laboratory
Washington, D. C. 20390

and

Dennis K. Clark
Naval Oceanographic Office
Washington, D. C. 20390

ABSTRACT

Multispectral photography, IR imagery, image enhancements, oceanographic, radiometric, and meteorological data are used in the study of temporal estuarine flow dynamics to increase our knowledge of nearshore circulation and the resulting dispersal of suspended and dissolved substances that are introduced from the continent.

Repetitive multispectral photography, IR imagery, surface truth, i.e. total radiance and irradiance, water surface temperatures, salinity, total suspended solids, visibility, current velocity, winds, dye implants, and high contrast image enhancements are used to observe and describe water mass boundaries in the nearshore zone and to attempt to establish on what repetitive scale these coastal features would be looked at to better understand their behavior.

Water mass variability patterns seen both naturally and with the use of dyes along the North Carolina coast and in the Chesapeake Bay are being studied as synoptic data that will lead to a better understanding of the basic dynamics of circulation, flushing and mixing in our coastal waters.

INTRODUCTION

One of the most immediate problems facing the world today is the management and understanding of our coastal environment and the impact made upon it by estuarine effluents. More and more demands are being placed on this natural resource without the background material needed for its total effective use. The knowledge of nearshore circulation

dynamics along the mid-Atlantic United States coasts and the resulting dispersal of suspended and dissolved substances that are naturally and culturally introduced from the continent is very fragmentary. This lack of comprehensive knowledge is proving costly in highly populated areas along our coastlines where man-introduced substances are threatening the natural utility of many coastal waterways.

With the rapid development of remote sensor technology, a new technique for ocean monitoring is developing. Remote sensors are capable of providing an overview of surface and near-surface conditions in real time over large geographical areas. This is not to suggest however, that remote sensing can replace in situ measurements but quite the contrary, very stringent in situ measurements must be used to fully interpret the data.

OBJECTIVES

The objectives of this nearshore remote sensing research which hopefully will lead to the solving of many of these problems are:

* attempt to describe surface and near-surface fluid flow dynamics in an estuarine environment using synoptic aerial photography and infrared imagery.

* attempt to establish the temporal characteristics of various surface and near-surface coastal features.

* correlate the spatial and temporal characteristics of estuarine effluents with other environmental parameters.

METHODS AND PROCEDURES

There are two fundamental properties of the ocean surface that require understanding when studying the ocean with electromagnetic sensors. The first property is the dynamic nature of the oceans surface; how it can change from a mirror smooth surface acting as a specular scatterer under no wind-wave conditions to white water under heavy winds. The second property is the degree to which electromagnetic energy can penetrate the water itself. Significant water penetration occurs only in two general regions of the spectrum; at very low frequencies on the order of 10^3 to 10^4Hz and at frequencies around 7×10^{14}HZ. Since it is

impractical to build remote sensors at low frequencies and long wavelengths, the only portion available lies in the visible region from about 400 to 600 nanometers.

The energy source for image formation on photographic film is the sun. The amount of solar energy which is recorded by photographic film in any particular wavelength band depends upon the energy which: (1) strikes the waters surface, (2) reaches a sub-surface object, (3) is reflected by the object, (4) makes its way coherently back through the water and across the water-air interface. Much of the image formation energy that reaches the camera from below the waters surface is concentrated in a spectral region extending from about 420 to 550 nanometers. In relatively clear oceanic waters, peak transmission lies near 480 nanometers but as one moves into coastal waters that are rich in particulate matter, this transmission peak shifts towards the green. Thus, depending upon the application and the type of water, there may be a preference in the portions of the visible spectrum to be used. The response of light energy interacting with the ocean can be illustrated on a qualitative basis by using a 6-band Hasselblad camera array which records on film several discrete portions of the visible spectrum (Figure 1).

In November 1970, the North Carolina coast was the site of an Earth Resources mission utilizing the NASA MSC RB57F aircraft. The flight objective was to obtain high-altitude mosaic multispectral photography over the coastal waters at least twice during a tidal cycle. Figure 2, shows 6 simultaneous multispectral photographs of an estuarine plume front adjacent to the North Carolina coast. A qualitative comparison of the 6 filter combinations for water mass delineation can be made by examining the frames. Starting at the blue end (47-B) of the spectrum very little contrast or definition can be seen in the water but as one moves to the blue-green (2E+38), the green (58), the yellow (21+57), and the red (25-A), increasing contrast and definition of the plume front can be observed. The near IR (89-B) energy is completely absorbed at the surface so gives no information on sub-surface phenomena but shows excellent shoreline definition. The 21+57 and the 25-A filter combinations seem to give the best depth penetration, contrast and definition for these particular coastal waters.

Figure 3 is a color photograph of an estuarine plume front taken during the same mission. The film density differences across this plume front are very small thereby making it difficult to examine the plume front lineation. A number of optical and photographic enhancement techniques were utilized in an attempt to increase the delineation of this plume front. No advantages could be found by using the optical

enhancers however, photographic techniques provided satisfactory contrast level information. Figure 4 is a high contrast enhancement of Figure 3 and clearly illustrates the increased plume front definition and the three separate water masses along the coastline. From water samples taken at the time of overflights, suspended particulate counts averaged approximately 8 mg/liter in this area. No correlation has yet been found between the densities of the film and the total suspended material found in the water. More research is needed on the physics of backscattered light from varying sizes, shapes, and types of particulate matter.

The plume front shown in Figure 4 was photographed three times during the day of 17 November spanning a total time of 146 minutes. The photographs were taken at 15:03, 15:26, and 17:29 GMT. High contrast enhancements were made from each of the three frames and a composite of the three enhancements was produced (Figure 5). Upon examination of this composite the movement of the plume becomes quite clear. The nearshore mass of water was moving at approximately 1.1 knot during this 146 minute period while the water mass offshore was only moving at 0.7 knot. This increased velocity (0.4 knot) in the nearshore zone is attributed to increased velocity due to the nearshore littoral current and/or increased velocity of the ebb flow discharge plume from Ocracoke Inlet as it progresses southward along the coastline.

In addition to these naturally occurring color fronts as indicators of circulation dynamics, dye tracer techniques are also being utilized to study the complex fluid flow dynamics in the estuarine system.

OBSERVATIONS AND RESULTS

During May 1971, the Naval Oceanographic Office conducted an investigation which provided simultaneous ground truth for a series of low-level overflights in the Patuxent River Estuary, Maryland. Dye tracer techniques were utilized to study the flow characteristics in an estuarine system and to aid in the interpretation of naturally occurring discontinuities detected by the remote sensors. The remote sensors operated on these missions were a CA-14 photogrammetric camera and a RECONOFAX IV infrared scanner. An extensive ground truth measurement program consisting of the following was conducted concurrently:

* Three water level stations
* Surface thermistor chain
* Surface temperature and salinity transects
* Three moored current meters

* Standard meteorological variables

* Smoke bombs for surface wind direction

* Point and continuous line dye sources

* Light penetration measurements

Although the analysis of this data resulting from this investigation is not yet complete, some of the preliminary results can be presented.

Two different observational sets will be discussed. The observations were taken on the same day at different tidal phases. The first set demonstrates a qualitative approach which is possible when flight track line spacing permits mosaics to be constructed. The second observational set, consisting of separate overflights of the same area with a short time separation, provides an example of a quantitative approach.

Mosaics constructed from the concurrent photography and IR imagery taken over the test area are presented in Figures 6 and 7. The photographic mosaic was made from Ektachrome positive transparancies and this, coupled with the reduction in size from the original mosaic, results in a very low photographic contrast level. Therefore, arrows were superimposed to indicate the direction of dye and smoke dispersal. The surface circulation within the test area is uniquely depicted in Figure 6 by the point and line dye sources. One of the areas of particular interest is the eddy which exists during flood tidal stage off Drum Point. The detail is difficult to distinguish in Figure 6 but in the original color photography, fluorescein dye from a point and a line source has been entrained into the eddy enhancing its visibility. This eddy also is observed in the IR imagery (Figure 7) where the warmer water flows out from a shallow pond just north of the Point. This outflow provides a sharp thermal contrast as this water flows around the Point into the eddy. Throughout the area the outflows of warmer water from the shallow creeks and coves provide sharp thermal discontinuities on the order of 1° to 2°C. The movements and positions of these thermal discontinuities in relation to the main stream flow provide such information as flow direction, points of flow separation, eddy size, upwelling, and lines of water mass convergence. However, the utility of the IR imagery decreases as an ebb tidal phase is impressed on the area; the warmer waters are entrained and mixed into the main stream flow and the thermal contrast is greatly diminished.

Moving further upstream the complex flow structure which occurs as the tidal current progresses through the river's successive bends can be

seen more clearly in Figure 8. Here the continuous line source, which was originally generated as a line between the tip of Point Patience and the opposite bank is rotating counter clockwise as the main flow is channeled along the southeastern side of the Point. The point sources also illustrates a "choking" effect with resulting partial flow reversal occurring along the lower bank. The "choking" effect is a result of insufficient specific energy* to pass the increased discharge per unit width in this area of extreme channel contraction.

A qualitative streamline analysis based on the composite photographic and IR imagery data is shown in Figure 9 and serves to illustrate the benefit of such an approach for developing conceptual models. The boundaries of the relatively unmixed Chesapeake Bay water were derived from positions of convergent line slicks in the photography and thermal discontinuities in the IR imagery. Ground truth surface temperature and salinity transects verified the upstream limit of this surface boundary. At this boundary the flow becomes increasingly unstable and less uniform as it passes into a contracting and bending channel. The Bay water is then mixed with and overridden by the warmes and less dense waters of the river only to reappear upstream in areas of upwelling.

Figures 10 and 11 are two photographs taken 396 seconds apart during an ebb flow at the mouth of the estuary. These photographs are used to illustrate a basic quantitative approach when using short term repetitive photography of dye tracers. In Figure 10, a continuous line source is in the process of being generated between Fishing Point and Drum Point. Two point sources are dispersing dye adjacent to the line source. In addition, bayward of the new line source, the remnant of an older line source can be seen. Figure 11 shows the displacement of the line source and the movement of the point sources during the 396 second time interval. The location of the dye images (with the exception of the new line source in Figure 11) were plotted after the photographs were corrected for altitude and tilt differences and are depicted in Figure 12. The center line of the line sources was then estimated and displacement measurements along with velocity calculations were made from these positions. In Figure 12, the cross-sectional variations of the surface velocities (V_1 through V_8) clearly indicate the high velocity area at the beginning of the abrupt channel contraction. The increased velocities of the point and remnant line sources (V_9 through V_{10}) are produced by the continuation of the narrowing channel and increased convergence. This further contraction of the channel

* Specific energy is defined here as the energy referred to the channel bed as datum.

bathymetry is not shown on the figure.

Three current meters were taut line moored 2.6 meters below the surface, between Drum Point and Fishing Point. The data from two of these current meters is not yet available. The other meter was moored at the position shown in Figure 12 in the vicinity of maximum displacement of the line sources. This displacement occurs to the right of the channel axis. The computed velocity (V_3) has a magnitude of .6 knot and the current meter position is shown indicating approximately the same direction with a .5 knot magnitude. This reasonable correlation was obtained from the water level and current speed data compiled in Figure 13. This Figure depicts the water level fluctuation for the photographic data acquisition time and an extrapolated current speed record. The extrapolation for current speed was necessitated by instrument failure prior to the overflight. The procedure for utilizing this data was to select a period in the water level data (when the current meter was functioning properly) that had approximately the same tidal phase and amplitude. Since the amount of energy contributed by the tidal force is approximately the same and that no large variation in discharge occurred; the extrapolation should be reasonable. Completion of the data processing of the other meters will provide a better correlation base.

CONCLUDING REMARKS

As has been shown in this preliminary analysis of a continuing Navy program to better understand nearshore circulation dynamics and its impact on the environment, a new look must be taken at the temporal scale at which coastal phenomena are to be studied. Coastal features are extremely dynamic; changing rapidly on the order of minutes and hours. With the deployment of satellites that look at one point every 18 days or even on the order of 4 days in future satellites, we will not be able to statistically examine and thereby understand many of the time dependent phenomena existing in the coastal zone. A well coordinated remote sensing aircraft program capable of repeat coverages on the temporal scale mentioned above is necessary if we wish to thoroughly understand the circulation dynamics in the nearshore zone.

BIBLIOGRAPHY

1. Duntley, S. Q., 1963, "Light in the Sea, "Jour. Opt. Soc. Am., Vol. 53.

2. Jerlov, N. G., 1968, Optical Oceanography, Elsevier, Amsterdam, 194 pp.

3. Henderson, F. M., 1966, Open Chennel Flow, MacMillan, New York, 522 pp.

4. Smith, J. T., editor, 1968, Manual of Color Aerial Photography, Am. Soc. Photo., Alexandria, Virginia, 550 pp.

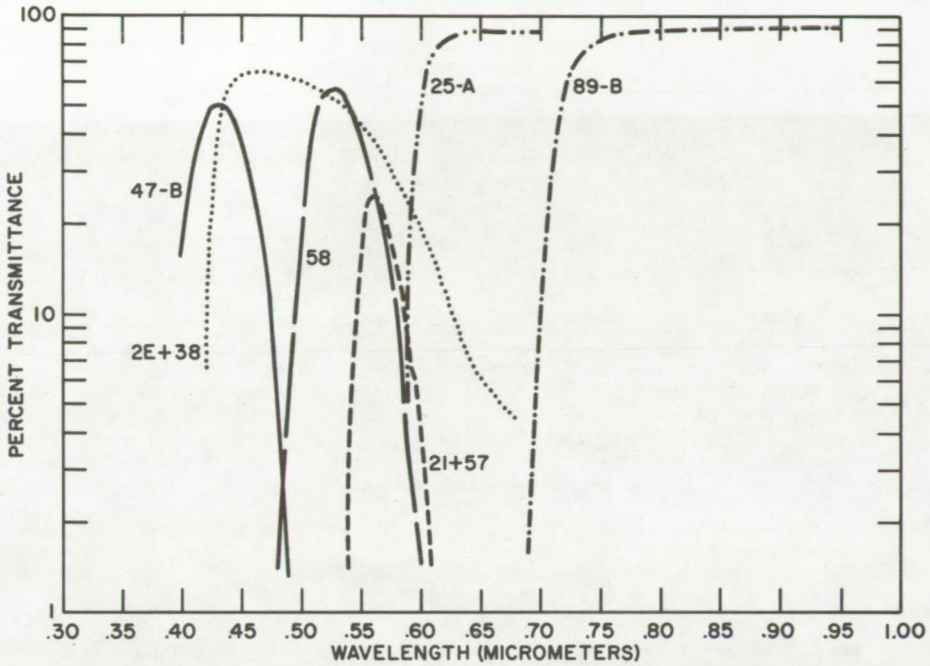

FIGURE 1. MULTISPECTRAL FILTER COMBINATION FOR NASA RB-57F HASSELBLADE ARRAY

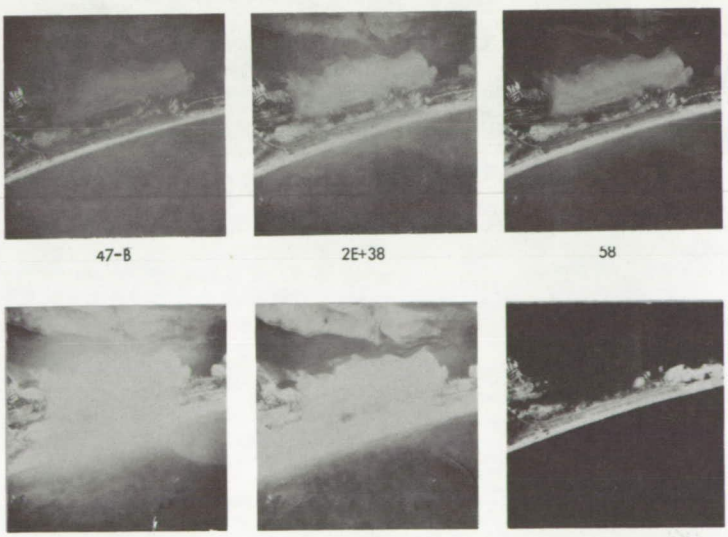

FIGURE 2. SIX SIMULTANEOUS MULTISPECTRAL PHOTOGRAPHS OF AN ESTUARINE PLUME FRONT NASA MSC MISSION NO. 147, 11-17-70

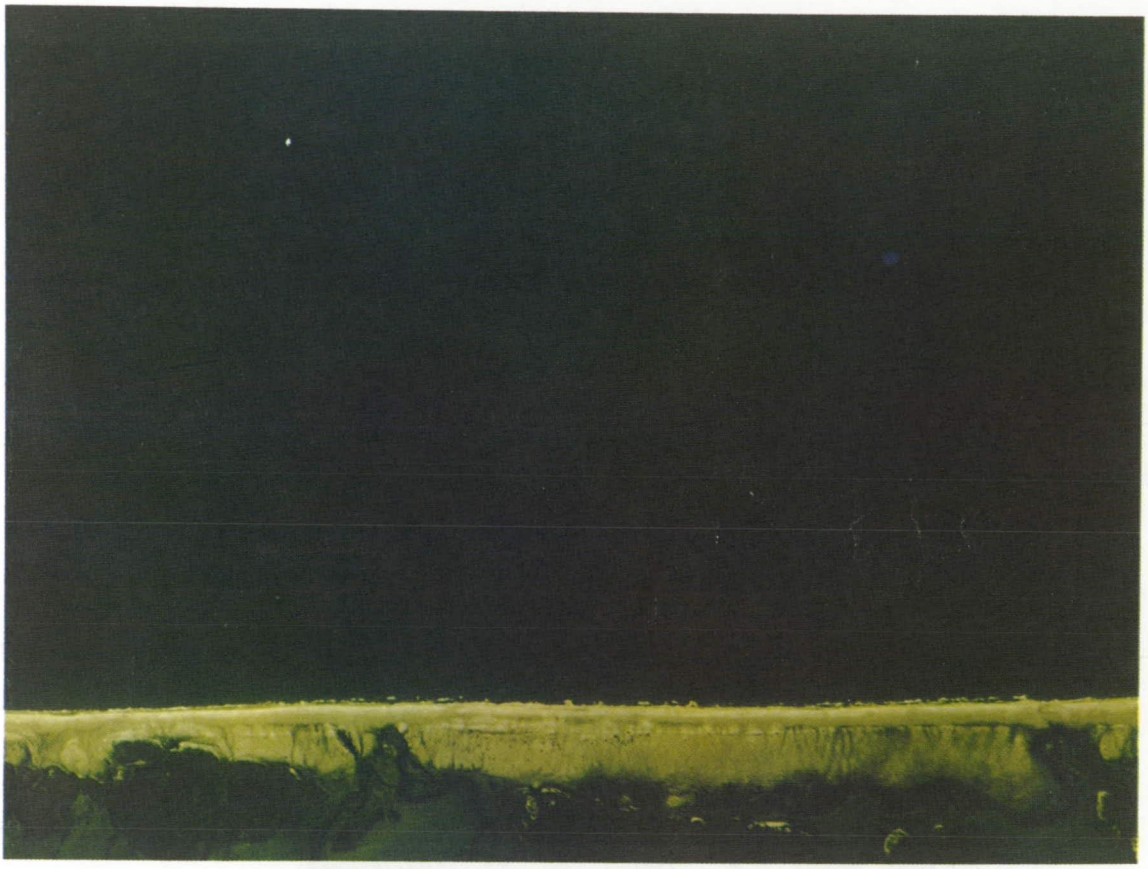

FIGURE 3. COLOR PHOTOGRAPH OF PLUME FRONT ADJACENT TO NORTH CAROLINA COAST.

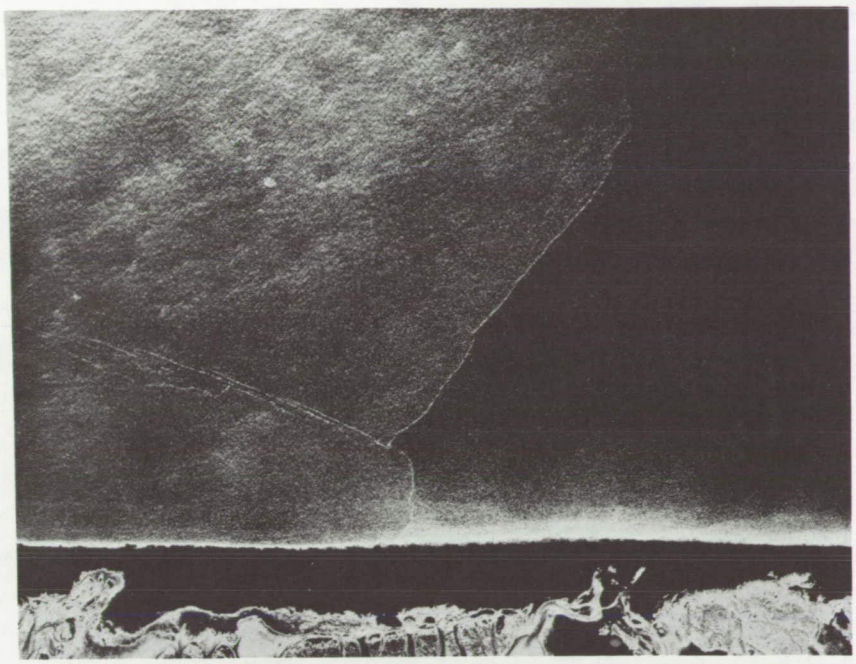

FIGURE 4. HIGH CONTRAST ENHANCEMENT FROM A COLOR PHOTOGRAPH OF AN ESTUARINE PLUME FRONT

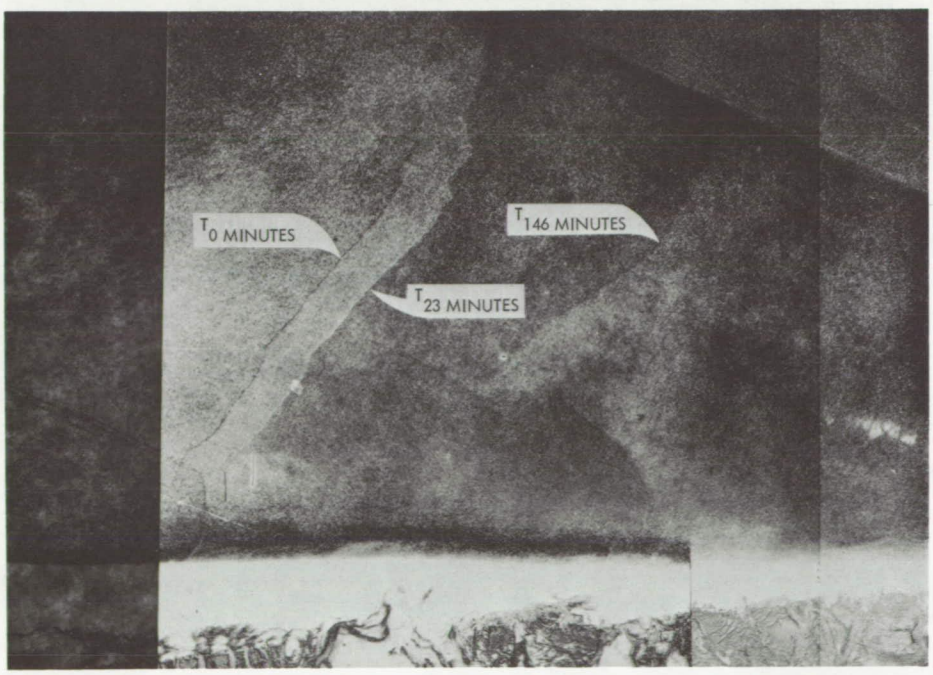

FIGURE 5. OVERLAY OF PLUME FRONTS PHOTOGRAPHED AT 15:03, 15:26, AND 17:29 GMT

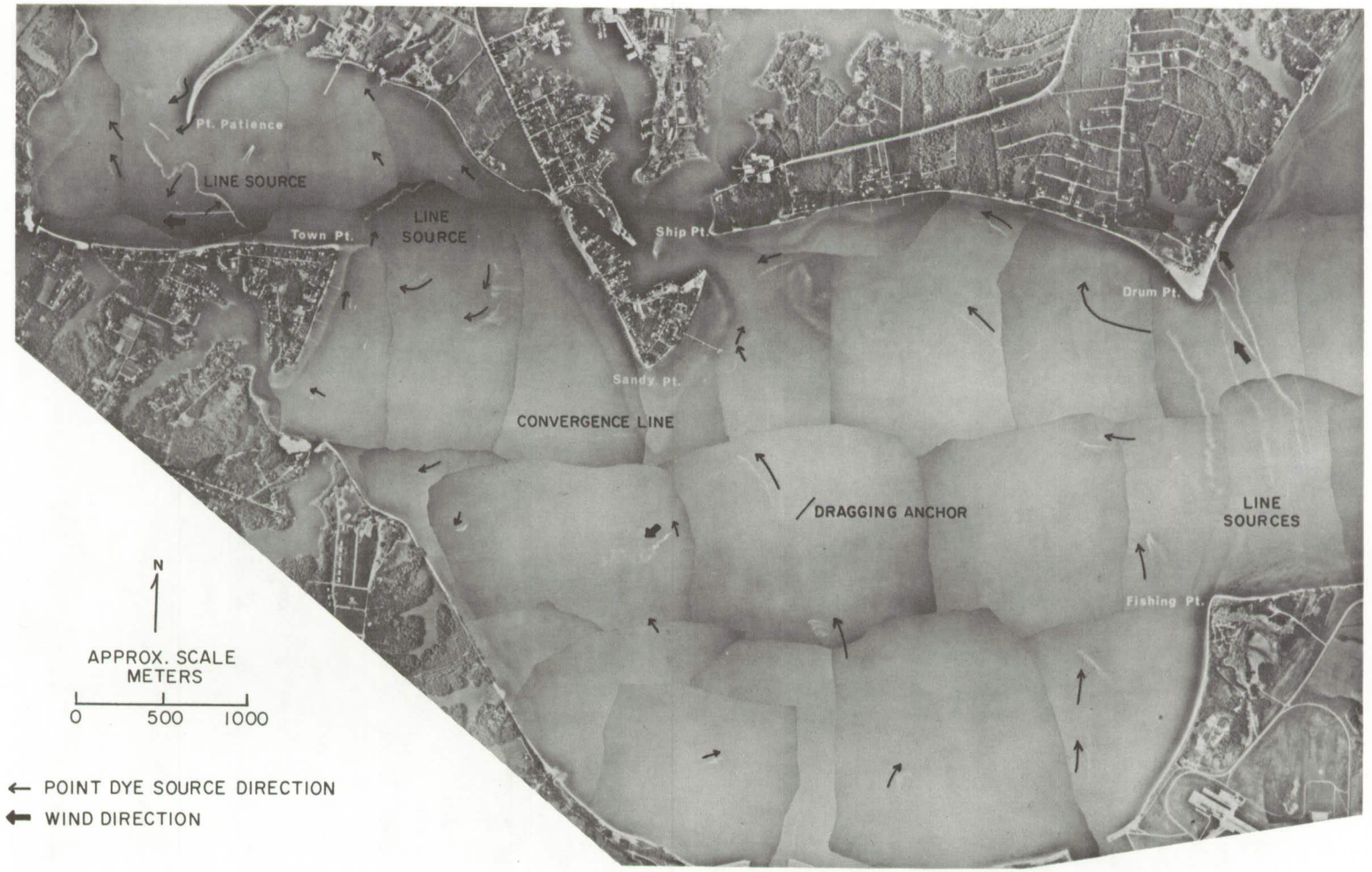

FIGURE 6. PHOTOGRAPHIC MOSAIC OF PATUXENT RIVER ESTUARY, 14 MAY 1971 (1642-1700 EDT).

FIGURE 7. INFRARED MOSAIC (8–14 μM), 14 MAY 1971 (1642–1700 EDT).

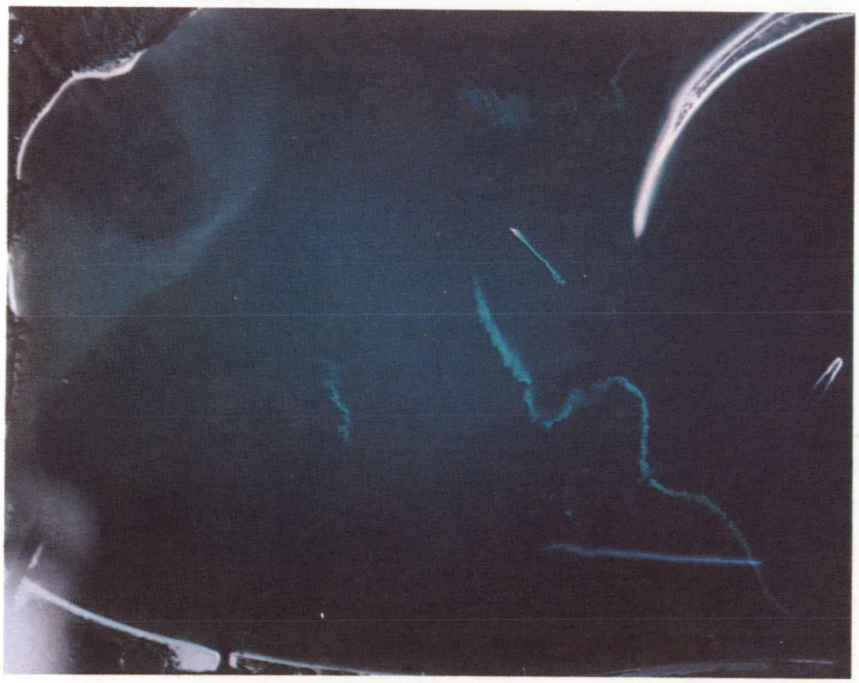

FIGURE 8. POINT AND LINE DYE SOURCES, POINT PATIENCE VICINITY, 14 MAY 1971 (1642 EDT).

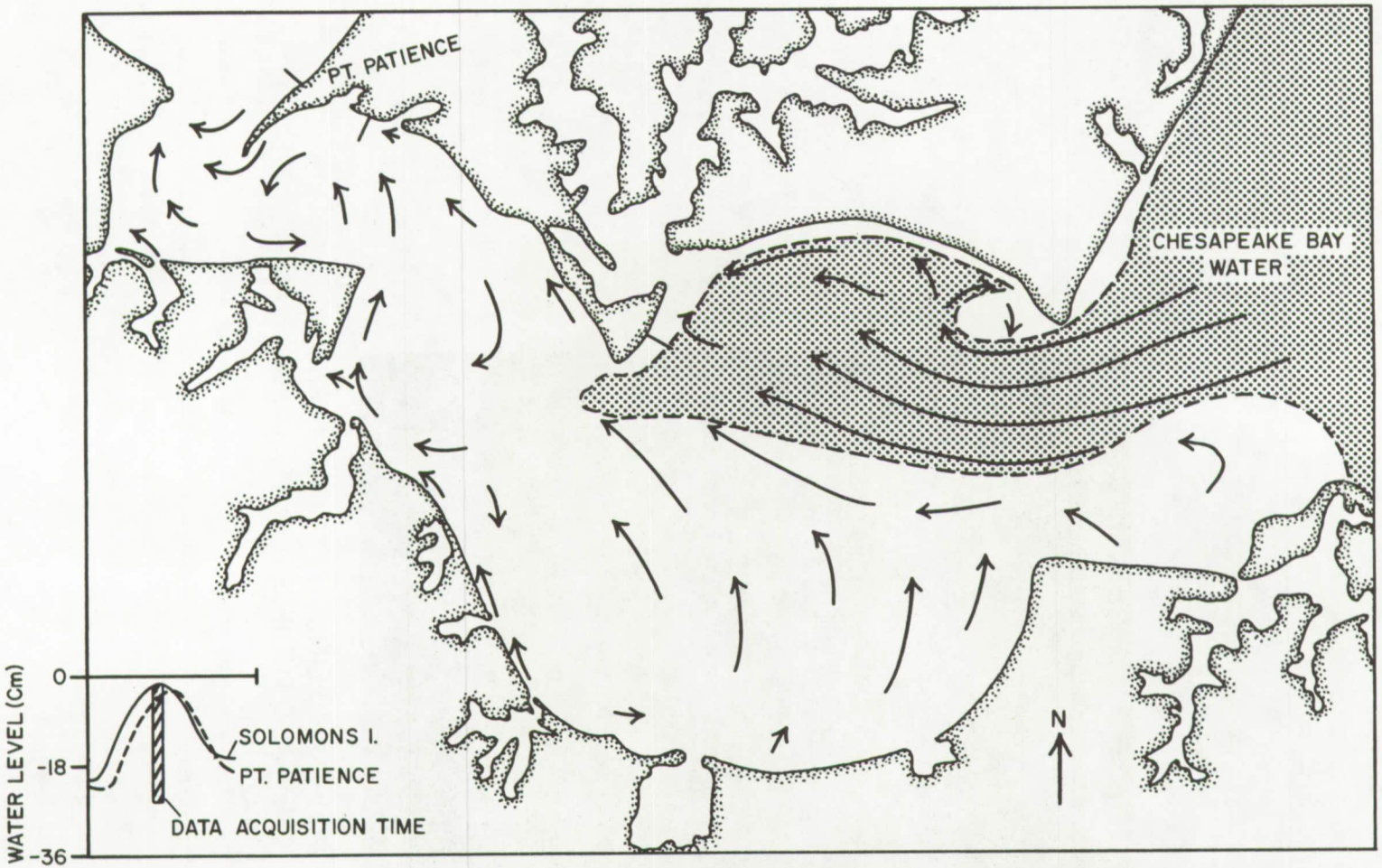

FIGURE 9. STREAMLINE ANALYSIS FROM COMPOSITE DYE TRACER AND IR IMAGERY DATA

FIGURE 10. POINT AND LINE DYE SOURCES BETWEEN DRUM AND FISHING POINTS, 14 MAY 1971 (0842 EDT).

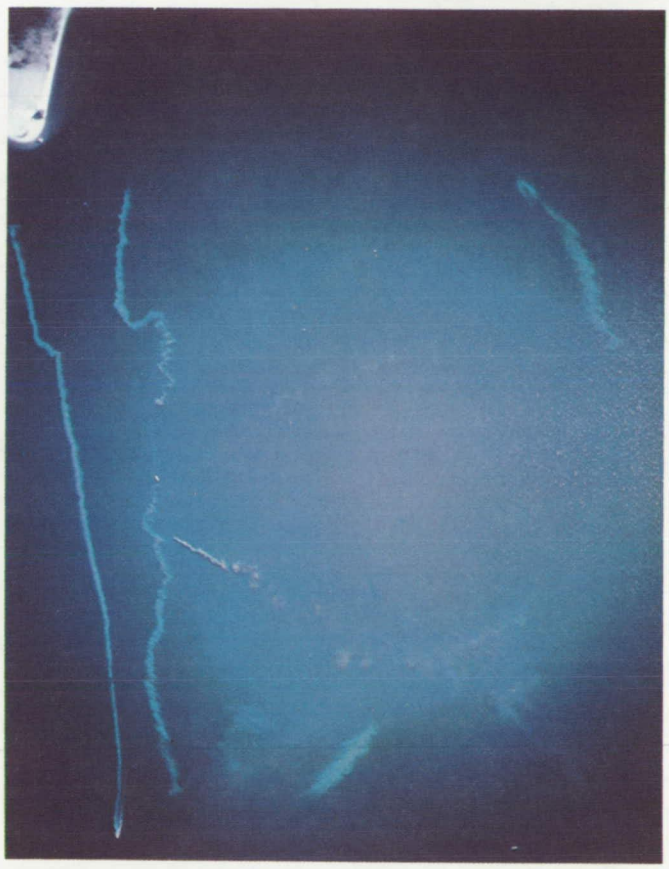

FIGURE 11. POINT AND LINE DYE SOURCES BETWEEN DRUM AND FISHING POINTS, 14 MAY 1971 (0848 EDT).

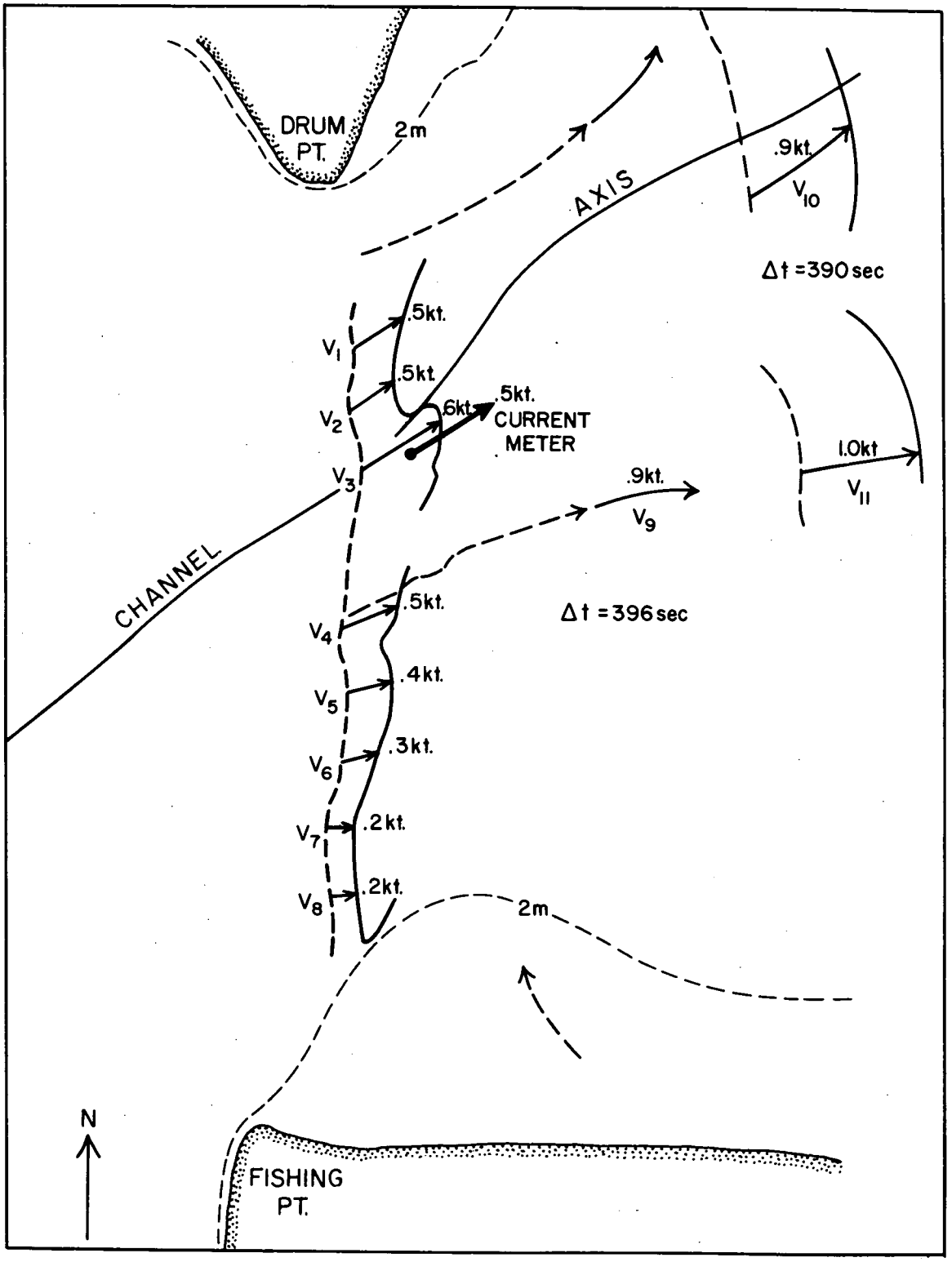

FIGURE 12. CROSS-SECTIONAL SURFACE VELOCITY CALCULATIONS FROM LINE AND POINT DYE TRACER SOURCES.

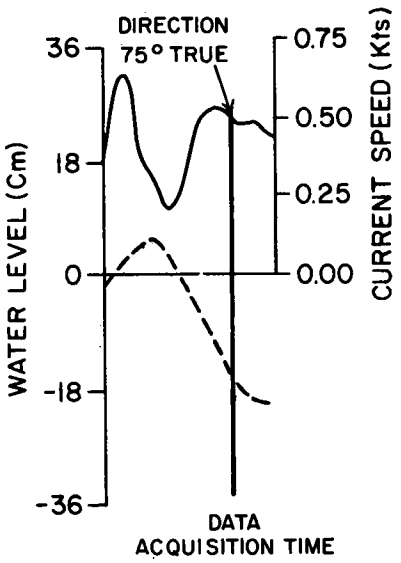

FIGURE 13. WATER LEVEL AND CURRENT SPEED DATA.

SECTION 113

THE TONGUE OF THE OCEAN AS A REMOTE SENSING OCEAN COLOR CALIBRATION RANGE

by

Leo V. Strees
Remote Sensing Oceanography Project
Naval Research Laboratory
Washington, D. C. 20390

INTRODUCTION

The land and ocean areas of the earth both receive, in the visible region of the electromagnetic spectrum, their energy from the same source - - - the sun. The spectral signature resulting from the interaction of the solar radiation with ocean areas differs, in several respects, from the spectral signatures of terrestrial scenes. In general, terrestrial scenes remain stable in content from both temporal and spacial considerations. Ocean scenes, on the other hand, are constantly changing in content and position. Additionally, the solar energy that enters the ocean waters undergoes a process of scattering and selective spectral absorption. The result of these processes is to produce an ocean scene of low level radiance and a spectral distribution which has the centroid of the spectrum shifted heavily toward the 450 nanometer wavelength. Ocean scenes are thus characterized as low level radiance with the major portion of the energy in the "blue" region of the spectrum. Terrestrial scenes are typically of high level radiance with their spectral energies concentrated in the "green-red" regions of the visible spectrum. Because of these differences, it appears that for the evaluation and calibration of ocean color remote sensing instrumentation, an ocean area whose optical ocean and atmospheric properties are known and remain seasonably stable over extended time periods is needed. The Tongue of the Ocean, or TOTO for short, is one ocean area for which we have a large data base of oceanographic information and a limited amount of ocean optical data (1).

PHYSIOGRAPHY OF TOTO

The Tongue of the Ocean is located about 220 nautical miles east of Key West, Florida. It is one of the two major submarine channels in the Bahama Banks. (See Figure 1) It is approximately 100 nautical miles long and 20 nautical miles wide, and one nautical mile deep. It is connected to the Atlantic Ocean by Northeast Providence Channel and Northwest Providence Channel and trends southeast into the Grand Bahama Bank, terminating in a circular cul de sac. (2)

Figure 2 is a photograph taken during the GEMINI V flights on August 22, 1965, 1839 hrs G.M.T. From this photograph we can view the southeastern portion of TOTO. The most striking features are the cul de sac where the water is over 750 fathoms deep and the sand bores which are covered by about six feet of water. Note the uniformity of the "water color" in the cul de sac.

Figure 3 is a later photograph taken during the APOLLO IX missions on March 8, 1969, 2010 hrs G.M.T. shows the axial portion of the TOTO channel and the near flank. The southern portion of Andros Island and Golding Cay, which lies in about the middle of Andros Island is also shown. Note again, as in Figure 2, the uniformity of the "color" of the deep TOTO waters.

The northwestern portion of TOTO and Andros Island are shown in this high altitude photograph taken from the NASA RB-57-F aircraft during Mission 147 in November 1970, Figure 4. The complex of buildings and harbor facilities are a part of the Navy Atlantic Undersea Test and Evaluation Center, abbreviated AUTEC.

OPTICAL CHARACTERISTICS OF TOTO WATERS

During the past two years AUTEC has been used as an operating area for conducting three "ocean color" remote sensing experiments. As part of the surface truth portions of these experiments radiometric and spectral radiometric measurements were made in both shallow and deep waters of TOTO.

A review and analysis of these measurements indicates that the intrinsic optical properties of the deep waters of TOTO are quite uniform and relatively stable over extended time periods.

One of the optical parameters used to characterize ocean waters is the diffuse light attenuation coefficient, "K", it is defined as the logarithm of the ratio of underwater irradiance to the surface solar irradiance per meter. In the graph of Figure 5 the curves shown as solid lines were derived from measurements taken with a Water

Clarity Meter which was designed by the Visibility Laboratory of Scripps Institution of Oceanography. (3) The dashed curve was obtained from measurements made by K. J. Hanson, NOAA, AOML-Sea-Air-Interaction Laboratory with an Eppley Underwater Pyranometer (Model 2). Note that the slope of this curve is approximately equal to those of the Water Clarity Meter curves. The differences in the position of the curves are due to the design of the two instruments. The pyranometer measures the broad band solar irradiance from 300 to 3,000 nanometer wavelengths while the Water Clarity Meter measures the solar irradiance corresponding to the sensitivity of the human eye to the visible spectrum.

A second optical parameter somewhat similar to the "K" coefficient employs the concept of the attenuation of a highly collimated beam of imagery forming light, i.e. beam transmittance (4). This is designated as the (α) coefficient per meter. In TOTO waters we have found the median value of $\alpha = 0.12(M^{-1})$ to be a fairly representative value. In Figure 6 is plotted the variation of "α" with depth, and on the same scale the temperature with depth. It is of some interest to note the trend of α to vary with temperature.

In Figure 7 is plotted the spectral irradiance of upwelled light in the deep TOTO waters. As mentioned earlier, the ocean is a low level radiance scene. Note that the maximum spectral irradiance is about 3.5 microwatts per square centimeter per nanometer and is centered at 460 nanometers. The solar incident power corresponding to this wavelength was 105 microwatts per square centimeter per nanometer, so we have had a peak attenuation of 30 fold. In Figure 8 for comparison also plotted are the energy curves for shallow water, that is for aobut six meters of water covering a white sand bottom. We see that the selective absorption processes have not proceeded to extinction in the shallow water and that some energy in the 600 to 700 nanometer band has been transmitted out of the water. It follows that if we have a knowledge of the shallow water depth and bottom reflectance characteristics, the water depth can serve as an optical filter to vary the spectral content of shallow water scenes.

CONCLUSION

In order to meaningfully evaluate the performance and to calibrate ocean color remote sensing instrumentation, a large area of the ocean, with a typical marine atmosphere, is needed. Terrestrial sites are not suitable since they do not have the characteristics of ocean scenes. Recent work in TOTO has indicated that these waters are ideal for an ocean color remote sensing calibration range.

REFERENCES

(1) "Environmental Atlas of the Tongue of the Ocean, Bahamas", SP-94, U.S. Naval Oceanographic Office, Washington, D.C. 20390, 1967.

(2) "Submarine Geogoly of the Tongue of the Ocean, Bahamas", TR-108, U.S. Naval Oceanographic Office, Washington, D.C. 20390, 1962.

(3) "An Oceanographic Illuminometer for Light Penetration and Reflection Studies" SIO Ref 68-11, July 1968, Scripps Institution of Oceanography, Visibility Laboratory, San Diego, California 92152.

(4) "Light in the Sea", S.Q. Duntley, Journal of the Optical Society of America, Vol. 53, No. 2 Feb 1963.

FIGURES

Figure 1. The Tongue of the Ocean is located about 220 nautical miles east of Key West, Florida. The boundary of TOTO is shown as the dashed line just east of ANDROS ISLAND.

Figure 2. From this photograph taken on orbit 19 of the GEMINI V mission on 22 August 1965 at 18:39 G.M.T. hrs we can view the southeastern portion of TOTO.

Figure 3. In this later photograph taken on 8 March 1969 at 20:10 hrs G.M.T. during the APOLLO IX mission shows the south end of ANDROS ISLAND up to Golding Cay.

Figure 4. The northwestern portion of TOTO, ANDROS ISLAND and AUTEC are shown in this high altitude photograph taken from the NASA RB-57F aircraft during mission 147.

Figure 5. "K" coefficient from TOTO waters.

Figure 6. "α" coefficient for TOTO waters and temperature variation with depth.

Figure 7. Upwelled spectral irradiance for deep TOTO waters.

Fugure 8. Shallow and deep water upwelled spectral irradiances for TOTO waters.

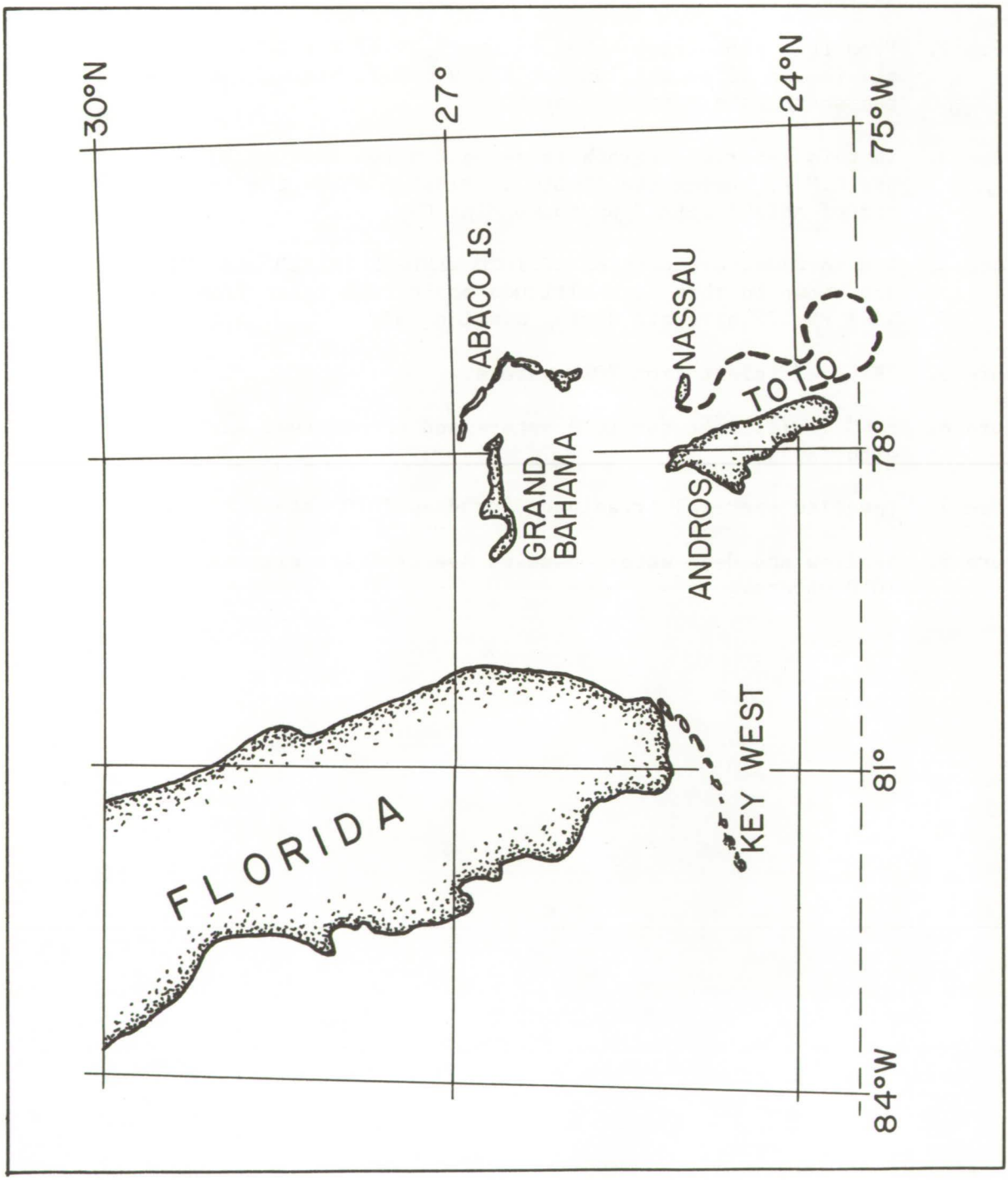
30°N
27°
24°N
75°W
78°
81°
84°W
ABACO IS.
GRAND BAHAMA
NASSAU
ANDROS
TO
TO
FLORIDA
KEY WEST

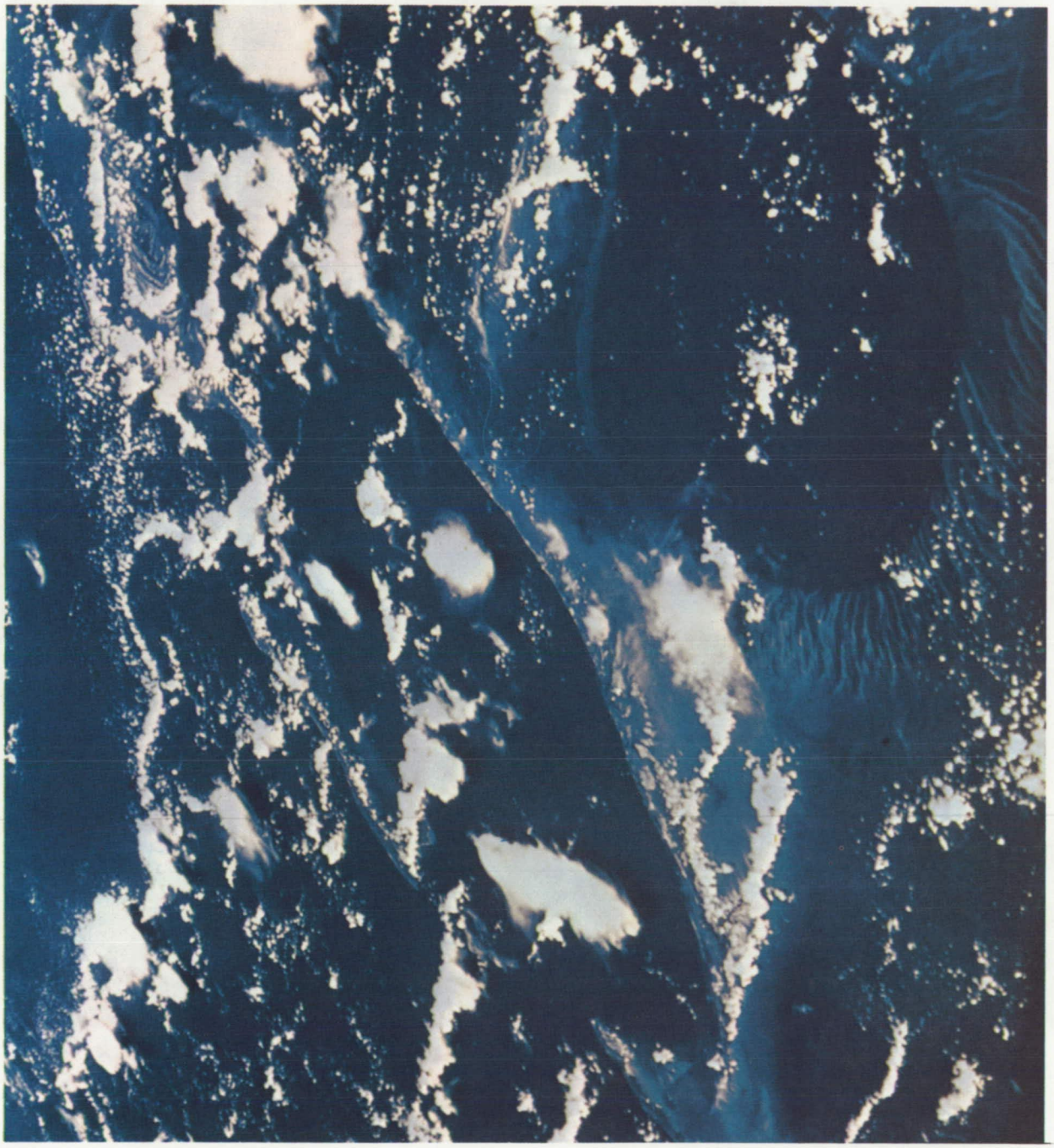

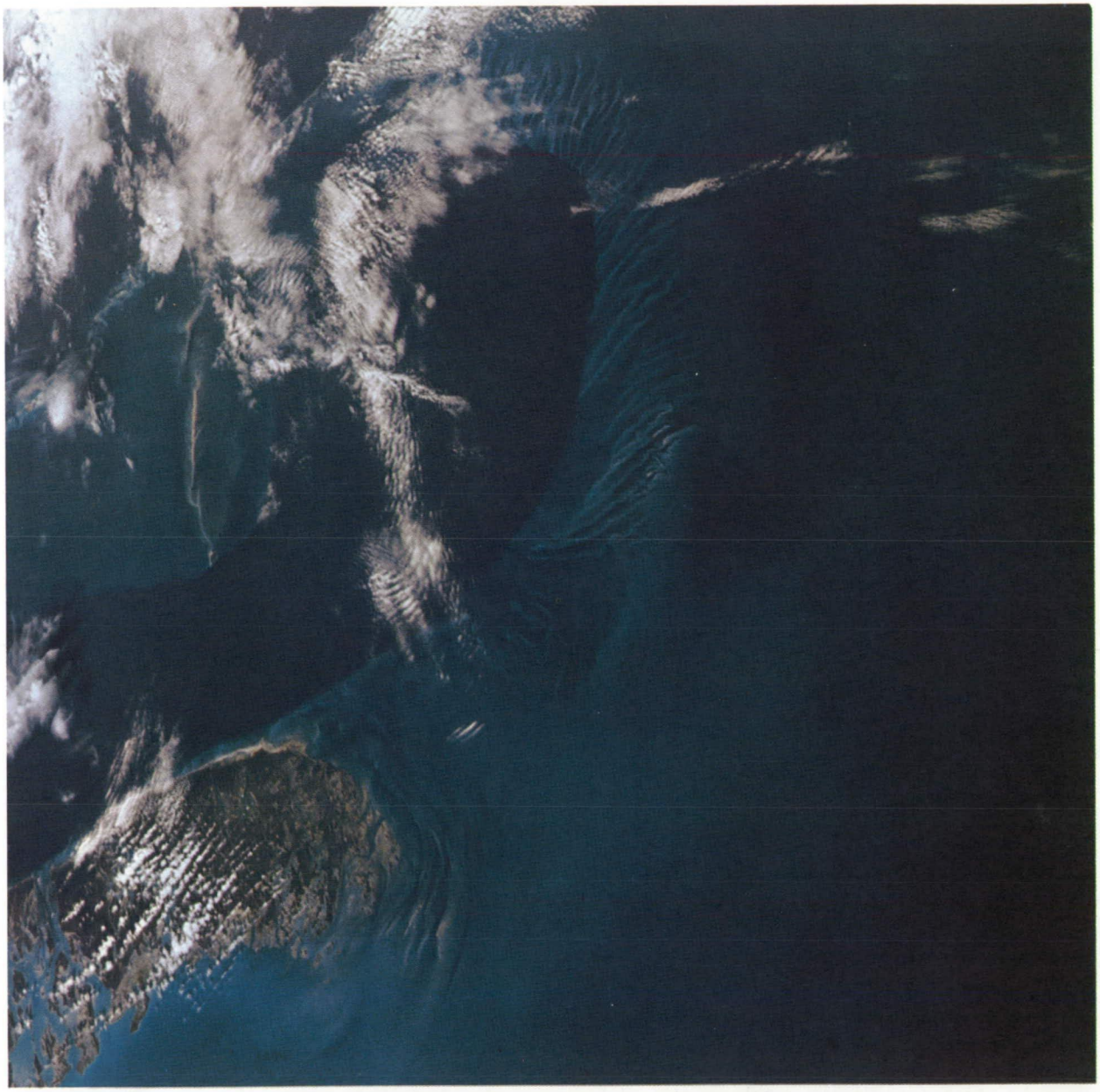

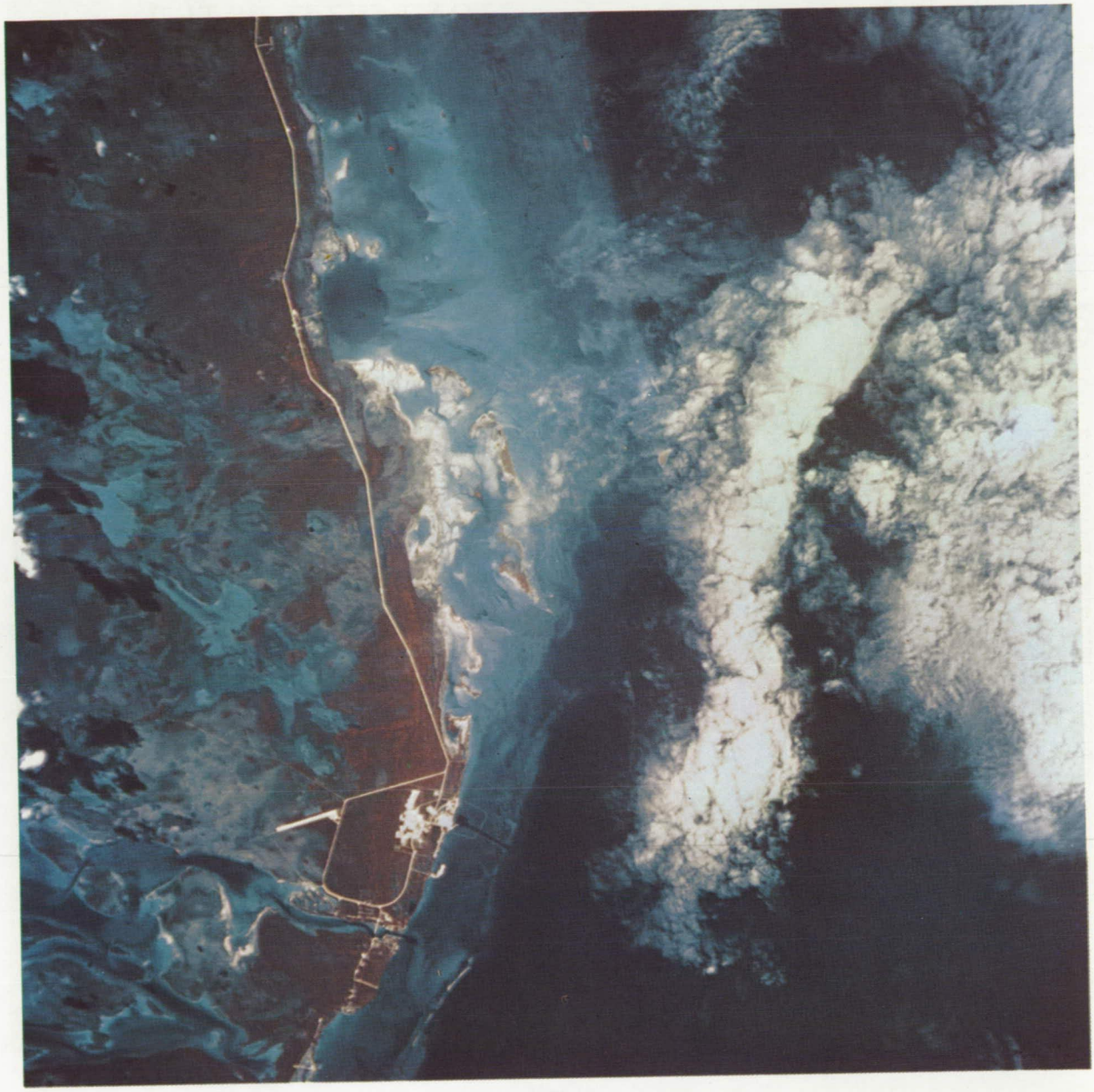

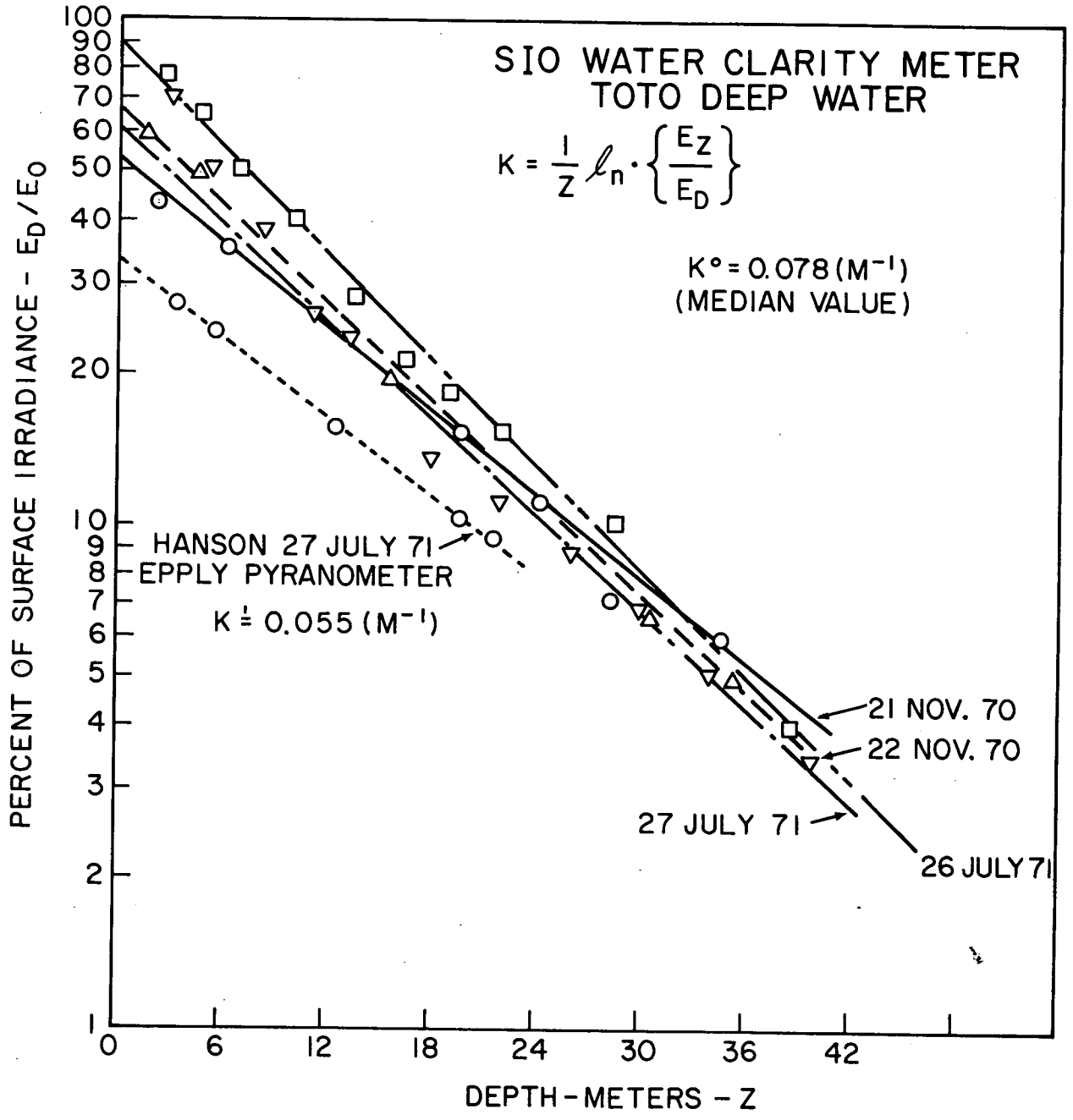
SIO WATER CLARITY METER
TOTO DEEP WATER
$K = \frac{1}{Z} \ell_n \cdot \left\{ \frac{E_Z}{E_D} \right\}$
K° = 0.078 (M⁻¹)
(MEDIAN VALUE)
HANSON 27 JULY 71
EPPLY PYRANOMETER
K ≒ 0.055 (M⁻¹)
21 NOV. 70
22 NOV. 70
27 JULY 71
26 JULY 71
PERCENT OF SURFACE IRRADIANCE - E_D/E_0
DEPTH - METERS - Z
100
90
80
70
60
50
40
30
20
10
9
8
7
6
5
4
3
2
1
0
6
12
18
24
30
36
42

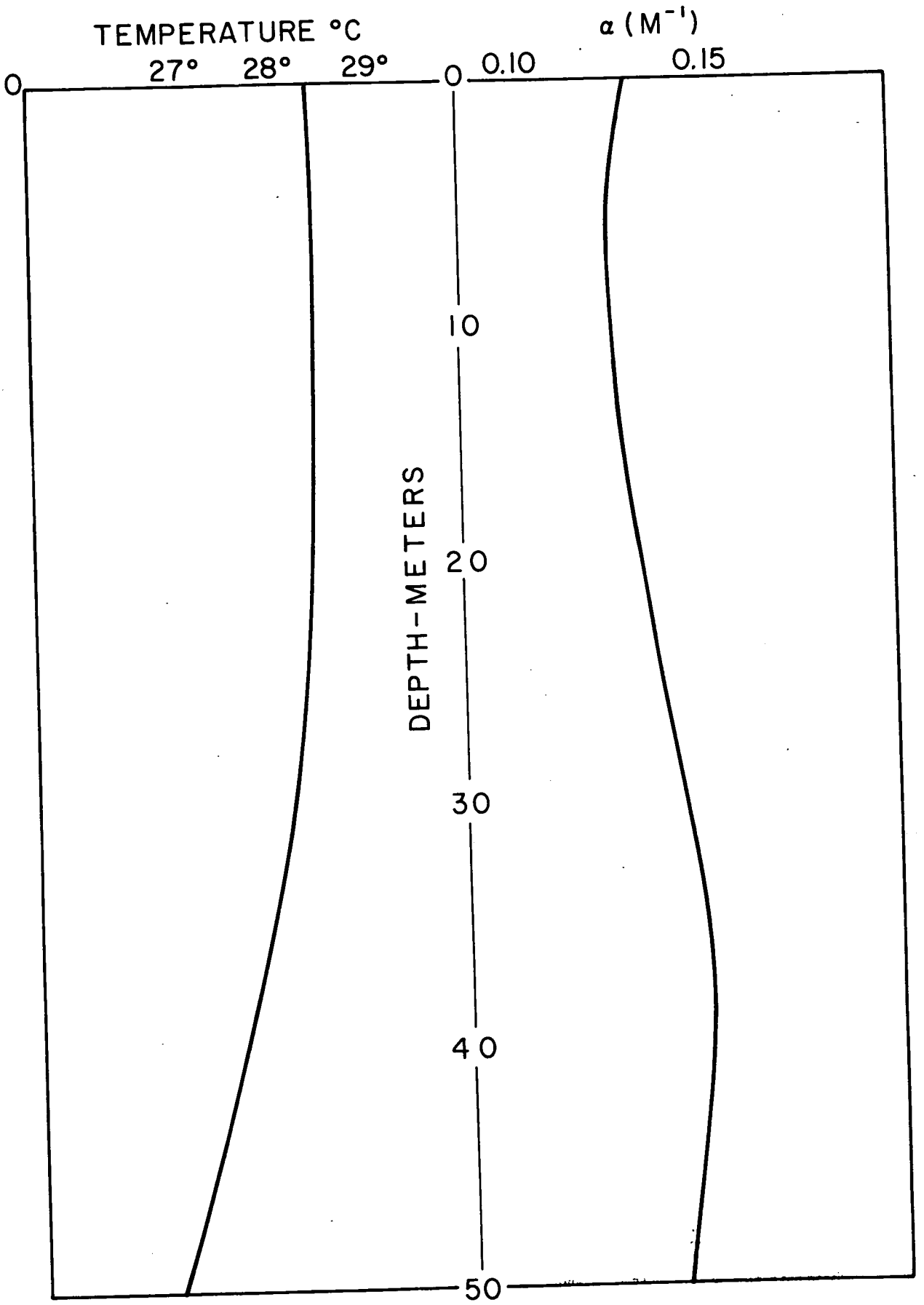
TEMPERATURE °C
27°
28°
29°
0
α (M⁻¹)
0.10
0.15
0
10
20
30
40
50
DEPTH-METERS

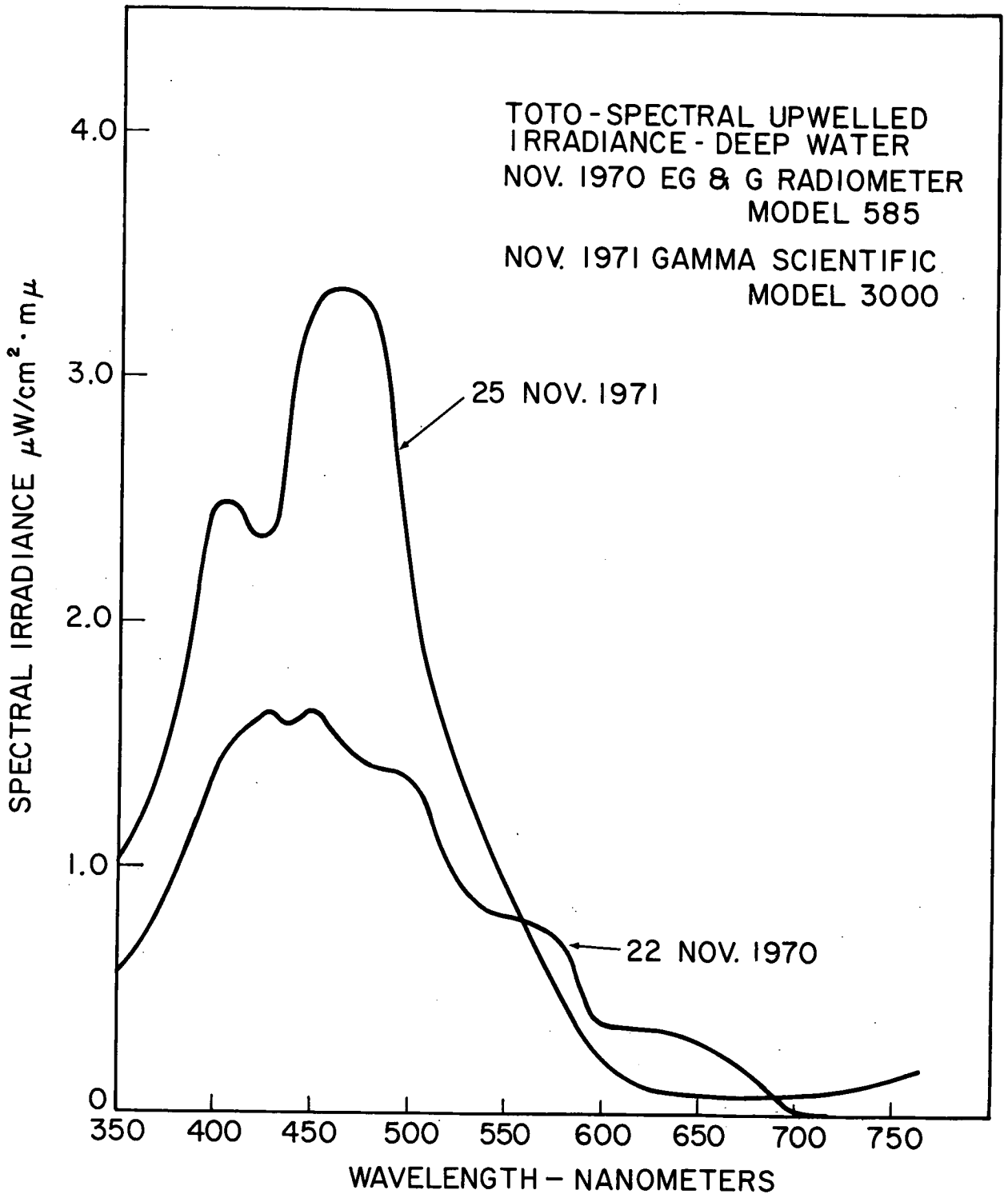
TOTO - SPECTRAL UPWELLED IRRADIANCE - DEEP WATER
NOV. 1970 EG & G RADIOMETER MODEL 585
NOV. 1971 GAMMA SCIENTIFIC MODEL 3000
25 NOV. 1971
22 NOV. 1970
SPECTRAL IRRADIANCE μW/cm² · mμ
4.0
3.0
2.0
1.0
0
350
400
450
500
550
600
650
700
750
WAVELENGTH – NANOMETERS

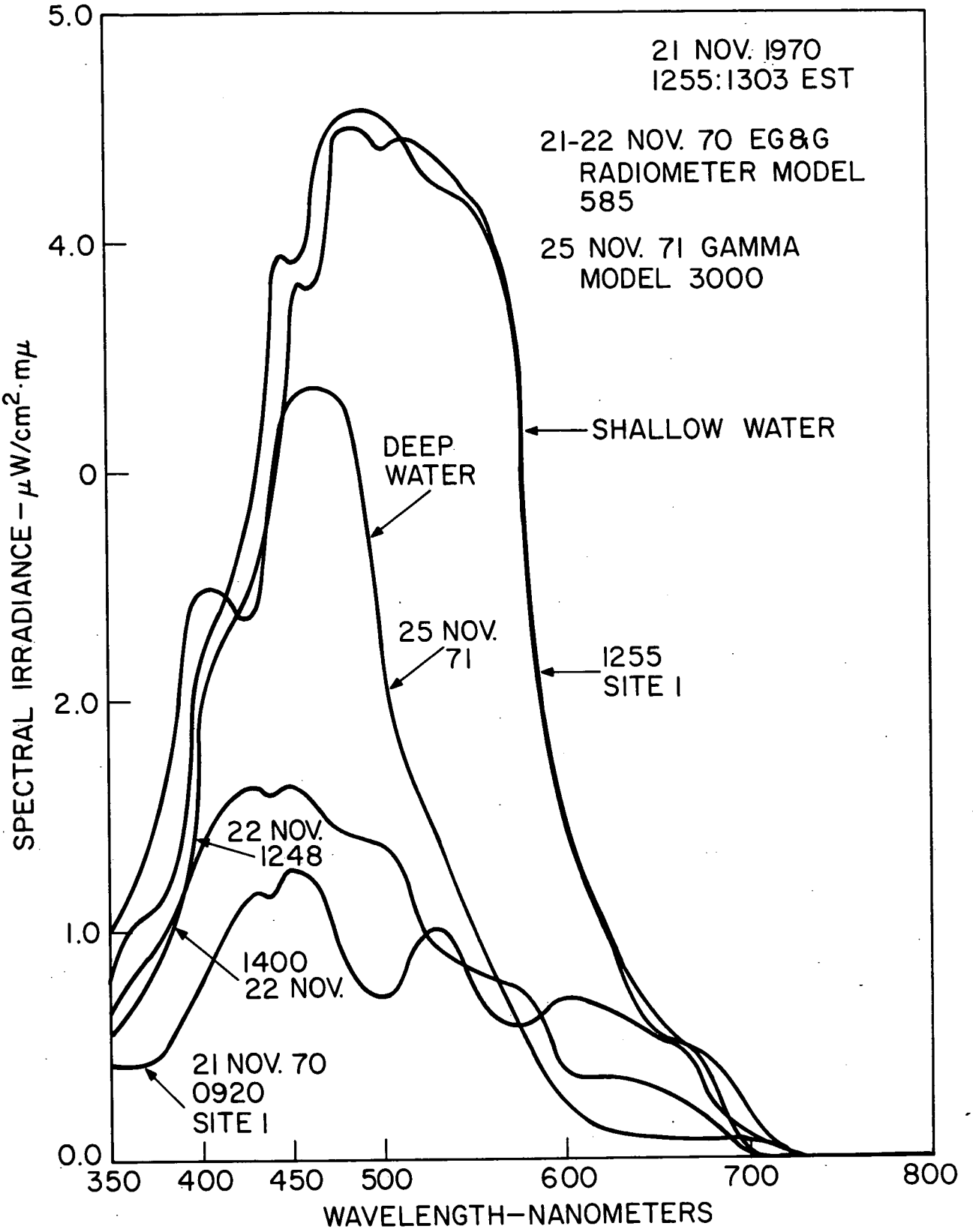
21 NOV. 1970
1255:1303 EST
21-22 NOV. 70 EG&G
RADIOMETER MODEL
585
25 NOV. 71 GAMMA
MODEL 3000
SHALLOW WATER
DEEP
WATER
25 NOV.
71
1255
SITE 1
22 NOV.
1248
1400
22 NOV.
21 NOV. 70
0920
SITE 1
SPECTRAL IRRADIANCE – μW/cm²·mμ
WAVELENGTH–NANOMETERS
5.0
4.0
0
2.0
1.0
0.0
350
400
450
500
600
700
800

SECTION 114

A PROGRAM TO ASSESS A THERMAL DISCHARGE ON TRINITY BAY, TEXAS

by

James B. Zaitzeff
U. S. Naval Research Laboratory
Washington, D. C.

Victor S. Whitehead
NASA-Manned Spacecraft Center
Houston, Texas

Estuarine processes are an area of great potential application in remote sensing. With increasing population growth and expansion of industrialization in coastal regions, estuaries are rapidly undergoing modifications of ecological and physical parameters, these being induced by man and by natural causes. In order for an efficient utilizations of estuary water resources (food, recreation, navigation, and as a disposal system) there is a need for a rapid accurate assessment of the effects of these modifications. This requirement complemented by the dynamic nature of the estuarine environment necessitates the spatial and temporal advantages of remote sensor instruments.

This requirement also has initiated a coordinated activity between several agencies, Figure 1, of which the overall objective is to establish a methodology whereby through the use of existing remote sensors, we can study the hydrodynamics, thermal, biological, and chemical characteristics of an estuary.

The construction of a large gas-fueled power generation plant, from which thermal waste water is discharged into a shallow estuary (Trinity Bay) has provided an opportunity to address a specific problem that is, to determine the impact of the thermal discharge on the bay. The bay and generation plant are well suited to the study, as both physical and mathematical hydraulic/thermal computer models of the bay are available. Also base-line data has been collected prior to and during the operation of the generation facility.

Specific objectives to data, to study the power plant effluent are:

a. To evaluate the application of a two dimensional mathematical model to the analysis of the thermal discharge, specifically, to verify the capability of the math model to predict the temperature distribution of Trinity Bay in the vicinity of the water outfall.

b. To compare the outputs of the Army Corps of Engineers physical model of Galveston--Trinity Bay and the mathematical models to the analysis of the thermal discharge plume characteristics.

c. To determine the heating affects by the discharge on key aquatic species specifically, the effects, if any, on "Ruppia maritima", a bottom grass that covers approximately 190 acres adjacent to the water outfall. The grass provides an important natural nursery for small shrimp, crabs, and young fish.

d. To evaluate the most effective balance between remote, in situ measurements and modeling in the determination of the discharge plume characteristics.

Objective number one will be discussed here. Basic date reported consists of aerial thermal infrared, and in situ measurements, as relating to the math model studies. In view of this objective, the key information to be determined is the extent and quantitative temperature determinations, of the outfall plume or mixing zone within the temperatures significantly above ambient are observed. The plume responds rapidly to winds and tides, and thus considerable quantities of synoptic temporal coverage via remote sensing provides an accurate assessment of temperatures and their release patterns. The assessment of ambient bay temperatures are also of much importance to this study, in particular, for a definition of real ambient bay values, and for a comparison to plume temperatures.

Trinity Bay is part of the Galveston Bay System, Figure 2, a typical gulf coastal plain estuary. The bay comprised approximately 90,000 acres or about 27% of the water area of the Galveston Bay System. It receives discharges from industrial and domestic sources, natural runoff, the Trinity River and other various smaller tributaries. The bay is relatively shallow, its central area is seven to eight feet deep, it has a complex circulation, and is biologically important to man.

The large gas fueled power generation plant now under construction by the Houston Lighting and Power Company, is located on Cedar Bayou, Figure 3. The plant is being built in six units, each unit planned to produce a capacity of about 750-800 megawatts and to circulate 750 c.f.s. of water through its condensers for cooling purposes. The ultimate capacity of the facility is 5000 megawatts and circulating 5000 c.f.s. of water by 1978.

In the planned configuration, water is drawn from upper Galveston Bay up Cedar Bayou and through the condensers where it will be heated approximately 20 degrees F. and discharged into a large cooling pond, (not yet completed) and Upper Trinity Bay, by a six mile canal. Houston Lighting and Power Company, estimate (based on model studies) that at the ultimate capacity, 2130 acres of Trinity Bay will be raised

1.5 degrees F. or more, and 1600 acres will have a temperature rise of 4 degrees F. or more. At the time of data acquisition for this report only one generating unit was in operation, discharging 750 c.f.s. into upper Trinity Bay.

OBSERVATIONAL PROGRAM

An observational and measurement program for Trinity Bay has been implemented, to meet the overall objectives. Emphasis of measurements are placed on those that are needed to provide an accurate description of the thermal and hydraulic structure of the bay, biological assessments, along with information concerning the operation of the power generation plant, meteorological and other physical conditions affecting the bay's ability to transfer heat. The observations are utilized for providing surface truth to, and a calibration of the remote sensors, as well as inputs to the mathematical models.

The observation program is in operation at selected periods in which concentrated measurements are made. These are:

a. Observations of tidal phases in Trinity and Galveston Bays.

b. Observations of meteorological parameters.

c. Inflow into the Galveston and Trinity Bays.

d. Measurements of outfall temperatures and flow rates of the discharge canal.

e. Airborne remote sensor measurements.

1. RS-14-infrared imaging scanner provides quantitized temperatures of the discharge plume.

2. PRT-5-provides surface radiation temperatures of plume and assessment of bay surface ambient temperatures; calibration for RS-14.

3. Cameras-water mass differentiation by color, measurement of advection and diffusivity water values through use of dye studies, "Ruppia maritima" inventory studies, indexing of infrared data.

4. Infrared spectrometer and radiometer.

f. Surface based in situ measurements taken prior to and during overflights.

1. Boats-surface and subsurface temperatures and salinities, turbidity, currents, biota.

2. Instrumented buoys-providing continuous surface and subsurface temperatures.

MODELING PROGRAM

In the present mathematical modeling program the waters of Trinity Bay are considered homogeneous, the bay is shallow and the mixing effects of waves is good. Therefore, the distribution of parameters in the bay is represented by vertically averaged models (that is with two horizontal spatial dimensions) to calculate current velocities for advection terms.

There are three specific models used in the study. These were initially developed by TRACOR and somewhat modified by NASA-Manned Spacecraft Center. These models consist of:

a. A large hydrodynamic model of the Galveston-Trinity Bay System.

b. A small hydraulic model of the Northwest part of Trinity Bay in the area of the discharge outfall.

c. A thermal model covering the same area as the small hydraulic model.

The hydraulic models are largely based on the numerical model of Reid and Bodine, 1968. The basic differential equations of motion and continuity are used and solved by finite difference methods. The effects of bottom friction, wind stress, rainfall, coriolis forces and advection of momentum are included in the basic equations. Allowances are made for submerged barrier reefs and the overflow of low-lying islands. The hydraulic models present a history of velocity patterns over the bay in two horizontal spatial dimensions.

The basic thermal math model uses the mass transport equations solved by finite difference methods similar to the method used to solve the hydraulic model. In practice the models are run for conditions prevailing at the time of the overflight experiments, and all three models are implemented for computing temperature contours in the vicinity of the outfall.

Figures 4 and 5 represent hydraulic and thermal model inputs supplied for Trinity Bay at a specific time. There are many other terms fixed in the computer program that apply for a specific estuary, though none are given here. For a detailed description of the models and their implementation in the Trinity Bay study, the reader is referred to "Trinity Bay Study, Status Report 5, October, 1971".

ANALYSIS PROGRAM

The aircraft and in situ data analysis is directed primarily toward a comparison with the output of the computer models. In the application of airborne infrared data, corrections are made for atmospheric effects, and the data precisely positioned with respect to the model output grid.

Figures 6 thru 10 present outputs of observed and model data obtained during May 17, 1971, at 1800 GMT. The direction of the winds were 160 degrees at 16 knots. Tidal phase was a flood tide at 1.1 feet above mean sea level.

The observed radiation temperature pattern contours obtained from the PRT-5 at an altitude of 2500 feet are shown in Figure 6. The equivalent data corrected for atmospheric effects is shown in Figure 7. Average surface ambient temperature in the bay shows 22.5 to 23.0 degrees C. The plume is 29.5 degrees C. at its outfall. The fine structure of the heated water plume are not resolved in detail by the non-imaging PRT-5. Figure 8, illustrates corresponding RS-14 infrared imagery, black and white film output and false color presentation. The RS-14 imagery can be compared with Figure 9, showing computed isotherms for the corresponding time in the vicinity of the discharge outfall. There is some similarity of distribution patterns and temperature contours. Temperature at the outfall computed from the math model program shows 30.0 degree C., and the actual observed temperature is 29.5 degree C. The displacement of the plume waters is eastward along the shore, largely influenced by winds and the flood tide.

The 25 degree C. isotherm obtained by boat traverse is placed over the model output, Figure 9. It can be noted that there is a tendency for the measured isotherm to be farther offshore, but that the model isotherm compared to isotherm patterns of the RS-14 imagery indicates the isotherm in question curves back towards the outfall. This difference may be due to near shore friction induced by grass beds.

As previously stated ambient temperatures of the bay and rise above ambient caused by the discharge plume are of critical importance to impact study evaluations, particularly its affects to the bay's ecology. Figure 10 illustrates the computed rise above ambient in the vicinity of the discharge.

CONCLUSIONS

While the initial analysis of at least, surface measurements, indicates there is some difference in placement of isotherms by the model

from that observed, the area enclosed by the isotherm does not appear to differ greatly from that recorded by the RS-14 imagery for the single case described here. The math model must be tested for a variety of extreme conditions for its overall validity to be evaluated. There are certainly some processes the two dimensional model cannot synthesize such as counter flow near the bottom or the sink of heated water discharge due to salinity differences.

The occurrence of subsurface heated water was recorded by a buoy October 6, 1971, one nautical mile south southwest of the discharge canal, as indicated in Figure 11. Temperatures observed at one foot below the surface were approximately 7 degrees F. higher than the surface waters.

Although the occurrence of both of the above phenomena have been observed, their significance to the problem has not yet been established.

REFERENCES

Reid, R. O. and Bodine, B. R., "Numerical Model for Storm Surges in Galveston Bay" Proceeding ASCE, WWI, February 1968.

Trinity Bay Study Status Report 5, complied by Application Office Earth Observation Division, NASA-Manned Spacecraft Center, October 1971.

Estuarine Modeling; An Assessment. Water Pollution Control Research Series, 16070 DZV 02/71, Environmental Protection Agency, February 1971.

NASA-S-71-4330-S

RELATIONSHIP OF PARTICIPATING AGENCIES

TRINITY BAY STUDY

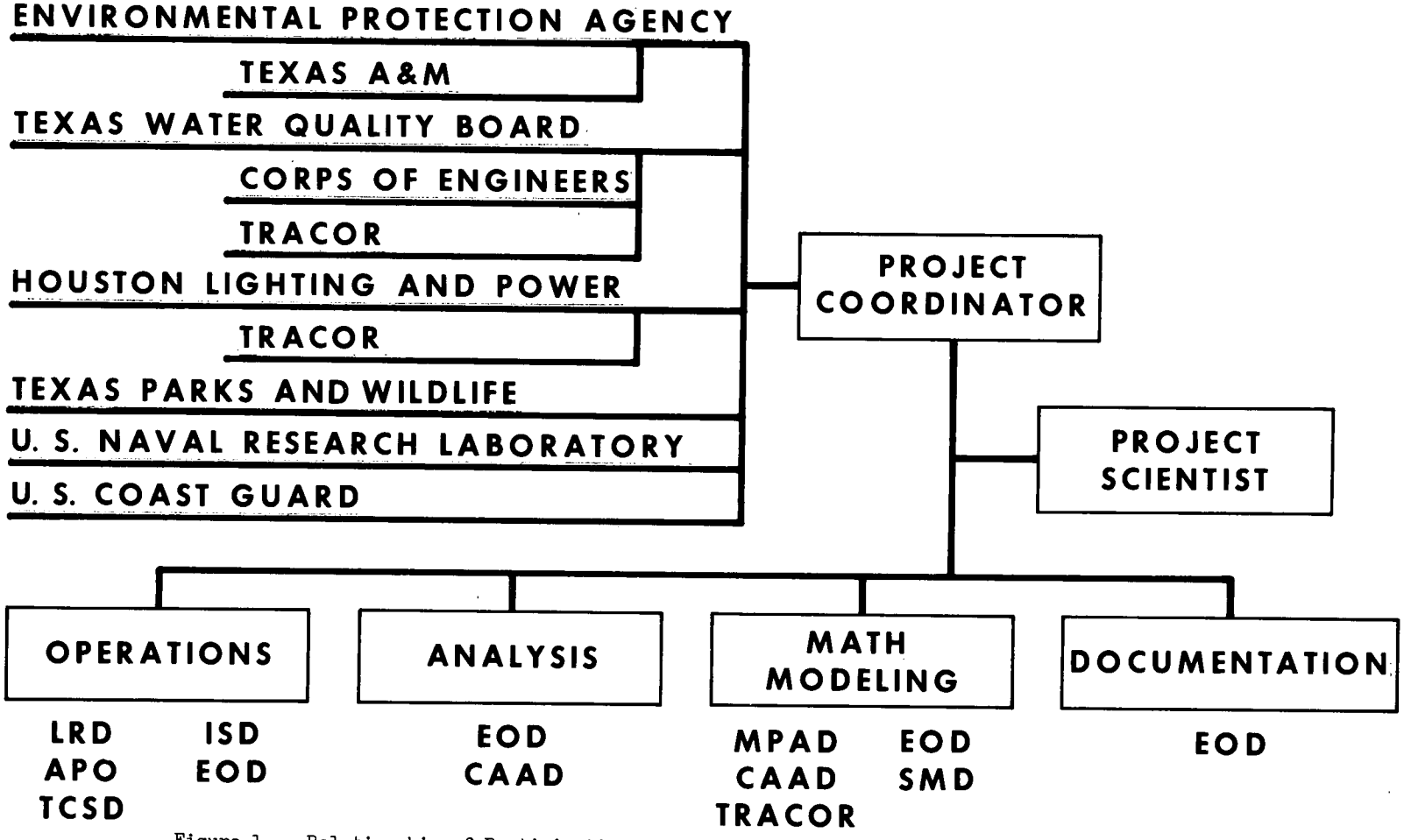

Figure 1. - Relationship of Participating Agencies in the Trinity Bay Study. Project Coordinator, NASA Manned Spacecraft Center. Project Scientist, U. S. Naval Research Laboratory

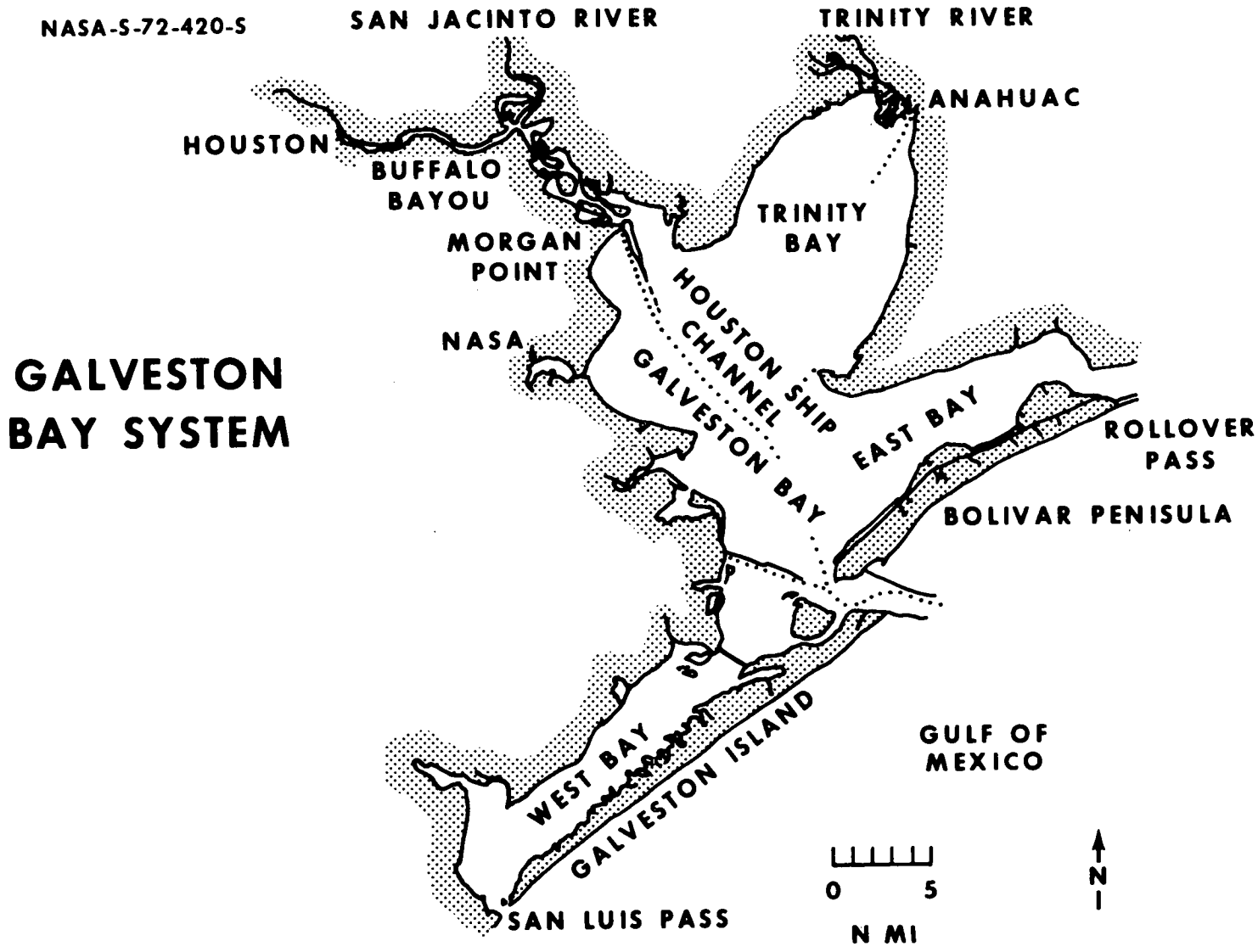

Figure 2.- The Galveston Bay System

NASA-S-72-421-S

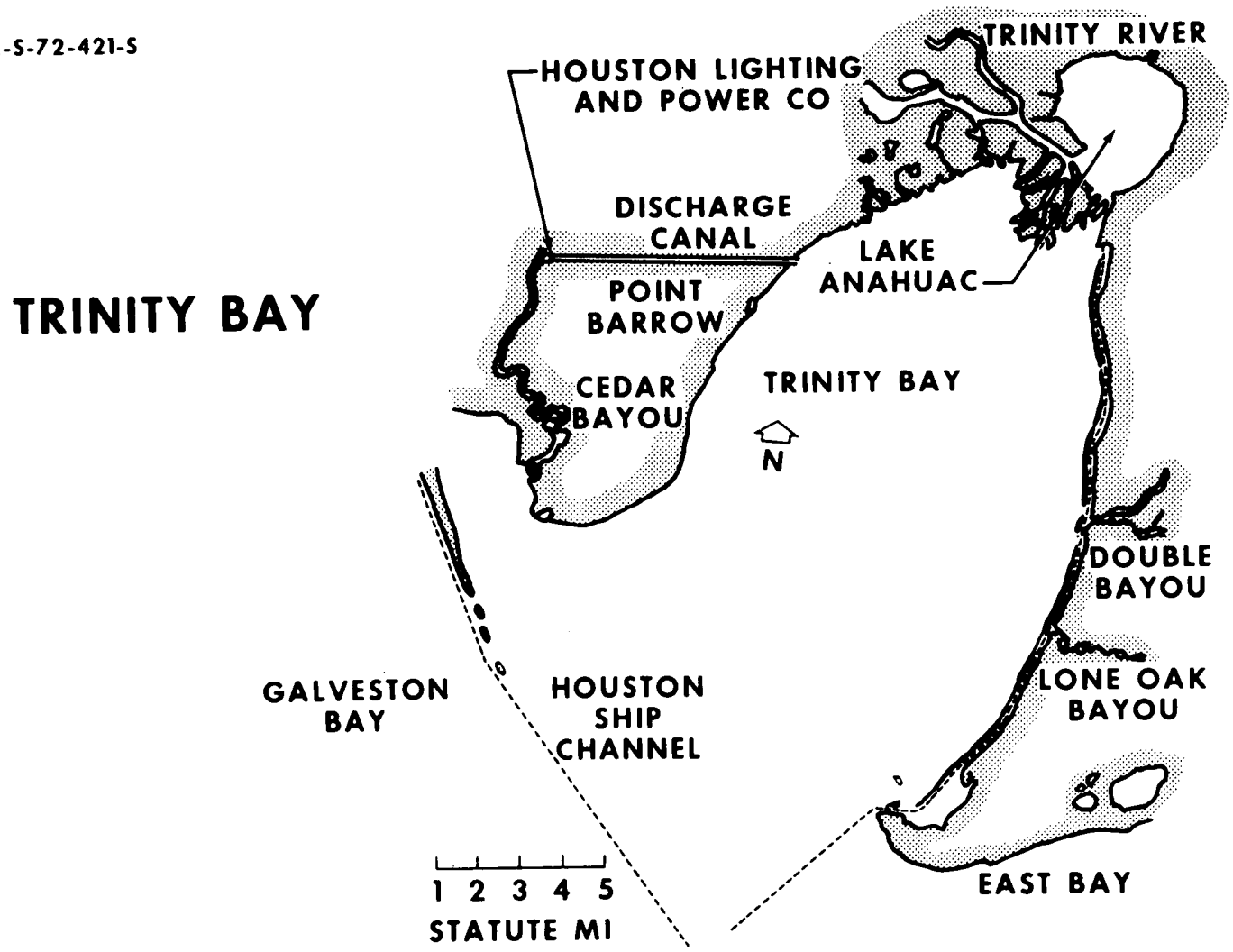

Figure 3.- Location of Houston Lighting and Power Company Discharge Canal

NASA-S-71-4357-S

HYDRAULIC MODEL INPUTS

- TIDAL HEIGHTS AT BOUNDRIES OF ESTUARY (HOURLY)
- WIND DIRECTION AND SPEED (HOURLY)
- CONTRIBUTING FRESH AND WASTE WATER INFLOWS
- RAINFALL RATE

Figure 4. - Hydraulic Model Inputs for Trinity Bay for a Specific Time

TEMPERATURE MODEL INPUTS

- TEMPERATURE OF STREAMS AND WASTES INTO ESTUARY
- AMBIENT WATER TEMPERATURE INITIAL VALUE
- X AND Y COMPONENTS OF WATER VELOCITY (FROM HYDRAULIC MODEL)
- ATMOSPHERIC PRESSURE
- AIR TEMPERATURE
- DEW POINT
- RELATIVE HUMIDITY
- PERCENT CLOUD COVER
- WIND DIRECTION AND SPEED
- RATE OF PRECIPITATION PER UNIT SURFACE AREA
- TEMPERATURE OF THE PRECIPITATION

Figure 5. - Temperature Model Inputs for Trinity Bay for a Specific Time

NASA-S-71-4322-S

MISSION 165 - FLIGHT 4

TRINITY BAY OVERFLIGHT - MAY 17, 1971

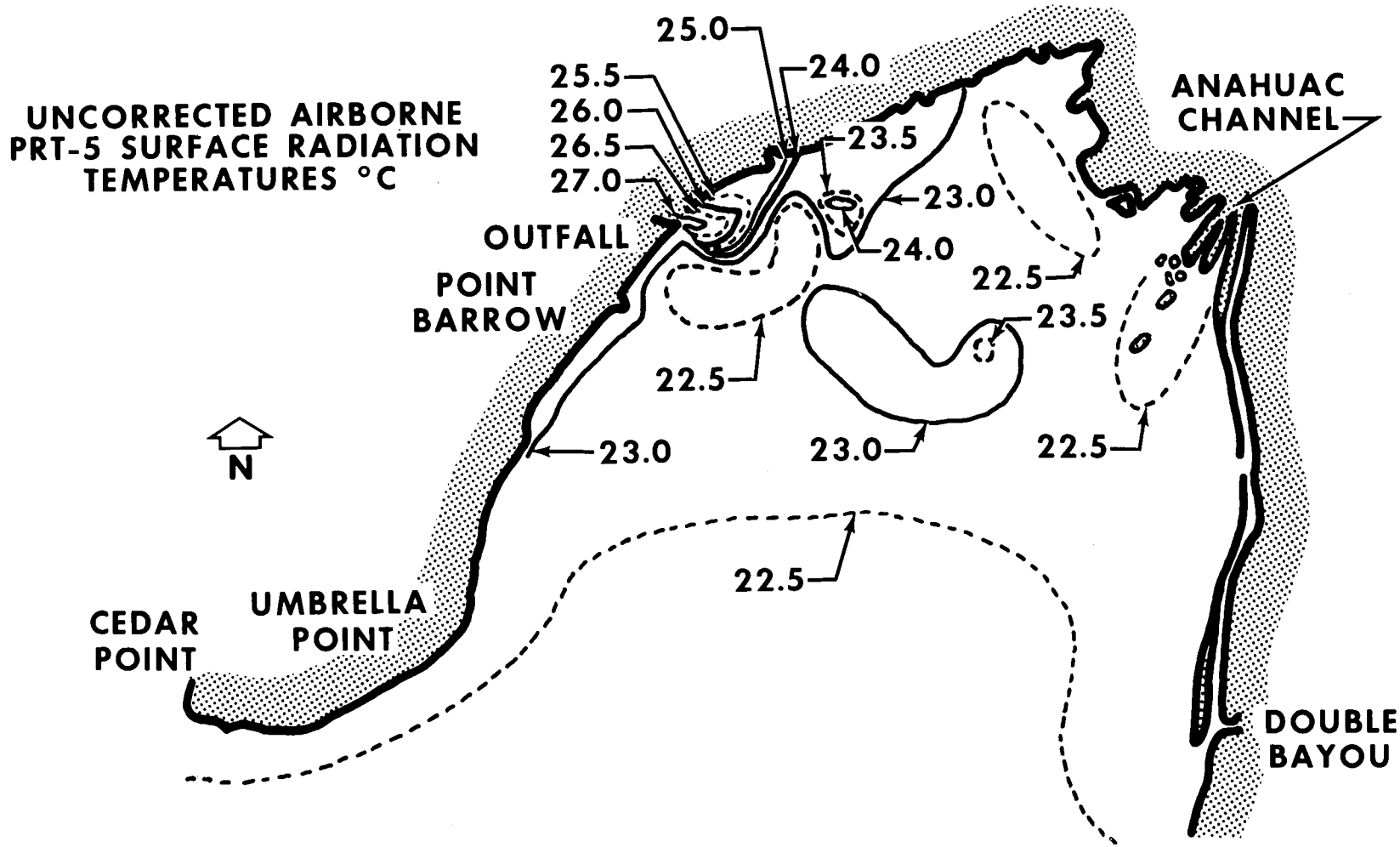

Figure 6. - Uncorrected Airborne Precision Radiation Thermometer (PRT-5) Surface Radiation Temperatures Degrees Centigrade. Trinity Bay Overflight, Mission 165, Flight 4, May 17, 1971.

NASA-S-71-4323-S

MISSION 165 - FLIGHT 4

TRINITY BAY OVERFLIGHT - MAY 17, 1971

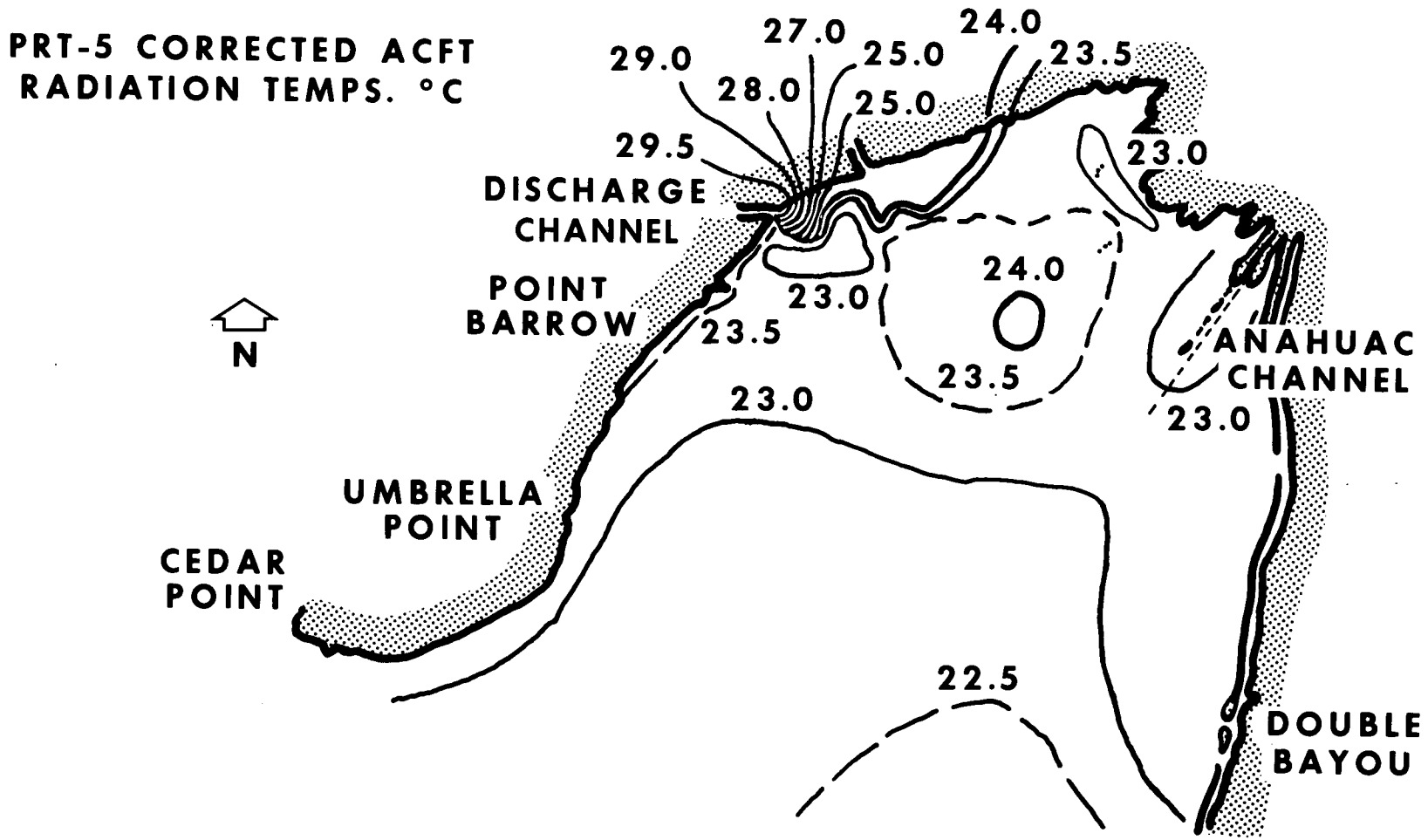

Figure 7. - Corrected Airborne Precision Radiation Thermometer (PRT-5) Surface Radiation Temperatures Degrees Centigrade. Trinity Bay Overflight, Mission 165, Flight 4, May 17, 1971.

NASA-S-71-4355-X

TRINITY BAY
WATER TEMPERATURE VARIANCES

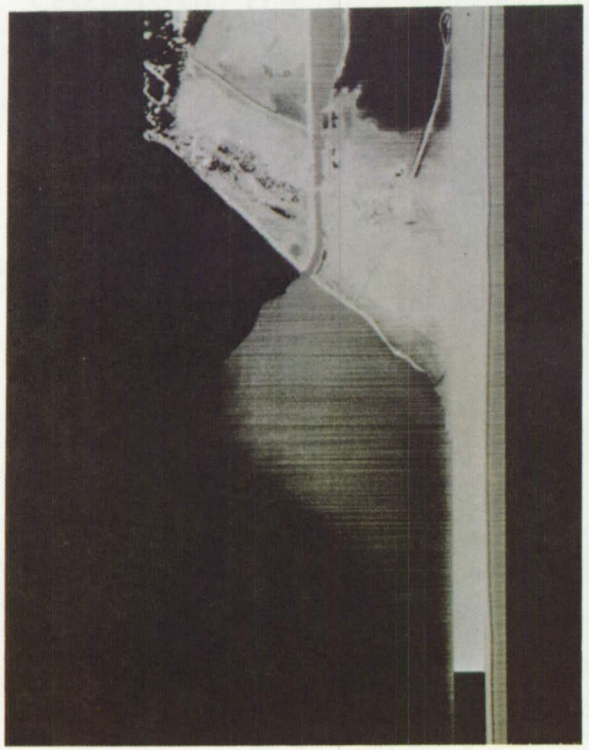

RS-14 INFRARED
SCANNER DATA

FALSE-COLOR
TELEVISION DISPLAY

Figure 8. - Trinity Bay Water Temperature Variances Displayed by RS-14 Infrared Scanner Imagery. Trinity Bay Overflight, Mission 165, Flight 4, May 17, 1971.

NASA-S-72-398-S

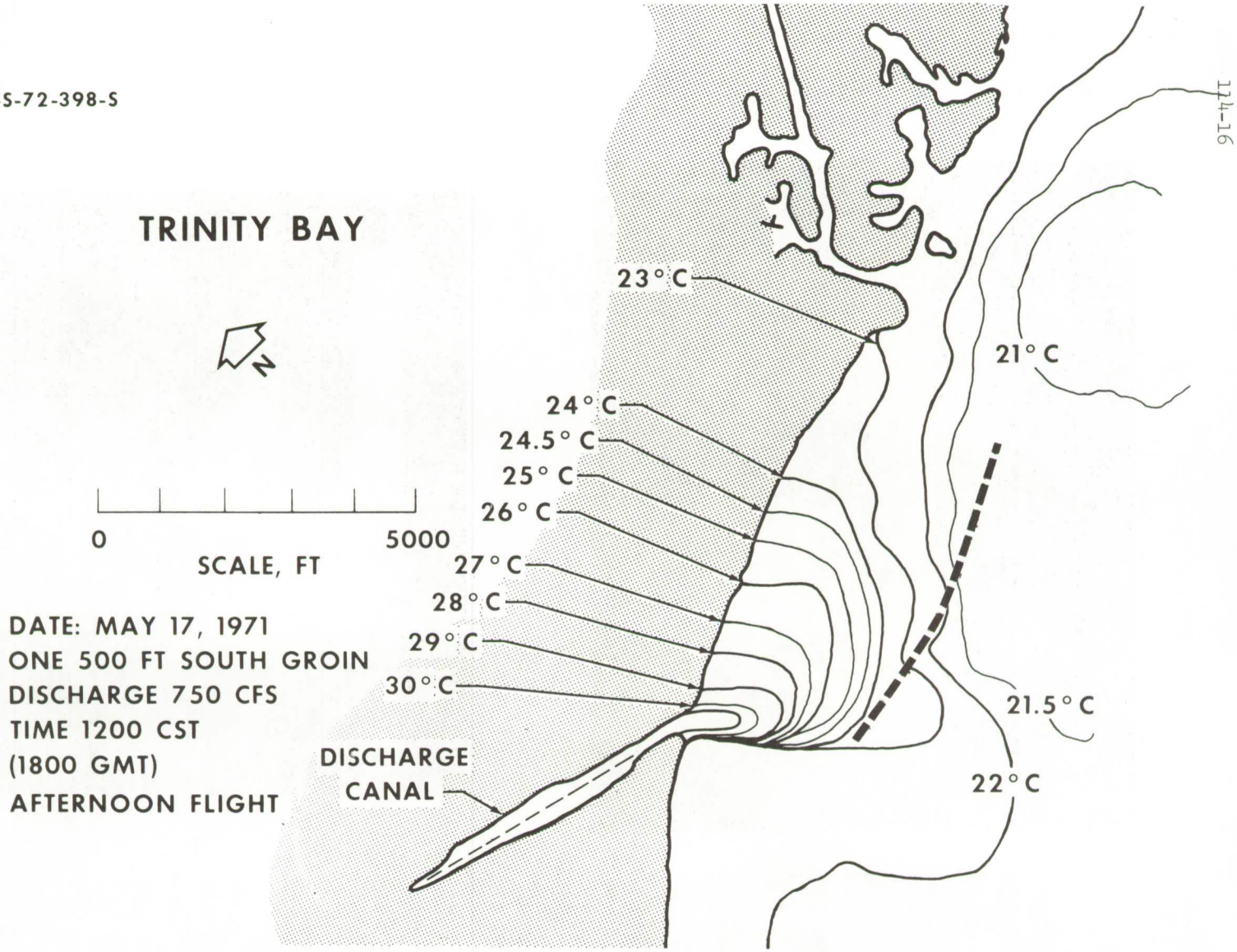

Figure 9.- Trinity Bay Computed Isotherms in Vicinity of Houston Lighting and Power Company Discharge Canal. 25 Degree C. Isotherm observed by surface measurements indicated by dashed line.

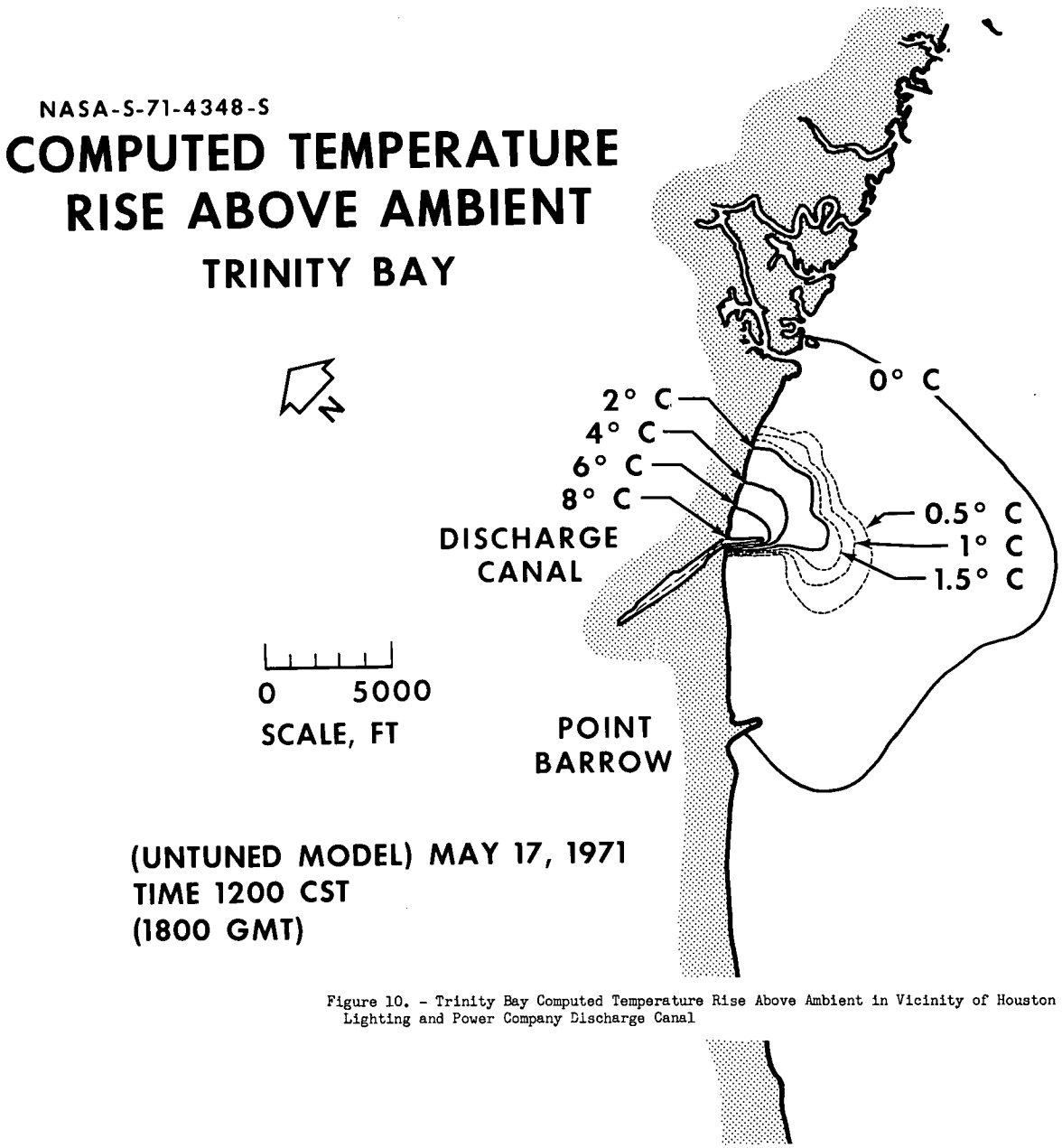

Figure 10. - Trinity Bay Computed Temperature Rise Above Ambient in Vicinity of Houston Lighting and Power Company Discharge Canal

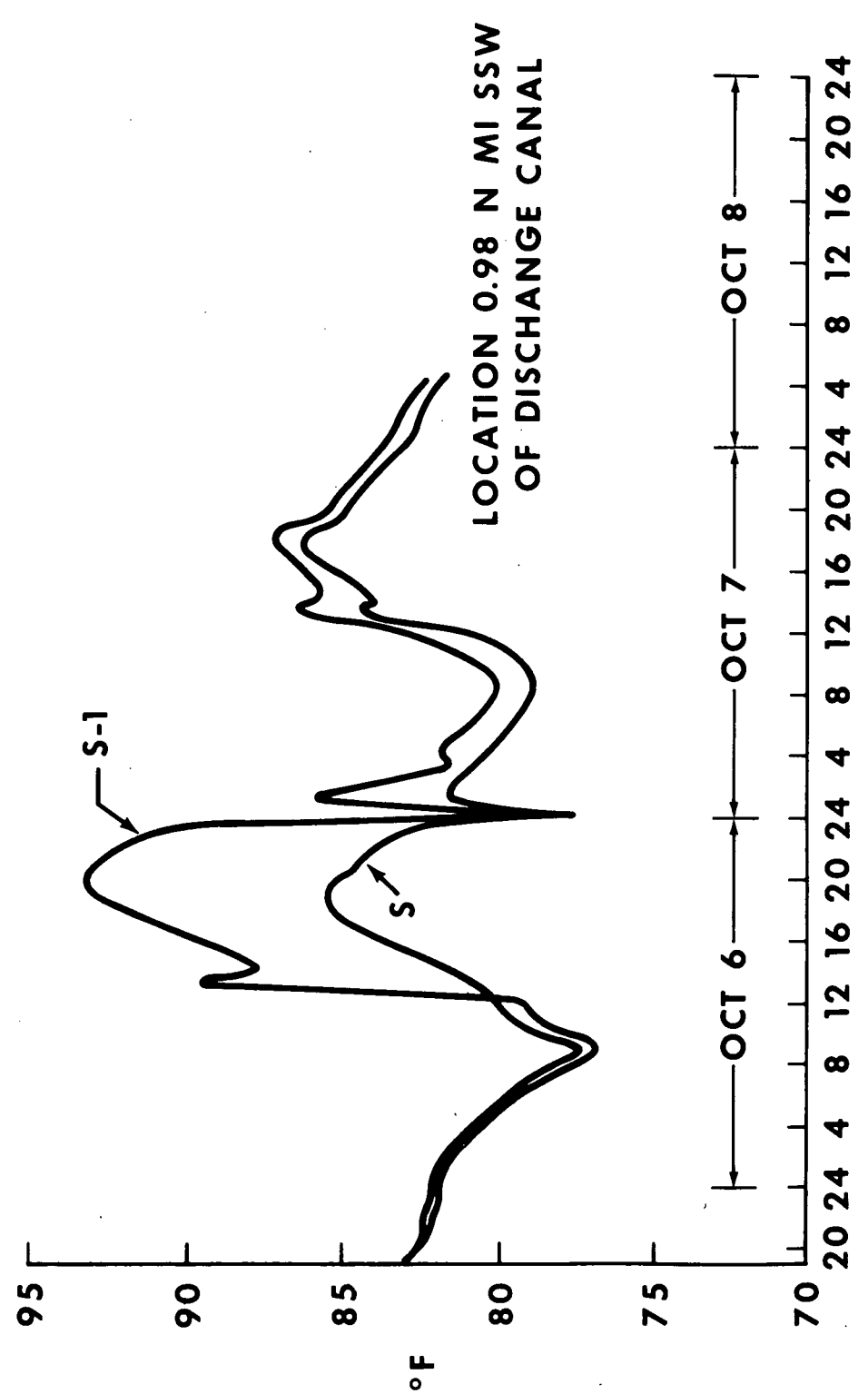

NASA-S-72-423-S

Figure 11.- Trinity Bay Buoy Number 4 Temperature Recorded for October 6-7, 1971. (S, surface record, S-1, one foot below surface record)

☆ U. S. GOVERNMENT PRINTING OFFICE: 1972—770-624